The 4th International Symposium on

One Health, One World

2025 HOW

Proceedings

November 20-22, 2025
CSIR CBRI, Roorkee, India

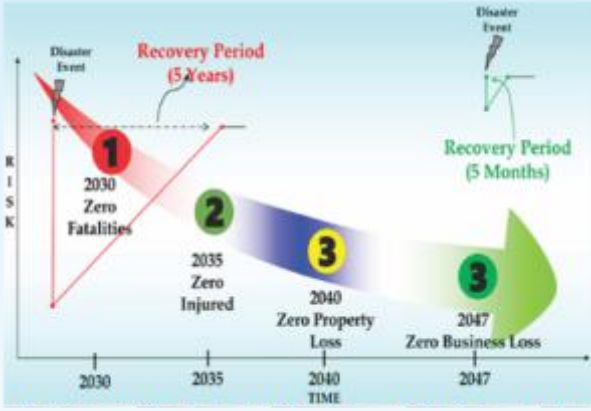

[IIS UTokyo SYMPOSIUM No.130]

Urban Safety | Disaster Mitigation | Infrastructure Management | Sustainable Built Environment | Climate Change | Green Recovery | Public Health

Organized by

CSIR Central Building Research Institute
Roorkee, India

OneHealth OneWorld

One Health One World Research Initiative
Institute of Industrial Science, Tokyo, Japan

Published by:

CSIR-Central Building Research Institute, Roorkee, INDIA

First Edition: 2025
ISBN

Content

ACKNOWLEDGEMENT

The Organising Committee of OHOW2025: The 4th International Symposium on Climate Change & Green Recovery, Urban Safety & Disaster Mitigation, Infrastructure Management, and Public Health Research in Asia, jointly organised by CSIR Central Building Research Institute (CBRI), Roorkee, and The University of Tokyo, Japan, extends its heartfelt gratitude to all those who have contributed to the successful organization of this international event and to the publication of this Souvenir Volume.

We express our deep appreciation to Dr. N. Kalaiselvi, Director General, CSIR & Secretary, DSIR, for her constant guidance, encouragement, and visionary leadership that continue to inspire scientific pursuits across the CSIR network. Our sincere thanks are due to Prof. R. Pradeep Kumar, Director, CSIR–CBRI, Roorkee, for his motivation, insightful leadership, and wholehearted support in conceptualizing and hosting this global symposium at Roorkee.

We gratefully acknowledge the distinguished collaboration of the University of Tokyo, Japan, and the invaluable contributions of our eminent partners, distinguished speakers, keynote speakers, bright spark speakers, delegates, and experts from India and abroad for enriching this conference with their ideas and experience. Special thanks are due to our international collaborators from Japan, Taiwan, New Zealand, Thailand, Nepal, Portugal, Malesia, Bangkok and other countries for strengthening the spirit of global cooperation in science and technology.

The Organising Committee records its appreciation for the dedicated efforts of the Advisory Committee, Technical Committee, Session Chairs, Reviewers, and all contributors of research papers, posters, and exhibits that have added exceptional value to the academic content of OHOW2025.

We also extend warm thanks to all members of the Publication Committee for their meticulous effort in compiling and designing this Souvenir Volume, and to the Secretariat and Support Teams for their tireless coordination in ensuring smooth conduct of the symposium.

Finally, we express our gratitude to all participants, sponsors, and well-wishers whose enthusiasm and cooperation have made OHOW2025. OHOW2025 will bring together leading researchers, engineers, academicians, practitioners, and policymakers from across the world to share insights, innovations, and experiences in the domains. The event will serve as a pulsating platform for scientific exchange, cross-sectoral collaboration, and advancement of sustainable and resilient development practices.

Nestled in the foothills of the Himalayas, **Roorkee** a historic and academic hub of India offers a unique setting combining heritage, natural beauty, and intellectual vibrancy. With its legacy in engineering and research excellence, Roorkee provides the perfect backdrop for deliberations on advancing knowledge and technology towards a safer, greener, and more sustainable future.

We are confident that participation in **OHOW2025** will be a **scientifically stimulating**, **professionally enriching, and personally memorable** experience. We look forward to warmly welcoming you to Roorkee, India!

Organising Committee
OHOW2025
CSIR Central Building Research Institute
Roorkee, India

डॉ० जितेन्द्र सिंह
राज्य मंत्री (स्वतंत्र प्रभार),
विज्ञान एवं प्रौद्योगिकी मंत्रालय;
राज्य मंत्री (स्वतंत्र प्रभार) पृथ्वी विज्ञान मंत्रालय;
राज्य मंत्री, प्रधान मंत्री कार्यालय;
राज्य मंत्री कार्मिक, लोक शिकायत एवं पेंशन मंत्रालय;
राज्य मंत्री परमाणु ऊर्जा विभाग तथा
राज्य मंत्री अंतरिक्ष विभाग
भारत सरकार

सत्यमेव जयते

Dr. JITENDRA SINGH
Minister of State (Independent Charge)
of the Ministry of Science and Technology;
Minister of State (Independent Charge)
of the Ministry of Earth Sciences;
Minister of State in the Prime Minister's Office;
Minister of State in the Ministry of Personnel,
Public Grievances and Pensions;
Minister of State in the Department of Atomic Energy and
Minister of State in the Department of Space
Government of India

MESSAGE

It gives me great pleasure to extend my greetings to all participants of the 4th International Symposium on "One Health, One World" (OHOW 2025), being hosted by the CSIR–Central Building Research Institute (CSIR–CBRI), Roorkee, from 20th to 22nd November 2025. The theme "One Health, One World" embodies a vision of collective well-being that unites human health, environmental balance, and sustainable development—an approach that lies at the heart of India's science-led progress towards Viksit Bharat @2047.

CSIR–CBRI has consistently demonstrated excellence in advancing research and innovation for resilient and sustainable infrastructure, disaster risk reduction, and environmental protection. By convening global experts, scientists, and policymakers through this Symposium, CBRI is reinforcing its leadership as a premier national institute committed to translating scientific knowledge into solutions that enhance safety, sustainability, and quality of life.

I am confident that the deliberations and outcomes of OHOW 2025 will inspire new collaborations, strengthen scientific preparedness, and contribute significantly to global efforts in achieving a healthier and more resilient world. I extend my best wishes to CSIR–CBRI for the grand success of this important initiative and for its continued pursuit of excellence in science and innovation for national development.

(Dr. Jitendra Singh)
MBBS (Stanley, Chennai)
MD Medicine, Fellowship Diabetes (AIIMS, New Delhi)
MNAMS Diabetes & Endocrinology
FICP (Fellow, Indian College of Physicians)

Anusandhan Bhawan, 2, Rafi Marg
New Delhi-110001
Tel. : 011-23316766, 23714230,
Fax : 011-23316745

Prithvi Bhawan, Lodhi Road,
Opp. India Habitate Centre,
New Delhi-110003
Tel. : 011-24629788, 24629789

South Block, New Delhi-110011
Tel. : 011-23010191 Fax : 011-23017931
North Block, New Delhi-110001
Tel. : 011-23092475 Fax : 011-23092716

सत्यमेव जयते

डॉ. (श्रीमती) एन. कलैसेल्वी
सचिव, वैज्ञानिक और औद्योगिक अनुसंधान विभाग
महानिदेशक, वैज्ञानिक तथा औद्योगिक अनुसंधान परिषद्
Dr. (Mrs.) N. Kalaiselvi
Secretary, DSIR and Director General, CSIR

भारत सरकार
विज्ञान एवं प्रौद्योगिकी मंत्रालय
वैज्ञानिक और औद्योगिक अनुसंधान विभाग
वैज्ञानिक तथा औद्योगिक अनुसंधान परिषद्
Government of India
Ministry of Science and Technology
Department of Scientific & Industrial Research
Council of Scientific & Industrial Research

MESSAGE

It gives me immense pleasure to convey my warm greetings to all participants of the *4th International Symposium on "One Health, One World" (OHOW 2025)* being organized by the CSIR–Central Building Research Institute, Roorkee, from 20th to 22nd November 2025. The theme, *"One Health, One World,"* is both timely and visionary, emphasizing the indivisible link between human health, environmental integrity, and sustainable development.

In an era marked by accelerating climate change, biodiversity loss, urban challenges, and public health crises, the One Health approach offers a transformative framework for integrated and science-driven solutions. It resonates deeply with CSIR's enduring commitment to deploy science, technology, and innovation for addressing complex and interconnected challenges that shape the nation's security, well-being, and resilience.

The Council of Scientific and Industrial Research, with its expansive network of laboratories across diverse domains—ranging from biotechnology and environmental sciences to infrastructure, materials, and climate adaptation—continues to advance mission-oriented R&D for societal benefit. The OHOW platform provides a vital opportunity to synergize these efforts, bridging scientific discovery with sustainable policy, disaster preparedness, and resilient infrastructure development.

I am confident that the deliberations of this Symposium will generate valuable insights to guide future research directions, foster inter-laboratory and international collaboration, and strengthen the translation of knowledge into practical solutions for health security, sustainability, and inclusive growth.

I congratulate CSIR–CBRI for this timely initiative and extend my best wishes for the grand success of OHOW 2025. May the Symposium serve as a catalyst for global partnerships and transformative innovations that truly embody the spirit of *One Health, One World.*

November 7, 2025
New Delhi

N. Kalaiselvi
(N. Kalaiselvi)

Prof. Kimiro Meguro
Dean, Professor,
Interfaculty Initiative in Information Studies/
Graduate School of Interdisciplinary Information Studies,
The University of Tokyo, Hongo, Japan

Professor, Industrial Institute of Sciences
The University of Tokyo, Komaba, Japan

Message

It is my great pleasure to extend heartfelt greetings to all participants of the *4th International Symposium on "One Health, One World" (OHOW 2025)*, being hosted by the *CSIR–Central Building Research Institute (CBRI), Roorkee, India*, from 20th to 22nd November 2025. The theme *"One Health, One World"* is both timely and profound, reflecting the growing realization that human well-being, environmental balance, and resilient infrastructure are inseparably linked and must be addressed through collective global action.

In today's interconnected world, challenges such as climate change, pandemics, rapid urbanization, and natural disasters transcend borders and disciplines. They call for integrated scientific approaches and sustained international partnerships. OHOW 2025 serves as a valuable platform for scientists, engineers, public health experts, and policymakers to exchange ideas and collaborate toward solutions that enhance community resilience and sustainability.

I deeply appreciate the initiative and leadership of *CSIR–CBRI* in organizing this significant global forum. The Institute's long-standing commitment to advancing disaster-resilient construction, sustainable habitats, and multidisciplinary research is commendable. Through its dedicated efforts under visionary leadership, CBRI has strengthened India's and the world's capacity to face emerging risks with scientific wisdom and practical innovation.

I am confident that *OHOW 2025* will foster enduring research collaborations, stimulate innovative thinking, and contribute meaningfully to the shared global mission of achieving safer, healthier, and more sustainable societies. I extend my best wishes to *CSIR–CBRI*, the organizing committee, and all participants for a highly successful and impactful Symposium.

(Prof. Kimiro Meguro)

Dr. Wataru Takeuchi
OHOW2025 Co-chair
Director, One Health One World research initiative, The University of Tokyo, Japan
Professor Institute of Industrial Science, The University of Tokyo, Japan

Message

The foundational concepts of OHOW—the interconnectedness of all life and the environment—gain increasing urgency as we face complex global challenges. This year marks 10 years since the devastating 2015 Nepal Earthquake, and the stark reality of natural disasters was brought home again with the 2025 Myanmar Earthquake. These events serve as powerful reminders of the need for robust, integrated approaches to infrastructure, resilience, and global cooperation.

We are delighted to announce that the 4th OHOW symposium will be held in Roorkee, India in 2025, following successful symposia in Bangkok, Thailand (2022), Dhaka, Bangladesh (2023), and Putrajaya, Malaysia (2024).

The OHOW symposium will include topics such as climate change and green recovery, international public health research in Asia, infrastructure management and sustainable built environment, and urban safety & disaster mitigation. These themes directly address the resilience needed in a world prone to both infectious diseases and natural catastrophes.

Beyond the academic program, we have curated networking opportunities, social events, and cultural experiences that will provide a platform for meaningful interactions, collaborations, and the forging of lifelong connections. We encourage all participants to take full advantage of these moments, as they often lead to serendipitous encounters and spark innovative ideas that transcend disciplinary boundaries.

We look forward to welcoming you to OHOW2025 in Roorkee, India, where we will collectively advance the mission of a healthier, safer world.

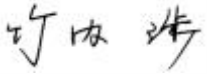

Dr. Wataru Takeuchi
OHOW2025 Co-chair
Director, One Health One World research initiative, The University of Tokyo, Japan
Professor Institute of Industrial Science, The University of Tokyo, Japan

प्रो. आर. प्रदीप कुमार
निदेशक
Prof. R. Pradeep Kumar
Director

सीएसआईआर–केन्द्रीय भवन अनुसंधान संस्थान
रुड़की – 247 667 (भारत)
CSIR-Central Building Research Institute
(A Constituent Establishment of CSIR)
ROORKEE - 247 667 (INDIA)

MESSAGE

It is a moment of immense pride and joy for *CSIR–Central Building Research Institute (CBRI), Roorkee* to host the *4th International Symposium on "One Health, One World" (OHOW 2025)* from 20th to 22nd November 2025. The theme, *"One Health, One World,"* beautifully captures the spirit of interconnectedness between human well-being, environmental balance, and sustainable living — values that lie at the heart of CBRI's research philosophy and institutional vision.

Over the years, CBRI has steadfastly advanced science and technology for the creation of safe, sustainable, and disaster-resilient habitats. The Institute's multidisciplinary research — spanning structural safety, sustainable construction materials, energy-efficient and healthy buildings, and disaster risk mitigation — reflects a deep commitment to serving society through innovation and excellence. OHOW 2025 provides a wonderful opportunity to showcase these endeavours and to engage with a distinguished global community of experts, researchers, and practitioners united by a shared purpose.

I take this opportunity to convey my heartfelt appreciation to all collaborators, contributors, and participants for their enthusiastic involvement and to the organizing team for their dedication in making this event a reality. I am confident that the deliberations of *OHOW 2025* will inspire meaningful discussions, enduring partnerships, and transformative ideas that will further the cause of a safer, healthier, and more sustainable world.

November 11, 2025
Roorkee

(R. Pradeep Kumar)

Tel : (+91) 1332 272243 (O), 272660 (R)
Website : www.cbri.res.in
Fax : (+91) 1332 272272
E-mail : director@cbri.res.in

About Organizer

CSIR Central Building Research Institute

(CSIR CBRI), Roorkee India

Website :- https://cbri.res.in/the-institute/about-institute/
Social Media : - Facebook

Established in 1947, the CSIR-Central Building Research Institute (CSIR CBRI), Roorkee, is India's premier research institute dedicated to building science, sustainable construction, and disaster-resilient infrastructure. Operating under the Council of Scientific and Industrial Research (CSIR), the institute plays a crucial role in advancing climate-responsive construction, structural safety, and smart urban planning.

CSIR CBRI focuses on key areas such as disaster-resilient structures, energy-efficient buildings, and sustainable materials, with innovative technologies like 3D Concrete Printing and Precast Prefinished Volumetric Construction (PPVC) revolutionizing modern housing solutions. The institute is also at the forefront of structural health monitoring, seismic risk assessment, and post-disaster rehabilitation. CSIR CBRI continues to drive innovation in smart cities, modular construction, and eco-friendly urban development, ensuring a safe, sustainable, and resilient built environment for the future.

One Health One World Research Initiative Secretariat

CSIR Central Building Research Institute

(CSIR CBRI), Roorkee India

The University of Tokyo
Website : - https://ohow.iis.u-tokyo.ac.jp/intro

The One Health and One World Collaborative Research Organization was established in 2021 at the University of Tokyo and has been operating a new academic research base for comprehensive science on common infectious diseases and health between humans and animals.

There is growing international recognition of the declaration, which argues that separate research by medical, veterinary, and environmental sciences is insufficient to deal with the risks of emerging infectious diseases that may occur in the future. Research institutes and faculties have been established at universities, and international joint research with African countries and other countries has been promoted.

About The Institute of Industrial Science, The University of Tokyo

Institute of Industrial Science, The University of Tokyo.

4-6-1 Komaba Meguro-Ku, Tokyo 153-8505, Japan

東京大学
生産技術研究所
Institute of Industrial Science,
The University of Tokyo

The University of Tokyo

Website : - https://www.iis.u-tokyo.ac.jp/en//
Social Media : - Facebook, Twitter, YouTube

The Institute of Industrial Science (IIS), The University of Tokyo, is a leading research institute dedicated to advancing science and technology across various engineering disciplines. Established in 1949, IIS has played a crucial role in pioneering cutting-edge research in fields such as robotics, artificial intelligence, materials science, and sustainable energy. With a strong emphasis on interdisciplinary collaboration, the institute fosters innovation by bringing together experts from different domains to tackle real-world challenges. IIS is home to numerous state-of-the-art laboratories and facilities, providing researchers with an ideal environment to conduct experimental and theoretical studies.

As part of The University of Tokyo, IIS maintains strong ties with both academia and industry, facilitating technology transfer and industry-academic partnerships. The institute collaborates with domestic and international organizations, contributing to the development of next-generation technologies that have practical applications in society. IIS also offers graduate education programs, nurturing the next generation of engineers and scientists through research-based learning. With a commitment to sustainability and social impact, the institute continues to push the boundaries of scientific knowledge, reinforcing its position as a global leader in industrial and engineering research.

About the Event

Recognizing the critical importance of urban safety and environmental management in today's rapidly urbanizing world, the Institute of **Industrial Science (IIS), University of Tokyo, and the Regional Network Office for Urban Safety (RNUS), Asian Institute of Technology (AIT)** have been jointly organizing the International Symposium on New Technologies for Urban Safety of Mega Cities in Asia (USMCA) since 2002. This annual event, hosted across various Asian cities, has become a prominent platform for experts, researchers, policymakers, and practitioners to exchange knowledge and ideas on innovative solutions for **urban safety, environmental sustainability, and resilience in the face of growing urban** challenges.

The recent **COVID-19 pandemic**, along with ongoing global issues such as **species loss, habitat degradation, pollution, invasive alien species,** and **climate change**, has highlighted the intricate interconnections between human activities, the natural world, and urban environments. These phenomena are fundamentally reshaping our way of life — from relatively untouched ecosystems to the densest and most complex urban habitats in human history. Addressing these transformations requires an integrated **approach** that not only mitigates immediate urban concerns but also ensures long-term **health, safety, and environmental sustainability**.

The concept of **"One Health, One World (OHOW)",** first articulated in the Manhattan Principles (2004), provides a comprehensive framework for understanding and addressing the interconnectedness of **human, animal, and environmental health**, alongside **urban safety and sustainable environmental management**. This holistic approach emphasizes that human well-being is inseparable from the health of ecosystems and the broader environment — a realization that is increasingly vital for managing challenges in urban settings where human and environmental systems closely interact.

The **4th International Symposium on One Health, One World (OHOW 2025),** jointly organized by the **One Health One World Research Initiative** and the **University of Tokyo, Japan**, in collaboration with the Council of **Scientific & Industrial Research – Central Building Research Institute (CSIR-CBRI), India**, aims to build upon insights from previous symposiums. The 2025 edition will delve deeper into key global challenges with a special focus on the following thematic areas:

- **Climate Change and Green Recovery** As cities face the escalating threat of climate change, adopting sustainable and adaptive approaches to urban development is imperative. This session will explore innovative solutions for **climate resilience, green recovery, and sustainable urban planning**, with an emphasis on protecting vulnerable urban populations.

- **International Public Health Research in Asia** Rapid urbanization across Asia has intensified public health challenges, including the spread of **zoonotic diseases, environmental pollution**, and the demand for resilient **health infrastructure**. This theme will highlight how international research collaborations can inform policy, guide interventions, and strengthen public health systems.

- **Infrastructure Management and Sustainable Built Environments** Robust and sustainable infrastructure systems are essential for ensuring urban safety and quality of life. This session will focus on sustainable infrastructure management, energy-efficient buildings, and eco-friendly urban design that contribute to the creation of safer and more resilient cities.

- **Urban Safety and Disaster Mitigation** With cities becoming increasingly dense and complex, the risks posed by **natural and human-induced disasters** have grown. This session will present strategies for improving **urban safety**, enhancing **disaster preparedness**, and implementing **risk reduction measures** to safeguard urban populations from earthquakes, floods, pandemics, and other emergencies.

The symposium will feature **state-of-the-art presentations, keynote lectures**, and **interactive sessions** led by eminent personalities from academia, research, and industry, offering valuable opportunities for knowledge sharing and collaboration.

Highlights of OHOW 2025 include:

- Participation of **over 200 delegates** from academia, research, industry, and professional sectors across the country.
- Presentation of **over 150 research papers** (oral and poster sessions), spanning from fundamental studies to field applications, covering diverse aspects of infrastructure in the Indian context.
- Publication of selected papers in **Springer Proceedings**, indexed in **Scopus**.
- **Industry-focused lectures** showcasing practical applications and aligning with **Government of India's National Missions** to bridge R&D and real-world implementation.
- **Technology exhibition and live demonstrations** of construction-related innovations, providing participants with hands-on exposure to current trends in engineering and sustainable technologies.

OHOW 2025 cordially invites researchers, practitioners, policymakers, and thought leaders to participate and contribute their work. Submissions should align with the symposium's themes, presenting **fresh perspectives, innovative methodologies**, and **practical insights** that advance the field of **structural and urban resilience engineering.**

Mark your calendars and **save the date** for this landmark event! Stay tuned for details on registration, speakers, and program highlights.

We look forward to welcoming you to **"One Health One World 2025"** — a global platform dedicated to discovery, collaboration, and transformation toward a **resilient, sustainable, and equitable built environment**. Together, we aim to lay the foundation for a future where **infrastructure serves as a catalyst for societal progress, economic prosperity, and environmental stewardship.**

COMMITTEE

Patron

Dr. N. Kalaiselvi
Director General
CSIR & Secretary DSIR, New Delhi

Conference Chair

Professor Wataru Takeuchi
Institute of Industrial Science
The University of Tokyo, Japan

Conference Chair

Professor R Pradeep Kumar
Director
CSIR-CBRI, Roorkee, India

Organising Secretary

Dr. Ajay Chourasia
Chief Scientist
CSIR-CBRI Roorkee, India

ADVISORY COMMITTEE

Prof. Kimiro Meguro	Professor,The University of Tokyo, Japan
Prof. Miho Ohara	Professor,The University of Tokyo, Japan
Prof. Masahiro Hashizume	Professor, The University of Tokyo, Japan
Prof. Pennung Warnitchai	Asian Institute of Technology, Thailand
Shri Krishna S. Vatsa	Member, NDMA, New Delhi
Prof. Mahesh Tandon	Chairman, Tandon Consultants Pvt Ltd
Prof. C. V. R Murty	Professor, IIT Madras
Prof Ravi Sinha	Professor, IIT Bombay
Dr. Rupen Goswami	Professor, IIT Madras
Prof STG Raghuknath	Professor, IIT Madras
Prof. Kamal Kishore Pant	Director, IIT Roorkee
Dr. N. Anandavalli	Director, CSIR-SERC
Dr. Virendra M. Tiwari	Director, CSIR-NEIST
Prof. Manoranjan Parida	Director, CSIR-CRRI
Dr. Avanish Kumar Srivastava	Director, CSIR-AMPRI
Dr. Yogendra Singh	Professor, IIT Roorkee
Dr. KVL Subramaniam	Professor, IIT Hyderabad
Prof. Suresh Bhalla	Professor, IIT Delhi
Dr. Shailesh Agrawal	Executive Director, BMTPC, MoHUA, New Delhi
Dr. P. K Das	Sr. Rural Housing Advisor UNDP, Noida

TECHNICAL COORDINATION COMMITTEE

Er. Ashish Kapoor	Scientist, CSIR-CBRI, Roorkee
Dr. Chandan Swaroop Meena	Principal Scientist, CSIR-CBRI, Roorkee
Er. Kanti Lal Solanki	Principal Scientist, CSIR-CBRI, Roorkee
Dr. Bharat Singh Chauhan	Senior Scientist, CSIR-CBRI, Roorkee
Mr. Chandrabhan Patel	Scientist, CSIR-CBRI, Roorkee
Dr. Chanchal Sonkar	Principal Scientist, CSIR-CBRI, Roorkee
Dr. Biswajit Pal	Scientist, CSIR-CBRI, Roorkee
Dr. Kishore S kulkarni	Principal Scientist, CSIR-CBRI, Roorkee
Dr. Tabish Alam	Senior Scientist, CSIR-CBRI, Roorkee
Mr. Amit Kush	Senior Technical Officer, CSIR-CBRI, Roorkee
Mr. Jalaj Parashar	Principal Technical Officer, CSIR-CBRI, Roorkee
Mr. Sameer	Senior Technical Officer, CSIR-CBRI, Roorkee
Mohd Jeeshan Khan	Senior Scientist, CSIR-CBRI, Roorkee

PRE WORKSHOP COMMITTEE

Dr. R. Siva Chidambaram	Principal Scientist, CSIR-CBRI, Roorkee
Er. Ashish Kapoor	Scientist, CSIR-CBRI, Roorkee
Dr. H.C Arora	Senior Principal Scientist, CSIR-CBRI, Roorkee
Dr. Debdutta Gosh	Principal Scientist, CSIR-CBRI, Roorkee
Dr. Bharat Singh Chauhan	Senior Scientist, CSIR-CBRI, Roorkee
Dr. Hina Gupta	Senior Scientist, CSIR-CBRI, Roorkee
Dr. Anindya Pain	Principal Scientist, CSIR-CBRI, Roorkee
Mr. Anup Kumar Prasad	Scientist, CSIR-CBRI, Roorkee
Dr. Biswajit Pal	Scientist, CSIR-CBRI, Roorkee
Er. M.M Dalbehera	Principal Scientist, CSIR-CBRI, Roorkee
Mr. B.K Kalra Senior	Technical Officer, CSIR-CBRI, Roorkee
Mr. Himanshu Sharma	Senior Technical Officer, CSIR-CBRI, Roorkee

PRINTING, STATIONERY AND CONFERENCE KIT COMMITTEE

Mr. Anup Kumar Prasad	Scientist, CSIR-CBRI, Roorkee
Dr. Veena Chaudhary	Scientist, CSIR-CBRI, Roorkee
Mr. Bharat Bhushan	Store and Purchase Officer, CSIR-CBRI, Roorkee
Dr. Chandan Swaroop Meena	Principal Scientist, CSIR-CBRI, Roorkee
Er. Ashish Pippal	Principal Scientist, CSIR-CBRI, Roorkee
Dr. Biswajit Pal	Scientist, CSIR-CBRI, Roorkee
Dr. Rajesh Kumar	Principal Scientist, CSIR-CBRI, Roorkee
Mr. Shyam Lal	Section Officer, CSIR-CBRI, Roorkee

FOOD & CATERING COMMITTEE

Dr. R.K. Verma	Senior Principal Scientist, CSIR-CBRI, Roorkee
Mr. Shyam Lal	Section Officer, CSIR-CBRI, Roorkee
Mr. Aman Kumar	Section Officer, CSIR-CBRI, Roorkee
Er. Ashish Pippal	Principal Scientist, CSIR-CBRI, Roorkee
Dr. Soumitra Maiti	Principal Scientist, CSIR-CBRI, Roorkee
Mr. Himanshu Sharma	Senior Technical Officer, CSIR-CBRI, Roorkee
Dr. Humaira Athar	Scientist, CSIR-CBRI, Roorkee
Mr. Ajay Dwivedi	Senior Technical Officer, CSIR-CBRI, Roorkee
Ms. Gayatri Devi	Senior Technical Officer, CSIR-CBRI, Roorkee

RECEPTION AND REGISTRATION COMMITTEE

Dr. Leena Chourasia	Senior Principal Scientist, CSIR-CBRI, Roorkee
Dr. Anindya Pain	Principal Scientist, CSIR-CBRI, Roorkee
Mr. Dinesh	Assistant Section Officer, CSIR-CBRI, Roorkee
Mr. Rahul	Assistant Section Officer, CSIR-CBRI, Roorkee
Ms. Hemlata	Senior Scientist, CSIR-CBRI, Roorkee
Mrs. Shaina	Senior Project Associate, CSIR-CBRI, Roorkee
Ms. Kavitasree	Senior PAT, CSIR-CBRI, Roorkee
Ms. Reetika Bisht	Admin. Staff, CSIR-CBRI, Roorkee
Ms. Ikra	Project Staff, CSIR-CBRI, Roorkee

CULTURAL PROGRAMME COMMITTEE

Mr. Arpan Maheshwari	Section Officer, CSIR-CBRI, Roorkee
Mr. Aman kumar	Section Officer, CSIR-CBRI, Roorkee
Mr. Anup Kumar Prasad	Scientist, CSIR-CBRI, Roorkee

DECORATION, LIGHTING, STAGE AND STALL MANAGEMENT COMMITTEE

Dr. Neeraj Jain	Senior Principal Scientist, CSIR-CBRI, Roorkee
Dr. Rajender	Technical Assistant, CSIR-CBRI, Roorkee
Sh. Rajneesh	Project Staff, CSIR-CBRI, Roorkee
Ms. Sanskriti	Project Staff, CSIR-CBRI, Roorkee
Dr. Tabish Alam	Senior Scientist, CSIR-CBRI, Roorkee
Mr. Naveen Nishant	Scientist, CSIR-CBRI, Roorkee

OFFICE SECRETARIAT COMMITTEE

Dr. Ajay Chourasia	Chief Scientist, CSIR-CBRI, Roorkee
Mrs. Shaina	Senior Project Associate, CSIR-CBRI, Roorkee
Ms. Kavitasree	Senior PAT, CSIR-CBRI, Roorkee
Mr. Sonu Pindwal	Project Staff, CSIR-CBRI, Roorkee
Mr. Manish Kumar Yadav	Project Staff, CSIR-CBRI, Roorkee
Ms. Sonali kohli	Project Staff, CSIR-CBRI, Roorkee
Mr. Govind	Project Staff, CSIR-CBRI, Roorkee
Ms. Reetika Bisht	Admin. Staff, CSIR-CBRI, Roorkee
Mr. Lakshay	Admin. Staff, CSIR-CBRI, Roorkee
Mr. Amaan Ullah	Admin. Staff, CSIR-CBRI, Roorkee

ONE TO ONE CONNECT COMMITTEE

Dr. Debi Prasanna Kanungo	Chief Scientist, CSIR-CBRI, Roorkee
Dr. Rajesh Kumar Das	Project Scientist, CSIR-CBRI, Roorkee
Mrs. Shaina	Senior Project Associate, CSIR-CBRI, Roorkee
Ms. Jyoti Yadav	PHD Student, CSIR CBRI, Roorkee
Mr. Shubham Chaudhary	PHD Student, CSIR CBRI, Roorkee
Ms. Prachi Chandna	PHD Student, CSIR CBRI, Roorkee
Mr. Nagesh Pratap Singh	PHD Student, CSIR CBRI, Roorkee
Mr. Amith K.S.	PHD Student, CSIR CBRI, Roorkee
Ms Shivani Devlal	Project Associate I, CSIR CBRI, Roorkee
Mrs. Monica Joseph	Senior PAT, CSIR CBRI, Roorkee
Dr. Pankaj Kundu	Project Scietinst, CSIR CBRI, Roorkee
Dr. Mugesh A	Project Scietinst, CSIR CBRI, Roorkee
Ms. Parul	Project Assistant II, CSIR CBRI, Roorkee
Mr. Dhirendra Kumar Kori	Project Associate, CSIR CBRI, Roorkee
Mr. Suraj Kumar	Project Associate, CSIR CBRI, Roorkee
Ms. Surbhi Choudhary	PAT I, CSIR CBRI, Roorkee
Mr. Akash	Project Associate, CSIR CBRI, Roorkee
Ms. Vaishnavi Agarwal	PAT-II, CSIR CBRI, Roorkee
Mr. Md Nafees Khan	Project Associate, CSIR CBRI, Roorkee
Ms. Rajashree Pati	PHD Student, CSIR CBRI, Roorkee
Mr. Virat Singh Chauhan	Senior PAT, CSIR CBRI, Roorkee
Mr. Sarath Rajeev	PA II, CSIR CBRI, Roorkee

OneHealth OneWorld

東京大学 生産技術研究所
Institute of Industrial Science, The University of Tokyo

CBRI

2025 HOW

PRE-CONFERENCE WORKSHOP

OHOW 2025

18, 19 NOVEMBER

Venue: CSIR CBRI, Roorkee, India

ENTER TO WIN PRIZES

EVENTS

1. One World, Many Hazards Workshop

(November 18, 2025)

- Presentation (On Spot)
- Panel Discussion

2. Student Competitions (November 19, 2025)

- Seismic Resistance Building Competition (Shake Table Test)
- Bridge Building Competition (Load Test)

Note: Max 4 Participants in a Team

Registration Fees: ₹1000 INR

To be paid at the venue

Email: ohowpcw@gmail.com
Contact: +91-01332 283387

For more details:
https://www.ohow2025.com

Scan To Register

https://forms.gle/3xZMryqYpPs4E7ya8

PRE-CONFERENCE WORKSHOP

ONE WORLD, MANY HAZARDS:

ARE WE READY FOR THE NEXT PANDEMIC?

LESSONS LEARNED

- COVID-19
- SARS
- EBOLA
- MISINFORMATTION
- OVERWHELMED SYSTEMS

ONE HEALTH

OUR TOOLKIT FOR THE FUTURE

- SURVEILLANCE
- GLOBAL SOLIDARITY
- RESEARCH
- ONE HEALTH APPROACH
- STRONGER POLICIES

ON SPOT PRESENTATION

4 Membersmaxperteam **Theme will be announced at the venue**

ohow2025@gmail.com

+91 01332 283387

for more details visit
www.ohow2025.in

18th NOVEMBER 2025

462629/2025/ABCD-CSIR-CBRI

OneHealth OneWorld

東京大学 生産技術研究所
Institute of Industrial Science, The University of Tokyo

CBRI

OHOW 2025

The 4th International Symposium on

One Health, One World

PRE CONFERENCE

Students Competition

CSIR CBRI, ROORKEE, INDIA

Seismic Resistant Building Competition (Shake Table Test)

Bridge Building Competition (Load test)

- **4 Members max per team**
- **Materials will be provided at the venue**

ohow2025@gmail.com

+ 91 01332 283387

for more details visit
www.ohow2025.in

19th NOVEMBER 2025

DISTINGUISHED SPEAKERS

Prof. Kimiro Meguro
Professor, Institute of Industrial Science, The University of Tokyo, Japan

Dr. Krishna S. Vatsa
Member, National Disaster Management Authority
New Delhi, India

Prof. Kimiro Meguro
Professor, Institute of Industrial Science, The University of Tokyo, Japan

Dr. Krishna S. Vatsa
Member, National Disaster Management Authority
New Delhi, India

Programme

OHOW 2025 Program At A Glance

DAY 1: Thursday, November 20, 2025

Venue: Hotel Clarks Safari, New Bahadarabad Bypass, Haridwar, Uttarakhand, India

Duration	Programme		
08:00 AM - 06:00 PM	**REGISTRATION – cum – HELP DESK** *Venue: Hotel Clarks Safari, New Bahadarabad Bypass, Haridwar, Uttarakhand, India*		
09:00 AM - 10:00 AM	**OPENING CEREMONY**		
10:00 AM - 6:00 PM	**EXHIBITION**		
10:00 AM - 10:30 AM	**HIGH TEA**		
10:30 AM - 12:00 PM	**DISTINGUISHED LECTURES** ○ **Prof. Kimiro Meguro**, Professor, Institute of Industrial Science, The University of Tokyo, Japan ○ **Shri Krishna S. Vatsa**, Member, National Disaster Management Authority (NDMA), New Delhi, India ○ **Dr. Juin-Fu Chai**, Deputy DG, NCREE, National Institutes of Applied Research, Taipei, Taiwan, ROC		
12:00 PM - 01:30 PM	**PARALLEL SESSIONS**		
	SURYA HALL	Urban Safety & Disaster Mitigation (USDM)	USDM-OP-01 to USDM-OP-10
	VAYU HALL	Infrastructure Management and Sustainable Built Environments (IMSBE)	IMSBE-OP-01 to IMSBE-OP-10
	JAL HALL	International Public Health Research in Asia (IPHAR)	IPHRA-OP-01 to IPHRA-OP-10
	PRITHVI HALL	Climate Change and Green Recovery (CCGR)	CCGR-OP-01 to CCGR-OP-10
01:30 PM - 02:30 PM	**LUNCH**		
02:30 PM - 04:00 PM	**PARALLEL SESSIONS**		
	SURYA HALL	Urban Safety and Disaster Mitigation	USDM-OP-17 to USDM-OP-25
	VAYU HALL	Infrastructure Management and Sustainable Built Environments	IMSBE-OP-11 to IMSBE-OP-20
	JAL HALL	International Public Health Research in Asia	IPHRA-OP-11 to IPHRA-OP-14
		Urban Safety and Disaster Mitigation	USDM-OP-11 to USDM-OP-16
	PRITHVI HALL	Climate Change and Green Recovery	CCGR-OP-11 to CCGR-OP-14
		Infrastructure Management and Sustainable Built Environments	IMSBE-OP-21 to IMSBE-OP-25

02:30 PM - 04:30 PM	**E - POSTER *Venue: Agni Sthal***		
	Screen-I	Climate Change and Green Recovery	CCGR-EP-01 to CCGR-EP-07
		Infrastructure Management and Sustainable Built Environments	IMSBE-EP-01 to IMSBE-EP-12
	Screen-II	Infrastructure Management and Sustainable Built Environments	IMSBE-EP-13 to IMSBE-EP-17
	Screen-III	International Public Health Research in Asia	IPHRA-EP-01 to IPHRA-EP-07
		Urban Safety and Disaster Mitigation	USDM-EP-01 to USDM-EP-10
	Screen-IV	Urban Safety and Disaster Mitigation	USDM-EP-11 to USDM-EP-14
04:00 PM - 04:30 PM	**TEA/ COFFEE BREAK**		
04:30 PM - 05:00 PM	**DISTINGUISHED LECTURE**		
	Prof. Paulo B. Lourenço, Professor, University of Minho, Portugal		
05:00 PM - 06:00 PM	**SURYA HALL**	Urban Safety and Disaster Mitigation	USDM-OP-26 to USDM-OP-32
	VAYU HALL	Infrastructure Management and Sustainable Built Environments	IMSBE-OP-26 to IMSBE-OP-32
	JAL HALL	Infrastructure Management and Sustainable Built Environments	IMSBE-OP-33 to IMSBE-OP-39
	PRITHVI HALL	Urban Safety and Disaster Mitigation	USDM-OP-33 to USDM-OP-39
07:30 PM onwards	**BANQUET DINNER** *Venue: Hotel Clarks Safari, New Bahadarabad Bypass, Haridwar, Uttarakhand, India*		

DAY 2 | Friday, November 21, 2025

Venue: Hotel Clarks Safari, New Bahadarabad Bypass, Haridwar, Uttarakhand, India

09:00 AM - 02:00 PM	**REGISTRATION (HELP DESK) and EXHIBITION** *Venue: Hotel Clarks Safari, New Bahadarabad Bypass, Haridwar, Uttarakhand, India*		
09:00 AM - 10:45 AM	**PARALLEL SESSIONS**		
	SURYA HALL	Urban Safety and Disaster Mitigation	**Keynote Lecture:** **Prof. Pennung Warnitchai**, Professor, Asian Institute of Tech., Thailand **Keynote Lecture:** **Mr. Jitendra K. Bothara**, Director, ResiPro Int. Engg. Ltd., New Zealand **Paper Presentations:** USDM-OP-40 to USDM-OP-45
	VAYU HALL	Infrastructure Management and Sustainable Built Environments	**Keynote Lecture:** **Dr. Ramesh Guragain**, Deputy Executive Director, National Society for Earthquake Technology, Nepal **Keynote Lecture:** **Dr. Shailesh Agrawal**, Executive Director, BMTPC, New Delhi, India **Paper Presentations**: IMSBE-OP-40 to IMSBE-OP-43
	JAL HALL	Infrastructure Management and Sustainable Built Environments	**Keynote Lecture:** **Dr. KVL Subramaniam**, Professor, Indian Institute of Technology, Hyderabad **Keynote Lecture:** **Dr. Tsuyoshi Minami**, Associate Professor., Institute of Industrial Science, University of Tokyo **Paper Presentations:** IMSBE-OP-44 to IMSBE-OP-47
	PRITHVI HALL	Urban Safety and Disaster Mitigation Infrastructure Management and Sustainable Built Environments	**Keynote Lecture**: **Shri Santanu Chakraborty**, Chief Executive Officer, Bal Raksha Bharat, New Delhi, India **Keynote Lecture**: **Er. Rajdeep Chowdhury**, Business Head, Biltech Building Elements Ltd. New Delhi **Paper Presentations**: USDM-OP-46 to USDM-OP-47 IMSBE-OP-48 to IMSBE-OP-50
10:45 AM - 11:00 AM	**TEA/ COFFEE BREAK**		

11:00 AM - 01:00 PM	**DISTINGUISHED LECTURES** ○ **Prof. C. V. R Murty**, PS Rao Chair Professor, Indian Institute of Technology Madras ○ **Mr. Yogesh P Kajale**, Director (Engineering), B G Shirke Construction Tech Pvt Ltd., Pune ○ **Dr. Shantanu Sarkar**, Director, Uttarakhand Landslide Mitigation & Management Center, Dehradun ○ **Prof. Daniel Vitorino de Castro Oliveira**, Associate Professor, University of Minho, Portugal
01:00 PM - 02:00 PM	LUNCH
02:00 PM - 02:30 PM	Transfer / Travel to CSIR CBRI, Roorkee
02:30 PM - 04:00 PM	Guided Visit to CSIR CBRI
04:00 PM - 04:30 PM	TEA/ COFFEE BREAK
04:30 PM - 5:30 PM	**BRIGHT SPARK LECTURES** ○ **Dr. L P Singh,** Director General, National Council for Cement and Building Materials, Ballabgarh, Haryana, India ○ **Mr. Saw Htwe Zaw,** Vice-Chairman, Myanmar Earthquake Committee in Myanmar ***Venue: Rabindranath Tagore Auditorium, CSIR CBRI, Roorkee***
05:30 PM - 06:30 PM	**CLOSING CEREMONY** ○ Conference Resolution ○ Awards ○ Announcements
06:30 PM – 07:00 PM	**TEA/ COFFEE BREAK**
07:00 PM – 07:30 PM	**IIS Alumni Meet**
07:30 PM Onwards	**FAREWELL DINNER (With Live Music Show)** **Venue: CSIR-Central Building Research Institute Lawns**

DAY 3 | Saturday, November 22, 2025

08:00 AM - 08:00 PM	**Technical Tour**

Live Telecast of Inaugural and Closing Ceremony shall be made on CSIR CBRI YouTube Channel and Facebook

Scan below

for Conference venue

Scan below

For Closing Ceremony / Farewell Dinner Venue venue

OneHealth OneWorld

東京大学 生産技術研究所

DETAILED PROGRAMME

DAY 1- Thursday, November 20, 2025

08:00 AM - 06:00 PM	**REGISTRATION**
Venue: Hotel Clarks Safari, New Bahadarabad Bypass, Haridwar, Uttarakhand, India	
09:00 AM - 10:00 AM	**OPENING CEREMONY**
10:00 AM - 06:00 PM	**EXHIBITION**
10:00 AM - 10:30 AM	**HIGH TEA**
10:30 AM - 12:00 PM	**DISTINGUISHED LECTURES:** ○ **Prof. Kimiro Meguro**, Dean, Professor, Interfaculty Initiative in Information Studies/ Graduate School of Interdisciplinary Information Studies, The University of Tokyo, Hongo, Japan, Professor, Industrial Institute of Sciences, The University of Tokyo, Komaba, Japan *Towards Ideal Disaster Countermeasures in Japan* ○ **Dr. Krishna S. Vatsa**, Member, NDMA, New Delhi, India *Post Disaster Needs Assessment* ○ **Dr. Juin-Fu Chai**, Deputy DG, NCREE, National Institutes of Applied Research, Taipei, Taiwan, ROC *NCREE-NIAR's Contributions to Earthquake disaster Mitigation and Community Resilience in Taiwan*

PARALLEL SESSION-1 (ORAL PRESENTATIONS: OP)

Venue: **SURYA HALL** | Date: November 20, 2025 | 12:00 PM to 01:30 PM

Theme: Urban Safety & Disaster Mitigation (USDM): USDM -OP-01 to USDM -OP-10

Chair: **Dr. Debi Prasanna Kanungo**, CSIR CBRI, Roorkee

Co-Chair: **Dr. Khin Myat Kyaw**, IIS, The University of Tokyo, Japan

12:00 PM	**USDM -OP-01** Abs. ID 95: Investigation on Shear Strength and Behaviour of Reinforced Concrete Short-Span T-Beams Strengthened By Concrete Jacket, *Vishnu T. Unni and* ***Amlan K. Sengupta***
12:10 PM	**USDM -OP-02** Abs. ID 58: Analysis and Design Methods of Piles: A Critical Review, ***Ganesh A. Suryawanshi*** *and Sachin M. Pore*
12:20 PM	**USDM -OP-03** Abs. ID 51: Rehabilitation of Severely Deteriorated RCC Elements in Operational Healthcare Facility: A Case Study on Material Techniques and Execution Monitoring, ***Aishwarya Gupta,*** *Niharika Nanduru and R. Pradeep Kumar*
12:30 PM	**USDM -OP-04** Abs. ID 9: Field data-based Landslide Hazard Assessment in parts of Munsyari, Pithoragarh, Uttarakhand, India, ***Kaushal Singh Barfal****, Siddhant Vaish and Ajay Kumar Arya*
12:40 PM	**USDM -OP-05** Abs. ID 53: Real-Time Landslide Hazard Assessment at Narendra Nagar using Acoustic Emission Sensor Technology, ***Ashish Pippal****, Kanti L Solanki, Chandrabhan Patel and S. K. Negi*

12:50 PM	**USDM -OP-06** Abs. ID 166: Performance evaluation of ANN and CNN models in fault localization of railway track using sensor data, ***Siya Srivastava****, Suman Dey and Aloke Kumar Datta*
01:00 PM	**USDM -OP-07** Abs. ID 154: Comprehensive Structural Health Monitoring Framework for Heritage Conservation, *Hina Gupta and* ***Debdutta Ghosh***
01:10 PM	**USDM -OP-08** Abs. ID 148: Assessment of Localized Damage in Reinforced Concrete Structural Elements Subjected to Confined Contact Explosions Using FE–SPH Hybrid Techniques, ***Suman Kumar*** *and Debdutta Ghosh*
01:20 PM	**USDM -OP-09** Abs. ID 147: Virtual Simulation of The Real Demolition Scenario Through The Removal Of Structural Elements With Time Delay Based on Computational Methods, ***Suman Kumar*** *and Debdutta Ghosh*
01:30 PM	**USDM -OP-10** Abs. ID 102: Need for Structural Health Monitoring (SHM) Code in India, ***P. D. Velani****, A. Bhalkikar, H. C. Dasari and R. Pradeep Kumar*
PARALLEL SESSION-2	
Venue: **VAYU HALL**	
Date: November 20, 2025 | 12:00 PM to 01:30 PM	
Theme: Infrastructure Management and Sustainable Built Environment (IMSBE): IMSBE -OP-01 to IMSBE -OP-10	
Chair: **Prof. Kazuyuki Takada**, The Tokyo Denki University, Japan	
Co-Chair: **Dr. Kishor S. Kulkarni**, CSIR CBRI, Roorkee	
12:00 PM	**IMSBE -OP-01** Abs. ID 187: Slope Monitoring System using Inclinometers and Soil Moisture Sensors, *T. Katayama , K. Goto, K. Fujimori and S. Konishi*
12:10 PM	**IMSBE -OP-02** Abs. ID 183: A Comprehensive Approach towards Enhancing Service Life of Marine Concrete Pile Structures Considering Depth-Varying Non-Uniform Corrosion Effects, ***Rishwanth Darun A S****, Lihai Zhang and Dimitrios Chronopoulos*
12:20 PM	**IMSBE -OP-03** Abs. ID 161: Effect of Paint Scrap Waste Based Accelerating Admixture on Setting Time, Compressive Strength and Hydration of Cement Paste, ***Jeeshan Khan****, P.C. Thapaliyal, Arun Kumar, Md. Reyazur Rahman and Neha Kumari*
12:30 PM	**IMSBE -OP-04** Abs. ID 131: Next-Generation Materials in Civil Engineering: Pioneering Sustainable Solutions for A Low-Carbon Built Environment, ***S.K. Singh****, Jyoti and Ajay P. Chourasia*
12:40 PM	**IMSBE -OP-05** Abs. ID 203: Durability performance of CO2 sequestered recycled aggregates, ***M. R. Rahman****, N. Mansuri and K.S. Kulkarni*

12:50 PM	**IMSBE -OP-06** Abs. ID 156: Comparative Assessment of Corrosion Susceptibility in E450 Carbon Steel and 450 Cr Stainless Steel Under Accelerated Exposure Conditions, ***A. Sharma****, P.C.A Kumar and G.P Chaudhary*
01:00 PM	**IMSBE -OP-07** Abs. ID 157: Decarbonising the Cement and Construction Sector using Low Carbon Cementitious System, ***P N Ojha****, Puneet Kaura, Brijesh Singh, Amit Trivedi, Arup Ghatak and L P Singh*
01:10 PM	**IMSBE -OP-08** Abs. ID 164: A Brief Overview of Major Challenges Occurred During Tunnelling and Associated Underground Structures in East West Metro Project, Kolkata, ***D. Kar****, P. Mitra, and B. Roy*
01:20 PM	**IMSBE -OP-09** Abs. ID 88: Eco-Cement Binders From Waste-Derived Raw Materials: A Route To Green Construction, ***R. Kumar***
01:30 PM	**IMSBE -OP-10** Abs. ID 130: Chloride Removal from Water Using Resin for Construction-Related Applications, ***Soumitra Maiti*** *and Neeraj Jain*
PARALLEL SESSION-3	
Venue: **JAL HALL**	
Date: November 20, 2025 | 12:00 PM to 01:30 PM	
Theme: International Public Health Research in Asia (IPHRA): IPHRA -OP-01 to IPHRA -OP-10	
Chair: **Dr. Arun Kumar,** Roorkee Child Hospital, Roorkee	
Co-Chair: **Dr. Dinesh Kumar**, National Institute of Health and Family Welfare, New Delhi	
12:00 PM	**IPHRA -OP-01** Abs. ID 80: Ultraviolet-C Disinfection Technologies During the COVID-19 Pandemic: Mechanisms, Efficacy, and Emerging Applications, ***Tabish Alam****, Nagesh Babu Balam, Kishor Kulkarni, Chandan S. Meena, Nirmal, Injamamul Haque and Naushad Ali*
12:10 PM	**IPHRA -OP-02** Abs. ID 184: One World One Health: Current Prospective, *M. K. Sinha and* ***P. C. Thapliyal***
12:20 PM	**IPHRA -OP-03** Abs. ID 160: Effect of Building Corner Shape Modification on Near-Field Pollutant Dispersion, ***Krishan Dutt Yadav*** *and Bharat Singh Chauhan*
12:30 PM	**IPHRA -OP-04** Abs. ID 155: Development in Bacteriology of Habitat and Marine Pathogen Monitoring Techniques, ***Vijay Wasudeorao Lande***
12:40 PM	**IPHRA -OP-05** Abs. ID 144: Randomised Double Blind Controlled Trial to Test The Efficacy Of Śuhyādi Kaāya Against Mahārāsnādi Kaāya In Knee Osteoarthritis, ***A Binitha*** *and M Jithesh*

12:50 PM	**IPHRA -OP-06** Abs. ID 140: Risk Factors for mpox Transmission Among Individuals in Case-Patient Households, Uganda, July 2024–February 2025, *Joyce Owens Kobusingye, Daniel Wenani, Richard Migisha, Ivan Lukabwe, Lillian Bulage, Stella Lunkuse, Michael Mwanga, Benon Kwesiga and Alex Riolexus Ario*
01:00 PM	**IPHRA -OP-07** Abs. ID 89: Sustainable Development Goals in Indian Healthcare: A Policy Analysis of the Post-Covid Period, ***A. Suytradhar****, N. Jaiswal and A. Shukla*
01:10 PM	**IPHRA -OP-08** Abs. ID 86: Time to Control of Anthrax Outbreaks In Africa, 2014–2023: A Systematic Review And Meta-Analysis, *Alex R. Ario, Esther Buregyeya, Elizeus Rutebemberwa, Abel W. Walekhwa, Rebecca Akunzirwe, Irene B. Kyamwine, Ronald Olum, Fred Nuwaha, David Serwadda and Rhoda K. Wanyenze*
01:20 PM	**IPHRA -OP-09** Abs. ID 62: Discussing Psychopathological Manifestations During Covid-19 Pandemic: A Public Mental Health Analysis, ***Chayan Munshi***
01:30 PM	**IPHRA -OP-10** Abs. ID 23: Dengue Transmission in India Under A Changing Climate, ***Srinivasa Rao Mutheneni*** *and Rajasekhar Mopuri*
PARALLEL SESSION-4	
Venue: **PRITHVI HALL**	
Date: November 20, 2025 | 12:00 PM to 01:30 PM	
Theme: Climate Change and Green Recovery (CCGR): CCGR-OP-01 to CCGR-OP-10	
Chair: **Dr. S. K. Panigrahi,** CSIR CBRI, Roorkee	
Co-Chair: **Dr. Soumitra Maiti**, CSIR CBRI, Roorkee	
12:00 PM	**CCGR-OP-01** Abs. ID 172: Carbon Emission by Steel Industry, ***Priti Jha***
12:10 PM	**CCGR-OP-02** Abs. ID 101: Exploring the Effect of Zeolite 13X and Olivine Sand on CO2 Sequestration in Concrete, ***Vedanshi Shah****, T. M. Joshi, M.J. Lashaki and U.V. Dave*
12:20 PM	**CCGR-OP-03** Abs. ID 6: Climate-Resilient Above-Ground Pest Control: Harnessing Sand and Entomopathogenic Nematodes, *Ratnakala and Kalleshwara Swamy C. M*
12:30 PM	**CCGR-OP-04** Abs. ID 96: Case Study of Urban Heat Island Impact through Surface Temperature Profiling in Ahmedabad using Thermal Infrared Imaging, *T.M. Joshi, N.N. Vanani,* ***J.H. Machchhoya****, V.A. Thakkar and U.V. Dave*

12:40 PM	**CCGR-OP-05** Abs. ID 162: Life Cycle Assessment of Artificial Light Weight Aggregates, *Brijesh Singh, Anand Bohra and L P Singh*
12:50 PM	**CCGR-OP-06** Abs. ID 125: Carbonation Behavior of Mortars Containing LD Slag: A Physical and Microstructural Investigation, *Kishor S. Kulkarni and Chandra Shekhar Sharma*
01:00 PM	**CCGR-OP-07** Abs. ID 33: Carbon-Cured Artificial Lightweight Aggregates from Municipal Solid Waste Incinerated Ash: A Cold Bonding Approach, ***Humaira Athar**, Deepika Saini, K.S. Kulkarni and D. Bhardwaj*
01:10 PM	**CCGR-OP-08** Abs. ID 100: Effect of Climate Change on Bridges, ***Prof. (Dr.) Rajeev Goel***
01:20 PM	**CCGR-OP-09** Abs. ID 54: A Dynamic Network Approach to Analyze the Impact of Crop Residue Burning on Urban Air Quality Using Time-Lagged Correlation, ***S. Anwar** and P. Misra*
01:30 PM	**CCGR-OP-10** Abs. ID 151: Toward Sustainable Cooling: Integrating Heat Pipes in Windcatchers for Passive Ventilation Systems, *Veena Chaudhary and Shubham Kumar*
LUNCH BREAK	
Venue: Clarks Safari, New Bahadarabad Bypass, Haridwar, Uttarakhand, India	
Date: November 20, 2025 | 01:30 PM to 02:30 PM	
PARALLEL SESSION-5	
Venue: **SURYA HALL**	
Date: November 20, 2025 | 02:30 PM to 04:15 PM	
Theme: Urban Safety & Disaster Mitigation (USDM): USDM -OP-17 to USDM -OP-25	
Chair: **Prof. S.K. Singh,** CSIR CBRI, Roorkee	
Co-Chair: **Dr. Debdutta Ghosh**, CSIR CBRI, Roorkee	
02:30 PM	**USDM -OP-17** Abs. ID 3: Identification of Optimum use of Iso*lation and Damping System For RCC Buildings,* **A. Das** and D. Bandyopadhyay
02:40 PM	**USDM –OP- 18** Abs. ID 115: 2D Digital Image Correlation-Based Impact Analysis of Rockfall Protection Tunnels Incorporating Energy Dissipation Systems, ***Sarath Rajeev** and Dr. S. Ganesh Kumar*
02:50 PM	**USDM -OP-19** Abs. ID 5: Rethinking Urban Resilience – Safety and Disaster Mitigation in a Rapidly Changing World, ***Deepak Gupta***
03:00 PM	**USDM -OP-20** Abs. ID 27: Artificial Intelligence-Based Modelling of Urban PM2.5 Concentration Considering Key Performance Indicators, *J. Pandya, D. Kaul, and D. Sarkar*

03:10 PM	**USDM -OP-21** Abs. ID 20: Optimal Subsidy to Reduce CO2 Emissions By Promoting Energy-Efficient Housing With A Balanced Approach To Demolition And Renovation, ***K. Isawa*** *and Y. Honma*
03:20 PM	**USDM -OP-22** Abs. ID 77: Diagonal Compression Tests on Autoclaved-Aerated Concrete (AAC) Blocks Walletes Reinforced With Prefabricated Wire Reinforcement, ***C. Sonkar,*** *A. Chourasia, R. Paswan,K.Sharma and S.kumar*
03:30 PM	**USDM -OP-23** Abs. ID 180: A Framework For Assessment of Multi Hazard Vulnerability and Risk Assessment, ***D.P. Kanungo****, Neha Gupta and Josodhir Das*
03:40 PM	**USDM –OP- 24** Abs. ID 205: Mapping and Analysis of Building Vulnerability to Rockfall Hazards in Ado Ekiti, Southwestern Nigeria, *Falae Philips Omowumi, Nkoyo Monday Asueiza and Ilevbare Martins*
03:50 PM	**USDM -OP-25** Abs. ID 142: Negative Stiffness Damper for Damage Mitigation of RC Buildings, *Ramyashree,* ***P. Kamatchi*** *and G. Raghava*
04:00 PM	Technical Presentation of SSA Techno Construction P. Ltd on Structural Retrofit
PARALLEL SESSION-6	
Venue: **VAYU HALL**	
Date: November 20, 2025 | 02:30 PM to 04:15 PM	
Theme: Infrastructure Management & Sustainable Built Env. (IMSBE): IMSBE -OP-11 to IMSBE OP-20	
Chair: **Mr. Parmanand Ojha,** NCCBM, Haryana	
Co-Chair: **Dr. Harish Chandra Arora,** CSIR CBRI, Roorkee	
02:30 PM	**IMSBE -OP-11** Abs. ID 129: Development of Perlite Based Sustainable Composite Plaster, *Neeraj Jain,* ***Soumitra Maiti*** *and Payal Bakshi*
02:40 PM	**IMSBE -OP-12** Abs. ID 91: Clogging and De-Clogging Potential Of Pervious Concrete Slices Using Falling Head Permeability Approach: An Experimental Analysis, ***Nagesh Pratap Singh****, Santha Kumar G and Ganesh Kumar S*
02:50 PM	**IMSBE -OP-13** Abs. ID 71: Adding Polypropylene Fibers to 3D Printable Concrete: Effects on Printability and Material Anisotropy, ***Ashish Kapoor,*** *Ajay Chourasia and Shamiyanka* ***Thakur***
03:00 PM	**IMSBE -OP-14** Abs. ID 67: Development of Microbial based Process for Bio-cement, Bio-brick and Self-Healing Concrete using locally available Resources, ***Sanjay Deori****, Dipak Basumatari, Masoom Saikia, Archana Yadav, Ratul Saikia, Leon Raj J. and Nibir Pran Borah*

03:10 PM	**IMSBE -OP-15** Abs. ID 13: Evaluation of seismic design parameters for 3D printed building: *A numerical study*, ***Phani Chandra Veligatla***
03:20 PM	**IMSBE -OP-16** Abs. ID 196: Decarbonization Of Limestone Through Hydrogenation – A Review, *L. P. Singh, A. K. Dikshit and* ***S. K. Chaturvedi***
03:30 PM	**IMSBE -OP-17** Abs. ID 138: Transforming Rubble To Resource By Performance Enhancement Of Recycled Aggregate Through Sustainable Treatment, ***A. Aggarwal****, S. K. Singh and G. Goel*
03:40 PM	**IMSBE -OP-18** Abs. ID 72: Characterization of Printing and Mechanical Properties of Agro-Waste Based Binary Cementitious Composite, ***B.Pal*** *and A. Chourasia*
03:50 PM	**IMSBE -OP-19** Abs. ID 113: Effect of Activator Dosage on the Compressive Strength of One-Part Alkali Activated Materials, ***Devesh Upadhyay****, Rinki Mehta and Sonal Thakkar*
04:00 PM	**IMSBE -OP-20** Abs. ID 32: Development of A Modular Large-Scale Gantry Based 3-D Concrete Printer, ***R. Sahai****, R. S. Bisht, S. Singh, Sameer, D. Kumar and S. K. Panigrahi*
04:10 PM	Technical Presentation of Tvasta Manufacturing Solutions Pvt. Ltd.: 3D Concrete Printing
PARALLEL SESSION-7	
Venue: **JAL HALL**	
Date: November 20, 2025 | 02:30 PM to 04:15 PM	
Theme: (a) International Public Health Research in Asia (IPHRA): IPHRA -OP-11 to IPHRA -OP-14 (b) Urban Safety & Disaster Mitigation (USDM): USDM -OP-11 to USDM -OP-16	
Chair: **Dr. Shorab Jain**, CSIR CBRI, Roorkee	
Co-Chair: **Dr. Anindya Pain**, CSIR CBRI, Roorkee	
02:30 PM	**IPHRA -OP-11** Abs. ID 4: Catalyst Free Synthesis Of Novel 6-Chloro-3-Isopropyl-1-Methylpyrimidine-2,4(1H,3H)-Dione Derivatives As Pharma Intermediate, ***R. S. Shingare****, A. Veeram, S. B. Andugulapati B.V. S. Reddy and S. Bansod*
02:40 PM	**IPHRA -OP-12** Abs. ID 190: Gender Estimation Using Sternum Medical Image Processing, ***Neha Pokhriyal*** *and Sanjay Sharma*
02:50 PM	**IPHRA -OP-13** Abs. ID 107: Integrating Climate and Disaster Resilience into MGNREGA: A Conceptual Framework, ***A. Singh****, R. Chaterjee and R. Shaw*
03:00 PM	**IPHRA -OP-14** Abs. ID OP-02: Issues and Challenges to Sustainability of Healthcare Waste Management in India: Call for One Health Approach, ***Dinesh Kumar***

03:10 PM	**USDM -OP-11** Abs. ID 99: Structural Performance Assessment of Buildings – A Key To Earthquake Disaster Preparedness, ***P.A. Bansode*** *and R. Goswami*
03:20 PM	**USDM –OP- 12** Abs. ID 38: Analysis of the Congestion Conditions of Highway Parking Area in Japan Using Probe Data and Drone Movie Data, *S.Y. Mon and* ***D. Watanabe***
03:30 PM	**USDM -OP-13** Abs. ID 90: Application Of MASW For Subsurface Characterization In Seismically Active Regions, *A. Dwivedi , S. Das,* ***K. Pandit*** *and A. Pain*
03:40 PM	**USDM -OP-14** Abs. ID 92: A Normative Procedure for Seismic Risk Assessment and Resilient Towns, ***Ajay Chourasia****, Pradeep Kumar R, Ashish Kapoor and Suvam Das*
03:50 PM	**USDM -OP-15** Abs. ID 179: A Study on the Effect Of Entrainment on 2024 Wayanad Debris Flow of Kerala, India, ***R.K. Dash****, D.P. Kanungo, Perry Bartelt, Yu Zhuang, Yves Bühler, Brian Mcardell and R. Pradeep Kumar*
04:00 PM	**USDM -OP-16** Abs. ID 168: Air Quality Index Trends In Indian Cities An Exploratory Analysis Of Urban Pollution Patterns, ***S.H. Pandit*** *and R.U. Patel*
04:10 PM	Technical Presentation of M/s ABC Solutions
PARALLEL SESSION-8	
Venue: **PRITHVI HALL**	
Date: November 20, 2025 | 02:30 PM to 04:15 PM	
Theme: (a) Climate Change and Green Recovery (CCGR): CCGR-OP-11 to CCGR-OP-14 (b) Infrastructure Management and Sustainable Built Environment: IMSBE OP-21 to OP-25	
Chair: **Dr. P. C. Thapliyal**, CSIR CBRI, Roorkee	
Co-Chair: **Dr. Neeraj Jain**, CSIR CBRI, Roorkee	
02:30 PM	**CCGR-OP-11** Abs. ID 175: Urban Heat Island (UHI) Phenomena in Indonesia Using Cloud Computing Google Earth Engine, ***S. Darmawan****, R. Hernawati and N.N. Nurulhakim*
02:40 PM	**CCGR-OP-12** Abs. ID 199: Development of a Soil Moisture Sensing IoT Device for Precision Agriculture, *Jyoti Pippal,* ***Neha Pokhriyal*** *and Neha Chaudhary*
02:50 PM	**CCGR-OP-13** Abs. ID 169: Sustainable Practices For A Steel Plants, ***P. Jha***
03:00 PM	**CCGR-OP-14** Abs. ID 177: Application of IoT And Remote Sensing Techniques To Investigates Water Status and Methene Emission from Rice Paddy Field, ***Md Rahedul Islam*** *and Wataru Takeuchi*

03:10 PM	**IMSBE -OP-21** Abs. ID 35: Approach to create long term sustainable water to solve water crisis, ***Anil Kumar***
03:20 PM	**IMSBE -OP-22** Abs. ID 200: Self-Sensing Geosynthetics (SSG) For Health Monitoring of Geotechnical Structures, *M Vinoth, Samreen Bano and Jaikey Saini*
03:30 PM	**IMSBE -OP-23** Abs. ID 158: Circular Economy Implementation in the Construction Sector through use of Alternate Aggregate, *P N Ojha,* ***Brijesh Singh****, Amit Trivedi, Puneet Kaura, Rohit Kumar and L P Singh*
03:40 PM	**IMSBE -OP-24** Abs. ID 93: Evaluating the Thermal Performance of Photovoltaic Cells Using Phase Change Materials and Geometric Enhancements: A Numerical Approach, ***Tabish Alam****, Nagesh B. Balam, Md Muslim Ansari, Kishor Kulkarni, Chandan S Meena, Injemamul Haque and Naushad Ali*
03:50 PM	**IMSBE -OP-25** Abs. ID 46: Urban Form And Shadow Impact On Pedestrian Environment, **H. Watanabe** and Y. Honma
04:00 PM	Technical Presentation of Punjab & Sind Bank
04:10 PM	Technical Presentation of TechFab (India) Industries Ltd.
e-POSTER-1 (EP)	
Venue: **Agni Sthal (Screen-I)**	
Date: November 20, 2025 | 02:30 PM to 04:30 PM	
Theme: (a) Climate Change and Green Recovery (CCGR): CCGR-EP-01 to CCGR-EP-07 (b) Infrastructure Management and Sustainable built Environment: IMSBE -EP-01 to IMSBE -EP-12	
Chair: **Dr. Nagesh Babu Balam**, CSIR CBRI, Roorkee	
02:30 PM	**CCGR-EP-01** Abs. ID 25: Bacteria Based Concrete Potential Negative Emission Technology: Critical Review, R*upali* ***R. Bhoir,*** *S.M. Pore and S.R. Bhagat*
02:37 PM	**CCGR-EP-02** Abs. ID 65: Carbon Taxation In India: A Policy Feasilbility Study on Economic Viability, Public Acceptance, and Global Lessons, ***Aviyush Sodhi***
02:44 PM	**CCGR-EP-03** Abs. ID 178: Comparative Life Cycle Assessment of Low Carbon Cements With Ordinary Portland Cement Production in India, ***Anand Bohra****, Varsha Liju, D K Panda, S K Chaturvedi and L P Singh*

02:51 PM	**CCGR-EP-04** Abs. ID 34: Beyond the Crisis: A Green Blueprint for Tomorrow, ***Deepak Gupta***
02:58 PM	**CCGR-EP-05** Abs. ID 143: Implication of Thermal Desiccation and Relative Gene Expression of HSP90 Among Marine Intertidal Barnacle, Amphibalanus Amphitrite: Climate Change Indicator???, ***Bidwan Sekhar*** *and Dattesh V. Desai*
03:05 PM	**CCGR-EP-06** Abs. ID 40: Biomimic Concrete: an Innovative Construction Material for Sustainable Build Environment, ***Farheen Jabeen****, Leena Chourasia and Srinivasaraonaik B*
03:12 PM	**CCGR-EP-07** Abs. ID 7: Polarity Assisted Pseudohalides Controllable Hetero-Aldazine Based Coordination Polymers: Crystal Engineering, Recognition of Explosive and Device Fabrication, *Mohit Kumar Chattopadhyay and* ***Priyabrata Banerjee***
03:19 PM	**IMSBE -EP-01** Abs. ID 82: Performance Assessment of Recycled Aggregate Concrete Sourced from Construction and Demolition Waste, ***Govind Gaurav*** *and Vishal Kumar*
03:26 PM	**IMSBE -EP-02** Abs. ID 150: Performance of Perforated Concrete-Filled Steel Tube (CFST) Under Flexural Loading Condition, *Preeti and* ***P. Kar***
03:33 PM	**IMSBE -EP-03** Abs. ID 195: Studies on Development of Portland Dolomite Cement (PDC) Using High MgO Limestone and Dolomitic Limestone, ***Varsha Liju****, Pinky Pandey, Diksha Rana, Mamta Pawar, S K Chaturvedi and L.P.Singh*
03:40 PM	**IMSBE -EP-04** Abs. ID 112: Thermally Treated Rice Husk Ash as A Sustainable Cement Substitute: Enhancing Strength and Carbon Sequestration in Mortars, ***Shrushti Patel****, Kshitij Parashar and Sonal Thakkar*
03:47 PM	**IMSBE -EP-05** Abs. ID 30: Portable Mud Block Machine for High Altitude Regions, ***R. S. Bisht****, D. Kumar, S. Singh, S. Yadav and S. K. Panigrahi*
03:54 PM	**IMSBE -EP-06** Abs. ID 55: GIS and Lidar Based Viewshed Analsysis of Uncontrolled Intersections,M. Bisht, K. Thakur and **P. Misra**
04:01 PM	**IMSBE -EP-07** Abs. ID 149: Structural Performance of CFST Beam-Column Connection under Combined Axial and Lateral Cyclic Loading ***P. Kar***
04:08 PM	**IMSBE -EP-08** Abs. ID 83: Evaluating Structural Performance through Numerical Models towards Earthquake Early Warning Application, ***A. Mugesh*** *and Ravi S Jakka*

04:15 PM	**IMSBE -EP-09** Abs. ID 42: Study of analysis of Precast / Partially Precast Pier-cap for 4 lane elevated corridor with cantilever pier, **Thirunavukkarasu M**
04:22 PM	**IMSBE -EP-10** Abs. ID 18: Development of an Automated Wall Plastering Machine for Indian Conditions, ***Chakradhar V***
04:29 PM	**IMSBE -EP-11** Abs. ID 87: Towards Sustainable Architecture: Data-Driven Geometry Optimization of a Funicular Arch, ***Aditi Singh****, Manas Sachin Deshmukh, Jay Sinha and Jofin George*
04:30 PM	**IMSBE -EP-12** Abs. ID 26: Efficacy of Co-calcined Red Mud and Kaolin Clay in Developing Low Carbon Cementitious Materials, *Nikhil Sanjay Nighot,* ***Rajesh Kumar*** *and Srinivasarao Naik B*

e-POSTER-2 (EP)

Venue: **Agni Sthal (Screen-II)**

Date: November 20, 2025 | 02:30 PM to 04:30 PM

Theme: Infrastructure Management and Sustainable built Environment: IMSBE -EP-13 to IMSBE -EP-16

Chair: **Dr. R. Siva Chidambaram,** CSIR CBRI, Roorkee

02:30 PM	**IMSBE -EP-13** Abs. ID 22: "A Sustainable Approach to High Performance Concrete using Industrial Wastewater: A Durability Perspective", ***Vijay Verma***
03:00 PM	**IMSBE -EP-14** Abs. ID 74: Performance Evaluation of High-Volume Fly Ash Concrete for Sustainable Construction, ***Jidnyasa Raut*** *, Dr. Harish Chandra Arora and Dr. B. K. Rao*
03:30 PM	**IMSBE -EP-15** Abs. ID PO-01 Axial Strength and Buckling Behavior of Cold-Formed Steel C-Sections and Built-Up Members: Experimental Investigation and Semi-Analytical Approach, ***S. Uniyal****, C. Sonkar, and S. Narayan*
04:00 PM	**IMSBE -EP-16** Abs. ID PO-02: Bond Shear Tests of Polypropylene Geo-grids strengthened on Masonry substrates, ***Deekshitha M K*** *and Siva Chidambaram R*

e-POSTER-3 (EP)

Venue: **Agni Sthal (Screen-III)**

Date: November 20, 2025 | 02:30 PM to 04:30 PM

Theme:
(a) International Public Health Research in Asia (IPHRA): IPHRA -EP-01 to IPHRA -EP-07
(b) Urban Safety & Disaster Mitigation (USDM): USDM – EP-02 to USDM – EP-10

Chair: **Mr. Ashish Pippal**, CSIR CBRI, Roorkee

02:30 PM	**IPHRA -EP-01** Abs. ID 128: Leveraging Ecological Intelligence in Ozone Based Technologies for Community and Industrial Applications– Futuristic Vistas, ***M.R. Asha****, S.N. Mudliar, Mekhala Huilgol, C.Nayana Nayaka*
02:38 PM	**IPHRA -EP-02** Abs. ID 189: Occupational Safety and Health Hazards of Construction Workers and Preventive Measures, ***Dr. Lakshmy Paramewswaran****, Dr. Swarna Parameswaran*
02:46 PM	**IPHRA -EP-03** Abs. ID 63: Complex Managerial Networks in Healthcare During the Covid-19 Pandemic Era, ***Ishika Pal****, Chayan Munshi*
02:52 PM	**IPHRA -EP-04** Abs. ID 61: Investigating the Contemporary Developments in Healthcare During The Covid-19 Pandemic Period, ***Swapnanil Mondal****, Chayan Munshi*
03:00 PM	**IPHRA -EP-05** Abs. ID 37: Diabetic Retinopathy Detection Model using Hybrid of U-Net and Vision Transformer Algorithms, ***Mudit Khater***
03:08 PM	**IPHRA -EP-06** Abs. ID 21: Recreational Games: A Comprehensive Literature Review on Pathway to better Health and Wellbeing, ***Tanmay Awasthi*** *and Sonal Atreya*
03:16 PM	**IPHRA -EP-07** Abs. ID 8: Harmonizing Health Horizons: Unraveling Public Health Innovations and Resilience, ***Diksha Tripathi***
03:24 PM	**USDM -EP-03** Abs. ID 191: Analysis of shared bikes combined with ETC2.0 data, ***Takashi Miyazawa***
03:32 PM	**USDM -EP-03** Abs. ID 191: Analysis of shared bikes combined with actual usage records, ***Takashi Miyazawa, Kazuyuki Takada***
03:40 PM	**USDM -EP-04** Abs. ID 114: Seismic Response Control of Buildings using FE-Based Shape Memory Alloy Base Isolators, ***Moka Eswar*** *and A. Chourasia*
03:48 PM	**USDM -EP-05** Abs. ID 98: Methods for Improving Earthquake Resistance of Non-Structural Elements, ***S. Saranya*** *and P. Sunitha*
03:56 PM	**USDM -EP-06** Abs. ID 207: Comparitive Seismic Assessment of Reinforced Concrete Buildings using Is:1893–2016 And Is:1893 (2023 Draft), ***D. Hima Chandan*** *and K. Akhil Kumar*
04:04 PM	**USDM -EP-07** Abs. ID 206: Deformation in Geosynthetic Reinforced Soil Wall during Seismic Event for Improved Risk Reduction, *Gopal Das and Manojit Samanta*
04:12 PM	**USDM -EP-09** Abs. ID 188: Use of Carbon Fiber Reinforced Polymer (CFRP) For Strengthening Shear and Flexural Capacities of Beam, ***Binay Karna***
04:20 PM	**USDM -EP-10** Abs. ID 137: Assessment of the Impact of Reduced Rendezvous Points on Doctor Helicopter Operations in the Noto Peninsula, ***Ryoma Arai, Kazuyuki Takada, Makoto Fujiu, Yuma Morisaki and Junichi Takayama***

e-POSTER-4 (EP)	
Venue: **Agni Sthal (Screen-IV)**	
Date: November 20, 2025 | 02:30 PM to 04:30 PM	
Theme: Urban Safety & Disaster Mitigation: USDM – EP-11 to USDM – EP-14	
Chair: **Dr. S. Ganesh Kumar**, CSIR CBRI, Roorkee	
03:40 PM	**USDM -EP-11** Abs. ID 29: Seismic Design and Performance Analysis of G+15 Building with Base Isolation (HDRB'S) and dampers (FVD), Satyam Murlidhar Shukla and Archana Dongre
03:50 PM	**USDM –EP-12** Abs. ID 50: Snow Avalanche Susceptibility Zonation Mapping along the Leh–Manali Highway of Himachal Pradesh and UT of Ladakh, India, *Jyoti Yadav, Rajesh Kumar Dash, Chandrabhan Patel,* ***Kanti L. Solanki,*** *D.P. Kanungo and S.K. Panigrahi*
04:00 PM	**USDM –EP-13** Abs. ID 208: Application of Seismic Method with In-ground Sensors for Detecting Geotechnical Cavities, ***S. Watanabe****, H. Yuki, Y. Hara and R. Kuwano*
04:20 PM	**USDM –EP-14** Abs. ID PO-03: Impact Resistance of GFRP-Reinforced Concrete Slabs: Experimental Evaluation, *S. Lokesh, R. Siva Chidambaram and T. Sai Sheshu*
04:00 PM- 04:30 PM	**TEA/ COFFEE BREAK**
04:30 PM- 05:00 PM	**DISTINGUISHED LECTURE** **Prof. Paulo B. Lourenço**, Professor, University of Minho, Portugal Disaster Multi-risk Reduction and Urban Resilience: A Selection of Concepts, Methods and Applications

PARALLEL SESSION-9	
Venue: **SURYA HALL**	
Date: November 20, 2025 | 05:00 PM to 06:00 PM	
Theme: Urban Safety & Disaster Mitigation (USDM): USDM -OP-26 to USDM -OP-32	
Chair: **Prof. Amlan Sengupta,** IIT Madras	
Co-Chair: **Dr. R. Siva Chidambaram**, CSIR CBRI, Roorkee	
05:00 PM	**USDM -OP-26** Abs. ID 108: Influence of Numerical Modelling Methods of URM Infills on Seismic Behaviour of Low-Rise RC Moment Frames, ***Y. Lakshmi Suupriya****, R. Pradeep Kumar and P. Sunitha*
05:09 PM	**USDM -OP-27** Abs. ID 24: Enhancing Urban Flood Resilience: A Flood Parameter Predictive Modelling with UAV-DEM and 1D Hydrodynamic Simulation for Non-Perennial River, ***Mrunalini Rana****, D. P. Patel and V. Vakharia*
05:18 PM	**USDM -OP-28** Abs. ID 186: Eye-Tracking Based Analysis of Driver Distraction Patterns in Urban Environments: A Delhi Study, *Romy Mathew, Merin Sara Mathew, Meenakshi Prasad, Kamini Guptha ,****Vinod Karar*** *and S. Velmurugan*
05:27 PM	**USDM -OP-29** Abs. ID 181: Analysis Of Driver Behavior In Urban Traffic Using Driving Simulator, Eye Tracker, And Vienna Test System, ***Nikhil Nandavane****, Gopika Manoj, Vinod Karar, Kamini Gupta, S. Velmurugan and Marisamynathan S*
05:36 PM	**USDM -OP-30** Abs. ID 173: Enhancing Urban Traffic Safety Through Optimized Heads-UP Display Systems, *Bhavika Arora, Divya Agrawal, Kamini Gupta, S. Velmurugan and Vinod Karar*
05:45 PM	**USDM -OP-31** Abs. ID 134: Route Choice Modeling Based on the Riding Environment of Bicycle Users, ***Rina Mizunoue*** *and Kazuyuki Takada*
06:00 PM	**USDM -OP-32** Abs. ID 133: Response Control of Steel MR Frames with Viscoelastic Damper for Enhanced Performance Objectives under MCE Hazard Level, ***Iwansh Gupta*** *and Saurabh Shiradhonkar*

PARALLEL SESSION-10	
Venue: **VAYU HALL**	
Date: November 20, 2025 | 05:00 PM to 06:00 PM	
Theme: Infrastructure Management and Sustainable Built Environment (IMSBE): IMSBE -OP-26 to IMSBE -OP-32	
Chair: **Dr. Rajesh Kr. Verma**, CSIR CBRI Roorkee	
Co-Chair: **Dr. Rajesh Sharma**, CSIR CBRI, Roorkee	
05:00 PM	**IMSBE -OP-26** Abs. ID 122: From Damage to Decision: Displacement-Based Methodology for Earthquake Recovery and Policy Planning in Masonry Buildings, ***Padalu P.K.V.R***
05:09 PM	**IMSBE -OP-27** Abs. ID 185: Post-Seismic Structural Integrity Assessment of Dams in Northern Myanmar After the 2025 Mw 7.7 Sagaing Earthquake using Multi-Technique InSAR Time-Series, ***Arliandy Pratama****, Wataru Takeuchi and Khin Myat Kyaw*
05:18 PM	**IMSBE -OP-28** Abs. Id 39: Traffic-Compatible Tunnel Health Screening With On-Vehicle Lidar, ***A. Regmi****, T. Mizutani, and K. Yamamoto*
05:27 PM	**IMSBE -OP-29** Abs. ID 132: Influence of CO2 Curing on the Performance of Construction and Demolition Waste-Based Cellular Lightweight Concrete, ***Santha Kumar G*** *and S. K. Singh*
05:36 PM	**IMSBE -OP-30** Abs. ID 15: Mitigating Pedestrian Heat Stress: An Optimization Approach for Shade Placement on Fixed-Routing Networks, *N. Adachi, H. Hasada, H. Watanabe and Y. Honma*
05:45 PM	**IMSBE -OP-31** Abs. ID 84: Numerical Investigation of Interlayer Characteristics on the Mechanical Properties of 3D Printed Concrete, ***B.Pal*** *and A. Chourasia*
06:00 PM	**IMSBE -OP-32** Abs. ID 73: Numerical Study on Seismic Performance Evaluation of 3D Printed Concrete Buildings, *Shubham Singhal, Phani Chandra Veligatla and* ***Dhananjay Tiwari***

PARALLEL SESSION-11	
Venue: **JAL HALL**	
Date: November 20, 2025 | 05:00 PM to 06:00 PM	
Theme: Infrastructure Management and Sustainable Built Environment (IMSBE): IMSBE -OP-33 to IMSBE -OP-39	
Chair: **Er. Yogesh P. Kajle**, Director (Design), BG Shirke Const. Tech. P. Ltd., Pune	
Co-Chair: **Ar.S. K. Negi,** Chief Scientist (Retd.), CSIR CBRI, Roorkee	
05:00 PM	**IMSBE -OP-33** Abs. ID 45: Comparison of Response of Single Cell and Double Cell Box Girder Decks, ***Arunprasath D***
05:09 PM	**IMSBE -OP-34** Abs. ID 174: Non-Contact Bridge Dynamic Displcement Monitoring using Mimo Radar, ***Y. Izumi****, M. Komuro and T. Kawarai*
05:18 PM	**IMSBE -OP-35** Abs. ID 85: Erection of Two Stage Cantilever Concourse and Platform Pier Arm for Elevated Metro Stations, ***Anshul Agrawal***
05:27 PM	**IMSBE -OP-36** Abs. ID 153: Multi Modal Imaging of Concrete Structures Using GPR and Ultrasound, *Debdutta Ghosh,* ***Hina Gupta****, Avinash Kumar and Sai Teja Kuchipudi*
05:36 PM	**IMSBE -OP-37** Abs. ID 56: Brick Kiln Detection using Geospatial Datasets: A Deep Learning Approach For Environmental Monitoring, ***A. Mehta****, P. Chaurasia, W. Takeuchi, R. Imasu and P. Misra*
05:45 PM	**IMSBE -OP-38** Abs. ID 66: Segment Anything Model Based Approach For Automating Rail Sleeper Spacing Estimation on Indian Tracks, ***S. Jaiswal*** *and T. Mizutani*
06:00 PM	**IMSBE -OP-39** Abs. ID 64: Behaviour of Pultruded GFRP Sections and Local Buckling Under Axial Compression, ***M.M. Ansari,*** *T. Alam and A. Chourasia*

PARALLEL SESSION-12	
Venue: **PRITHVI HALL**	
Date: November 20, 2025 | 05:00 PM to 06:00 PM	
Theme: Urban Safety & Disaster Mitigation (USDM): USDM -OP-33 to USDM -OP-39	
Chair: **Mrs. Niharika Nanduru**, NVLN Constructions Pvt Ltd, Hyderabad	
Co-Chair: **Dr. Nawal Kishor Banjara**, CSIR CBRI, Roorkee	
05:00 PM	**USDM -OP-33** Abs. ID 176: A Preliminary Seismic Risk Assessment of Built Environment, ***D.Yogeswar*** *and C. Sashidhar*
05:10 PM	**USDM -OP-34** Abs. ID 19: Earthquake Risk Assessment of Wooden Houses for Spatial Delineation of Critical Areas in Tokyo Prefecture, ***Arpan Singh****, Kenjiro Yamamoto and Kimiro Meguro*
05:20 PM	**USDM -OP-35** Abs. ID 152: Influence of Fiber Reinforced Composite on the Cyclic Behaviour Beam-Column Joints, ***R. Siva Chidambaram*** *and Pankaj Agarwal*
05:30 PM	**USDM -OP-36** Abs. ID 78: Structural Integrity assessment of an Existing Newspaper Printing Press Building Using Non-destructive Evaluation and Finite Element Modelling, ***Ashish Kapoor*** *and A. Chourasia*
05:40 PM	**USDM -OP-37** Abs. ID 75: Third-Party Quality Assurance: A Strategic Approach to Disaster Management in Construction, ***Jidnyasa Raut*** *and Harish Chandra Arora*
05:50 PM	**USDM -OP-38** Abs. ID 59: Smart Geosynthetics for Monitoring Dynamic Response of Geosynthetic-Reinforced Structures, ***G. Sakthivel*** *and Dr. S. Ganesh Kumar*
06:00 PM	**USDM -OP-39** Abs. ID 79: Out-of-Plane Behaviour of AAC Wall Panels Reinforced with Prefabricated Wire Reinforcement In Comparison to RCC Bands, ***Chanchal Sonkar****, R. Chowdhury, A. Chourasia, R. Paswan, M. M. Dalbehera, S. Kumar, K. Sharma and M.K Yadav*
07:30 PM onwards	**BANQUET DINNER** Venue: Hotel Clarks Safari, New Bahadarabad Bypass, Haridwar, Uttarakhand, India

DAY 2 - Thursday, November 20, 2025

PARALLEL SESSION-13	
Venue: **SURYA HALL**	
Date: November 21, 2025 | 09:00 AM to 10:45 AM	
Theme: Urban Safety & Disaster Mitigation (USDM): USDM -OP-33 to USDM -OP-39	
Chair: **Dr. Juin-Fu Chai,** DDG, NCREE, Taiwan	
Co-Chair: **Ms. Hina Gupta,** CSIR CBRI, Roorkee	
09:00 AM - 10:45 AM	**KEYNOTE LECTURES**
	Prof. Pennung Warnitchai, Professor, Asian Institute of Tech., Thailand *Understanding Earthquake Risk in Thailand: Reflections on the 28 March 2025 Event*
	Mr. Jitendra K. Bothara, Director, ResiPro Int. Engg. Ltd., New Zealand *Rethinking Seismic Safety: A Public Health approach for Inclusive Risk Reduction*
	ORAL PRESENTATIONS
	USDM -OP-40 Abs. ID 02: Structural Performance of Bamboo – EPS Sandwich Core Panel under Uniaxial Compression, *Ajay Chourasia, **Mickey Mecon Dalbehera** and Chanchal Sonkar*
	USDM -OP-41 Abs. ID 10: Reconstruction of Housing Process after Disasters: Trends, Challenges & Opportunities, ***V Srinivasan** and K Sivasubramanian*
	USDM -OP-42 Abs. ID 49: IoT-Based Subsurface Snow Temperature Profiling Unit For Avalanche Forecasting, *Chandrabhan Patel, **Kanti Lal Solanki**, Prateek Kumar, Komal Joshi, Dr. DP Kanungo and Dr SK Panigrahi*
	USDM -OP-43 Abs. ID 209: Fire Performance Evaluation of Ultra-High-Performance-Concrete, ***Nawal Kishor Banjara**, and R.R.Kumbhoje*
	USDM -OP-44 Abs. ID 201: Numerical Assessment of Topographic-Soil–Structure Interaction Effects On Mid-Rise Buildings Adjacent to Slopes, ***Adnan Ansari** and Manojit Samanta*
	USDM -OP-45 Abs. ID OP-04: Applicability of Hilbert Huang Transform Based Approach in Structural Health Monitoring, ***Gayatri Devi**, S.K.Panigrahi, A. Kumar, N. K. Banjara and N. Kumarand N. Kumar*

PARALLEL SESSION-14	
Venue: **VAYU HALL**	
Date: November 21, 2025 | 09:00 AM to 10:45 AM	
Theme: Infrastructure Management and Sustainable Built Environment	
Chair: **Prof. Kimiro Meguro**, Professor, IIS, Japan	
Co-Chair: **Dr. Siddharth Behera**, CSIR CBRI, Roorkee	
09:00 AM - 10:45 AM	**KEYNOTE LECTURES**
	Dr. Ramesh Guragain, Deputy Executive Director, National Society for Earthquake Technology, Kathmandu, Nepal *Lessons on Promoting Seismic Retrofitting Of Buildings and Infrastructures in Nepal*
	Dr. Shailesh Agrawal, Executive Director, Building Materials & Technology Promotion Council (BMTPC), New Delhi, India *Technology Transition through Light House Projects under Pradhan Mantri Awas Yojana – URBAN (PMAY-U)*
	ORAL PRESENTATIONS
	IMSBE -OP-40 Abs. ID 52: Automated Assessment Of Overhead Wires Geometry In Railway Tunnels, ***Fahad Mohammed Khan***, *T. Mizutani, and A.Regmi*
	IMSBE -OP-41 Abs. ID 165: Indigenous Antimicrobial Polymeric Nanofiber Membrane As An Air Filter, ***R.V.N. Gundloori***, *S. Jha, S.Ghodke, P. Bijjargi, K. Sundaraganesan, T.R. Gautum and S.Ghosh*
	IMSBE -OP-42 Abs. ID 69: Behaviour of Load Bearing Prefabricated Bamboo Wall Panel With Magnesium Oxide Sheathing Board Under Monotonic Lateral Loading, ***M M Dalbehera***, *A. Chourasia, C. Sonkar and S. Kumar*
	IMSBE -OP-43 Abs. ID 68: Determination of Modulus Of Elasticity of Bamboo Culm Parallel to Fiber Direction Under Compressive Loading, ***M M Dalbehera***, *A.Chourasia and C. Sonkar*

PARALLEL SESSION-15	
Venue: **JAL HALL**	
Date: November 21, 2025 | 09:00 AM to 10:45 AM	
Theme: Infrastructure Management and Sustainable Built Environment	
Chair: **Dr. Shantanu Sarkar,** Director, ULMMC, Dehradun	
Co-Chair: **Er. Ranu Chauhan**, NDMA, New Delhi	
09:00 AM - 10:45 AM	**KEYNOTE LECTURES**
	Dr. KVL Subramaniam, Prof. IIT Hyderabad *Engineered Material-Efficient Systems towards Net Zero Construction: Case Studies with 3D Printing and Geopolymer Sandwich Core Construction*
	Dr. Tsuyoshi Minami, Asso. Prof., Institute of Industrial Science, University of Tokyo, *Organic Electronic Devices for Chemical Sensing*
	ORAL PRESENTATIONS
	IMSBE -OP-44 Abs. ID 17: Commercial Agglomeration Induced By Local Currency Introduction Analyzed Through The Balancing-Mechanism, ***Hiroaki Kato***, *H. Hasada, H. Watanabe and Y. Honma*
	IMSBE -OP-45 Abs. ID 141: Pre-Engineered Buildings –Innovative Structural Systems For Sustainable Built Environment, ***Dr Padmaja Gokaraju***
	IMSBE -OP-46 Abs. ID 81: Flexural Behaviour of Recycled Aggregate Concrete (RAC) Precast Concrete Sandwich Panel, ***Govind Gaurav*** *and Vishal Kumar*
	IMSBE -OP-47 Abs. ID 48: Affordable Semi-Automatic Casting Machine For Lightweight Panels In Climate-Resilient Construction, ***Kanti Lal Solanki***, *Dr. SK Panigrahi, Chandrabhan Patel, Anuj Kumar and Dr. Ajay Chourasia*

PARALLEL SESSION-16	
Venue: **PRITHVI HALL**	
Date: November 21, 2025 | 09:00 AM to 10:45 AM	
Theme: Urban Safety and Disaster Mitigation	
Chair: **Dr Neeraj Jain**, CSIR CBRI, Roorkee	
Co-Chair: **Dr Manojit Samanta**, CSIR CBRI, Roorkee	
	KEYNOTE LECTURES
	Shri Santanu Chakraborty, Chief Executive Officer, Bal Raksha Bharat, New Delhi *Relevant Experiences on Working for and With Children on Climate Change*
	Er. Rajdeep Chowdhury, Business Head, Biltech Building Elements Ltd. New Delhi *Sustainable Walling Solutions*
	ORAL PRESENTATIONS
09:00 AM - 10:45 AM	**USDM -OP-46** Abs. ID 8: Sustainable On-Demand Transit Under Demographic Shift Via A Scenario-Based Behavioral Modeling Framework, ***H. Hasada****, A. Mizuno, S. Kitamura and R. Kanamori*
	USDM –OP-47 Abs. ID 159: Police Activities at the Time of the Great Kanto Earthquake and the future Great Tokyo Earthquake, ***Tetsuro Ito*** Abs. ID OP-01: The Evolution of Evacuation Shelter Management in Japan, ***Osamu Murao*** *and Kei Matsuzaki*
	IMSBE -OP-49 Abs. ID OP-03: Smartphone-Based Ground Penetrating Radar for Millimeter-Scale Damage Assessment in Concrete Structures, ***Tsukasa Mizutani*** *and S. Iwai*
10:45 AM - 11:00 AM	**TEA/ COFFEE BREAK**
	DISTINGUISHED LECTURES
11:00 AM - 01:00 PM	**Prof. C. V. R. Murty**, TS Rao Chair Professor, IIT Madras *Model Earthquake Safety Standards for Alpine Himalayan Belt*
	Er. Yogesh P Kajale, Director (Engineering), B G Shirke Const Tech Pvt Ltd., Pune *Innovative and sustainable Precast Technology for Mass Housing*
	Dr. Shantanu Sarkar, Director, Uttarakhand Landslide Mitigation & Management Center, Dehradun *Landslide Hazards: Challenges, Issues and Opportunities for Risk Reduction*
	Prof. Daniel Vitorino de Castro Oliveira, University of Minho, Portugal *Improving the Seismic Resistance of Masonry Heritage Buildings: From Concepts to Inorganic Matrix Composites*

01:00 PM - 02:00 PM	**LUNCH**
02:00 PM - 02:30 PM	**Transfer / Travel to CSIR CBRI**
02:30 PM - 4:00 PM	**Guided Visit to CSIR CBRI**
04:00 PM - 4:30 PM	**TEA/COFFEE BREAK**
04:30 PM - 05:30 PM	**BRIGHT SPARK LECTURES** Venue: Rabindranath Tagore Auditorium, CSIR CBRI, Roorkee Chair: **Prof. R. Pradeep Kumar**, CSIR CBRI, Roorkee Co-Chair: **Dr Ajay Chourasia**, CSIR CBRI, Roorkee **Dr. L P Singh**, Director General, NCCBM, Ballabhgarh, Haryana, India *Preparedness for Climate Change Amidst Accelerated Growth for India's Cement Sector* **Mr. Saw Htwe Zaw**, Vice-Chairman, Myanmar Earthquake Committee in Myanmar *M7.7 2025 Mandalay Earthquake; Review from Myanmar Earthquake Clinics*
05:30 PM - 06:30 PM	**CLOSING CEREMONY** ○ Conference Resolution ○ Awards ○ Announcements
06:30 PM - 07:00 PM	**TEA/ COFFEE BREAK**
07.00 PM - 7:30 PM	**ISS Alumni Meet**
07:30 PM Onwards	**FAREWELL DINNER (With Live Music Show)** **Venue: CSIR Central Building Research Institute Lawns**

PROGRAMME: GUIDED TOUR TO CSIR CBRI

Date: Friday, November 21, 2025
Time: 14:30 hrs – 16:30 Hrs.

Time (Hrs.)	Activity	Venue (Responsible Group)
14:30 – 14:45	**CSIR CBRI Exhibition Gallery** *Showcasing Institute's R&D Achievements and Societal Contributions*	Exhibition Gallery (Dr Neeraj Jain & Team)
14:45 – 14:55	**National Earthquake Engineering Test Facility** *Advanced Pseudo-dynamic Test, Structural Health Monitoring, Tests on Building / Building Components*	NEETF Lab. (Dr Chanchal Sonkar & Team)
14:55 – 15:05	***Geotechnical Test Facility*** *Debris flow, Liquefaction Test on Shake Table*	Geotech. Test Lab. (Dr Ganesh, Rajesh & Team)
15:05 – 15:15	***3D Concrete Printing Lab.*** *3D Concrete Printing of building components*	3DCP Lab. (Dr Ashish Kapoor & Team)
15:15 – 15:30	***Fire Research Lab.*** *Fire test of building components; Live Tank Fire*	FRL Lab (Dr Shorab Jain & Team)
15:30 – 15:40	***Rural Technology Park*** *Low cost rural housing technologies*	RT Park (Dr Nagesh & Team)
15:40 – 15:50	***Adv. Concrete & Steel Composite Lab.*** *Corrosion tests, Test on joints using couplers, Waste utilization in Construction*	ACSC Lab (Dr Siva C, Rajesh S & Team)
15:50 – 16:15	***Construction Technology Demonstration Park*** *Emerging construction technologies for housing, Climate Resiliency Evaluation*	Demo Park (Dr Ashish Pipple, Kishore K, Chanchal S, A. Kapoor, Himanshu Sharma)
16:15 – 16:30	***High Tea & Knowledge Sharing Interaction*** *Scientist – Participants Interaction*	Museum Hall

Note: All visitors are requested to adhere to the time schedule to ensure a smooth and enriching visit experience.

Overall visit shall be coordinated by Dr Neeraj Jain & Team.

DAY 3- Saturday, November 22, 2025

Technical Site Visits and Suggested Tour to Indian Culture, Heritage, Traditions- cum-Adventure Sports

Narendra Nagar Landslide Area : The Himalayan terrain in Uttarakhand is geologically weak with steep slopes, tectonic activity, and heavy rainfall that make it prone to landslides. Heavy rain often triggers landslides, and road construction or widening increases the risk. Locals said landslides have risen since the all-weather road work on NH-94. Falling rocks and debris are dangerous, as seen in 2019 when vehicles were stranded, Distance from Conference Venue: 65 Kms



Tehri Dam (Tehri District) in Uttarakhand: Tehri Garhwal (Tehri District), Uttarakhand, hosts one of India's tallest and most complex hydroelectric projects on the Bhagirathi River, providing power, irrigation, and drinking water. Built in challenging Himalayan terrain, it showcases advanced engineering, safety, and sustainability, symbolizing India's innovation and resilience, Distance from Conference Venue: 127 Km


The Mansa Devi area in Haridwar, Uttarakhand:
A localized landslide occurred due to intense rainfall and unregulated slope cutting. The weathered rocky terrain, weakened by erosion and construction near the temple route, led to slope instability. Increased surface runoff raised pore-water pressure, triggering failure. Mitigation: improve drainage and stabilize slopes with retaining structures, Distance from Conference Venue: 20 Km


Traditional Heritage of India

Har Ki Pauri: is the most famous ghat in Haridwar, Uttarakhand, revered as the "Steps of the Lord" because it is believed Lord Vishnu left his footprint here. Devotees flock to witness the spiritually mesmerizing Ganga Aarti every evening, and the site is a major hub during the Kumbh Mela, offering a serene and culturally rich atmosphere.
Distance from Conference Venue: 16 Kms.



The Patanjali Herbal Garden in Haridwar, Uttarakhand: is a serene, lush destination showcasing a wide variety of medicinal plants and herbs used in Ayurvedic products, where visitors can gain knowledge about herbal remedies and natural healing through tours, workshops, and demonstrations. Distance from Conference Venue: 2 Kms.




Laxman Jhula in Rishikesh, Uttarakhand: is a famous suspension bridge over the Ganges River. Surrounded by temples, ashrams, and scenic hills, it attracts pilgrims and tourists alike. The iconic bridge offers breathtaking views, spiritual vibes, and a serene atmosphere, Distance from Conference Venue: 45 Kms.



Traditional Heritage of India

Triveni Ghat in Rishikesh, Uttarakhand: is a serene riverside spot along the Ganges. Known for its tranquil environment, it attracts pilgrims and tourists alike for spiritual activities, morning yoga, and peaceful walks. The ghat offers scenic views of the flowing river, surrounded by lush greenery and distant hills. Distance from Conference Venue: 45 Kms.



Adventure Tour
Experience India's Most Thrilling Adventure Destination!

Rishikesh City, located in Uttarakhand: is a global hotspot for adventure and spiritual tourism. It is Situated on the banks of the River Ganga and surrounded by the Shivalik Hills, (Part of Himalaya area) it offers a unique blend of natural beauty, thrill, and tranquility.
Distance from Conference Venue: 50 kms

Popular Adventure Sports (01:00PM – 2:00PM : LUNCH)

River Rafting
Team-based activity across River Ganga rapids

Bungee Jumping
India's highest fixed platform (272 ft) at Mohan Chatti Safe thrill jump from 20–30 ft into the Ganga

Zip Lining
Glide across the River Ganga with Himalayan Mountain views

Cliff Jumping
On natural cliffs near Shivpuri Rishikesh

Rock Climbing & Rappelling
Trails to Neer Garh Waterfall and Kunjapuri Temple.

Sky Swinger
An exhilarating freefall experience followed by a massive pendulum-like swing

Advertisements

PLATINUM SPONSOR

Built to Innovate

FULL - SCALE EXPERIMENTAL EVIDENCE OF PERFORMANCE

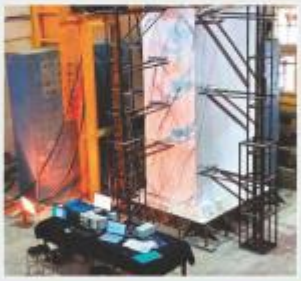

TRIED - TESTED - CERTIFIED 3S PREFAB / PRECAST SYSTEM

SHIRKE®

QUALITY | TECHNOLOGY | CUSTOMER SATISFACTION

B G SHIRKE CONSTRUCTION TECHNOLOGY PVT. LTD.

72-76, Industrial Estate, Mundhwa, Pune - 411 036

Tel.: +91 (20) 2670 8100 | contracts@shirke.co.in | www.shirkegroup.com

PUNE | MUMBAI | BENGALURU | NEW DELHI | NAGPUR | HYDERABAD | CHENNAI

GOLD SPONSOR

Tvasta Manufacturing Solutions

DIGITIZING CONSTRUCTION

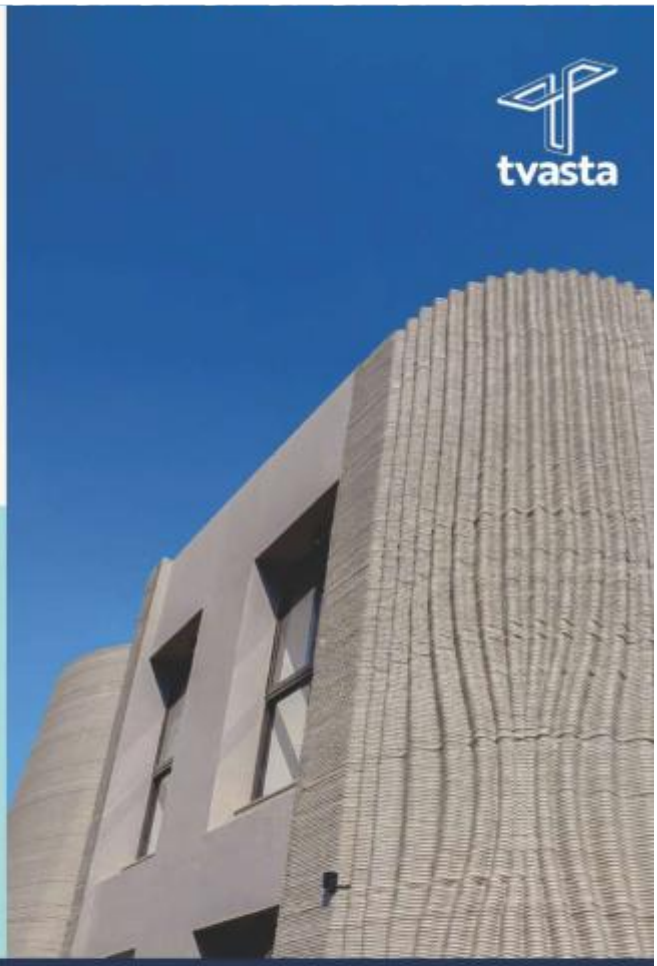

Innovative Construction Solutions

Tvasta Manufacturing Solutions is pioneering innovative construction techniques with advanced 3D printing technology, ensuring a sustainable future for modern building practices and creating efficient, eco-friendly solutions for various construction needs.

Empowering the future of construction with innovation, sustainability, and precision

CORE OFFERINGS

- Industry scale machineries & accessories
- Concerete 3D Printed Construction
- Architectural & Landscape Elements
- Coral Reef Restoration
- Custom 3D Printing Solutions

Why Choose TVASTA?

- Swift construction timelines
- Minimized material waste
- Exceptional design flexibility
- Sustainable and efficient practices
- Demonstrated technology with practical applications

Tvasta Manufacturing Solutions

+91 89258 12337

info@tvastagroup.in

No.172 (Old No.345), Bala estate, Rajiv Gandhi Salai (OMR), Sholinganallur, Chennai – 600119. India

Scan for more information

GOLD SPONSOR

tvasta

CONSTRUCTION

Innovative 3D printed buildings transforming the construction industry for the future.

ARCHITECTURE

Unique architectural elements enhancing aesthetic and functional aspects of modern spaces.

ENVIRONMENT

Sustainable marine interventions promoting biodiversity and ecosystem restoration efforts worldwide.

tvasta

Tvasta Manufacturing Solutions

+91 89258 12337

info@tvastagroup.in

No.172 (Old No.345), Bala estate, Rajiv Gandhi Salai (OMR), Sholinganallur, Chennai – 600119. India

Scan for more information

SILVER SPONSOR

biltech | SIPOREX

Biltech Building Elements Limited

Since 1993, Biltech Building Elements Ltd. (BBEL) has been at the forefront of introducing and shaping the Autoclave Aerated Concrete (AAC) revolution in India. As the country's largest manufacturer of AAC, we have redefined how India builds — with lighter, stronger, and more sustainable solutions. With over 10 lakh cubic meters of AAC manufacturing capacity across 5 plants and 14 delivery points, BBEL has powered 4000+ landmark projects nationwide.

Our product range today includes AAC Blocks, Jointing Mortar, Masonry Reinforcement (Murfor® Compact), and Ready-Mix Plaster — helping create homes and structures that are durable, eco-friendly, and future-ready. BBEL continues to lead with innovation, quality, and trust — building a greener tomorrow, one block at a time.

MEMBER

Bureau of Indian Standards

GRIHA

BBEL products are BIS certified, ensuring the highest standards of quality and safety. The company also actively supports the Green Building Movement through its membership in leading sustainability bodies such as IGBC and TERI–GRIHA, reinforcing its commitment to environmentally responsible construction practices.

Contact persons: Mr Rajat Bahl - CEO; Mr Rajdeep Chowdhury, Business Head – VAP & AAC TPO

FOR TRADE ENQUIRIES PLEASE CONTACT:

BILTECH BUILDING ELEMENTS LIMITED
H.O.: 71& 83, Okhla Industrial Estate, Phase III, New Delhi-110020
L- 011-49696600 ; E: info@biltechindia.com ; W:biltechindia.com

SILVER SPONSOR

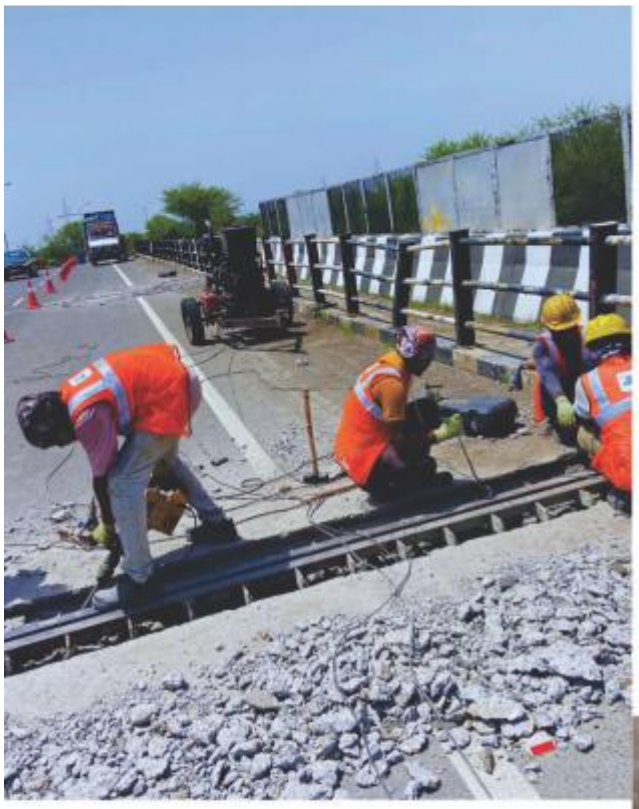

NVLN CONSTRUCTIONS PVT LTD

With proven expertise in repair, retrofitting, and strengthening, we deliver solutions that restore confidence and extend the service life of critical assets.

Our works span diverse sectors — from infrastructure, industrial, and institutional to commercial, residential, and pharmaceutical projects — consistently upholding the highest standards of quality and precision.

OUR SERVICES:

- **Concrete Repairs**
- **Structural Strengthening and Retrofitting**
- **Bridge Repair & Rehabilitation**
- **Repair of Concrete Pavements**
- **Protective Coatings**
- **Non-Destructive Testing Systems**
- **Concrete demolition**

TO KNOW MORE ABOUT US, PLS SCAN

Contact Details : +91 9121333302, Email ID: info@nvlnconstructions.com, Website: www.nvlnconstructions.com

BRONZE SPONSOR

Manufacturer's of PUF Panels (Polyurethane Foam Insulated Panels & PIR Panels (Polyisocyanurate Rigid Foam Insulated Panels) for Walls, Ceiling Floor Roofing, Clean Room Solutions, Modular Panels, Cold Storages, Prefab cottages & Habitats, FRP Insulated Shelters, UPVC Doors, Windows, Ventilators and Glazing's, PUF Insulated Water Storage Tanks.

ACEprefab
Builders & Engineers

Mobile : +91 9888300888, 9463962358, 9888088560, 9876564422
Email : info@aceprefab.com, sales@aceprefab.com
Website : www.aceprefab.com

BRONZE SPONSOR

GROUP PROFILE

The Journey of Excellence began in 1999. It has been on the rise ever since its inception. **Aqua Group** is committed to secure people and premises, wherever lives and property are at risk. Having annual Turnover of more than **150 Crore** we give them the best quality products & services for their needs.

With us you can feel safe. We offer you an extensive portfolio of innovative, high-quality, products, solutions, services and systems for various needs, featuring intelligent functionality and modular concepts that grow with your requirements.

Offering an unrivaled choice and an integrated approach, our company offers a complete range of specialized state-of-the-art products and services for standard or customized applications and projects.

- Highly qualified and technically sound staff has made us competitive in completing the projects within the stipulated timelines.
- We have secured the appreciation of customers, suppliers and peers for quality execution, integrity, efficiency and abilities.

Aqua Group:

1. **Aqua Puf Panels & Heating System**
2. **Aqua Engineers & Fabricators**
3. **Aqua Pharma**
4. **Aqua Motors**
5. **AB Engineering**

(1) Aqua Puf Panels & Heating System is one of the leading providers of turnkey solution for innovative and efficient building products and packaging solution. Organization principal activity comprises of insulated sandwich panel manufacturing, light gauge steel framing and protective Foam packaging.
Cell: +91 9419424038, Email: aquapuf@aquagroup.me

(2) Aqua Engineers & Fabricators help keep pre-engineered steel construction strong and productive through top quality management and supervisory training and participation in departmental and industry related initiatives.
Cell: +91 9797794180, Email: aquaengineers@aquagroup.me

(3) Aqua Pharma is a leading distribution house in valley and are committed to widening our distribution base, so more people can benefit from our world class health products.
Cell: +91 9419075771, Email: aqua_pharma@yahoo.com

(4) Aqua Motors is known for selling genuine auto parts which are tested under various simulated extreme conditions to ensure Quality, Reliability and Durability.
Cell: +91 9906585758, Email: aquamotorskmr@gmail.com

(5) AB Engineering, is the only Authorized Fabricators of OKOTECH uPVC profiles in J&K wherein we fabricate a whole range of innovative uPVC doors & windows for our clients.
Cell: +91 9797794180, Email: abengrs0303@gmail.com

CEO

BRONZE SPONSOR

BRONZE SPONSOR

Bal Raksha Bharat

ABOUT BAL RAKSHA BHARAT

Bal Raksha Bharat (also known as Save the Children) is a registered entity under the Societies Registration Act 1860, working in India since 2004. We are one of the country's leading organisations working for and with children, in alignment with the government's mission. Bal Raksha Bharat functions as an independent Indian organisation, connected with Save the Children Association. This association encompasses Save the Children International and its 30 member countries working to deliver positive change for children through developmental and humanitarian support across 113 countries. With a strong presence across 19 states and 3 Union Territories, our work spans critical child focused areas, including **Education**, **Health & Nutrition**, **Protection**, **Skill-Building & Livelihood**, as well as **Humanitarian and Child-Centric Disaster Risk Reduction.**

COLLABORATIVE APPROACH

Our strategic approach revolves around collaborating with governmental systems, extending support to various Ministries and engaging closely with esteemed institutions such as NITI Aayog, National Institute of Disaster Management, and National Skill Development Corporation. We envision to positively impact the lives of children in India and to ensure full participation of Bal Raksha Bharat with all stakeholders, in the journey of developed India (Viksit Bharat) —where every child enjoys a healthy, nourished, protected and inclusive childhood, to fulfil their aspirations.

IMPACT

Since 2021, we have impacted the lives of approximately **35 lakh children** through our focused interventions. This scale of impact, across India, has been achieved through the successful implementation of **234** projects, in collaboration with **160** generous Corporate and Institutional donors along with numerous individual supporters.

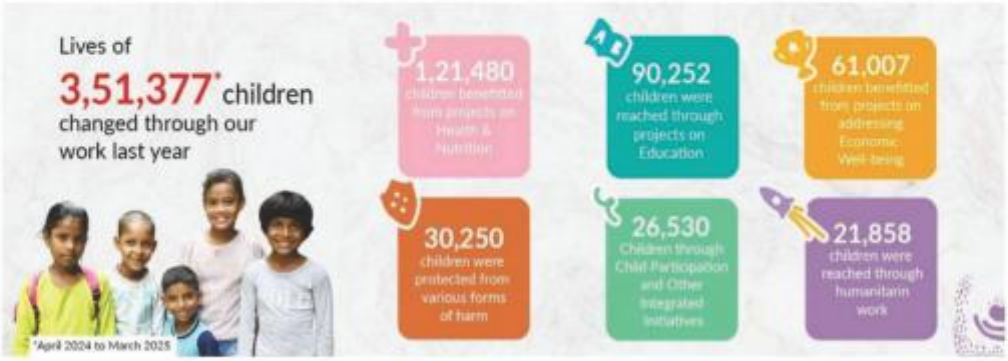

BRONZE SPONSOR

TECHFAB INDIA

At the Heart of Geosynthetic Activity

MASTERING GEOTECHNICAL CHALLENGES

INNOVATING WITH GEOSYNTHETICS FOR 22 YEARS

Your Trusted Partner in Geosynthetic & GeoHazard Mitigation Innovation

We, at TechFab India, are committed to Excellence in everything we do. Our unwavering dedication to quality, innovation and customer satisfaction drives us to consistently deliver products and services that exceed expectations.

Our Offerings are :

- ***Geogrid***
- ***TechLink***
- ***Geocell***
- ***Gabion***
- ***GeoMattress***
- ***Polymeric Strip***
- ***Erosion Control Mat***
- ***Fabric Form Grout Mattress***
- ***Woven & Nonwoven Geotextiles***
- ***Geotextile Bags & Tubes***
- ***Drainage Geocomposites***
- ***Prefabricated Vertical Drains (PVD)***
- ***Rhomboidal Steel Cable Mesh Panels***
- ***High Tensile Steel Wire Mesh***
- ***Self Drilling Anchors***
- ***Weld Mesh***

GET IN TOUCH

+91 - 22 - 2287 6224
+91 - 22 - 4186 0100

info@techfabindia.com
www.techfabindia.com

46/47, Maker Chambers VI,
Nariman Point, Mumbai - 400021

SUPPORTING SPONSOR

TICENT ENERGY

India is now the world's third-largest automobile market — yet only about 2% of vehicles on our roads are electric. At the same time, the country ranks as the third-largest emitter of greenhouse gases.

The opportunity and the responsibility to accelerate clean mobility is immense. At Ticent Energy, we are committed to transforming India's mobility landscape by rapidly increasing EV adoption. Our mission is to build a high-performance EV charging network through a chain of large-scale, rapid charging hubs/stations located in prime and premium zones across the 15 busiest Indian cities by 2030.

We believe it is time to move beyond traditional deployment of EV chargers i.e. isolated, unmanned and unreliable public chargers - Instead pioneer Next-Generation EV Charging Landmarks. Our vision is to build human-assisted, state-of-the-art EV charging landmarks — each equipped with 8 to 32 simultaneous fast-charging guns, guaranteeing 80% SOC within 30 minutes and backed by a 24×7 uptime promise for unmatched reliability and seamless customer experience.

We are proud to introduce India's first 4-gun high-performance DC fast charger - engineered to be the most efficient and intelligent EV charger available in the country today. Purpose - built for Indian use conditions, it is an ideal product offering unmatched reliability and performance.

The genesis of our innovation lies in addressing two major limitations of existing EV chargers in India: Foreign-Centric Charger Designs and poor Software – Hardware Integration

VISION

Pioneer in establishing a reliable network of high-speed charging stations for electric vehicles.

MISSION

Accelerating clean mobility through innovative fast charging solutions.

WE ARE BACKED BY

DPIIT #startupindia · DST NIDHI PRAYAS · TIDES · IIMB · NSRCEL

TICENT ENERGY PRIVATE LIMITED
HOUSE NO. 54, B.T. GANJ, ROORKEE, UTTARAKHAND-247667
GSTIN: 05AALCT4762E1Z9 | CIN: U27200UT2024PTC018356
+91-7022621707 | ENQUIRY@TICENTENERGY.COM | WWW.TICENTENERGY.COM

SUPPORTING SPONSOR

I. R. TECHNOLOGY SERVICES PVT. LTD.
9th Floor, C-0901 Tower-C, ATS Bouquet, Plot- A2/2, Sector-132,
Noida, Gautam Buddha Nagar, Uttar Pradesh, 201305, India
Ph: +91-120-4530800 || Email: sales_del@irtech.in

Since its inception in 1961, **I. R. TECHNOLOGY SERVICES PVT LTD,** has been in the field of marketing sophisticated analytical and medical instruments in India. This company has pioneered in introducing the 'state-of-the –art' instruments technology in India with over four decades of experience of experience in various leading industries and research laboratories of India. I R Tech has been associated with a number of reputed and most prestigious instrument manufactures from U.S.A, Japan, Germany, Canada, Finland etc. To provide support to the customers I R Tech has offices all over India at strategic locations like Mumbai, Noida, Kolkatta, Bangalore, Hyderabad, Chennai & Jamshedpur. Each of the offices has technically qualified sales and services personnel to support the customers. Coupled with quality and effective support, you can rely on IRTECH as your reliable partner in research instrumentation.
We have partnered with some of the best manufactures of analytical instruments.

Rigaku

Since its inception in Japan in 1951, Rigaku Corporation has been at the forefront of analytical and industrial instrumentation technology. With hundreds of major innovations to its credit, Rigaku and its subsidiary companies are world leaders in the fields of X-ray spectrometry, X-ray diffraction, X-ray optics, as well as small molecule and protein crystallography.

- WD XRF (Bench top- 50W and 200W, Floor Model – 3KW XRF, 4KW XRF, Tube above configuration, tube below Configuration) (inverted optics for analysis for pressed pellets or fusions, inclusion analysis, Homogeneity testing with ration mapping, formula calculations, Ratios of distributions, C114 accreditation Analysis without standards, Automation)
- XRD (Bench top-450W, Floor Model – 3KW, 9KW, 18KW, 2e/e, e/e)
- Thermal Analyser (TG/DTA/DSC/TMA)
- Protein Crystallography System
- **Handheld Raman Spectrometer- Progeny**


Xtalab Synergy


Miniflex


SmartLab


Supermini200


ZSX Primus


Progeny

LECO
Delivering the Right Results

Since 1936 LECO is first choice for scientists all around the World for below instruments.

- Isoperibol Bomb Calorimeter for Gross Calorific Content, Proximate Analyzer, GD based Optical Emission Spectrometer.
- Pegasus® 4D GCxGC-TOFMS, High resolution GC TOF MS and 2D Gas Chromatography.
- Elemental analyzer – Carbon, Hydrogen, Nitrogen, sulfur and Oxygen in both organic and inorganic samples.

Pegasus 4D GC TOFF MS


CHN628


Bomb Calorimeter AC500


GDOES

MILESTONE
MICROWAVE

Milestone vision is to help chemist in the field of AAS and ICP by providing the most technologically advanced microwave instrumentation for sample preparation in research and quality control

OLYMPUS

Mumbai	Bangalore	Kolkata	Hyderabad
EL - 91, TTC INDUSTRIAL AREA, ELECTRONIC ZONE, MIDC, MAHAPE, NAVI MUMBAI - 400 710	208, SWISS COMPLEX, 33, RACE COURSE ROAD, BANGALORE – 560 001	22, ASHUTOSH CHOWDHURY AVENUE, FLAT NO. 12, 1ST FLOOR, KOLKATA – 700 019	406, AGARWAL CHAMBERS, 5-9-1121, KING KOTHI, HYDERABAD – 500 001
TEL : 022 - 41571111 / 27611228	TEL : 080 – 2225 5936 / 22203173	TEL : 033 – 2461 5831 /2461 5832	TELEFAX : 040 – 66842401 / 02
FAX : 022 - 41571155	FAX : 080 – 51136045	FAX : 033 – 2461 5021	EMAIL : sales_hyd@irtech.in
EMAIL : sales_newbom@irtech.in	EMAIL : sales_blr&@irtech.in	EMAIL : sales_cal@irtech.in	

SUPPORTING SPONSOR

apple chemie

triggering transformation

3D CONCRETE

Apple Chemie offers all solutions to 3D concrete construction

Materials ▪ Additives

CONTACT US:

APPLE CHEMIE INDIA PVT LTD

E: sales@applechemie.com
M: 9822471468 / 9822471455
W: www.applechemie.com

TERMIPORE INSTALLATION:

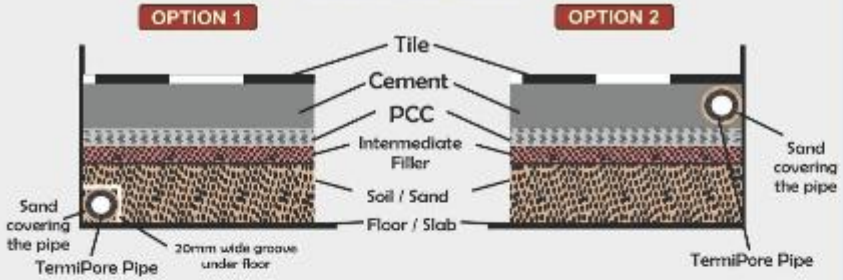

- ☑ Lay TermiPore on a bed of coarse sand and cover it with coarse sand or small pebbles. Ensure it has a cover of coarse sand or small pebbles on all sides.
- ☑ Use clamps and cable tie to secure TermiPore Pipe in place
- ☑ Use a junction box at every 25 to 40 meters of TermiPore Pipe
- ☑ Ensure that the open ends of the pipe in junction box are properly closed with end plugs. Open them only at the time of injecting termiticide.
- ☑ For best results, dilute water based termiticides with low TDS soft water
- ☑ After injecting SC termiticide, you can choose to flush out the heavy suspension with a small quantity of clean, soft water after the injection and clear the pipe holes
- ☒ TermiPore should not come in direct contact with wet cement
- ☒ Do not bend TermiPore at sharp corners, use elbows instead
- ☒ Do not bring TermiPore above floor / ground level. Use plain plastic pipe or even better, use metal nipples and expose only that part in the junction box.

CONTACT US:

+91 63592 92525 / +91 84010 17087

marketing@termipore.com

FOLLOW US:

Termipore

www.termipore.com

SUPPORTING SPONSOR

TermiPore

ANTI-TERMITE RETICULATION PIPE

INTERNATIONALLY PROVEN TERMITE PREVENTION TECHNOLOGY

Effective and safe termite prevention solution

Install a network of TermiPore Anti-Termite Reticulation Pipes

Inject termicide at regular intervals and bid good-bye to termites

TERMIPORE ADVANTAGES:

- ☑ Concealed installation
- ☑ Easy to install
- ☑ High thickness
- ☑ Manufactured by an ISO 9001:2015 certified company
- ☑ Stringent quality control
- ☑ Long lasting
- ☑ Consistent flow
- ☑ Uniform micro holes throughout the pipe (50-80 per meter)

www.termipore.com

TermiPore

TermiPore offers multiple product options:

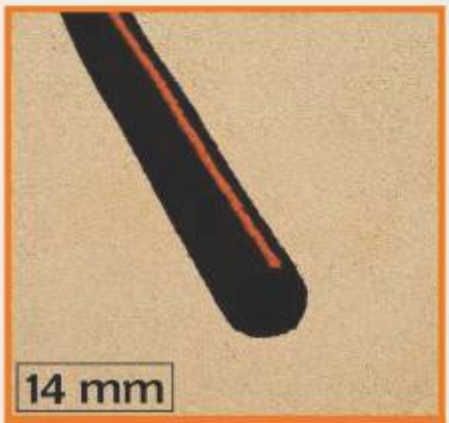

14 mm

- Size 9.5X14.5 mm commonly called 14mm(Orange Line)
- Supplies pesticides in long lengths with less outlets

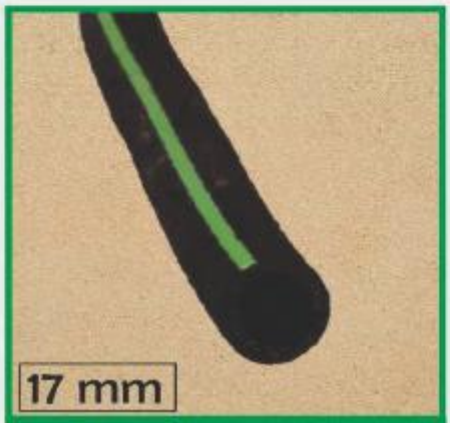

17 mm

- Size 12.5X17.5 mm commonly called 17mm (Green Line)
- Higher inside diameter for improved pesticide flow

19 mm

- Size 12.5X19.5 mm commonly called 19mm (Red Line)
- High thickness premium pipe for more load bearing and high consistency of flow

TERMIPORE ACCESSORIES:

Elbow

Tee

Jointer

Feeder Pipe

End Plug

Barbed Clamp

Junction Box

FOLLOW US: Termipore

SUPPORTING SPONSOR

ANTI - TERMITE RETICULATION PIPE

TermiPore is manufactured by an ISO 9001:2015 certified company.
Quality and proper systems come naturally to us.
Every single roll is tested for 9+ quality parameters, including:

- Inside and outside dimensions
- Wall thickness and concentricity
- Bending radius and locking angle
- Micro hole performance at various pressures
- Flow rate at various pressures
- Flow distance covered
- Flow uniformity along length and circumference
- Material dispersion uniformity
- Accuracy in length and uniformity in weight

We don't just do sample testing, but check 20% to 40 % length of pipe for proper flow in every single roll

TermiPore is also tested in-house and by authorized laboratories for:

- AWT – Accelerated Weathering Test
- ESCR – Environment Stress Crack Resistance
- RoHS – Restriction of Hazardous Substances
- Compatibility with various termiticides like Imida Clorpid, Fipronil, Chloropyrophos, etc
- Uniformity in flow rate over multiple injections over many months
- Durability and structural integrity over many years in soil and under PCC

TermiPore Pipe can be installed at various stages of construction.

AT PLINTH / GROUND LEVEL

BELOW TILES

AROUND BUILDING PERIPHERY

+91 63592 92525 marketing@termipore.com

PLATINUM SPONSOR

Built to Innovate

FULL - SCALE EXPERIMENTAL EVIDENCE OF PERFORMANCE

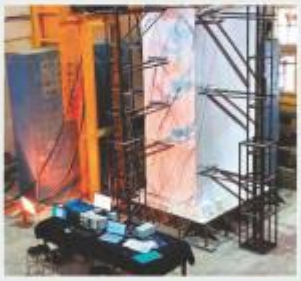

TRIED - TESTED - CERTIFIED 3S PREFAB / PRECAST SYSTEM

SHIRKE®

QUALITY | TECHNOLOGY | CUSTOMER SATISFACTION

B G SHIRKE CONSTRUCTION TECHNOLOGY PVT. LTD.

72-76, Industrial Estate, Mundhwa, Pune - 411 036

Tel.: +91 (20) 2670 8100 | contracts@shirke.co.in | www.shirkegroup.com

PUNE | MUMBAI | BENGALURU | NEW DELHI | NAGPUR | HYDERABAD | CHENNAI

2025

HOW

The 4th International Symposium on

One Health, One World

Organised By

CSIR

CBRI
केंद्रीय भवन अनुसंधान संस्थान, रुड़की
Central Building Research Institute, Roorkee
सुरक्षित और टिकाऊ आवास
Safe & Sustainable Habitat

OneHealth OneWorld
ワンヘルス・ワンワールド連携研究機構

INSTITUTE OF INDUSTRIAL SCIENCE · THE UNIVERSITY OF TOKYO

Co-sponsor

NATIONAL DISASTER MANAGEMENT AUTHORITY

USDMA

Platinum Sponsor

SHIRKE®

QUALITY | TECHNOLOGY | CUSTOMER SATISFACTION

Gold Sponsor

NBCC (INDIA) LIMITED

tvasta

Punjab & Sind Bank

Silver Sponsor

AVLA®

UltraTech CEMENT
INDIA'S NO. 1 CEMENT

magicrete®
magic behind happy homes

biltech™

IRCLASS
SYSTEMS AND SOLUTIONS PRIVATE LIMITED

Bronze Sponsor

AQUA GROUP

REBUILD
TECHNOLOGIES SERVICES PVT. LTD.

ABC
Amata Build Care Solutions

ACE prefab

TECHFAB INDIA
At the Heart of Geosynthetic Activity

IHMS

Supporting Sponsor

IR TECH

apple chemie
triggering transformation

TermiPore

Bal Raksha Bharat
Also known as Save the Children

bmtpc

Theme

Climate Change and Green Recovery (CCGR)

Distinguished Speakers

Keynote Speakers

ABS ID: KN-02

Organic Electronic Devices for Chemical Sensing

T. Minami
Associate Professor, Institute of Industrial Science, The University of Tokyo, Tokyo, Japan Correspond to T. Minami (tminami@g.ecc.u-tokyo.ac.jp)

Keywords: *Organic Transistor, Chemical Sensor, Molecular Recognition, Real-Sample Analysis.*

1. GENERAL INSTRUCTIONS

Real samples contain abundant chemical species playing crucial roles in environmental assessments, food analysis, and diagnostic fields. Conventionally, large-sized analytical instruments have been widely applied to real-sample analysis owing to their accuracy. However, the applicability of such a well-established instrumental approach is still a concern in on-site analysis because of the complicated detection principle that requires trained personnel and time-consuming operation. Herein, the author introduces an approach for the development of chemical sensor devices based on organic field-effect transistors (OFETs). OFETs, consisting of gate, source, and drain electrodes, are electronic devices showing switching characteristics by applying voltage [1]. The applicability of solution processes in device fabrication has accelerated the manufacturing of OFET-based chemical sensors. By combination with appropriate molecular recognition materials, the OFET can demonstrate quantitative changes in transistor characteristics such as threshold voltages (VTHs) and drain currents (IDSs) upon analyte capture [2]. Notably, the amplification ability of OFETs contributes to sensitive detection over conventional electrochemical methods. Meanwhile, the instability of organic semiconductive layers of OFETs under ambient conditions is a bottleneck for chemical sensing in aqueous media. Considering this, an extended-gate structure was selected as a configuration of an OFET-based chemical sensor in this study (Figure 1). The OFET device is isolated from a sensing gate in this structure, which qualitatively and quantitatively detects changes in transistor characteristics upon analyte capture at an electrode functionalized with a molecular recognition material.

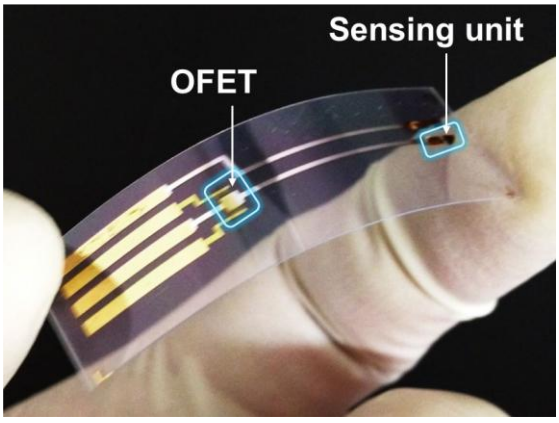

Figure 1. Photograph of the manufactured extended-gate-type OFET chemical sensor.

2. DESIGN OF MOLECULAR RECOGNITION MATERIALS

Chemical species detected in real samples show various molecular geometries, sizes, and charges. Therefore, receptors are designed based on molecular recognition chemistry,

considering the above factors. Among the selection of materials, biological materials such as enzymes and antibodies have been employed in analytical chemistry fields, owing to their favorable specificities to analytes based on the lock-and-key recognition principle. However, detectable analyte structures are limited by a library of these biological materials. Therefore, artificially synthesized receptors based on molecular recognition chemistry are promising approaches in the design of recognition sites. In this study, molecularly imprinted polymers (MIPs) were applied to molecular recognition materials for selective detection [3][4]. MIPs provide three-dimensional recognition networks against specific analytes. A pre-organized structure constructed by a template (i.e., analyte) and functional monomers can be optimized using quantum chemical calculation methods. Such optimized MIP structures contribute to selective detection even in the presence of interferents. In contrast, cross-reactive artificial receptors can be applied to the simultaneous detection of multiple analytes by using pattern recognition methods [5][6] (Figure 2).

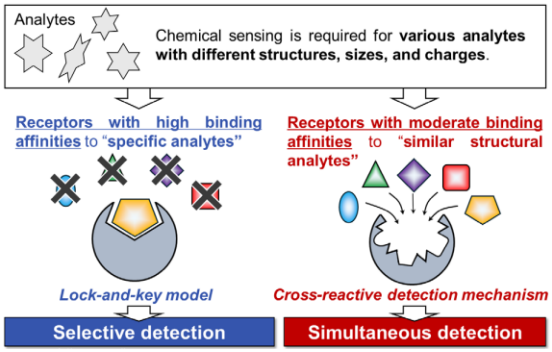

Figure 2. Conceptual illustration of molecular recognition materials and their detection mechanisms.

3. CONCLUSIONS

The author has revealed the potential of OFETs as chemical sensor platforms for real-sample analysis by combining with artificially synthesized receptors. This presentation will discuss the usability of OFET-based chemical sensor devices based on fusion technologies of organic electronics and molecular recognition chemistry.

REFERENCES:

[1] T. Minami et al., ACS Sens. 4 (2019) 2571–2587 (Invited Perspective, Cover).

[2] T. Minami et al., ACS Appl. Mater. Interfaces 17 (2025) 31165–31173 (Invited Perspective, Cover).

[3] T. Minami et al., Sens. Actuators B Chem. 382 (2023) 133458 (Invited Paper).

[4] T. Minami et al., Chem. Commun. 61 (2025) 9872–9875 (Invited Paper, Cover).

[5] T. Minami et al., J. Mater. Chem. C 9 (2021) 11690–11697. (Invited Paper, Cover).

[6] T. Minami et al., ACS Appl. Mater. Interfaces 14 (2022) 22903–22911 (Invited Paper, Cover).

ABS ID: KN-016

Translating the one Health Framework into Action: A Case of Bal Raksha Bharat's Integrated Health and Climate Resilience Programs

Santanu chakraborty[1], Dr. Tanvi chauhan[2], mintu debnath[3], naveen shukla[4]
[1]*Chief Executive Officer, Bal Raksha Bharat, New Delhi, India*
[2]*Senior National Manager, Health Programmes, Bal Raksha Bharat, New Delhi, India*
[3]*Head- Humanitarian, DRR and Climate Action, Bal Raksha Bharat, New Delhi, India*
[4]*National Manager, Humanitarian, DRR and Climate Action, Bal Raksha Bharat, New Delhi, India*
Correspond to S. CHAKRABORTY (s.chakraborty@balrakshabharat.org)

1. UNDERSTANDING THE ONE HEALTH APPROACH

The One Health approach recognizes that the health of people, animals and the environment are deeply interconnected. It promotes collaborative, multi-sectoral and transdisciplinary action to prevent, detect and respond to health threats that arise at the interface of these three domains. By integrating efforts across public health, veterinary, agriculture, environment and community systems, One Health aims to build resilience against zoonotic diseases, antimicrobial resistance (AMR), foodborne infections and climate-related health impacts.

Globally and nationally, this approach is embedded within the National One Health Mission, National Programme for Prevention and Control of Zoonoses (NCDC) and Delhi Declaration on AMR, calling for a unified response that bridges human and animal health with environmental stewardship and behavioral change.

Climate change poses a profound and accelerating threat to child health, intensifying vulnerabilities across generations. Children born in 2020 will face, on average, twice as many wildfires, 2.8 times more crop failures, 2.6 times more droughts, 2.8 times more river floods, and 6.8 times more heatwaves compared to their grandparents born in 1960. By 2050, climate change is projected to cause 40 million more children to be stunted and 28 million more to suffer from wasting, reflecting the compounding impacts of food insecurity and disease burdens.

In India, rising temperatures and erratic rainfall have increased the incidence of vector- and water-borne diseases such as malaria, dengue, cholera, jaundice, and diarrhoea—conditions that disproportionately affect children. Post-disaster contamination of water sources often leads to more child deaths from diarrhoeal illnesses than the disaster itself. Unsafe drinking water, poor sanitation, and open drains contribute to recurrent infections, chronic malnutrition, and weakened immunity among children.

Community-level evidence, drawn from a national study conducted by Save the Children and PwC (2020), underscores the magnitude of this crisis:

- Over 90% of households in Purulia, South 24 Parganas, and Uttarkashi reported health impacts of climate change.
- In Purulia and South 24 Parganas, 58% of parents reported children suffering from dehydration, skin diseases, and allergies due to rising temperatures.

• In Madhya Pradesh, about 50% of households reported similar heat-related illnesses among children.

• In Uttarakhand, 30% of families reported that children were injured during floods and landslides.

• In Haridwar and Uttarkashi, over 50% of parents reported that children fell ill post-extreme events, and 39% required hospitalization.

These realities make clear that climate change is not only an environmental crisis but a child survival and development emergency, amplifying disease, malnutrition, and inequity among India's most vulnerable populations.

This paper positions Bal Raksha Bharat (BRB) as an on-ground implementer translating the One Health framework into action — bridging community behavior, food safety and health system resilience through integrated programs on nutrition, safe food practices and climate-linked health preparedness. BRB demonstrates how One Health can be operationalized from households to health systems, advancing India's vision for a resilient and sustainable public health ecosystem.

2. CONNECTING ONE HEALTH TO BRB'S WORK

BRB (Save the Children) translates the One Health vision into practical, community-driven action by linking nutrition, food safety, hygiene, and health system preparedness, BRB operationalizes One Health principles from the household to system level. Some of the examples from BRB's work include;

• Through collaboration with FSSAI under the Eat Right initiative, BRB promotes safe food handling, responsible consumption and antimicrobial stewardship — addressing the human and food system dimensions of One Health.

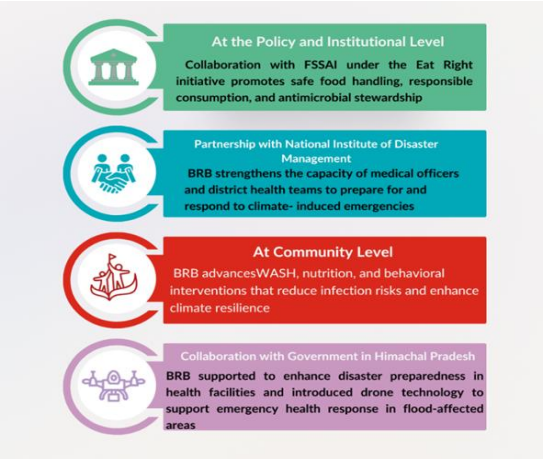

Figure 1. Framework into action

• In partnership with the National Institute of Disaster Management (NIDM), BRB builds the capacity of medical officers and district health teams to prepare for and respond to climate-induced emergencies, reinforcing the health system and environmental dimensions of the framework.

• At the community level, BRB strengthens WASH, nutrition and behavioral interventions that reduce infection risks, enhance climate resilience— bringing One Health principles into everyday practice.

• Through the Himachal Pradesh Flood Response project, BRB strengthened the disaster preparedness and resilience in 15 health facilities in Mandi and Solan districts by developing Health Facility Disaster Management Plans, risk profiling and conducting mock drills with active participation from medical and community staff. These initiatives enhanced the readiness of health centres to remain functional during any future extrema weather event, improved coordination among frontline workers and built local capacity to respond swiftly to health emergencies, ensuring uninterrupted essential healthcare services during future climate shocks. The initiative has also successfully introduced drone technology to

strengthen emergency health response in flood-affected areas of Himachal Pradesh to deliver essential medical supplies to remote and cut-off areas, ensuring timely access to life-saving medicines and continuity of healthcare services during climate-induced disasters.

Together, these initiatives demonstrate how One Health

can move beyond policy into operational resilience —

protecting children, families and ecosystems through an integrated, prevention-focused approach.

3. CONCLUSION

Bal Raksha Bharat's experience demonstrates that One Health must be people-centered and child-focused to drive real impact. Strengthening the interface between human, animal, and environmental health requires:

• Integrating climate resilience into public health systems.

• Empowering children and youth as agents of change in climate and health advocacy.

• Leveraging technology and partnerships for timely, inclusive responses.

Operationalizing One Health at the community level ensures that India's most vulnerable—especially children—are not left behind. A healthy planet is the foundation of a healthy child and a sustainable future.

REFERENCES:

[1] Save the Children & PwC India, Protect a generation, climate security for India's Children Save the Children, New Delhi, 2020

[2] Save the Children, Born into the Climate Crisis2: An Unprecedented Life: Protecting Children's Rights in a Changing Climate Save the Children International, London, 2025.

Bright Spark Lecture

Oral Presentations

ABS ID: 172
Code No: CCGR-0P-01

Ms. Priti jha

ABS ID: 101
Code No: CCGR-0P-02

Exploring The Effect of Zeolite 13x And Olivine Sand on Co2 Sequestration in Concrete

V.n. Shah[1], t. M. Joshi[2], m.j. Lashaki[3], and u.v. Dave[4]
[1]*Ph.D. Student, Civil Engineering Department, Nirma University, Ahmedabad, India,*
[2]*Assistant Professor, Civil Engineering Department, Nirma University, Ahmedabad, India,*
[3]*Assistant Professor and Graduate Program Director, Department of Civil, Environmental and Geomatics Engineering, Florida Atlantic University, Boca Raton, USA,*
[4]*Professor, Civil Engineering Department, Nirma University, Ahmedabad, India,*
Correspond to Dr. Tejas Joshi (tejas.joshi@nirmauni.ac.in)

Keywords: *Carbon Sequestration in Concrete, Zeolite 13X, Olivine Sand, High-purity CO2 curing environment, Sustainable Construction Materials, Thermogravimetric Analysis, Green Construction.*

1. INTRODUCTION

The cement and concrete industry contribute nearly 8% of global CO2 emissions, challenging sustainable development. Conventional mitigation alone is insufficient, prompting interest in mineralization-based CO2 sequestration in concrete, which enables permanent storage while improving performance. Zeolite 13X offers high CO2 adsorption, and Olivine Sand facilitates irreversible mineral carbonation. This study investigates their separate use in concrete to enhance CO2 uptake and mechanical properties, providing a scalable approach for green construction.

2. LITERATURE REVIEW

Zeolites are highly efficient porous materials for CO2 adsorption due to their tunable frameworks, surface chemistry, and ion-exchange properties. Advances include wash coating of 13X onto microchannel monoliths, maintaining thin layers for effective uptake [1], and solar driven synthesis of 4A and 13X from kaolin and halloysite, achieving CO2 capacities up to 2.15 mmol/g with calcination temperature control [2]. Zeolite assisted internal carbonation in BOFS - OPC systems enhanced early-age strength via CaCO3 precipitation, especially at 20 wt% CO2 impregnated zeolites [3], while 13X and 4A effectively upgraded biogas, with 13X showing superior CO2 selectivity and enhanced uptake under humid conditions [4]. Na^+ exchanged erionite improved micropore accessibility and adsorption capacity [5]. Olivine, a naturally abundant silicate, enables durable mineral carbonation for CO2 sequestration. Its reactivity depends on CO2 partial pressure, temperature, stirring, and sodium salts, which enhance ionic strength and carbonate crystallization [6]. Biotic and physical factors in natural settings accelerate weathering, while ultramafic rocks like dunite can simultaneously generate H2 and sequester CO2 [7,8]. Mechanical activation of olivine increases lattice disorder, promoting formation of stable carbonates such as hydro magnesite [9]. However, large scale coastal spreading is limited by kinetics, logistics, and health concerns, with terrestrial tropical applications offering better feasibility [10]. Although both zeolites and olivine have significant CO2 sequestration potential, their individual integration into concrete remains underexplored, particularly regarding mechanical properties, durability, and long-term stability. This study investigates the

separate use of Olivine Sand (10 - 40% sand replacement) and Zeolite 13X (2.5 - 10% cement addition) on the compressive strength and CO2 uptake of M30 concrete.

3. MIX DESIGN AND PROCEDURE

For the Olivine Sand mix design, OPC 53 grade cement, natural fine aggregates, Olivine Sand as partial replacement of fine aggregates, 10 mm coarse aggregates, and a PCE-based superplasticizer were used to achieve the desired workability. For the Zeolite mix design, OPC 53 grade cement, natural fine aggregates, Zeolite 13X as a cement additive, 10 mm coarse aggregates, and a PCE-based superplasticizer were used. All materials conform to relevant IS specifications. The detailed mix proportions for both designs are summarized in Table 1 below. For each mix design, two sets of nine concrete cubes (100 mm × 100 mm × 100 mm) were prepared. Normal mixing procedures were followed, with the exception that Zeolite 13X was thermally activated at 400 °C for 3 hours prior to incorporation into the mix. After casting, one set of cubes was left to dry under ambient air for 24 hours, while the other set was placed in a sealed CO2 curing chamber maintained at 0.2 psi with 99.9% pure industrial-grade CO2. All cubes were then demoulded. The air-dried cubes were kept in water curing until the testing day. The CO2 cured cubes were further exposed to CO2 curing for an additional 24 hours, completing a total of 48 hours, after which they were transferred to water to compensate for moisture loss until testing. Cube weights were recorded at each stage of the procedure. The CO2 curing chamber set up is shown in Figure 1 below.

4. RESULT AND DISCUSSION

Compressive strength of all concrete mixes will be evaluated at 7, 14, and 28 days using 10 × 10 × 10 cm cubes. Two sets, air-dried and CO2-cured, will allow comparison of normal hydration and accelerated.

Fig. 1 CO2 Curing Chamber

carbonation. CO2 uptake will be measured via the analytical weight gain method and verified

by Thermogravimetric Analysis (TGA) to assess carbonation extent. The evaluation of compressive strength and CO2 uptake for the prepared concrete mixes is currently underway.

Table 1 Mix Design

Mix ID	Cement	Natural Fine	Coarse Aggregate	Water	Olivine Sand	Zeolite 13X	Super plasticizer
NC	322	862	1020	176	0	0	1.61
OS1	322	776	1020	176	86	0	1.61
OS2	322	690	1020	176	172	0	1.61
OS3	322	603	1020	176	259	0	1.61
OS4	322	517	1020	176	345	0	1.61
Z1	322	857	1014	176	0	8	1.61
Z2	322	851	1007	176	0	16	1.61
Z3	322	846	1000	176	0	24	1.61
Z4	322	840	994	176	0	32	1.61

The use of Olivine Sand and Zeolite 13X in concrete has the potential to reduce the carbon footprint of construction materials by enhancing CO2 sequestration, making it suitable for precast elements, pavements, and non-structural components where sustainable solutions are prioritized. By lowering embodied CO2 in concrete, such mixes support Sustainable Development Goals (SDGs) related to climate action and sustainable infrastructure. Future studies should focus on long-term durability, carbonation depth, and performance under varied environmental conditions to ensure practical applicability and structural reliability of carbon-sequestering concrete.

REFERENCES:

[1] Bondugula, M. S. R., Ege, F., & Pahinkar, D. G. (2024). Ethanol-enhanced wash-coating of zeolite 13X on microchannel walls for CO2 capture. Separation and Purification Technology, 345, 127411.

[2] Pasabeyoglu, P., Deniz, E., Moumin, G., Say, Z., & Akata, B. (2024). Solar-driven calcination of clays for

sustainable zeolite production: CO2 capture performance at ambient conditions. Journal of Cleaner Production, 477, 143838.

[3] Wang, Z., Pham, B. T., Wang, X., & Ling, T. C. (2025). Understanding the synergistic effects of CO2-impregnated zeolite in cement pastes blended with 70% BOFS. Journal of Industrial and Engineering Chemistry.

[4] Montanari, T., Finocchio, E., Salvatore, E., Garuti, G., Giordano, A., Pistarino, C., & Busca, G. (2011). CO2 separation and landfill biogas upgrading: a comparison of 4A and 13X zeolite adsorbents. Energy, 36(1), 314-319.

[5] Hernandez, M. A., Pestryakov, A., Portillo, R., Salgado, M. A., Rojas, F., Rubio, E., ... & Petranovskii, V. (2015). CO2 sequestration by natural zeolite for greenhouse effect control. Procedia Chemistry, 15, 33-41.

[6] Wang, F., Dreisinger, D., Jarvis, M., & Hitchins, T. (2019). Kinetics and mechanism of mineral carbonation of olivine for CO2 sequestration. Minerals Engineering, 131, 185-197.

[7] Schuiling, R. D., & De Boer, P. L. (2010). Coastal spreading of olivine to control atmospheric CO2 concentrations: A critical analysis of viability. Comment: Nature and laboratory models are different. International Journal of Greenhouse Gas Control, 4(5), 855-856.

[8] Al Kalbani, M., Serati, M., Hofmann, H., Bore, T., & Roshan, H. (2025). In-situ low-temperature CO2 mineralization and hydrogen tracing using ultramafic rocks from Australia and New Zealand. Gas Science and Engineering, 134, 205531.

[9] Turianicová, E., Baláž, P., Tuček, Ľ., Zorkovská, A., Zeleňák, V., Németh, Z., ... & Kováč, J. (2013). A comparison of the reactivity of activated and non-activated olivine with CO2. International Journal of Mineral Processing, 123, 73-77.

[10] Hangx, S. J., & Spiers, C. J. (2009). Coastal spreading of olivine to control atmospheric CO2 concentrations: A critical analysis of viability. International Journal of Greenhouse Gas Control, 3(6), 757-767.

ABS ID: 06
Code No: CCGR-0P-03

Ms. Ratnakala

ABS ID: 96
Code No: CCGR-0P-04

Case Study of Urban Heat Island Impact Through Surface Temperature Profiling in Ahmedabad Using Thermal Infrared Imaging

T.m. Joshi[1], n.n. Vanani[2], j.h. Machchhoya[2], v.a. Thakkar[2] and u.v. Dave[3]
[1]Assistant Professor, Civil Engineering Department, Institute of technology, Nirma University, Ahmedabad, India,
[2]UG Student, Civil Engineering Department, Institute of technology, Nirma University, Ahmedabad, India,
[3]Professor, Civil Engineering Department, Institute of technology, Nirma University, Ahmedabad, India,
Correspond to Dr. T.M. JOSHI (tejas.joshi@nirmauni.ac.in)

Keywords: *Urban Heat Island (UHI), Surface Temperature Analysis, Thermal Infrared Imaging, Pavement Heat Retention, Sustainable Urban Planning, Ahmedab*

1. INTRODUCTION

The Urban Heat Island (UHI) effect, characterized by elevated temperatures in metropolitan cores relative to rural environs, poses a significant environmental challenge in rapidly urbanizing regions. This phenomenon is exacerbated in semi-arid cities like Ahmedabad, India, where intense solar insolation and the proliferation of low-albedo, impervious surfaces such as asphalt and concrete synergistically intensify thermal stress [1]. Conventional UHI assessments, often reliant on satellite-derived Land Surface Temperature (LST) data, lack the spatial resolution to resolve micro-scale thermal variations dictated by specific material properties and urban morphology [2]. The location of the 12 study sites within Ahmedabad is illustrated in Figure 1. This study addresses this critical gap by employing high-resolution, ground-based thermal infrared imaging to quantitatively profile the surface thermal behavior of common urban materials in Ahmedabad, providing granular data to inform climate-resilient urban planning and material selection.

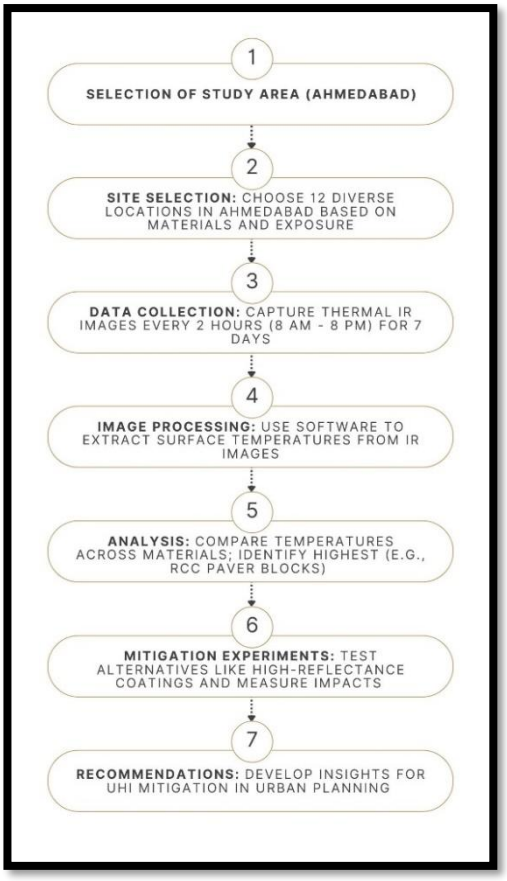

Fig 1. Flowchart for Methodology

2. METHODOLOGY

A systematic field campaign was conducted across 12 representative urban sites in Ahmedabad, selected to encapsulate a spectrum of surface typologies: asphalt roads, reinforced cement concrete (RCC) pavements, interlocking paver blocks, Kota stone flooring, vegetated lawns, rooftops, and semi-conditioned indoor spaces. To isolate the effect of shading, paired observations (exposed vs. shaded) were conducted for applicable surfaces.

Data acquisition was performed using a calibrated handheld thermal infrared camera. A representative thermal image (thermogram) capturing the contrast between different surfaces is shown in Figure 2. Sampling was strategically scheduled to capture key diurnal thermal phases: peak insolation (14:00–15:00 hrs) and the primary radiative cooling period (20:00–21:00 hrs). At each site, triplicate measurements were obtained from a standardized height and averaged to ensure statistical robustness. The resultant dataset was validated against concurrent air temperature records from the India Meteorological Department (IMD) and broad-scale thermal patterns from the Landsat Thermal Infrared Sensor (TIRS).

3. RESULTS AND DISCUSSION

The analysis revealed pronounced disparities in the thermal performance of urban surfaces, with significant implications for UHI intensity.

• Material-specific thermal response

Impervious, low-albedo materials exhibited the most extreme thermal behavior, confirming their role as primary UHI drivers [2]. Unshaded asphalt surfaces recorded a peak temperature of 56.2°C, exceeding ambient air temperature by approximately 15°C. RCC pavements and exposed paver blocks also functioned as pronounced heat sinks, reaching 51.4°C and 54.1°C, respectively. The comparative peak surface temperatures for all materials are summarized in Figure 3.

• Efficacy of shading interventions

The moderating effect of shading was substantial across all material types. Shaded asphalt surfaces exhibited a peak temperature reduction of ~9°C. The most significant differential was observed for paver blocks, where shading resulted in a ~15°C reduction, underscoring the profound impact of urban canopy cover on surface thermal regulation, a finding supported by other studies in hot climates [5].

• Cooling capacity of permeable surfaces

Vegetated lawns consistently maintained the lowest surface temperatures, peaking at 34.5°C and cooling rapidly to 28.7°C by evening, highlighting the dominant role of evapotranspiration [6]. Kota stone demonstrated more rapid cooling than asphalt or concrete, suggesting its potential as a sustainable urban surface material.

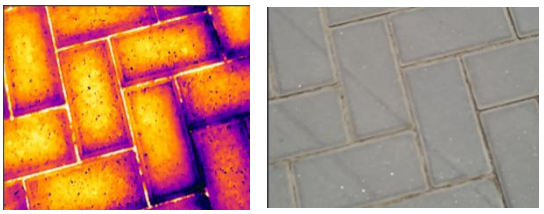

Fig 2 Normal and Thermal Gun photo of pavement surface

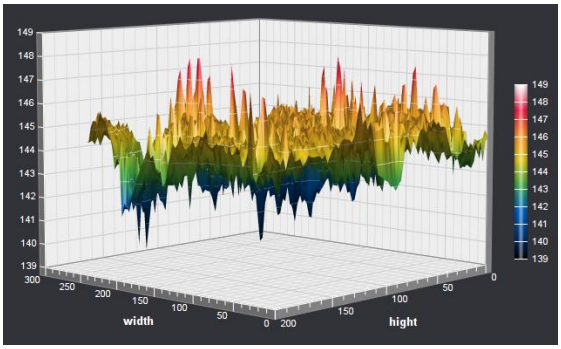

Fig 3 Graph for pavement surface

4. CONCLUSIONS

This study quantitatively establishes that UHI intensity at the micro-scale is a direct function of surface material properties and urban design. The findings lead to three principal conclusions: The selection of construction materials is a primary determinant of urban thermal load; Architectural and natural shading constitutes one of the most effective passive cooling strategies; and Permeable and vegetated surfaces offer optimal thermal performance. Based on these conclusions, the following evidence-based interventions are recommended: promote high-albedo materials and permeable pavements in building codes; integrate strategic shading through urban forestry; expand green infrastructure; and implement reflective or green roof technologies [7]. This work establishes a framework for material-specific UHI mitigation, offering a pathway toward enhanced thermal comfort and climate resilience in rapidly developing cities.

REFERENCES:

[1] M. Santamouris, Energy and Buildings. 103 (2015) 2–9.

[2] A. Mohajerani, J. Bakaric, T. Jeffrey-Bailey, Urban Climate. 21 (2017) 126–140.

[3] Y. Zhang, et al., Science of The Total Environment. 870 (2023) 161921

[4] I.D. Stewart, T.R. Oke, Bulletin of the American Meteorological Society. 93 (2012) 1879–1900

[5] S. F. M. Rafiee, A. A. D. A. Dias, E. M. D. S. L. C. M. P. A. C. G. I. D. A. F. T. M. J. C. Silva, Climate. 10 (2022) 11.

[6] C. S. B. Grimmond, M. Roth, T. R. Oke, Y. C. Au, M. Best, R. Betts, Bulletin of the American Meteorological Society. 91 (2010) 1015–1057.

[7] H. Akbari, S. Konopacki, Energy and Buildings. 37 (2005) 1297–1305.

ABS ID: 162
Code No: CCGR-0P-05

Life Cycle Assessment of Artificial Light Weight Aggregates

Brijesh Singh[1], Anand Bohra[2] and L P Singh[3]
[1]*General Manager, National Council for Cement and Building Materials, Faridabad, India*
[2]*Group Manager, National Council for Cement and Building Materials, Faridabad, India*
[3]*Director General, National Council for Cement and Building Materials, Faridabad, India*
Correspond to Mr. Anand Bohra. (anand.bohra@ncbindia.com)

Keywords: Life cycle assessment, artificial lightweight aggregates, sintered flyash aggregate, natural aggregate, Global Warming Potential, Uncertainty analysis.

The focus on infrastructure growth and housing in India requires huge quantity of coarse aggregates for manufacturing of concrete and it is expected that about 4000 million tonnes of coarse aggregates will be required in 2050. The use of natural aggregates results in ecological impact due to crushing of mountains. India is having huge stocks of 206.8 million tonnes of legacy fly ash and about 24.8 million tonnes of flyash generated in 2022-23 remained unutilized. The replacement of natural aggregates by artificial light weight aggregates (ALWA) based on waste materials/by-products like fly ash can help in achieving sustainability and circular economy. Life cycle assessment (LCA), an environment impact assessment tool, is used to compare the potential environment impacts associated with the production of artificial light weight aggregates like sintered flyash aggregates and cold bonded aggregates with natural aggregates. The study was undertaken from 'cradle to gate' and the functional unit was taken as 1 tonne of aggregate. In this study, an excel based LCA model was developed for ALWA covering all the inputs like raw materials, heat and electricity and outputs like product and emissions. The potential life cycle environment impacts were assessed in terms of Global Warming Potential, Acidification Potential, Eutrophication Potential and Abiotic Depletion Potential. The study highlights that the impacts associated with ALWA vary considerably as compared to natural aggregates, depending upon the heat and electricity inputs. Three alternative scenarios were developed replacing grid power with renewable based power and replacement of fossil fuel with biomass/biofuels. Sensitivity analysis was also carried out to assess the robustness of LCA model. This paper helps in selection of sustainable construction materials and planning of waste management strategies.

1. INTRODUCTION

The growing focus on infrastructure development and housing in India has led to a tremendous rise in the demand for construction materials, particularly coarse aggregates used in concrete production. It is estimated that by the year 2050, approximately 4000 million tonnes of coarse aggregates will be required to meet the country's construction needs. At present, these aggregates are primarily obtained by crushing natural rocks and mountains, a process that significantly disturbs the ecological balance by causing habitat loss, deforestation, and landscape degradation. This scenario highlights the urgent need to identify and adopt sustainable and eco-friendly alternatives to natural coarse aggregates, ensuring that infrastructure growth can continue without compromising environmental integrity. [1, 2].

Over the past few decades, considerable attention has been directed towards producing high-quality aggregates through the recycling of construction and demolition (C&D) waste. However, the widespread use of C&D waste–based aggregates in concrete production remains limited due to challenges such as inconsistent material quality, inadequate processing infrastructure, and the presence of adhered contaminants. Alternatively, various industrial by-products, including fly ash, LD slag, ferrochrome slag, and residual powders, are being explored as potential sources for manufacturing artificial aggregates, offering a promising and sustainable substitute for natural materials. [3-4].

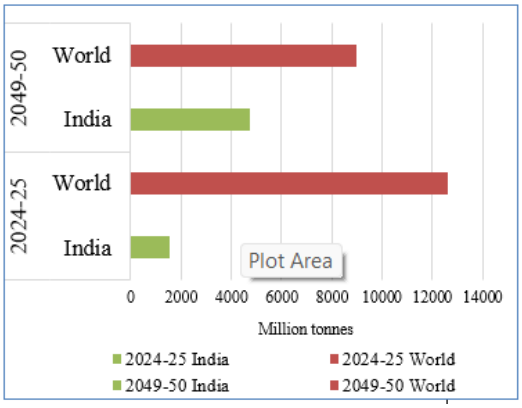

Figure 1: Aggregates demand in India

Now a day, artificial lightweight aggregates (ALWA) are increasingly getting used in concrete because of properties like low density, better thermal insulation and enhanced durability performance [5]. Natural type of lightweight aggregates such as pumice or volcanic ash, diatomite etc. are less in quantum than conventional aggregates available on earth. The processing of these aggregates to make them usable also leads to high energy consumption and environmental pollution. Therefore, the utilization of artificial aggregates can pave a feasible pathway for tackling the issue of scarcity of natural aggregates and reduces the negative impact on environment.

Artificial lightweight aggregates are usually made from various raw materials and production techniques such as ash based, expanded slate, expanded clay, expanded shale, expanded slag, etc. Amongst the various types of artificial lightweight aggregates, sintered flyash lightweight aggregates are more sustainable as they contain 95% of flyash, a by-product generated in coal based thermal power plants [5-7]. In India, as per CPCB, the flyash generated in the year 2022-23 was 291.7 million tonnes out of which 266.9 million tonnes was utilized, resulting in unutilized flyash stock of 24.8 million tonnes with a legacy stock of 206.8 million tonnes [8]. The unutilized flyash can be readily consumed for production of ash based lightweight aggregates.

Life Cycle Assessment (LCA) is an environment management tool used for assessing the potential environment impacts associated with a product or process through its entire life cycle. Researchers have indicated in past that novel construction materials are not getting adopted easily by construction fraternity due to apprehension about its environmental, social and economic impacts, which are key for informed decision making and policy formulation [9-10]. Therefore, LCA will be a useful tool for the large-scale acceptability of sintered flyash lightweight aggregates in the construction fraternity involving practitioners, end users, policy makers and code formulation bodies. LCA study has also been widely used for comparative environment assessment of two products or products with its alternatives [11-13].

The main issue faced in LCA studies is the lack of accurate data driven life cycle inventory (LCI) primarily due to factors like lack of primary data, assumptions, emission factors, different methodologies and secondary data used in the study [11-12].

2. MATERIALS AND METHOD

2.1 Material

The flyash based artificial lightweight aggregates (ALWA) are mainly produced through three routes (a) sintering (b) cold bonding and (c) hydro-thermal treatment. Out of the three routes, sintering route has maximum ash utilisation efficiency of 95% and has shorter curing periods. Apart from this, aggregates produced through sintering methods have superior mechanical properties [8-9]. It mainly consists of preparation of raw meal and its blending, pelletisation, sintering between 900-1200oC and screening for final product as shown in Fig 2 [3,6].

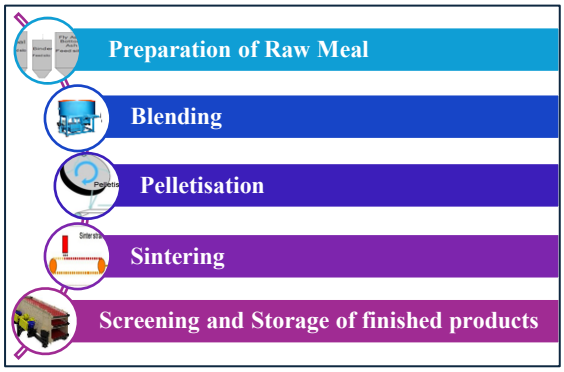

Figure 2: Production process of ALWA

In this study, the aggregates are manufactured using flyash generated from coal based thermal power plants along with coal and bentonite. The production process of ALWA is discussed below:

i. The first step involves handling/conveying of raw materials to respective silos

ii. In the second step, the raw materials like flyash, coal in grinded form and bentonite, are mixed in a blender along with water required for desired consistency, for preparing a homogenous mix. Typically, the raw mix used for production of green ALWA pellets consists of 91-96 % flyash, 0.8-3.0 % bentonite and 3.6-4.5 % coal along with 25% water. The green pellets have been prepared by agglomerating finer particles of flyash using bentonite in disc type palletizer. The pellet dimensions are usually controlled by adjusting the disc angle (35◦-55◦) and by varying the speed of palletizer (35-55 rpm).

iii. In the third step, the green pellets are hardened by heating and fusing of fly ash particles with coal & bentonite at a temperature of 900-1200°C followed by cooling.

Table 1: Raw materials & fuels

Baseline	Quantity (kg per t of ALWA)	t-km	Source	Mode of transportation
Fly Ash	925	1.0	CPP	Conveyor Belt
Coal	45	4.0	Eastern India	Trucks
Bentonite	30	20.0	North-west India	Trucks

The energy inputs (MJ) in the form of thermal, electrical, diesel and coal to each of the four steps of manufacturing process of ALWA were calculated in this study as shown in Table 2.

Table 2: Energy inputs at various stages of LCA

Process Parameters	Energy (in MJ)			
	Thermal	Electrical	Diesel	Coal
Handling of Materials to silos	-	80.0	2.0	-
Blending Unit & Pelletisation	-	70.0	1.8	-
Sintering Process	382.1	100.0	27.6	847.2
Screening and Handling of product	-	37.2	0.9	-

-

iv. In the final step, the cooled and hardened pellets are passed through breaker, wherein the fused pellets are broken into aggregates pellets. The aggregates are then segregated as per the size (4 mm to 16 mm) by passing through a screener.

2.2 LCA Methodology

A life cycle assessment (LCA) is a tool used for assessment of potential environment impacts covering entire life cycle of a product or process. In a LCA study, all inputs and outputs through each of the unit processes are inventoried and classified and characterized into various impacts. The common impact categories to assess the environment impacts are global warming potential (GWP), eutrophication potential (EP), acidification potential (AP), resource depletion (ADP) etc. The LCA study is carried out as per ISO: 14049:2012 [13] ISO 14040:2006 [14] and 14044:2006 standards [15].

i. Goal and Scope: The first phase involves defining the functional unit, system boundary, assumptions, cut off etc.

ii. Life Cycle Inventory (LCI): The second phase involves identifying, quantifying and compiling the input and outputs through each of the unit process in the entire life cycle of the product.

iii. Life Cycle Impact Assessment (LCIA): The third step involves characterization of the input and outputs into potential environmental impacts.

iv. Interpretation: The fourth and final step of LCA study is the most important part as the results of LCIA are analysed and reviewed for making informed decisions and recommendations.

To assess the environment impacts an excel based model was developed [16-25]. The three alternative scenarios are prepared based on the contribution analysis carried out. As sintering and electricity consumption are the main contributors for various impact categories, accordingly the alternative scenarios are designed as given below in

Table 3:

Table 3: Description of Baseline and Alternative Schemes

Particulars		Base-line	1st Alternate	2nd Alternate	3rd Alternate
Electrical Energy	CPP	100 %	50%	0%	0%
	Solar	0%	25%	25%	50%
	Grid	0%	25%	75%	50%
Thermal Energy	Biomass	0%	0%	15%	25%
	Coal	100 %	100%	85%	75%

3. RESULT AND DISCUSSION

3.1 Contribution analysis of unit processes for various impacts

The contribution analysis for assessing the contribution of various unit process to each of the 4 impact categories is shown in Fig 3.

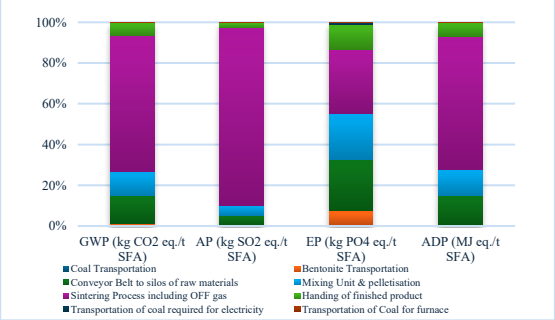

Figure 3: Contribution Analysis

As highlighted in the Fig 3, sintering process is having maximum contribution towards each of the impact categories ranging from 43% to 64% followed by electricity consumption in various unit processes contributing 15% to 43 % in various impact categories.

In view of above, the alternative scenarios are processes based on the alternatives for electricity consumption from captive power plant and use of biomass in place of coal.

3.2 Impact Assessment

One alternative to ALWA is natural aggregates, which is presently being produced by crushing of natural rocks and used in all construction activities. The comparative impact assessment of ALWA and natural aggregates is shown in

Fig 4.

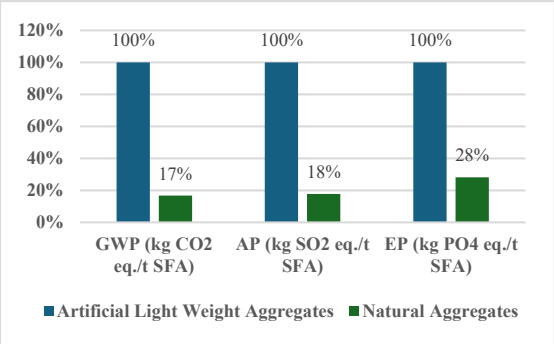

Figure 4: Comparison of impacts of ALWA and natural aggregates

The life cycle impact assessment has been carried out for ALWA production in India and three alternative scenarios (1st, 2nd and 3rd) as shown in Table 4 and Fig 5. The impact assessment was carried out in terms of GWP impacts in the four scenarios is 216.81 kg CO2 eq., 178.39 kg CO2 eq., 149.65 kg CO2 eq. and 131.57 kg CO2 eq. respectively. This shows that the 3rd alternative scenario is having the lowest GWP impacts. Similarly, AP impacts per tonne of ALWA in the four scenarios is 0.79 kg SO2 eq, 0.71 kg SO2 eq., 0.61 kg SO2 eq. and 0.59 kg SO2 eq. respectively. This shows that the 3rd alternative scenario is having the lowest AP impacts. Similarly, EP impacts per tonne of ALWA in the four scenarios is 0.11 kg PO4 eq., 0.06 kg PO4 eq., 0.01 kg PO4 eq. and 0.01 kg PO4 eq. respectively. This shows that the 2nd alternative scenario is having the lowest EP impacts. Similarly, ADP impacts per tonne of ALWA in the four scenarios is 3852 MJ eq., 3091 MJ eq., 2496 MJ eq. and 2197.6 MJ eq. respectively. This shows that the third alternative scenario is having the lowest ADP impacts.

Table 4: Impact Assessment of ALWA

Scenario of ALWA Production	GWP (kg CO_2 eq./t ALWA)	AP (kg SO_2 eq./t ALWA)	EP (kg PO_4 eq./t ALWA)	ADP (MJ eq./t ALWA)
Baseline	216.81	0.79	0.11	3851.61
1st Alternate Scenario	178.39	0.71	0.06	3091.30
2nd Alternate Scenario	149.65	0.61	0.01	2496.39
3rd Alternate Scenario	131.57	0.59	0.01	2191.37

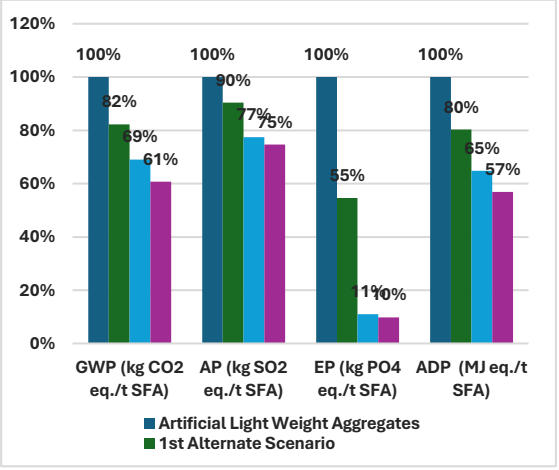

Figure 5: Comparative impact assessment of four scenarios of ALWA

3.3 Sensitivity Analysis

Sensitivity analysis (SA) is a significant tool for studying the robustness of results and their sensitivity to uncertainty factors in life cycle assessment (LCA). Sensitivity analysis highlights the most important set of model parameters to enhance the interpretation of LCA results and to determine whether data quality needs to be improved. The input variables used in the study for calculation of life cycle impacts were identified and listed in Table 5.

S.No.	Parameters

1.	Coal required for electricity in captive thermal power plant
2.	SO_2 and NOx emission factor for coal
3.	Carbon % of coal
4.	Grid CO_2 Emission Factor
5.	Coal requirement for electricity production in grid
6.	SO_2 and NOx emission factors of Grid & CPP
7.	CO_2 emission factor for truck transportation
8.	SO_2 and NOx emission factors for truck transportation
9.	Density of Diesel
10.	Mileage of Truck

Table 5: Input variable parameters of LCA study

The sensitivity analysis was carried out to assess the most important set of model parameters, whether the data quality needs to be improved, and to enhance interpretation of results. The parameter values were changed by a unit value or unit % and the impacts on model outputs were determined. The SO2 and NOx emission factors for electricity generated at captive thermal power plant and coal combustion in sintering process have higher impact on model output especially AP and EP upto 35%. The emission values were provided by the plant. Further, coal requirement for electricity and bentonite requirement are the major parameters having impact upto 10% on GWP impact on unit change in values of parameters.

4. CONCLUSION

This paper contributes for the study of environment impacts associated with the artificial light weight aggregates like sintered flyash lightweight aggregates (ALWA) produced in India and its comparison with natural and alternative scenarios of ALWA production. Based on the results and discussions, it was found that natural aggregates are having much lower (i.e. 55 to 90%) environment impacts as compared to present baseline scenario of ALWA production. However, with alternative scenario like usage of biomass and grid-based electricity will help in reduction of the environment impacts and make it comparable with natural aggregates as shown in Fig 6.

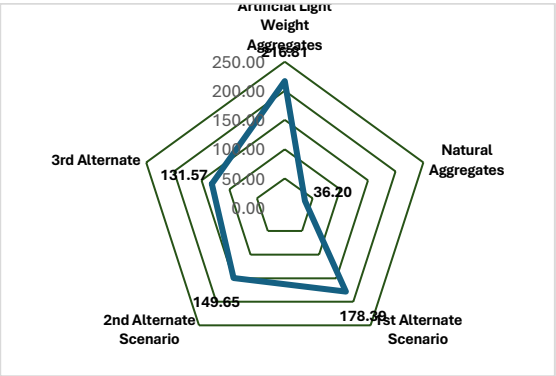

Figure 6: Comparison of GWP impacts of SFA with NA and three alternative scenarios

REFERENCES:

1. Grand View Research (2020–2027). Aggregates market size, share and tends analysis report by type (gravel, crushed stone, sand), By application (concrete, road base and coverings), By region (APAC, MEA), and segment forecasts, 2020.

2. Gonzalez, M. J., Navarro, J. G. Assessment of the decrease of CO emissions in the construction field through the selection of materials: practical case study of three houses of low environmental impact. Build Environment. 503 4(17), 902–909, 2006.

3. Shang. X., Yang. J., Wang. S., Zhang. M., Fractal analysis of 2D & 3D mesocracks in recycled

aggregate concrete using X-ray computed tomography images. J. Cleaner Prod. 304, 127083, 2021.

4. Shi, M., Ling, T., Gan, B., Guo, M. Turning concrete waste powder into carbonated artificial aggregates. Constr. Build. Mater. 199, 178-184, 2019.

5. Singh, B., Singh, S.B., Barai S.V. Performance of concrete made using sintered flyash lightweight aggregate- A review, Indian Concrete Journal, July, Vol. 97(7), pp.41-59, 2023.

6. Ojha, P.N., Singh, B., Behera, A. K. Sintered flyash lightweight aggregate-Its properties and performance in structural concrete, Indian Concrete Journal, Vol. 95 (6), pp.20-30, (2021).

7. Singh, B., Singh, S.B., Barai, S.V., Bohra, A. Life cycle assessment of artificial sintered flyash lightweight aggregate produced in India using OFF

gas and coal based thermal power. Innov. Infrastruct. Solut. 10, 113 (2025).

8. Central Pollution Control Board, Fly Ash Mission, 2023 accessed on 18.04.2025.

9. Kockal, N. U., Ozturan, T. Effects of lightweight fly ash aggregate properties on the behavior of lightweight concretes. J. Hazard. Mater. 179, 954-965, 2010.

10. Rigamonti, L., Grosso, M., Giugliano, M. Life cycle assessment for optimizing the level of separated collection in integrated MSW management systems. Waste Management, 29, 934-944, 2009.

11. Ben-Alon, L., Loftness, V., Harries, K. A., Cochran, H. E. Life cycle assessment (LCA) of natural vs conventional building assemblies. Renewable Sustainable Energy Review 144, 110951, 2021.

12. Park, J., Yoon, J., Kim K. H. Critical review of the material criteria of building sustainability assessment tools. J. Sustain. 9(2), 186-186, 2017.

13. ISO:14049. 2012. Environmental management - Life cycle assessment – Illustrative examples on how to apply ISO 14044 to goal and scope definition and inventory analysis

14. ISO 14040. 2006. Environmental management—life cycle assessment—principles and framework. ISO: Geneva, Switzerland,

15. ISO 14044. 2006. Environmental management—life cycle assessment—requirements and guidelines. ISO: Geneva, Switzerland

16. Singh, B., Singh, S.B., Bohra, A. et al. Probabilistic life cycle assessment of ash-based sintered lightweight aggregates manufactured with producer gas and coal-operated thermal power. Innov. Infrastruct. Solut. 10, 483 (2025). https://doi.org/10.1007/s41062-025-02287-1

17. Bohra, A., Nema, A. K. and Ahluwalia, P., Global warming potential of waste management options: case study of Delhi. International Journal of Environmental Technology and Management, Vol. 15, No. 3-6, 2012. https://doi.org/10.1504/IJETM.2012.049233

18. Pradhan, S., Tiwari, B., Kumar, S., Barai, S. 2019. Comparative LCA of recycled and natural aggregate concrete using Particle Packing Method and conventional method of design mix. Journal of Cleaner Production. 10.1016/j.jclepro.2019.04.328.

19. CO2 baseline database for the Indian power sector. 2023. User guide. Central Electricity Authority, Ministry of Power, Government of India, Delhi, India.

20. Emission Calculations SO2 and NOx, Mizoram Pollution Control Board (MPCB) & Its Constitution, mizoram.gov.in

21. India specific road transport emission factors. 2015. India GHG Program, India

22. BPCL: High Speed Diesel (BS VI), Bharat Petroleum Corporation Limited, https://www.bharatpetroleum.in/images/files/high%20speed%20diesel_pds.pdf

23. IPC-II Division, Environmental regulations for thermal power plants, https://cpcb.nic.in/uploads/thermal_power_plant_overview.pdf

24. Shang X, Chang J, Yang J, Ke X, Duan Z. 2022. Life cycle sustainable assessment of natural vs artificial lightweight aggregates, Journal of Cleaner Production, 133064, doi: https://doi.org/10.1016/j.jclepro.2022.

25. Gaurav Jha, S. Soren, Kapil Deo Mehta, Life cycle assessment of sintering process for carbon footprint and cost reduction: A comparative study for coke and biomass-derived sintering process, Journal of Cleaner Production, Volume 259, 2020, 120889, https://doi.org/10.1016/j.jclepro.2020.12089

4th International Symposium on One Health, One World
November 20 – 22, 2025

ABS ID: 125

Code No: CCGR-0P-06

Carbonation Behavior of Mortars Containing Ld Slag: A Physical and Microstructural Investigation

C. S. Sharma[1], and k.S. Kulkarni [2]
[1]*Research Scholar, Academy of Scientific Innovative Research, Ghaziabad- 220020, India*
[2]*Principal Scientist, CSIR-Central Building Research Institute, Roorkee, India,*
Correspond to Dr. K.S. KULKARNI (kishorsk.cbri@csir.res.in)

***Keywords**: LD steel slag; Carbonation curing; Compressive Strength; Microstructure.*

1. INTRODUCTION

The cement and construction industries face major challenges of high carbon emissions and depletion of natural resources like sand, limestone, and clay. The Global Cement and Concrete Association (GCCA) warns that limestone, essential for clinker production, could be exhausted within 25–30 years. Cement manufacturing contributes about 8% of global CO_2 emissions (around 2.8 billion metric tons annually due to the calcination of limestone [1-2]. To address these issues, researchers are exploring steel slag, a by-product of steel manufacturing, as a partial replacement for Ordinary Portland Cement (OPC), combined with Carbon Capture and Utilization (CCU) and Accelerated Carbonation Curing (ACC) techniques [3]. Steel slag's pozzolanic properties enhance the mechanical strength and durability of cement mortar while sequestering CO_2 during curing, reducing carbon footprints and conserving natural resources [4-6]. This approach supports the development of eco-friendly, high-performance materials, aligning with global sustainability goals [7-8].

This study explores the effects of accelerated CO_2 curing on the physical, mechanical, and microstructural characteristics of accelerated Carbonation Cured Slag (ACCS) mortar. The mortar was formulated using basic oxygen furnaces (LD) slag, combined with 4.5 mm down fine aggregates and a chemical admixture.

2. MATERIALS AND COMPOSITION

LD slag for this experiment was obtained from (M/s. JSW steel factory Vijayanagar, Karnataka, India). The raw LD slag was ground using a motorized ball mill to produce finer particles of LD material. This process makes the slag particles finer and activates them for use as cementitious material. Tables 1 provide the physical and chemical properties of LD slag.

Table 1. Physical characteristics of LD slag

Properties	LD Slag
Color	Gray
Fineness (m^2/kg)	479
Bulk density (kg/m^3)	3210
Specific gravity	3.19
Lime reactivity index	0.83
Specific Gravity	2.81
pH	11.52
Refractivity index	1.69

Table 2. Chemical composition of LD slag

Chemical composition	%	Chemical composition	%
Na_2O	0.19	CaO	43.99
MgO	13.40	MnO	2.22
Al_2O_3	3.65	Fe2O3	0.95
SiO_2	30.03	Loi	2.87

For the experimentation on Accelerated Carbonation Curing Slag (ACCS) mortar the OPC is partially replaced with LD steel slag, the different mixes were prepared as per Table 3. The LD steel slag, cement, fine aggregate, and water were thoroughly mixed in an automatic electric mortar mixer at a speed exceeding 140

rpm for 10 minutes. After testing the flowability property of the ACCS mortar determined by a flow table apparatus, ACCS mortar was filled into 50 mm cubical molds. The mortar specimens were demolded 18 hours after casting. After de-molding, the ACCS mortar specimen cubes were subjected to accelerated carbonation curing for 24 hours using an automatically operated carbonation chamber machine. Following the curing process, the mortar samples were subjected to various tests. After the carbonation curing the specimens were tested for carbonation depth, water absorption, pH and compressive strength.

Table 3. Mix proportion of ACCS mortar mix

Sl. No.	OPC (gm)	LD (gm)	Fine Sand (gm)	Water (gm)
1	900	100	750	230
2	800	200	750	230
3	700	300	750	230
4	600	400	750	230
5	500	500	750	230

3. RESULTS AND DISCUSSION

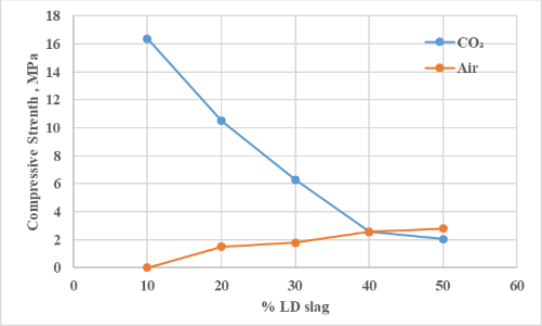

Figure 1 Compressive Strength of LD slag sample

The effect of CO2 concentration, acceleration curing of ACC chamber on the compressive strength of concrete samples is presented in the Figure 1. It is observed that when specimen subjected to CO2 curing there is an increase the compressive strength. This is due to the fact that as the samples as exposed to more amount of CO2, the CO2 will ingress more into the concrete specimen. 10% LD slag is replaced with cement then maximum strength comes to 16.38 MPa.

Figure 2 Water Absorption of LD slag Sample

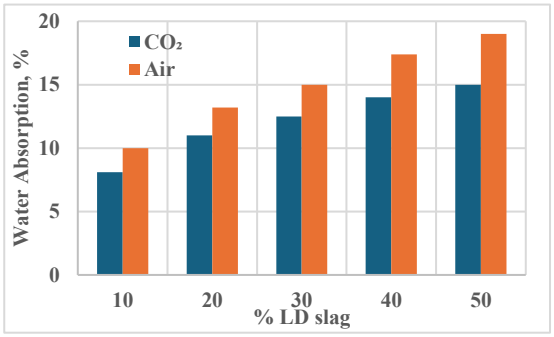

The LD slag mortar exhibited reduced water absorption after the carbonation. LD slag mortar samples shown minimum water absorption (8.1%) at 10% slag replacement

Figure 3 Carbonated LD slag samples

The carbonation depth was quantified using depth of carbonation and the effect of ACC on hardened properties, minerals formed and morphology was confirmed using XRD and SEM analysis.

The pH of the sample decrease because of the carbonation involves reaction of carbon dioxide with calcium hydroxide in the cement to form calcium carbonate, hence lowering the pH of the material. In the noncarbonated state, pH is quite high because the cement is alkaline however for the LD sample the pH is observed as lower as 10.66. For the LD slag samples, the carbonation depth was measured up to 10 mm. The findings indicated that CO_2 curing shortened the

carbonation depth from 2 mm to 20 mm, improved mechanical properties by 3 MPa to 14 MPa, reduced water absorption by 20%, and enhanced mortar density.

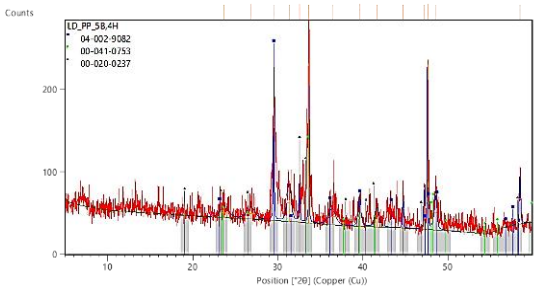

Figure 4 XRD of LD Slag carbonated sample

A Field Emission-Scanning Electron Microscope (FE-SEM) analysis and X-ray diffraction (XRD) test demonstrated that the ACCS mortar matrix was denser compared to non-carbonated mortar specimens without LD slag.

4. CONCLUSIONS

The study investigates the influence of steel slag content and curing duration on cement mortar performance. Among various mixes, a 1:3 binder ratio with 10% LD slag showed optimal results. The impact of ACCS on compressive strength and carbonation depth was analyzed, and mineralogical and microstructural changes were confirmed through XRD and SEM analyses. The integration of LD slag not only enhances the material's performance but also aligns with sustainable development objectives by promoting industrial waste valorization and reducing cement dependency. This approach offers a cost-effective and environmentally responsible pathway for the production of durable and affordable building materials suitable for large-scale infrastructure and housing applications.

REFERENCES:

[1] A. Mushaer, I. Bashar, S. T. Alam, A. Wasi, I. Jerin, S. Khatun, and M. Rahman. Sustainable Production and Consumption 28 (2021) 1018-1039.

[2] D. Ravikumar, D. Zhang, G. Keoleian, S. Miller, V. Sick, and V. Li. Nat. Commun. 12(1) (2021) 855.

[3] S.Y. Pan, T. C. Chung, C. C. Ho, C.J. Hou, Y. H. Chen, and P. C. Chiang, Sci. Rep.,7(1) (2017) 17227.

[4] M. Mahoutian, Z. Ghouleh, and Y. Shao, Constr. Build. Mater., 66 (2014) 214–221.

[5] C. J. Shi and Q. Y. Zou, Key Eng. Mater., 400–402 (2008) 81–87.

[6] M. Bodor, R. M. Santos, G. Cristea, M. Salman, O. Cizer, R. I. Iacobescu, Y. W. Chiang, K. Van Balen, M. Vlad, and T. Van Gerven, Cement and Concrete Composites, 65 (2016) 55-66.

[7] B. Zhan, C. Poon, and C. Shi, Cement and Concrete Composites,42 (2013)1-8.

[8] X. Wang, W. Ni, J. Li, S. Zhang, M. Hitch, and R. Pascual, Cem. Concr. Res., 125 (2019) 105893.

ABS ID: 33
Code No: CCGR-0P-07

Carbon-Cured Artificial Lightweight Aggregates from Municipal Solid Waste Incinerated Ash: A Cold Bonding Approach

H. Athar[1], d. Saini[2], k.s. Kulkarni[3] and d. Bhardwaj[4]
[1]*Scientist, CSIR-Central Building Research Institute, Roorkee, India*
[2]*Project Associate, CSIR-Central Building Research Institute, Roorkee, India*
[3]*Principal Scientist, CSIR-Central Building Research Institute, Roorkee, India*
[4]*Deaprtment of Civil Engineering, University Institute of Technology, H. P. University, Shimla India*
Correspond to Humaira Athar (humaira.cbri@csir.res.in)

Keywords: *Artificial lightweight aggregates; Municipal solid incinerated bottom ash; Cold-bonding; Mineral Carbonation; Individual grain strength.*

ABSTRACT

The increasing demand for sustainable construction materials has accelerated efforts to incorporate industrial and municipal wastes into building applications. Lightweight aggregates (LWA) play a vital role in reducing structural load, improving thermal insulation, and enhancing energy efficiency in construction. This study focuses on the development of artificial lightweight aggregates (ALWA) using municipal solid waste incineration bottom ash (MSWIBA) and Portland Pozzolana Cement (PPC) through a cold-bonding pelletization process. A single-step disc pelletization method was employed with optimized parameters of 35–45 rpm speed, 20–25 minutes' duration, and a water-to-solid ratio of 0.30–0.35. The prepared aggregates were air-dried for 24 hours, water-cured for 1, 3, 7, 14, and 28 days, and subsequently carbonated with 99% pure CO_2 under 4 bar pressure and 65–70% relative humidity for 24 hours. Carbonation significantly enhanced performance, leading to a ~34% increase in single pellet strength, a 16% reduction in water absorption, and the

formation of additional calcite that refined the microstructure. At 7 days, bulk density and specific gravity of carbonated aggregates were ~1170 kg/m³ and ~1.96, respectively. pH values decreased from 11.74 (non-carbonated) to 9.86 (carbonated), reflecting carbonation reactions. Thermogravimetric analysis confirmed a CO_2 uptake of 5–6%, while microscopic studies showed denser and less porous structures. The aggregates were rounded to sub-rounded (4–16 mm) and suitable for non-structural applications such as bricks, blocks, and roof insulation. This work demonstrates the dual benefits of valorizing MSWIBA and sequestering CO_2, aligning with circular economy practices and offering technical, environmental, and economic advantages for sustainable construction.

1. INTRODUCTION

The construction industry is one of the largest consumers of natural resources and a significant contributor to environmental pollution, largely due to the intensive use of cement and aggregates in concrete production (Hussin et al., 2013; Aslam et al., 2016). Aggregates account for nearly 70–80% of concrete volume, and excessive quarrying of natural aggregates leads to land degradation, energy consumption, and ecosystem disruption (Oktay et al., 2015). To address these concerns, artificial aggregates produced from industrial and municipal wastes have gained considerable attention for their potential to conserve resources and transform waste into value-added products (Kayali, 2008). Among the various production techniques, cold bonding has emerged as an energy-efficient and environmentally friendly process compared to sintering, which requires high-temperature treatment (Baykal and Doven, 2000; Bijen, 1986). Cold-bonded aggregates are typically produced by pelletizing fine waste powders such as fly ash, quarry dust, or bottom ash, followed by curing under ambient or accelerated conditions (Chi et al., 2003; Geetha and Ramamurthy, 2010). The process relies on the pozzolanic reactivity of wastes in the presence of calcium hydroxide or cement, forming calcium silicate hydrate (C–S–H) gel that provides strength and durability (Manikandan and Ramamurthy, 2008). Studies have shown that cold-bonded aggregates can be successfully used in concrete with strengths up to 30–40 MPa (Joseph and Ramamurthy, 2008; Güneyisi et al., 2015; Thomas and Harilal, 2015). Moreover, their production reduces embodied energy, promotes waste valorization, and enhances sustainability performance in construction projects (Thomas and Harilal, 2015; J. Thomas and Harilal, 2019). Given the abundance of waste streams such as fly ash and municipal solid waste incineration residues, cold bonding provides a viable pathway to develop sustainable aggregates for future infrastructure.

2. MATERIALS AND TEST METHODS

Municipal Solid Waste Incineration Bottom Ash (MSWIBA), rich in SiO_2 (35–50%), Al_2O_3 (10–25%), CaO (10–30%), and Fe_2O_3 (5–15%), was used as the primary raw material, while finely ground Portland Pozzolana Cement (PPC), containing 25–38% SiO_2, 5–12% Al_2O_3, and 50–60% CaO, served as the binder. Cold-bonded aggregates were produced using a disc pelletizer inclined at 45° and operated at 30–40 rpm. The dry-mixed MSWIBA–PPC blend was fed into the disc, where water spraying induced agglomeration into spherical pellets. Fresh aggregates were air-dried for 24 hours, water-cured for 1, 3, 7, and 14 days, and then carbonated in a carbonation chamber prior to testing. Performance evaluation included water absorption (IS 2386 Part 3), single pellet strength (IS 2386 Part 4), bulk density, specific gravity (oven-dry, SSD, and

submerged), and pH, determined using a 1:10 aggregate-to-water solution with a calibrated pH meter.

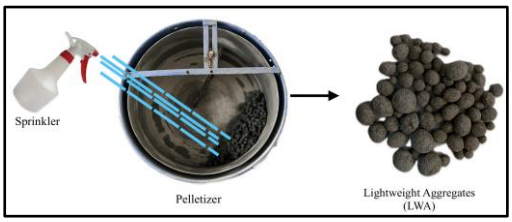

Figure 1. Preparation of lightweight aggregates

3.RESULTS AND DISCUSSION

The physical and mechanical properties of artificial aggregates produced from municipal solid waste incineration bottom ash (MSWIBA) and Portland Pozzolana Cement (PPC) through the cold-bonding method were evaluated at different curing ages, and the results are summarized in Table 1.

Single Pellet Strength (SPS): The development of strength with curing age was evident in both non-carbonated (NC) and carbonated (C) aggregates. At early ages, the SPS of carbonated aggregates was significantly higher compared to non-carbonated ones. For instance, at 1 day, the SPS of C aggregates (2.24 MPa) was about 41% higher than NC aggregates (1.59 MPa). This improvement is attributed to the accelerated hydration and precipitation of calcium carbonate during carbonation, which densifies the aggregate microstructure [1]. At 7 days, the SPS of C aggregates (5.34 MPa) exceeded that of NC aggregates (3.99 MPa). However, the difference narrowed at 28 days, where both exhibited comparable values (4.69 MPa vs. 4.60 MPa), suggesting that carbonation enhances early strength development, while long-term hydration reduces the gap between NC and C aggregates.

Bulk Density: Carbonated aggregates consistently exhibited higher bulk densities than NC aggregates throughout the curing period. At 28 days, C aggregates achieved 1083 kg/m³ compared to 1079 kg/m³ for NC aggregates. The increase in density can be linked to the filling of voids by calcium carbonate and other hydration products, thereby reducing porosity [2].

Water Absorption: Water absorption decreased steadily in both NC and C aggregates with curing age, with carbonated aggregates consistently showing lower values. At 28 days, C aggregates recorded 8.04% absorption compared to 10.05% in NC aggregates. This reduction reflects the densification of the aggregate matrix caused by carbonation and hydration reactions, which block capillary pores and restrict water ingress [3].

Specific Gravity: The specific gravity of aggregates increased with age, with C aggregates showing higher values than NC aggregates at all ages. At 28 days, C aggregates reached a specific gravity of 1.95, while NC aggregates attained 1.93. This enhancement further supports the hypothesis of reduced porosity and denser packing of hydration and carbonation products [4].

pH: A significant difference was observed in the alkalinity of NC and C aggregates. At 14 days, NC aggregates showed a pH of 11.74, whereas C aggregates dropped to 9.84. This reduction indicates the neutralization of free lime and alkalinity by carbonation, leading to a chemically stable aggregate surface [5].

Overall, these results confirm that the cold-bonding pelletization of MSWIBA with PPC, followed by carbonation, yields aggregates with improved early strength, higher density, reduced water absorption, and stabilized pH. Carbonation not only enhances performance but also contributes to CO_2 sequestration, aligning with sustainable construction practices.

Table 1: Physico-mechanical properties of cold-bonded aggregates

Properties	1 day		3 days		7 days		14 days		28 days	
	NC*	C*	NC	C	NC	C	NC	C	NC	C
Single pellet strength (MPa)	1.59	2.24	2.58	4.93	3.99	5.34	4.10	4.67	4.60	4.69
Bulk density (Kg/m^3)	840	931	1008	1020	1043	1061	1068	1075	1079	1083
Water absorption (%)	11.50	10.74	10.59	9.13	10.28	8.29	10.16	8.10	10.05	8.04
Specific gravity	1.56	1.59	1.61	1.78	1.84	1.86	1.88	1.91	1.93	1.95
pH					11.74	9.84				

*NC: Non-Carbonated
*C: Car

REFERENCES:

[1] Zhang, T., et al. "Carbonation of artificial aggregates: Strength development and microstructural evolution." Construction and Building Materials (Year).
[2] Gunning, P., et al. "Cold-bonded artificial aggregates from fly ash and waste residues: Performance and properties." Cement and Concrete Composites (Year).
[3] Yao, J., et al. "Influence of carbonation on pore structure and durability of waste-based aggregates." Journal of Cleaner Production (Year).
[4] Cioffi, R., et al. "Cold-bonded lightweight aggregates made from industrial wastes." Waste Management (Year).
[5] Kuo, W., et al. "The effect of accelerated carbonation on the properties of lightweight aggregates." Cement and Concrete Research (Year).

4. CONCLUSIONS

This study demonstrates that artificial lightweight aggregates (ALWA) can be successfully developed from municipal solid waste incineration bottom ash (MSWIBA) and Portland Pozzolana Cement (PPC) through a cold-bonding pelletization process, with carbonation serving as a key performance enhancer. Carbonated aggregates exhibited significantly higher early-age single pellet strength, reaching ~41% improvement at 1 day compared to non-carbonated aggregates, owing to accelerated hydration and the precipitation of calcium carbonate that densified the microstructure. Improvements were also evident in bulk density, specific gravity, and water absorption, with carbonated aggregates recording ~16% lower absorption and higher density values than non-carbonated counterparts at 28 days. Additionally, carbonation reduced pH from 11.74 to 9.84, stabilizing the aggregate matrix by consuming free lime. Thermogravimetric and microstructural analyses further confirmed CO_2 uptake and densification effects. The produced aggregates were well-graded, rounded to sub-rounded (4–16 mm), and suitable for non-structural applications such as blocks, bricks, and roof insulation. Overall, the process not only valorizes MSWIBA but also sequesters CO_2, aligning with circular economy principles and contributing to sustainable construction practices.

REFERENCES:

Aslam, M., Shafigh, P., Jumaat, M.Z. and Lachemi, M., 2016. Benefits of using blended waste coarse lightweight aggregates in structural lightweight aggregate concrete. *Journal of Cleaner Production*, 119, pp.108–117. https://doi.org/10.1016/j.jclepro.2016.01.071

Baykal, G. and Doven, A.G., 2000. Utilization of fly ash by pelletization process – theory, application areas and research results. *Resources, Conservation and Recycling*, 30(1), pp.59–77.

Bijen, J.M., 1986. Manufacturing processes of artificial lightweight aggregates from fly ash. *International Journal of Cement Composites and Lightweight Concrete*, 8(3), pp.191–199.

Chi, J.M., Huang, R., Yang, C.C. and Chang, J.J., 2003. Effect of aggregate properties on the strength and stiffness of lightweight concrete. *Cement and Concrete Composites*, 25(2), pp.197–205.

Geetha, S. and Ramamurthy, K., 2010. Reuse potential of low-calcium bottom ash as aggregate through pelletization. *Waste Management*, 30(8–9), pp.1528–1535. https://doi.org/10.1016/j.wasman.2010.03.027

Güneyisi, E., Gesoglu, M., Ozturan, T. and Ipek, S., 2015. Fracture behaviour and mechanical properties of concrete with artificial lightweight aggregate and steel fibre. *Construction and Building Materials*, 84, pp.156–168.

Hussin, J., Rahman, I.A. and Memon, A.H., 2013. The way forward in sustainable construction: Issues and challenges. *International Journal of Advanced and Applied Sciences*, 2(1), pp.15–24.

Joseph, G. and Ramamurthy, K., 2008. Effect of cold bonded aggregate on workability and mechanical properties of concrete. *The Institution of Engineers (India) Journal*, 89, pp.33–38.

Kayali, O., 2008. Fly ash lightweight aggregates in high performance concrete. *Construction and Building Materials*, 22(12), pp.2393–2399.

Manikandan, R. and Ramamurthy, K., 2008. Effect of curing method on characteristics of cold bonded fly ash aggregates. *Cement and Concrete Composites*, 30(10), pp.848–853.

Oktay, H., Yumrutas, R. and Akpolat, A., 2015. Mechanical and thermophysical properties of lightweight aggregate concretes. *Construction and Building Materials*, 96, pp.217–225.

Thomas, J. and Harilal, B., 2015. Properties of cold bonded quarry dust coarse

aggregates and its use in concrete. *Cement and Concrete Composites*, 62, pp.67–75.

Thomas, J. and Harilal, B., 2019. Green rating credits for waste utilization in construction. In: Drück, H., Pillai, R.G., Tharian, M.G. and Majeed, A.Z. (eds.) *Green Building and Sustainable Engineering*. Singapore: Springer, pp.189–201.

Chen, Z.X., Jiang, Y., Liu, F., Zhang, J., Liu, Q. and Wang, Z., 2023. Carbonation characteristics and microstructural evolution of cementitious materials with recycled concrete fines. Cement and Concrete Composites, 139, p.105044. https://doi.org/10.1016/j.cemconcomp.2023.105044

Garcia-Lodeiro, I., Fernandez-Jimenez, A. and Palomo, A., 2016. Variation in hybrid cements over time. Alkali Activated Materials: RILEM State-of-the-Art Reports, 13, pp.169–209.

Jad, Y.E., Hossain, M.U., Poon, C.S. and Tsang, D.C.W., 2021. Sustainable treatment and recycling of municipal solid waste incineration bottom ash for construction materials – A review. Resources, Conservation & Recycling, 168, p.105366. https://doi.org/10.1016/j.resconrec.2020.105366

Joel, M., Ayuba, A. and Akinyemi, B., 2021. Properties of self-compacting concrete incorporating municipal solid waste incineration bottom ash as partial replacement for fine aggregate. Case Studies in Construction Materials, 15, 0739. https://doi.org/10.1016/j.cscm.2021.e00739

Kaliyavaradhan, S.K., Ling, T.C., Mo, K.H., Yap, S.P. and Yang, J., 2020. Valorisation of concrete slurry waste as supplementary cementitious material through accelerated carbonation. Journal of Cleaner Production, 245, p.118715. https://doi.org/10.1016/j.jclepro.2019.118715

Shi, C., Zhuang, X., Tang, M. and Hu, S., 2016. Utilization of municipal solid waste incineration (MSWI) bottom ash in blended cement. Journal of Cleaner Production, 112, pp.653–661. https://doi.org/10.1016/j.jclepro.2015.07.004

Tang, P., Florea, M.V.A., Spiesz, P. and Brouwers, H.J.H., 2019. Application of thermally treated municipal solid waste incineration bottom ash fines as binder substitute. Cement and Concrete Composites, 95, pp.10–21. https://doi.org/10.1016/j.cemconcomp.2018.10.010

Tang, P., Chen, W., Yang, T. and Brouwers, H.J.H., 2020. Carbonation of MSWI bottom ash and its effect on the strength and microstructure of cementitious systems. Construction and Building Materials, 243, p.118250. https://doi.org/10.1016/j.conbuildmat.2020.118250

ABS ID: 100
Code No: CCGR-0P-08

Effect of Climate Change on Bridges

Prof. (dr.) Rajeev goel
Chief Scientist & Head, Bridge Engineering and Structures, CSIR-Central Road Research Institute, Delhi-Mathura Road, New Delhi -110025 INDIA Email: rgoel.crri@csir.res.in

Keywords: *Bridges, Climate Change, Temperature, Rainfall, Snowfall, Cyclone, Deterioration.*

1. INTRODUCTION

Bridges are lifeline of a Nation's road infrastructure and massive investments are being made in the Highway Sector year after year in India. In India, there are several lakhs of existing bridges and many more bridge are under various stages of construction / planning.

Climate change is the significant variation of average weather conditions over several decades or longer. It is the longer-term trend that differentiates climate change from natural weather variability. Thus, climate change refers to long-term shifts in temperatures and weather patterns.

Climate change poses significant risks to bridges, including accelerated degradation of materials, increased flood levels, and damage to pavements. These impacts can lead to structural damage, reduced safety, and increased maintenance costs.

This paper gives details of effect of Climate change on various design loads of the bridges including temperature, wind, snowfall, rainfall, water currant, impact on bridges due to floating bodies or vehicles, buoyancy etc. This paper also provides present strategy to mitigate the effect of climate change on bridges.

2. ABOUT CLIMATE CHANGE

Climate change refers to long-term shifts in temperatures and weather patterns. These shifts can be due to following reasons:

• Natural, due to changes in the sun's activity or large volcanic eruptions.

• Human activities primarily burning of fossil fuels like coal, oil and gas, since 1800s.

Human beings are responsible for global warming and Climate Change over the last 200 years. Human activities are causing greenhouse gases that are warming the world faster than at any time, atleast in the last two thousand years. The average temperature of the Earth's surface is now about 1.2°C warmer than it was in the late 1800s (before the industrial revolution) and warmer than at any time in the last 100,000 years.

Many people think climate change mainly means warmer temperatures. But temperature rise is only the beginning of the story. Because the Earth is a system, where everything is connected, changes in one area can influence changes in all others.

Burning of fossil fuels generates greenhouse gas emissions that act like a blanket wrapped around the Earth, trapping the sun's heat and raising temperatures.

Lesser heat escapes into space from earth due to generation of higher greenhouses gases by the humans (refer Figure-1)

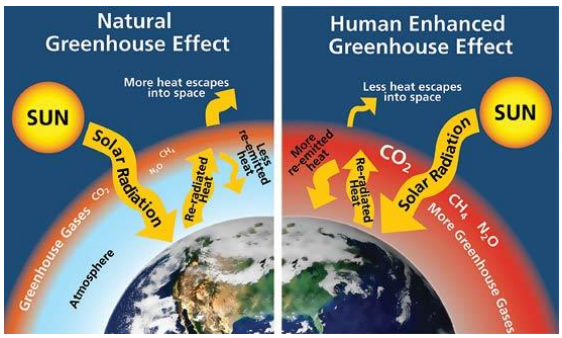

Figure-1: Lesser heat escapes into space from earth due to generation of higher greenhouses gases by the humans

The main greenhouse gases that are causing climate change include Carbon dioxide and Methane. These gases come from using gasoline for driving a car or coal for heating a building, for example. Clearing land and cutting down forests can also release Carbon dioxide. Agriculture, oil and gas operations are major sources of Methane emissions. Energy, industry, transport, buildings, agriculture and land use are among the Main Sectors causing greenhouse gases.

3. EFFECTS OF CILMATE CHANGE

Deserts are expanding, while heat waves and wildfires are becoming more common. Rise in global temperatures, resulting in more intense storms, droughts, and other weather extremes. Rise in sea levels. More frequent and intense extreme weather events. Changes in precipitation patterns

Effect on Global Temperature

Global temperature is rising since 1880 as shown in Figure-2.

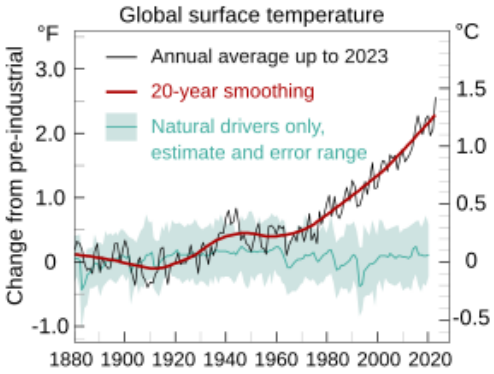

Figure-2: Rise in Global temperatures since year 1880

Effect on Rainfall

Climate change is changing rainfall patterns by increasing the intensity and frequency of precipitation in some areas, while decreasing it in others. This can cause crop damage, soil erosion, and increased flood risk. The interval between precipitation events can also change, which can lead to changes in overall precipitation totals.

Effects on Cyclones

Climate change is making tropical cyclones more intense and destructive, though it may also reduce their frequency. Cyclones may have stronger winds, may dump more rain, may bring more dangerous storm surges and flooding, may retain their strength for longer duration, and may move more slowly, resulting in more rainfall, stronger storm surge and prolonged wind damages.

Effects on Snowfalls

Climate change has caused a decrease in snowfall in many parts of the world. This is due to warmer temperatures, which cause more precipitation to fall as rain instead of snow. Snowpack has decreased at most sites in the Western United States since 1955. Peak snowpack is happening earlier in the season.

The number of heavy snowfall days has decreased.

4. EFFECTS ON BRIDGES

Bridges are designed for the following nineteen forces in India namely Dead Load, Live Load, Snow Load, Impact Factor on Vehicular Live Load, Impact Due to Floating Bodies or Vehicles, Vehicle Collision Load, Wind Load, Water Current, Longitudinal Forces due to Tractive/ Braking efforts of Vehicles, Centrifugal Force, Buoyancy, Earth Pressure, Temperature Effects, Deformation Effects, Secondary Effects, Erection Effects, Seismic Force, Wave Pressure, and Grade Effects.

Out of these nineteen forces, eight forces namely Snow Load, Impact Due to Floating Bodies or Vehicles, Vehicle Collision Load, Wind Load, Water Current, Buoyancy, Temperature Effects, and Wave Pressure are affected by Climate Change.

Effects of Excessive Rains on Bridges

Flooding is one of the most damaging hazards to the bridges which are designed for 100 year return period of Floods. However, it is anticipated that frequency of return period may reduce to 20 years return period, in next 30-40 years. Thus, Higher risk of crossing HFL very frequently. Thus, there is higher risk of landslide / slope failures due to higher precipitation; Higher Scour depth, due to higher average annual run-off; Additional loads on foundations; Higher risk of liquefaction of soil, due to higher ground water table; Higher risk of settlement of foundations; and Higher risk of accidents due to slippery roads.

Effects of Higher Temperatures on Bridges

• Melting of snow at higher rate, resulting in additional run-off

• Higher risk of damages of bridges due to impact by Avalanches

• Higher expansion of bridge may lead to damages to bridge bearings and bridge expansion joints

• Reduction in remaining fatigue life

• Higher thermal stresses in the bridges

• Higher temperature gradient across the depth of bridge deck

• Effects of Higher and Intensive Storms on Bridges

• Higher forces on the various members of the bridges

• Higher wind speeds and more frequent rains may increase the risk of instability of cables of Cable stayed bridges / Extradosed bridges

• Higher risk of damages in Long-span bridges

• Higher frequency of vehicle collision, resulting in damages due to impact and fire

More adverse effects on Bridges

• Accelerated deterioration of concrete and steel due to higher values of temperatures, rainfall, relative humidity and carbon dioxides.

• Higher Ground water table may result in formation of acids from the Sulphates and Chlorides, resulting in increased risk of damages to the foundations

• Due to rise in sea levels, higher corrosion probability in those areas of substructures which were earlier not in splash zones

• Higher long-term deflections of concrete members due to higher creep values

• Higher losses in the prestressing forces in PSC structures, due to higher creep values

• Higher chances of damages to bridge, near the Wild fire areas

5. WAY FORWARD

• Assessment of expected discharges considering effects of Climate change

• Studies on Creep and Shrinkage on the basis of changed climatic conditions and relative humidity

• Studies on various properties of materials such as strength, fatigue, corrosion etc. due to change in temperatures

• Studies on Wind and Flood to assess their impact on structures, substructures and foundations

• Studies on effective temperature ranges and temperature gradients

6. CONCLUSIONS

Like other structures, bridges are also affected by the climate change. Climate adapted new codes and guidelines need to be prepared. Existing provisions in various codes and guidelines need to be relooked and updated, based on the recent experience and research studies. In India, work has already been started. Presently, new document on "Hydraulics of Bridges" is being prepared in India, considering the effects of climate change.

REFERENCES:

[1] Wikipedia
[2] Websites of NASA, United Nations, etc.
[3] Materials from Internet

ABS ID: 54
Code No: CCGR-0P-09

A Dynamic Network Approach to Analyze the Impact of Crop Residue Burning on Urban Air Quality Using Time-Lagged Correlation

S. Anwar[1], p. Misra[2]
[1]*M Tech. Geospatial Engineering, Department of Civil Engineering, IIT Roorkee, Roorkee, India*
[2]*Assistant Professor, Department of Civil Engineering, IIT Roorkee, Roorkee, India*
Correspond to Prof. P. MISRA (prakhar.misra@ce.iitr.ac.in)

***Keywords**: Air Pollution, Crop Residue Burning, Fire Detection Counts, $PM_{2.5}$, Spatial Correlation Network, CUPI-G Sensor, Time-lagged Correlation*

1. ABSTRACT

Air pollution is a serious concern worldwide in recent decades as it poses a significant threat to both the environment and human health. In India, post-monsoon crop residue burning (CRB) in Punjab and Haryana is considered to cause severe air pollution in Delhi-NCR region. Despite extensive research on impact of CRB on urban air quality, existing studies fall short of explaining the full complexity of pollution transport from rural areas in Punjab and Haryana to urban centres such as Delhi-NCR. The existing studies utilizing HYSPLIT and other traditional models does not measure actual pollution interaction between areas. Satellite measurements also have certain limitations, especially due to presence of clouds during CRB events. This study introduces a novel approach of utilizing Spatial Correlation Network (SCN) to investigate the spatiotemporal dynamics of extreme pollution events induced by CRB. While SCNs have previously been employed in wildfire studies, their use in context of agricultural residue burning in the IGP region remains unexplored. The study utilized hourly $PM_{2.5}$ observations from Compact and Useful $PM_{2.5}$ measuring Instrument-Gases (CUPI-G) network deployed across Punjab, Haryana and Delhi-NCR for the post-monsoon period for 2022-2024 to create SCN using time-lagged correlation. The network exhibits an increase in average degree of the SCN that reaches a maximum value of 4.5 with mean concentration of $PM_{2.5}$ reaching up to 300 $\mu g/m^3$ over the study region indicating shift from local correlation to region correlation during peak burning events. The SCN approach reveals significant $PM_{2.5}$ anomalies during the peak burning events in October and November even when fire detection counts (FDCs) are hindered by clouds. This novel approach of SCN highlights the limitations of traditional models such as HYSPLIT and satellite-derived measurements and emphasize the role of SCNs in effective environmental monitoring and air quality management.

2. INTRODUCTION

Air pollution is an increasing concern worldwide in recent decades, especially for developing countries like India. The cities in the IGP region experience severe air pollution during winter [1] [2]. Post-monsoon CRB in Punjab and Haryana is considered as one of the main reasons attributed to increased pollutant levels in the IGP region during winter [4]. CRB, popularly referred to as stubble burning, is one of the indigenous cropland management activities practiced for preparing fields for the next cropping cycle in several parts of the country [2][4]. The widespread stubble burning in the IGP region results in emission of massive amounts of harmful air pollutants such as CO (carbon monoxide), CO_2 (carbon dioxide), CH_4 (methane), NO_X (nitrogen oxides), SO_X (sulphur oxides) and particulate matter ($PM_{2.5}$, PM_{10}) [1][2] [4][5]. Post-monsoon CRB is a major contributor to $PM_{2.5}$ pollution in the IGP region [1][6].

Punjab and Haryana are considered as the rice and wheat bowls of India and are also responsible for the highest residue burning in India [8][9]. In Punjab and Haryana, the main reason for stubble burning is a limited time frame for farmers to prepare fields for next crop due to enactment of Preservation of Subsoil Water Act (SSWA, 2009) [4][6][8]. This act requires transplanting rice to start by 20 June, which was enacted for reviving

groundwater table in Punjab and Haryana and which results in delay in rice harvesting and reduces the time for preparing fields for wheat crop to just 20-25 days [6][8]. The use of mechanized harvesting and lack of affordable options for managing leftover crop residue, forces farmers to burn crop residue in open fields [4] [10]. The north-western winds from Punjab and Haryana cause the dispersal of pollutants emitted due to CRB towards the Delhi-NCR region, causing severe air pollution [4][8] [11].

Despite extensive research on the impact of CRB on air quality in the IGP region, existing studies fall short of explaining the full complexity of pollution transport from source regions to receptor regions such as Delhi-NCR [1][4][5][12]. Traditional monitoring networks focus more on urban areas and do not reveal how pollutants spread over time from rural regions to urban centres [13][14]. Satellite measurements also have various limitations especially during cloudy and hazy conditions during CRB events [8][11][12]. Previous researches have utilized HYSPLIT (Hybrid Single Particle Lagrangian Integrated Trajectory) model to assess the impact of CRB on urban air quality, but these models have also various limitations [2][4]. The HYSPLIT trajectory model lacks quantitative measures of influence between monitoring locations and does not capture temporal synchronizations in pollutant dynamics, particularly under various episodic events like CRB.

Recent studies have emphasized on the application of SCN for assessing the spatio-temporal dynamics of $PM_{2.5}$ and other pollutants[13][15] [16]. A. Gozolchiani et al., [16] established a climate network using time-lagged correlation to track the influence of El Niño across the globe and enabled the identification global impacts of El Niño events through changes observed in correlation patterns. Vlachogiannis et al., [15] proposed a framework of time-evolving directed and weighted correlation networks in China and California, USA, utilizing an hourly $PM_{2.5}$ dataset. Bashan et al., [13] presented a novel dynamic network approach to uncover the spatiotemporal dynamics of extreme pollution events. The study utilized a Spatial Correlation Network approach using hourly $PM_{2.5}$ data from monitoring stations distributed across the contiguous United States to reveal significant $PM_{2.5}$ anomalies during the 2020 and 2021 wildfire seasons in the United States [13]. This study enhances the understanding of spatiotemporal dynamics of $PM_{2.5}$ establishing SCNs as valuable tools for effective environmental monitoring and air quality management [13].

The present study highlights an efficient and unique approach that employs Spatial Correlation Network using a time-lagged correlation of hourly $PM_{2.5}$ to assess the impact of CRB on urban air quality in the IGP region. The SCN approach employed in this study helps in comprehensive understanding of pollution pathways and reveal significant regional correlation during peak burning events. The objective of the study to utilize SCN to investigate how $PM_{2.5}$ emissions from CRB events move from rural burning hotspots in Punjab and Haryana to urban centres like Delhi-NCR. The study highlights the limitations of traditional models like HYSPLIT and satellite measurements and further seeks to improve our understanding of transboundary air pollution which helps us with better public health responses and more efficient environmental policies.

3. STUDY AREA AND DATASETS

The study area encompasses the regions of Punjab, Haryana and Delhi-NCR as Punjab and Haryana form major part of the region where post-monsoon CRB is practiced for clearing fields for the next crop. Punjab and Haryana are the major producers of rice and wheat in India [6][8]. These two states are accountable for the maximum residue burning in the country [9]. The study area has been shown in Figure 1.

This study utilizes hourly $PM_{2.5}$ dataset from CUPI-G sensors installed across Punjab, Haryana and Delhi NCR region for creating Spatial Correlation Networks for the study period between September and November (2022-2024). The CUPI-G sensor network

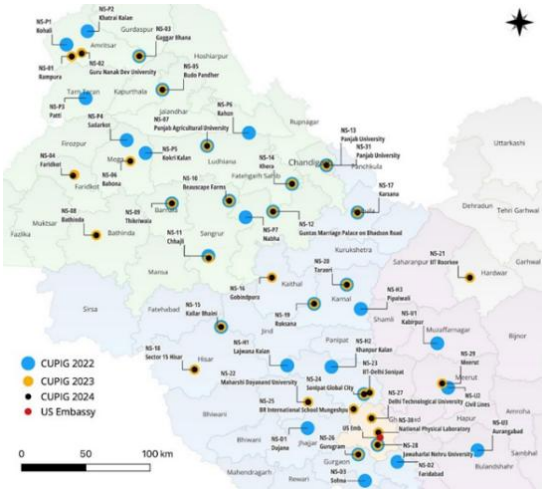

installation was part of the Aakash Project titled "An Interdisciplinary Study toward Clean Air, Public Health and Sustainable Agriculture: The case of Crop Residue Burning in North India" which was initiated as a research project at the Research Institute for Humanity and Nature (RIHN) Japan in April 2020 to address the problem of air pollution caused by large-scale rice stubble burning in the IGP region [10][14][17].

Table 1 Datasets used in the study

Dataset	Product	Spatial resolution	Temporal resolution
CUPI-G Dataset	CUPI-G sensor network	30 Sensors	Hourly data
VIIRS-SNPP FDCs	VNP14A1	750 m	Daily (2 Times, 1:30 AM, 1:30 PM)
Sentinel-5P Daily Cloud Fraction	S5P/OFFL/L3/CLOUD	1113.2 m	Daily (1:30 PM)
ERA-5 Dataset	ERA-5 ECMWF	27.75 km (0.25° x 0.25°)	Hourly

4. METHODOLOGY

The methodology of the study includes creation of daily Spatial Correlation Network, calculation of FDCs using VIIRS-SNPP Active Fire Product, and calculation of daily wind speed and planetary boundary layer height (PBLh) using ERA-5 ECMWF Climate Reanalysis dataset. The overall methodology has been shown in Figure 2. The study has utilized hourly $PM_{2.5}$ data from CUPI-G sensor network installed in the study area. The CUPI-G sensor dataset consists of hourly $PM_{2.5}$ data for three years from 2022 to 2024 for the month of September, October and November.

In this study, we conceptualize CUPI-G sensors as nodes of the network and constructed undirected, weighted networks. An edge or link is formed between two nodes if their time series of $PM_{2.5}$ concentrations exhibit a statistically significant time-lagged correlation.

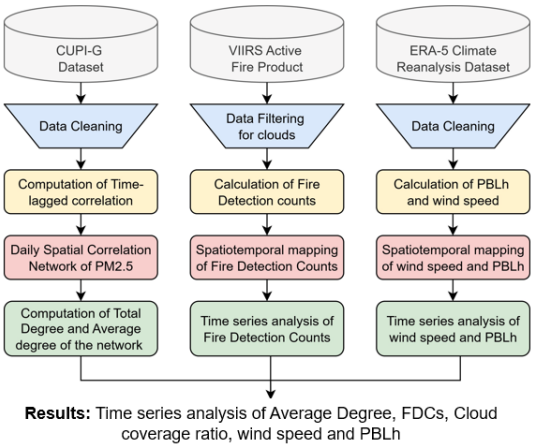

Figure 2. Overall Methodology

Mathematically, a link between two nodes i and j is established if the maximum of the absolute value of their cross-correlation function, denoted as Cij over a range of time lags $\tau \in [-\tau_{max}, \tau_{max}]$, exceeds a predefined critical bonding threshold $\hat{C}_{ij}(\tau)$. These complex networks are spatially constrained as we employ the voronoi diagram to ensure connections only among neighbouring nodes. The result is a dynamic network that evolves with time, reflecting the spatial propagation of pollutants across a region. The cross-correlation between pair of monitoring stations is calculated using eq. (1).

$$\hat{C}_{ij}^{(\tau)} = \frac{\langle gX_i(t).gX_j(t+\tau)\rangle}{\sqrt{\langle [gX_i(t)]^2\rangle} * \sqrt{[gX_j(t+\tau)]^2}} \qquad (1)$$

where τ denotes the time-lag, bounded within the interval $-\tau_{max} < \tau < \tau_{max}$. The variable X_i refers to the $PM_{2.5}$ concentration recorded by sensor i at time t. The fluctuation component is defined as $gX_i(t) = X_i(t) - \langle X_i \rangle$, which measures deviations from the temporal mean value $\langle X_i \rangle$, calculated over T time steps as:

$$\langle X_i \rangle = \frac{1}{T}\sum_{t=1}^{T} X_i(t) \qquad (2)$$

We calculated the total degree and average degree of the Spatial Correlation Network for measuring the overall impact of CRB on the network. The total degree of the network ($2L$) is determined by adding all edges formed between sensor locations [13]. The average degree (μ) of the network is calculated by dividing the total degree by the number of monitoring stations of the network [13].

We selected an optimal time lag by using statistical correlation between average degree of the network and mean values of $PM_{2.5}$ for different time lags ranging from 0 to 15 hours. We adopted a value of 0.7 as a critical threshold value, which was determined by analysing the slope of curve between average degree and different threshold values ranging from 0 to 1.

5. RESULTS AND DISCUSSION

The Spatial Correlation Network approach employed in our study leverages hourly datasets of $PM_{2.5}$ measurements from CUPI-G sensors across Punjab, Haryana and Delhi-NCR. We utilized time-lagged correlations to model the interrelationships between $PM_{2.5}$ measurements among neighbouring CUPI-G monitoring sites in the study region. Figure 4 shows SCN for 9th September 2022, 9th October 2022, and 8th November 2022 and 9th November 2022. The network shows localized correlation with low network density ($\mu = 2.44$) during 9th September 2022, when FDCs are very low (28) and average value of $PM_{2.5}$ is also low (<100 $\mu g/m^3$). On 9th October 2022, the average degree increases to 2.81, accompanied by an increase in $PM_{2.5}$ levels, indicating early stage crop residue burning and inter-regional pollution transport in the study region (Figure 4). On 8th November and 9th November 2022, there is significant increase in total degree and average degree of the network, as the average degree reached 3.94 and 3.31 on these days respectively (Figure 4). The network during 8th November 2022 and 9th November 2022 shows regional correlation due to significant rise in number of crop residue fires (Figure 4). The dense network suggests persistent transport of pollutants during crop residue burning and indicates long-range transport of $PM_{2.5}$ from source to receptor regions. The increase in average degree of the network during peak burning events is consistent with the study by Bashan et al., [13] which showed an increase in total degree and average degree due to wildfires and dust storm events in Southern California, USA.

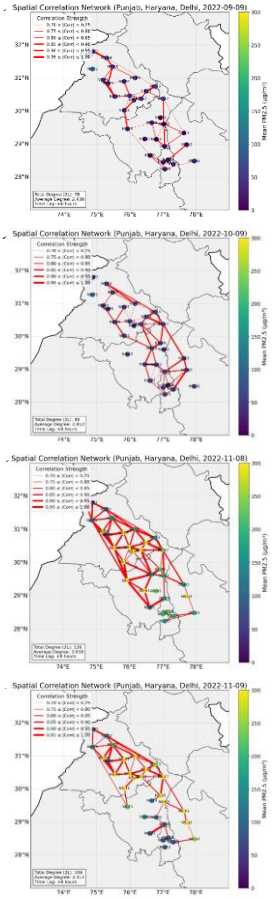

Figure 3 Spatial Correlation Network for (a) 9th September 2022, (b) 9th October 2022 (c) 8th November 2022 and (d) 9th November 2022.

The FDCs during 8th November 2022 and 9th November 2022 are 971 and 1342 respectively (Figure 5). The network exhibits an increase in average degree that reaches a maximum value of 4.5 with mean concentration of $PM_{2.5}$ reaching up to 300 µg/m^3 over the study region

indicating shift from local correlation to region correlation during peak burning events (Figure 5).

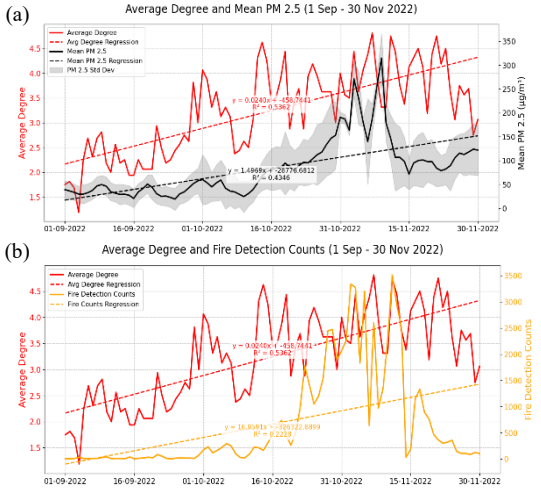

Figure 4. (a) Average degree and Mean $PM_{2.5}$ over the study region during September -November 2022 (b) Average degree of the network and FDCs in the study region during Sep-Nov 2022.

The FDCs on 8th November (971) are lower than FDCs on 9th November (1342) as shown in Figure 3. However, the average degree of the network on 8th November (3.94) is higher than average degree on 9th November (3.31). This significant observation can be attributed to the impact of cloud cover on satellite detection of FDCs, as many crop residue fires remain undetected due to high cloud coverage ratio (>0.75) on 8th November 2022 (Figure 3). The cloud coverage ratio on 9th November (<0.4) is lower as compared to 8th November 2022. The SCN approach shows widespread impact of pollution caused due to crop residue fires using measures of SCNs such as average degree (μ) and total degree ($2L$) even when FDCs are not detected due to presence of clouds.

Figure 5 Fire Detection Counts and Cloud Coverage Ratio for Sep -Nov 2022

6. CONCLUSION

The study demonstrates the efficacy of SCN approach to understand the spatiotemporal dynamics of $PM_{2.5}$ during extreme pollution events like CRB. The key findings of this study include a high average degree (up to 4.5) of the SCN during peak burning events in October and November, correlated with elevated $PM_{2.5}$ levels (up to 300 $\mu g/m^3$). The study successfully highlighted the limitations of traditional models like HYSPLIT and satellite based FDCs due to presence of clouds, and established SCN as an efficient tool for environmental monitoring. These insights have significant implications for air quality management, suggesting targeted policy interventions such as real time monitoring to mitigate the adverse effects of CRB on urban air quality in the IGP region.

REFERENCES:

[1] D. H. Cusworth *et al.*, 'Quantifying the influence of agricultural fires in northwest India on urban air pollution in Delhi, India', *Environmental Research Letters*, vol. 13, no. 4, Sep. 2018, doi: 10.1088/1748-9326/aab303.

[2] M. Nair, H. Bherwani, S. Kumar, S. Gulia, S. Goyal, and R. Kumar, 'Assessment of contribution of agricultural residue burning on air quality of Delhi using remote sensing and modelling tools', *Atmos Environ*, vol. 230, Sep. 2020, doi: 10.1016/j.atmosenv.2020.117504.

[3] P. Das, M. D. Behera, and P. C. Abhilash, 'A rapid assessment of stubble burning and air pollutants from satellite observations', *Trop Ecol*, vol. 65, no. 1, pp. 152–157, 2024, doi: 10.1007/s42965-022-00291-5.

[4] N. K. Maurya, P. C. Pandey, S. Sarkar, R. Kumar, and P. K. Srivastava, 'Spatio-Temporal Monitoring of Atmospheric Pollutants Using Earth Observation Sentinel 5P TROPOMI Data: Impact of Stubble Burning a Case Study', *ISPRS Int J Geoinf*, vol. 11, no. 5, 2022, doi: 10.3390/ijgi11050301.

[5] P. K. Nagar and M. Sharma, 'A hybrid model to improve WRF-Chem performance for crop

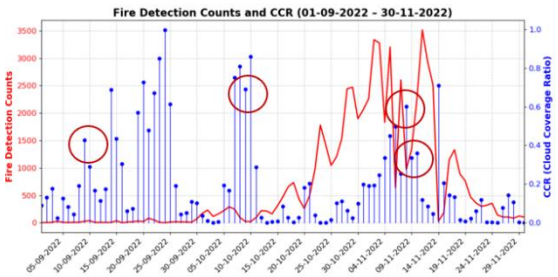

burning emissions of PM2.5 and secondary aerosols in North India', *Urban Clim*, vol. 41, no. August 2021, p. 101084, 2022, doi: 10.1016/j.uclim.2022.101084.

[6] H. Sembhi *et al.*, 'Post-monsoon air quality degradation across Northern India: Assessing the impact of policy-related shifts in timing and amount of crop residue burnt', *Environmental Research Letters*, vol. 15, no. 10, 2020, doi: 10.1088/1748-9326/aba714.

[7] R. Sawlani *et al.*, 'Crop Residue Burning: A Threat to South Asian Air Quality', *Atmos Pollut Res*, vol. 10, no. 3, pp. 868–879, 2019, doi: 10.1016/j.apr.2018.12.015.

[8] H. Jethva, O. Torres, R. D. Field, A. Lyapustin, R. Gautam, and V. Kayetha, 'Connecting Crop Productivity, Residue Fires, and Air Quality over Northern India', *Sci Rep*, vol. 9, no. 1, Sep. 2019, doi: 10.1038/s41598-019-52799-x.

[9] K. C. Thumaty *et al.*, 'Maurya', *Curr Sci*, vol. 109, no. 10, p. 1850, 2015, doi: 10.18520/v109/i10/1850-1868.

[10] S. Hayashida, 'Tackling Air Pollution from Agricultural Residue Burning: The Aakash Project: Challenge for Reduction of Rice-Stubble Burning in the Indian Punjab Region', 2023. [Online]. Available: https://www.chikyu.

[11] T. Liu, L. J. Mickley, S. Singh, M. Jain, R. S. DeFries, and M. E. Marlier, 'Crop residue burning practices across north India inferred from household survey data: Bridging gaps in satellite observations', *Atmos Environ X*, vol. 8, no. September, p. 100091, 2020, doi: 10.1016/j.aeaoa.2020.100091.

[12] K. P. Vadrevu, E. Ellicott, K. V. S. Badarinath, and E. Vermote, 'MODIS derived fire characteristics and aerosol optical depth variations during the agricultural residue burning season, north India', *Environmental Pollution*, vol. 159, no. 6, pp. 1560–1569, Sep. 2011, doi: 10.1016/j.envpol.2011.03.001.

[13] N. F. Bashan, W. Li, and Q. R. Wang, 'Dynamics of PM2.5 and network activity during extreme pollution events', Sep. 2024, *Nature Research*. doi: 10.1038/s41612-024-00716-z.

[14] T. Singh *et al.*, 'Very high particulate pollution over northwest India captured by a high-density in situ sensor network', *Sci Rep*, vol. 13, no. 1, Sep. 2023, doi: 10.1038/s41598-023-39471-1.

[15] D. M. Vlachogiannis, Y. Xu, L. Jin, and M. C. González, 'Correlation networks of air particulate matter (PM 2.5): a comparative study', *Appl Netw Sci*, vol. 6, no. 1, Sep. 2021, doi: 10.1007/s41109-021-00373-8.

[16] A. Gozolchiani, K. Yamasaki, O. Gazit, and S. Havlin, 'Pattern of climate network blinking links follows El Niño events', *Europhys Lett*, vol. 83, no. 2, p. 28005, Jul. 2008, doi: 10.1209/0295-5075/83/28005.

[17] P. Mangaraj *et al.*, 'Weak coupling of observed surface PM2.5 in Delhi-NCR with rice crop residue burning in Punjab and Haryana', *NPJ Clim Atmos Sci*, vol. 8, no. 1, Sep. 2025, doi: 10.1038/s41612-025-00901-8.

ABS ID: 151
Code No: CCGR-0P-10

Toward Sustainable Cooling: Integrating Heat Pipes in Windcatchers for Passive Ventilation System

Veena Chaudhary[1], Shubham Kumar[2]
[1,2]*CSIR- Central Building Research Institute Roorkee (CBRI), Uttarakhand, India*
[1*]*Corresponding Author: veenachaudhary.cbri@csir.res.in*

***Keywords**: Passive cooling, Natural ventilation, low carbon cooling, Heat transfer device, climate change, Windcatcher.*

Abstract

Low-carbon cooling systems preserve global community well-being and thermal comfort while minimizing the negative environmental effects. Rethinking building services is necessary to safeguard inhabitants at a low energy cost in an era of the global energy crises, and escalating effects of climate change and global warming The significance of low-carbon cooling systems cannot be emphasized in the battle against climate change, energy conservation, air quality improvement, boosting resilience to climate risks, advancing sustainable development goals, and financial benefit. Since fans account for 25% of a building's energy usage, traditional HVAC (heating, ventilation, and air conditioning) systems are not sustainable for the built environment of the future. Thus, from the standpoints of energy consumption and occupant well-being, natural ventilation technologies—like windcatchers—present a benefit over mechanical systems. In order to improve the cooling efficiency of windcatchers for buildings in hot climates, a single-sided windcatcher incorporating a Heat Transfer Device has been developed numerically. Geometric parameters, operating condition assessments, and ventilation need assessments are all part of the numerical model used to evaluate the windcatcher's ventilation and cooling performance using a heat transfer device. Variations of damper angle on ventilation rate, mean age of air, and ventilation efficiency are investigated. Based on typical India hot climate, this unique approach produced a significant temperature drop range of 6 K–12K for outdoor at 45°C. The main goal was to evaluate how geometrical compactness affected the windcatcher's ability to ventilate and cool using a heat transfer device. The airflow distribution, streamlined flow, and temperature distribution are utilized to determine the performance of a wind-driven ventilation system. It could be a sustainable space conditioning solution from an energy consumption point of view and also help to mitigate the impact of climate change.

Introduction

In the quest for sustainable and efficient architectural solutions, mankind often turns to nature for inspiration. One such marvel of biomimicry is the Unidirectional Windcatcher with Heat Transfer Device, which blends ancient wisdom with modern technology. This structure not only captures the cool breeze but also channels it with precision, enhancing ventilation and cooling within buildings [1], [2], [3], [4]. The application of windcatchers [2], [4], [5], [6], [7] for cooling in contemporary architecture was studied by various researchers, who show the impact of modern windcatchers on the indoor air quality, thermal comfort, and energy consumption, which leads to a sustainable cooling approach without

harming the climate. Now, imagine this windcatcher integrated with a sophisticated heat transfer mechanism, capable of harnessing the thermal energy of ambient air for heating or cooling purposes [5], [6], [8], [9]. This amalgamation of passive cooling techniques with active thermal management represents a groundbreaking approach toward sustainable building design. This innovative synergy between passive airflow control and active thermal regulation reduces reliance on mechanical heating and cooling systems, significantly lowering energy consumption and carbon emissions. As we strive toward a greener future, embracing such transformative technologies holds the promise of not only enhancing the comfort and efficiency of our environments but also contributing to the global imperative to mitigate climate change. Numerous studies [9], [10], [11], [12], [13]have focused on evaluating the thermal performance of this system and its ability to provide thermal comfort for occupants. Most of the studies [14], [15] have been carried out using numerical and analytical modeling, validated by laboratory scale or wind tunnel test data. Recently, several studies have focused on addressing one of the limitations of the windcatcher by incorporating evaporative cooling [16], [17] and heat transfer devices within the airflow channel to enhance its cooling capabilities in hot outdoor conditions [8], [18], [19], [20]. Chohan et al [21] presented the role of windcatcher in UAE heritage architecture as an approach to achieve zero-energy cooling solutions. Their study focuses on the role of the windcatcher as a traditional element that improves natural ventilation and minimizes energy consumption in buildings, specifically in hot and arid climatic regions. Mamari et al[22] discussed the optimized design of windcatchers in order to identify the impact on thermal comfort and indoor air quality in contemporary houses. Computational analysis of windcatcher design was conducted, where the orientation was at 30 degrees. Authors observed the improvement in comfort levels in terms of predicted mean vote and reduction in carbon dioxide with windcatcher application. Figure 1 represents the traditional windcatcher and the working principle of the heat pipe. Windcatchers capture the air and direct it into the indoor environment, which provides natural ventilation and cooling. The windcatcher performance is influenced by the orientation of the wind capture direction. In current research, the influence of the damper angle of louvers on the performance of a single-sided windcatcher is studied using a computational approach, and the results are validated with the literature. This traditional windcatcher was used in arid countries, especially in Persian countries, and a few applications were found in India also. There is a strong need to explore the windcatcher possibility in Indian climatic conditions. Since windcatcher is passive approach to cool down the building with the integration of other passive cooling technologies. In current research, a heatpipe, which is a passive heat transfer device, was integrated with a single-sided compact windcatcher to provide comfortable cooling inside the building without any electricity consumption. Following sections presented the adopted computational methodology in current research.

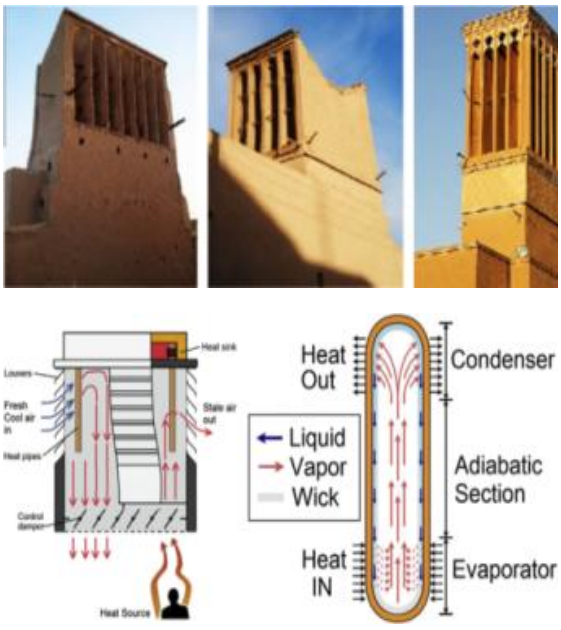

Fig.1: Traditional windcatchers and working principle of heat pipe

1. Modelling and Simulation

A proposed windcatcher model of 1*1*1.2 m dimensions is designed using ANSYS Design Modeler software. This model has an integrated heat transfer device and a cooling sink arrangement to lower the incoming air. The damper angle of the louvers is varied from 30 degrees to 90 degrees to identify the optimum damper angle. Here, the proposed windcatcher was modified in order to reduce its height. It is a single-sided windcatcher with eight louvers/ To effectively guide the incoming cooled fresh air into the room, an adjustable damper arrangement is placed at the outlet of the windcatcher. To visualize the room's thermal comfort and air flow, as well as to replicate the room's internal climate, a micro-climate model is created at the outlet of the windcatcher, using Ansys Design Modeler. Additionally, a macro-climate model is created above the room, containing the windcatcher body. This larger model captures the external environment and the wind flow around the windcatcher. Table 1 depicts the details of the computational model geometry.

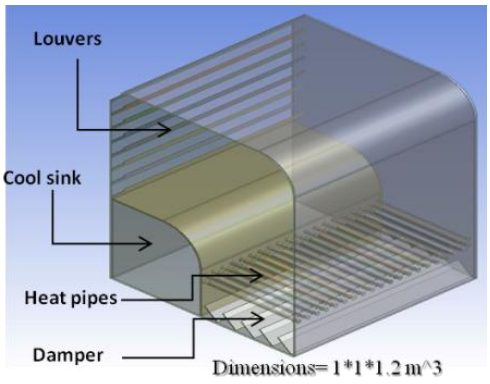

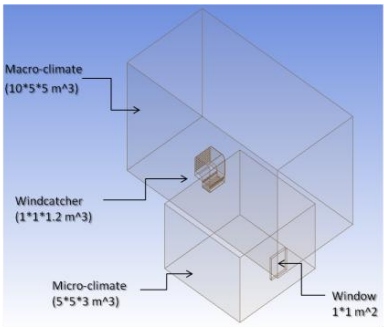

Fig.2: windcatcher with heat pipe and macroclimate.

Table 1: Details of the geometry model of windcatcher

Component Name	Material of construction	Dimensions (m)	Surface Roughness (μm)
Wind catcher body	Steel	Dimensions= 1*1*1.2 Wall thickness= 0.01	15
Louvers	Aluminum	No. of louvers= 8	1
Heat pipes	Copper	Dia= 0.02	1
Dampers	Aluminum	Thickness= 0.005 No of dampers= 5	1
Room walls	Concrete-aerated	Dimensions= 5*5*3 Wall thickness= 0.1	300

I. Mesh generation and grid independence analysis

The proposed windcatcher system is designed to evaluate both ventilation efficiency and passive cooling performance under controlled conditions. The model setup comprises three main components: a macro-climate chamber, a windcatcher module integrated with thermal enhancement features, and a micro-climate chamber.

Macro-Climate Chamber: This section represents the simulated outdoor environment. It is designed to replicate various external climatic conditions, such as wind speed, direction, ambient temperature, and

solar radiation. The macro-climate boundary provides realistic inflow conditions for wind and heat transfer, allowing accurate prediction of how the windcatcher responds to different environmental scenarios.

Windcatcher Module: Positioned between the macro- and micro-climate chambers, this central component includes a windcatcher shaft integrated with passive heat transfer enhancement devices. These may include internal vanes, a wing wall for improved airflow directionality, and cooling elements such as heat pipes or radiative cooling panels. The module is connected to a cooling sink—either a water-based or PCM-based thermal storage unit—designed to absorb and dissipate the heat extracted from the incoming air. The integration of these elements aims to improve both the convective and conductive cooling efficiency of the windcatcher.

Micro-Climate Chamber: This part of the model simulates the indoor conditions of a room or enclosed space. It is used to study airflow distribution, air change effectiveness, temperature stratification, and overall thermal comfort within the occupied zone. Key performance indicators such as air velocity, mean radiant temperature, and thermal comfort indices (e.g., PMV, PPD) are evaluated in this domain.

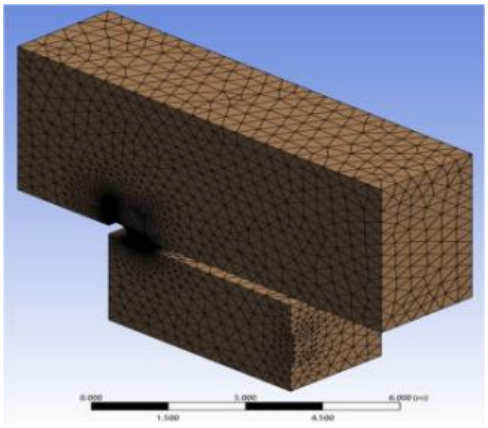

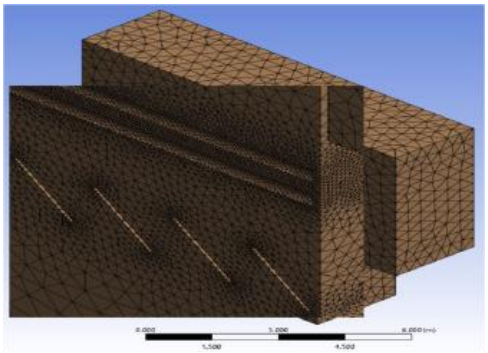

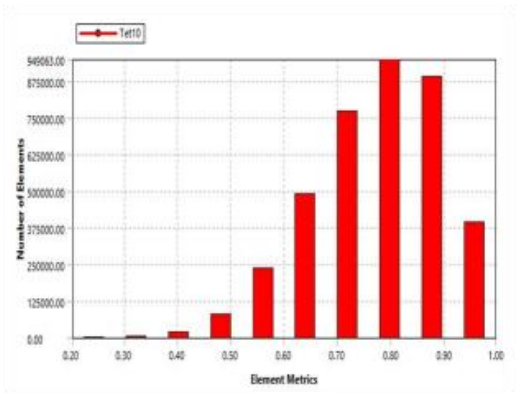

Fig.3: Orthogonal quality metrics

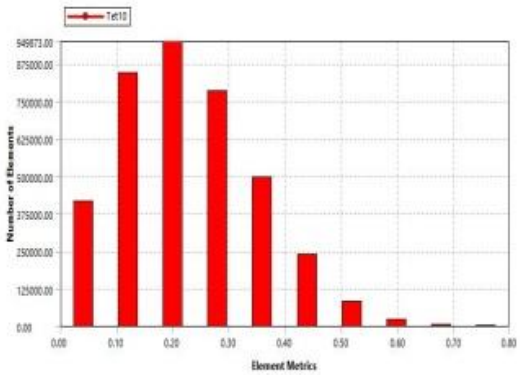

Fig.4: Skewness metrics

To optimize the computational resources and reduce simulation time without compromising the accuracy of results, the complete windcatcher system model is bisected along a central vertical symmetry plane. This approach effectively halves the domain, assuming mirrored airflow and thermal behavior on both sides. The symmetric half-model significantly decreases the total number of computational cells required for meshing. Meshing of the model is performed using the ANSYS Meshing tool. An unstructured mesh consisting of

tetragonal (tetrahedral) elements is employed, which offers greater flexibility in capturing complex geometries such as the internal contours of the windcatcher and heat exchanger components. Local mesh refinement is applied in critical zones—such as the windcatcher throat, around heat exchange surfaces, and in the micro-climate outlet region—to ensure accurate resolution of flow and thermal gradients. Mesh quality metrics such as skewness, orthogonality, and aspect ratio are monitored to maintain numerical stability and solution accuracy during simulation.

At the initial stage of the CFD analysis for the proposed windcatcher system, a grid independence (mesh convergence) study is conducted to verify that the simulation results are not significantly influenced by the mesh density. This is a crucial step to ensure the reliability and accuracy of the numerical results while optimizing computational resources. To perform this assessment, three different mesh resolutions are developed using ANSYS Workbench:

• Coarse mesh comprising approximately 633,588 elements

• Medium mesh with 3,839,380 elements

• Fine mesh consisting of 5,304,258 elements

All three mesh configurations are generated with the same geometry and boundary conditions, maintaining consistency across simulations. The key performance metric selected for comparison is the area-averaged air velocity across a horizontal plane located at 1.5 meters above the floor level, representing the average breathing zone height in the micro-climate (room) domain. Upon evaluation of simulation results, the transition from the coarse to the medium mesh results in a 20.51% increase in area-averaged velocity, indicating that the coarse mesh lacks sufficient resolution to capture critical flow features. However, when transitioning from the medium to the fine mesh, only a marginal 0.451% increase in velocity is observed, suggesting that further mesh refinement yields negligible improvement in solution accuracy. Based on these observations, the medium mesh configuration is selected for all subsequent simulations. This choice strikes a balance between computational efficiency and result accuracy, ensuring a sufficiently resolved flow field without incurring excessive simulation time or computational cost.

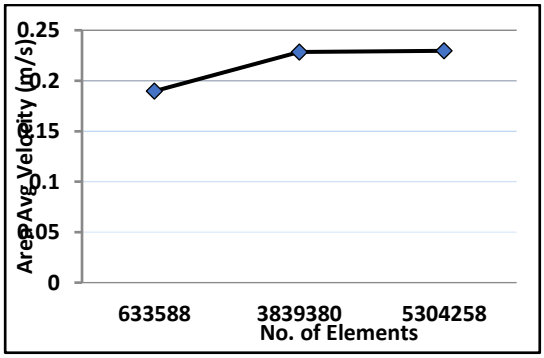

Fig. 5: Grid Independence Test

II. CFD Methodology

In this study, Computational Fluid Dynamics (CFD) simulations are carried out using ANSYS FLUENT to analyze the airflow and passive cooling performance of the proposed windcatcher system. The windcatcher is integrated with heat pipes to enhance cooling through natural ventilation by facilitating heat extraction from incoming air. The simulation involves solving the governing equations of mass, momentum, and energy conservation, which describe airflow and heat transfer within the system. To model turbulence effects, the standard k–ε turbulence model with standard wall functions and curvature correction is employed. This model is widely used in natural ventilation studies due to its balance of accuracy and computational efficiency [6]. The pressure-based solver is used in conjunction with the Semi-Implicit Method for Pressure-Linked Equations (SIMPLE) algorithm for pressure-velocity coupling. A second-order upwind scheme is applied to discretize all governing equations, ensuring accurate resolution of velocity and temperature

gradients with minimal numerical diffusion. Boundary conditions, such as inlet velocity and temperature profiles, are consistently applied across all simulations. Surface materials and heat pipe properties are also specified to simulate realistic thermal interactions within the windcatcher system.The governing equations used in this study are shown below:

$$\frac{\partial \rho}{\partial t} + \nabla \times (\rho u) = 0 \quad (1)$$

$$\frac{\partial (\rho u)}{\partial t} + \nabla \times (\rho u u) = -\nabla P + \rho g + \nabla \times (\mu \nabla u) - \nabla \times \tau_t \quad (2)$$

Wheret is time and and u is the fluid density and velocity vector respectively.P denotes the pressure;g is gravitational acceleration vector, is molecular dynamic viscosity of fluid and represents the divergence of the turbulence stresses which accounts for auxiliary stresses due to velocity fluctuations.

$$\frac{\partial (\rho e)}{\partial t} + \nabla \times (\rho e u) = \nabla \times \left(k_{eff} \nabla T\right) - \nabla \times \left(\sum_i h_i j_i\right) \quad (3)$$

Where represents specific internal energy, is effective heat conductivity, T is air temperature, and are the specific enthalpy and mass flux of the fluid.

$$\frac{\partial (\rho k)}{\partial t} + \nabla \times (\rho k u) = \nabla \times \left[\alpha_k \mu_{eff} \nabla k\right] + G_k + G_b - \rho_\varepsilon \quad (4)$$

$$\frac{\partial (\rho \varepsilon)}{\partial t} + \nabla \times (\rho \varepsilon u) = \nabla \times \left[\alpha_\varepsilon \mu_{eff} \nabla \varepsilon\right] + C_{1\varepsilon} \frac{\varepsilon}{k} (G_k + C_{3\varepsilon} G_b) - C_{2\varepsilon} \rho \frac{\varepsilon^2}{k} \quad (5)$$

Where represents the source term of turbulent kinetic energy(TKE) due to average velocity gradient, is the source term of TKE due to buoyancy force, and are the turbulent Prandtl's numbers, , and are empirical model constants.

III. Boundary conditions and convergence of solution

The boundary conditions for the numerical model are defined in accordance with best practice guidelines from the literature on natural ventilation airflow modeling. The standard k–ε turbulence model with standard wall functions is selected, as it has been widely validated for similar naturally ventilated systems. Air density is assumed constant (incompressible flow) throughout the domain, which is a valid assumption for low-speed natural ventilation scenarios.At the micro-climate window and the macro-climate outlet, atmospheric pressure is applied as the outlet boundary condition, set at 0 Pa gauge pressure. No-slip wall conditions are assigned to all solid surfaces to represent realistic boundary layer development and surface interaction. The macro-climate domain simulates external wind conditions. Air enters through a vertical face designated as a velocity inlet, while the opposite face is set as a pressure outlet. A uniform inlet velocity profile is applied, with the ambient wind temperature set to 318 K. The surface temperature of the heat pipes within the windcatcher is fixed at 293 K, enabling convective heat transfer that cools the incoming air before it enters the indoor (micro-climate) space.To account for buoyancy effects due to temperature differences, gravitational acceleration is included in the simulation, applied as –9.81 m/s² in the y-direction. All boundary walls are treated as no-slip surfaces with specified roughness height (ks = 0.5 m) and roughness constant (cs = 0.5) to simulate surface friction effects accurately. The second-order upwind scheme is used to discretize all transport equations for improved accuracy. For pressure-velocity coupling, the SIMPLE algorithm is employed for steady-state simulations, while the PISO algorithm is used for transient simulations to capture dynamic airflow behavior effectively. The convergence limit for residuals is set to 10-3 for all equations solved in this numerical study.

Table 2: Details of ANSYS model.

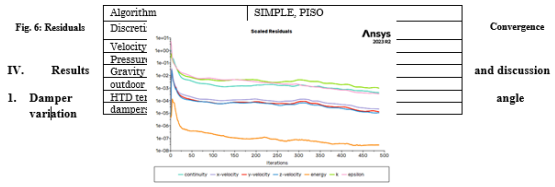

Fig. 6: Residuals

IV. Results and discussion

1. Damper angle variation

To evaluate the influence of damper orientation on the internal airflow dynamics and thermal comfort, the angle of the dampers located at the windcatcher outlet is varied systematically. These angles are defined clockwise from the horizontal plane, and four distinct configurations are investigated: 30°, 45°, 60°, and 90°. The purpose of this parametric variation is to identify the damper angle that provides optimal fresh air distribution, enhances ventilation effectiveness, and supports thermal comfort within the occupied zone of the room. Each damper configuration is simulated under identical boundary and environmental conditions to isolate the effect of damper angle. The results are analyzed based on parameters such as air velocity distribution, recirculation zones, and air change effectiveness within the micro-climate space.

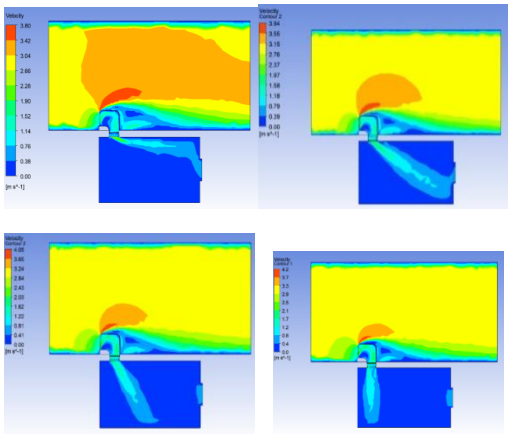

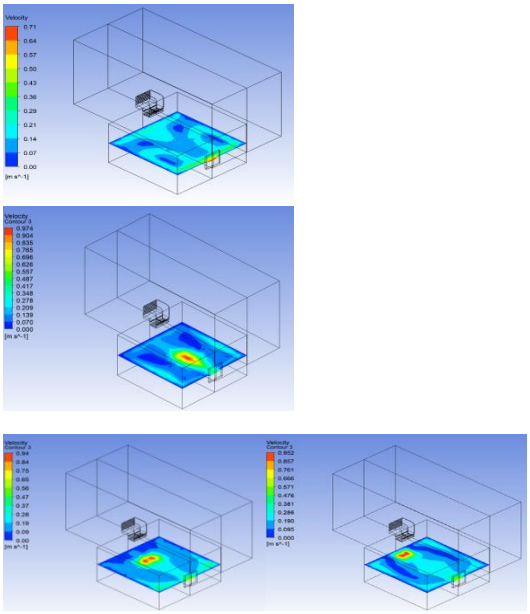

Fig. 7: damper angle variation and velocity contour at breathing height (1.1 m)

Among the four tested angles, the 60° damper setting demonstrates the most favorable airflow characteristics. Specifically, it facilitates smooth redirection of the incoming airstream, minimizes flow stagnation, and enhances cross-room air mixing, leading to a uniform distribution of fresh air throughout the space.At this angle, a satisfactory ventilation rate is maintained, with improved airflow penetration depth and reduced stratification. This configuration strikes a balance between adequate air momentum and directional control, allowing the cooled air—conditioned by the heat pipes—to effectively reach the lower occupied zone. Visualization of the airflow streamlines (see Fig. 7) confirms consistent flow patterns and minimal dead zones compared to the 30°, 45°, and 90° cases. Based on these results, the 60° damper angle is selected as the optimal configuration for further in-depth analysis, including thermal performance evaluation, occupant comfort studies, and energy efficiency assessments.

2. Simulation results at 600 damper angle

For the numerical analysis of the proposed windcatcher system, a fixed damper angle of 60° is employed, based on prior parametric optimization which demonstrated superior airflow and ventilation performance at this configuration. Additionally, the louver angle at the windcatcher inlet is fixed at 45°, a value widely reported in the literature to enhance the capture and redirection of ambient airflow into indoor spaces through natural ventilation. Climatic boundary conditions for the simulation are derived from on-site weather data corresponding to the actual location of the planned or implemented field study. These include external air temperatures and humidity levels representative of typical warm-season conditions, with values set at 318 K (45°C) and 20% relative humidity, respectively. To assess the effect of varying wind intensities, the simulation is conducted across five inlet wind velocities: 1, 2, 3, 4, and 5 m/s.

The airflow within the windcatcher and the indoor micro-climate is modeled using the standard k–ε turbulence model, incorporating standard wall functions and curvature correction to improve accuracy in curved and complex geometries commonly found in natural ventilation flows. This two-equation model is well-suited for predicting the turbulent behavior of air under buoyancy-driven and wind-driven conditions. Figure 8 illustrates the streamline distribution inside the windcatcher and room for varying inlet wind velocities. The visualizations indicate that with increasing wind velocity, there is a marked improvement in the circulation of fresh air within the room, resulting in more efficient mixing of cooled air delivered by the heat pipe-integrated windcatcher system. To quantitatively assess airflow and thermal distribution, a horizontal plane is defined at mid-room height (1.5 meters above floor level), corresponding to the average breathing zone height for occupants. At this plane, velocity, temperature, and pressure profiles are extracted and analyzed to evaluate thermal comfort and ventilation performance within the occupied space. Figure 9 presents the temperature distribution at mid-room height for different inlet wind velocities. The results demonstrate that the cooled air from the windcatcher is effectively distributed throughout the room. However, it is also observed that as wind velocity increases, the extent of cooling at the inlet decreases slightly. This occurs because the larger volume of incoming air at higher speeds results in a portion of the airflow bypassing contact with the heat pipe surfaces, thereby reducing the amount of heat extraction per unit of incoming air.

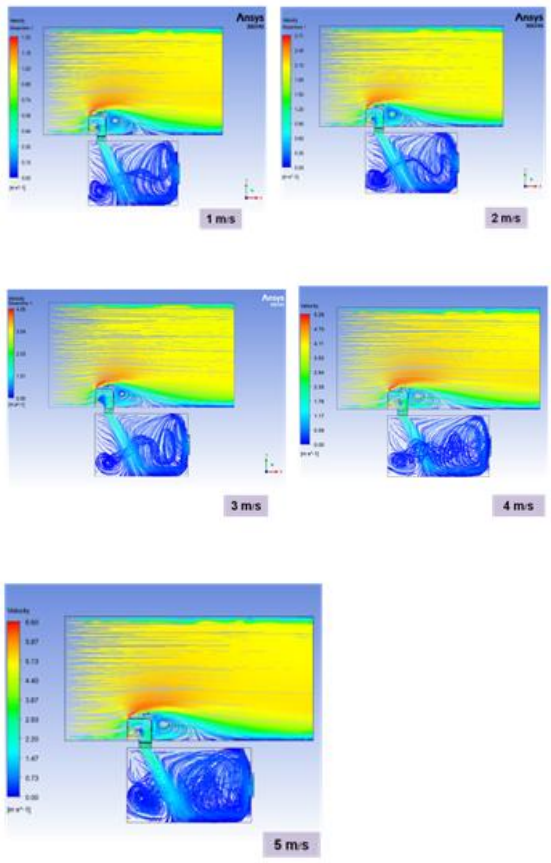

Fig.8: Flow streamline at optimized damper angle

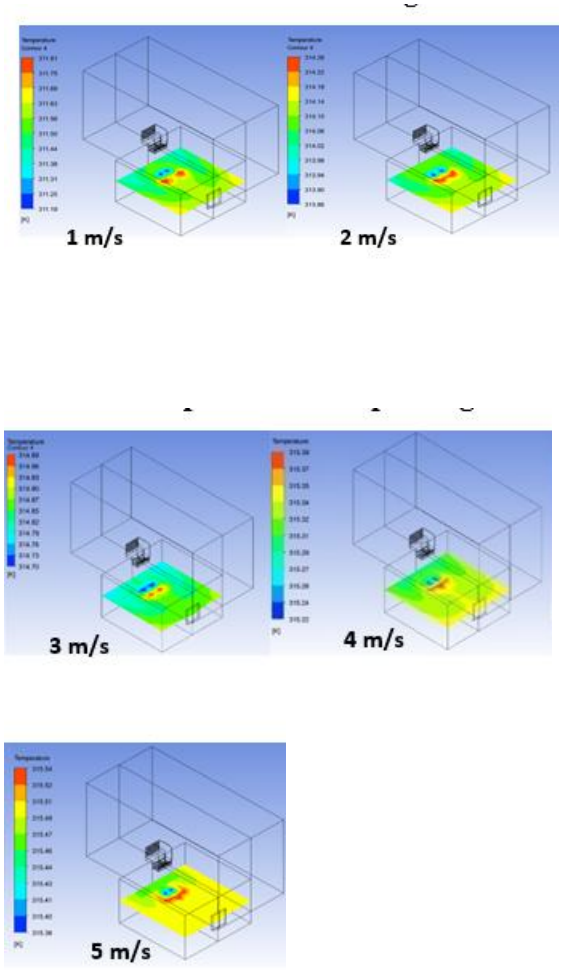

Fig. 9: Temperature distribution at mid-room height (1.5 m)

These findings underscore the trade-off between airflow volume and cooling effectiveness, highlighting the importance of optimizing windcatcher and heat pipe design to maintain both adequate ventilation rates and desired indoor air temperatures across a range of external wind conditions.

Figure 10 illustrates the air velocity distribution inside the room at a height of 1.5 meters from the floor, representing the typical occupant breathing zone. This horizontal cross-section is used to assess the ventilation effectiveness and air movement characteristics under various external wind conditions.To observe the time-dependent behaviour of the proposed windcatcher system, transient analysis is performed using the ANSYS software package. The system domain is discretized using the PISO second-order upwind discretization scheme with bounded second-order for better accuracy of the simulation. The simulation runs for 1200 seconds, to observe the transient behaviour of the system while the system approached towards a steady state. Figure 11 shows the variation of area-weighted average temperature at room floor over time. Analysis of the curves show that the temperature drops sharply at higher wind velocities, while the temperature drop is less compared at lower wind velocities.The simulation results reveal that as the external wind velocity increases from 1 m/s to 5 m/s, there is a corresponding enhancement in indoor airflow intensity. The airflow patterns indicate improved circulation, reduced stagnation zones, and enhanced mixing of the incoming fresh air with the indoor environment. These outcomes suggest that higher external wind speeds lead to more effective natural ventilation, thereby contributing to improved thermal comfort.

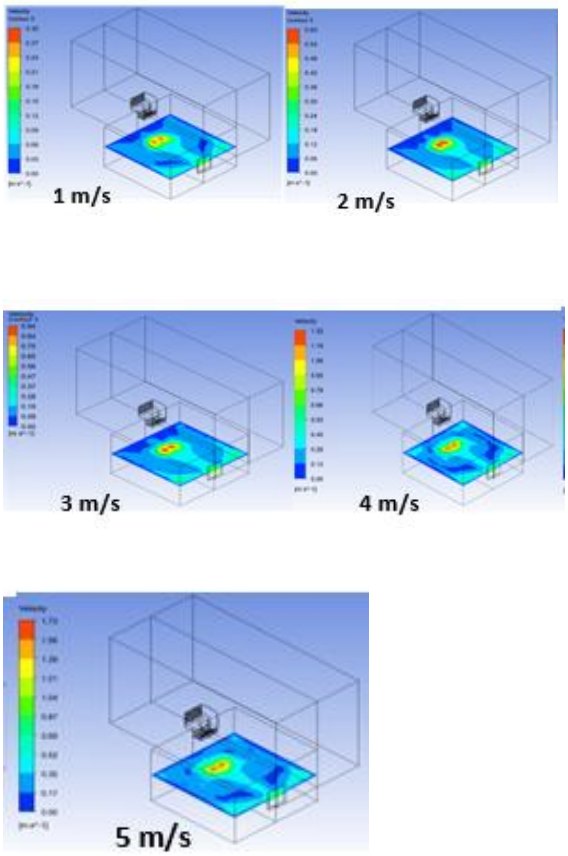

Fig.10: Velocity distribution at mid room height (1.5 m)

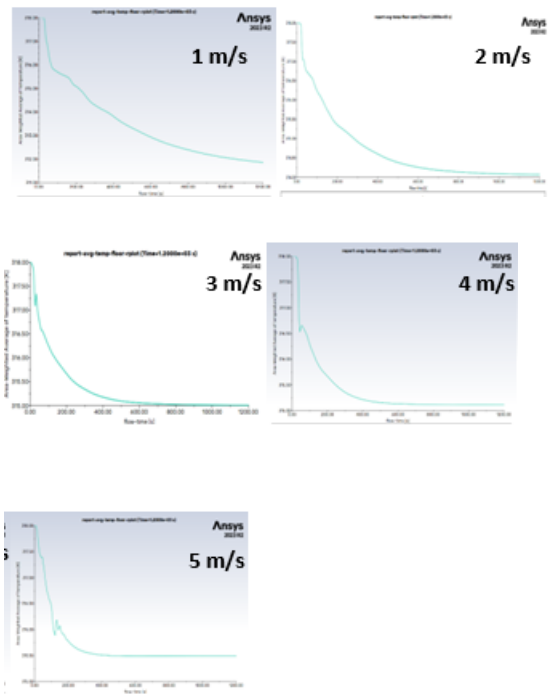

Fig.11: Variation of area weighted average of temperature at floor

To quantitatively assess ventilation performance, the area-averaged velocity at this 1.5 m plane is calculated for each case and plotted against the corresponding external wind velocity. The results are then compared with recommended indoor air velocity ranges for naturally ventilated spaces, as established in previous studies [12] and ventilation standards found in the literature. The findings demonstrate that, under the simulated conditions, the area-averaged indoor velocities remain within or near the optimal range for comfort (typically 0.2–0.8 m/s, depending on activity level and clothing insulation). This confirms the windcatcher's capacity to deliver effective passive ventilation even at relatively low external wind speeds, and its potential to maintain acceptable indoor environmental conditions across varying climatic scenarios.

3. Ventilation performance

The ventilation performance of the proposed windcatcher system is further evaluated by calculating the volume flow rate (in liters per second, L/s) and the air change per hour (ACH) within the occupied zone of the room, across a range of external wind velocities from 1 to 5 m/s. These metrics provide a comprehensive assessment of the system's capacity to supply adequate fresh air and maintain healthy indoor air quality under varying environmental conditions. For this analysis, the simulation assumes a total of five occupants within the room.

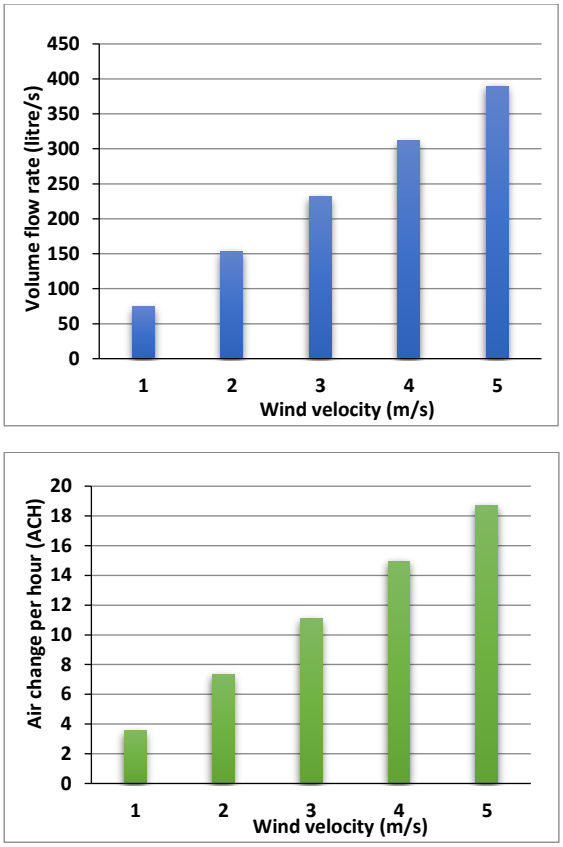

Fig.12: a) Volume flow rate (L/s) within the room at 1-5 m/s wind velocity b) Air change per hour (ACH) within the room at 1-5 m/s wind velocity

The results, presented in Figures 12a and 12b, illustrate the variation of both total ventilation rate and ACH with increasing external wind speed. The ventilation rate per person is derived by dividing the total volumetric airflow by the number of occupants. According to the simulation data, the ventilation rate per person ranges from approximately 15 L/s to 70 L/s, depending on the external wind velocity. These values are found to exceed the minimum requirement of 10 L/s per person, as stipulated by ASHRAE Standard 62.1 for acceptable indoor air quality in naturally ventilated spaces.

This indicates that the proposed windcatcher system can provide more than sufficient fresh air supply, ensuring both occupant health and comfort, even under lower wind conditions. Furthermore, the calculated ACH values show that the system achieves multiple air changes per hour, contributing to the effective dilution and removal of indoor pollutants, heat, and moisture. These findings highlight the windcatcher's potential as a passive ventilation strategy, particularly suited for hot and dry climates where mechanical ventilation may not be energy-efficient or feasible.

4. Mean age of air and air change effectiveness at breathing height (1.1 m)

The proposed windcatcher system is designed to accommodate five occupants. To evaluate the system's ventilation performance, the mean age of air (MAA) is calculated across different wind velocities ranging from 1 to 3 m/s. The mean age of air is a key metric used to assess the time elapsed since the air entered the system, providing insight into how effectively the air is distributed and replaced within the room. At 3 m/s wind velocity

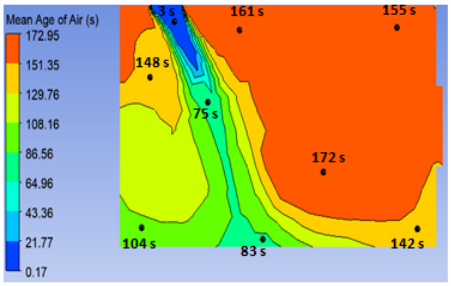

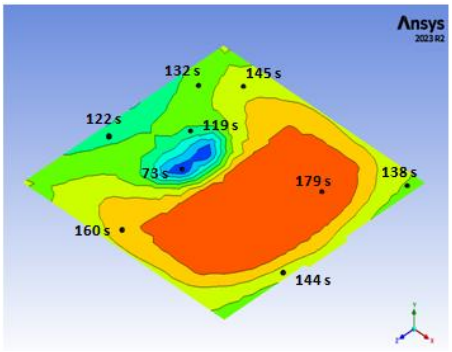

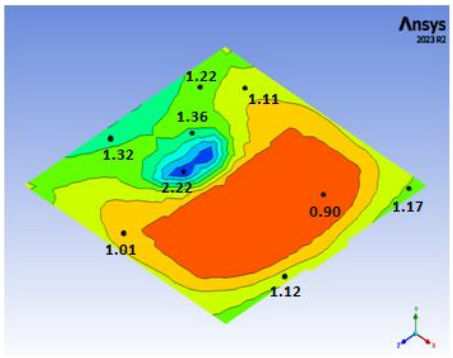

Fig.13: At 3 m/s wind velocity

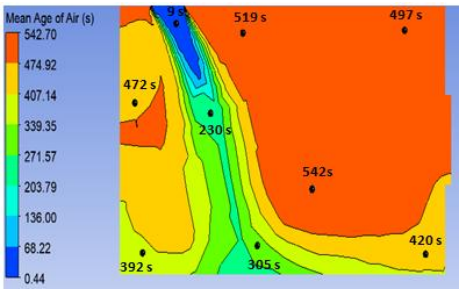

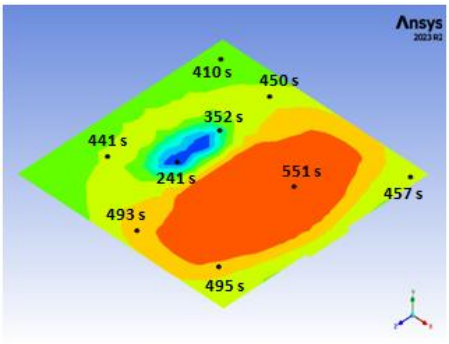

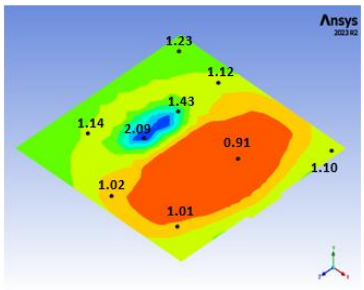

Fig.14: At 1 m/s wind velocity

Figure 13 presents the mean age of air at nine distinct points located on a vertical surface in the middle of the room. This vertical distribution provides valuable data on how air is transported and mixed within the vertical dimension of the room, which can be crucial for understanding stratification or stagnant zones at different levels. Figure 14 shows the

mean age of air at several points on a horizontal surface located at breathing height (1.1 meters above the floor), which represents the typical occupant breathing zone. This helps evaluate the air distribution effectiveness in the zone where occupants are most sensitive to indoor air quality. The results show how quickly air is exchanged at this height, which is directly related to thermal comfort and air quality for the occupants.

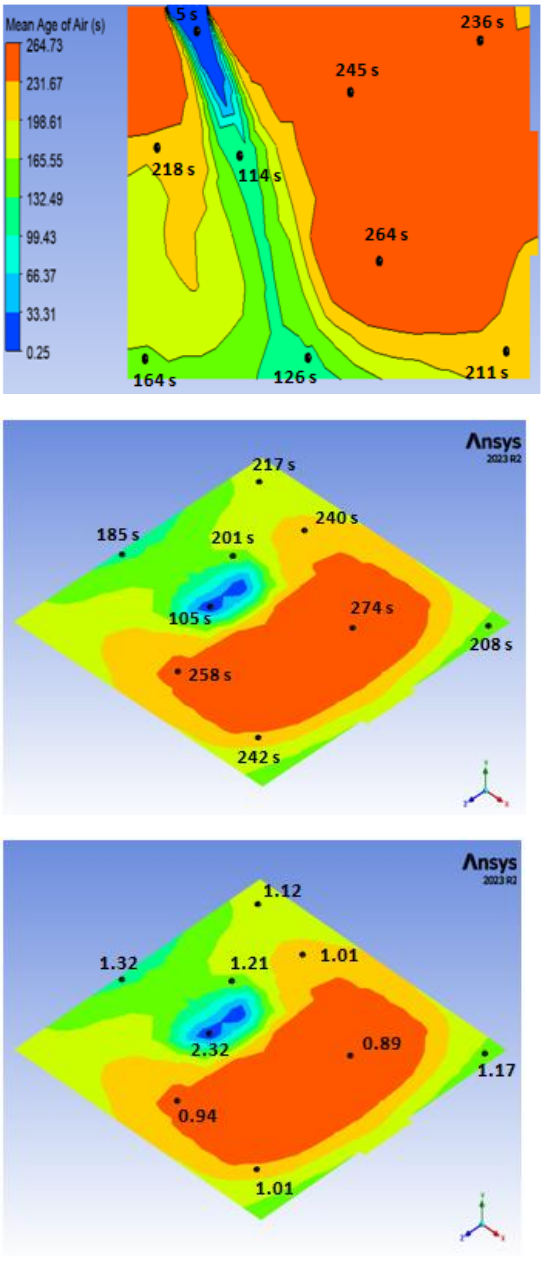

Fig.15: At 2 m/s wind velocity

Figure 15 depicts the Air Change Effectiveness (ACE) values, which represent the ratio of the air exchange rate at the occupied zone to the total air exchange rate within the room. A higher ACE indicates better ventilation efficiency and air distribution within the room. According to ASHRAE standards, an ACE value higher than 0.95 is considered ideal for proper ventilation performance. The results show that the majority of the room area achieves ACE values well above the minimum required threshold, confirming that the windcatcher system provides effective air exchange and meets the necessary standards for natural ventilation, even under varying external wind conditions. This highlights the system's potential to improve indoor air quality and thermal comfort while maintaining energy efficiency.

5. Conclusions

This study critically analyzes the performance of a modern single-sided hybrid windcatcher system, focusing on the effects of varied damper angles (30°, 45°, 60°, and 90°) and wind velocities ranging from 1 to 5 m/s. The results indicate that the system achieves optimal ventilation performance when the damper is positioned at a 60° angle. Additionally, the windcatcher's positioning on the windward side of the room further enhances the system's ability to capture and direct air effectively into the room. Regarding cooling performance, the system can achieve a temperature drop of 7-8 K at lower wind velocities (1-3 m/s). This cooling effect can be further improved by integrating extended surfaces, such as fins on the heat pipes, which increase the heat transfer area and enhance the system's heat extraction capability. The performance of the system is also shown to be sensitive to the number and configuration of heat pipes, suggesting that a higher number or different arrangement of pipes can further optimize the cooling effect.The study also evaluates key ventilation parameters like volume flow rate and air change per hour (ACH). The simulation results confirm that the

proposed windcatcher system consistently meets or exceeds the minimum required air flow rates per person, in accordance with ASHRAE standards, even at varying outdoor wind velocities between 1 and 5 m/s. Additionally, the analysis of the mean age of air (MAA) and air change effectiveness (ACE) provides valuable insights into the distribution and quality of fresh air inside the room. The mean age of air at breathing height (1.1 m) indicates good ventilation efficiency, with the windcatcher system achieving ACE values higher than the minimum required value of 0.95, as prescribed by ASHRAE. This result demonstrates that the system is not only capable of delivering adequate fresh air but also ensuring uniform distribution and effective air exchange within the occupied zone, promoting thermal comfort and indoor air quality.

REFERENCES:

[1] H. Sirror, "Innovative Approaches to Windcatcher Design: A Review on Balancing Tradition Sustainability and Modern Technologies for Enhanced Performance," Energies, vol. 17, no. 22, p. 5770, Nov. 2024, doi: 10.3390/en17225770.

[2] F. Jomehzadeh et al., "A review on windcatcher for passive cooling and natural ventilation in buildings, Part 1: Indoor air quality and thermal comfort assessment," Renewable and Sustainable Energy Reviews, vol. 70, pp. 736–756, Apr. 2017, doi: 10.1016/j.rser.2016.11.254.

[3] Q. Ma, G. Qian, M. Yu, L. Li, and X. Wei, "Performance of Windcatchers in Improving Indoor Air Quality, Thermal Comfort, and Energy Efficiency: A Review," Sustainability, vol. 16, no. 20, p. 9039, Oct. 2024, doi: 10.3390/su16209039.

[4] H. Ghandi and M. F. Leone, "The Potential of One-Sided Traditional Windcatchers for Outdoor Use as a Sustainable Urban Feature," Urban Science, vol. 8, no. 4, p. 229, Nov. 2024, doi: 10.3390/urbansci8040229.

[5] J. K. Calautit, P. W. Tien, S. Wei, K. Calautit, and B. Hughes, "Numerical and experimental investigation of the indoor air quality and thermal comfort performance of a low energy cooling windcatcher with heat pipes and extended surfaces," Renewable Energy, vol. 145, pp. 744–756, Jan. 2020, doi: 10.1016/j.renene.2019.06.040.

[6] M. Liu, P. Nejat, P. Cao, C. Jimenez-Bescos, and J. K. Calautit, "A critical review of windcatcher ventilation: Micro-environment, techno-economics, and commercialisation," Renewable and Sustainable Energy Reviews, vol. 191, p. 114048, Mar. 2024, doi: 10.1016/j.rser.2023.114048.

[7] M. Mayhoub, H. Selim, and A. Abuzaid, "Roadmap to developing a geometrical design guide for windcatchers," Front. Built Environ., vol. 11, p. 1534284, Mar. 2025, doi: 10.3389/fbuil.2025.1534284.

[8] H. N. Chaudhry, J. K. Calautit, and B. R. Hughes, "Computational analysis of a wind tower assisted passive cooling technology for the built environment," Journal of Building Engineering, vol. 1, pp. 63–71, Mar. 2015, doi: 10.1016/j.jobe.2015.03.004.

[9] S. Jafari and V. Kalantar, "Numerical simulation of natural ventilation with passive cooling by diagonal solar chimneys and windcatcher and water spray system in a hot and dry climate," Energy and Buildings, vol. 256, p. 111714, Feb. 2022, doi: 10.1016/j.enbuild.2021.111714.

[10] S. H. Hosseini, E. Shokry, A. J. Ahmadian Hosseini, G. Ahmadi, and J. K. Calautit, "Evaluation of airflow and thermal comfort in buildings ventilated with wind catchers: Simulation of conditions in Yazd City, Iran," Energy for Sustainable Development, vol. 35, pp. 7–24, Dec. 2016, doi: 10.1016/j.esd.2016.09.005.

[11] P. Nejat, J. K. Calautit, M. Z. Abd. Majid, B. R. Hughes, and F. Jomehzadeh, "Anti-short-circuit device: A new solution for short-circuiting in windcatcher and improvement of natural ventilation performance," Building and Environment, vol. 105, pp. 24–39, Aug. 2016, doi: 10.1016/j.buildenv.2016.05.023.

[12] L. Li and C. M. Mak, "The assessment of the performance of a windcatcher system using computational fluid dynamics," Building and Environment, vol. 42, no. 3, pp. 1135–1141, Mar. 2007, doi: 10.1016/j.buildenv.2005.12.015.

[13] P. Nejat, Y. Fekri, M. Sheikhshahrokhdehkordi, F. Jomehzadeh, H. Alsaad, and C. Voelker, "The Windcatcher: A Renewable-Energy-Powered Device for Natural Ventilation—The Impact of Upper Wing Walls," Energies, vol. 17, no. 3, p. 611, Jan. 2024, doi: 10.3390/en17030611.

[14] M. Afshin, A. Sohankar, M. D. Manshadi, and M. K. Esfeh, "An experimental study on the evaluation of natural ventilation performance of a two-sided wind-catcher for various wind angles," Renewable Energy, vol. 85, pp. 1068–1078, Jan. 2016, doi: 10.1016/j.renene.2015.07.036.

[15] F. Jomehzadeh et al., "A review on windcatcher for passive cooling and natural ventilation in buildings, Part 1: Indoor air quality and thermal comfort assessment," Renewable and Sustainable Energy Reviews, vol. 70, pp. 736–756, Apr. 2017, doi: 10.1016/j.rser.2016.11.254.

[16] A. Abdullah, "Experimental study of natural materials for an evaporative cooling design in hot-arid climate," Building and Environment, vol. 207, p. 108564, Jan. 2022, doi: 10.1016/j.buildenv.2021.108564.

[17] J. P. Harrouz, K. Ghali, and N. Ghaddar, "Integrated solar – Windcatcher with dew-point indirect evaporative cooler for classrooms," Applied Thermal Engineering, vol. 188, p. 116654, Apr. 2021, doi: 10.1016/j.applthermaleng.2021.116654.

[18] J. K. Calautit and B. R. Hughes, "A passive cooling wind catcher with heat pipe technology: CFD, wind tunnel and field-test analysis," Applied Energy, vol. 162, pp. 460–471, Jan. 2016, doi: 10.1016/j.apenergy.2015.10.045.

[19] J. K. Calautit, D. O'Connor, and B. R. Hughes, "A natural ventilation wind tower with heat pipe heat recovery for cold climates," Renewable Energy, vol. 87, pp. 1088–1104, Mar. 2016, doi: 10.1016/j.renene.2015.08.026.

[20] D. N. P. Group, "The Basics of Heat Pipes – Their History, Principle, and Varieties explained | Colomn | Solutions/Products/Services | DNP Dai Nippon Printing," Dai Nippon Printing Co., Ltd. Accessed: Aug. 31, 2024. [Online]. Available: https://www.global.dnp/biz/column/detail/10162360_4117.html

[21] A. H. Chohan, J. Awad, Y. Elkahlout, and M. Abuarkub, "Evaluating windcatchers in UAE heritage architecture: A pathway to zero-energy cooling solutions," Ain Shams Engineering Journal, vol. 15, no. 10, p. 102936, Oct. 2024, doi: 10.1016/j.asej.2024.102936.

[22] M. A. Mamari, H. M. Khan, S. Al Saadi, and A. Al Hashim, "Impact of windcatcher on the thermal comfort and indoor air quality in a modern house," Building Research & Information, vol. 53, no. 1–2, pp. 204–219, Feb. 2025, doi: 10.1080/09613218.2024.2386580.

ABS ID: 175
Code No: CCGR-0P-11

Associatie Prof. Soni Darmawan

ABS ID: 199
Code No: CCGR-0P-12

Mrs. Jyoti Pippal

ABS ID: 169
Code No: CCGR-0P-13

Ms. Priti Jha

ABS ID: 177
Code No: CCGR-0P-14

Application of Iot and Remote Sensing Techniques to Investigates Water Status and Methene Emission from Rice Paddy Field

Md Rahedul Islam[1*] Wataru Takeuchi[2]
[1*]*Associate Professor, Dept. of Geography and Environment*
Pabna University of Science and Technology, Bangladesh
[2]*Professor, Institute of Industrial Science, University of Tokyo, Japan,*
Correspond to Associate Professor, Md Rahedul Islam
Email: rahe_ge@pust.ac.bd

***Keywords**: Synthetic Aperture Radar, Time series, Backscatter, Machine learning, Bangladesh.*

1.INTRODUCTION

Alternate wetting and drying (AWD) irrigation system is a efficient and proven irrigation practice for rice paddy cultivation. The AWD irrigation practice is a periodic irrigation system which allow the paddy field dry up periodically except in rooting and flowering stages (Islam, M.R., Kim, H., Takeuchi, 2024). The AWD irrigation system reduce irrigation water use up to 40%, reduced methane emission up to 70% and yield increased up to 10% is found in different studies(Alam et al., 2010; Basak, 2016; Hasan et al., 2016; Runkle et al., 2019). Although the system shown numerical socio-economic and environmental advantages but in Bangladesh field level adaptation rate comparatively very slow. Moreover, AWD could be a great potential tool for Bangladesh to get carbon credit in terms of CH4 emission reduction sources. As the Joint Crediting Mechanism (JCM), The verified Carbon Standard (VCS), and gold standard monitoring, verification and reporting is very crucial for achieving such standards. The AWD irrigation system implementation and ensure the co-benefit, the most important task its proper monitoring. To wide scale adaptation of AWD irrigation practice the monitoring system is very important. There are a number of studies has been conducted on the assessing the socio-economic benefit and impacts of AWD irrigation. Along with manual observation, IoT devices, UAV, and satellite-based application are the potential tools for AWD irrigation monitoring (Krishnaveni et al., 2020). But the IoT device-based monitoring is also a in situ solution and challenging to implemented in large scale monitoring. There are some individual studies on AWD irrigation monitoring likes, i) manually monitoring with perforated water pipe, ii) IoT device-based water level monitoring, and iii) remote sensing based irrigated field monitoring. The remote sensing techniques based studies mostly used Synthetic Aperture Radar (SAR) data and machine learning techniques to detect the agriculture field either irrigated or not (Gao et al., 2018; Wei et al., 2023). Above mentioned discussion noted that, none of them are adequate to monitor AWD irrigation in a larger scale with a good efficiency. Hence, this study is an attempt to combinedly use the IoT based device, UAV and remote sensing techniques to monitor AWD irrigation practices in the Bangladesh. The objectives of the study, i) To monitor AWD irrigation water level and CH4 emission with low cost IoT devices; ii) To compare the irrigated water condition and CH4 emission with manual, IoT and satellite data.

2. DATA AND METHODOLOGY

2.1 Data: The irrigation schedule data collected through the volunteers from the farmer's field (90), IoT based low-cost water level monitoring sensor have been installed (90), the manual close chamber CH4 estimation (24), IoT sensor based CH4 chamber (06) have been installed in the field area. The Japan Aerospace Exploration Agency (JAXA) SAFE initiative ALOS-2 SacnSAR data along with Sentinel-1 data during the rice growing period used for the study.

2.2 Methodology

The study has conducted in both field and desktop mode. The low-cost water level monitoring sensors are installed in the six field from the different part of the country. This IoT devices water level monitored data received via the central server via online platform. The SAR data from syntinel-1 dual polarized C band data used. The Sentinel -1A backscatter data with 10-meter spatial resolution with 12-day temporal resolution.

3. RSULTS

The results showed that the low cost IoT device-based water level data and manually collected water level data shown very high agreement (85.34%) among the 89 different plots. The IoT sensors-based water level status and satellite-based irrigation water status results show very good agreement (78.56%) in our project sites. The details result shown in Fig. 1.

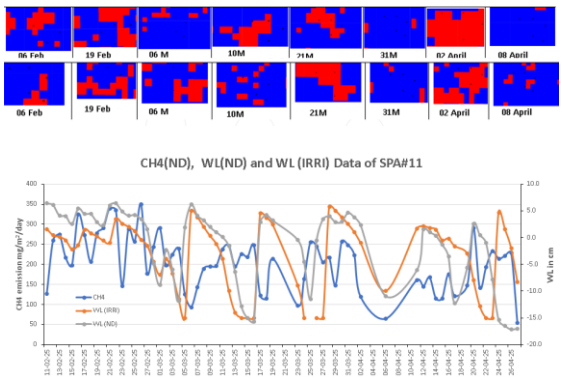

Figure 1. Irrigated water status monitoring result from (a) satellite-based monitoring result; (b) Low cost IoT sensor-based water level and manually collected water level data.

Along with the water level of rice paddy field means as irrigated condition is closely correlated with CH4 emission from rice paddy field. The three different techniques (Manually chamber, Sensors based and satellite based) were used in to estimated CH4 emission from rice paddy fields. The CH4 emission estimation with manual and automated sensors-based estimation shown high correlation and average 2 to 4% over estimation in sensors-based estimation. The satellite based CH4 estimation is challenging task and, in this study, we used Sentinel 5P methene data. Moreover, the IPCC tier 2 irrigation emission factors as water regime management used to estimated CH4 emission. The estimated CH4 emission with satellite based shown high discrepancy but emission factor-based estimation shows very good agreement. The lower spatial resolution of satellite data and small or fragmented size of irrigated rice paddy field. The details result shown in Fig.2.

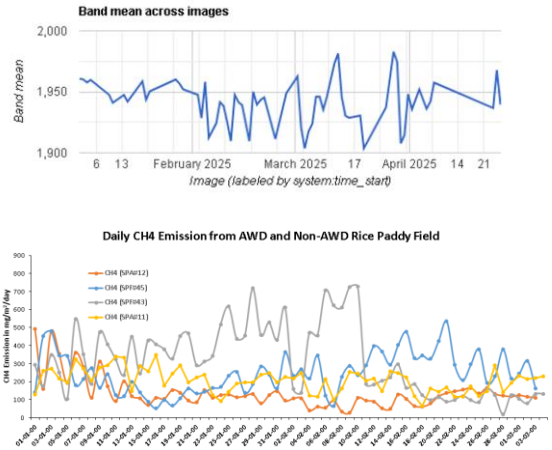

Figure 2. CH4 emission estimation from AWD and Non-AWD rice paddy field with (a) satellite-based estimation result; (b) Low cost IoT sensor-based CH4 emission estimation.

4. CONCLUSION

The results shows that the manual, sensors based and satellite-based irrigation water level estimation of AWD and Non-AWD rice paddy filed are very high agreement (up to 96%). In case of CH4 estimation with manual chamber and automated automatic sensors shows 4% variation. The water regime adjusted emission factor based CH4 illustrated high agreement with manual and sensors-based estimation but satellite-based estimation shows high discrepancy with others. The outcome of the study could be potential tool for AWD irrigation system monitoring, reporting and verification for policy making.

REFERENCES:

Alam, M. S., Islam, M., Salam, M., & Islam, M. (2010). Economics of Alternate Wetting and Drying Method of Irrigation: Evidences from Farm Level Study. The Agriculturists, September 2014, 82–89. https://doi.org/10.3329/agric.v7i1.5258

Basak, R. (2016). Benefits and costs of climate change mitigation technologies in paddy rice: focus on Bangladesh and Vietnam. CCAFS Working Paper, 160, 52-pp. https://cgspace.cgiar.org/rest/bitstreams/79059/retrieve

Gao, Q., Zribi, M., Escorihuela, M. J., Baghdadi, N., & Segui, P. Q. (2018). Irrigation mapping using Sentinel-1 time series at field scale. Remote Sensing, 10(9), 1–18. https://doi.org/10.3390/rs10091495

Hasan, K., Habib, A., Bhattacharjee, D., & Afrad, S. I. (2016). Impact of Alternate Wetting and Drying Technique on Rice Production in the Drought Prone Areas of Bangladesh. Indian Research Journal of Extension Education, 16(1).

Islam, M.R., Kim, H., Takeuchi, W. (2024). Springer-Nature-BookChapter-Rahe (1).pdf. New Frontiers in Regional Science: Asian Perspectives, vol 77. Springer, Singapore. https://doi.org/https://doi.org/10.1007/978-981-97-1188-8_14

Krishnaveni, M., Praveen Kumar, S. K., Arul Muthusamy, E., Kowshick, J., & Arunya, K. G. (2020). Real-time monitoring of water level and storage dynamics of irrigation tank using IoT. H2Open Journal, 3(1), 392–400. https://doi.org/10.2166/h2oj.2020.123

Palanisami, K.; Kakumanu, K. R.; Nagothu, U. S.; Ranganathan, C. . (2019). Climate Change and Future Rice Production in India: A Cross Country Study of ... - K. Palanisami, Krishna Reddy Kakumanu, Udaya Sekhar Nagothu, C. R. Ranganathan - Google Books. Springer Nature Singapore Pte Ltd. https://doi.org/https://doi.org/10.1007/978-981-13-8363-2_2

Electronic Poster Presentations

ABS ID: 25
Code No: CCGR-EP-01

Bacteria Based Concrete Potential Negative Emission Technology: Critical Review

Rupali R. Bhoir[1], S.M. Pore[2], and S.R. Bhagat[3]
[1]*Research Scholar, Department of Civil Engineering, Dr. Babasaheb Ambedkar Technological University, Lonere, Raigad, Maharashtra, India,*
[2]*Head & Professor, Department of Civil Engineering, Dr. Babasaheb Ambedkar Technological University, Lonere, Raigad, Maharashtra, India,*
[3]*Professor, Department of Civil Engineering, Dr. Babasaheb Ambedkar Technological University, Lonere, Raigad, Maharashtra, India,*
Correspond to Rupali R. Bhoir (rupali.bhoir7@gmail.com)

Keywords*: Bacteria based concrete, Self-healing concrete, MICP, Biomineralization, Negative Emission Technology.*

1. SIGNIFICANCE OF RESEARCH

out of all the greenhouse gases, carbon dioxide is the most prevalent and primary one. Amongst the most global carbon emission contributing material is concrete, which is nearly 8% [1]. It requires frequent replacement or repair, because of its inherent fragility, which is expensive and produces a significant quantity of CO2. Therefore, this sequestration of CO2 through concrete healing and repair will lower the amount of CO2 in the atmosphere; more precisely, it will partially offset the amount of CO2 released by the building sector. The MICP method can stop CO2 as carbonate from leaking into the environment.

Even while MICP and concrete healing have been the subject of multiple separate review publications, there are few studies in the area that address the research gap that denotes both the concrete healing element and its use in CO2 sequestration. As a result, this study tackles the new research area of using MICP to mend concrete cracks while maintaining the goal of removing CO2 from the atmosphere.

2. ROLE IN SELF HEALING OF CONCRETE

Due to extensive urbanization, industrialization, and other human activities reliant on fossil fuels, the concentration of CO2, the primary greenhouse gas, has been rising, contributing to global warming. Consequently, climate change. The growth of the building sector also led to increased cement manufacturing, which raised CO2 emissions into the atmosphere. As a result, the need for efficient carbon footprint management is crucial. CO2 sequestration, sometimes referred to as "Carbon trap" or "CO2 arrestation," is a technique for long-term atmospheric storage of CO2 or its related forms [2]. In this case, using microbes to sequester CO2 is a practical and cost-effective strategy that is also advantageous for a sustainable ecosystem. We call this biological sequestration of CO2. From a structural perspective, the self-healing concrete crack technique, known as MICP (bacteria-induced calcium carbonate, or calcite) precipitation, is a very efficient way to sequester CO2. The microbes primarily sequester CO2 from the atmosphere and fix it into various carbonate minerals, including dolomite, calcite, and magnesite [3]. Much research has been done on MICP technology,

with a focus on ureolytic bacteria for concrete structural crack repair.

3. ADVANTAGES AND DISADVANTAGES OF DIFFERENT MICP CYCLES USED IN CONCRETE

Since various cyanobacteria, including Dichothrix, Lyngbya, Gloeocapsa, and Synechococcus species, can survive in alkaline environments with pH values between 11 and 13, their use of oxygenic photosynthesis may be a crucial step in the healing of concrete cracks. Using methane oxidation, some researchers [6] also proposed that bacteria could use the environmentally hazardous gases, like CH4 and H2S, which are bad for concrete, in their metabolism process, which would then lead to the precipitation of calcite. On the other hand, the sulphur cycle damages concrete's health by generating the dangerous corrosive chemical H2S, which causes the concrete structure to deteriorate quickly. The ureolytic pathway, in which the microbial urease hydrolyses urea mixed with various calcium compounds as nutrients to produce ammonia and CO2, is the most often employed MICP mechanism for MICP in concrete. This process improves concrete's compressive strength, crack-healing ability, material permeability, and other qualities, but it has some significant disadvantages. For example, it is a temperature-dependent mechanism that releases the hazardous gas nitrogen oxide into the atmosphere, and it increases the risk of salt damage in concrete by converting it to nitric acid because too much ammonia is produced in the matrix. The concept of metabolic conversion of organic compound (organic acid salt) to calcium carbonate was introduced to address the problem of excessive ammonium ion production of ureolytic. In this scenario, the bacteria directly use the organic material for their metabolism, producing CaCO3 as a by-product, increasing the production of CaCO3 without any ammonium.

3. EFFECTS OF CARBONATE PRECIPITATION IN BACTERIA BASED CONCRETE

The usage of MICP is not limited to solving environmental problems like storing CO2, but it also works well for structural engineering problems like concrete fractures that mend themselves [7]. In contrast to traditional methods for concrete crack treatment, calcium carbonate bio-deposition by MCP (Table 1) also prevents aggressive chemicals from penetrating. The efficiency of surface crack repair in MICP is significantly influenced by the quantity and quality of precipitated crystal in terms of density, thickness, cohesiveness, and effective bond with the concrete matrix [8].

Bacteria	Nutrients and chemical added	References
Sporosarcina pasteurii	Urea, Yeast extract, Tris-buffer, Ammonium Sulfate, Calcium chloride	Wang et al. [4]
Bacillus megaterium	Peptone, yeast extract, beef extract, sodium chloride, Agar, Urea, Calcium Chloride	Kaur et al. [5]
Bacillus alkalinitrilicus	Calcium lactate and yeast extract	Wiktor and Jonkers [6]
B. cohnii	Calcium lactate and yeast extract	Seifan M and Berenjian A [7]
S. pasteurii	Urea and calcium chloride	Ramachandran [10]
B. Subtilis	Urea, Peptone, meat extract and	Nosouhian et al [11]

	calcium chloride	

Table 1 Different microorganisms and nutrients used to create CaCO3 in concrete/mortar matrix in Ureolytic mechanism of Precipitation

3. CONCLUSIONS

According to the MICP approach, microbial self-healing concrete has the ability to sequester CO2, making it a viable solution to the global warming problem. Furthermore, it has a favourable impact on concrete's mechanical qualities. These MICP mechanisms for concrete crack healing can make use of the massive CO2 output from the cement industry, which poses a serious environmental danger in the current situation. Although the MICP methods have their own advantages and disadvantages, this can also serve as a method of sequestering CO2 from the environment. It is already known that the ureolytic mechanism and cyanobacteria's oxygenic photosynthesis both use ambient CO2 in the MICP process. MICP by means of replacement of urea to CO2 influx can effectively contribute to CO2 arrestation from the atmosphere. Moreover, the mostly used pathway, i.e., using cyanobacteria also bears the potential of repairing concrete cracks alongside the major contribution to CO2 arrestation in the process. However, the applicability of optimum conditions as well as of effective microorganisms and its pathway needs more rigorous study to establish a mechanism of MICP for concrete crack healing which will also act as an effective solution in atmospheric CO2 sequestration. Even so, it can be concluded that MICP can bear a significant role in arrestation as well as sequestration of CO2, under proper atmospheric conditions with a cautious selection of microorganisms and its nutrient for the MICP procedure.

It is strongly advisable doing a thorough experimental study on the application of ambient CO2 in MICP for concrete crack healing, taking into account and putting into practice the different aspects and parameters needed for the same. After that, an assessment of the restored concrete's performance in a real-world setting is also required. With a successful outcome, a workable plan for a more environmentally friendly world can be developed. In addition to concrete repair, the use of MICP technology as a negative emission technology has significant potential in the fields of solid waste treatment and soil remediation. This can also be investigated through appropriate and thorough experimental procedures for a more sustainable and greener environment.

REFERENCES:

[1] Ellis LD, Badel AF, Chiang ML, Park RJY, Chiang YM, Proc Natl Acad Sci 117(23) (2020) 12584–12591.
[2] Atrayee Bandyopadhyay, Anwesha Saha, Diya Ghosh, Bomba Dam, Amiya K. Samanta and Susmita Dutta, Beni-Suef University Journal of Basic and Applied Sciences 12:7 (2023) 1-13.
[3] Dhami NK, Mukherjee A, Reddy MS, Appl Biochem Biotechnol 172 (2014) 2552–2561.
[4] Wang JY, Soens H, Verstraete W, Belie ND, Cem Concr Res 56 (2014) 139–152.
[4] Bharti RK, Srivastava S, Thankur IS, J Environ Chem Eng 2 (2014)31–39.
[5] Kaur G, Dhami NK, Goyal S, Mukherjee A, Reddy MS, Constr Build Mater 123 (2016) 527–533.
[6] Wiktor V, Jonkers HM, Cem Concr Compos 33 (2011) 763–770.
[7] Seifan M, Berenjian A, Appl Microbiol Biotechnol 103 (2019) 4693–4708.
[8] Li L, Xue S, Xi J, J Environ Sci 76 (2019) 238–248.
[9] Seifan M, Samani AK, Burgess JJ, Berenjian A, Nova Science Publishers Inc, New York, (2016) 97–124.
[10] Ramachandran SK, Ramakrishnan V, Bang SS, ACI Mater J 98 (2001) 3–9.
[11] Nosouhian F, Mostofinejad D, Hasheminejad H J Mater Civ Eng 04015064 (2016) 1–12.

ABS ID: 65
Code No: CCGR-EP-02

Mr. Aviyush Sodhi

ABS ID: 178
Code No: CCGR-EP-03

Mr. Anand Bohra

ABS ID: 34
Code No: CCGR-EP-04

Beyond The Crisis: A Green Blueprint for Tomorrow

Deepak Gupta[1]
[1]*Assistant Professor, Department of Aerospace Engineering, GNA University, Phagwara, India*
Correspond to DEEPAK GUPTA (deepakgupta7060@gmail.com, deepak.gupta@gnauniversity.edu.in)

***Keywords**: Global Warming, politicization of climate change, Sustainability, Urban Resilience.*

Climate change and environmental degradation have pushed humanity toward a critical juncture, where the decisions made today will profoundly shape the future of ecosystems, economies, and societies. Rather than treating these challenges as isolated crises that demand short-term reactions, this paper promotes a visionary "green blueprint" for sustainable development—one designed not only for recovery but for deep renewal and resilience. This framework integrates cutting-edge research and innovative solutions to embed sustainability as the foundation of urban planning, industrial processes, and policy-making at all levels. At the heart of this blueprint lies the concept of leveraging integrated blue-green infrastructure, sustainable architecture, renewable energy innovation, and circular economy principles. Combined, these approaches form a cohesive strategy to address multiple interconnected risks: climate disruption, resource depletion, environmental injustice, and social inequities. Key future goals include accelerating decarbonization through widespread renewable energy adoption, restoring ecosystems at scale, enhancing urban resilience via nature-based solutions, and fostering socio-technical systems that prioritize inclusive governance and participatory decision-making. Technologies today such as precision AI-driven agriculture, smart water management, green building standards, and net-zero engineering are critical enablers that spark holistic transformation. However, technology alone is insufficient without policy frameworks that emphasize social participation, distributive equity, and adaptive capacity building—elements necessary to ensure that benefits of green growth are shared broadly across societies. Research emerging from diverse fields shows that this future blueprint is not simply corrective, but rather transformative in scope: it aims to regenerate natural capital, minimize lifecycle carbon footprints, and nurture communities capable of thriving within planetary boundaries. Empirical studies reinforce this vision, demonstrating, for example, that green architecture significantly lowers greenhouse gas emissions while improving energy efficiency. Similarly, urban blue-green infrastructure—by combining natural water management with green urban spaces—contributes to social wellbeing, reduces heat islands, and enhances biodiversity. Decentralized water conservation initiatives also show promise as levers of both climate resilience and socioeconomic development in vulnerable regions. Collectively, this living framework will evolve continuously through global cooperation, interdisciplinary innovation, and locally adapted action plans, providing scalable pathways toward sustainable futures. Re conceptualizing Climate Change: From Crisis to Climate Epic Much of recent popular and policy dialogue casts climate change as an urgent "crisis" or "emergency," emphasizing the need for rapid, sometimes drastic, interventions. While this framing mobilizes immediate action, it risks oversimplifying the complexity and duration of

climate challenges [1]. Recent scholarship introduces an alternative perspective by describing climate change as an ongoing "epic"—a long-term, multifaceted process unfolding over decades and centuries rather than a short-lived emergency. Viewing climate change as a political epic reshapes how governments, communities, and institutions approach environmental stewardship. Unlike crises, epics demand endurance, adaptability, and long-range planning. They require policies that evolve in response to changing conditions, institutions prepared for sustained collaborative governance, and societies oriented toward resilience rather than quick fixes. This paradigm shift also invites reflection upon traditional democratic mechanisms, which often excel at responding to short-term emergencies but may falter when addressing protracted challenges of epic scale. In place of episodic emergency measures, an epic framework prioritizes evolutionary adaptability, continual preparedness, and collective efforts. Such an approach acknowledges the deep entanglement of environmental, social, and political factors shaping climate outcomes, encouraging inclusive and flexible responses. Ultimately, this reconceptualization fosters a more realistic, sustained commitment to climate action—enabling communities to navigate the unprecedented changes of today and tomorrow with resilience and hope. Transforming the Workforce for a Sustainable Future Alongside technological and infrastructural transitions, human capital is pivotal for realizing green futures. The IEMA and Deloitte study underscores that as environmental imperatives grow, so too does the demand for "green skills"—specialized knowledge and competencies that equip workers to mitigate climate impacts, conserve biodiversity, and manage waste more effectively[2]. By 2050, green skills are expected to become essential qualifications across most professions, akin to digital literacy today. However, transforming the workforce is not without challenges. Surveys and interviews reveal barriers such as inertia in existing career paths, unclear progression opportunities in green sectors, prevalent skill gaps, and underrepresentation of diverse groups. Overcoming these obstacles requires multi-pronged strategies: government policies that incentivize green workforce development, tailored training and upskilling programs, leadership commitment from organizations, and cultural shifts toward sustainability orientation. Case studies provide compelling examples. The automotive industry is retraining workers for electric vehicle production, plastics-sector employees are adapting to recycling mandates, and oil and gas companies are pivoting toward offshore wind and hydrogen technologies. Encouragingly, many skills from traditional sectors are transferable, smoothing the transition for affected workers. Additionally, regional and government programs promoting carbon capture, hydrogen economies, and home retrofitting accelerate this green occupational shift. Ultimately, workforce transformation is a key pillar of the green blueprint—ensuring that the people powering industries are equipped not only technically but also with sustainability mindsets necessary for systemic change. Blue-Green Infrastructure: Enhancing Urban Resilience and Wellbeing Urban environments are frontline arenas where climate risks collide with dense populations, infrastructure vulnerabilities, and social disparities. Promoting integrated blue-green infrastructure—a synergy of urban greenery and natural water management—emerges as a powerful strategy for increasing urban resilience and sustainability. Examples include urban trees, green roofs, permeable pavements, wetlands, and bioswales[3]. Research demonstrates multifaceted benefits: increasing biodiversity, reducing urban heat island effects, improving water quality, and mitigating flooding events. These elements collectively enhance ecosystem services that underpin human health, social interaction, and environmental sustainability. Importantly, this approach advocates inclusion, ensuring

equitable access to green amenities for marginalized and vulnerable populations. New technologies such as artificial intelligence further enable optimization of green infrastructure design and management, making cities more responsive to evolving climate uncertainties. Urban greening also aids stormwater management, air purification, and carbon sequestration, contributing to cities that are both healthier and more climate-resilient[4].

Solution

Long-Term Adaptation and Resilience: New stress shifting from short-term emergency responses to long-term resilience building. They emphasize decentralized climate governance with empowered local governments being critical to tailor solutions to regional vulnerabilities and to engage communities in climate adaptation planning[5].

Green Finance and Innovative Funding: Multiple editorials note the need for innovative green financing mechanisms, including green bonds, climate insurance, debt-for-nature swaps, and dedicated climate funds to mobilize the trillions of dollars needed. The establishment of the Loss and Damage Fund and international commitments under COP29 and COP30 are highlighted as important but insufficient steps toward equitable climate finance[6].

Green Bonds and Climate Finance Innovations: Encouraged to fill funding gaps for adaptation and mitigation, alongside new financial instruments like debt-for-nature swaps to support developing countries (GCA)

Research for Net Zero Technologies: Investing in breakthrough technologies beyond 2030 including hydrogen, carbon capture, and AI applications for sustainability (UKRI)

Conclusion

Key References: Previous Authors' Work

Today's environmental crisis must be met with a fundamental shift in mindset and action. Moving beyond reactive, short-term emergency responses, a multi-dimensional green blueprint offers a pathway for sustained ecological and social renewal. Recognizing climate change as a prolonged, complex "epic" guides governance toward adaptability, resilience, and inclusive collaboration. Central to this vision is a transformed workforce armed with green skills, coupled with innovations in technology and integrated urban ecological design. This framework aspires not merely to address present threats but to restore natural capital, reduce carbon footprints, and build thriving, equitable societies capable of withstanding future shocks. Through interdisciplinary innovation, global cooperation, and local adaptation, the green blueprint stands as an evolving, scalable model—helping humanity move beyond crisis toward a sustainable and just tomorrow.

Title & Year	Focus Area	Major Achievements/Findings
Beyond Crisis and Emergency: Climate Change as Political Epic (2024)	Political framing of climate crisis	Advocates for long-term, adaptive policy beyond emergency models, centering crisis as a catalyst for transformation
Blueprint for Green Workforce Transformation (2022)	Industrial decarbonization, workforce skills	Projects AI-driven industry, integrated renewable grids, and circular economy as foundational for green transition
Blueprint for A Greener Future (2024)	Sustainable architecture, carbon reduction	Demonstrates significant carbon savings via green architecture; highlights material circularity as crucial
Promoting Integrated Blue–Green Infrastructure (2024)	Urban resilience, nature-based solutions	Case studies show improved health, social cohesion, and adaptable cities via blue-green infrastructure

REFERENCES:

[1] J. S. Maloy, "Beyond Crisis and Emergency: Climate Change as a Political Epic," Ethics Int. Aff., vol. 38, no. 1, pp. 103–125, 2024, doi: 10.1017/S0892679424000030.

[2] Deloitte and IEMA, "A Blueprint for Green workforce transformation," Deloitte, p. 55, 2022, [Online]. Available: https://www2.deloitte.com/content/dam/Deloitte/uk/Documents/consultancy/deloitte-uk-a-blueprint-for-green-workforce-transformation.pdf

[3] S. Jagadisan, "Promoting integrated blue–green infrastructure for urban resilience—lessons learned from case studies," Front. Water, vol. 6, no. November, pp. 1–11, 2024, doi: 10.3389/frwa.2024.1474411.

[4] P. Kumar et al., "Urban greening for climate resilient and sustainable cities: grand challenges and opportunities," Front. Sustain. Cities, vol. 7, 2025, doi: 10.3389/frsc.2025.1595280.

[5] "Rain and," 2015.

[6] J. Handy, "What to Expect in https://gca.org/what-to-expect-in-climate-change-in-2025-opportunities-amid-challenges/," 2015.

Code No: CCGR-EP-05

Mr. Bidwan Sekhar

ABS ID: 40
Code No: CCGR-EP-06

Biomimic Concrete: An Innovative Construction Material for Sustainable Build Environment

Farheen jabeen[1] leena chaurasia;srinivasa rao naik[b]
[1]*Project Associate CSIR-Central Building Research Institute, Roorkee, India*
Corresponding author (email id:leenachaurasia@gmail.com;sriniva.s@cbri.res.in

***Keywords**: MICP, Crack sealing agent-Bacteria, CO2 sequestration, Biomimic cement.*

Cementitious composites inevitably suffer from cracking that allow easy access of moisture and contaminants into the structure. Micro-cracks may originate in concrete just after construction or at advanced stage which is often unnoticed until it leads to major durability or structural issues. Cracks can be manually repaired but manual repair and maintenance operations face challenges including emission of carbon dioxide, poor quality and limited accessibility. In addition, it is a financial burden to carry out routine repair operations on facilities. This study, therefore, explores integrated approach of bio-based self-healing in which bacterial spores used to heal cracks automatically by MICP (Microbial-induced calcium carbonate precipitation and carbon sequestration) to deliver smart crack healing and develop cementitious composites as 'Biomimic Cement'. The urgent need to mitigate climate change has driven innovation in sustainable construction practices. The promising approach is the integration of biochar into construction materials to enhance carbon sequestration. Its microparticles were used both as a filler inside the cement paste and mortar composites and as a substitute for the cement powder inside the mixes [1]. Biochar, a carbon-rich byproduct produced from the pyrolysis of biomass under limited oxygen conditions, possesses a stable carbon structure that resists degradation, allowing it to store carbon for centuries. When incorporated into materials such as concrete, bricks, and insulation composites, biochar not only helps reduce the overall carbon footprint of buildings but also improves thermal insulation, moisture regulation, mechanical properties and also plays a significant role in reducing environmental pollution. Its porous structure and chemical stability enable long-term carbon storage, effectively sequestering CO_2 that would otherwise be released into the atmosphere. This study explores the potential of biochar as a multifunctional additive in construction, focusing on its role in long-term carbon storage, material performance, and environmental sustainability. By replacing conventional high-emission materials and sequestering atmospheric CO_2, biochar-infused construction presents a dual benefit. Overall the combination of biochar-spore could be a new option for the construction industry to develop smart infrastructure with improved serviceability and pollution free sustainable environment.

There are synergistic benefits when bacteria and biochar are combined in cementitious materials or concrete. Biochar serves as a biological carrier and structural addition, improving the performance and survivability of bacteria. The synergistic effect of biochar and bacteria in self-healing concrete arises from their mutual reinforcement—biochar protects and nourishes bacteria, while bacteria produce $CaCO_3$, which is enhanced by biochar's nucleation and moisture retention. Biochar can provide nucleation sites for chemical

reactions and exhibit compatibility with cement, asphalt, and polymer materials [2]. This combination significantly improves the self-healing efficiency, mechanical strength, and durability of the concrete.

From the following figures it can easily observe that biochar and bacteria together heals the crack.

Fig 1. Biochar+cement paste sample without bacteria

Fig 2. Biochar+cement paste sample with bacteria

An Advancement includes developed the light weight yet robust structures by imitating the interior geometry of natural material like bamboo, diatoms, and bird bones which maximize material distribution for strength and flexibility. By lowering structural weight and material consumption, these bio-inspired designs contribute to reducing the carbon impact of building and transportation.

Additionally, by taking inspiration from creatures that naturally regulate temperature—like termite mounds, which use passive ventilation systems to maintain interior climate stability—biomimic concrete can help enhance thermal regulation and energy efficiency. By incorporating these techniques into building materials and facades, artificial heating and cooling systems can be used less frequently, resulting in more energy-efficient buildings.

COMPRESSIVE STRENGTH

One of most important factor in construction material is compressive strength and in case of biomimic concrete it is optimized that after 28 days the values of compressive strength of mixes with biochar have shown up to 10-15% increase compared to control specimens.

CONCLUSION

Biomimic concrete, which draws inspiration from nature's 3.8 billion years of evolutionary creativity, signifies a revolutionary change in the way we plan and construct our infrastructure. Biomimic concrete stands out as a progressive option that can improve structural performance while reducing ecological impact as the construction industry shifts towards greener and more adaptable approaches. Biomimic concrete has the ability to reshape the built environment in a more sustainable and harmonious manner with further study, development, and incorporation into conventional building.

REFERENCES:

[1] D. Suarez-Rieraa *, L. Restucciaa , G.A. Ferroa

The use of Biochar to reduce the carbon footprint of cement-based materials

[2] Yuying Zhang1, Mingjing He1, Lei Wang2*, Jianhua Yan2, Bin Ma3, Xiaohong Zhu4, Yong Sik Ok5, Viktor Mechtcherine6 and Daniel C. W. Tsang1,2,7* Biochar as construction materials for achieving carbon neutrality.

ABS ID: 07
Code No: CCGR-EP-07

Mr. Mohit Kumar Chattopadhyay

Theme

International Public Health Research in Asia (IPHRA)

Distinguished Speakers

Keynote Speakers

Bright Spark Lecture

Oral Presentations

ABS ID: 80
Code No: IPHRA-OP-01

Ultraviolet-C Disinfection Technologies During the Covid-19 Pandemic: Mechanisms, Efficacy, and Emerging Applications

Tabish alam[1], nagesh babu balam[2], kishor kulkarni[3], chandan s. Meena[3], nirmal[4], injamamul haque[5], and nausahd ali[5]

[1]Senior Scientist, APEE, CSIR-Central Building Research Institute, Roorkee, India,
[2]Senior Principal Scientist, APEE, CSIR-Central Building Research Institute, Roorkee, India,
[3]Principal Scientist, APEE, CSIR-Central Building Research Institute, Roorkee, India,
[4]Scientist, APEE, CSIR-Central Building Research Institute, Roorkee, India,
[5]Project Associate, APEE, CSIR-Central Building Research Institute, Roorkee, India,
Correspond to Dr. Tabish Alam (tabish.cbri@csir.res.in)

Keywords: *COVID-19, SARS-CoV-2, ultraviolet-C (UVC), disinfection, far-UVC, surface decontamination, airborne pathogens.*

1. ABSTRACT

The COVID-19 pandemic prompted urgent advancement in disinfection strategies to mitigate the transmission of SARS-CoV-2, particularly in high-contact and enclosed environments. This review summarizes the range of disinfection technologies that evolved during this period, encompassing chemical, thermal (e.g., autoclaving, dry heat), and radiation-based methods. This review chronicles the transition in UVC technology. Experimental data indicate that UVC doses between 1.2 and 3.7 mJ/cm² can achieve >99.9% inactivation of SARS-CoV-2 on various surfaces and in aerosols. Recent innovations, such as far-UVC (222 nm), pulsed UVC, and UVC-based robotic units, have expanded the safe and effective use of this technology in healthcare facilities, public transport, and commercial buildings. The review further highlights the regulatory landscape, practical implementation challenges, and ongoing standardization efforts.

2. INTRODUCTION

The pandemic originated in Wuhan, China at the end of the year 2019[1]. The detection of the new virus, severe acute respiratory syndrome coronavirus 2, or the SARS-CoV-2, at the end of 2019 radically changed infection control and environmental disinfection procedure on the global scale, thus generating interests in ultraviolet-C (UV-C) disinfection technologies for health-care, commercial, and residential applications. While the germicidal properties of ultraviolet light have been arguably known for over a century, the COVID-19 pandemic acted as a watershed moment that provided momentum to the furtherance, acceptance, and mass implementation of UV-C-based pathogen inactivation technologies[2]. This technological renaissance, as it may be called, was fuelled by the urgent necessity for disinfectants capable of acting swiftly without chemicals and residues against the newly unique challenge of an airborne respiratory pathogen with significant environmental persistence.

The germicidal properties of light were first discovered in 1877 by Downes and Blunt, who found that the efficacy of light depends on the intensity and duration (dose) and that shorter wavelengths are more effective[3]. The clinical

studies about UVC disinfection of air were carried out in the early 1900s, even before the actual mechanistic understanding was obtained[2]. In a study spanning many years culminating in 1942 in Philadelphia schools, the rate of measles infection in typical classrooms was reported to have plummeted from > 50% to less than 16% with the application of upper-air UVC irradiation, and during the 1957 Influenza epidemic, infection rates plummeted from 19% to less than 2% in hospital wards under upper-room UVC irradiation[4,5].

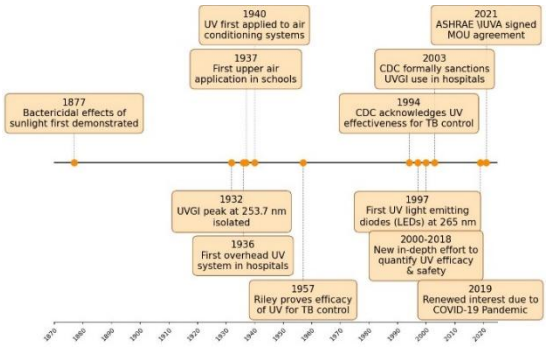

Figure 1. Key events in historical background of UVC air disinfection[6].

3. MECHANISM OF UVC INACTIVATION

Photo-inactivation or photolysis is UVC inactivation of viruses[7]. The main means by which UVC radiation exerts its germicidal effect is by disrupting the genetic mechanism of the virus, thus blocking its ability to replicate and infect host cells[8]. UVC irradiation could be defined as being short in wavelength, hence higher in energy, especially in the range of 200-290 nm. DNA/RNA absorbs wavelengths in the range from 200 to 300 nm, with the peak absorbance occurring around 260 nm. The most common wavelengths used germicidally are in the region between 254 and 260 nm[7]. They are absorbed intensely by telltale nucleic acids, DNA/RNA present in microbial cells and viruses. The intensity with which it is absorbed is so great that it damages or completely destroys the germs' genetic material. The genetic damage involves the photo-dimerization between adjacent pyrimidine molecules of the nucleotides, mainly the thymine/uracil dimerization in nucleic acids[7]. The other components outside of the genetic core can also be targeted by UVC irradiation, which denatures enzymes required in DNA repair under the photoreactivation mechanism in the case of viruses and phages[7].

3. APPLICATIONS AND EMERGING TECHNOLOGIES

UVC light based are the main form of technology and equipment used for the environmental decontamination of SARS-CoV-2, which is used by a variety of specialized devices. These include whole-room UVC units with low-pressure mercury vapor lamps operating at 254 nm, those with very strong germicidal activity against those organisms[7]. For cleaning room terminals and surfaces, commercial products such as UVC disinfection chambers (e.g. A. Skytron technologies) that ensure accurate germicidal dosages, as well as pulsed-xenon UV robots (e.g. A. model PXUV4D) are employed. Far-UVC (222 nm) is mostly obtained from KrCl excimer lamps is explored as a safer alternative for use in occupied spaces, UVC-LEDs are the compact sterilizers that are replacing older mercury sources because of their small size, long life, ability to arbitrarily control irradiance, and because they are free of hazardous mercury[7,9].

The UVC technology has been one input that quickly entered different equipment types, from specialized air cleaners and centralized HVAC systems to different automated and manual surface disinfectors for environmental disinfection. In ducts, HVAC-type raisers and upper-room UVCs are some specialized ways in which conventional UVC-type systems are often applied, basing basically on 254nm. In-duct systems treat the air as it passes through the AHUs; for big buildings, the usual objective is 85 percent single-pass inactivation. The upper-room UVC system radiates the upper air space of the occupied room. Added as a commercial example of HVAC integration, Rheem's third-generation RM3 UV-

C units are for cleaning SARS-CoV-2-loaded air in HVAC ducts[7,10]. Portable UV-C air purification devices, which use germicidal-UV lamps, are used to remove aerosols from air through circulation in a UV-C reactor, with efficacy reported to be 99 percent (in laboratory settings). New emitters, such as Deep UV-LEDs at 280 nm, are used in compact systems where air is channeled through a conduit to inactivate viruses[11]. Other small devices emerged include portable UVC disinfection lamps, the Handsfree UVC decontamination device, which uses intelligent sensing to remotely decontaminate large areas, and the UVC Scanz Plus sanitizing machine, an ultraviolet scanning machine that disinfects objects in a 360-degree manner[7].

3. CONCLUSIONS

The COVID-19 pandemic instigated a turning moment, initiating the hurried development and certain widespread applications of various UVC disinfection technologies. UVC (200–290 nm) has long been acknowledged for its germicidal effects-heavily inactivating viruses such as SARS-CoV-2 by photoinactivation through DNA/RNA rupture. Experimental data have shown that UVC doses between 1.2 and 3.7 mJ/cm² gave rise to a virus inactivation rate of more than 99.9. This need for rapid disinfection without the use of chemicals drove a technological revolution. Far-UVC (222 nm), UVC-LEDs, and fully automated robotic UVC systems have forged the way for decontamination applications on surfaces, in air, and inside HVAC systems as well as portable air purifiers-all these across a handful of occupied and commercial spaces

REFERENCES:

1 Zhu N, Zhang D, Wang W, Li X, Yang B, Song J, et al. A Novel Coronavirus from Patients with Pneumonia in China, 2019. New England Journal of Medicine 2020;382.

2. Reed NG. The history of ultraviolet germicidal irradiation for air disinfection. Public Health Reports 2010;125.

3.DOWNES A, BLUNT TP. The Influence of Light upon the Development of Bacteria 1. Nature 1877;16.

4. JORDAN WS. The mechanism of spread of Asian influenza. Am Rev Respir Dis 1961;83.

5. Wells WF, Wellsi MW, Wilder TS. The environmental control of epidemic contagion: I. An epidemiologic study of radiant disinfection of air in day schools. Am J Epidemiol 1942;35.

6 Kowalski W. Ultraviolet germicidal irradiation handbook: UVGI for air and surface disinfection. 2009.

7 Bhardwaj SK, Singh H, Deep A, Khatri M, Bhaumik J, Kim KH, et al. UVC-based photoinactivation as an efficient tool to control the transmission of coronaviruses. Science of the Total Environment 2021;792.

8 Sellera FP, Sabino CP, Cabral F V., Ribeiro MS. A systematic scoping review of ultraviolet C (UVC) light systems for SARS-CoV-2 inactivation. J Photochem Photobiol 2021;8.

9 Chiappa F, Frascella B, Vigezzi GP, Moro M, Diamanti L, Gentile L, et al. The efficacy of ultraviolet light-emitting technology against coronaviruses: a systematic review. Journal of Hospital Infection 2021;114.

10 Abkar L, Zimmermann K, Dixit F, Kheyrandish A, Mohseni M. COVID-19 pandemic lesson learned- critical parameters and research needs for UVC inactivation of viral aerosols. Journal of Hazardous Materials Advances 2022;8.

11 Hiep NT, Nguyen MK, Nhut HT, Hung NTQ, Manh NC, Lin C, et al. A review on sterilization methods of environmental decontamination to prevent the coronavirus SARS-CoV-2 (COVID-19 virus): A new challenge towards eco-friendly solutions. Science of the Total Environment 2023;904.

ABS ID: 184
Code No: IPHRA-OP-02

One World One Health: Current Prospective

M. K. Sinha[1] and P. C. Thapliyal[2, 3]
[1]*Medical Officer, CSIR-Central Building Research Institute, Roorkee-247667, India.*
[2]*Chief Scientist, CSIR-Central Building Research Institute, Roorkee-247667, India.*
[3]*Professor, Academy of Scientific and Industrial Research, Ghaziabad-201002, India.*
Correspond to Prof. P. C. THAPLIYAL (pcthapliyal.cbri@csir.res.in)

Keywords: *Health, Diseases, OWOH approach, Endemic, Zoonotic.*

ISSUES

One world one health issues include emerging, re-emerging, and endemic zoonotic diseases, neglected tropical diseases, vector-borne diseases, antimicrobial resistance, food safety and food security, environmental contamination, climate change and other health threats shared by people, animals, and the environment. For example, antimicrobial-resistant germs can quickly spread through communities, the food supply, healthcare facilities, and the environment (soil, water), making it harder to treat certain infections in animals and people.

Vector-borne diseases are on the rise with warmer temperatures and expanded mosquito and tick habitats. Diseases in food animals can threaten supplies, livelihoods, and economies. The human-animal bond can help improve mental well-being.

Contamination of water used for drinking, recreation, and more can make people and animals sick. Even the fields of chronic disease, mental health, injury, occupational health, and noncommunicable diseases can benefit from the One world one health approach involving collaboration across disciplines and sectors.

WORKING OF THIS APPROACH

One world one health is gaining recognition in the United States and globally as an effective way to fight health issues at the human-animal-environment interface, including zoonotic diseases. One world one health approach by involving experts in human, animal, environmental health, and other relevant disciplines and sectors in monitoring and controlling public health threats and to learn about how diseases spread among people, animals, plants, and the environment.

Successful public health interventions require the cooperation of human, animal, and environmental health partners. Professionals in human health (doctors, nurses, public health practitioners, epidemiologists), animal health (veterinarians, paraprofessionals, agricultural workers), environment (ecologists, wildlife experts), and other areas of expertise need to communicate, collaborate on, and coordinate activities (Figure 1). Other relevant players in the One world one health approach could include law enforcement, policymakers, agriculture, communities, and even pet owners. No one person, organization, or sector can address issues at the animal-human-environment interface alone.

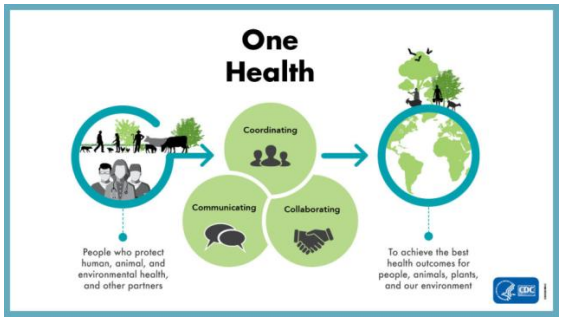

Figure 1: The Foundation of One world one health: communication, coordination, and collaboration among human, animal, environmental health, and other relevant partners.

By promoting collaboration across all sectors, the One Health approach can achieve the best health outcomes for people, animals, and plants in a shared environment [1].

IMPACT

COVID-19 has led to the loss of millions of lives and trillions of dollars from the global economy, an impact that needs to be avoided in the future. The emergence of the SARS-CoV-2 virus has underlined the need to strengthen the One world one health approach, with a greater emphasis on connections to the environment, as well as promoting a healthy and green recovery from COVID-19, as described in the WHO manifesto for a healthy recovery from COVID-19. Human health is a pillar of global health security that is sustained directly and indirectly through access to clean air and fresh water, safe food and healthy sustainable diets, and the availability of and access to medicines.

As we come together as a community in the aftermath of this global pandemic, we have an unprecedented opportunity to strengthen cross-sectoral collaboration; increase policy coordination and coherence supported by a more systematic use of robust scientific evidence; and promote the development of integrated indicators and safeguards to address upstream drivers of disease, with a focus on prevention. These efforts will not only contribute to the prevention of future pandemics but will help to build more resilient and equitable systems, environments, economies and societies.

RESPONSE

In the context of the renewed interest from Member States to strengthen work on One Health and prevention of emerging zoonoses and the work of WHO Governing bodies on One Health, the WHO One Health Initiative team was set up to serve as the Secretariat of One Health High-Level Expert Panel (OHHLEP), WHO coordination mechanism for its One Health activities and the quadripartite collaboration.

Investing in One world one health contributes to WHO's vision to promote health, keep the world safe and serve the vulnerable. WHO works to integrate the One Health approach into the global health narrative, grounded in strong political leadership, technical expertise and inclusive implementation led and owned by countries.

WHO and partner organizations are working to increase the adoption of the One Health approach in national, regional and international health policies through intersectoral political and strategic leadership; operationalizing responses and scaling up of country support, including research and policy assessment; strengthening country capacities; and monitoring of risks and preparedness for early detection and response to emerging pathogens.

Through combined energies of the Quadripartite organizations (FAO, OIE, UNEP and WHO), a comprehensive One Health Joint Plan of Action is in development, supported and advised by the One Health High-Level Expert Panel. The Plan aims to mainstream and operationalize One Health at the global, regional and national levels;

support countries in establishing and achieving national targets and priorities for interventions; mobilize investment; promote a whole of society approach; and enable collaboration, learning and exchange across regions, countries and sectors [2].

KEY ASPECTS OF THE ONE WORLD ONE HEALTH CONCEPT

- Interconnectedness

Recognizes that human as well as animal health and ecosystem health influence each other.

- Multi-sectoral collaboration

Requires collaboration and communication between medical, veterinary, environmental, and other relevant sectors to address complex health issues.

- Holistic approach

Emphasizes the need to consider the broader context of health, including environmental factors, social determinants, and cultural practices.

- Focus on prevention

Aims to prevent disease emergence and spread by addressing the underlying causes and promoting healthy ecosystems.

- Global perspective

Acknowledges that health challenges transcend national borders and require international cooperation and coordination.

EXAMPLES OF ONE WORLD ONE HEALTH IN ACTION

1. Zoonotic disease control

By understanding the animal origins of diseases like COVID-19, Ebola, and influenza, One Health approaches can help prevent future outbreaks by improving surveillance, vaccination programs, and public health infrastructure.

2. Antimicrobial resistance

By promoting responsible antibiotic use in both human and animal health, and by implementing effective infection control measures, One world one health can help combat the growing threat of antimicrobial resistance.

3. Climate change and health

Recognizing the impact of climate change on disease patterns and human health, One world one health can help develop strategies for climate adaptation and mitigation that also promote human and animal health.

4. Food safety

By ensuring safe food production practices and effective food safety systems, One world one health can help prevent foodborne illnesses and promote overall well-being.

5. Environmental health

By addressing pollution, habitat destruction, and other environmental factors that affect human and animal health, One world one health can contribute to a healthier planet.

The One world one health approach is not just a scientific concept; it's a call for a more integrated and collaborative way of thinking about health that recognizes the interconnectedness of all living things and the environment. It's a vital framework for addressing the complex health challenges of the 21st century and building a healthier, more sustainable future for all.

REFERENCES:

1. https://www.cdc.gov/one-health/about/index.html;

Accessed on 27/08/2025 at 2.30 PM.

2. https://www.who.int/health-topics/one-health#tab=tab_3;

Accessed on 27/08/2025 at 2.45 PM.

ABS ID: 160
Code No: IPHRA-OP-03

Effect of Building Corner Shape Modification on Near-Field Pollutant Dispersion

KRISHAN DUTT YADAV[1,2], BHARAT SINGH CHAUHAN[1,2]
[1]*Heritage and Special Structure Group, CSIR- Central Building Research Institute Roorkee, Uttarakhand, India-247667.*
[2]*Academy of Scientific and Innovative Research, Ghaziabad, Uttar Pradesh, India-201 002.*
Correspond to Mr. Krishan Dutt Yadav (krishandutt.cbri@gmail.com)

Keywords: *Point Source, Pollutant Dispersion, OpenFOAM CFD, k−ϵ Turbulence Model, Scalar Transport, Environmental Fluid Dynamics, Air Quality Modeling.*

ABSTRACT

This study presents an investigation of the complex phenomenon of passive scalar pollutant dispersion from a ground-level point source close to a building having different corner shapes through Computational Fluid Dynamics (CFD). Understanding and accurately predicting such dispersion is paramount for environmental protection, urban planning, and public health, particularly in scenarios involving vehicular emission, industrial emissions, or accidental releases in the atmospheric boundary layer. The study utilizes a steady-state Reynolds-Averaged Navier-Stokes (RANS) framework, coupled with the robust k−ϵ turbulence model, to numerically resolve the intricate turbulent flow field and subsequent scalar transport. Simulations were meticulously conducted using OpenFOAM, demonstrating CFD capability to provide high-fidelity insights beyond simplified analytical approaches. The results vividly illustrate the characteristic plume development, revealing a rapid decay in pollutant concentration both laterally and vertically downstream of the source. This research not only advances the fundamental understanding of localized pollutant releases in atmospheric environments but also provides a vital tool for informed decision-making in air quality management and environmental risk assessment.

1. INTRODUCTION

Sharp corner buildings induced turbulent flow patterns, which produce wake cavities and prolonged recirculation, which constitute the primary cause of urban pollutant emission close to buildings [1]. For the betterment of public health, these high near field concentrations need to be mitigated [2]. This flow and dispersion are primarily governed by the geometric shape of the building [3]. Building morphology controls near field pollutant dispersion by influencing wake turbulence [4], [5]. Sharp corners on square buildings induce intense shear separation, creating large, polluted recirculation zones [6]. This research uses high fidelity CFD to investigate the effect of specific, targeted corner modifications: R10 fillet and 10×45˚ chamfer on a rectangular building. While previous work broadly addresses shape, this study isolates and quantifies the aerodynamic impact of these two widely applicable, simple architectural treatments against the sharp corner baseline. Current study novelty lies in providing a direct, quantitative comparison of these common design adjustments, establishing a clear link between specific

corner geometry and its effect on local pollutant concentration and wake structure.

1.1 Building Configurations

A scaled-down model at a ratio of 1:200 is used to analyze a tall building with dimensions of (L×B×H=20m × 60m × 100m). Computational Fluid Dynamics (CFD) study is used to investigate various geometric modifications effect on wind-flow and pollution dispersion on various building configurations. A rectangular building with sharp edges serves as the study baseline model [Fig.1(a)]. In subsequent configurations, the vertical edges are supplemented with fillet corners [Fig. 1(b)] and chamfer corners [Fig. 1(c)] at 10% of the building length (L=100 mm).

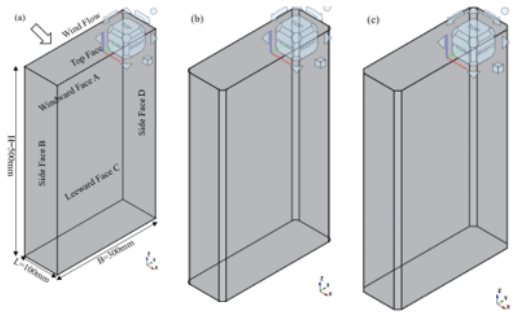

Fig. 1 Different building configurations

2. METHODOLOGY

Methodology employs CFD using a compiled OpenFOAM solver, turbScalarTransportsimpleFoam complied by binayakl, based on combinations of simpleFoam and scalarTransportFoam Solvers. The standard k-ϵ model is used for turbulence.

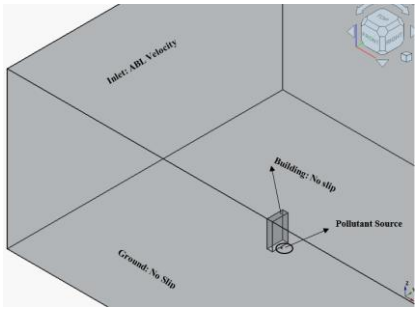

Fig. 2 Near field allocation of pollutant source

A hex dominant cfMesh is generated with refinement around building and nearfield pollutant point source shown in Fig.2 with sufficient domain size, applying ABL boundary conditions to ensure accuracy. The ABL profile used, based on the power law correlation from Bharat et al. (2021) (α=0.3 in the BLWT), is defined by a reference velocity of Uref=9.55 m/s at a reference height of zref=0.5 m and a roughness length z0=0.01 m. The governing equation [Eqns. 1 and 2] are:

RANS Momentum Equation:

$$\nabla\cdot(UU)-\nabla\cdot(v_{eff}\ \nabla U)=-\nabla p_r\ +〚R〛_{terms} \quad (1)$$

Passive Scalar Transport:

$$\nabla\cdot(UT)-\nabla\cdot(D_{eff}\ \nabla T)=0 \quad (2)$$

Where:

U: Mean fluid velocity vector.

T: Pollutant concentration (passive scalar).

Turbulent diffusivity (Dt)

$$D_t=v_t/〚Sc〛_t$$

〚Sc〛_t: Turbulent Schmidt number. [0.6 used for this]

3. RESULTS AND DISCUSSIONS

The visualization [Fig. 3 (a-b)] of the dimensionless pollutant mass fraction (T), which ranges from 0 to 1 confirms that the highest concentrations are localized immediately downstream of the source, situated at the bottom center of the building leeward face. This source is modeled as a 10 mm point source 25 mm away from the building, defined by a constant mass emission rate of 0.096 g/s (via scalarSemiImplicitSource in fvOptions). This small emission magnitude ensures the simulation remains within the trace atmospheric dispersion regime. Comparing the three corner geometries (Sharp, Fillet, and Chamfer), results indicate that edge modification impacts pollutant dispersion in the wake. The Sharp Corner

configuration yields the lowest near-face concentration, suggesting stronger flow separation and enhanced mixing. Conversely, the Fillet and Chamfer geometries result in slightly higher peak pollutant accumulation near the leeward face, potentially due to a dampened recirculation zone that retains the pollutant mass for a longer duration.

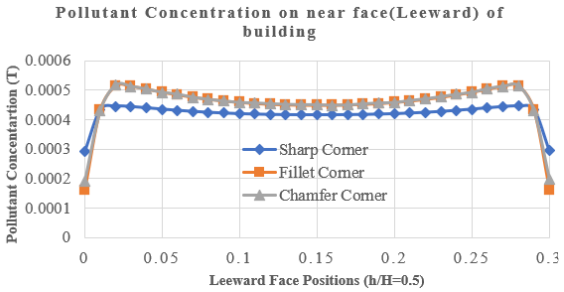

Fig. 3(a) Pollutant Concentration at horizontal centre of leeward face

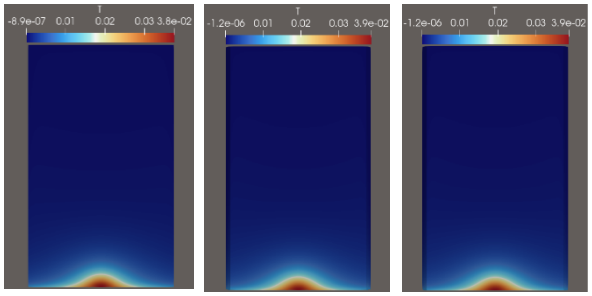

Fig. 3(b) Pollutant Concentration on nearer face (leeward face) to pollutant source

4. CONCLUSIONS

Sharp corners promote superior pollutant dispersion if provide on leeward side of building by enhancing wake turbulence and mixing. Fillet and Chamfer corners slightly hinder this effect, resulting in marginally increased near-wall pollutant retention.

5. REFERENCES:

[1] T. R. Oke, Boundary Layer Climates. Routledge, 2002.

[2] S. Vardoulakis, B. E. A. Fisher, K. Pericleous, and N. Gonzalez-Flesca, “Modelling air quality in street canyons: a review,” Atmos Environ, vol. 37, no. 2, pp. 155–182, Jan. 2003.

[3] J. Hang, Y. Li, M. Sandberg, R. Buccolieri, and S. Di Sabatino, “The influence of building height variability on pollutant dispersion and pedestrian ventilation in idealized high-rise urban areas,” Build Environ, vol. 56, pp. 346–360, Oct. 2012.

[4] L. Meng, B. Li, X. Si, and C. Cao, “Wind environment and pollutant dispersion around high-rise buildings with different void space structures,” J Build Phys, vol. 48, no. 5, pp. 738–766, Mar. 2025.

[5] B. Hajra, T. Stathopoulos, and A. Bahloul, “A wind tunnel study of the effects of adjacent buildings on near-field pollutant dispersion from rooftop emissions in an urban environment,” Journal of Wind Engineering and Industrial Aerodynamics, vol. 119, pp. 133–145, Aug. 2013.

[6] E. Keshavarzian, R. Jin, K. Dong, and K. C. S. Kwok, “Effect of building cross-section shape on air pollutant dispersion around buildings,” Build Environ, vol. 197, p. 107861, Jun. 2021.

ABS ID: 155
Code No: IPHRA-OP-04

Dr. Vijay Wasudeorao Lande

4th International Symposium on One Health, One World
November 20 – 22, 2025

ABS ID: 144
Code No: IPHRA-OP-05

Randomised Double Blind Controlled Trial to Test the Efficacy of Śuṇṭhyādi Kaṣāya Against Mahārāsnādi Kaṣāya in Knee Osteoarthritis

A Binitha [1], M Jithesh [2]

[1]*Professor, Department of Panchakarma , VPSV Ayurveda College Kottakkal, Kerala, India,*

[2]*Professor, Department of Kayachikitsa, VPSV Ayurveda College Kottakkal, Kerala, Indiary,*

Correspond to drbinithaunni@gmail.com

Keywords: *Mahārasnādi Kaṣāya, Śuṇṭhyādi Kaṣāya, Knee Osteoarthritis, Sandhigatavata, Kashaya extract, Non inferior RCT, Decoction.*

Introduction

Knee osteoarthritis is a prevalent degenerative joint disease with significant impact on older adults and has no curative treatment [1]. A randomized double-blind controlled clinical trial investigated the efficacy of Śuṇṭhyādi Kaṣāya [2] extract compared to Mahārasnādi Kaṣāya [3] extract, a formulation used in Sandhigatavata which is symptomatically similar to Osteoarthritis, in managing knee osteoarthritis.The study aimed to assess the non-inferiority of Śuṇṭhyādi Kaṣāya.

Methodology

114 subjects meeting the American College of Rheumatology diagnostic criteria for knee osteoarthritis [4] were randomized into two groups, each receiving either 60ml of Śuṇṭhyādi Kaṣāya or Mahārasnādi Kaṣāya twice daily for 60 days. The Kaṣāya extracts were prepared under Good Manufacturing Practice standards, ensuring uniformity and blinding. Assessments done at 30th, 60th, and follow up at 90th day, using the Visual Analogue Scale (VAS) and the modified WOMAC (Western Ontario and McMaster Universities Arthritis Index) score (modified – CRD Pune version).[5] focusing on primary efficacy variables and degree of knee flexion.

Preparation of Kaṣāya extract

The Kaṣāya extracts were prepared without any preservatives or additives, by a GMP company (Sreemed Labs). Mahārāsnādi Kaṣāya drugs were made into Kaṣāya in standardized form [6] and converted into extract form using Vacuum spray dry method, filled in sachet and packed in bottles labelled A. Similarly Balā , Atibalā and Śuṇṭhī in the ratio 5:5:2 was made into Kaṣāya and converted into extract form, filled in sachet and packed in bottle labelled B. The sachet and bottles were of the same colour and size and identity remained concealed with the guide. Each sachet contained 1.5 gm of powder and was equivalent to 15 ml of concentrated Kaṣāya which was taken by adding 45 ml of lukewarm water.

Analyses

Primary analyses included all participants who were randomized, following an intention-to-treat principle. Statistical analysis was conducted using SPSS version 27. The Shapiro-Wilk test was employed to assess normality, and as the data did not follow a normal distribution, non-parametric tests were subsequently used. The overall effectiveness of the treatment was evaluated using Friedman's test. For pair-wise comparisons of effectiveness within groups, the Wilcoxon

signed-rank test was utilized, while the Mann-Whitney U test was applied for comparisons of effectiveness between groups. The level of significance for all analyses was set at 5%. The Protocol was approved by the Institutional Review Board and also registered in the Clinical trial registry of India (CTRI/2021/07/035148CTRI). There were no conflicts of interest for the study.

Results

Both Group A and Group B demonstrated significant improvement in their WOMAC scores over time, indicating a reduction in pain and stiffness and an improvement in physical function. Pairwise comparison also confirmed significant improvements at all time points (all $p < 0.001$). The mean change in WOMAC from baseline increased over time. There was no statistically significant difference between Group A and Group B at 30th, 60th, or 90th day. Though there was significant difference within groups ($p<0.05$), in WOMAC Subscores (Pain, Stiffness, Function, Optional) except for functional score, there was significance at $p<0.05$ in between group analysis.

Both groups showed a statistically significant reduction in VAS scores over time, indicating a decrease in perceived pain. While baseline VAS scores at Day 0 were not significantly different between the groups ($Z = -1.770$, $p = 0.077$), the Mann-Whitney U Test revealed a significant difference in VAS scores between Group A and Group B from Day 30 onwards. There was no significant change in the degree of knee flexion from Day 0 to Day 90 within their respective groups

Inferiority analysis

The analysis consistently demonstrates that Group B is non-inferior to Group A across all assessed pain and functional outcomes over a 90-day period. This conclusion is supported by non-inferiority t-tests at 30th, 60th, and 90th day, which uniformly yielded p-values less than 0.001, indicating that the null hypothesis of inferiority for Group B was statistically rejected.

Discussion

This double-blind Randomized Controlled Trial (RCT) involving 114 participants evaluated the efficacy of Mahārasnādi Kaṣāya and Śuṇṭhyādi Kaṣāya extracts for knee osteoarthritis over two months, followed by a one-month follow-up. Both formulations significantly reduced symptoms, with no reported adverse effects despite 14 dropouts. Among the dropouts, six from Group A and eight from Group B, none were due to treatment-related adverse events, rather, they were primarily attributed to external factors such as job relocation, accidental trauma, and travel commitments, with the few instances of symptom aggravation remaining within manageable limits and linked to non-compliance with lifestyle advice or excessive travel in an outpatient setting. The two-month treatment duration, coupled with the ready-to-use extract form, likely optimized dosage and patient compliance, enhancing efficacy. Functional limitation is influenced by chronic joint degeneration, lifestyle, and psychological factors, not just symptomatic relief. Even if pain/stiffness improves, the functional score may not shift significantly, because activities like climbing stairs or squatting demand structural improvement, which Kaṣāya alone may not be achieved in the study duration.

Hence, functional improvement may require longer duration of therapy, supportive Panchakarma (e.g., Abhyanga, Swedana, Vasti), and physiotherapy, along with Kaṣāya administration

Mahārasnādi Kaṣāya is a classical polyherbal formulation with a broad therapeutic spectrum. Traditionally, it has been indicated in a wide range of disorders including neurological conditions (such as neuropathies, hemiplegia, and other vāta-related disorders), gynaecological ailments (like dysmenorrhea, pelvic pain, and postpartum complications), as

well as musculoskeletal diseases including arthritis, low back pain, and joint disorders. Its multidimensional pharmacological actions,Balya (strengthening), Vātahara (alleviating Vāta), and Śūlapraśamana (analgesic)make it versatile across several systems of the body supported by the anti-inflammatory, analgesic, anti-arthritic, and antioxidant actions of its ingredients[7]. In contrast, Śuṇṭhyādi Kaṣāya has a relatively targeted therapeutic application, being predominantly used in musculoskeletal conditions. Its formulation emphasizes ingredients with properties like Śūlapraśamana (pain-relieving), Āma-pācana (digestive and anti-inflammatory), and Vāta–Kapha hara (pacifying Vāta and Kapha). Hence, it is specifically effective in conditions such as Osteoarthritis, Rheumatoid arthritis, and other painful inflammatory disorders of the joints and soft tissues. Specifically, Balā root (Sida cordifolia) inhibits protein denaturation and proteinase enzymes, while Atibalā root shows superior anti-arthritic action compared to acetylsalicylic acid. Shunṭi (Zingiber officinale) in Shuntyadi Kashaya is crucial, with its gingerols, shogaols, and volatile oils providing anti-inflammatory, analgesic, and antioxidant effects by targeting COX/LOX pathways and cytokines, effectively reducing pain and swelling, and improving mobility with fewer side effects than NSAIDs [8,9,10]. Thus, while Mahārasnādi Kaṣāya offers a broader systemic utility spanning multiple specialties of Ayurveda, Śuṇṭhyādi Kaṣāya is more focused in action, primarily targeting musculoskeletal pathologies with a distinct emphasis on pain and inflammation management accounting for the differential outcomes observed.

Conclusion

Mahārasnādi Kaṣāya (Group A) and Śuṇṭhyādi Kaṣāya (Group B) significantly improved the Visual Analog Scale (VAS) for pain and the WOMAC subscores, except functional score both within and between groups. WOMAC total score, functional score and degree of flexion were insignificant between groups. While both treatments were effective, Śuṇṭhyādi Kaṣāya demonstrated a slightly higher effect on WOMAC and VAS scores and was found to be non-inferior to Mahārasnādi Kaṣāya. This led to the rejection of the null hypothesis, confirming Śuṇṭhyādi Kaṣāya 's comparable efficacy.

References:

1. Mahajan A, Chopra A. Osteoarthritis. In: Munjal YP, editor. API Textbook of Medicine. 9th ed. Mumbai: The Association of Physicians of India; 2012. p. 1093–6.

2. Aravattazhikathu K, Anekkaleelil S. Sahasrayoga. 19th ed. Sujanapriya commentary. Kerala: Vidyarambham Publishers; June 1993. p.78

3. Aravattazhikathu K, Anekkaleelil S. Sahasrayoga. 19th ed. Sujanapriya commentary. Kerala: Vidyarambham Publishers; June 1993. p.82

4. R. Altman, E. Asch, D. Bloch, G. Bole, D. Borenstein, K. Brandt, et al. The American College of Rheumatology criteria for the classification and reporting of osteoarthritis of the knee. Arthritis Rheum 1986;29:1039—1049

5. Chopra A, Saluja M, Tillu G, Venugopalan A, Sarmukaddam S, Raut AK, et al. A randomized controlled exploratory evaluation of standardized Ayurvedic formulations in symptomatic osteoarthritis knees: a Government of India NMITLI project. Evid Based Complement Alternat Med. 2011;2011:724291. doi:10.1155/2011/724291.

6. Śārṅgadhara. Śārṅgadhara Saṃhitā. In: Murthy KR, editor and translator. Madhyama Khaṇḍa, Chapter 2 (Kwātha Kalpanā), Verse 2. 6th ed. Varanasi: Chaukhambha Orientalia; 2007. p. 48

7. Sruthi CV, Sindhu A. A comparison of the antioxidant property of fi ve Ayurvedic formulations commonly used in the management of vata vyadhis. J Ayurveda Integr Med 2012; 3:29-32

8. Grzanna R, Lindmark L, Frondoza CG. Ginger—an herbal medicinal product with broad anti-inflammatory actions. J Med Food. 2005;8(2):125–132.

9. 22. Daily JW, Yang M, Park S. Efficacy of ginger for alleviating the symptoms of primary osteoarthritis. Osteoarthritis Cartilage. 2000;8(9):567–572.

10. 23.Altman RD, Marcussen KC. Effects of a ginger extract on knee pain in patients with osteoarthritis. Arthritis Rheum. 2001;44(11):2531–253

ABS ID: 140
Code No: IPHRA-OP-06

Mrs. Joyce Owens Kobusingye

ABS ID: 89
Code No: IPHRA-OP-07

Mrs. Ananya Sutradhar

ABS ID: 86
Code No: IPHRA-OP-08

Associatie Prof. Alex Riolexus Ario

ABS ID: 62
Code No: IPHRA-OP-09

Dr. Chayan Munshi

ABS ID: 23
Code No: IPHRA-OP-10

Dr. Chayan Munshi

4th International Symposium on One Health, One World
November 20 – 22, 2025

ABS ID: 04
Code No: IPHRA-OP-11

Catalyst Free Synthesis of Novel 6-Chloro-3-Isopropyl-1-Methylpyrimidine-2,4(1h,3h)-Dione Derivatives as Pharma Intermediate

R. S. SHINGARE,[1] A. VEERAM,[2,3] S. B. ANDUGULAPATI,[2.3] B.V. S. REDDY,[1,3] and S. BANSOD [1,3]

[1]Department of Fluoroagrochemicals, CSIR-Indian Institute of Chemical Technology, Hyderabad-500007 (TS), India.

[2]Department of Applied Biology, CSIR-Indian Institute of Chemical Technology, Hyderabad-500007 (TS), India.

[3]Academy of Scientific and Innovative Research (AcSIR), Ghaziabad-201002(UP), India.

ABSTRACT

We synthesised novel compounds containing 6-chloro-3-isopropyl-1-methylpyrimidine-2,4(1H,3H)-dione derivatives without a catalyst. These molecules can potentially demonstrate exceptional anticancer, antiviral, and bactericidal properties while being safe for use. These compounds represent a minor modification of Mavacamten. Additionally, we can efficiently produce them on an industrial scale. They may also serve as active components in medicinal and veterinary antifungal agents.

INTRODUCTION

Acute Lung Injury (ALI) and acute respiratory distress syndrome (ARDS) are serious pulmonary disorders characterised by excessive inflammation and cytokine storms, which frequently lead to respiratory failure and high mortality rates, particularly when left untreated [1]. Mavacamten, a pioneering small-molecule cardiac myosin ATPase inhibitor, is recognised for its ability to reduce pathological hypercontractility, yet its potential role in ALI/ARDS remains largely unexplored [2]. To address this gap, we synthesised novel mavacamten derivatives that incorporate the 6-chloro-3-isopropyl-1-methylpyrimidine-2,4(1H,3H)-dione scaffold using a catalyst-free method. We then evaluated the anti-inflammatory and antioxidant properties of mavacamten and its derivatives (5d and 5o) through LPS-induced inflammation models, both in vitro and in vivo. Initial assays for IL-6 indicated that mavacamten and its derivatives significantly lowered IL-6 levels compared to the LPS control [3].

Further in vitro analysis demonstrated a notable downregulation of pro-inflammatory markers (IL-1β, IL-6, TNF-α, CCL2, and F4/80) along with oxidative stress indicators (ROS, nitric oxide, and cofilin), while also restoring caveolin levels. In vivo, compounds 5d and 5o were tested in an LPS-induced (intra-tracheal administration) ALI mouse model. Both derivatives significantly reduced the LPS-induced increases in lung and heart indices, as well as systemic inflammatory markers such as monocytes, white blood cells (WBCs), and neutrophils. They also restored platelet and lymphocyte levels, suggesting reduced inflammatory cell infiltration at the injury site [4].

Gene and protein expression analyses confirmed a decrease in inflammatory marker expression, and histopathological examinations revealed that 5d and 5o significantly alleviated the LPS-induced damage to lung (including alveolar oedema and wall thickening) and heart (myocardial

inflammation) tissues. These findings suggest that compounds 5d and 5o effectively reduce LPS-induced inflammation and tissue injury through the modulation of NF-κB signalling, underscoring their potential as therapeutic candidates for the treatment of ALI/ARDS [5].

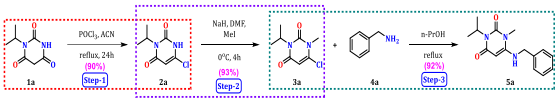

Figure 1: Scheme of total Synthesis of Products.

Discussion

Mavacamten is mainly used to treat hypertrophic cardiomyopathy, but its effects on lung inflammation are still largely unknown. Understanding how mavacamten influences lung inflammation is important, especially since the heart and lungs are closely linked in many health issues. There is a need for research on how mavacamten and similar drugs could impact lung inflammation.

Acute lung injury (ALI) often begins with infections or harmful agents like LPS. This type of injury doesn't just affect the lungs; it can cause inflammation in other vital organs, especially the heart. This systemic inflammation contributes to problems with bloodvessels and may worsen damage beyond the lungs. Lung injuries can also lead to issues with other organs, particularly the heart, linked to excessive activation of neutrophils and increased cell death in lung tissue.

Mavacamten works as an allosteric inhibitor of cardiac myosin ATPase, addressing the excessive heart contractions seen in affected patients. Clinical studies show that it can greatly relieve symptoms, improve patients' health, and reduce the need for surgery. However, doctors must monitor its use closely because itmay lower left ventricular ejection fraction (LVEF). These concerns are part of the FDA's Risk Evaluation and Mitigation Strategy (REMS). Additionally, the high cost of mavacamten can limit its availability, especially outside specialized centers.

Given these challenges, it's important to develop new mavacamten-based drugs that are safer and have broader uses. New versions of the drug could reduceheart-related side effects while also helping with inflammation in conditions like ALI, where lung and heart issues are connected. Advancements like these could provide better treatment options for complex heart and lung diseases.

Mavacamten, created for heart issues, may also help with lung diseases due to its anti-inflammatory and muscle-relaxing effects. It might lower levels of cytokines like IL-6, reduce airway tightening, and slow down scarring in lung diseases like asthma or pulmonary fibrosis. However, more studies are needed to confirm these possible benefits. Monoclonal antibodies such as dupilumab, benralizumab, and itepekimab are being tested for lung inflammation. They target specific cytokines involved in airway diseases but come with downsides like high costs, infection risks, uneven patient responses, and limited safety data.

Because of mavacamten's limitations, including the need for careful monitoring and availability issues, our study focused on creating modified versions of the drug with better benefits, especially for reducing inflammation. LPS triggers pro-inflammatory cytokine production, causing inflammation in both lung and heart tissues. Our research aimed to test the effects of these new compounds on inflammation both in lab settings and in live models. We created 18 new compounds derived from mavacamten and first tested their anti-inflammatory effects using ELISA-based assays. In this initial screening, two compounds, 5d and 5o, showed significantly better inhibition of pro-inflammatory cytokines than mavacamten alone. We chose

compounds 5d and 5o for further study because of their stronger effects.

Table 1: List of mouse primer sequences

SN	Name of the gene	Forward primer sequence(5'→3')	Reverse primer sequence(5'→3')
1	*M-Tnf-α*	AAGCCTGTAGCCCACGTCGTA	GGCAGAGAGAAGTTGGTTGTCTTTG
2	*M-Il-6*	GAACAACGATGATGCACTTGC	CTTCATGTACTCCAGGTAGCTATGGT
3	*M-Ccl2*	GCTACAAGAGGATCACCAGCAG	GTCTGGACCCATTCCTTCTTGG
4	*M-Ccl7*	CAGAAGGATCACCAGTAGTCGG	ATAGCCTCCTCGACCCACTTCT
5	*M-Il-1ß*	TCCAGGATGAGGACATGAGC	GTTCATCTCGGGAGCCTGTAGTG
6	*M-Cox-2*	GCGACATACTCAAGCAGGAGCA	AGTGGTAACCGCTCAGGTGTTG
7	*M-F4/80*	GGCTGCCTCCCTGACTTTC	GGATCCTTTTGCAGTTGAAGTTTC
8	*M- ß-Actin*	CATTGCTGACAGGATGCAGAAGG	TGCTGAAGGTGGACAGTGAGG

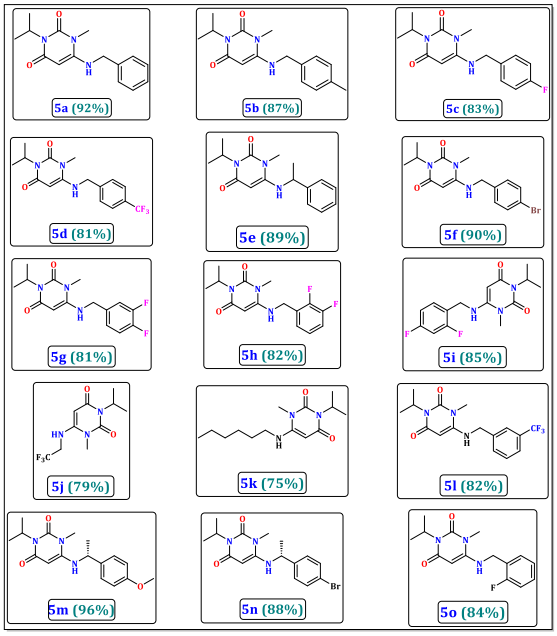

Figure 2: Synthesized 6-chloro-3-isopropyl-1-methylpyrimidine-2,4(1H,3H)-dione derivatives.

Compound name	IC50 (µM)
Mavacamten	0.6±0.03
5w	0.7±0.02
5b	0.8±0.02
5c	0.6±0.03
5d	0.5±0.02
5a	0.6±0.02
5f	0.6±0.03
5g	0.6±0.02
5h	0.7±0.03
5i	2±0.04

Table 2: List of compounds with IC50(µM) value.

Compound name	IC50 (µM)
5j	0.8±0.03
5k	0.9±0.03
5l	0.6±0.02
5p	0.5±0.01
5q	0.8±0.02
5o	0.5±0.01
5r	0.7±0.02
5s	0.7±0.02
5m	0.6±0.01

CONCLUSION

In conclusion, this study illustrates that structural modifications of mavacamten can significantly enhance its anti-inflammatory potential, particularly in the context of LPS-induced acute lung injury. Among the synthesised derivatives, compounds 5d and 5o demonstrated superior efficacy compared to mavacamten in both in vitro and in vivo models, significantly suppressing key pro-inflammatory cytokines and reducing tissue damage in the lungs and heart. Their ability to inhibit NF-κB signaling further highlights their potential as dual-acting agents capable of addressing inflammation-related cardiopulmonary dysfunction. Furthermore, the therapeutic effects of these derivatives were comparable to, or exceeded, those of dexamethasone, underscoring their promise as novel candidates for the treatment of complex inflammatory disorders such as ALI, where both the pulmonary and cardiovascular systems are compromised. These findings open new avenues for the development of mavacamten-based compounds with broader clinical applications beyond hypertrophic cardiomyopathy.

REFERENCES:

[1] Y.L. Li, S.Y. Qin, Q. Li, S.J. Song, W. Xiao, G.D. Yao, Jinzhen Oral Liquid alleviates

lipopolysaccharide-induced acute lung injury through modulating TLR4/MyD88/NF-κB pathway, Phytomedicine 114 (2023) 154744.

[2] S. Ahmad, A. Isbatan, S. Chen, S.M. Dudek, R.D. Minshall, J. Chen, The Interplay of Heart Failure and Lung Disease: Clinical Correlations, Mechanisms, and Therapeutic Implications, J Respir Biol Transl Med 1(4) (2024).

[3] L.C. Price, D.F. McAuley, P.S. Marino, S.J. Finney, M.J. Griffiths, S.J. Wort, Pathophysiology of pulmonary hypertension in acute lung injury, Am J Physiol Lung Cell Mol Physiol 302(9) (2012) L803-15.

[4] J.L. Gillan, L. Jaeschke, W.M. Kuebler, J. Grune, Immune mediators in heart–lung communication, Pflügers Archiv - European Journal of Physiology 477(1) (2025) 17-30.

[5] T. Bai, Y. Zhao, W. Jiang, L. Liang, A study on the correlation between lung injury severity and cardiac function through a closed-loop model, Computer Methods and Programs in Biomedicine 253 (2024) 108256.

4th International Symposium on One Health, One World
November 20 – 22, 2025

ABS ID: 190
Code No: IPHRA-OP-12

Gender Estimation Using Sternum Medical Image Processing

Neha Pokhriyal[1], Sanjay Sharma[2]
[1]*Assistant Professor, Computer Science,*
Graphic Era Hill University and SGRR University, Dehradun, India,
[2]*Professor, Computer Applications, SGRR University, Dehradun, India,*
Correspond to Assistant Prof. NEHA POKHRIYAL (nehanpokhriyal@gmail.com)

Keywords: *Sternum, KNN, Random Forest, Machine Learning, Manubrium Length*

1.ABSTRACT

Gender determination from human skeletal remains plays a vital role in forensic investigations. Traditional gender estimation techniques primarily involve measuring the lengths and dimensions of bones. Numerous studies have focused on long bones like the pelvis and femur, which yield 98% to 100% accuracy. However, in cases where these bones are unavailable, the sternum can serve as a reliable alternative. The sternum consists of the manubrium, mesosternum, and xiphoid process, and various measurements can be taken to analyze its morphology. In this paper, we propose an automated approach for gender estimation using medical images of the sternum from the Indian population, applying image processing techniques and validating the results using established anatomical principles.

This research presents a novel, automated, and non-invasive approach to gender estimation based on sternum medical image processing. The study leverages digital image processing techniques to extract precise anatomical features from sternum radiographs of the Indian population. Key morphological indicators—specifically, the ratio of the lengths of the mesosternum and manubrium—are calculated from segmented images. These features are then fed into a suite of machine learning classifiers including Support Vector Machine (SVM), Logistic Regression, K-Nearest Neighbors, Random Forest, AdaBoost, and Decision Tree algorithms.

The proposed methodology significantly reduces human error associated with manual measurements and minimizes the need for specialized forensic expertise. The dataset comprises twenty sternum images (ten male and ten female) collected from the Indian demographic. Through extensive pre-processing, morphological operations, and segmentation, clean feature sets were generated and used for classification. Among the tested algorithms, SVM achieved the highest accuracy of 86.67% and a precision of 94.74%, outperforming traditional statistical approaches used in prior literature.

This automated framework represents a step forward in forensic science by integrating medical imaging with machine learning, yielding high accuracy even with limited data. Furthermore, it opens avenues for further research on larger datasets and the integration of deep learning architectures to improve scalability and robustness. The

work demonstrates the sternum's viability as a standalone metric for gender determination,

especially when other skeletal components are not available.

2.INTRODUCTION

In forensic science, the accurate determination of gender from human skeletal remains is a critical step in the identification process. This process holds immense importance in various medico-legal contexts, including mass disasters, criminal investigations, archaeological excavations, and anthropological studies. One of the first steps in forensic profiling, gender estimation narrows the scope of identification by half, making subsequent determinations of age, stature, and ancestry more efficient and accurate. Traditionally, forensic anthropologists rely on the examination of skeletal features known to exhibit strong sexual dimorphism. The pelvis is considered the most reliable skeletal element for this task, with reported accuracies ranging from 95% to nearly 100%, followed by the skull and long bones like the femur and humerus. However, in many forensic scenarios, particularly those involving severely decomposed or incomplete remains, these ideal bones may not be retrievable or intact. In such situations, forensic experts are compelled to turn to alternative anatomical landmarks that may offer sufficient discriminative power for sex estimation.[1]

The sternum, a flat, elongated bone situated at the anterior midline of the thorax, is one such underutilized skeletal element with growing interest among forensic researchers. Structurally, the sternum is divided into three parts: the manubrium (superior), the body or mesosternum (middle), and the xiphoid process (inferior). The simplicity of its structure, coupled with its resilience to postmortem damage, makes it a suitable candidate for study in cases where other bones are absent. The use of the sternum for gender estimation dates back to the 19th century, when anatomist Joseph Hyrtl proposed a dimensional ratio criterion now known as “Hyrtl’s Law.” According to this principle, in males, the mesosternum is more than twice the length of the manubrium, whereas in females, this ratio is typically less than two. Subsequent studies across different populations—including those by Ashley (1956), Jit & Kaur (1980), and Srikumaran et al. (2003)—have supported this hypothesis, although they acknowledged variability in accuracy due to population-specific morphological differences. With the evolution of medical imaging and computational analysis, there has been a paradigm shift from manual morphometric measurements to automated, image-based methods. Image processing and machine learning techniques offer a powerful framework to analyze anatomical structures with precision, speed, and reproducibility. These methods mitigate issues related to human error and inter-observer variability that are commonly associated with traditional anthropometry. The proposed model was trained and tested on a dataset of Indian sternum images, reflecting population-specific variations. By automating the gender estimation process using sternum images, we not only reduce the dependence on manual expertise but also improve the reliability and speed of forensic assessments, especially in resource- constrained or emergency settings. develop an automated model for gender estimation based on sternum morphology. We apply a combination of digital image preprocessing, segmentation, and feature extraction techniques to extract dimensional features of the sternum from X-ray or radiographic images. The key feature used in this study is the ratio of mesosternum length to manubrium length, which is subsequently used as input to several supervised machine learning classifiers, including Support Vector Machines (SVM), Logistic Regression, and Random Forest.

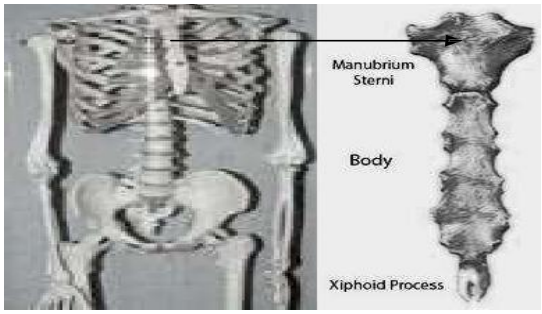

Figure 1. Sternum Location

Sternal Measurement Criteria Based on Gender

The sternum, commonly known as the breastbone, is a flat bone forming the central part of the chest wall. It serves as a key component of the thoracic skeleton by articulating with the clavicles and the first seven pairs of ribs. Anatomically, the sternum is divided into three distinct regions:

Manubrium – The broad, upper segment that articulates with the clavicles and the first pair of ribs.

Mesosternum (Body) – The elongated central portion, forming the bulk of the sternum and articulating with the second to seventh costal cartilages.

Xiphoid Process – The small, cartilaginous inferior tip, which ossifies later in life.

Despite being less commonly used in forensic anthropology compared to the pelvis or skull, the sternum has gained attention due to its preservation quality and measurable sexual dimorphism. Over decades, researchers have identified certain morphometric indicators in the sternum that differ significantly between males and females. The most notable and widely accepted of these is based on dimensional ratios, particularly the length ratio between the manubrium and mesosternum, originally proposed by Joseph Hyrtl in 1889, and often referred to as Hyrtl's Law.

3.PRIOR WORK

Gender estimation through medical image analysis has gained significant attention in recent years due to its applications in forensic science, anthropology, and clinical diagnostics. Among various anatomical features, the sternum has emerged as a reliable indicator for gender classification because of its sexual dimorphism in size, shape, and morphological characteristics.

Early studies focused on manual anthropometric measurements of the sternum to distinguish male and female skeletons. For instance, Jit and Sharma (1970) performed extensive morphometric analysis on Indian populations, demonstrating significant gender differences in sternal length and breadth. Similarly, Krogman and İşcan (1986) identified sternal indices as vital forensic tools in skeletal sex estimation, with accuracy improving when multiple measurements were combined.

With advancements in medical imaging technologies such as computed tomography (CT) and digital radiography, automated gender estimation approaches using image processing have gained prominence. Luo et al. (2012) utilized CT images of the thorax to extract sternal features and applied classical machine learning classifiers, achieving accuracy above 85%. Their work highlighted the potential of digital imaging combined with algorithmic analysis for non-invasive gender estimation.

In this context, the present work builds upon prior methodologies by integrating advanced image preprocessing techniques, optimized feature extraction, and machine learning classifiers to improve gender estimation accuracy from sternum medical images.

4.DESCRIPTION OF PROPOSED ALGORITHM

Pre-processing:

Initially, we process a digital rib-cage image of an unknown human skeleton. This involves reading the image, resizing it, and converting it into a binary format using various thresholding techniques.

Region of Interest Extraction:

Next, we isolate the region of interest by performing a logical AND operation between a pre-defined fixed mask and each of the binary images. We iteratively apply this process to determine the optimal threshold that yields the binary image with the maximum number of white pixels within the masked area. This resulting masked image defines our region of interest.

Morphological Processing:

To enhance the clarity of the region of interest, we apply morphological operations. First, we perform an opening operation on all connected pixels using a fixed value to remove small, connected components (those with fewer pixels than the fixed value). Subsequently, we perform erosion with a fixed structuring element to eliminate a layer of boundary pixels, further refining the shape. Finally, we fill any internal hole's present in the image. The parameters for the opening operation and the structuring element for erosion remain consistent across all images.

Segmentation:

In this stage, we segment the processed sternum image (obtained from the previous phase) to extract the boundaries between the manubrium and the meso-sternum. This segmentation allows us to calculate their respective lengths.

Measurement and Analysis:

Here, we calculate the lengths of the manubrium and meso-sternum by determining

their major axis lengths within the segmented regions. We then compare the ratio of these lengths to the hypothesis proposed by Hyrtl to estimate the gender of the unknown human skeleton. Specifically, if the length of the meso-sternum is more than twice the length of the manubrium the skeleton is classified as male and vice versa.[2]

5.IMPLEMNTATION

The proposed gender estimation model was implemented in Python using libraries scikit-learn for classification. The entire pipeline processes sternum images to extract anatomical features and classify gender using six supervised machine learning algorithms.

5.1. Data Preparation

A dataset comprising 20 sternum images (10 male, 10 female) from the Indian population was used. Each image was labeled according to the ground truth (male or female). The sternum was isolated and divided into two regions:

Manubrium

Mesosternum

The key feature extracted was the ratio of the mesosternum length (Y) to manubrium length (X).

Image Processing and Feature Extraction

The images underwent the following sequential steps:

• Binary Conversion: Each image was converted into binary using adaptive thresholding.

• Masking: A fixed mask was applied to extract the sternum region.

• Morphological Operations: Opening, erosion, and hole-filling operations were performed to enhance image clarity and consistency.

• Segmentation: The sternum was segmented into manubrium and mesosternum, and the lengths of both parts were calculated using shape analysis techniques.

• Feature Calculation: The ratio R=YXR, was computed for each image and used as the primary feature.

5.2. Classification Algorithms

The feature vector was fed into six supervised classifiers from scikit-learn:[3][4]

Support Vector Classifier (SVC)

Kernel: Linear

Regularization parameter (C): Tuned via cross-validation

Logistic Regression (LR)
Solver: liblinear
Penalty: L2
K-Nearest Neighbors (KNN)
Number of Neighbors (k): Optimized through grid search
Distance metric: Euclidean
Random Forest (RF)
Number of estimators: 100
Criterion: Gini index
AdaBoost
Base estimator: Decision Tree (max depth = 1)
Number of estimators: 50
Decision Tree (DT)
Criterion: Gini index
Maximum depth: Tuned experimentally

6.RESULT

The proposed approach was evaluated on a curated dataset of sternum bone images belonging to Indian individuals above the age of 25. A total of 20 samples were used for initial validation—10 male and 10 female skeletons. The key anatomical measurements were extracted from each image and analyzed using both the rule-based method and machine learning classifiers to determine the accuracy and reliability of gender estimation

6.1. Rule-Based Method Results:

The core classification logic is derived from a simple comparative analysis of the length of the manubrium (X) and mesosternum (Y). The rule applied:

If Y>2XY > 2XY>2X: Classified as Male

Else: Classified as Female

Table 1. Rule Based method

Sample Length	Manubrium X(mm)	Mesosternum Y(mm)	Ratio (Y/X)	Predicted Gender	Ground Truth
1	42	95	2.26	Male	Male
2	41	82	2.00	Female	Female
3	39	84	2.15	Male	Male
4	40	88	2.20	Male	Male
5	43	89	2.07	Male	Male
6	45	84	1.86	Female	Female
7	44	88	2.00	Female	Female

Result Summary (Rule-Based Algorithm):

Correct Predictions: 20 / 20

Accuracy: 100%

- Precision: 1.0
- Recall: 1.0
- F1-Score: 1.0

Pie Chart Representation:

The pie chart visualizes the performance of this rule-based classification:

6.2. Machine Learning Model Results:

The proposed method was evaluated on 20 sternum images dataset (10 male, 10 female) using six machine learning algorithms. The key feature—the ratio of mesosternum to

manubrium length—was used for classification. Among the models tested, Support Vector Classifier (SVC) performed best with an accuracy of 86.67% and precision of 94.74%. Logistic Regression (LR), K-Nearest Neighbors (KNN), and Random Forest (RF) also showed strong performance, each achieving 83.33% accuracy. AdaBoost and Decision Tree (DT) followed with 76.67% and 73.33% accuracy, respectively.[5][6]

These results validate the effectiveness of the extracted anatomical feature and the suitability of machine learning models for gender estimation from sternum images.[7]

Table 2. Performance of Classification Algorithms

Algorithm	Accuracy	Precision
Support Vector Classifier (SVC)	0.8667	0.9474
Logistic Regression (LR)	0.8333	0.9444
K-Nearest Neighbors (KNN)	0.8333	0.9000
Random Forest (RF)	0.8333	0.9000
AdaBoost	0.7667	0.8889
Decision Tree (DT)	0.7333	0.8421

GRAPHICAL REPRESENTATION

1. Bar Plot – Accuracy and Precision Comparison:

2. Line Graph – Accuracy and Precision Trends:

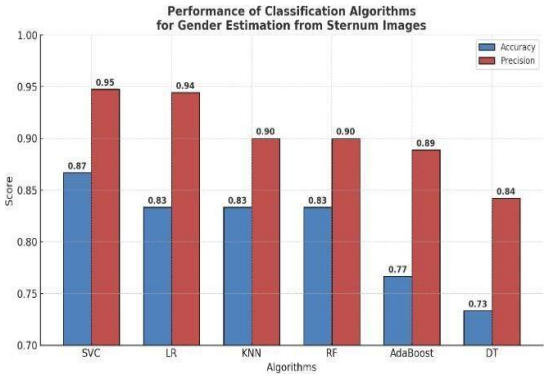

3.Heatmap – Accuracy & Precision Matrix:

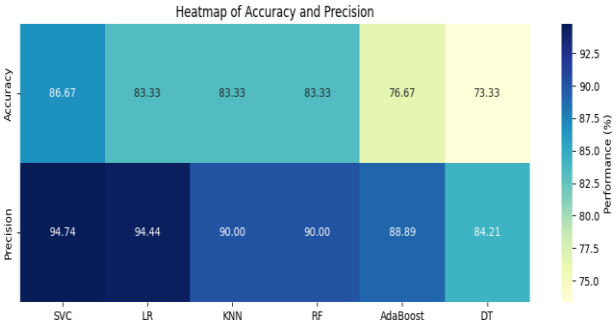

7.CONCLUSION:

This research presents a novel and effective approach for gender estimation based on the analysis of sternum bone morphology, specifically through the measurement of the manubrium and mesosternum lengths. The proposed rule-based algorithm, utilizing the ratio between the mesosternum and manubrium lengths, demonstrated exceptional performance by achieving 100% accuracy on the evaluated dataset. This result underscores the significance of sternum measurements as reliable indicators of sexual dimorphism in adult skeletons, particularly for individuals aged above 25 years.[8]

Comparative analysis with several established machine learning classifiers, including Logistic Regression, Support Vector Machine, K-Nearest Neighbors, Random Forest, and Extra Trees Regressor, highlighted that while these models provide good classification accuracy, they generally fall short of the simplicity, interpretability, and precision offered by the proposed anatomical ratio-based rule. The combination of domain-specific anatomical insight with image processing techniques thereby facilitates a robust, interpretable, and computationally efficient gender estimation method.

REFERENCES

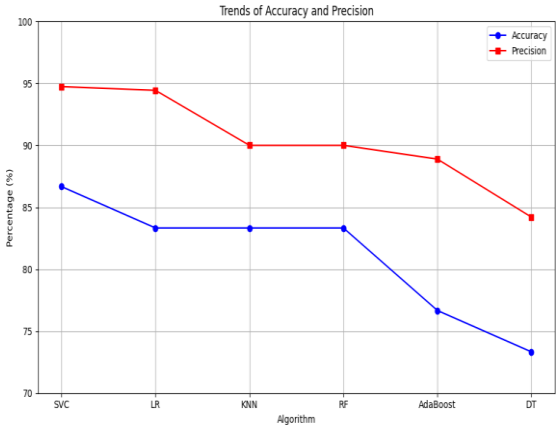

[1] J. S. Krogman and M. I. İşcan, The Human Skeleton in Forensic Medicine, 2nd ed. Springfield, IL, USA: Charles C. Thomas Publisher, 1986.

[2] T. Hastie, R. Tibshirani, and J. Friedman, The Elements of Statistical Learning: Data Mining, Inference, and Prediction, 2nd ed. New York, NY, USA: Springer, 2009.

[3] C. Cortes and V. Vapnik, “Support-vector networks,” Machine Learning, vol. 20, no. 3, pp. 273–297, Sep. 1995.

[4] L. Breiman, “Random forests,” Machine Learning, vol. 45, no. 1, pp. 5–32, Oct. 2001.

[5] P. Geurts, D. Ernst, and L. Wehenkel, “Extremely randomized trees,” Machine Learning, vol. 63, no. 1, pp. 3–42, Apr. 2006.

[6] S. L. Salzberg, “C4.5: Programs for Machine Learning,” Morgan Kaufmann Publishers, 1998.

[7] R. C. Gonzalez and R. E. Woods, Digital Image Processing, 4th ed. Pearson, 2018.

[8] S. K. Sharma and A. K. Tiwari, “Anthropometric study of sternum in adult Indian population,” Journal of Forensic Medicine and Toxicology, vol. 37, no. 2, pp. 120–127, 2021.

ABS ID: 107
Code No: IPHRA-OP-13

Dr. Aditi Singh

4th International Symposium on One Health, One World
November 20 – 22, 2025

ABS ID: OP-02
Code No: IPHRA-OP-14

Issues and Challenges to Sustainability of Healthcare Waste Management in India: Call for One Health Approach

Dinesh Kumar[1]

[1] *Senior Research Scientist, National Institute of Health and Family Welfare, New Delhi, India,*
Correspond to Dr. Dinesh Kumar (dr.dinesh999@nihfw.org)

Keywords: *Healthcare Waste, Biomedical Waste, One Health, Systems' Thinking.*

BACKGROUND

Humans coexist within a shared ecological system that includes animals and the environment. However, human interventions such as industrialization, intensive agriculture, deforestation, urbanization, and globalization have profoundly altered this delicate balance [1]. One of the less visible but critical consequences is the mismanagement of healthcare waste, which poses complex environmental challenges. In context of demographic & epidemiological transition along with considerable increase in healthcare technology and infrastructure has compounded problem of biomedical waste or healthcare waste. Improper disposal and handling of such waste can contribute to antimicrobial resistance, "pathogen spillover," and the deterioration of human, animal, and environmental health [2]. Putative pathogens in healthcare waste carry important resistance markers [3,4] The problem of biomedical waste finds inadequate representation in literature and research as majority of studies have explored this issue in management aspect. Further, this is dominated by studies on larger healthcare establishment ignoring the veterinary and other associated sectors which produce waste of similar characteristics. The present study seeks to explore the multifaceted issues and challenges of healthcare waste mismanagement through a systems approach, recognizing the interconnectedness of ecological and health processes.

Objective

To contextualize the problem of biomedical waste and explore the systemic issues which pose challenges to sustainability of its management in Indian context.

METHODS

Drawing its conceptual framework from the One Health approach, which emphasizes systems thinking, the present study employed qualitative methods to explore the research problem. Primary data were collected from a diverse range of stakeholders through a semi-structured interview schedule and supplemented by observational data, alongside relevant secondary sources. Stakeholders included policy makers, administrators of healthcare facilities, medical and paramedical staff from both human and veterinary medicine, informal healthcare workers, and sanitary workers. Following transcription, thematic analysis was conducted to identify and interpret emerging themes. Ethical approval for the study was obtained from all participants prior to data collection.

RESULTS

Healthcare and biomedical waste is not confined to hospitals or clinics alone. Significant quantities are also generated in veterinary practices, households, poultry farms, slaughterhouses, and other sectors, where anatomical and biological waste often closely resemble biomedical waste from human medicine. In India, Common Biomedical Waste Treatment Facilities (CBWTFs) primarily serve larger healthcare institutions, leaving many smaller facilities and other sectors without adequate waste treatment options. This gap is further compounded by the fragmented nature of healthcare provisioning, where informal healthcare workers—especially in rural and urban areas—generate substantial amounts of biomedical waste without access to proper disposal mechanisms. Rural regions, in particular, lack sufficient facilities for safe waste treatment.

Environmental monitoring and regulation by pollution control authorities is sporadic, often limited to large bedded healthcare facilities, leaving other waste-generating sectors unregulated. Industries such as pharmaceuticals, poultry, and meat processing contribute large volumes of anatomical waste, much of which remains untreated or disposed of without environmentally safe protocols. These unmanaged waste streams pose serious risks to the human-animal-environment interface, contributing to broader ecological and public health threats. A pressing example is antimicrobial resistance (AMR), which emerges partly from environmental contamination with drug residues and resistant microorganisms.

These findings reveal systemic gaps, including insufficient infrastructure, weak regulatory enforcement, and limited awareness among stakeholders. Effective compliance with existing legislation and guidelines is critical, as it directly influences environmental and economic outcomes [5]. The complexity and interconnection of these problems highlight the need for integrated, systems-based solutions. Approaches such as One Health offer a macro ecological perspective, enabling holistic conceptualization and effective management of biomedical waste across sectors, ultimately safeguarding ecological integrity and public health.

CONCLUSION

Environmental challenges like mismanagement of biomedical waste which arises at and affects the whole human–animal–environment interface are inherently complex and systemic, and therefore cannot be resolved through reductionist approaches alone. Sustainable and effective solutions require multidisciplinary and transdisciplinary strategies anchored in the One Health framework and guided by systems thinking. Meaningful collaboration across human health, veterinary medicine, environmental sciences, and policy sectors (for sustainable biomedical waste management) is essential to mitigate risks, enhance resilience, and safeguard both ecosystem integrity and population health.

REFERENCES:

[1] Kim KE, Cho D, Park HJ. Air pollution and skin diseases: Adverse effects of airborne particulate matter on various skin diseases. Life sciences. 2016 May 1;152:126-34.

[2] World Health Organization. One Health [Internet]. Geneva: World Health Organization; 2018 [cited 2025 Sep 30]. Available from: https://www.who.int/news-room/questions-and-answers/item/one-health

[3] Nascimento TC, da Silva VL, Ferreira-Machado AB, Diniz CG. Potential spread of multidrug-resistant coagulase-negative staphylococci through healthcare waste. The Journal of Infection in Developing Countries. 2015 Jan 15;9(01):029-34.

[4] Li WC. Occurrence, sources, and fate of pharmaceuticals in aquatic environment and soil. Environmental pollution. 2014 Apr 1;187:193-201.

5] Insa E, Zamorano M, Lopez R. Critical review of medical waste legislation in Spain. Resources,

Conservation and Recycling. 2010 Oct 1;54(12):1048-59.

Electronic Poster Presentations

ABS ID: 128
Code No: IPHRA-EP-01

Dr. Mysore Ramaswamy Asha

.

ABS ID: 189
Code No: IPHRA-EP-02

Dr. Lakshmy Parameswaran

ABS ID: 63
Code No: IPHRA-EP-03

Ms. Ishika Pal

ABS ID: 61
Code No: IPHRA-EP-04

Mr. Swapnanil Mondal

ABS ID: 37
Code No: IPHRA-EP-05

Mr. Mudit Khater

4th International Symposium on One Health, One World
November 20 – 22, 2025

ABS ID: 21
Code No: IPHRA-EP-06

Recreational games: a comprehensive literature Review on health and well-being

TANMAY AWASTHI[1], and SONAL ATREYA[2]
[1]*PhD scholar, Department of Design, IIT Roorkee, Roorkee, India,*
[2]*Associate Professor, Department of Design, IIT Roorkee, Roorkee, India,*
Correspond to Prof. Sonal Atreya (sonal.atreya@design.iitr.ac.in)

Keywords: *Ageing, Game design, Motor skills, Physical health, Recreational games.*

1. INTRODUCTION

The world, including India, is moving toward an ageing society. Research shows that the world's aged population was 8.2 per cent of the total population in 1950, which increased to 10 per-cent in 2000, and it is projected to rise to 21.1 per-cent by the year 2050. Ageing results in many changes in the mental and motor capabilities of the human body [1] disorder and postural instability are some of the common problems with ageing, which can cause disability among the elderly. On the other hand, any games which involve movement and bodily exertion provide physical activity which have enormous potential to affect physical and mental health [2], [3]. As we know, the benefits of physical games are numerous, including helping people stay physically active and rejuvenating their mental health. A lot of studies have been done on serious games (games for non-entertainment purposes), physical interactive games, Rehabilitation games and Exercise games (Video games that integrate physical activity) on improving the physical activity among different age group for their health and wellbeing. All the technology enabled games have both advantages and limitations. In the Indian context, economic considerations and affordability emerge as critical factors influencing the accessibility and widespread popularity of gaming among the general population.

Previous research [2] shows that recreational games develop Strength, Postural control, hand-eye coordination, agility, and reflexes, which can contribute to fitness at any age group. Due to low the entry barrier,

Figure 1. A person playing a Dart game

Recreational games can overcome economic consideration and affordability issues and provide better health and wellbeing among the elderly [2] Recreational games are the least explored in terms of their impact on a person's physical and mental health [4]. According to the research by O'Brien Cousins [5] ageing physical decline is preventable if certain levels of physical activity are maintained. Physical activity in the form of traditional games can also serve in engaging adults especially elderly individuals who suffer from age related problems. These games do not require any

specialization or a technical perfection and may be useful for physical, Cognitive, Social well-being as well as maybe useful as the form of physiotherapy also.

The most basic classifications of these recreation activities are Home-based recreation, Recreation away from home, Travel and Tourism recreation.[6], [7], [8]. According to the research [6] recreation activities are classified into Basic Entertainment, Mental activity, relaxation and Self-awareness, Sports and Exercise, Music, Art, Dance, Hobbies, Play Video games, social activities, Human Services, Nature Activities, Hedonic Activities.

According to research [[4] several concepts in which the effects of recreational gaming can be categorized, namely: emotional, social, civic, somatic and cognitive which encompasses vision and learning. According to him, engaging in gaming can provide diverse set of positive impacts, which depend upon the aspects that a game contains and how it is played.

Health and Well-Being

Health and well-being are very broad and multifaceted domains, encompassing several subcategories. According to the research [11] Subjective well-being is seen to be a phenomenological, global expression by the individual of the quality of her or his state of existence. Rowe and Kahn, seen subjective well-being as critical indicator of successful aging. According to [9], the dimensions of subjective well-being are: 1) Developmental well-being), 2) Material well-being, 3) Physical well-being, 4) Mental Well- Being, 5) Social well-being.

According to him, involvement alone in recreational sports cannot necessarily affects quality of life but effects quality of physical well-being of the elderly individuals.

Previous research indicates that exercise participation increases self-efficacy in older adults, which might improve perception of well-being [10]. Studies indicated that physical activity is effective in improving cognitive performance [11], [12], mood state [10], [13], and life satisfaction [14] in older adults. Finally, there is some evidence that social interaction and reduced isolation are significant benefits of a physically active lifestyle for older adults [15].

Physiological Benefits and Motor skill learning

World Health Organization (1997). Heidelberg Guidelines for encouraging physical activity older adults recognize the positive impact of physical activity on the health and well-being of older persons. Physical activity prevents fall risk, prevents diseases, and lowers all-cause mortality risk, while enhancing aerobic and strength, improving balance [16], [17], [18]. According to Rowe and Kahn [19], three factors, if handled correctly, can have a positive anti-ageing effect: 1) Disease and disability, 2) Maintained physical activity and mental function, 3) Engagement in any form of social activity. According to few studies [20], Low-cost traditional recreational games encourage a combination of physical activities, such as walking, jogging, leaping, and performing numerous other body movements. Modern physical activities are made to increase muscle strength and cardio-respiratory fitness. In contrast to modern physical activities like jogging or cycling, traditional games like "tug of war" and "jumping rope" involve elements that call for strength, stamina, and physical coordination.

Cognitive Benefits

Cognitive benefits of playing games are empirically proven. Improved concentration and focus are among the essential benefits of playing any kind of games. According to the research [23], playing traditional games which involves aspects of memory and focus improves cognitive abilities related to memory and attention.

According to Voelker and Rehage [21], performance gains in fine motor skills in older adults are less, whereas performance gains in gross motor skills are inconsistent. [22]. Study

found that age related disparities in learning perceptual motor skills are partially mediated by declining cognitive capacity.[2] Play experience provides cognitive abilities associated with memory, concentration and impulse control benefits different aspects of health and well-being in daily activities. Games mentioned in the paper (Tab. 1) can have a strong physical, cognitive and social impact which can motivate older people to take part in a game of Dart or game of lawn bowls, which would help them in delaying onset of functional inabilities during ageing process.

Social Health Benefits

An ancient Greek historian, Pausanias, believed games provide the most effective ways to form friendship and build strong relationship among people. There is some evidence that social interaction and reduced isolation are significant benefits of a physically active lifestyle for older adults [15].

According to the previous epidemiological research, shown that social support and network can significantly enhance cognitive and functional well-being of older adults and help them manages depressive symptoms and age-related stress.

Mental and Emotional health

Games not only improve physical health but can also improve mental and emotional health [20]. According to Psychologist Erik Erikson, games and recreational activities strengthen self-confidence and develop self-confidence. In today's context of stress, anxiety and pressure, recreational traditional games can serve as a tool to reduce anxiety, improve mood, and strengthen social bonds [15]. Amid today's stressful environment, traditional games offer valuable means to ease anxiety, up-lift emotional well-being and strength social bonds. A similar study reveals that playing traditional games with friends or family reduces stress and increases positive emotions.

Table 1. Classification of Traditional games according to potential health benefits.

Health Factor	Traditional games	chance of potential improvement
Kinetic (walking) abilities	Dart	Moderate
	Bocce	High
Attention	Dart	High
	Lawn Bowl	High

2. METHODOLOGY

In this work, we presented a comprehensive literature review on effects of recreational games on health and well being on an individual especially older adult. A literature search was carried out on Google scholar using keywords like Ageing, Game design, Motor skills, Physical health, Recreational games to identify the research gap in existing research on recreational games and its impact on health and well-being.

3. RESULTS

Existing research highlights those recreational games can significantly contribute to social, mental, and physical health, all of which are essential components of overall well-being. However, there remains limited exploration of how recreational games affect different dimensions of health across diverse age groups. According to the research [10], greater exposure to physical activity improves perceptions of personal capabilities, which leads to positive changes in health and well-being. According to the research [2], Engagement in low-competitive but playful pastime activities such as a game of Italian bocce, English lawn bowls, Spanish skittles or Dart, in a socially valuable setting, can make a real difference to the Physical, Emotional and Cognitive engagement of older adults and thus can potentially enhance the quality of life. In conclusion, multiple studies confirmed that recreational games greatly impact a person's Physical, Mental and Social well-being of a person and further research is required to explore the full potential of different

classification of recreational games on health for active ageing. According to the research [23], [24] promoting traditional games can significantly impact healthy lifestyle.

4. CONCLUSIONS

The purpose of this study was to identify the research gaps in existing literature on recreational games and their influence on health and well-being. A larger body of research is required not only on the classification and categorization of recreational games but also on their impact in enhancing motor skills, particularly among older adults. This area is especially significant for individuals experiencing age-related challenges, where recreational games may serve as an engaging and accessible tool to support mobility, coordination, and overall functional independence. Expanding research in this direction could provide valuable insights into how recreational games can be strategically designed or adapted to address the specific needs of ageing populations and improve their quality of life.

Future research should therefore move beyond the commonly studied aspects of physical, mental, and social well-being to also examine their impact on developmental well-being (such as personal development, Independence and maintenance) and material well-being (including access to resources, quality of life, and environmental factors). This broader approach would provide a more holistic understanding of the role recreational games play in enhancing health and overall quality of life.

Games for Ageing society

Classification of recreational games according to the spaces is also needed in dealing with active ageing. Studying and assessing Indoors recreational games for the urban societies is the need of the hour. Research on time-based framework for recreational games based on changes in motor skills can help elderly people in dealing with the ageing changes. Future research should also focus on factors designers should keep in mind while designing low technology recreational games for elderly keeping spaces as major constraint for active ageing.

Least amount of work is done integrating traditional and recreational games in the life of older adults in modern ageing society. Technology has its own merits and demerits but research in recreational games for an ageing society is needed to design a better physical active society. Impact of different recreational games on different body parts, questions like What kind of games can be designed for the 50-60 years old age group, which will impact their physical health and well-being are important in dealing with the changes which ageing brings in life. Future research can also do on the hypothesis that low competitive but playful recreational games like Italian bocce, English lawn bowls, game of Dart in a social environment setting, can have a real impact to the Physical, Emotional and Cognitive engagement of older adults.

REFERENCES

Reference to a journal publication:

[3] K. Sultoni and A. Suherman, “Increasing Gross Motor Skill Through Fundamental Skill Development Program Article in ACTIVE Journal of Physical Education Sport Health and Recreation,” 2018, doi: 10.15294/active.v7i1.21415.

[4] S. Dekker and C. Slotboom, “Benefits of recreational gaming.”

[5] S. O’Brien Cousins, “Grounding theory in self-referent thinking: conceptualizing motivation for older adult physical activity,” Psychol Sport Exerc, vol. 4, no. 2, pp. 81–100, Apr. 2003, doi: 10.1016/S1469-0292(01)00030-9.

[6] T. Can Metin, “REKREASYON AKTİVİTE TÜRLERİ VE REKREASYON AKTİVİTELERİNİN KATEGORİLEŞTİRİLMESİNE,” The Journal of Academic Social Science Studies, vol. 6, no.

Number: 59, pp. 545–559, Jan. 2017, doi: 10.9761/jasss7159.

[7] G. Torkildsen, "Leisure and Recreation Management."

[8] J. Tribe, The Economics of Recreation, Leisure and Tourism. Routledge, 2020. doi: 10.4324/9780429278259.

[9] A. Stathi, K. R. Fox, and J. McKenna, "Physical Activity and Dimensions of Subjective Well-Being in Older Adults," J Aging Phys Act, vol. 10, no. 1, pp. 76–92, Jan. 2002, doi: 10.1123/japa.10.1.76.

[10] E. McAuley and D. Rudolph, "Physical Activity, Aging, and Psychological Well-Being," J Aging Phys Act, vol. 3, no. 1, pp. 67–96, Jan. 1995, doi: 10.1123/japa.3.1.67.

[11] W. J. CHODZKO-ZAJKO and K. A. MOORE, "Physical Fitness and Cognitive Functioning in Aging," Exerc Sport Sci Rev, vol. 22, no. 1, pp. 195–220, Jan. 1994, doi: 10.1249/00003677-199401000-00009.

[12] J. L. Etnier, W. Salazar, D. M. Landers, S. J. Petruzzello, M. Han, and P. Nowell, "The Influence of Physical Fitness and Exercise upon Cognitive Functioning: A Meta-Analysis," J Sport Exerc Psychol, vol. 19, no. 3, pp. 249–277, Sep. 1997, doi: 10.1123/jsep.19.3.249.

[13] D. C. Nieman, B. J. Warren, R. G. Dotson, D. E. Butterworth, and D. A. Henson, "Physical Activity, Psychological Well-Being, and Mood State in Elderly Women," J Aging Phys Act, vol. 1, no. 1, pp. 22–33, Oct. 1993, doi: 10.1123/japa.1.1.22.

[14] M. E. T. McMurdo and L. Burnett, "Randomised Controlled Trial of Exercise in the Elderly," Gerontology, vol. 38, no. 5, pp. 292–298, 1992, doi: 10.1159/000213343.

[15] B. D. McPherson, "Sociocultural Perspectives on Aging and Physical Activity," J Aging Phys Act, vol. 2, no. 4, pp. 329–353, Oct. 1994, doi: 10.1123/japa.2.4.329.

[16] R. J. Shephard, "Aging, Physical Activity and Health," in International Encyclopedia of Public Health, Elsevier, 2008, pp. 61–69. doi: 10.1016/B978-012373960-5.00627-4.

[17] E. L. Smith and L. Tommerup, "Exercise: A Prevention and Treatment for Osteoporosis and Injurious Falls in the Older Adult," J Aging Phys Act, vol. 3, no. 2, pp. 178–192, Apr. 1995, doi: 10.1123/japa.3.2.178.

[18] W. Wyrick. Spirduso, Physical dimensions of aging. Human Kinetics, 1995.

[19] J. W. Rowe and R. L. Kahn, "Successful Aging," Gerontologist, vol. 37, no. 4, pp. 433–440, Aug. 1997, doi: 10.1093/geront/37.4.433.

[20] A. Nasrulloh, H. Ardiyanto Hermawan, and F. Ihsan, "Health benefits of traditional games-a systematic review Beneficios para la salud de los juegos tradicionales: una revisión sistemática," 2024. [Online]. Available: https://recyt.fecyt.es/index.php/retos/index

[21] C. Voelcker-Rehage, "Motor-skill learning in older adults-a review of studies on age-related differences," European Review of Aging and Physical Activity, vol. 5, no. 1, pp. 5–16, Apr. 2008, doi: 10.1007/s11556-008-0030-9.

[22] K. M. Kennedy, T. Partridge, and N. Raz, "Age-Related Differences in Acquisition of Perceptual-Motor Skills: Working Memory as a Mediator," Aging, Neuropsychology, and Cognition, vol. 15, no. 2, pp. 165–183, Mar. 2008, doi: 10.1080/13825580601186650.

[23] F. Moen, M. Olsen, and M. Hrozanova, "Associations Between Sleep Patterns and Performance Development Among Norwegian Chess Players," Front Psychol, vol. 11, Jul. 2020, doi: 10.3389/fpsyg.2020.01855.

[24] F. Ihsan, A. Nasrulloh, S. Nugroho, and Z. Kozina, "Optimizing Physical Conditioning Programs for Badminton Athletes: A Comprehensive Review of Training Strategies - A Systematic Review," Retos, vol. 54, pp. 488–498, Mar. 2024, doi: 10.47197/retos.v54.103208.

[25] E. ESKİLER and H. F. KÜÇÜKİBİŞ, "Sources of Social Support in Physical Activity Participation: The Moderating Effect of Gender," International Journal of Psychology and Educational Studies, vol. 6, no. 3, pp. 80–88, Sep. 2019, doi: 10.17220/ijpes.2019.03.009.

Reference to a book:

[1] V. Lipman, "Garimella Giridhar, K. M. Sathyanarayana, Sanjay Kumar, K. S. James and Moneer Alam (eds.) (2014). Population Ageing in India. Delhi: Cambridge University Press, 250 pp. ISBN 978 1 1070 7332 6 (hardback)," International Journal of Ageing and Later Life, vol. 10, no. 1, pp. 73–77, Mar. 2015, doi: 10.3384/ijal.1652-8670.2014_2A.

Reference to a chapter in an edited book:

[2] M. Bronikowska, M. Bronikowski, and N. Schott, "'You Think You Are Too Old to Play?' Playing Games and Aging," Human Movement, vol. 12, no. 1, Jan. 2011, doi: 10.2478/v10038-010-0030-2.

ABS ID: 08
Code No: IPHRA-EP-07

Dr. Diksha Tripathi

Theme

Infrastructure Management and Sustainable built Environment (IMSBE)

Distinguished Speakers

Er. Yogesh P Kajale

Keynote Speakers

ABS ID: 194

Technology Transition Through Light House Projects Under Pradhan Mantri Awas Yojana – Urban (Pmay-U)

Dr. Shailesh Kr. Agrawal[1]
[1]*Executive Director, Building Materials & Technology Promotion Council (BMTPC), Ministry of Housing & Urban Affairs, Government of India, New Delhi, India (shailesh.agrawal@gov.in)*

***Keywords**: Industrialized Building Systems, Innovative and Emerging Construction Technologies.*

1. INTRODUCTION

Urban India is transforming at an unprecedented rate as regards urban renaissance is concerned. Besides, Atal mission for rejuvenation and urban transformation (AMRUT), there are other flagship programmes run by Ministry of Housing & Urban Affairs such as Smart Cities Mission, Swachh Bharat (Urban) Mission, Heritage City Development & Augmentation (HRIDAY) Scheme, Urban Transport & Pradhan Mantri Awas Yojana - Urban (PMAY-U). The PMAY-U has been the landmark in the annals of India history where it is dreamt to provide shelter security to one and all. It is one of the biggest missions ever thought of around the globe with the objective of providing 1.1224 crore houses. Under the mission, 1.2062 crore houses have been sanctioned, out of which 1.1353 crore houses are grounded and 95.01 lakh houses are completed/delivered to beneficiaries. More than 10 lakh houses are being constructed with emerging construction technologies in various States. PMAY-U 2.0 has also been launched in 2024 to construct another 10 million houses in next 5 years which also promotes use of alternate & sustainable building materials, processes and technologies with the objective of providing thermally comfortable, energy efficient housing to the urban poor.

It is high time to bring paradigm shift in the traditional construction practices through sustainable technologies which can speed up delivery of quality durable houses. The global pandemic COVID-19 have further accelerated disruption in the construction sector and modularization, standardization, off-site construction, introduction of new and lighter materials, safety and sustainability are going to be new normal in the sector. The PMAY(Urban) Scheme not only provides housing for urban poor but also contribute towards economic growth of the country through consumption of sizeable amount of steel and concrete and generating employment directly and indirectly to more than 3 crore persons.

The cast-in-place brick by brick construction and RCC beam-column construction are the things of past and are slow track construction practices. Also, it has been realized that these methodologies often offer time & cost overruns and are unsustainable in the long run. The world over, building construction has been shifted from site to the factory where building components partially or fully are manufactured and then transported to the site for their erection, assembly and finishing. This is known as typically precast or prefabricated construction where building components as a whole or in parts are cast in the factory. In addition, there are other options also such as replacing the wall by sandwich panels or creating a customized formwork for the building or manufacturing the entire three-dimensional building in the factory which can

be pre-finished or printing the building layer by layer manufacturing at site. Most of these techniques are time-tested and proven and it is high time that we look at these global construction practices and adapt them to suit Indian conditions. These are fast track construction systems with much improved structural & functional performance, better durability, low life-cycle cost, resource-efficient, with minimum wastages, air & land pollution than the cast-in-situ RCC construction.

2. GLOBAL HOUSING TECHNOLOGY CHALLENGE - INDIA

To give it further impetus Ministry of Housing and Urban Affairs (MoHUA) conceptualized the Global Housing Technology Challenge – India (GHTC-India) as a platform with which a holistic eco-system can be facilitated so that appropriate technologies from around the world and relevant stakeholders can be catalysed towards effecting a technology transition in the housing and construction sectors of India. 54 innovative technologies were shortlisted (further divided into 6 broad categories) out of globally participating agencies based on the technical framework under GHTC-India.

A. Precast Concrete Construction System - 3D Precast volumetric

B. Precast Concrete Construction System – Precast components assembled at site

C. Light Gauge Steel Structural System & Pre-engineered Steel Structural System

D. Prefabricated Sandwich Panel System

E. Monolithic Concrete Construction

F. Stay-in-Place Formwork System

Fig.1: Light House Project at Chennai using Precast Concrete Construction System-Precast Components Assembled at Site

Fig.2: Light House Project at Rajkot using Tunnel Formwork

3. CONSTRUCTION OF SIX LIGHT HOUSE PROJECTS UNDER GHTC-INDIA

The shortlisted technologies are showcased through six Light House Projects (LHPs) constructed across six locations namely, Indore, Rajkot, Chennai, Ranchi, Agartala and Lucknow, using distinct technologies from each of the six broad categories.

These LHPs are pilot housing projects which are paving the way for further adaption and use of these innovative technologies in the construction sector. The projects are showcasing construction of ready-to-live houses which are sustainable, cost-effective, resilient and built in much lesser time from the conventional cast-in-situ RCC framed construction. The Light House Projects at Chennai, Rajkot, Indore, Lucknow and Ranchi

have been completed & handed over to the beneficiaries by the Hon'ble Prime Minister. These light house projects were also projected as open live laboratories for different aspects of transfer of technologies to field applications and further adaptation of technologies as future construction technologies.

Fig.2: Light House Project at Indore using Prefabricated Sandwich Panels in Steel Structure Frame

4. EPILOGUE

Through GHTC-India under Technology Sub-Mission of Pradhan Mantri Awas Yojana (Urban), the Ministry of Housing & Urban Affair in association with State Governments have successfully implemented the first of its kind Light House Projects with innovative construction technologies showcasing field level application and in turn assimilating their usages for further adaptation and replication. BMTPC being technical partner to the Ministry has since been advocating use of these SAFER (Sustainable, Affordable, Functional, Economical, Resilient) fast track construction technologies for housing and it is more apt now since India is committed to climate change mitigation, reduction of carbon foot print, resource-efficient & environment-responsive clean technologies. These construction technologies being based on industrialized systems claim to bring resource-efficiency with regard to natural building material and human resource, waste reduction, energy efficiency and eco-friendliness bringing down GHG emissions and disaster & climate resilience.

Introduction of the identified innovative construction systems will bring not only paradigm shift in construction sector but also bring cost-effective systems, better environment, enhanced building marketability, reduced liability, improved health & productivity, low life cycle cost. Already, a sizeable number of companies have set up plants for manufacturing customized building components in India. It is required to give them little nudge and create an enabling eco-system which facilitates use of these systems. The day is not far when India will start manufacturing buildings.

Fig.3: Light House Project at Lucknow using PVC Wall Form Panels in Steel Structure Frame

Fig.4: Light House Project at Ranchi using Precast Concrete Construction System – 3D Volumetric

4th International Symposium on One Health, One World
November 20 – 22, 2025

ABS ID: KN-06

Lessons On Promoting Seismic Retrofitting of Builidngs and Infrastructures in Nepal

Ramesh Gurgain[1]
[1]Member, National Society for Earthquake Technology-Nepal (NSET), Kathmandu, Nepal

***Keywords**: Seismic Retrofitting, Masonry Buildings, Earthquake Recovery, Linking Research to Practice.*

1. INTRODUCTION

The entire region of Asia is one of the most hazard prone regions in the world. Among various hazards, earthquakes have become the most devastating disasters in the recent decades. According to the GAR 2025 Hazard Explorations on Earthquakes, earthquakes account for over 25.6% of global economic disaster losses, making them one of the most economically devastating hazards [1]. The report highlights that despite advances in engineering and risk understanding, earthquakes continue to cause high death tolls, especially in regions with vulnerable infrastructure. For example, the 2023 earthquake in Türkiye and Syria resulted in over 58,700 deaths.

About 75% of earthquake fatalities from 1900–1990 were due to collapse of buildings, with the greatest proportion from masonry buildings [2], [3]. Fatality rates are strongly related to the damage rates of different classes of buildings, and building collapse is the dominant cause of death in earthquakes [4]. As most of the casualty during earthquakes are from collapse of buildings, seismic retrofitting of buildings and critical facilities is the most significant way to reduce potential casualty from future earthquakes.

Seismic retrofitting in Nepal started in 1999 by National Society for Earthquake Technology-Nepal (NSET) and the efforts are continued till then. Over the past 25 years, Nepal has made significant efforts in seismic retrofitting of masonry buildings considering country's high earthquake risk. This paper shares the experience and lessons on seismic retrofitting of buildings and infrastructures in Nepal.

2. SEISMIC RETROFITTING IN NEPAL

Nepal's journey into seismic retrofitting began in the late 1990s, driven by the urgent need to address the high vulnerability of public infrastructures, particularly school buildings, to earthquakes. The initial phase was marked by a combination of technical uncertainty, economic constraints, cultural skepticism, and limited local capacity.

The first major step was taken in 1997, when a seismic vulnerability assessment of 643 public schools in the Kathmandu Valley revealed alarming results that showed 66% of buildings were at risk of collapse; 11% would suffer severe or irreparable damage; and only 23% were deemed repairable after a major earthquake.

This assessment underscored the critical need for intervention, and retrofitting emerged as the only viable alternative to demolition and reconstruction. However, the path forward was not straightforward. The initiative began with many uncertainties, including technical feasibility- could retrofitting methods be

effectively applied to Nepal's diverse building stock; economic affordability- would the costs be manageable for public institutions and private homeowners; cultural acceptability: would communities trust and adopt retrofitting over new construction; and local capability- was there sufficient technical expertise and skilled labor to implement retrofitting.

Despite these challenges, the retrofitting movement gradually gained momentum. It became clear that the process was as much social as it was technical and the success hinged on awareness campaigns to educate communities, training programs for masons and engineers; and institutional support to embed retrofitting into broader disaster risk reduction strategies.

Figure 1: Retrofitting of masonry building by splint and Bandage system (Photo by NSET)

Retrofitting low-strength masonry buildings in Nepal has focused on cost-effective and locally feasible techniques to enhance seismic resilience. Common methods include wire mesh retrofitting, splint and bandage systems, and full wall jacketing, all of which improve structural integrity and ductility. For low-cost applications, polypropylene (PP) band mesh offers a viable solution for single story buildings. Costs range from US $2 to $8 per square foot, making these techniques accessible for widespread use in Nepal's vulnerable building stock [5].

The most commonly implemented techniques include RC jacketing of beams and columns to improve flexural and shear strength, steel profile jacketing for passive confinement and shear enhancement, addition of wing walls to increase lateral strength with minimal structural intervention and strengthening of infill masonry walls using splint and bandage or full wall jacketing methods. These approaches address deficiencies in strength, ductility, and integrity, especially in non-engineered residential buildings with lean columns and inadequate reinforcement. While RC jacketing is more suitable for medium-rise buildings due to space and aesthetic constraints, steel jacketing and masonry wall strengthening are more adaptable for low-rise residential structures, making them practical solutions for Nepal's vulnerable building stock [6].

3. KEY LESSONS

1) High Level Meetings and Exposure Visits are important activities at the initial stage:

When top government officials engage directly with global experts during high-level meetings, they gain valuable insights into the life-saving and economic benefits of retrofitting, helping build strong policy-level commitment. Exposure visits further reinforce this understanding by allowing leaders and engineers to witness successful retrofitting projects firsthand, especially in contexts similar to their own. Seeing practical applications and interacting with experienced practitioners boosts confidence and motivation, making it easier to envision and implement similar efforts locally. Together, these activities foster informed decision-making and accelerate the adoption of retrofitting as a strategic investment in disaster resilience.

2) Identification and use of right technologies is important during pilot projects:

The success of a pilot project depends on selecting technologies that is not only technically sound but also contextually appropriate. This involves selecting a right

technology that is technically feasible, economically affordable, socially acceptable, locally available and finally easy to design, construct, and maintain.

3) Starting with simple public buildings like schools help:

School buildings are the recommended structures for pilot projects due to multiple reasons. Schools are ideal to start retrofitting as they play central role in engagement of multiple stakeholders; they can be highly visible and accessible as demonstration sites; these buildings are typically modest in scale and design; their public ownership ensures fewer legal or bureaucratic hurdles; and they often have existing infrastructure that can be upgraded rather than built from scratch. Moreover, involving schools fosters community engagement and awareness, as students, teachers, and parents become direct beneficiaries and advocates of the new concept. Schools are ideal also to monitor performance, gather feedback, and make improvements before scaling to more complex or private structures. Overall, starting with schools helps build trust, demonstrate feasibility, and lay a strong foundation for broader adaptation.

4) Targeting two representative members of community for pilot project for housing retrofit helps build confidence of whole community:

It is crucial to target two representative members of the community, a respected community leader and a representative from a marginalized group, for the pilot retrofitting project. A community leader often holds influence, trust, and visibility within the broader population. Their endorsement can lend credibility to the project, encourage wider participation, and help overcome resistance to change. As a role model, they can demonstrate the benefits of retrofitting, such as improved safety, energy efficiency, beautification etc. so that others will follow. Equally important is the inclusion of a representative from a marginalized community. If only a person from well off family is chosen, community may think retrofitting is doable only for richer people. These individuals often face economic, social, or infrastructural challenges. Involving them directly, the project shows that retrofitting is possible even for marginalized community.

5) Using multi-front approach for awareness raising can create necessary demand for retrofitting:

A multi-front approach to awareness raising is essential for effectively reaching diverse segments of the population. By utilizing various communication channels such as television, radio, hoarding boards, leaflets, and information calendars, messages can be tailored to suit different audiences and contexts. Television and radio are powerful tools for reaching a broad audience quickly. Hoarding boards placed in strategic public locations serve as constant visual reminders. Leaflets and information calendars provide tangible materials that people can refer to repeatedly, making the information more memorable and accessible.

6) Trainings should prioritize hands on exercise and case studies for development of required skills:

Prioritizing hands-on exercises and case studies in training is essential, especially for engineers who may not have experience on retrofitting. Hands on training helps bridge the gap between theory and practice and allow participants to learn the techniques, tools, and challenges involved in retrofitting. Case studies provide real-life example and highlight successful implementations, lessons learned and challenges. Similarly, hands-on exercises build confidence in applying technical knowledge.

7) Physical demonstrations are helpful for confidence buildings: Physical demonstrations

help trainees build confidence and they are especially useful for learning complex concepts like retrofitting. It helps the participants understand how the theory works in real life and makes the steps for implementation clearer. It also gives engineers the confidence to try retrofitting themselves.

8) Provision of financial incentives are important to promote: In most of the developing countries, it is challenging to implement building code even for new buildings where the additional cost is just 5-10%. The retrofitting cost is about 20-30% even for residential buildings and is more difficult for communities to get convinced and invest fully by them. However, small financial support with a provision of technical support encourages communities to retrofit. Provision of USD1000 after 2015 Gorkha Earthquake with additional socio-technical support was good enough to promote the seismic retrofitting [7].

9) Unless there is mandatory requirement in the code for assessment and retrofitting, it is difficult for large scale implementation: In Nepal, there is no mandatory requirement for seismic assessment and retrofitting of buildings and without that it is difficult for the local governments to implement seismic retrofitting at large scale. There are examples like New Zealand Building Regulation "Building (Specified Systems, Change the Use, and Earthquake-prone Buildings) Amendment Regulations 2017" clearly gives what the territorial authorities should do if the buildings are rated less than some threshold. Buildings with less than 34% capacity in comparison to the new code compliance buildings and buildings with less than 20% capacity in comparison to the new code compliance buildings need to be recommended either for retrofitting of demolition in a certain time frame. Similar provision is required for wider promotion and large scale implementation of retrofitting.

10) Priority of actions will differ in different stage of overall retrofitting activities in the country: based on Nepal's experience we can divide the progress of promoting retrofitting in three stages: a) Start-up stage, b) Promotion Stage and c) Large scale implementation stage. The priorities of activities will also change as per the progress. At the start-up phase, getting political buying-in, developing core group of experts, implementing pilot projects and developing technical guidelines are important. At the promotion stage, implementing massive awareness and capacity building programs, revising building act and code, creating system for financial support and incentives et are critical. At the large-scale implementation stage, developing national program for retrofitting and implementation of large-scale retrofitting work and continuous revision of act and code might be critical.

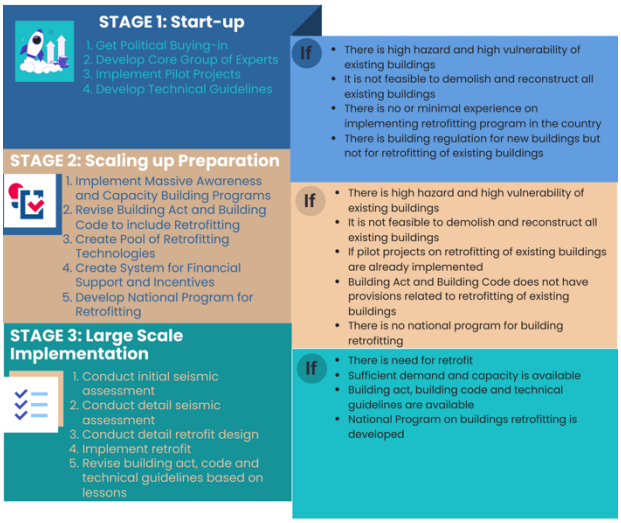

Figure 2: Priority activities at different stages of retrofitting

3. CONCLUSIONS

In 25 years of promoting seismic retrofitting in Nepal, several lessons are learned. Retrofitting efforts faced early challenges including limited technical capacity, financial constraints, cultural resistance, and lack of replicable models. Despite these hurdles, approximately 300 school buildings were successfully retrofitted before the 2015 Gorkha Earthquake. Remarkably, all retrofitted schools withstood the earthquake without damage,

while thousands of non-retrofitted schools in the same regions collapsed, validating the effectiveness of retrofitting.

The priority of actions will differ in different stage of overall retrofitting activities. Getting political buying-in, developing core group of experts, implementing pilot projects are important at the initial stage while revision of act and code with the provision of mandatory assessment and retrofitting is important after the ground work is done.

REFERENCES:

[1] UNDRR. (2025). Global Assessment Report on Disaster Risk Reduction 2025: Resilience Pays- Financing and Investing for Our Future. United Nations Office for Disaster Risk Reduction.

https://www.undrr.org/gar/gar2025

[2] Coburn, A., & Spence, R. (2002). Earthquake Protection (2nd ed.). John Wiley & Sons. https://www.wiley.com/en-us/Earthquake+Protection%2C+2nd+Edition-p-9780470849231

[3] Guragain, R., Shrestha, S. N., Maharjan, D. K., & Pradhan, S. (2018). Lessons from building damage patterns during April 25, 2015 Gorkha earthquake in Nepal. In R. Spence, E. So, & C. Scawthorn (Eds.), Living Under the Threat of Earthquakes (pp. 65–84). Springer. https://doi.org/10.1007/978-3-319-68044-6_5

[4] So E, Spence R (2013) Estimating shaking-induced casualties for global earthquake modelling. Bull Earthquake Eng 11: 1757–1775.

https://doi.org/10.1007/s10518-013-9462-0

[5] Hima Shrestha, Suman Pradhan, Ramesh Guragain (2012) Experiences on Retrofitting of Low Strength Masonry Buildings by Different Retrofitting Techniques in Nepal. 15WCEE, Portugal

[6] Rajani Prajapati, Hima Shrestha, Ramesh Guragain (2019) Exploration of Different Retrofitting Options for RC Frame Buildings in Kathmandu. USMCA2019, Kathmandu

[7] Nicola Giordano, Alastair Norris, Vibek Manandhar, Liva Shrestha, Dev R. Paudel, Natalie Quinn, Elizabeth Rees, Hima Shresth, Narayan P. Marasini , Rajani Prajapati, Ramesh Guragain, Flavia De Luca, Anastasios Sextos (2021), Financial assessment of incremental seismic retrofitting of Nepali stone-masonry buildings, International Journal of Disaster Risk Reduction, Volume 60. https://doi.org/10.1016/j.ijdrr.2021.102297

2025 HOW

4th International Symposium on One Health, One World
November 20 – 22, 2025

ABS ID: KN-11

Engineered Material-Efficient Systems Towards Net Zero Construction: Case Studies With 3d Printing And Geopolymers

K.V.L. Subramaniam[1], S.T. Maganty[2], R[3], and R. Vemuri[3]
[1]*Professor, Department of Civil Engineering, Indian Institute of Technology Hyderabad, Hyderabad, India,*
[2]*Senior Research Fellow, Department of Civil Engineering, Indian Institute of Technology Hyderabad, Hyderabad, India,*
[3]*Director, SL Structural Consortium, Hyderabad, Telangana, India, City,*
Correspond to Prof K.V.L. Subramaniam (kvls@ce.iith.ac.in)

***Keywords**: Sustainable Construction, Net Zero, Concrete, Geopolymer, From optimization, material-efficient systems.*

Sustainable construction practices primarily focus on mitigating the environmental impact and minimizing the carbon footprint. The primary focus of getting to net zero carbon emissions has focused on three scales: (a) binder level; (b) concrete level; (c) structure level. Most of the attention has focused on binder and concrete-level solutions, with efforts made to reduce the clinker content in cement, decrease the energy requirements in binder processing, decrease the binder content in concrete, and improve its long-term durability. Little attention has been paid to the structural scale and the utilization of concrete. At the structural scale, producing and erecting concrete structures with a low carbon impact focuses on developing lean construction methods and structural forms with a lower quantum of concrete usage. Therefore, a holistic approach towards achieving sustainability in concrete structures should involve producing structures designed for comparable performance as those produced by conventional procedures.

Material-efficient designs explore structural efficiency using structural forms that place material judiciously. Reducing self-weight contributes to lowering stress levels in the members. This allows for exploiting the upward spiral in design, contrary to conventional design, which relies on increasing the cross-sectional dimensions to provide increased capacity. This produces a downward spiral that makes design difficult with an increasing span. A significantly larger percentage of material resistance is consumed in supporting self-weight as the member size increases. Structural forms are developed using material-efficient designs, and two case studies are presented. In the first, the concept of form optimization is explored to develop a lightweight, structurally efficient bridge with a significant reduction in quantum consumption. In the second, lightweight geopolymer slab panels are presented.

Sustainability in concrete construction requires consideration of reducing the carbon in binders and minimizing material consumption. Material-efficient systems utilizing low-carbon binders offer solutions for a significant reduction in Global Warming Potential (GWP), assessed in terms of kilograms of CO_2 equivalent.

ABS ID: KN-12

Er. Rajdeep Chowdhury

Bright Spark Lecture

ABS ID: 196

Preparedness for Climate Change Amidst Accelerated Growth for India's Cement Sector

L.P. Singh
Director General
National Council for Cement and Building Materials
Ballabgarh- 121004, Haryana, India

In the fast-growing infrastructure of our country, use of sustainable materials is the key in the circular economy. Environment-friendly materials (also known as green building materials) are those in which, for their production, placing and maintenance, actions of low environmental impact have been performed. They have to be durable, reusable or recyclable. These materials also have to be natural and must not be spoilt by cold, heat or humidity. Concrete is the most widely used man-made material on earth and approximately, 2.0-2.5 m3 of concrete person is used. Though concrete is not a natural material but due to its superiority features it's a material of choice for infrastructure development. It forms the foundations of cities and connects communities and without it, many of the elements of modern life wouldn't be possible. The basic ingredient of concrete is cement and 7-8% of total CO2 emission in the world is by the cement production only. Due to the increasing concerns of climate change, cement industries are on the radar of policy makers to lower their carbon foot-prints. Cement industries have been asked to be carbon neutral by 2050. There is a significant challenge involved in achieving sustainability by cement industry. India is the second largest producer of cement after China and therefore, to meet the target of 2050 innovative indigenous efforts are required. The present talk will provide an overview of the Research & Development efforts being undertaken in achieving the concrete sustainability.

Oral Presentations

4th International Symposium on One Health, One World
November 20 – 22, 2025

ABS ID: 187
Code No: IMSBE -OP-01

Slope Monitoring System Using Inclinometers And Soil Moisture Sensors

T. Katayama [1], K. Goto [1], K. Fujimori [1], S. Konishi [1]
[1]Manager (T.K.), Engineer (K.G.), Technical Staff (K.F.), and Chief Engineer (S.K.), Technical Development Office, Project Promotion Division, Asano Taisei Kiso Eng Co., Ltd., Tokyo, Japan, Correspond to Teruhiko Katayama (katayama-tr@atk-eng.eng)

***Keywords**: Slope management system, Soil moisture sensor, Inclination sensor, Volumetric water content, Railway slope.*

1. INSTRCUTIONS

Heavy rainfall disasters have become more severe in recent years due to extreme weather conditions, and damage caused by landslides has been reported in many areas. Slope failures that can be expected on cut slopes include slope erosion caused by concentrated inflow of surface water (gully erosion) and slope slides caused by slope instability due to a rise in the groundwater table. The railway companies that own many small-scale slopes are required to respond to small-scale slope failures as shown in Figure 1.

To respond to such social needs, the Technical Development Office has been developing and commercializing a slope monitoring system using a soil moisture meter buried underground and a slope sensor installed on the ground surface since 2018 as a response to the risk of slope instability associated with rising groundwater levels.

This time, we have installed the developed slope monitoring system for such small-scale slope failures on the slope and started its measurement.

Figure 1. Example of surface collapse of a railway cutting slope

2. Outline of the Slope Management System

Figure 2 shows an overview of the installed slope management system. This system was developed by ATK and consists of the main unit of the measuring instrument, which incorporates a 3-axis tilt sensor, temperature sensor, and communication module shown in Figure 3 a soil moisture sensor, and a power supply. The main unit is fixed to a pile driven into the ground and measures the slope angle of the ground surface in the vertical and horizontal directions. The soil moisture sensor is buried in the soil and measures changes in soil moisture as volumetric moisture content.

The measurement of volumetric moisture content was introduced in reference to the results of a basic study on the sophistication of highway regulatory standards, which showed a strong relationship between changes in soil moisture content on slopes and slope stability [1]. Figure 4 shows the relationship between volume water content and displacement in a small-scale model experiment.

Measurement data is stored in the cloud via NB-IoT communication, and the system is designed to share measurement data among the parties concerned.

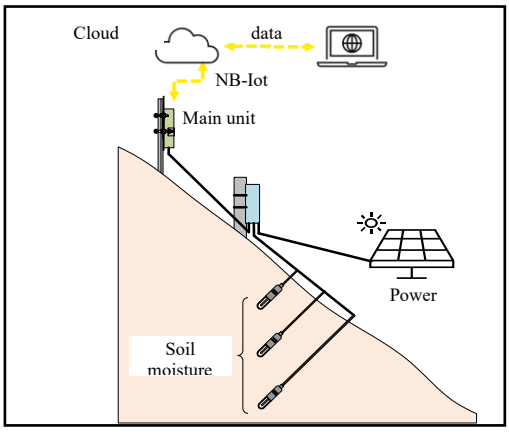

Figure 2. Overview of the observation

Figure 3. Equipment used in the observation system

(From left: main unit, soil moisture sensor, power supply)

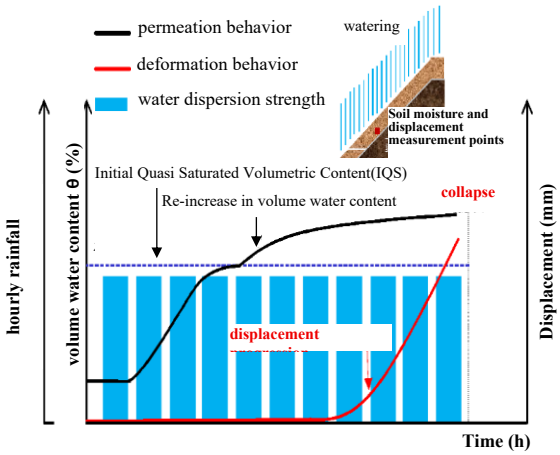

Figure 4. Relationship between volume water content and displacement in small-scale model experiments [1]

3. Location of the observation system

3.1 Site A

Figure 5 shows the installation situation. The installation site is a cut slope of Kanto loam adjacent to the Keio railway line. The observation system was installed at the end of the slope near the railroad line, taking into consideration the impact on the railway line when deformations occur. In order to understand the rainwater infiltration process in detail, soil moisture sensors were installed at three depths: 28 cm, 60 cm, and 78 cm. The power source was a 100 V power supply provided at the site where the system was installed.

Figure 5. Observation system installation status

3.2 Site B

Figure 6 shows the installation situation. The installation site is a landslide area in Tokushima Prefecture, which was kindly provided by the Shikoku Mountain Erosion Control Office as part of the field demonstration test of the "Consortium for Market Development of Slope Monitoring Using Inclination Sensors," in which we are participating. The observation system was installed on a natural slope consisting mainly of weathered muddy schist and weathered sandy schist with a slope gradient of about 1:1.5 to 1:1.0, which is somewhat unstable. The solar panels installed at the site were powered by the solar panels and the solar panels were installed at the site. Solar panels installed at the site were used as the power source.

Figure 6. Observation system installation status

4. Measurement Results

4.1 Site A

Figure 7 shows the measurement results and hourly precipitation. Data from the Hachioji observatory, which is closest to the measurement site, was used for the hourly precipitation. During the measurement period (December 10-31, 2022), continuous rainfall occurred three times. The maximum rainfall was 23 mm on December 22.

Looking at changes in volumetric water content during rainfall, changes in volumetric water content due to rainfall were observed at the sensor with a depth of 28 cm, which is closest to the ground surface, indicating that volumetric water content increases with the amount of rainfall. On the other hand, no significant change in volumetric water content was observed during rainfall at the 60 cm and 78 cm depths. Therefore, it is assumed that at the rainfall intensities that occurred during the measurement period, rainwater infiltration was limited to very shallow depths on the ground surface.

Since the tilt sensor maintained a nearly constant angle of inclination in both the vertical and horizontal directions of the slope, it is assumed that no displacement that could lead to slope failure occurred during the measurement period.

4.2 Site B

At Site B, measurements began on July 12, 2022. During the observation period, the tilt sensor detected a variation in the tilt angle during a heavy rainfall in September, but the situation remained relatively stable thereafter. However, on March 23, 2022, a large change in tilt angle was captured. The situation is described below, and Figure 8 shows the time-series data for that day.

According to the data from the observation station near Site B, the site had rainfall of about 4 mm maximum hourly rainfall from around 8:00 on that day. Soil moisture sensors installed at the site also confirmed an increase in volumetric moisture content from the same

time, suggesting that rainfall also occurred at the site. The tilt angle in the Y-axis direction, which is orthogonal to the slope, began to increase slightly around 11:00 a.m. under such rainfall, and the sensor was observed to begin to tilt toward the valley side. It is assumed that the tilt displacement was increasing with increasing speed. After that, around 17:00, the tilt angle in the Y-axis direction increased rapidly to more than 50°, and a change that foreshadowed slope displacement was confirmed; after 17:00, the values of tilt angle and angular velocity varied, and it is assumed that the tilt sensor continued to move erratically.

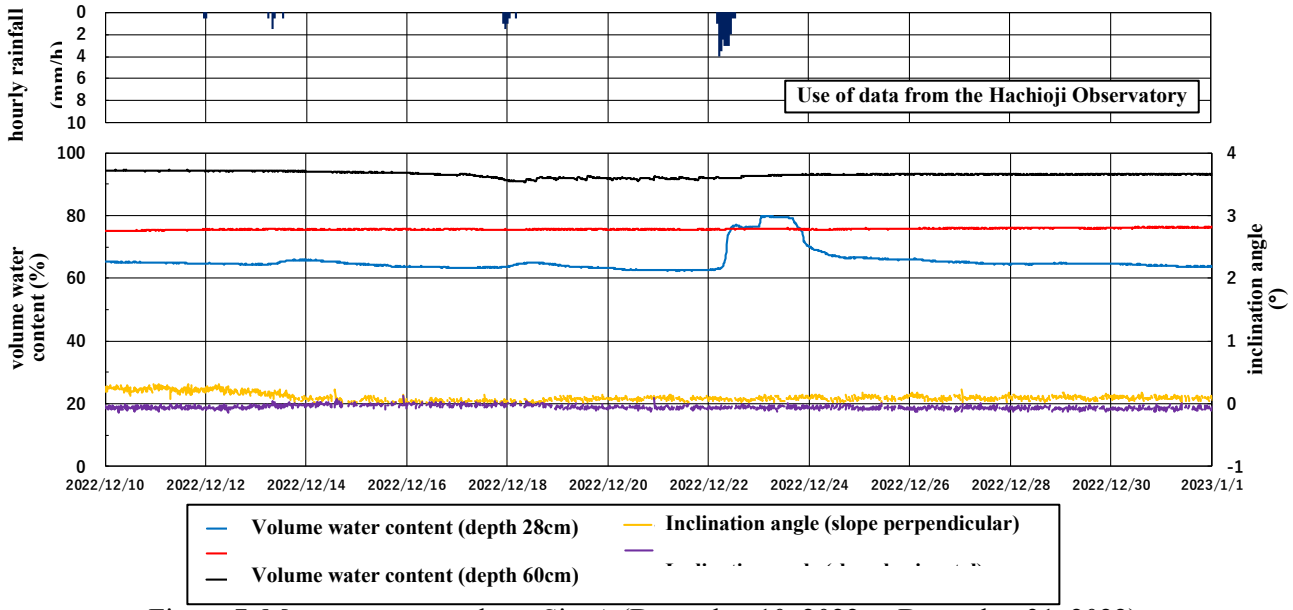

Figure 7. Measurement results at Site A (December 10, 2022 to December 31, 2022)

4.2 Site B

At Site B, measurements began on July 12, 2022. During the observation period, the tilt sensor detected a variation in the tilt angle during a heavy rainfall in September, but the situation remained relatively stable thereafter. However, on March 23, 2022, a large change in tilt angle was captured. The situation is described below, and Figure 8 shows the time-series data for that day.

According to the data from the observation station near Site B, the site had rainfall of about 4 mm maximum hourly rainfall from around 8:00 on that day. Soil moisture sensors installed at the site also confirmed an increase in volumetric moisture content from the same time, suggesting that rainfall also occurred at the site. The tilt angle in the Y-axis direction, which is orthogonal to the slope, began to increase slightly around 11:00 a.m. under such rainfall, and the sensor was observed to begin to tilt toward the valley side. It is assumed that the tilt displacement was increasing with increasing speed. After that, around 17:00, the tilt angle in the Y-axis direction increased rapidly to more than 50°, and a change that foreshadowed slope displacement was confirmed; after 17:00, the values of tilt angle and angular velocity varied, and it is assumed that the tilt sensor continued to move erratically.

Later, as a result of on-site confirmation, we found that the surface collapse shown in Figure 9 had occurred, and the area of the collapse was approximately 5 m wide and 10 m long. It was confirmed that our sensor was washed down the valley side due to the collapse.

Based on the variation in slope angle and angular velocity, and the on-site conditions confirmed later, it is assumed that a surface collapse occurred at the site, and that the time of occurrence was around 17:00, with slope failure continuing until around 18:30.

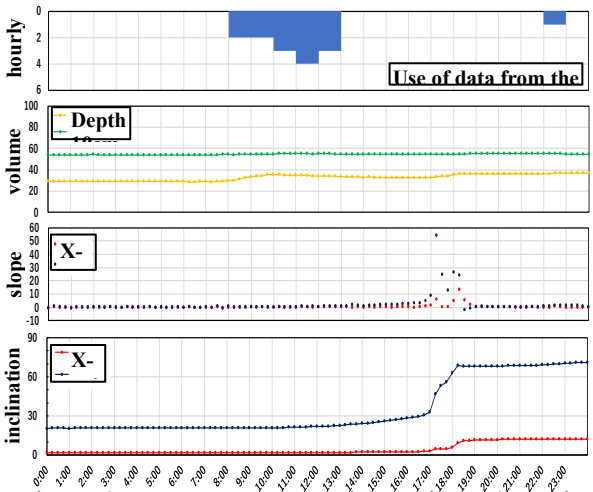

Figure 8. Measurement results at Site B (March

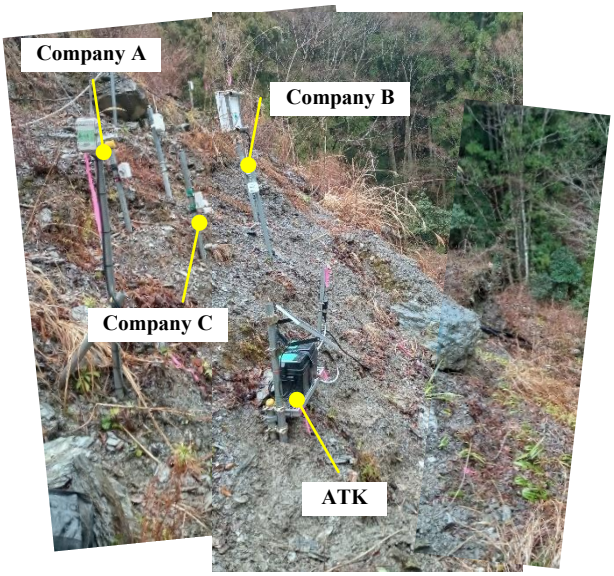

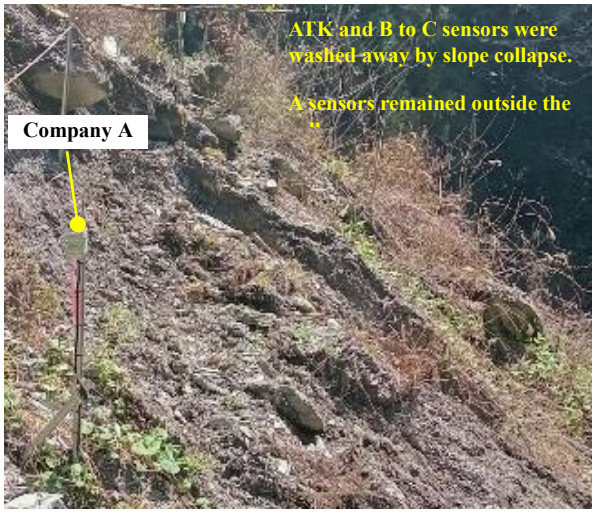

Figure 9: Observation system installation locations

(Top: Before collapse, March 2, 2023; Bottom: After collapse, March 28, 2023)

5. Discussion

At Site B, we were able to obtain measurement data before and after the slope failure. Therefore, based on the obtained data, we will discuss the changes in measurements during slope failure with the keyword "creep".

In general, there are various patterns of landslide and slope failures. One concept for predicting these collapses is the creep deformation concept. The creep deformation concept is based on the creep curves obtained from the results of creep tests of soil and rock shown in Figure 10, and the creep curves are classified into three regions, from first to third creep, according to the progression of strain.

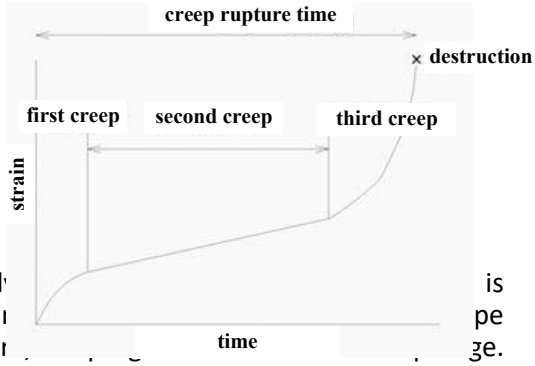

Figure 10. Creep curve diagram [2]

Therefore, we applied the prediction method using the inverse of the surface movement velocity by Fukuzono[3] to the case of this collapse. In other words, this is an attempt to show the slope failure by the relationship between the inverse of the movement velocity and time. Specifically, we obtained the relationship between the inverse of the angular velocity of the slope and time, and attempted to determine whether the inverse of the angular acceleration shows first to third creep movement. The results of the trial are shown in Figure 11.

Although further study is needed, the series of creep curves shown in Figure 9 was confirmed, and it is possible that the change from first to third creep was captured by the slope of the inverse of the angular acceleration.

6. summary and future issues

In this study, a slope measurement system developed by the Technical Development Office was installed on a cut slope and a landslide site, respectively, as a method of monitoring slope management, and changes in slope displacement and volumetric water content over time were monitored.

As a result, changes in volumetric water content and slope displacement in response to rainfall intensity were clarified.

In particular, we were able to obtain data before and after slope failure at the landslide site, which is very useful information when considering management methods in the future.

However, since this study focused on changes in slope angle, we would like to focus on changes in volumetric water content to discover the relationship between the two, and to use this data to predict slope failure in the future.

Currently, as one of the collapse prediction methods, we would like to try to identify anomalies in measured data by using a recurrent neural network (RNN).

In other words, it is a method to determine "abnormal trends" that deviate from the conventional range of expectation by learning the "normal trend of change" based on time-series data (information) of daily volume moisture content, inclination angle, and inclination angular velocity.

If this judgment method can be established and an alarm can be issued immediately after the occurrence of the first-order creep, we believe that the first-order to second-order creep can be used as the lead time necessary for evacuation, leading to safe evacuation.

REFERENCES:

[1]Keigo Koizumi, Keiji Sakuradani, Kazuhiro Oda, Shinichi Ito, Yoshio Fukuda, Maria Q.FENG, and Masashi Takemoto: Fundamental study for upgrading highway traffic control criteria against surface failure during rainfall, Journal of JSCE, C (Geosphere Engineering), Vol. 73, No. 1, 93-105, 2017

[2]M. Saito: Prediction of slope failure timing by tertiary creep, Landslide, Vol.4, No.3, pp.1-8, 1968

[3]Teruki Fukuzono: Prediction of slope failure time due to rainfall using inverse of surface movement velocity, Landslide, Vol.22, No.2, 8-13, 1985

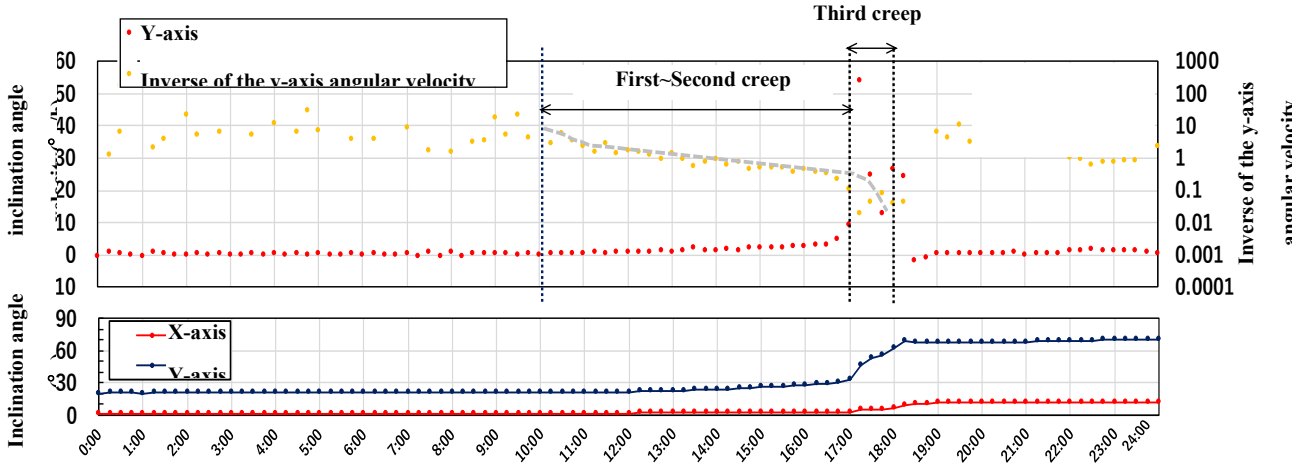

Figure 11. Changes in tilt angle velocity before and after collapse based on measurement results (March 23, 2023)

ABS ID: 183
Code No: IMSBE-OP-02

Mr. Rishwanth Darun Annamalaisamy Sannasiraj

4th International Symposium on One Health, One World
November 20 – 22, 2025
ABS ID: 161
Code No: IMSBE-OP-03

Effect Of Paint Scrap Waste Based Accelerating Admixture on Setting Time, Compressive Strength and Hydration of Cement Paste

Jeeshan Khan[1], P.C Thpaliyal[2,5], Arun Kumar[3], Reyazur Rahman[1] and Neha Kumari[4]
[1]*Senior Scientist, Advanced Concrete, Steel and Composites Group, CSIR-Central Building Research Institute (CSIR-CBRI), Roorkee, Uttarakhand, 247667, India*
[2]*Chief Scientist, Advanced Concrete, Steel and Composites Group, CSIR-Central Building Research Institute (CSIR-CBRI), Roorkee, Uttarakhand, 247667, India*
[3]*Project Assistant, Advanced Concrete, Steel and Composites Group, CSIR-Central Building Research Institute (CSIR-CBRI), Roorkee, Uttarakhand, 247667, India*
[4]*Technical Assistant, Advanced Concrete, Steel and Composites Group, CSIR-Central Building Research Institute (CSIR-CBRI), Roorkee, Uttarakhand, 247667, India*
[5]*Professor, Academy of Scientific and Innovative Research (AcSIR), Ghaziabad, 201002, India*
Correspond to Dr. Jeeshan Khan (jeeshank@cbri.res.in)

Abstract

Building renovation and repairing work generated a huge amount of old paint scrap. This waste left-over in landfill as part of the household or demolition waste, which is a major environmental concern. The objective of this paper is to convert powdered paint scrap waste into a liquid accelerating admixture using dilute acid and investigates effects of accelerating admixture on setting time, compressive strength and hydration of cement paste. This paper aimed to investigate effects of different percent of accelerating admixture on setting time of cement paste with different water cement ratios of 0.4, 0.45 and 0.5. The result indicates that accelerating admixture reduces setting time of cement paste with different water cement ratios. The findings reveal that accelerating admixture enhances hydration and slightly improved compressive strength of cement paste. Thus, paint scrap waste can be utilized in making of setting accelerator for cement-based materials

Keywords: *Paint scrap waste, Accelerating admixture, Setting time, Cement hydration, Compressive strength.*

1. INTRODUCTION

Construction industry around the world is one of the largest sources of economic growth. Nevertheless, its wide range of operations leads to generation of huge waste, which creates difficulties in environmental sustainability and resource management. The fast-growing cities, the constant changing of infrastructures and renovation works that are frequently undergoing have very rapidly increased the construction and demolition (C&D) wastes [1, 2].

Paint scrap is one of the most neglected wastes from repair and refurbishment works. It is non-biodegradable materials which tend to be buried at the landfills, where they cause contamination of both the soil and water. Yet, this discarded paint scrap waste is high in synthetic polymer and other functional additives that bear resemblance to concrete admixtures. The paint scrap normally carries pigments, fillers, polymers which have dried, surfactants and coalescing agents which are not easily biodegraded and as a result a source of pollutant to the environment [3,4]. The reuse of such waste will fit into the process of sustainable development within the construction and circular economy.

Cement and concrete have become the most popular forms of construction materials all over the world on which the infrastructure like buildings, bridges, and roads [5, 6]. Nevertheless, their performance depends on various factors that include temperature,

humidity, and requirements of properties [7-9]. Chemical admixtures are normally used in order to strengthen or alter concrete properties in different conditions. Such admixtures, may enhance workability, change setting times, diminish water requirement, and enhance mechanical properties and durability of concrete.

For greater than 70 years the polymeric admixtures have influenced the concrete performance positively by boosting workability, shortening setting time and reinforcing the cement-matrix-aggregate bond, structural integrity and reliability to the concrete. Interestingly, the polymers contained in waste latex paint i.e styrene butadiene resins, acrylics, and polyvinyl acetates, have closely related structures to those present in commercial admixtures [10-12]. These polymers, when well processed, they can perform as bonding agent, water reducer, and the modifier of setting time of the cementitious materials. Further, architectural paint scrap is a blend with inorganic fillers (e.g. calcium carbonate, titanium dioxide) and organic polymers which on reaction with dilute acids can produce reactive species [13]. It is through these elements that it would be possible to create an accelerating admixture that furthers enhances early age reaction of cementitious materials [14-16]. Therefore, the reuse of paint scrap not only reduces the waste in landfills but also reduces the reliance on expensive commercial admixtures thus leading to more sustainable methods of construction.

Based on that, the current research suggests a method to valorize paint scrap wastes. In particular, it focuses on the development of liquid setting accelerator by dilute acid treatment of powdered paint scrap waste. Performance and technical viability of this accelerating admixture are surveyed based on determining on main properties of cement paste. The study will concentrate on determining the variations in initial and final setting times at various water cement ratios (0.4, 0.45 and 0.5) and compressive strength of cement paste at different ages.

2. MATERIALS AND EXPERIMENTAL METHODS

2.1 Materials

OPC 43 (Ordinary Portland Cement) in acquiescence with IS 8112: 2013 [17] was used in this paper. Waste old paint scrap was collected locally generated from building renovation shown in Figure 1. Collected paint scrap grinded and powdered to below 300 micron size in mortar pestle. Dilute acid was prepared from concentrated inorganic acid and water in the ratio of 1:4. Further, 8% paint scrap powder slowly added and dissolved in dilute acid until saturation of solution and this solution denoted paint scrap based accelerating admixture.

Figure 1. Waste paint scrap from building.

2.2 Experimental Methods

The setting time of cement paste was determined using vicat apparatus in acquiescence with IS 4103: 2005 part 5 [18]. Accelerating admixture dosages of 0% (Control), 5% (PAD 5), 10% (PAD 10) and 15% (PAD 15) by weight of cement were mixed with water for making of cement paste specimens with different water cement ratios 0.4, 0.45 and 0.5. Cement paste mix are prepared with varying water cement ratios and admixture dosages for initial and final setting time determination are given in Table 1. The mechanical behavior of the casted specimens 50x50x50mm^3 was determined through compressive strength tests according to the ASTM C 109 [19]. The casted specimens contain 0% (Control), 5% (PAD 5), 10% (PAD 10) and 15% (PAD 15) of accelerating admixture by cement weight and water cement ratio 0.4. The cement paste mix details of four different mixes for compressive strength were given cement in Table 2. These specimens kept for 24 hr at room temperature after that they were demoulded and subjected to water curing until required for compressive strength testing.

The study of the hydration process carried out through isothermal calorimetric tests using TAM Air isothermal calorimeter incompliance with standard ASTM C 1679 [20]. The samples were prepared externally and approx. 5 gm cement paste incorporated accelerating admixture 0% (Control) and 15% (PAD 15) of

water cement ratio 0.4 and perform for a period of 3 days at 25°C temperature.

Table 1. Mixes investigation for setting time of cement paste

Mixes Designation	Accelerating admixture (%)	Water cement ratios	Cement weight (gm)	Water (gm)	Accelerating admixture (gm)
Control	0	0.4	500	200	-
PAD 5	5		500	175	25
PAD 10	10		500	150	50
PAD 15	15		500	125	75
Control	0	0.45	500	225	-
PAD 5	5		500	200	25
PAD 10	10		500	175	50
PAD 15	15		500	150	75
Control	0	0.5	500	250	-
PAD 5	5		500	225	25
PAD 10	10		500	200	50
PAD 15	15		500	175	75

Table 2 Mixes investigation for compressive strength of cement paste

Mixes Designation	Accelerating admixture (%)	Water cement ratios	Cement weight (gm)	Water (gm)	Accelerating admixture (gm)
Control	0	0.4	3000	1200	-
PAD 5	5		3000	1050	150
PAD 10	10		3000	900	300
PAD 15	15		3000	750	450

3. RESULTS AND DISCISSIONS

3.1 Initial and final setting time

The initial and final setting times of cement paste with waste old paint scrap based accelerating admixture dosages of 0% (Control), 5% (PAD 5) 10% (PAD 10) and 15% (PAD 15) by weight of cement were evaluated at different water cement ratios (0.4, 0.45 and 0.5) shown in Figure 2, 3 and 4. The addition of accelerating admixture dosages, setting time reduces significantly compared to control at different water cement ratios. Cement setting behavior is affected by the development of calcium sulphoaluminate hydrates. The making of this phase depending on the accessibility of the aluminate phases, reaction rate, gypsum retarder and the liberation of portlandite during the hydration of C_3S and β-C_2S phases. The addition of accelerating admixture not only reduces setting times and accelerate formation of ettringite but also enhances the hydration of the C_3S and β-C_2S phases. The increase in the rate of cement paste setting at in the presence of admixtures can be explained on the basis of needle like morphology of the ettringite which contributes to a quicker stiffening of the cement paste [21]. As illustrated in Figure 2. paint scrap based accelerating admixture at water cement ratio of 0.4 significantly reduces initial and final setting times. For PAD 5 initial setting time is shortened by 30 mins and final setting time by 50 mins compared with control mix; for PAD 10 initial setting time is shortened by 50 mins and final setting time by 90 mins; and for PAD 15 the initial setting time is shortened by 80 mins and final setting time by 120 mins compared with the control mix. Further, in Figure 3. results of the initial and final setting time of the cement paste at 0.45 water cement ratio are displayed. The accelerating admixture containing PAD 5 mix showed a decrease of 30 mins in the initial and final setting times, PAD 10 showed a decrease of 50 mins in initial setting time and 60 mins in final setting time whereas the PAD 15 decreased the initial and finial setting times by 70 and 120 mins respectively. Furthermore, Figure 4. shown initial and final setting times of the cement paste at water cement ratio of 0.5. In this case PAD 5 mix decreases initial setting time by 40

mins and final setting time by 30 mins, PAD 10 decreases initial setting time by 60 mins and final setting time by 70 mins and for PAD 15 the initial and final setting times were decreased by 90 and 120 mins respectively compared to control mix. In all these mixes old paint scrap based accelerating admixture performed well and was consistent in all the studies of various water cement ratios. For further studying the strength performance and hydration behavior, the water cement ratio of 0.4 was fixed for all cement paste mixes.

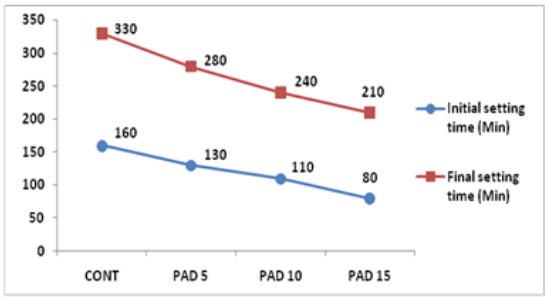

Figure 2. Effect of accelerating admixture on setting time of cement paste at water cement ratio 0.4.

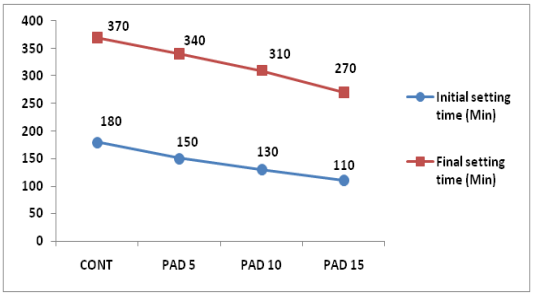

Figure 3. Effect of accelerating admixture on setting time of cement paste at water cement ratio 0.45.

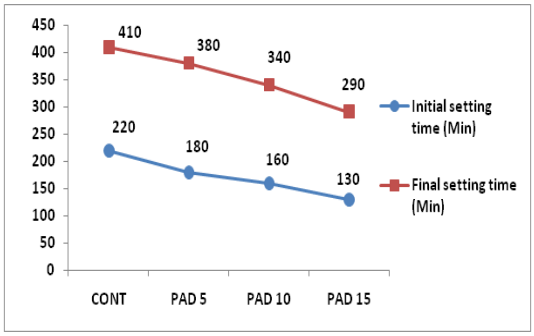

Figure 4. Effect of accelerating admixture on setting time of cement paste at water cement ratio 0.5.

3.2 Compressive strength

The bar graph diagram in Figure 5. represents comparison of cement paste specimens compressive strength incorporating 0%, 5%, 10%, and 15% of the accelerating admixture. Strength of the specimens was determined at 3 days and 28 days. The compressive strength of accelerating admixture specimens PAD 5 increases strength by 5.2% and 0.95% compared to control, PAD 10 by 6.5% and 3.6% compared to control and PAD 15 by 9.8% and 3.9% compared to control at 3 and 28 days respectively, this is because of accelerating effect of admixture. The accelerating admixture significantly increased the early strength at 3 days and slightly improvement in strength was also observed at 28 compared to control.

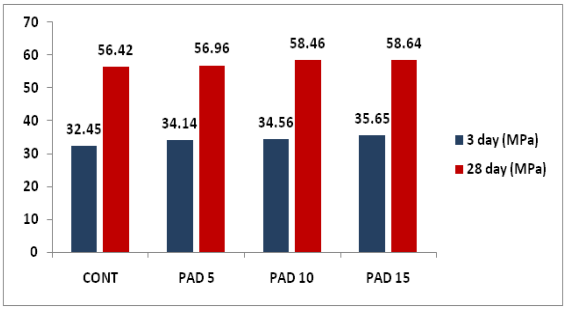

Figure 5. Effect of accelerating admixture on compressive strength of cement paste at water cement ratio 0.4.

3.3 Hydration study

The measurement of exothermic heat of cement paste was done to determine the effect of paint scrap based accelerating admixture on the hydration reaction and compare with control (Fig. 6 and Fig. 7). The early acceleration stage induction period is a slow process and linked with hydration of C_3S. After, end of induction period acceleration period

starts where C-S-H are formed which develop on the face of the initial grains of cement. A dense interior product of C-S-H is later formed between the expanding C-S-H needles and the original cement grains [22]. Heat flow and cumulative heat evolution of the PAD 15 cement paste, which had the paint scrap as the accelerating admixture, were compared to the control mix at water cement ratio of 0.4 (Fig. 6 and Fig. 7). The addition of the admixture significantly changed hydration behaviour as shown by the exothermic heat release profiles. In the PAD 15 mix, the induction period was shortened, the acceleration peak appeared at the earlier stage, and the release of cumulative heat is higher than that of the control. Furthermore, the accelerating peak of the admixture containing mix reached much earlier than that of the control, which clearly indicates that the admixture considerably shortened the time to reach the main hydration peak and effectively accelerated the overall hydration process of the cement paste.

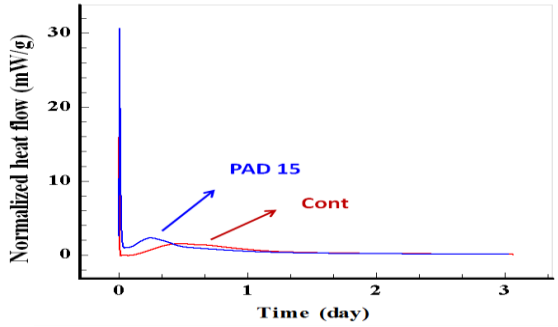

Figure 6. Normalized heat flow of cement pastes with and without admixture at 25°C.

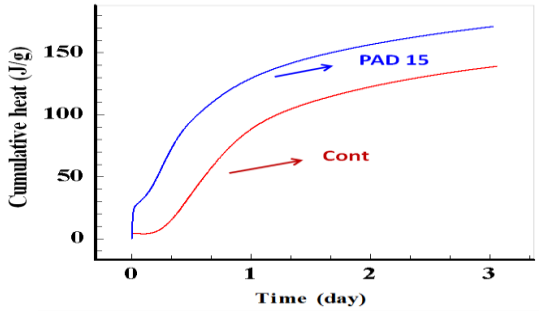

Figure 7. Cumulative heat of cement pastes with and without admixture at 25°C.

4. CONCLUSIONS

The main conclusions are

• The powdered paint scrap waste converted into a liquid accelerating admixture for cement paste.

• This accelerating admixture of different dosages significantly reduces setting time of cement paste at 0.4, 0.45 and 0.5 water cement ratio.

• The accelerating admixture slightly improved compressive strength of cement paste at 0.4 water cement ratio.

• The exothermic heat release profile of control and accelerating admixture (15%) cement mix showed that admixture considerably shortened time to reach of acceleration peak compared to control and accelerates the reactions of hydration.

Acknowledgments

The authors are thankful to CSIR- Central Building Research Institute, Roorkee (U.K.) for granting permission to publish this research work and for financial support under research grant OLP-2301.

REFERENCES

[1] L. A. López Ruiz, X. Roca Ramón, S. Gassó Domingo, J. Clean. Prod., 248 (2020) 119238.

[2] M. Menegaki, D. Damigos, Curr. Opin. Green Sustain. Chem. 13 (2018) 8–15.

[3] Q. Ding, H. Zhu, Polym., 15 (2023) 1485.

[4] A. H. Noruzman, N. Mohd Apandi, ARBMS 20 (2020) 28–33.

[5] S. Griffiths, B. K. Sovacool, D. D. F. Del Rio, A.M. Foley, M. D. Bazilian, J. Kim, J. M. Uratani, Renew. Sustain. Energy Rev., 180 (2023) 113291.

[6] C. R. Gagg, Eng. Fail. Anal., 40 (2014) 114–140.

[7] A. Keshmiry, S. Hassani, M. Mousavi, U. Dacker mann, Buildings., 13 (2023) 918.

[8] C. Lu, W. Wang, J. Jiang, M. Hao, Adv. Cem. Res., (2017) 1–10.

[9] H. Zhao, K. Jiang, R. Yang, Y. Tang, J. Liu, Int. J. Heat Mass Transf., 146 (2020) 118784.

[10] S. A. Osemeahon, A. Akinterinwa, E. Fasina, F. P. Andrew, M. H. Shagal, S. A. Kareem, U. Reuben, P. U. Onyebuchi, A. R. Olubukola, D. Esenowo, A. Aminu, Prog. Rubber Plast. Recycl. Technol., (2024) 14777606241281624.

[11] X. Zhang, M. Du, H. Fang, M. Shi, C. Zhang, F. Wang, Constr Build Mater., 299 (2021) 124290.

[12] M. Novak, B. Ormsby, Poly(Vinyl Acetate) Paints, Polym. 15 (2023) 4348.

[13] J. Atílio Fritz Fidel Rocco, R. Francisco Boschi Gonçalves, M. Galizia Domingues, Physicochemical Behavior of Concretes Admixed with Water-Based Polymers (PMC: Polymer-Modified Concrete), in: H.M. Saleh, M. Mhadhbi, A.I. Hassan (Eds.), Design and Analysis, Intech Open, 2023.

[14] N. Almesfer, C. Haigh, J. Ingham, Cem. Concr. Compos., 34 (2012) 627–633.

[15] N. Almesfer, J. Ingham, Cem. Concr. Compos., 46 (2014) 19–25.

[16] Y. R. Patil, V. A. Dakwale, R. V. Ralegaonkar, Adv. Civ. Eng., 2024 (2024) 6234010.

[17] IS 8112: 2013, Indian Standard code of practice, Ordinary Portland Cement 43 grade Specification, Bureau of Indian Standard, New Delhi.

[18] IS 4103: 2005 part 5, Indian Standard code of practice, Methods of physical tests for hydraulic cement, Bureau of Indian Standard, New Delhi.

[19] ASTM C109/109M, Standard test method for compressive strength of hydraulic cement mortars, ASTM, West Conshohcken, PA, USA.

[20] ASTM C1679-2014, Standard practice for measuring hydration kinetics of hydraulic cementitious mixtures using isothermal calorimetry, ASTM, West Conshohocken, PA. USA.

[21] M. Heikal, Cem. Concr. Res., 34 (2004) 1051–1056.

[22] Y. L. Yaphary, Z. Yu, R. H. W. Lam, D. Lau, Constr. Build. Mater., 141 (2017) 94–103.

4th International Symposium on One Health, One World
November 20 – 22, 2025

ABS ID: 131
Code No: IMSBE-OP-04

Next-Generation Materials in Civil Engineering: Pioneering Sustainable Solutions for A Low-Carbon Built Environment

S. K. Singh[1,2], Jyoti [1,2] And Ajay P. Chourasia[1,2]
[1]*CSIR-Central Building Research Institute, Roorkee-247667, India*
[2]*Academy of Scientific and Innovative Research (AcSIR), Ghaziabad-201002, India*
Correspond to Prof. S. K. Singh (sksingh.cbri@csir.res.in)

Keywords: *Engineering innovation; Green binder; Quaternary binder; Sustainable materials; Ternary binder.*

EXTENDED ABSTRACT

1. INTRODUCTION

The increase in climate change and its related environmental impacts has placed the construction sector under increasing scrutiny, given its considerable carbon footprint and high resource consumption. In this context, Portland cement production appears as one of the most energy-intensive processes, accounting for approximately 7–8% of global anthropogenic CO_2 emissions [1,2]. Therefore, the need to reduce greenhouse gas emissions, due to rapid urbanisation and infrastructure development, imposes an urgent transition towards greener alternatives. Sustainable construction materials, specifically alternative binders, have therefore become the focus of intense research and development worldwide [3].

The environmental drawbacks associated with ordinary Portland cement (OPC), such as high resource consumption, high calcination-based emissions, and substantial fossil fuel demand, are prompting both academia and industries to adopt supplementary cementitious materials (SCMs). These by-products, generated from various sectors, offer dual advantages, for instance, mitigating waste accumulation and simultaneously serving as cement substitutes to a greater extent [4,5]. Fly ash, silica fume, Ground granulated blast furnace slag (GGBFS), metakaolin, and geopolymers are among the most prominent alternatives. Initially, binary binders have gained industrial acceptance, particularly OPC–fly ash-based and OPC–GGBFS-based systems. While these binders reduce clinker factor to a greater extent and also improve various performance parameters [6], the potential of two or more SCM-based binders with OPC remains underexplored. Recent research studies have shown that ternary and quaternary SCM combinations with OPC, upon optimisation, can lead to improved hydration, microstructural refinement, and superior strength. The rational design of such multi-blended composites thus represents a significant leap toward next-generation sustainable binders.

Binder Development and Testing

The present study explores the performance of ternary and quaternary binder systems encompassing OPC, GGBFS, Linz-Donawitz Slag (LDS), and Ladle Furnace Slag (LFS). Both LDS and LFS are by-products of steelmaking and remain underutilised compared to GGBFS; however, they present promising hydraulic and pozzolanic properties if processed appropriately. In this work, chemical processing using alkalis was employed to enhance dissolution and promote the development of additional calcium-silicate-hydrate (C-S-H) gel and other strength-imparting hydration compounds. The binders were prepared in two formats: a ternary blend consisting of OPC, GGBFS, and LDS, and a quaternary blend comprising OPC, GGBFS, LDS, and LFS. Mechanical strength performance was examined across 7, 28,

56, and 90 days. In addition, microstructural measurements were conducted using Scanning Electron Microscopy (SEM) and X-Ray Diffraction (XRD). These tests were supported by Thermal Gravimetric Analysis (TGA) and Differential Scanning Calorimetry (DSC) for monitoring the phase transformation. Durability assessments included tests such as resistance to sulphate attack, acid attack and drying shrinkage.

Analysis and Interpretation

Based on various test results, the study concluded that the superior properties of both ternary and quaternary binder systems over conventional OPC. In compressive strength analysis, the ternary formulation demonstrated considerable improvements over OPC, particularly at later ages. However, the prepared quaternary binder formulation surpassed both OPC and ternary binders, exhibiting 18–22% higher strength at 90 days. Microstructural examination revealed a denser matrix in quaternary binder samples, characterised by fewer voids and a refined structure compared to other binder systems. SEM micrographs highlighted the homogeneity and compactness of hydrates in quaternary binder samples. In contrast, XRD analysis confirmed the development of additional hydration products, including C-S-H, hydrotalcite-like phases and calcium aluminosilicate hydrates. Thermogravimetric profiles showed enhanced thermal stability in quaternary binders compared to OPC. Exposure to sulphate and acidic environments revealed better durability performances of both ternary and quaternary binders. Ternary binders showed improvement, but quaternary samples recorded the lowest weight loss. For acid attack resistance, the quaternary blend exhibited nearly 40% lower mass loss relative to OPC. In drying shrinkage analysis, quaternary binders showed modest shrinkage compared to OPC, attributed to controlled pore water redistribution and a denser microstructure. Fig. 1 shows the overview of the study.

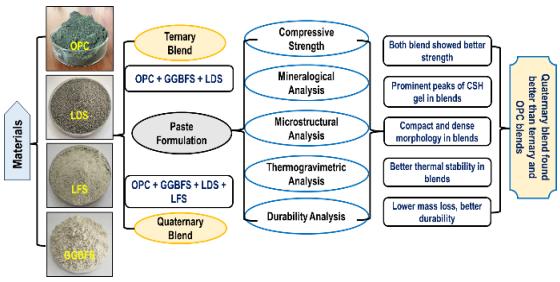

Fig. 1: Overview of study

Challenges

While these outcomes underscore the technical feasibility and environmental potential of steel and iron slags as supplementary binders, several challenges must be addressed before large-scale implementation can be realised. Chief among these are the issues of raw material heterogeneity, variable chemical composition, and the need for standardised pre-processing methods to ensure consistent performance. Additionally, the successful integration of such materials into mainstream construction practices will require comprehensive codal recognition, robust performance verification mechanisms, and clear cost-benefit assessments to convince stakeholders of their viability. Equally important is the application of life-cycle assessment (LCA) methodologies to quantify the long-term environmental benefits of these materials, including their carbon savings, energy footprint, and recyclability at the end of life.

CONCLUSION

The findings of this study underscore the immense potential of quaternary binder systems as sustainable yet high-performance alternatives to OPC. Their ability to integrate a broader spectrum of

industrial by-products not only reduces reliance on clinker but also diverts metallurgical slag away from landfills. Additionally, the demonstrated mechanical, thermal, and durability enhancements make these systems attractive for deployment in infrastructure operating under aggressive environmental conditions. From a life-cycle perspective, the net environmental gain is twofold: significant CO_2 savings from reduced clinker production and ecosystem benefits from the efficient utilisation of industrial waste.

ACKNOWLEDGEMENT

The authors are grateful to the CSIR-CBRI for granting permission to publish this work.

REFERENCES:

[1] Barbhuiya, S., Kanavaris, F., Das, B.B. and Idrees, M., 2024. Decarbonising cement and concrete production: Strategies, challenges and pathways for sustainable development. *Journal of Building Engineering*, *86*, p.108861

[2] Chen, B., Liu, M., Wang, Q., Wang, L., Guo, Q. and Zhou, S., 2025. Analysis of industrial solid waste and the possibility of recycling and utilisation. *Green Chemistry Letters and Reviews*, *18*(1), p.2493155.

[3] Birgonda, S. and Senthilkumar, R., 2025. Long-term performance and phase characterisation of Quaternary Blended Self-Compacting Concrete incorporating IFSS aggregates: A multidisciplinary investigation. *Journal of Building Engineering*, *102*, p.111966.

[4] Li, L., Shao, X. and Ling, T.C., 2023. Life Cycle Assessment of Coal Gangue Composite Cements: From Sole OPC to Low-Carbon Quaternary Binder. *Journal of Cleaner Production*, *414*, p.137674.

[5] Kumar, P.R., Murthi, P. and Poongodi, K., 2024, June. Development of low-carbon binder from quaternary blending of cement for sustainable construction: A review on current materials, properties, and applications. In *AIP Conference Proceedings* (Vol. 3122, No. 1, p. 070003). AIP Publishing LLC.

[6] Zhang, J., Li, S. and Li, Z., 2020. Investigation of the synergistic effects in quaternary binder containing red mud, blast furnace slag, steel slag and flue gas desulfurization gypsum based on artif neural networks. Journal of Cleaner Production, 273, p.122972.

2025 HOW

4th International Symposium on One Health, One World
November 20 – 22, 2025

ABS ID: 203
Code No: IMSBE-OP-05

Durability Performance of Co_2 Sequestered Recycled Aggregates

M.R. Rahman[1], N. Mansuri[2], And K.S. Kulkarni[3]
[1] *Senior Scientist, ACSC, CSIR-Central Building Research Institute, Roorkee, India,*
[2] *Project Associate, ACSC, CSIR-Central Building Research Institute, Roorkee, India,*
[3] *Senior Scientist, APEE, CSIR-Central Building Research Institute, Roorkee, India,*
Correspond to M.R. RAHMAN (reyaz.cbri@csir.res.in)

***Keywords**: Recycled aggregate, Durability, Carbonation, Sequestration, CCUS, C&D waste.*

ABSTRACT

Global warming stands as one of the most significant environmental challenges globally, primarily driven by the increasing concentration of greenhouse gases in the atmosphere. Carbon dioxide (CO_2) is the most abundant greenhouse gas on Earth, and its atmospheric level is rising at an accelerating pace due to infrastructure development and industrial emissions. Construction and demolition (C&D) waste is another challenge for the environment again due to newer infrastructure coming up and old construction getting demolished. Recycled aggregates (RAs), derived from C&D waste, offer a sustainable alternative to finite natural resources. A promising and increasingly important method for waste valorization is the process of mineral carbonation. This technology chemically locks carbon dioxide (CO_2) into a stable, solid form, simultaneously improving the material properties of the RA. In this work, concrete prepared using CO_2 sequestered recycled aggregates have been investigated for durability properties under aggressive chemical environment by exposing them to sulphate, acid and chloride ingress after curing. The performance in terms of water absorption, compressive strength and weight change has been evaluated at various age till 90 days. It is concluded that CO_2 sequestration on recycled aggregate is a viable, cost-effective, and eco-friendly method for future decarbonization efforts.

1. INTRODUCTION

The issue of global warming and climate change caused by increasing greenhouse gases mainly carbon dioxide (CO_2) is a point of concern in present world. Therefore, it is imperative to reduce greenhouse gas emissions, especially CO_2 [1]. One potential approach involves implementing strategies such as carbon capture utilization and storage (CCUS), which enable the capture and long-term storage of emitted CO_2. At the same time, the global construction industry faces a dual challenge of managing the immense volume of waste generated by demolition activities of concrete structures while simultaneously reducing its substantial carbon footprint and resource depletion [2]. The major challenge with construction and demolition (C&D) waste management lies in its volume, complexity, and often, inadequate infrastructure for handling and processing it. Production of recycled aggregates from C&D waste provides a significant solution in mitigating C&D waste issues and growing demand for aggregates for future construction [3]. Recycled aggregates are generally found to be adhered with cement paste and mortar from previous concrete. The adhered cement mortar, which is rich in calcium hydroxide and calcium silicate hydrate, is regarded as a promising calcium source for CO_2 sequestration [4]. The sequestration of CO_2 in cement-based materials, such as recycled concrete aggregate, occurs through a process known as carbonation. This is a chemical reaction in which CO_2 reacts with the alkaline compounds present in the cementitious materials leading to the formation of thermodynamically stable carbonate minerals. The recycled aggregate is found to have improved physical and mechanical properties after CO_2 sequestration [5].

To enhance the efficiency and speed of this natural process, several methods of accelerated carbonation have been developed. One common approach is to treat the recycled aggregates with pressurized CO_2 in a controlled environment. Pre-treatment with other calcium-rich solutions, such as calcium

hydroxide, can further improve the properties of recycled aggregates and the concrete in which they are used [6]. Pressurized carbonation, such as at a pressure of 0.10 MPa, has been shown to produce a large quantity of calcite on the surface of the aggregates, which provides nucleation sites for C-S-H and contributes to the formation of stable calcium carbonate [7]. Beyond treating the aggregates themselves, CO_2 sequestration can also be achieved by injecting the gas directly into fresh concrete during the mixing process or by curing precast concrete products in a CO_2-rich atmosphere. In both scenarios, the gaseous CO_2 diffuses into the fresh concrete and is transformed into solid calcium carbonates, filling the pore spaces [8]. The porosity of recycled aggregates, which is typically seen as a defect, provides a greater number of reaction sites and a more extensive network for CO_2 diffusion and precipitation. Thus, the very characteristic that makes recycled aggregates weaker actually makes them a more effective medium for carbon sequestration. The process of carbonation, by filling these pores with solid carbonates, directly addresses and remedies the material's primary weakness [9].

2. MATERIALS AND METHOD

The material used in this study includes OPC (43 grade), natural aggregates (coarse and fine) and recycled concrete aggregates (coarse and fine). Locally available natural crushed stone of maximum nominal size 20 mm and 12.5 mm were used as coarse aggregate. Locally available natural river sand was used as the natural fine aggregate (NFA) in dry condition confirming to IS: 383. The recycled coarse and recycled fine aggregates were obtained from a commercial recycling plant at Burari, New Delhi. The specific gravity and water absorption of 20 mm natural coarse aggregate (NCA) was 2.61 and 0.70 % respectively. For 12.5 mm NCA the specific gravity and water absorption was 2.58 and 1.30 % respectively while for NFA it was 2.5 and 2.05 % respectively. NCA and NFA were used to prepare the control concrete mix. The recycled coarse aggregate (RCA) and recycled fine aggregate (RFA) were used to produce recycled aggregate concrete (RAC). These recycled aggregates both coarse and fine were exposed to CO_2 in a carbonation chamber for 24 hours at 30°C, 60% relative humidity and 10 % CO_2 concentration. These carbonated recycled concrete aggregates were used to make carbonated recycled aggregates concrete (CRAC). The specific gravity and water absorption of recycled concrete aggregates are given in Table 1.

Table 1. Properties of recycled concrete aggregates

Property	RCA		RFA	
	Before carb.	After carb.	Before carb.	After carb.
Sp. gravity	2.46	2.43	2.24	2.27
Water abso (%)	4.17	3.67	6.36	5.87

Concrete cubes of size 100 mm were casted with control concrete (NAC), RAC and CRAC mixes for immersion into the aggressive chemical solution and compression test. The durability performance of all the mixes has been studied under exposure to sulphate

(a)

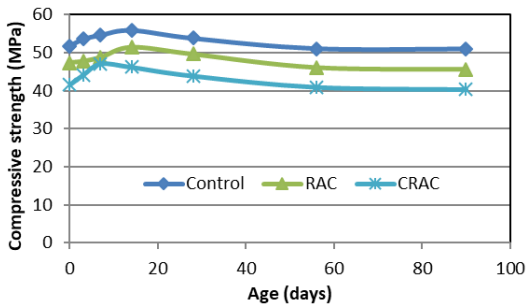

(b)

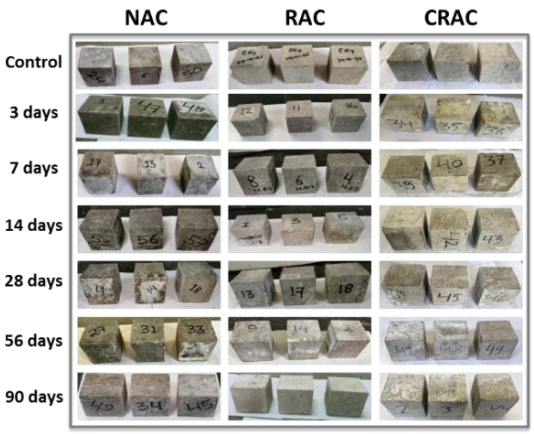

Fig. 2 Cube specimens exposed to sulphate attack and compressive strength after exposure

attach ($MgSO_4$) and acid resistance (H_2SO_4). The test specimens were immersed in magnesium sulphate ($MgSO_4$) solution with 5% concentration in a plastic tank (Fig. 1). The volume proportion of sulphate solution to specimens is kept 4:1. The specimens were also soaked in 2% sulphuric acid (H_2SO_4) solution with measured pH of < 2. The concentrated sulphuric acid (98% concentration) is used to prepare 2% concentrated solution. The durability performance of the concrete mixes has been evaluated based on the change in compressive strength and the change in mass after 3, 7, 14, 28, 56 and 90 days of immersion. Corrosion in reinforcement happens after the dissolution of the passive layer on the outer surface of the reinforcement mainly due to the ingress of chloride ions into the concrete.

Fig.1Cubes kept for durability study in the acid solutions

In order to access the chloride ion ingress in concrete a quick test known as rapid chloride penetration test (RCPT) is used. For RCPT disc specimens of 100 mm diameter and 50 mm thickness were prepared from all the mixes. In this study RCPT is conducted for all the mixes as per ASTM C 1202.

3. RESULTS AND DISCUSSION

The durability of a material has a significant influence on its service behaviour, design life and safety. The deterioration of materials may occur through a variety of chemical or physical processes, especially when it is exposed to aggressive environment.

Effect of $MgSO_4$

Fig. 2a shows the surface of cubes taken out from sulphate solution after different exposure duration. On visual inspection, it is found that the samples exposed to sulphate solution are intact and free from cracks or pits. No deposition of salt has taken place on the surface. Fig. 2b shows the compressive strength of all the mixes after different exposure duration. It is found that there is an initial gain in strength till 14 days in control and RAC mixes and in CRAC mix the strength gain is till 7 days. After this there is gradual decrease in strength in all the mixes. The initial gain in strength is primarily due to the formation of expansive reaction products such as ettringite and gypsum that fill the original pore structure, leading to densification. Once all the available pore space is filled, the continuing crystallization and expansion of ettringite and gypsum generate significant internal tensile stresses. These stresses exceed the tensile strength of the concrete, causing micro-cracking, followed by cracking, spalling, and mass loss. This ultimately leads to progressive reduction in strength and durability.

Effect of H_2SO_4

The samples exposed to acid attack are also examined continuously and on visual inspection, it is noticed that there is a white deposit on the surface due to dissolution of surface layer of the cubes (Fig. 3a). The compressive strength of samples after different exposure duration in sulphuric acid is shown in Fig. 3b. It is observed that there is rapid strength loss upto 14 days in all the mixes and after that the loss in strength was slow. After an exposure of 90 days the control mix lost 23% of its strength while RAC and CRAC lost about 18% and 15% of its strength respectively. The strength loss is due to rection of acid with paste materials in concrete causing its dissolution. The dissolution of the paste material increases the porosity and creates a soft, degraded layer, which can be easily washed away or spalled off, exposing fresh concrete to further attack.

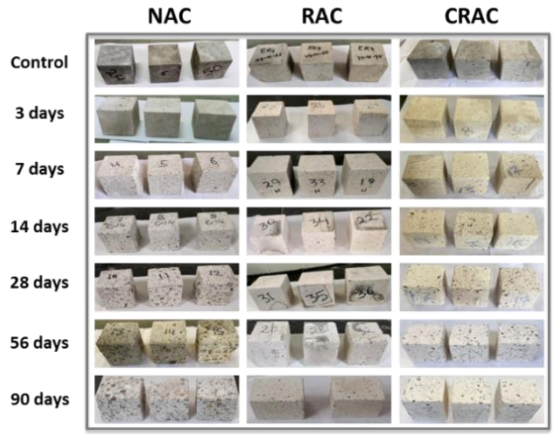

(a)

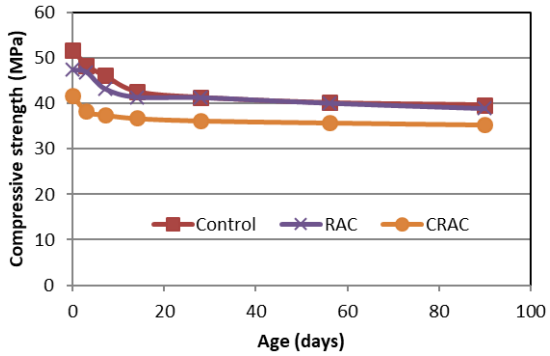

(b)

Fig. 3 Cube specimens exposed to acid resistance and compressive strength after exposure

Effect on weight change

The weight measurement was also taken after each exposure time for all the mixes (Fig. 4). The samples immersed in $MgSO_4$ gained weight up to a level of 0.7%, being maximum in the RAC mix. It is noticed that weight gain in the samples increases up to 28 days immersion and then flatten out with the subsequent exposure. In contrary to this, samples exposed to H_2SO_4 solution continuously lost weight with slight gain in weight at 3 days and after 90 days the maximum weight loss was in control mix (2.9%) while in CRAC weight loss was found to be about 1.6%.

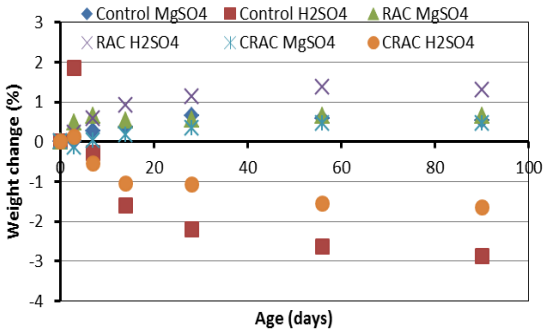

Fig. 4 Weight change in different mixes with exposure time

Chloride ion penetration

The Rapid Chloride Permeability Test (RCPT) is conducted as per ASTM C1202 (Fig. 5) for control concrete, RAC and CRAC mixes to assess a concrete's resistance to chloride ion penetration which is a primary cause of steel reinforcement corrosion and structural deterioration. For this disc specimens of 100 mm diameter and 50 mm thickness cured for 28 days. Before the test pre-conditioning of specimens is done using a vaccum pump set-up. The RCPT is then performed as per standard by applying a voltage of 60 V across the specimen in the cell which is filled with 0.3 N NaOH on one side and 3% NaCl solution on the other side. The current is recorded after 30 minute interval for 6 hours. Then the charge passed is calculated for each mix. It is found that the charge passed in control mix is lowest and in CRAC it was more than control mix but considerably lower than the RAC mix (Table 1). This is due to the dense pore structure of the CRAC mix compared to RAC as a result of aggregate carbonation. CRAC benefits from densification of the ITZ and the matrix due to $CaCO_3$ formation during carbonation, which impedes chloride ion movement. All the mixes are found to be under 'low' chloride ion penetrability category.

Fig. 5 Rapid Chloride Permeability Test

Table 1. RCPT values

Mix	**Charge passed** (coulombs)	**Chloride ion penetrability**
Control	1822.97	Low
RAC	1880.36	Low
CRAC	1839.95	Low

4. CONCLUSIONS

Following conclusions are made from this study on durability performance of concrete made using recycled concrete aggregate that has been exposed to CO_2.

- The CO_2 exposure of RCA lead to reduction in the water absorption due to filling of the pores in the adhered mortar present outside the RCA by the carbonate precipitation.
- Under magnesium sulphate solution, all the concrete mixes gained strength initially and after 90 days of exposure there is not much significant deterioration in the compressive strength.
- Suplhuric acid has a corrosive effect on the surface of concrete in initial exposure

period and rapid strength loss due to dissolution of C-S-H and calcium hydroxide.

- Chloride ion penetrability of all the mixes was characterized as low as per ASTM with much improvement in chloride ion penetration resistance of CRAC over RAC.
- CO_2 sequestration in RCA is a viable solution for CO_2 mitigation from atmosphere and valorization of RCA for sustainable infrastructure development.

REFERENCES:

[1] A. Parekh, G. Chaturvedi, A. Dutta, Sustainable Energy Tech. Assessments 55 (2023) 102942.

[2] M.A.T. Alsheyab, Int. J. Env. Sci Tech. 19(3) (2022) 2129-2138.

[3] S. Ghaffar, Hamidreza, M. Burman, N. Braimah. J. clean. Prod. 244 (2020) 118710.

[4] P.M. Borges, J.Z. Schiavon, S.R. da Silva, E. Rigo, A.N. Junior, E. Possan, J.J.O. Andrade, Const. Build. Mater. 387 (2023) 131600.

[5] B. Zhan, C.S. Poon, Q. Liu, S. Kou, C. Shi. Const. Build Mater 67 (2014) 3-7.

[6] W. Jun, D. Yahong, X. Ping, Z. Meixiang, G. Meng, G. Shuqi, Ceramics-Silikáty 66(1) (2022) 113-127.

[7] K. Liu, W. Xu, D. Sun, J. Tang, A. Wang, D. Chen, Materials Express 11(9) (2021): 1439-1452.

[8] D.S. Gill, S.M. Abraham. Materials Today: Proceedings (2023).

[9] S. Kashef-Haghighi, S. Ghoshal. Indust. Eng. Chem. Res. 52(16) (2013) 5529-5537.

4th International Symposium on One Health, One World
November 20 – 22, 2025
ABS ID: 156
Code No: IMSBE-OP-06

Comparative Assessment of Corrosion Susceptibility in E450 Carbon Steel And 450 Cr Stainless Steel Under Accelerated Exposure Conditions

A. Sharma[1], P.C.A Kumar[2], And G.P Chaudhary[3]
[1] *Research Scholar, IIT, Roorkee, India,*
[2] *Assistant Professor, IIT, Roorkee, India,*
[3] *Professor, IIT, Roorkee, India,*
Correspond to A. Sharma (aashima_s@eq.iitr.ac.in

***Keywords**: ASTM G31, corrosion, IRS-450CR, stainless-steel.*

1. INTRODUCTION

Corrosion is a critical degradation mechanism that significantly undermines the durability and safety of steel structures, particularly when exposed to aggressive service environments. The susceptibility of structural steels to corrosion directly affects their load-bearing capacity, service life, and maintenance requirements [1], [2]. E450 carbon steel and equivalent grade have been widely used for structural applications due to their strength and economic viability; however, their resistance to corrosion is limited under aggressive marine conditions. Frequent repainting and maintenance costs are generally quite higher. To address these limitations, ferritic–martensitic stainless steels such as IRS-450CR have been developed, offering improved corrosion resistance while maintaining adequate mechanical properties for infrastructure use.

A systematic comparison of the corrosion susceptibility of these two grades is essential for informed material selection in bridges, railways, and coastal structures where exposure to accelerated deterioration processes is inevitable. Previous studies have primarily focused on mechanical performance or generalized corrosion rates, but detailed experimental assessment under controlled accelerated environments remains limited. Moreover, comparative mass loss and surface degradation data are necessary to establish quantifiable benchmarks for service performance.

This study aims to experimentally evaluate and compare the corrosion susceptibility of E450 carbon steel and IRS-450CR stainless steel under accelerated exposure conditions. Controlled laboratory experiments were performed to simulate immersed corrosive environments, and weight-loss measurements were systematically recorded at different intervals. By analyzing the progression of mass loss, surface morphology, and relative susceptibility indices, this work provides critical insights into the comparative degradation behaviour of the two grades. The findings are intended to support the development of predictive models for service life estimation and guide material selection strategies for long-term structural durability.

2. EXPERIMENTAL DATA

The specimens were cut to a size of 20 mm x 50 mm along the rolling direction as per provisions given in ASTM G31[3]. Before immersing, the specimens were polished with emery paper and then kept in a 3.5% NaCl solution for 7 days, 14 days and 28 days. During the corrosion duration, samples are regularly stirred and oxygenated by an air diffusing pump. After respective days of immersion, the samples are cleaned as per the standard solutions given in ASTM G01[4]. The specimens are weighed, and the mass loss has been calculated. The corrosion rate is calculated as per equation 1:

$$CR = (k \times w)/ (A \times T \times D) \qquad \textit{Equation 1}$$

Where k is a constant, w is weight loss in g, A is exposed area in cm^2, T is time in hours, D is density of material in g/cm^3. Table 1 demonstrates the chemical composition of both E450 carbon steel and IRS450CR stainless steel.

Table 1: Chemical composition of E450 and IRS-450CR

Chemical composition	E450	IRS-450CR
%C	0.182	0.020
%Mn	1.460	1.260
%S	0.0031	0.003
%P	0.0124	0.030
%Si	0.325	0.520
%Ni	<0.005	0.840
%Cr	0.0042	11.30
%N	-	0.032
%Mo	<0.005	0.240
%Al	0.0223	-
%Nb	0.0469	-
%V	0.0418	-
%Ti	0.0065	-

3. RESULTS

Fig.1 shows the mass loss and corrosion rate values for both E450 and the IRS-450CR grade. It is observed from the results that with the passage of time, the mass values increase for both grades. Also, the comparative analysis showed that the E450 grade shows higher mass loss in comparison to IRS-450CR. After 7 days, E450 is 86.4% more susceptible to corrosion than IRS-450CR and this value reduces to

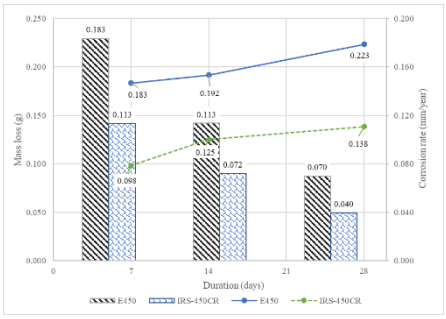

Figure 1:Mass loss and corrosion rate for E450 and IRS-450CR

61.4% after 28 days. The corrosion rate values also tend to reduce with the passage of time. The highest value of corrosion rate is 0.183 mm/year and 0.113 mm/year for E450 and IRS-450CR after 7 days of corrosion. This value reduces to 0.070 mm/year and 0.040 mm/year after 28 days for E450 and IRS-450CR respectively. The reason behind this behaviour is the passivity provided in stainless steel due to the formation of a chromium oxide layer. But in carbon steels, no passive layer formation takes place, so the rust layer formed on the surface acts as a barrier between the uncorroded steel and the corrosive environment. This causes the corrosion rate to reduce until the passive layer and the rust layer protection are breached by some chemical or mechanical process. The higher mass loss in E450 leads to a major reduction in cross-sectional area, ultimately affecting the mechanical properties of the material. Further, prolonged exposure could lead to pitting on the surface of the material, which could change the fracture behavior and leads to prior failure [5].

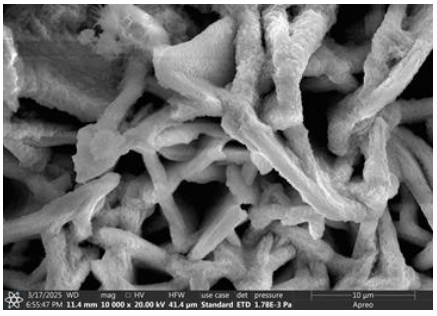

a)

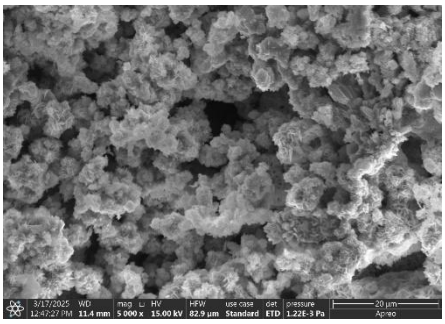

b)

Figure 2: Morphology of a) Lepidocrocite and b) goethite

The corroded samples are also tested for rust morphology in a scanning electron microscope (SEM). Figure 2 shows the general morphology of the rust product observed in both carbon and stainless-steel grades observed. Lepidocrocite, a needle-shaped structure and goethite, a globular structure, are the oxidised forms of iron [6]. Lepidocrocite is formed in the initial days of corrosion and goethite, a more stable form, is found in more rusted situations. There are various other morphological features formed in rust layer of carbon and stainless

steel, but a long-term experiment is required to analyze those features.

4. CONCLUSIONS

The study was conducted to understand the material behavior in a corrosive environment, which helps in choosing a better material for structural applications in harsh environmental conditions. The following conclusions can be drawn from the study:

a) IRS-450CR is more corrosion resistant than E450 grade steel. After 28 days of immersion, E450 shows 61.4% more mass loss than IRS-450CR.

b) General morphology observed in both the steel grades is lepidocrocite and goethite.

The study concluded that IRS-450CR stainless-steel is a better material in comparison to E450 carbon grade in highly corrosive conditions.

REFERENCES:

[1] A. Cinitha, P. K. Umesha, and N. R. Iyer, “An overview of corrosion and experimental studies on corroded mild steel compression members,” KSCE J. Civ. Eng., vol. 18, no. 6, pp. 1735–1744, 2014, doi: 10.1007/s12205-014-0362-0.

[2] X. Zhang, S. Zheng, and X. Zhao, “Experimental and numerical study on seismic performance of corroded steel frames in chloride environment,” *J.* Constr. Steel Res., vol. 171, p. 106164, 2020, doi: 10.1016/j.jcsr.2020.106164.

[3] NACE TM0169/G31, “Standard Guide for Laboratory Immersion Corrosion Testing of Metals,” 2021.

[4] ASTM G1-03, "Standard practice for preparing, cleaning, and evaluating corrosion test specimens.”

[5] J. Xing, D. Dilixiati, N. Yang, and Q. Yang, “Fracture properties of corroded steel under monotonic tension load,” Constr. Build. Mater., vol. 437, no. December 2023, p. 136918, 2024, doi: 10.1016/j.conbuildmat.2024.136918.

[6] D. de la Fuente, I. Diaz, J. Simancas, B. Chico and M. Morcillo, “Long term atmospheric corrosion of mild steel”,Corros. Sci., vol. 53, no. 2, pp 604-617,2011, doi: 10.1016/j.corsci.2010.10.007.

4th International Symposium on One Health, One World
November 20 – 22, 2025

ABS ID: 157
Code No: IMSBE-OP-07

Decarbonising The Cement and Construction Sector Using Low Carbon Cementitious System

P N Ojha[1], Puneet Kaura[2], Brijesh Singh[3], Amit Trivedi[4], Arup Ghatak[5] and L P Singh[6]
[1]*Joint Director, National Council for Cement and Building Materials, Ballabgarh, India*
[2] *Group Manager, National Council for Cement and Building Materials, Ballabgarh, India*
[3]*General Manager, National Council for Cement and Building Materials, Ballabgarh, India*
[4]*Joint Director, National Council for Cement and Building Materials, Ballabgarh, India*
[5]*Group Manager, National Council for Cement and Building Materials, Ballabgarh, India*
[6]*Director General, National Council for Cement and Building Materials, Ballabgarh, India*
Correspond to Puneet Kaura (puneet.kaura@ncbindia.com)

Keywords: *Low-carbon cement, clinker substitution, composite cement, limestone, calcined clay, LD slag.*

Abstract

The cement and construction sector is a major contributor to global greenhouse gas emissions, with Ordinary Portland Cement (OPC) production accounting for approximately 6-7% of anthropogenic CO_2 emissions. In order to cater environmental concerns and regulatory pressures of cement and construction sector, significant research has been directed toward the development of low-carbon cementitious systems which is considered to be one of the important levers to reduced carbon footprint. The present study explores several alternative cement formulations - fly ash - slag composite cement, Portland limestone cement (PLC), Portland limestone calcined clay cement (PLCCC), LD slag-based Portland slag cement, and fly ash-limestone composite cement-as viable solutions for decarbonising the sector.

Experimental investigations focused on reducing the clinker factor through the incorporation of supplementary cementitious materials (SCMs) such as fly ash, ground granulated blast furnace slag (GGBS), calcined clay, Linz Donawitz (LD) slag and alternative materials such as ground limestone. Fly ash-slag composite cement blends with clinker content ≥ 45%, fly ash 10-25%, and GGBS 25-40% demonstrated performance on par with or superior to Portland Pozzolana Cement (PPC), particularly in terms of durability and resistance to carbonation-induced corrosion. PLC, with up to 15% finely ground limestone, met required standards for mechanical and durability performance, provided the overall fineness of cement exceeded 425 m²/kg. PLCCC showed significant CO_2, reduction potential-up to 30% lower than OPC-while maintaining early strength and improving microstructure. LD slag, when used to partially replace GGBS, produced Portland slag cement with acceptable performance with compared to control PSC. Fly ash-limestone composite cement, incorporating 60-65% clinker, 15-30% fly ash, and 5-10% limestone, yielded durable and sustainable concrete mixes.

The results affirm that low-carbon cementitious systems can significantly reduce environmental impact without compromising durability of concrete. These findings support the revision of existing standards and promote broader adoption of sustainable binders in modern construction, aligning with global decarbonisation objectives.

1.INTRODUCTION

The global construction industry, particularly the cement sector, is one of the most carbon-intensive industrial activities, contributing approximately 6–7% of global anthropogenic carbon dioxide (CO_2) emissions through Ordinary Portland Cement (OPC) production alone [1]. This substantial carbon footprint arises primarily from the calcination of limestone and the high energy consumption

associated with clinker production, the key constituent of OPC. As the world grapples with accelerating climate change and environmental degradation, decarbonising the cement and construction industry has become an urgent priority [2]. In response to these concerns, research has intensified around developing low-carbon cementitious materials that reduce clinker content by integrating supplementary cementitious materials (SCMs) such as fly ash, ground granulated blast furnace slag (GGBS), calcined clay, and industrial by-products like LD slag. These alternatives not only lower the carbon footprint but also enhance the durability and performance of concrete when optimally formulated [3]. Moreover, incorporating locally available materials like LD slag and ground limestone enhances the sustainability and economic viability of these solutions. By facilitating wider acceptance of such low-carbon binders, the construction sector can align more closely with international sustainability frameworks and national carbon neutrality targets [4]

In the present work, five different types of low carbon cementitious system were formulated and studied for its application in concrete, the details of the same are mentioned below

i. Fly ash - slag composite cement,
ii. Portland limestone cement (PLC),
iii. Portland limestone calcined clay cement (PLCCC),
iv. LD slag-based Portland slag cement, and
v. Fly ash-limestone composite

2.DEVELOPMENT OF LOW CEMENTITIOUS SYSTEMS

2.1 Development of Fly ash –slag composite cement

Developing Low-Portland clinker cement is one of the best solutions, the cement industry can offer to reduce CO_2 emissions. Composite cement is a low-clinker cement in which a combination of fly ash and granulated slag replaces a significant proportion of the clinker. In India, composite cement typically consists of 35%-65% Portland cement clinker/ ordinary Portland cement (OPC) along with 15%-35% fly ash and 20%-50% GBFS. However, using composite cement with such a varied clinker content may not be suitable for RCC structures due to potential carbonation and carbonation-induced corrosion issues. The study conducted by researchers like V V Arora et al. [5], and Cheah et al. [6] shows insignificant improvement in the microstructure of the composite cement blends made by various combinations of fly ash and slag. This is mainly due to the formation of secondary C-S-H gels due to pozzolanic reaction at the later ages that creates a closely-packed geometry, contributing to further densification of the binder phase matrix. However, replacing the Portland cement clinker significantly with fly ash and slag will also influence the pore chemistry. Although the carbonation process has been studied extensively, the behaviour of rebar in carbonated concrete has not gained adequate attention. To investigate this, a study was conducted using five possible specifications of composite cement. Ten concrete mixtures of composite cement were designed at a 0.60 water-cement ratio. The performance of these mixtures against carbonation and carbonation-induced corrosion was compared to concrete mixtures made with Portland Pozzolana Cement (fly ash based) and Portland Slag Cement (PSC). The compressive strength study was carried out at two ages, i.e., 7 days and 28 days, and the results are mentioned in Table 1. From the study, it was observed that compressive strength values are influenced by parameters like percentage of OPC content and fly ash content. Further, it was also observed that when OPC content is > 50%, the composite cement mixes had compressive strength at par with concrete mixes designed with conventional Portland systems like OPC, PPC, and PSC [7]. It was recommended to keep OPC content at least 50% or clinker content at least 45%, fly ash in the range of 10-25% and GGBS in the range of 25-40 % to achieve performance equivalent or better than PPC.

Table 1. Compressive strength, carbonation depth and corrosion rate of concrete

S.No.	Composition (OPC:FA:GGBS)	water cement ratio = 0.60					
		Compressive Strength (MPa)		Carbonation Depth (mm) at exposure period of		carbonation front progress from 70 days to 140 days in mm (B-A)	Corrosion rate when carbonation front reaches beyond 22 mm (in mm/yr)
		7-day	28-day	70 days (A)	140 days (B)		
1	Control	22.6	26.0	9.97	16.40	6.43	0.0057
2	65:35:00	13.0	20.8	17.00	26.34	8.62	0.0063
3	40:0:60	19.7	27.9	15.25	23.87	9.34	0.0065
4	35:15:50	14.7	22.0	22.15	33.62	11.47	0.0109
5	35:25:40	11.0	21.8	24.93	37.56	12.63	0.0098
6	40:10:50	19.2	24.0	17.53	27.09	9.56	0.0087
7	40:25:35	17.9	23.1	19.92	30.47	10.55	0.0075
8	45:10:45	18.8	28.9	15.92	24.81	8.89	0.0064
9	45:25:35	15.6	25.2	17.39	26.89	9.50	0.0058
10	50:10:40	23.0	28.6	12.92	20.57	7.65	0.0055
11	50:25:25	19.0	27.7	14.93	23.41	8.48	0.0048
12	55:10:35	21.4	28.0	10.45	17.08	6.63	0.0041
13	55:25:20	16.6	26.5	12.50	19.98	7.48	0.0039

2.2 Development of Portland limestone cement

Portland Limestone Cement (PLC) is a type of blended cement that incorporates a significant amount of finely ground limestone into the cement matrix. Typically, PLC contains between 5% and 35% limestone by mass, mixed with Portland cement clinker and gypsum. The inclusion of limestone improves the cement's workability, reduces its heat of hydration, and enhances durability while lowering its carbon footprint compared to traditional Portland cement [8,9]. Previously conducted studies in NCCBM shows that limestone addition influences the mechanical as well as the durability behaviour of mortar and concrete [10]. To achieve performance comparable to conventional Portland cement based concrete it was suggested that appropriate quality of limestone up to 15% with a resultant fineness of more than 425 m^2/kg should be used. For the verification and validation of the conclusions drawn from the previous study, additional study on Portland limestone cement (PLC) was carried out on 8 concrete mixes. Some of the results of the study are shown in fig. 1 and fig. 2. On the basis of present test results corresponding to mechanical as well as durability aspect, it can be concluded that PLC blends designed with limestone content up to 15 %, overall fineness of PLC blends as well as limestone more than 425 m^2/kg and 600 m^2/kg respectively, performance of the concrete is at par to that of concrete made with OPC.

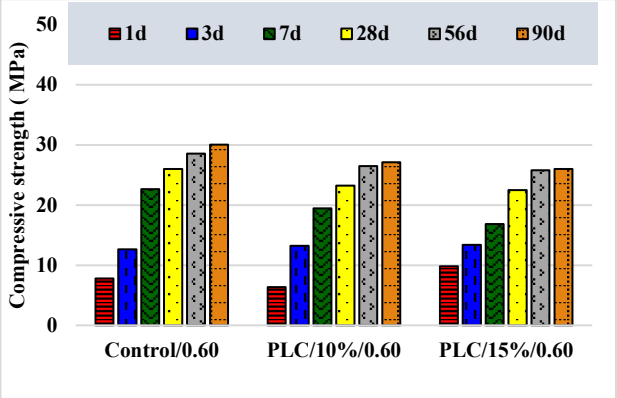

Figure 1. Compressive strength development in concrete mixes at various ages

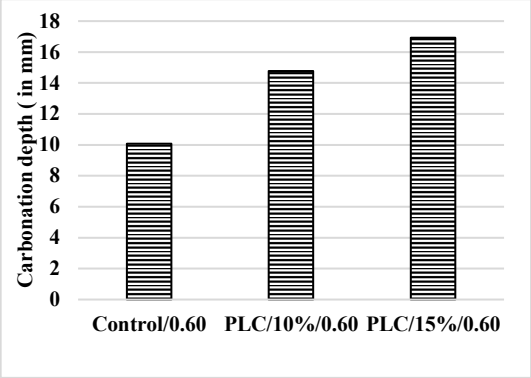

Figure 2. Carbonation depth of concrete mixes

2.3 Development of Portland limestone calcined clay cement

Ternary cements with low clinker contents have been demonstrated to be technically and environmentally beneficial in many scenarios. The manufacture of ternary cements through inter-grinding of its components requires that sufficient care is taken to ensure that all constituents are ground to requisite fineness. Individual constituents, especially clinker, remaining coarse after grinding can significantly hamper the performance of the cement. The advantage of Portland calcined clay limestone cement is known to be the dual hydration of its additions, namely, the formation of calcium alumino-silicate hydrate from the hydration of calcined clay with lime and the formation of carbo-aluminate phases from the hydration of limestone with aluminates from the calcined clay and clinker [11]. The production of these solid hydration products improves the mechanical properties and durability of the cement at relatively lower clinker content.

Recently, based on the work done by IIT-Delhi as well as NCCBM, code on Portland Limestone Calcined Clay Cement was published by BIS. Some of the highlights of the specifications are as follows:

1. Portland Cement Clinker::The content of Portland cement clinker should be between 50% and 80% by mass of the total binder content.
2. Calcined Clay: The calcined clay should be between 10% and 35% by mass of the total binder content.
3. Limestone: The limestone should constitute between 5% and 20% by mass of the total binder content.

2.4 Development of LD slag based Portland Slag cement

LD slag is a by-product of primary steel making in the basic oxygen furnace (BOF) and therefore it is also known as BOF slag. At present, granulated Blast Furnace Slag (GBFS) is used for preparation of PSC along with clinker and gypsum. GBFS is amorphous in nature and has amorphous content in excess of 90%. Whereas, amorphous content in LD slag is in the range of only about 10-30%. Due to significantly lower amorphous content, LD slag cannot be used alone for manufacturing PSC along with clinker, as minimum specified value of amorphous content in slag to be used in the manufacture of PSC as per Indian Standards is 85%. Therefore, in order to investigate the utilization of LD slag in the preparation of PSC, LD slag shall be used as partial replacement the granulated BF slag for preparing PSC. In view of above, NCCBM carried out experimental investigations to utilize LD slag as partial replacement of granulated BF slag for preparing composite slag which will subsequently be used for preparation of Portland Slag Cement (PSC) [12]. The study aimed to investigate the possibility to utilize LD slag as one of the cementitious materials for preparation of composite slag (having 8% and 15% LD slag) which will subsequently be used for manufacturing Portland slag cement (PSC). PSC samples (having overall 4% to 9% LD slag) were prepared using LD slag from two sources in a laboratory ball mill. PSC samples were analysed for various chemical characteristics and physical properties. All the PSC

samples containing LD slag showed their conformance to the chemical and physical requirements of PSC as specified in Indian standard (IS 455:2015) with comfortable margin and comparable to control PSCs. Studies were conducted on concrete mixes prepared at water to cement ratio of 0.65 and 0.40. All the fresh, hardened and durability properties of concrete mixes prepared using experimental PSCs made with composite slag having up to 15% LD slag, were found to be comparable with their corresponding control mixes prepared using control PSCs.

2.5 Development of Fly Ash-Limestone composite cement

Fly ash-limestone composite cement represents a significant advancement in the field of concrete technology, combining the benefits of both fly ash and limestone powder to enhance the performance and sustainability of concrete. NCB has conducted a detailed investigation on the mechanical and durability aspects of concrete made with Fly ash-limestone composite cement [13,14]. A total 24 mixes were cast using two type of limestone used = Cement grade (L) and Dolomitic limestone (D) with overall fineness of cement was kept in the range of 400-410 m^2/kg. Some of the test results are shown in fig.3 and fig.4.Based on the mechanical as well as durability test results, especially carbonation as well as carbonation induced reinforcement corrosion, it was recommended to keep OPC content at least 65% or clinker content at least 60%, fly ash in the range of 15-30% and limestone in the range of 5-10 % to achieve performance equivalent or better than PPC.

By incorporating fly ash-limestone composite cement into concrete mixes, builders and engineers can achieve a more durable, sustainable, and cost-effective construction material. This approach not only enhances the performance characteristics of concrete but also supports broader environmental goals by reducing reliance on traditional Portland cement and utilizing industrial by-products.

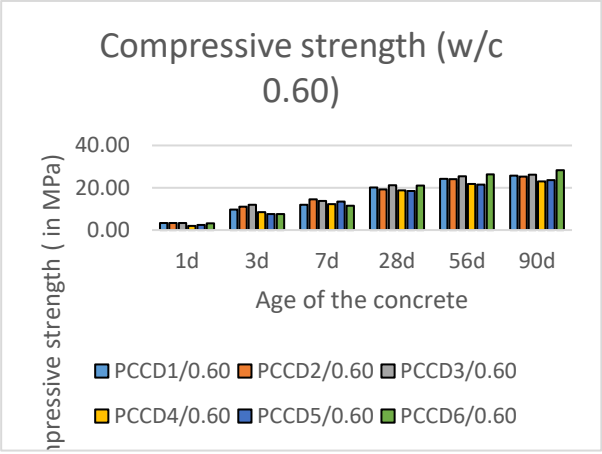

Figure 3. Compressive strength (in MPa) of concrete mixes made with Portland fly ash limestone cement (Dolomitic limestone) at 0.60 w/c

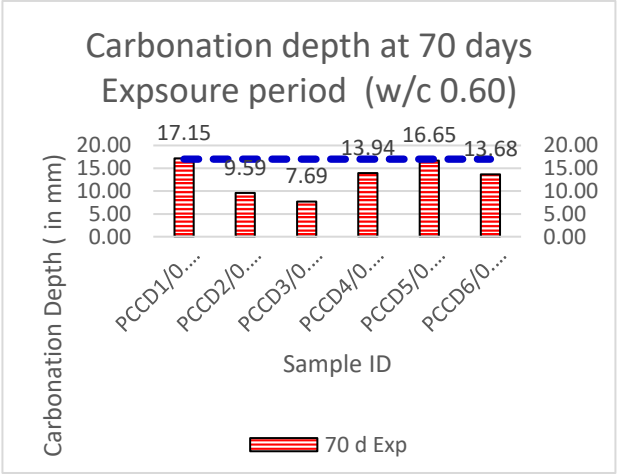

Figure 4. Carbonation depth of concrete mixes made with Portland fly ash limestone cement (Dolomitic limestone) at 0.60 w/c

3.CARBON FOOT PRINT OF THE LOW CARBON CEMENTITIOUS SYSTEM

The carbon footprint of cementitious materials is primarily dictated by the amount of clinker present, as clinker production is responsible for approximately 90% of the total CO_2 emissions in Ordinary Portland Cement (OPC) manufacture [15]. Low-carbon cementitious systems aim to significantly reduce this footprint by substituting a portion of the clinker with supplementary cementitious materials (SCMs) such as fly ash, slag, calcined clay, and ground limestone—each with substantially lower embodied emissions. In general carbon footprint is typically measured in tonnes of carbon dioxide equivalent (CO2e), often per year, while determining carbon print of the low carbon cementitious system as mentioned in table 2 following assumptions are considered [16-17]

Table 2. Carbon foot print of the conventional and low carbon cementitious system

Type of cementitious system	Clinker Content, %	Type of SCM or alternative materials, %					Carbon footprint Range (kg CO_2e / t)	Reduction % in comparison to OPC*
		Fly ash	GGBS	Limestone	Calcined clay	LD slag		
Portland Pozzolana Cement (PPC)	≥ 60	15-35	-	-	-	-	575 – 750	20 %– 40%
Portland Slag Cement (PSC)	≥ 25	-	25-70	-	-	-	235 – 700	25 %– 70%
Fly ash - slag composite cement	≥ 45	10-25	25-40	-	-	-	450-600	35%-55%
Portland limestone cement (PLC)	≥ 80	-	-	10-15	-	-	700 – 750	20%-25%
Portland limestone calcined clay cement (PLCCC)	50-80	-	-	5-20	10-35	-	450 – 800	30%- 50%
LD slag-based Portland slag cement	≥ 40	-	51	-	-	≤ 9	350 – 430	50% – 60%
Fly ash-limestone composite	≥ 60	15-30	-	10-15	-	-	490 -670	30% – 50%

*For Baseline study, Carbon footprint of OPC is assumed as 900 kg CO_2/t

- Clinker (calcination + fuel): 806 kg CO_2 per tonne clinker
- Typical values in case of SCM or filler
  - GGBS (ground granulated blast furnace slag) ≈ 42–70 kg CO_2 / t
  - Fly ash ≈ 27 kg CO_2 / t
  - Limestone (filler) ≈ 75 kg CO_2 / t
  - Calcined clay ≈ ~250 kg CO_2 / t
  - LD (steel) slag ≈ 50 kg CO_2 / t

4. CONCLUSION

The present investigation clearly establishes that the systematic reduction of clinker content, coupled with the judicious incorporation of supplementary cementitious materials (SCMs) such as fly ash, ground granulated blast furnace slag (GGBS), finely ground limestone, calcined clay, and LD slag, can deliver substantial benefits in terms of both performance and sustainability.

From a carbon footprint perspective, the clinker substitution strategy yielded notable reductions in embodied CO_2 emissions compared to OPC, which was taken as a baseline of approximately 900 kg CO_2/t. LD slag-based PSC (clinker ≥ 40%, GGBS 51%, LD slag ≤ 9%) and Fly ash–slag composite cement (clinker ≥ 45%, fly ash 10–25%, GGBS 25–40%) achieved the most significant reductions—up to 60% and 55%, respectively. PLCCC, with clinker contents as low as 50%, offered a balanced solution with up to 30% reduction in CO_2 emissions. PLC and Fly ash–limestone composites also demonstrated substantial savings, achieving reductions of up to 25% and 50%, respectively. These results confirm that low-carbon cementitious systems can deliver a two-fold benefit—ensuring durability of concrete while contributing meaningfully to national and global decarbonisation targets.

REFERENCES:

[1] P N Ojha, Brijesh.Singh, Puneet.Kaura, Abhishek Singh, Light Weight Geopolymer Fly Ash Sand: An

Alternative to Fine Aggregate for Concrete Construction" Research on Engineering Structures & Materials (2021).

[2] International Energy Agency (IEA), Cement – Analysis (2023), Retrieved from https://www.iea.org/reports/cement

[3] Scrivener. K. L., John.V. M., Gartner. E. M, Eco-efficient cements: Potential economically viable solutions for a low-CO_2 cement-based materials industry,Cement and Concrete Research (2018), 114, 2–26.

[4] United Nations Environment Programme (UNEP), Global Status Report for Buildings and Construction (2020), Retrieved from https://www.unep.org/resources/report/2020-global-status-report-buildings-and-construction

[5] V.V. Arora, Puneet.Kaura, Piyush.Mittal, Bikekananda.Mohapatra, Performance assessment of concrete made with ternary cementitious blends against chloride ingress and CO2 attack, Civil Engineering and Construction Review (May 2020)

[6] Cheah.Chee Ban, Ling. Ling. Tiong, Eng. Poh. Ng, Chuan. Wei. Oo, the engineering performance of concrete containing high volume of ground granulated blast furnace slag and pulverized fly ash with polycarboxylate-based superplasticizer, Construction and Building Materials 202 (2019): 909-921.

[7] P.N. Ojha, Puneet.Kaura, Carbonation and corrosion rate of concrete made with composite cement, 10th International Conference on Concrete under Severe Conditions – Environment and Loading (CONSEC24), Chennai, India,2024

[8] Puneet.Kaura, Brijesh.Singh, Ojha, P.N. Ojha, L.P. Singh,Performance of Portland limestone cements under sulphate environment,10th International Conference on Concrete under Severe Conditions – Environment and Loading (CONSEC24), Chennai, India,2024.

[9] P.N. Ojha, Brijesh.Singh, Pranay.Singh, Abhishek. Singh, Manish. Kumar. Mandre, Study on effect of fly ash and limestone powder on compressive strength of roller compacted concrete for dam construction, Asian Concrete Federation Journal (2022), Vol. 8(1), pp.37-50

[10] Puneet.Kaura, P.N. Ojha, Hardik.Jai,Mechanical and Durability performance of Portland limestone cement (PLC) made with intergrinding having high fineness limestone in concrete,17th NCB International Conference on cement, concrete and building materials, New Delhi, India,2019.

[11] Bishnoi.S, Standardisation of LC3 in India: Lessons and Way Forward for Global Acceptance. In International Conference on Calcined Clays for Sustainable Concrete (pp. 17-23). Cham: Springer Nature Switzerland (2022).

[12] P.N. Ojha., A.Singh., Brijesh.Singh., Sen.S. Kumar, B.M. Patra, Studies on Portland Slag Cement Made Using Blast-Furnace and Linz-Donawitz Slag. ACI Materials Journal (2023), 120(1).

[13] B.N.Mohapatra, Puneet.Kaura, P.N. Ojha, Brijesh.Singh, Sumit.Kumar, Varsha. Liju, Fresh, hardened and durability properties of concrete
made with Fly ash and limestone based Portland composite cement, Asian Concrete Federation Journal (2023), Vol. 9, No. 1.
made with Fly ash and limestone based Portland composite cement, Asian Concrete Federation Journal (2023), Vol. 9, No. 1.
[14 Puneet.Kaura, P.N. Ojha, Brijesh.Singh. Amit. Trivedi, Investigation of mechanical and durability performance of concrete made with flyash limestone composite cement,18th NCB International Conference and exhibition on Cement, Concrete and Building Materials at Yashoobhumi, Dwarka, Delhi, 2023.

[15] P.N. Ojha, P. Mittal, Abhishek.Singh, Brijesh.Singh, V.V.Arora, Optimization and Evaluation of Ultra-High Performance Concrete, Asian Concrete Federation Journal (2020), Volume 6, No.1, pp 26-36

[16]Scrivener.K, Martirena .F, Bishnoi. S,Maity.S, Calcined clay limestone cements (LC3). Cement and concrete research (2018), 114, 49-56.

[17] Guo.Y, Luo.L, Liu.T, Hao. L, Li. Y, Liu. P, Zhu.T. A review of low-carbon technologies and projects for the global cement industry. Journal of Environmental Sciences (2024), 136, 682-697.

4th International Symposium on One Health, One World
November 20 – 22, 2025

ABS ID: 164
Code No: IMSBE-OP-08

A Brief Overview Of Major Challenges Occurred During Tunnelling And Associated Underground Structures In East West Metro Project, Kolkata

D. Kar[1], P. Mitra[1], and B. Roy[2]
[1]*Associate Director, AECOM, Kolkata, India,*
Email: debjyoti.kar@aecom.com
Email: prithviraj.mitra@aecom.com
[2]*Associate, AECOM, Kolkata, India,*
Email: bodhisatwa.Roy@aecom.com

Keywords: *Excavation, Tunnelling, Ventilation Shaft, Cross Passage, Underground, Flyovers, Dilapidated Buildings.*

1. INTRODUCTION

Due to its geographical position, Kolkata is the most important metropolitan city in Eastern India. This British-era city consisted of several age-old facilities and thereby needed rapid modernization of transportation for the overall development of the eastern part of the country. East-West Metro Project is one of such iconic infrastructure projects connecting east end with the west end of the city.

Kolkata East-West metro corridor starts from Howrah Maidan in the West following with the passage of Tunnel Boring Machine (TBM) below the existing railway track and flyovers, TBM driving below river Hooghly, crossing below the existing metro line1 at Esplanade. Through its advancement from Howrah Maidan towards Sealdah, by touching all the important structures and facilities of the city, the alignment passes below the age-old congested area. Thereafter the alignment passes beneath Sealdah railway yard to Phoolbagan and subsequently it becomes an elevated corridor up to Salt Lake Sector V, which is the terminal station at the east.

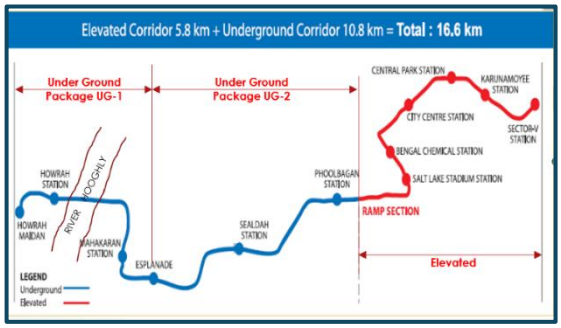

Figure 1. Alignment of the Project

The underground stretch starts from Ramp section near subhas sarobar in the East and ends at Howrah Maidan Station in the West covering six stations along with one ventilation shaft. The underground stretch between Sealdah and Howrah Maidan as depicted in figure 1, had undergone various design and construction challenges which are briefly described in the subsequent sections.

2. BRIEF OVERVIEW OF MAJOR CHALLANGES

The following are the major construction challenges that occurred during the construction of the East-West corridor:

2.1. Passage of TBM below Railway yard at Howrah

The operation of TBM below Railway Yard had been challenging due to the 228m radius of curvature when passed below in one of the busiest railway networks consisting of several crossings. Therefore, any excessive ground settlement could have led to the derailment of trains. As a mitigation measure, extensive instrumentation and monitoring had been carried out along with extensive grouting below high electric masts.

2.2. Water ingress due to piping in Howrah Station during Excavation

Howrah Metro station, having depth of 30 m from ground level, is the deepest underground metro station in India. It is a 4-tier station with 46 m depth of diaphragm wall and 60 m deep barrettes. Due to the presence of silty-sand layer at 10 m below base slab during excavation

of base slab, sudden water ingress due to piping action through the pressure relive well occurred. To mitigate this, the pressure relief wells were closed, and excavation of base slab was split into small zones of construction for better control over exigency.

2.3. Passage of TBM below River Hooghly

This is first under river twin tunnel metro alignment in India. As no bore log had been possible to conduct within the river width of a stretch zone of 540 m, no geological profile was available in this zone. Therefore, uncertainty along with risk was present from the beginning due to non-availability of bore log data and no scope for TBM maintenance. To mitigate this, mining below the river had been performed without any stoppage, with prior thorough maintenance by experts. Continuous monitoring with disciplined crew working in shifts around the clock and a well-coordinated logistics system for a constant supply of materials and the daily disposal of up to 1200 m3 of muck has been performed during the operation. This rigorous preparation and execution allowed the tunnel construction to be completed in just 66 days, significantly faster than the planned 127 days.

2.4. Construction of 42.1m Deep Ventilation Shaft Between Two Existing Tunnels in Close Proximity along with Live Railway Line

In between Howrah and Mahakaran Station, an intermediate ventilation shaft of 42.1 m depth and 10.3 m internal diameter had been constructed as a fire exit as presented under ref [1]. The major challenges were construction of 56 m Diaphragm wall, excavation of shaft at 5m away from the suburban railway track and 2.5m away from already constructed main tunnels of the project. To overcome the soil piping effect, the depth of excavation had been reduced to 2.5 m so that there may be sufficient thickness of clay overburden layer at bottom plug.

2.5 Passage of TBM below Brabourne Road Flyover

Brabourne road flyover is located along the tunnel alignment after crossing the Hooghly River. Commuters availing Howrah Railway station encounter this flyover just after crossing the iconic Howrah Bridge. The tunnel alignment is located around 100m along the flyover alignment with a minimum distance of 0.85 m from the centerline of existing pile of the flyover as described in ref [2]. Pre-tunnelling and post-tunnelling ground improvement by suitable grouting along with extensive monitoring of settlement at each pier location of the flyover was conducted during the TBM operation.

2.6. Driving TBM below existing north south metro line at Esplanade and H-Pile Intervention

The tunnel alignment was crossing beneath the existing Esplanade Metro Station, of North-South Corridor, at 2.0m below the existing diaphragm walls. Further, there was no stoppage of operation in the existing Esplanade station of North South metro line, during TBM mining. Any distress in the existing operating metro structure would be catastrophic. To mitigate the risk, rigorous instrumentation and monitoring of the existing platform, track and structural elements were performed and speed restriction up to 10 Km/hr.

2.7. TBM passing beneath age-old dilapidated buildings

As the alignment passed beneath the congested area of the city, many age-old dilapidated buildings of British era, had been encountered during the tunnelling, which are prone to collapse due to any ground movement. After rigorous assessment of building condition survey and damage assessment, several mitigation measures had been applied, such as applying low grouting pressure adjacent to the building foundations, propping extensively beneath the beam supporting floors and staircases etc., to carry out the operation safely, without damaging the existing buildings. Round-the-clock instrumentation and monitoring were ensured.

Figure 2. Supporting Arrangement of dilapidated building

2.8. Passage of TBM below Vidyapati Setu at Sealdah

Before reaching Sealdah station, TBM had to almost perpendicularly cross the articulated spans of Vidyapati Setu (Flyover) having piers at an interval of 20m connecting pile cap by a hinged joint.

The TBM passed beside the pile foundation at a clear gap of 1.5 m only, which was the main concern during tunnelling. During TBM operation, continuous monitoring of the flyover had been performed by installing measuring instruments on the flyover. Flyover span in the zone had been supported by suitable propping arrangement and vehicle movement on the flyover was restricted as a precautionary measure.

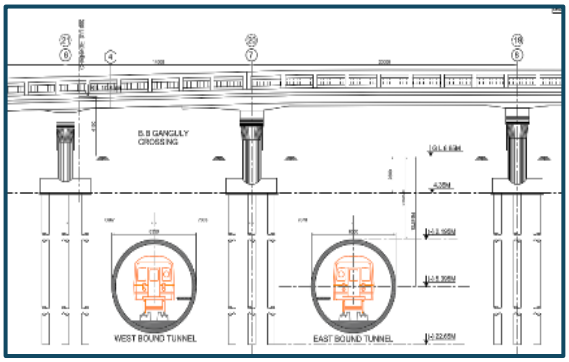

Figure 3. Cross Section of TBM below Flyover

2.9. Construction of Cross passage in silty-sand layer

In between the stretch of Esplanade to Sealdah, there were seven cross passages. Patch of silty-sand layers with sand content of 65% to 70%, in between two clay layers, were encountered in this zone from Subodh Mullick square to Bank of India Building near Bow bazar. Due to such stratigraphy, the sand layer behaves like a water bearing strata. Thereby, during cross passage construction, stabilization of the surrounding soil may become difficult in achieving strength and impermeability with cementitious grouting material. As a mitigation, trial mixes with different chemical compositions had been performed and proper admixture had been selected for application for grouting to mitigate the risk of piping of soil during excavation. In areas, where the soil stabilization is found to be not possible, alternate solution has been worked out to eliminate the Cross Passage with alternate egress path, complying codal provisions.

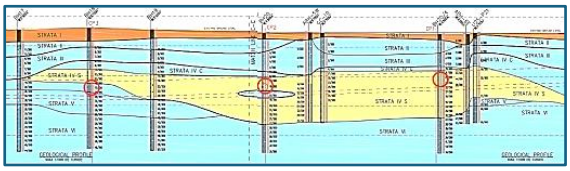

Figure 4. Geological Profile near Cross Passages

The subsequent section represents a case study related to the challenges faced during the construction of cross passage, CP2 and how the situation has been handled to ensure site safety as well as the safety of the residents without hampering operational hazard.

3. CONSTRUCTION OF CROSS PASSAGE CP2-A CASE STUDY

Cross Passage CP2 was planned near Bow bazar area, close to Sealdah Station. The depth of CP2 was around 16.5m from ground level. As per available borehole in this location, a silty sand / sandy silt layer is present at a depth of 14 m to 32 m from ground.

During construction of CP2, grouting with OPC cement and sodium silicate was undertaken. However, due to the presence of water inflow during probe drilling, composition of grouting material had been changed to MFC with sodium silicate along with colloidal silica. After a number of successful probe drilling outcomes, the excavation of heading, by opening the face of the tunnel liner, commenced. After one round of top heading excavation, substantial water ingress was observed. Additional cementitious grouting had been taken up after erecting the bulkhead, but excavation work could not be resumed due to consistent water inflow. After that, chemical admixtures, i.e., PU grout was applied, and the water ingress could have been controlled. Ensuring face stability, heading excavation was successfully completed for the entire length of the cross passage. The benching excavation started after that. During the benching operation, suddenly huge soil ingress, with flowing of soil particles, was observed and the ingress became uncontrollable with rapid pace. Gush of water with silt flooded into the tunnel. The intensity and volume of ingress was so high that shotcrete could not be sprayed, as the pump was getting frequently buried in the silt deposit. Large volume of water, at a rate of approximately 1000 l/min had been

experienced during the ingress. The mechanism of such high-volume water ingress was due to soil piping. Once the ground water, which was approximately at 1.8 bar, found a pathway into the excavation, it began to carry away the soil particles with it. As a result, rapidly the silt began to collapse, and water/silt mix flowed like a liquid. The collapse of the soil structure made it very difficult to control the subsidence. The work was immediately stopped. Ingress had been stopped by placing temporary bulkhead, two layers of shotcrete application and by continuous application of PU grout.

Figure 5. Cross Passage CP-2 after stoppage of water ingress

The impact of this huge soil/water ingress, causing volume loss, was visible in the tunnel liners and on the above ground buildings. Surface settlement and the development of severe cracks in some of the adjacent buildings were reported. The immediate concern was the health of existing twin tunnels as the tunnels were subjected to settlement and convergence due to huge ingress. A fresh wriggle survey and crack mapping for both the tunnels had been carried out and compared with original wriggle survey data. Accordingly, necessary strengthening measures for tunnels had been performed with installation of steel liners at the damaged zone.

Thereby, to eliminate the construction risks associated with cross passages in highly pressurized saturated silty sand layer, suitable alternate options were explored. National Building Code (NBC) 2016 Annex K-4.1.3 stipulates emergency exits be located at distance of 750m and the first cross passage be located at distance of 500m from the end of the platform or mid-tunnel exit. In addition to that, as per Annex K-4.1.9 of NBC 2016, maximum variation of 10% is permitted for the above-mentioned distances. Therefore, an egress shaft at Bow bazar at a distance of 821 m from Sealdah Station was constructed in accordance with Fire Department's regulation in lieu of three cross passages, i.e., CP1, CP2 and CP3 in this zone. The revised executed scheme from Esplanade to Sealdah stretch has been illustrated in diagram below.

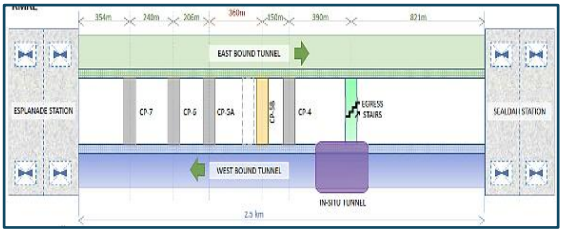

Figure 6. Schematic Line diagram between Esplanade and Sealdah

4. BRIEF DESCRIPTION OF ALTERNATE SCHEME:

As an alternate scheme of constructing CP1, CP2 and CP3, 13.2mx 2.7m egress shaft have been constructed at Bow-

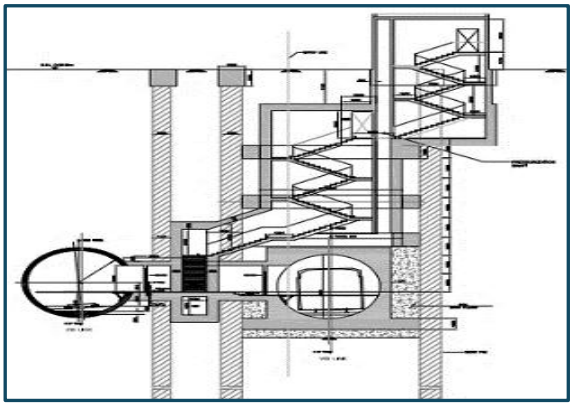

Figure 7. Egress Shaft at Bow bazar

Bazar location, at a depth approximately 22.5 m from ground level. Further, to establish proper evacuation paths as per standard regulation, additional land had been acquired by the concerned authority.

5. CONCLUSION:

As mentioned in the above illustrations, the East-West metro project had undergone several construction hurdles and had been successfully countered technically by appropriate measures. This has resulted in achieving the target of successful completion and subsequent commercial operation of the project.

The East West Metro Project aimed to address increasing transportation demand in Kolkata and its surroundings, which has reduced traffic

congestion and environmental pollution. This line connects with the existing North-South metro at Esplanade Metro Station. It has also interchange facilities with the planned Joka-Esplanade Metro Line at Esplanade as per the revised alignment. Additional interchange options are available at Sealdah and Howrah Stations for access to Eastern Railway, as well as at the major bus terminal at Esplanade. The East-West Line thus became a major commuter to support regional economic activity and contribute to improvements in urban traffic flow by reducing the travel time to 35 minutes from 2 hrs. and air quality by reducing carbon emission. Projections estimate that approximately 1 million people will use this system daily by 2035.

ACKNOWLEDGEMENT

The support received from Kolkata Metro Railway Corporation (KMRCL) for allowing to use the project data through Consultative Collaboration is gratefully acknowledged. The guidance rendered by Mr. Shailesh Kumar, (GGM CIVIL), KMRCL, is also sincerely avowed.

REFERENCES:

[1] D. Kar, S. Dutta, B. Roy, A. Ghosh. Construction of Deep Ventilation Shaft & Its Impact in Adjoining TBM Tunnels– A Case Study on a Deep Excavation in Between Two Bored Tunnels Within Soft Soil in East-West Metro Corridor Kolkata, India. Proceedings GEO-RARP 2023, pp. 289-299.

[2] S. Dutta, D. Kar, A. Bagchi, B. Roy, A. Ghosh. Impact Of Tunnelling on Piled Structure– A Case Study on Brabourne Road Flyover in Kolkata East-West Metro Corridor. Proceedings GEO-RARP 2023, pp. 277-288.

4th International Symposium on One Health, One World
November 20 – 22, 2025

ABS ID: 88
Code No: IMSBE-OP-09

Eco-Cement Binders from Waste-Derived Raw Material: A Route to Green Construction

R. Kumar
Principal Scientist & Associate Head, Advanced Concrete, Steel & Composites (ACSC) Division, CSIR- Central Building Research Institute, Roorkee, Uttrakhand, 247 667, India
**Correspond to Rajesh Kumar (rajeshkumar.cbri@csir.res.in)*

***Keywords**: Low carbon cement, Waste utilization, Stone waste, Portland Limestone Cement.*

1. ABSTRACT

At present, India is world's second-largest consumer of cement, behind China. The rising demand for Ordinary Portland Cement (OPC) due to rapid urbanization highlights the depletion of finite natural resources necessary for its production. India's rapid urbanization has significantly increased the demand for Ordinary Portland Cement (OPC), raising concerns regarding the environmental impact of its production. This study investigates sustainable alternatives, specifically through the development of low-carbon cement, namely Portland Limestone Cement (PLC), by incorporating waste materials such as microfine thermally processed low-grade limestone slurry into OPC clinkers. This approach aims to produce an energy-efficient, environmentally friendly binder without compromising performance. The developed PLC binder achieved desirable properties in accordance with BS:7979, including initial and final setting times of 112 minutes and 7.5 hours, respectively, and compressive strengths of 35.8 and 45.7 MPa at 7 and 28 days, respectively, with an optimized 20% replacement of OPC with thermally processed stone slurry. Following the synthesis of the new PLC binder, specific strength attributed to aircrete, commonly known as cellular foamed concrete (CFC), was developed by further replacing unprocessed stone slurry with fine river sand, with replacement levels ranging from 0 to 100%.

2. INTRODUCTION

Cement production is a vital global industry, yet it presents significant environmental issues due to its high CO_2 emissions and consumption of raw materials. The process of manufacturing cement is responsible for approximately 8% of carbon dioxide emissions worldwide, mainly due to the clinkerization process. This involves heating limestone ($CaCO_3$) to create lime (CaO), which releases CO_2as a byproduct **[1].** Considering environmental concerns and the pressing need to reduce carbon emissions, sustainable alternatives are being investigated to lessen the carbon footprint of cement production **[2,3].** Various waste materials are being utilized to develop cementitious binders. One such challenge is the disposal of stone slurry, which generates considerable environmental concerns due to the accumulation of waste from stone processing operations **(Figure 1).** Incorporating low-grade limestone in cement production has garnered significant research and industrial interest because it directly decreases clinker content, thus reducing both CO_2 emissions and resource consumption **[4,5].** The use of limestone as a cement component is further encouraged by its global availability and its potential to enhance the sustainability of cement production. Since limestone is easily accessible, its use in the cement mix diminishes the dependence on clinker, which requires substantial heating and energy. Recent research has shown that the physical and chemical properties of limestone can actively improve the hydration process of cement,

influencing both its microstructure and overall durability **[6,7].** Therefore, substituting a portion of clinker with limestone serves a dual purpose: it reduces the carbon footprint of cement and can enhance the specific performance characteristics of the product. As a result, the use of limestone is increasingly seen as a key element of low-carbon strategies in the cement industry **[8,9].**

Figure. 1. Hazardous Stone slurry deposited in Rajasthan, India.

This study introduces a sustainable cement binder for green construction in India, developed by thermally processing low-grade limestone slurry waste (LSW) – a novel use of an abundant stone-cutting byproduct. By replacing up to 20% of OPC clinker with LSW, the eco-cement significantly lowers clinker consumption and CO_2 emissions, while diverting industrial waste from landfills. The work demonstrates one-of-its-kind utilization of LSW as a value-added cementitious material, combining environmental benefits with solid technical performance (hydration and strength) and offering a viable green binder solution for sustainable infrastructure in India.

3. MATERIALS AND METHODS

In this study, locally sourced raw materials were utilized, including ordinary Portland cement (OPC-43G), which was transformed into Portland limestone cement (PLC) through the addition of thermally processed limestone slurry waste (LSW), along with standard sand and potable water. Ultratech Vikram premium cement (OPC-43G) was employed as the cementitious binder in accordance with **IS:8112** standards **[10].** The physical and chemical properties of OPC were assessed following the guidelines of **IS 4031: Part I-VI, XI [11-17]**. The outcomes of these evaluations are detailed in Table 1, confirming adherence to the specifications delineated in **IS 8112 [10]**. The cement exhibited a standard consistency of 26% and setting times within the prescribed range. Compressive strength (CS) measurements at 3, 7, and 28 days surpassed the minimum requirements. The soundness of OPC (1.9 mm) and its fineness (355 m^2/kg) were well within the established limits.

Table 1
Physical and chemical properties of OPC-43G.

Parameters	**Value**	**IS: 8112-2013 [10]**
(A). Physical properties		
Setting time (min.)		
Initial	140	30 (Min.)
Final	467	600 (Max.)
CS (MPa)		
3 Days	27.50	23(Min.)
7 Days	36.30	33(Min.)
28 Days	48.40	43(Min.)
Bulk specific gravity, (SSD)	3.15	-Not specified-
B. Chemical properties, *% by mass*		
Magnesium oxide (MgO)	0.85	6.00 (Max.)
LOI	0.08	0.10 (Max.)
Sulphur oxide (SO_3)	2.48	3.50 (Max.)

X-ray fluorescence (XRF) analysis of cement has identified the presence of several key chemical compounds and cement phases. The major oxides detected include calcium oxide (CaO) at 63.81%, silicon dioxide (SiO_2) at 19.53%, aluminum oxide (Al_2O_3) at 5.78%, iron oxide (Fe_2O_3) at 5.05%, and magnesium oxide (MgO) at 0.85%. These compounds contribute to the formation of the primary cement phases, specifically alite (65.24%), belite (6.78%), tricalcium aluminate (C_3A) (6.77%), and tetracalcium aluminoferrite (C_4AF) (15.37%).

After development of slurry induced PLC binder; apart from the determination of compressive strength, Isothermal calorimetry was utilized to investigate the heat generation

and hydration processes of cementitious materials incorporating both processed and unprocessed LSW. This technique facilitates the measurement of exothermic reactions that occur when water interacts with cementitious substances. In this study, a TAM Air thermostat was employed to detect the heat emission from the ampoules. The composite cement paste was prepared at ambient temperature, and its isothermal heat was analyzed at 27°C. An 8-channel calorimeter within the TAM Air thermostat was used for this experiment. The sample preparation involved mixing the binder and water in a glass ampoule using a glass rod. Following the mixing process, the samples were sealed and placed in a TAM Air thermostat to measure the heat output.

4. RESULTS AND DISCUSSIONS

4.1 Physico- Mechanical Properties

In the synthesis of Portland Limestone Cement (PLC) as a low-carbon cementitious binder, LSW was evaluated as a cement substitute in proportions ranging from 5% to 20%, both with and without thermal treatment, in accordance with **BS 7979 [18].** The analysis of the limestone sample reveals essential chemical and physical characteristics pertinent to its application in cement production. Chemically, the calcium carbonate content in unprocessed LSW was determined to be 66.26%, which is below the minimum requirement of 75% as specified in the codal provision. The chloride content (0.12%) slightly exceeds the maximum permissible limit of 0.10%, while the total sulfur content (0.728%) remains within the acceptable maximum of 1.0%. The clay content, assessed via the methylene blue index (MBI), was 1.33 g/100g, marginally surpassing the maximum limit of 1.2 g/100g. Similarly, the organic material content (0.60%) exceeds the maximum allowable limit of 0.50%. Physically, the fineness (%) of the limestone sample significantly deviates from the standards, with 26% retained on a 45 mm sieve, considerably higher than the maximum limit of 10.0%. However, the fraction passing through a 300 µm sieve and retained on a 45 mm sieve (6.33%) was within the acceptable range. The initial setting time of 132 minutes satisfies the minimum requirement of 75 minutes, and the soundness (0.50 mm) was well within the maximum limit of 10 mm. The moisture content (10.50%) substantially exceeds the maximum allowable limit of 0.50%. The compressive strength of a mixture comprising 80% Ordinary Portland Cement (OPC) and 20% of the sample (LSW) meets the standard requirements, with 7-day and 28-day strengths of 18.57 MPa and 34.44 MPa, respectively. The loss on ignition is 32.02%, for which no specific codal provision is provided. However, it is evident that the compressive strength does not conform to IS: 8112 (minimum 43 MPa at 28 days) due to the slightly higher replacement of inert filler and high clay content. Consequently, thermal treatment was conducted for up to 4 hours at a temperature of 900ºC. Following the thermal treatment, various physical and chemical characterizations were performed again in accordance with the BS code. The results are presented in Table 2.

The characterization of processed LSW in accordance with **BS:7979-2001 [18]** indicates significant alterations in its chemical and physical properties over varying processing durations. Chemical analysis reveals a gradual reduction in chloride content, decreasing from 0.099% at ½ hour to 0.071% at 4 hours. Similarly, total sulfur content shows a notable decline, from 0.275% to 0.137% over the same period. The clay content, assessed via the Methylene Blue Index (MBI), decreases markedly from 1.17 g/100g to 0.50 g/100g, with the most pronounced change occurring between ½ hour and 2 hours. The content of organic material, as indicated by Total Organic Carbon (TOC), significantly diminishes from 0.16% to 0.02%. The physical properties of processed LSW also exhibit variations with processing time. The fineness, measured as the percentage retained on a 45mm sieve, remains constant at approximately 24.8% across all durations. The initial setting time decreases from 125 minutes at ½ hour to 112 minutes at 4 hours, suggesting enhanced reactivity. Soundness, an indicator of volume stability, shows a slight increase from 0.56 mm to 1.90 mm. For samples processed for ½ hour, compressive strength increases from 20.7 MPa at 7 days to 36.3 MPa at 28 days. Similarly, for 1-hour processing, the strength rises from 23.6 MPa at 7 days to 38.4 MPa at 28 days. After 2 hours of processing, the strength further improves from 35.8 MPa at 7 days to 45.7 MPa at 28 days. Finally, with 4-hour processing, compressive strength reaches its highest values, increasing from 37.3 MPa at 7 days to 48.4 MPa at 28 days. These findings suggest that extended processing time generally enhances the chemical and physical characteristics of LSW, potentially improving its suitability for PLC synthesis. According to **IS:8112 [10],** limestone is permissible as a mineral additive or performance enhancer in

quantities up to 5%. However, the primary aim of the current study was to maximize the utilization of LSW as a component of the cementitious binder. Consequently, thermally processed LSW was substituted for OPC-43 in proportions ranging from 5% to 20%. The synthesized low-carbon cement based on OPC-43 exhibits desirable properties in accordance with IS:8112 **[10],** at a LSW replacement level of 20% following a thermal processing duration of 2 hours.

Table 2

Characterization of processed LSW as per BS:7979 [18].

Properties		Results			
		½ hr.	1 hr.	2 hrs.	4 hrs.
Chemical	Chloride (%)	0.099	0.096	0.096	0.041
	Total Sulfur (%)	0.275	0.192	0.165	0.137
	Clay content (MBI, g/100g)	1.17	0.83	0.50	0.50
	Organic material content (TOC%)	0.16	0.053	0.046	0.02
Physical	Fineness, % (retained on 45 µm sieve)	24.6	24.8	24.7	24.8
	Initial setting time (min.)	125	119	116	112
	Soundness (mm)	0.56	0.58	0.59	1.9
Compressive strength (MPa) (80% OPC + 20% LSW)	7 days	20.7	23.6	35.8	37.3
	28 days	36.3	38.4	45.7	48.4

4.2 Hydration Properties

As illustrated in Fig. 2, the blue curve (b), which represents OPC with 20% unprocessed LSW, not only demonstrates the lowest total heat evolution compared to pure OPC (curve- a), but also remains lower than that of the processed slurry waste mixture. The unprocessed LSW primarily functions as an inert filler, offering some advantages in particle packing while contributing minimally to the hydration reaction itself. Consequently, the cumulative heat was relatively lower due to the dilution effect, indicating limited long-term hydration enhancement. The green curve (c), representing OPC with 20% processed LSW, exhibited the highest total heat evolution among the three compositions. This suggests that the processed LSW possessed the highest reactivity, significantly contributing to the hydration process. The increased cumulative heat can be attributed to the nucleation effect and enhanced reactivity of the thermally activated LSW, which actively participates in hydration reactions. This resulted in the formation of additional hydration products, leading to a higher overall heat evolution. In conclusion, the incorporation of processed LSW maximized the total heat evolution and indicated higher long-term hydration, rendering it a more effective additive than unprocessed slurry waste. This observation aligns with hydration heat flow data, where the nucleation and reactivity of thermally activated LSW were shown to enhance hydration and cumulative heat, supporting its suitability as a supplementary material for optimizing cement hydration. Therefore, the strength development rate for the thermally activated LSW mix was higher at 7 and 28 days, as shown in Table 2. The compressive strength of a mixture comprising 80% OPC and 20% of the sample (inert LSW) was recorded as 18.57 MPa and 34.44 MPa at 7 days and 28 days, respectively. After 2 hours of processing, the strength further improved to 35.8 MPa at 7 days and 45.7 MPa at 28 days.

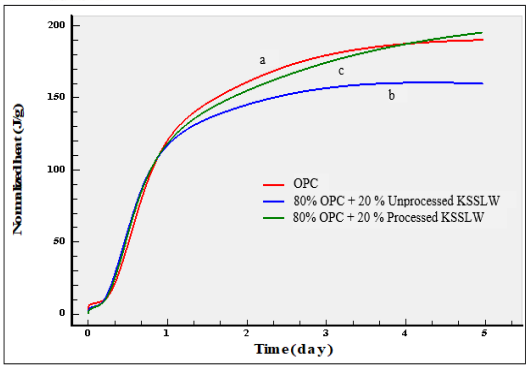

Figure. 2. Total heat evolution of (a). 100% OPC, (b). 80% OPC with 20% unprocessed LSW/KSSLW, and (c). 80% OPC with 20% processed LSW/KSSLW.

5. CONCLUSIONS

This study demonstrates the successful development of a sustainable cement binder for green construction in India by utilizing thermally processed low-grade limestone slurry waste (LSW). The research highlights the potential of this eco-cement to significantly reduce clinker consumption and CO_2 emissions while diverting industrial waste from landfills. Key findings were observed as-

i. Thermal processing of LSW for 2 hours at 900°C resulted in optimal chemical and physical properties for use in Portland Limestone Cement (PLC).
ii. The developed PLC binder, with 20% replacement of OPC by processed LSW, achieved desirable properties in accordance with BS:7979 and IS:8112 standards.
iii. Compressive strength of the PLC binder reached 35.8 MPa at 7 days and 45.7 MPa at 28 days, surpassing the minimum requirements.
iv. Isothermal calorimetry revealed that processed LSW exhibited higher reactivity and contributed more effectively to the hydration process compared to unprocessed LSW.
v. The incorporation of processed LSW resulted in increased cumulative heat evolution, indicating enhanced long-term hydration and strength development.

This research presents a novel approach to utilizing limestone slurry waste as a value-added cementitious material, offering a viable solution for sustainable infrastructure in India. The developed eco-cement not only addresses environmental concerns by reducing CO_2 emissions and waste accumulation but also demonstrates solid technical performance in terms of hydration and strength properties. These findings pave the way for further exploration and implementation of low-carbon cement alternatives in the construction industry.

ACKNOWLEDGEMENT

The author is thankful to the CSIR-CBRI, Roorkee, India for granting permission to publish this research work. The author is grateful to MoEF&CC, New Delhi, Government of India, for financial support (File Number: 19-45/2018/RE).

REFERENCES:

(1) Nighot, N. S., & Kumar, R. (2023). A comprehensive study on the synthesis and characterization of eco-cementitious binders using different kind of industrial wastes for sustainable development. Developments in the Built Environment, 14, 100135. https://doi.org/10.1016/j.dibe.2023.100135
(2) Srivastava, A., Kumar, R., & Lakhani, R. (2022). Low energy/Low carbon eco-cementitious binders as an alternative to ordinary Portland cement. Handbook of Smart Materials, Technologies, and Devices, 2619-2640. https://doi.org/10.1007/978-3-030-84205-5_143
(3) Kumar, R. (2022). Recent progress in newer cementitious binders as an alternative to Portland cement: Need for the 21st century. Lecture Notes in Civil Engineering, 797-812. https://doi.org/10.1007/978-981-19-4040-8_63
(4) Anurag, Kumar, R., & Goyal, S. (2023). Recycling of calcined low-grade limestone slurry in producing low carbon cementitious binder towards sustainable environment: ANOVA, statistical modeling & microstructural performance. Environmental Development, 47, 100910. https://doi.org/10.1016/j.envdev.2023.100910
(5) Guo, Y., Luo, L., Liu, T., Hao, L., Li, Y., Liu, P., & Zhu, T. (2024). A review of low-carbon technologies and projects for the global

cement industry. *Journal of Environmental Sciences, 136*, 682–697. https://doi.org/10.1016/j.jes.2023.01.021

(6) Panesar, D. K. & Zhang, R. (2020). Performance comparison of cement replacing materials in concrete: limestone fillers and supplementary cementing materials – a review. *Construction and Building Materials, 251*, 118866. https://doi.org/10.1016/j.conbuildmat.2020.118866

(7) Anurag, Kumar, R., Goyal, S., & Srivastava, A. (2021). A comprehensive study on the influence of supplementary cementitious materials on physico-mechanical, microstructural and durability properties of low carbon cement composites. Powder Technology, 394, 645-668. https://doi.org/10.1016/j.powtec.2021.08.081

(8) Lakhani, R., Kumar, R., & Tomar, P. (2014). Utilization of stone waste in the development of value-added products: A state of the art review. Journal of Engineering Science and Technology Review, 7(3), 180-187. https://doi.org/10.25103/jestr.073.29

(9) Gupta, S., Mohapatra, B. N., & Bansal, M. (2020). A review on the development of Portland limestone cement: A step towards a low-carbon economy for the Indian cement industry. *Current Research in Green and Sustainable Chemistry, 3*, 100019. https://doi.org/10.1016/j.crgsc.2020.100019

(10) IS: 8112 (2013). Specification for 43 grade ordinary Portland cement. Bureau of Indian Standards, New Delhi, India.

(11) IS: 4031(i) (1996). Physical tests for hydraulic cement: Determination of fineness by dry sieving. Bureau of Indian Standards, New Delhi, India.

(12) IS: 4031(ii) (1999). Physical tests for hydraulic cement: Determination of fineness by specific surface using the Blaine air permeability method. Bureau of Indian Standards, New Delhi, India.

(13) IS: 4031(iii) (1988). Methods of physical tests for hydraulic cement: Determination of soundness. Bureau of Indian Standards, New Delhi, India.

(14) IS: 4031(iv) (1988). Methods of physical tests for hydraulic cement: determination of the consistency of standard cement paste. Bureau of Indian Standards, New Delhi, India.

(15) IS: 4031(v) (1988). Physical tests for hydraulic cement: determination of initial and final setting times. Bureau of Indian Standards, New Delhi, India.

(16) IS: 4031(vi) (1988). Physical test methods for hydraulic cement: Determination of the compressive strength of hydraulic cement. Bureau of Indian Standards, New Delhi, India.

(17) IS: 4031(xi) (1988). Methods of physical tests for hydraulic cement: Determination of density. Bureau of Indian Standards, New Delhi, India.

(18) BS 7979:2016 - Specification for Limestone Fines for Use with Portland Cement (2016).

Mr. Kaiga Shimmori

4th International Symposium on One Health, One World
November 20 – 22, 2025
ABS ID: 130
Code No: IMSBE-OP-10

Chloride Removal from Water Using Resin for Construction-Related Applications

Soumitra Maiti [1,2*], Neeraj Jain [1,2]
[1]*Building Materials and Environmental Sustainability (BMES) Group, CSIR-Central Building Research Institute (CBRI), Roorkee, Uttarakhand 247667, India*
[2]*Academy Of Scientific and Innovative Research (Acsir), Ghaziabad 201002, India*
**Corresponding Author:* Soumitra@Cbri.Res.In

Keywords: *Water treatment, Chloride Absorption, Gibbs Free energy.*

Abstract:

The present work utilizes a commercial-grade anion exchange resin for the removal of chloride from contaminated water. The impacts of different operational parameters, such as initial concentration (500 mg/l – 2000 mg/l), time (0-360 min), resin dosage (20 g/l - 100 g/l), and temperature (30 to 60 °C) on removal efficiency were investigated. It was noticed that with a rise in initial concentration from 500 to 2000 mg/L, removal efficiency decreased from 84% to 77%. Equilibrium time was found to be around 180 minutes. The pseudo-second-order kinetic model better described the adsorption process, and it followed both Langmuir and Freundlich isotherms. Thermodynamic studies revealed that the adsorption of chloride was spontaneous and endothermic and the point zero charge of resin is 8.5. SEM and FTIR results indicate that this resin effectively adsorbs chloride.

Batch adsorption of chloride ions onto resins was systematically investigated to determine the optimal amount of resin required to minimize chloride ion concentration effectively (Hekmatzadeh et al., 2012) using a water shaker bath.

The plot of ln (qe – qt) versus t was used to determine the value of adsorption rate k1 for the adsorption of chloride onto anion exchange resin Doshion GA-13 (OH) (Fig 1.)

SEM images demonstrate a substantial decrease in the porosity of the resin and a noticeable smoothing of its surface. This change suggests that the adsorption of chloride ions has filled the pores and smoothed out the surface irregularities.

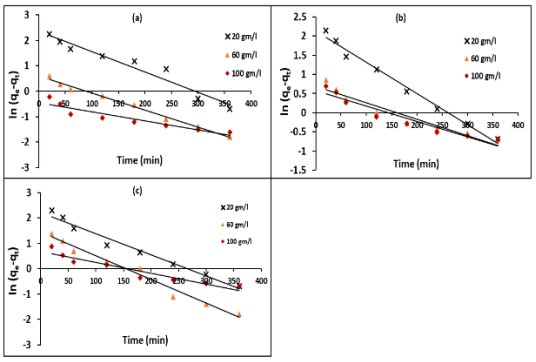

Fig 1. The plot of the pseudo-first-order for chloride adsorption onto anion exchange resin at different initial concentrations (a)500 ppm, (b) 1000 ppm, and (c) 2000 ppm

The plot of t/qt versus t was used to determine the value of adsorption rate k2 for the adsorption of chloride onto anion exchange resin Doshion GA-13 (OH) (Fig 1.)

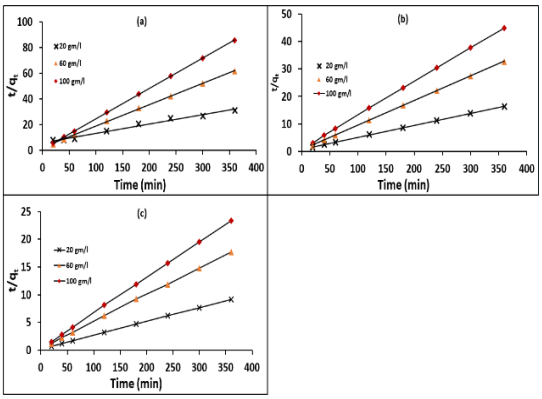

Fig. 2. The pseudo-second-order plot of chloride adsorption onto anion exchange resin at different initial concentrations (a) 500 ppm, (b) 1000 ppm, (c) 2000 ppm.

Consequently, the surface morphology alterations provide visual evidence of the resin's adsorption efficiency and capacity for removing chloride ions from water. Fig.3 showed the SEM Image of resin (a) Before treatment with contaminated water, (b)After treatment with water

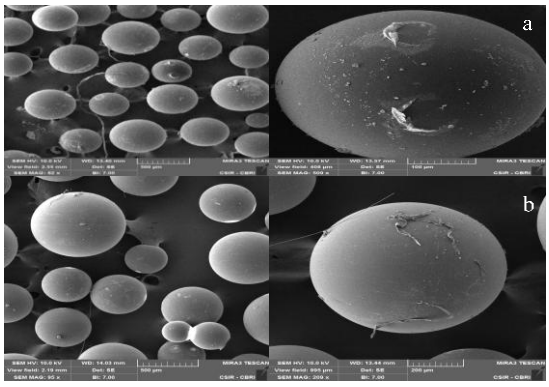

Fig 3. SEM Image (a) Before treatment with water, (b)After treatment with water

The successful application of the pseudo-second-order kinetic model suggests that chemisorption is likely involved. The adsorption followed the Langmuir isotherm, as indicated by the separation factor RL being between 0 and 1. Additionally, the adsorption process followed the Freundlich isotherm, with the value of n ranging from 1.35 to 1.49. The Dubinin-Radushkevich isotherm confirmed that the adsorption is chemical ion exchange in nature, as the value of E was between 20 -28.867 KJ/mol

Furthermore, the negative Gibbs free energy change (ΔG) observed in the study implies that the adsorption process is spontaneous and thermodynamically favorable, while the positive ΔH value indicates that the process is endothermic in nature.

CONCLUSIONS:

This study analyzed the removal of chloride from water using the anion exchange resin DOSHION GA-13(OH) via batch experiments, applying kinetic, isotherm, and thermodynamic studies. The effects of contact time and resin dosage were also examined, revealing that equilibrium was reached at approximately 120 minutes, and the maximum dosage required for optimal chloride removal was 100 g/l. SEM and FTIR images confirmed that chloride was effectively adsorbed by the Resin.

The successful application of the pseudo-second-order kinetic model suggests that chemisorption is likely involved. The adsorption behavior of chloride onto the chosen adsorbent was well-described by the Langmuir, Freundlich, and Dubinin-Radushkevich (D-R) isotherms. The adsorption followed the Langmuir isotherm, as indicated by the separation factor RL being between 0 and 1. Additionally, the adsorption process followed the Freundlich isotherm, with the value of n ranging from 1.35 to 1.49. The Dubinin-Radushkevich isotherm confirmed that the adsorption is chemical ion exchange in nature, as the value of E was between 20 -28.867 KJ/mol

Furthermore, the negative Gibbs free energy change (ΔG) observed in the study implies that the adsorption process is spontaneous and thermodynamically favorable, while the positive ΔH value indicates that the process is endothermic in nature. Overall, anion exchange resins prove to be highly effective for

removing anions from contaminated water, offering a reliable and efficient method for water treatment that is both cost-effective and environmentally sustainable

REFERENCES:

[1] Nematzadeh, A., Karimi-Jashani, A., Talebbeydokhti, N. & Kløve, B.: 2012, Desalination 284, 22-31

[2] Khan, T. A., Sharma, S. & Ali, I.: 2011, J Toxicol Environ Health Sci 3, 286-297.

4th International Symposium on One Health, One World
November 20 – 22, 2025
ABS ID: 129
Code No: IMSBE-OP-11

Development of Perlite Based Sustainable Composite Plaster

Neeraj Jain[1], Soumitra Maiti[2], Payal Bakshi[3]

[1]Neeraj Jain, Senior Scientist, Building Materials and Environmental Sustainability (BMES) Group, CSIR-Central Building Research Institute (CBRI), Roorkee, Uttarakhand 247667, India
[2]Soumitra Maiti, Scientist, Building Materials and Environmental Sustainability (BMES) Group, CSIR-Central Building Research Institute (CBRI), Roorkee, Uttarakhand 247667, India
[3]Payal Bakshi, Post-Doc, Academy of Scientific and Innovative Research (Acsir), Ghaziabad 201002, India

Abstract

Perlite is a glassy volcanic rock that expands into a lightweight, high-density material when rapidly heated under controlled conditions. Its applications are primarily driven by its unique physical and chemical characteristics (1,2). Expanded perlite ranges in color from snow-white to grey-white, while raw perlite varies from translucent and light grey to glossy black. In Portland cement or gypsum-based plasters, expanded perlite enhances thermal insulation, fire resistance, and other desirable performance traits(3-5). It has long been used as a lightweight substitute for cement and mortar. Perlite is a mineral scarcely found in India but is processed by some industries into lightweight aggregates. Expanded perlite is a desirable material for many goods, including lightweight panels, glass, and other materials, due to its lightweight, superior thermal insulation, and fire resistance. Since these materials have not yet been produced in India, no guidelines or criteria have been established. On the usage of perlite in gypsum, Indian Standard Specifications IS: 948812 and IS: 2547 (Part 11) are available (Singh & Garg, 1991). In comparison to vermiculite and cement, perlite appears to be a better additive to enhance the composite's thermal insulator performance. Perlite does improve the matrix's porosity rate and thus its thermal qualities as an insulator. During sample preparation, it appears that water is trapped between layers of perlite, increasing the thermal conductivity of the composite A combination of FGD gypsum and perlite has been used to develop Gypsum Perlite Plaster (GPP). Table 1 shows the mix composition of perlite plaster.

Table 1: Mix compositions of Gypsum Perlite plasterPlaster (GPP)

Mix Designations	Hemihydrate plaster (%)	Perlite (%)	Retarder dose (DTPA) (%)
GPP1	96.0	4.0	0.05
GPP2	95.0	5.0	0.05
GPP3	94.0	6.0	0.05

The physical and mechanical properties of three formulations GPP1, GPP2, and GPP3 were evaluated and compared against the standards specified in IS: 2547.

Water absorption tests indicate that the plaster is unsuitable for external applications in regions with persistent moisture or rainfall. Nevertheless, the findings confirm that perlite, when combined with gypsum and cement, holds promise as a viable material for use in building construction. Table 2 demonstrate the Physio-mechanical properties of Gypsum Perlite Plaster

Table 2: Physio-mechanical properties of Gypsum Perlite Plaster

Parameters	Values		
	GPP1	GPP2	GPP3
Colour	Creamy white	Creamy white	Creamy white
pH	7.30	7.28	7.26
Loss on ignition (LOI)	9.47%	9.23 %	8.90 %
Dry Bulk Density (powder)	740 kg/m^3	717 kg/m^3	687kg/m^3
Set Bulk density of cube(dried at 42°C)	1100-1120 kg/m^3	1010-1030 kg/m^3	1000-1010 kg/m^3
Specific gravity	1.96	1.86	1.76
Consistency	55.00 %	57.00%	60.00 %
Fineness: RetRetention on 45 µmsieve	10.0-15.0 %	10.0-15.0 %	10.0-15.0 %
Setting time	20-25 min	20-25min	20-25 min
Compressive strength 7 days 28 days	11.72 MPa 11.5 MPa	10.93 MPa 10.83 MPa	10.08 MPa 10.08 MPa
Flexural Strength 7days 28days	4.50 MPa 4.50 MPa	4.05 MPa 4.05 MPa	3.6 MPa 3.6 MPa
Soundness (Max. 5. As as per IS:6909 -1990)	~1.5 mm	~1.5 mm	~1.5 mm

Conclusion

(i) The physical and mechanical properties of all the mixes (GPP1, GPP2, and GPP3) were determined which showed that the bulk density and compressive strength of mix GPP1 complied with IS: 2547. Therefore, the mix GPP1 has been recommended for commercial exploitation as premixed lightweight plaster.

(ii) The results of water absorption and porosity of plaster cubes (GPP1) showed that these parameters increased with the increase in immersion period in water (2 hours to 24 hours). Water absorption and porosity observed were very high and were about 33 % and 41 %, respectively, making them unsuitable for external use.

Based on the experimental results obtained, technical specifications of the Gypsum Perlite Plaster (GPP) have been compared with IS: 2547. The comparison showed that it complied with all the parameters of the standard. The GPP1 has also been compared with the properties of other plasters or similar products available in the market

REFERENCES:

[1] Abidi, S., Nait-Ali, B., Joliff, Y., & Favotto, C. (2015). 392–400.

[2] Erbs, A. Nagalli, K. Querne de Carvalho, V. Mymrin, F.H. Passig, W. Mazer, J. Clean. Prod. 183 (2018) 1314–1322.

[3] Alkan, M., Karadaş, M., Doğan, M., & Demirbaş, Ö. (2005). Journal of Colloid and Interface Science, 291(2), 309– 318.

[4] Austin, G. S., & Barker, J. M. (1998).

[5] Celik, A. G., Kilic, A. M., & Cakal, G. O. (2013). 49(2), 689–700.

2025 HOW

4th International Symposium on One Health, One World
November 20 – 22, 2025

ABS ID: 91
Code No: IMSBE-OP-12

Clogging And De-Clogging Potential Of Pervious Concrete Slices Using Falling Head Permeability Approach : An Experimental Analysis

Nagesh Pratap Singh[1,1], Santha Kumar G[2] And Ganesh Kumar S[3]

[1,1]*Research Scholar, Csir- Central Building Research Institute, Roorkee-247 667, India*
Academy Of Scientific And Innovative Research (Acsir), Ghaziabad-201002, India
[2]*Senior Scientist, Csir- Central Building Research Institute, Roorkee-247 667, India*
Assistant Professor, Academy Of Scientific And Innovative Research (Acsir), Ghaziabad-201002, India
[3]*Principal Scientist, Csir- Central Building Research Institute, Roorkee-247 667, India*
Assistant Professor, Academy Of Scientific And Innovative Research (Acsir), Ghaziabad-201002, India
**Correspond To Nagesh Pratap Singh (Nagesh.Cbri20a@Acsir.Res.In)*

***Keywords**: Pervious concrete, Permeability, Clogging, De-clogging.*

1. INTRODUCTION

Pervious concrete (PC) is a highly porous material that shows superior hydraulic performance. PC is generally made of coarse aggregate, binder, and water. Typically, little or no fine aggregate is used in order to achieve high porosity in PC. PC is used in various field applications such as pavement, groundwater recharge, water treatment, PC pile for ground improvement, and acoustic purposes [1]. Clogging is a major drawback of the PC during ingress of sediments into the PC and block the pores of PC, causing a reduction in the hydraulic performance of the PC [2]. Clogging of PC is influenced by depth of PC layer, type of sediments, and concentration of sediments. Studies need to be addressed in relevance with the clogging behavior of PC under the influence varying layer of PC and type of sediments. Considering the above gaps, this paper focuses on examining the clogging behavior of the PC to determine which depth of the PC structure is more susceptible to clogging.

2. MATERIALS AND METHODOLOGY

2.1 Materials

OPC 43 grade cement and coarse aggregate (CA) of size range 10-20 mm were used as raw material for making PC. The water-to-cement (W/C) ratio was kept 0.32 for all the mix designs. Three design void content-based PC, such as 15, 20, and 25 % were designed as per ACI522R-10 guidelines [3]. The mix design details of PC are given in Table 1. For the clogging, two types of sediments, such as sand and clayey silt, were used to prepare a clogging sediment solution for the clogging test. The sand was categorized as fine-graded sand and clayey silt as low plasticity soil. Clogging sediment solution was prepared by mixing 100g of soil sediment in 1 litre of water, resulting in a concentration of the clogging solution of 100g/l.

Table 1 Mix proportions used in PC mixes.

Batch ID	CA (kg/m^3)	Cement (kg/m^3)	Design Void (%)
PC-15	1646	385.38	15
PC-20	1646	306.64	20
PC-25	1646	227.90	25

2.2 Experimental methodology

The PC cylindrical specimens of size 200 mm in length and 100 mm in diameter were used for clogging. The soil sediment clogging solution was prepared by mixing the sediment with clean water with a stirrer for 1 minute. Two different soil sediments, such as sand and clayey silt were used. Initially, the PC specimen was fixed into falling head permeability test setup, and the clogging sediment solution was passed over top of PC specimens and filled upto 50 cm head. The clogging cycle was repeated till the PC specimen clogged, i.e., permeability reached < 0.14 cm/sec as minimum permeability specified in ACI522R-10. After clogging, the accumulated sediment at the top surface of the specimen was removed from the clogged PC. The clogged PC specimen was sliced into three equal lengths

(L) of 66.6 mm, such as top slice, middle slice, and bottom slice. The clogged permeability (kC) of the sliced specimen was measured by filling fresh water in a graduated cylinder of a falling head setup up to initial water head (h0) of 50 cm and allowing it to pass through the clogged PC slice specimen untill the final water head 10 mm (h1) was reached. Figure 1 shows the permeability test setup. The permeability was calculated by Eq. (1).

$$k = \frac{Ap*L}{Ac*t} \ln \frac{h_0}{h_1} \quad (1)$$

Where Ac (in cm2) is the cross-sectional area of the PC slice specimen, Ap (in cm2) is the cross-sectional area of the pipe, t (in sec) is the time required to water from water head h0 to h1.

Figure 1. Permeability test setup

For the de-clogging, the fresh water passed through the clogged sliced specimen, and the permeability recovery (kR) was measured, and the total quantity of water required for de-clogging (WR) was also estimated. The de-clogging indicator (IDC) was calculated as per Eq. (2) [1].

$$I_{DC} = \frac{(k_{Rmax} - k_C)}{W_R}) \quad (2)$$

3. RESULTS AND DISCUSSIONS

3.1 Clogged permeability of PC slices

Figure 2 shows the clogged permeability of the PC slices clogged with different types of clogging sediment solutions. The clogged permeability of the PC is higher in the case of PC-25 than in PC-20 and PC-15. It shows that a higher void has less clogging potential. The permeability of top slice was lower for the sand-clogged PC, whereas the permeability of bottom slice was lower for clayey silt-clogged PC. Therefore, the top slice of PC under the influence of sand sediment solution and bottom portion of PC under the influence of Clayey silt sediment solutions were more prone to clogging.

Figure 2. Permeability PC slices clogged with (a) sand sediment (b) Clayey silt sediment

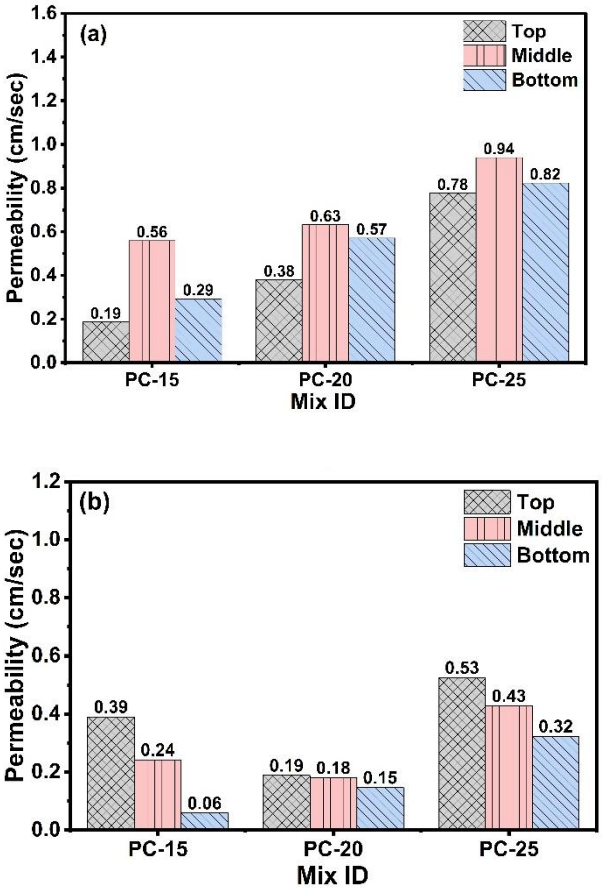

3.2 De-clogging indicator of PC slices

Figure 3 shows the de-clogging indicator of the various clogged PC slices. The value of de-clogging indicator of the top slice is highest among others for of clayey silt clogged PC, whereas the value of middle slice layer was highest for sand-clogged PC. The de-clogging potential of middle slice layer was highest among others for sand clogged PC, whereas, the de-clogging potential of top slice layer was highest among others for clayey silt clogged PC.

Figure 3. De-clogging indicator of PC slices clogged with (a) sand sediment (b) Clayey silt sediment

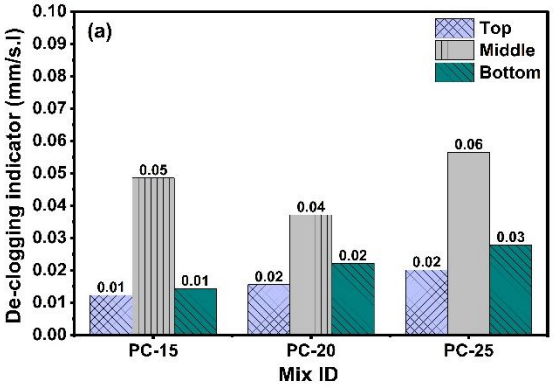

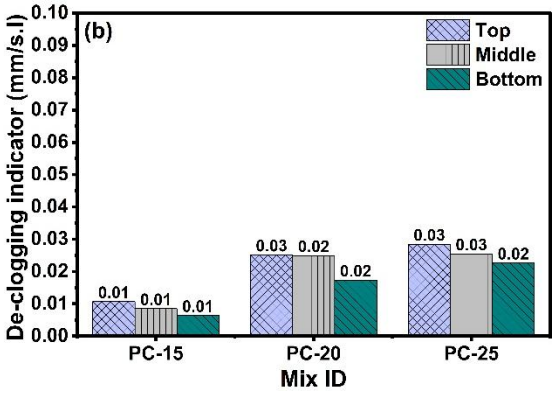

4. CONCLUSIONS:

The following is the summary and conclusion of this study:

- PC with higher void content exhibited lower clogging potential.
- The top slice layer of PC was more prone to clogging under the influence of sand sediment clogging solutions, whereas bottom slice of PC for clayey silt sediment solutions.
- The de-clogging potential was higher for the middle portion of the sand clogged PC, whereas the top portion of clayey silt clogged PC

REFERENCE:

[1] Singh NP, Santha Kumar G, Ganesh Kumar S. Influence of soil-contaminated water on clogging phenomenon of pervious concretes with different void contents. Magazine of Concrete Research 2024:1–17.

[2] Sandoval GFB, Pieralisi R, Dall Bello de Souza Risson K, Campos de Moura A, M. Toralles B. Clogging phenomenon in Pervious Concrete (PC): A systematic literature review. Journal of Cleaner Production 2022;365:132579.

[3]ACI. American Concrete Institute (ACI) ACI 522R-10 - Report On Pervious Concrete 2010.

4th International Symposium on One Health, One World
November 20 – 22, 2025
ABS ID: 71
Code No: IMSBE-OP-13

Adding Polypropylene Fibers To 3d Printable Mortar: Effects on Printability and Material Anisotropy

A. Kapoor[1,2], A. Chourasia[3] and S. Thakur[4]
[1] *Scientist, Structural Engineering Department, Csir-Cbri, Roorkee,India,*
[2]*acsir- Academy Of Scientific and Innovative Research, Roorkee,India.*
[3]*chief Scientist, Structural Engineering Department, Csir-Cbri, Roorkee,India,*
[4]*project Associate, Structural Engineering Department, Csir-Cbri, Roorkee,India*

***Keywords**: 3D concrete printing, Polypropylene (PP) fibers, Extrudability, Buildability.*

Abstract

This study investigates how polypropylene (PP) fibers affect the printability and mechanical performance of 3D-printed mortar. Mortar mixtures with different PP fiber contents (0–0.5%) and water-to-cement ratios (0.28–0.40) were tested, maintaining a constant cement-to-sand ratio of 1:1.3. Moderate fiber addition (≤0.2%) improved extrudability, buildability, and flexural strength, while higher contents reduced compressive strength and caused extrusion issues. The results emphasize the importance of balancing fiber dosage and water content to ensure stable, high-quality 3D-printed mortars for digital construction.

1. Introduction

3D concrete printing (3DCP) is transforming digital construction by enabling flexible designs, cutting material waste, reducing labor, and speeding up projects [1,2]. The success of 3D printing in construction depends on cementitious materials with optimized rheological and mechanical properties for proper printability and structural performance [3]. Polypropylene (PP) fibers are valued for their strength, durability, chemical resistance, and low cost [5,6]. Despite their benefits, the impact of PP fiber content on the anisotropic behavior of 3D-printed elements is underexplored. This study examines how varying fiber content and water-to-cement ratios affect printability and mechanical performance, including extrudability, dimensional stability, buildability, and strength

2. Materials and Methods

2.1 Raw Materials

The raw materials used in this study included Ordinary Portland Cement (OPC) of 43 grade conforming to IS: 8112–2013, locally available river sand as fine aggregate, polypropylene (PP) fibers, potable tap water, and a polycarboxylate-based superplasticizer (SP). The cement had a specific gravity of 3.15. The fine aggregate had a maximum size of 1.18 mm, specific gravity of 2.65, water absorption of 1.20%, and moisture content of 0.10%. The PP fibers were monofilament type, with a specific gravity of 0.91, diameter of 20–25 µm, and length of 12 mm. The SP used was a third-generation polycarboxylate ether-based admixture with a solid content of 20% and specific gravity of 1.03.

Table 1 presents the mix design matrix with PP fiber content, W/C ratio VMA and SP dosage.

	M1	M2	M3	M4	M5	M6
Water: Binder	0.4	0.4	0.4	0.4	0.4	0.4
Total Binder (Kg/m³)	833	833	833	833	833	833
Sand (Kg/m³)	1113	1113	1113	1113	1113	1113
SP (%)	1	1	1	1	1	1
VMA (%)	0.4	0.4	0.4	0.4	0.4	0.4
PP Fiber(%)	0	0.1	0.2	0.3	0.4	0.5

Fig.1. (a) PP fibers; (b) Polycarboxylate ether-based Sp.

2.2 Mix Proportions

A total of fifteen 3D printable mortar mixtures were formulated by varying PP fiber content and W/C ratio. The fiber contents were set at 0.00%, 0.10%, 0.20%,0.30%, 0.40% and 0.50 by weight of cement,while the W/C ratios were chosen as 0.28, 0.32, and 0.40. For all mixes, the cement-to-sand ratio was fixed at 1:1.3 by mass. Each mix was identified using a code in the format X–Y, where X denotes fiber content and Y denotes the compressive strength. The optimum SP dosage required to achieve the desired flow spread was determined experimentally for each mix.

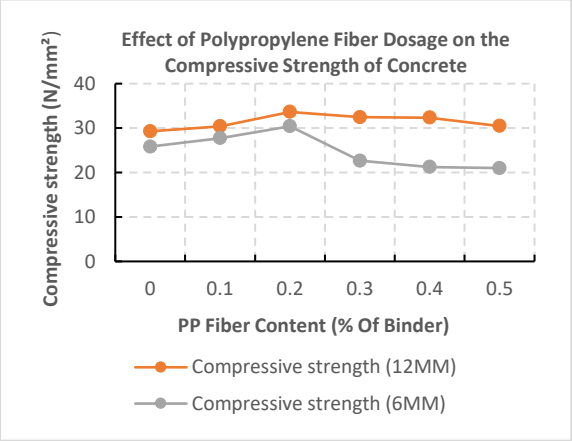

Fig.2. Impact of PP Fiber on Compressive Strength

Fig.3. Impact of PP Fiber on Flexural Strength

Compressive strength increases with PP fiber addition up to 0.2%, reaching a maximum of ~35 N/mm² for 12 mm fibers, then decreases at higher dosages. Overall, 12 mm fibers outperform 6 mm fibers, showing that longer fibers improve strength. The optimal fiber content is 0.2%. beyond which strength declines.

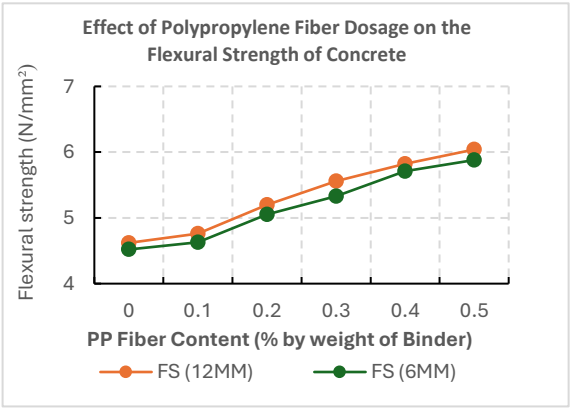

(a) (b) (c) (d) (e)

Fig.4. Effect of PP Fiber Content (0.1%–0.5%) on 3D Concrete Printing Extrudability (Fig. 4a–4e).

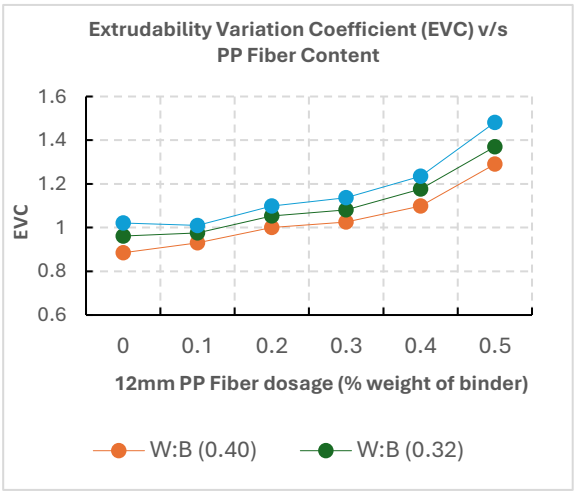

Fig.5.Extrudability Variation Coefficient v/s PP Fiber

Extrudability was evaluated using the Extrudability Variation Coefficient (EVC), defined as the ratio of designed width to actual printed width (lower EVC = better extrudability). The final average height was recorded to evaluate buildability and the Buildability Variation Coefficient (BVC) was calculated as:"

$$\frac{\text{Total designed height- Actual height}}{\text{Total designed height}}$$

Lower BVC values indicate improved buildability.

Fig.6. Check Rheological Behavior Through Printing Tests on PP Fiber.

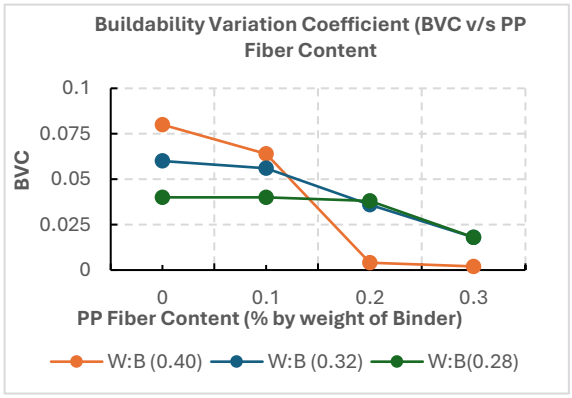

Fig.7. Buildability Variation Coefficient v/s PP Fiber

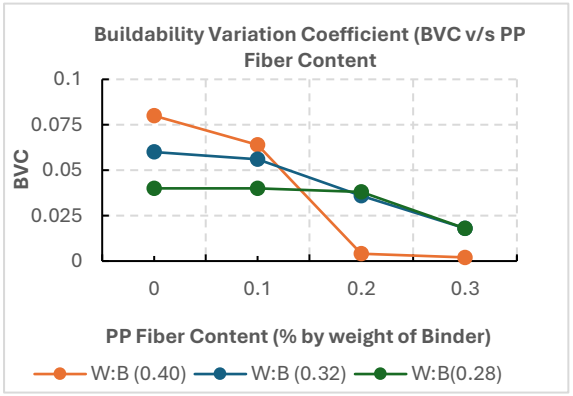

Water-to-Binder ratio of 0.40 with 0.2%

polypropylene fiber content (by binder weight) results in an EVC of approximately 1.0, indicating stable and uniform extrudability with sufficient workability and minimal blockage or segregation, suitable for extrusion-based applications.

At 0–0.1% fiber, the mix flows easily but lacks strength. At 0.2%, it shows a good balance between flow and strength, allowing smooth and stable extrusion. When fiber content exceeds 0.2% (0.3–0.5%), the mix becomes stiff, causing uneven flow, clogging, and poor layer quality.

2.3 Flow Table Test

Flowability was tested using the flow table method as per IS: 1199 (Part 6) – 2018 [35]. The average spread after 25 drops was measured and recorded as the flow spread. A target value of 160 ± 10 mm was set, based on trials and literature, to maintain a balance between extrudability and buildability.

Fig.8. flow table test

3. Conclusion

This study highlights the significant impact of polypropylene fibers on the printability and mechanical behavior of 3D printable mortars. Higher PP fiber content, particularly with 12mm fibers, enhance flexural strength, extrudability and buildability. However excessive fiber addition reduces compressive strength and may cause extrusion blockage, reflecting anisotropic effects. These results highlight the need to optimize fiber dosage and W/B ratio to achieve a balance between fresh and mechanical properties for effective 3D printed construction.

REFERENCES

[1] Le, T. T., Austin, S. A., Lim, S., Buswell, R. A., Gibb, A. G., & Thorpe, T. (2012). Mix design and fresh properties for high-performance printing concrete. Materials and Structures, 45(8), 1221–1232.

[2] Bos, F. P., Wolfs, R. J. M., Ahmed, Z. Y., & Salet, T. A. M. (2016). Additive manufacturing of concrete in construction: potentials and challenges of 3D concrete printing. Virtual and Physical Prototyping, 11(3), 209–225.

[3] Panda, B., & Tan, M. J. (2018). Experimental study on mix proportion and fresh properties of fly ash based geopolymer for 3D concrete printing. Ceramics International, 44(9), 10258–10265.

[5] Banthia, N., & Gupta, R. (2006). Influence of polypropylene fiber geometry on plastic shrinkage cracking in concrete. Cement and Concrete Research, 36(7), 1263–1267.

[6] Singh, S., Singh, L. P., & Thakur, A. (2021). Polypropylene fiber-reinforced concrete: A review. Construction and Building Materials, 278, 122347.

[7] Rahul, A. V., Santhanam, M., Meena, H., & Ghani, Z. (2019). 3D printable concrete: Mixture design, printing parameters and their effects on mechanical properties. Cement and Concrete Composites, 97, 13-23.

[8] IS: 1199 (Part 6) – 2018. Fresh Concrete – Method of Test – Flow Test. Bureau of Indian Standards, New Delhi.

4th International Symposium on One Health, One World
November 20 – 22, 2025
ABS ID: 67
Code No: IMSBE-OP-14

Development Of Microbial Based Process for Bio-Cement, Bio-Brick and Self-Healing Concrete Using Locally Available Resources

Sanjay Deori[1*], Dipak Basumatari[2], Masoom Saikia[3], Archana Yadav[4], Ratul Saikia[5], Leon Raj J[6]., And Nibir Pran Borah[7]

[1]*senior Principal Scientist & Group Leader, Applied Civil Engineering Group, Engineering Sciences And Technology Division, Csir-Neist, Jorhat, Assam India*

[2] *Principal Scientist, Applied Civil Engineering Group, Engineering Sciences And Technology Division, Csir-Neist, Jorhat, Assam India*

[3]*research Scholar, Biotechnology Group, Biological Sciences And Technology Division, Csir-Neist, Jorhat, Assam India*

[4]*senior Technical Officer, Biotechnology Group, Biological Sciences And Technology Division, Csir-Neist, Jorhat, Assam India*

[5]*chief Scientist & Head, Biological Sciences And Technology Division, Csir-Neist, Jorhat, Assam India*

[6]*principal Scientist, Applied Civil Engineering Group, Engineering Sciences And Technology Division, Csir-Neist, Jorhat, Assam India*

[7]*senior Technical Officer, Applied Civil Engineering Group, Engineering Sciences And Technology Division, Csir-Neist, Jorhat, Assam India*

**Corresponding Author's E-Mail : Sanjaydeoricrri@Gmail.Com*

ABSTRACT

Microorganism based bio-cementation process has revealed a new path in the field of construction engineering. The concept of Bio-Cement", Bio-Brick" and Microbial concrete or Self-healing Concrete" are the promising alternative construction materials produce from the process of microbial induced carbonate precipitation (MICP). Bacterial cement can be a better replacement of conventional cement as it is highly environmentally friendly also can heal minor damages in structure.

In this study, many resources were tested for calcium carbonate precipitation found locally, a previously isolated bacterium from orchid called Crinum Asiaticum found to be highly calcium carbonate precipitator. The bacteria known as Brevibacterium Sediminis is gram positive and can survive in alkaline environment. The bacteria were further optimised for MICP, and it showed maximum precipitation in pH level of 9 and at a temperature of 37℃. For bio cement mortar we used locally available sand from river Brahmaputra (zone 4) and Kanaighat (zone 2). Mixture of both sands showed the best result when tested for compressive strength following IS code 4031(Part 6). Further rice husk ash having specific gravity 1.75 of locally available rice Joha dhan used for improvement of compressive strength. This bio cement is not as consistent as conventional cement also needs 14 hours for loose plasticity and more than 24 hours for complete hardening process. For evidence of bacteria in calcite precipitation SEM (Scanning Electron Micrography) was done is CSIR-NEIST lab and the result was quite impressive.

Keywords: Bio-cementation, Crinum Asiaticum, Brevibacterium Sediminis, Brahmaputra Sand, Kanaighat Sand

1. INTRODUCTION

Now a days, air pollution is found to be the major issue globally, among the highest contributor of air pollution, cement production (at 1440℃) is at the top. Every 1 kg of cement production contributes 1 kg of Carbon-dioxide to the environment. So, this concept of bio-cement has turned out to be in trending. These can also act as a healing agent, when hair cracks are occurred in concrete structures. Microbial induced Carbonate precipitation is where urease positive bacteria can precipitate Calcium carbonate which act as the main binding material in case of conventional cement.

There are many orchids found in North-Eastern states of India. The Crinum asiaticum is mainly found in sub-tropical reasons like North-Eastern part of India. It is a bulb-forming perennial producing an umbel of large, showy flowers that are prized by gardeners.

There are many bacteria of Bacillus group, which were found to be precipitator and a large depositor of Calcium Carbonate. Many researches are now on process for optimisation of deposition as it is a very valuable process. Bio-cementation process takes place when micobially induced calcium carbonate precipitation (MICP) occur by the urease activity of halo tolerant and alkaliphilic microorganisms. The urease producing bacteria (UPB) in presence of urea and calcium ions creates MICP crystallization of calcite on to solid particle surface.

Assam is one of the main contributors to the rice production in India. Varieties of local rice such as Joha dhan, Sali Dhan, Ahu Dhan are cultivated everywhere in North-East. The rice husk ash is a major source of silica, almost 90% of silica is present in rice husk ash. The role of silica in conventional cement is to provide strength by forming Di Calcium Silicate and Tri Calcium silicate, which is responsible for both initial and late strength development in concrete. As rice husk ash is a waste product and pollute our air, so use of this ash can be a good waste product management.

The mighty River Brahmaputra has been treating as lungs of Assam since early civilisation days, providing mainly water and navigation facilities. But every year its depositing silts result in devastating flood mainly in the Brahmaputra valley. The sand and silt of this river is not being used for construction purposes as it belongs to the Zone-4 gradation. The purpose of use of this sand in this study to reduce this deposition, so that probability of occurrence of flood can be reduced and navigation of large ships can be improved during the winter season. Also, there is another river present in Golaghat district of Assam called Kanaighat river is a contributor of Zone 2 sand.

The Scanning Electron Microscope (SEM) is state-of-art equipment which scans a focused electron beam over a surface to create an image. The electrons in the beam interact with the sample, producing various signals that can be used to obtain information about the surface topography and composition.

The consistency of bio-cement paste is defined as the percentage of requirement of bio-cement paste at which the viscosity of paste in such a way that it determines the amount of water needed to make a cementation solution paste. The standard consistency of a cement paste determines using Vicat Apparatus that will permit the plunger to penetrate to a point 5 to 7 mm from the bottom of the cement paste. The consistency plays a vital role in the determination of compressive strength of bio cement or workability test for bio cement.

2. MATERIALS AND METHODOLOGIES

2.1 Collection, enrichment of sample and bacteria Isolation

Various samples were collected aseptically in different locations in sterilized polyethene zipper bag and pH was recorded to be in the range of 4-10 indicating both acidic and alkaline environment. The samples were suspended in a sterile saline solution (0.9 % NaCl), potential isolates were obtained by the serial dilution method and by plating the samples on nutrient agar. The plates were then incubated at 30◦C and subsequent subculture was done until pure distinguishable single bacterial colonies were obtained. In total 359 bacterial strain were isolated and 51 strains were revived in nutrient broth as given in the Figure-1.

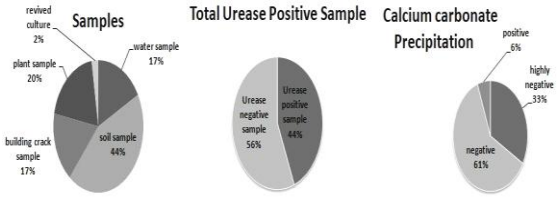

Figure 1. Bacterial isolation source with total number of isolates and urease positive and calcium carbonate precipitation.

2.2 Ureolysis or Degradation of Urea

The microbial urease hydrolysis urea into Ammonium and Carbonate. One mole of urea is hydrolysed intracellularly to Ammonia and Carbamic acid, then forms bicarbonate, Ammonium and hydroxide ions in water. The production of hydroxide ions results in the increase of pH, which in turn can shift the bicarbonate equilibrium, resulting in the formation of carbonate ions. The produced carbonate ions precipitates in the presence of calcium ions as calcium carbonate crystals.

2.3 Selection of urease-producing bacteria

Potential urease producing isolates were screened using Christensen's medium or urea agar 2% filter sterilized urea were supplemented. Single colony was selected and inoculated on medium and then incubated at 30◦C for 5 days. E. Coli was used as a negative control and Proteus vulgaris was used as a positive control. The urease production was examined through visual observation every day throughout the incubation period for colour changes in medium from pale yellow to pink red recorded as a urease-positive (Figure-2). Out of 359 bacterial isolates 30 isolates designated as urease positive and were selected for further studies-based on screening results of urea agar as shown in the Figure-1.

Figure 2. (Top) E. coli (negative control) showed no colour change and (Bottom) Proteus vulgaris (positive control) showed urease positive.

2.4 Screening for Calcium Carbonate (CaCO3) precipitation

The ability of the 30 isolated urease positive bacteria to precipitate carbonate were tested according to (Stabnikov et al.2013). Briefly, 90 ml of 0.5 M anhydrous CaCl2 was mixed with 90 ml of filter sterilized 1 M urea and 20 ml of culture liquid of each bacterial isolate. Negative control was prepared without inoculums. Positive control was inoculated with Proteus vulgaris Cultures were incubated for 48 h at 37◦C. Calcium concentration was determined in the liquid after bio-cementation using EDTA titration (APHA, 1999).

Briefly, 1 ml of sodium hydroxide buffer was added to 15 ml liquid sample to maintain the pH at 10 then few drops of pH indicator (0.5% Eriochome black T) were added and the sample was titrated with 0.01 MEDTA until the colour changed (Zaghloul et al. 2020). Colour changes to blue colour considered as positive whereas pink colour was considered as negative. Out of 30 bacterial isolates only one strain i.e.,Brevibacterium Sediminis showed precipitation of calcium carbonate (Figure 3).

Fig 3 (Left) Calcium carbonate precipitation test and (Right) Calcium Carbonate precipitated by B. Sediminis against control sample

Brevibacterium Sediminis an endophytic strain isolated from aerial root of orchid Crinum asiaticum was used throughout this study. The culture was previously isolated in the Biological Sciences and Technology Division of CSIR-NEIST. The culture was maintained at nutrient agar medium (pH 6.8 ±2). Nutrient broth medium was used to grow the isolate. Bacterial culture was grown at 37°C under shaking condition (150 rpm).

2.5 Optimization

Various parameters were optimised for maximum CaCO3 precipitation. The different parameters were Urea, Calcium chloride, pH, temperature and time interval. The precipitation versus the parameters is discussed in the Table no 1.

Characterization of colony and cell morphology was observed under visual observation while gram staining was observed under compound microscope as shown in the Table-1.

Table 1. Characterization of colony and cell morphology

Bacterial culture	Colony size	Color	Shape	Gram staining
Brevibacterium Sediminis	Small	Slightly brown	Circular, raised elevation, soft surface	Gram +Ve

2.9 Compressive strength of bio-cement mortar

To study the compressive strength test of cement mortar Brevibacterium Sediminis was grown in nutrient agar. An optimised cementation solution containing 1.5 M Urea + 0.75 M CaCl2 + 25 mM NaHCO3 + 150 mM NH4Cl was used with bacterial solution which was kept at 37℃ for 48 hours in incubator. The total solution required was calculated by the following method.

As a first trial, above solution was mixed with Brahmaputra sand (fine, medium and coarse mixed uniformly) and cured for 28 days. Three cubes of the mixes in the cement testing mould sizes of 7.06cm x 7.06cm x7.06cm were casted as per IS 4031-1988 method. The samples were casted with 5, 10 and 15% cementation solution to sand. After that samples were cured at a controlled temperature of 37℃ in incubator for 28 days. No noticeable result was found in compressive strength (Fig.5).

Figure 5. Bio-Cement mould with 5, 10 and 15 percent cementation solution

3.VIABILITY TEST

3.1 Scanning Electron Microscopy (SEM) analysis

To study the role of microbial induced calcite precipitation, specimens were observed under Scanning Electron Microscope (SEM). After the calcite precipitation the samples were collected and dried at 60°C for 24 h. The samples were gold-coated with a sputter coating machine (Emitech K575) and examined using a JEOL JSM-5410LV (JEOL, United Kingdom) SEM at accelerating voltages ranging from 15 to 35 kV.

4. CONCLUSIONS

Brevibacterium Sediminis which is an endophytic strain and isolated from locally available aerial roots of orchid in North East Region of India was found Urease positive and a large precipitator of CaCO3. Till now there is no any study reported on Bio-Cementing and Self-Healing Concrete using Brevibacterium Sediminis bacteria as a potential precipitator of CaCO3.

- After optimization the maximum of 3.13 gm of CaCO3 was precipitated, when 10 ml of bacterial solution was mixed with 90 ml of cementation solution containing 1.5 M Urea + 0.75 M CaCl2 at pH 11 after 72 hours of incubation at 37℃.
- Rice husk ash was introduced in the Bio-cement as there was a lack of silica in the sand and bacterial solution mixture, as silica is needed to introduce strength after hardening. So locally available Rice husk ash of specific gravity 1.75 and 90% of silica content was used which is being considered as waste materials. The utilization of such waste material can reduce the burden on environment.
- The consistency of Bio-cement is found out to be 105%, which is very high as compared to conventional cement (25-35%). Also, initial setting time of Bio-cement is 14 hours, which is very slow in losing elasticity and become a plastic paste.
- After numbers of trials with different proportions, the mixture of Kanaighat river sand (Zone-2) and Brahmaputra river sand (Zone-4) with rice husk ash, lime and cementation solution after 28 days showed strength of 0.89 Mpa when kept at 37℃. The Brahmaputra river sand with Kanaighat river sand produced more strength compared to when tested for Brahmaputra river sand alone, which is zone 4. Also, after 30, 60 and 90 days the compressive strength of the mixed sand samples are 0.89, 1.66 and 1.89 Mpa. So, it is be concluded that hardening process in case of bio-cement is slow and requires more time when compared to Ordinary Portland conventional cement.
- The Bio-cement cubes were kept at two different conditions of dry and wet curing at the temperature of 37℃. The compressive strength of cubes were found about 0.89 Mpa after 28 days of dry curing and after the wet curing it was found about 0.78 Mpa.

REFERENCES:

Viktor Stabnikov, Chu Jian,Volodymyr Ivanov, Yishan Li (2013) Halotolerant, alkaliphilic urease-producing bacteria from different climate zones and their application for biocementation of sand. World J Microbiol Biotechnol (2013) 29:1453–1460 DOI 10.1007/s11274-013-1309-1.

APHA (1999) Standard Methods for the Examination of Water and Wastewater. American Public Health Association, Washington DC.

Eman H. Zaghloul, Hassan A.H. Ibrahim, Dalia El S. El-Badan (2020) Production of biocement with marine bacteria; Staphylococcus epidermidis EDH to enhance clay water retention capacity. Egyptian Journal of Aquatic Research, Volume 47, Issue 1, March 2021, Pages 53-59.

Indian Standard IS : 6932 (Part I) -1973 Methods of Tests for Building Limes.

Indian Standard IS: 4031 (Part 4)-1988 (Reaffirmed 1995) Methods of Physical Tests for Hydraulic Cement. Part 4-Determination of Consistency of Standard Cement Paste (first revision)

Indian Standard IS: 383 -1970 (Reaffirmed 2002) Specification for Coarse and Fine Aggregates from Natural Sources for Concrete (Second Revision)

Mr. Phani Chandra Veligatla

4th International Symposium on One Health, One World
November 20 – 22, 2025

ABS ID: 138
Code No: IMSBE-OP-16

Transforming Rubble to Resource by Performance Enhancement of Recycled Aggregate Through Sustainable Treatment

A. Aggarwal[1,2], S. K. Singh[1], And G. Goel[2]
[1]*CSIR-Central Building Research Institute, Roorkee 247667, Uttarakhand, India*
[2]*Thapar Institute of Engineering and Technology, Patiala, 147004, India,*
Correspond to Prof S. K. Singh, Chief Scientist (sksingh.cbri@csir.res.in)

***Keywords**: Circular economy; Recycled aggregate; Sustainable construction; Treatment and processing.*

1. INTRODUCTION

The construction sector generates approximately 20% of global greenhouse gas (GHG) emissions and consumes nearly 50% of the world's natural resources, resulting in a substantial environmental burden [1]. The global construction industry is witnessing a surge in construction and demolition (C&D) waste generation, which exceeds 3.57 billion tons annually and is projected to rise to 27 billion tons by 2050 [2]. India, as a representative case, generates around 350 million tons of C&D waste annually but recycles less than 1% formally, primarily due to limited infrastructure, poor enforcement, and inadequate awareness [3]. There is an urgent need for sustainable alternatives, such as recycled aggregates (RA), to reduce pressure on natural resources and decrease environmental impact. The number of publications from the past two decades is represented in Fig. 1(a), illustrating the temporal distribution of scholarly publications indexed in Scopus from 2005 to 2025 based on the keyword “Recycled aggregate in concrete construction”. Furthermore, Fig. 1(b) illustrates research conducted in various countries, highlighting the global contributions to this research domain. China (CH) emerges as the predominant contributor, followed by India (IN) and Australia (AU).

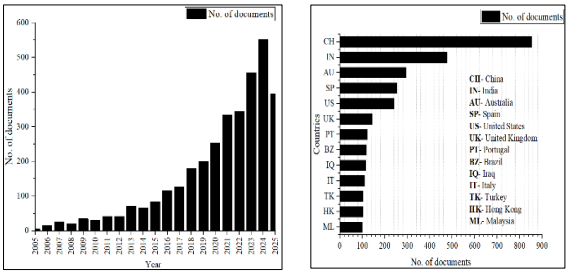

Figure 1. Number of documents in the field of RA (data obtained from Scopus): a) Annual count of major publications from 2005 to 2025, b) Publications by country.

RA is generally considered inferior to NA due to its porous structure, lower density, and weaker surface properties [4,5]. Pre-treatment methods have thus gained prominence as strategies to enhance RA quality [6,7]. Acid soaking using strong acids, such as Sulfuric acid (H2SO4) and Hydrochloric acid (HCl), efficiently dissolves cementitious phases [8]. However, they also induce micro-cracking, alter aggregate mineralogy, and can compromise the long-term strength and durability of treated RA, raising environmental concerns.

To overcome these limitations, oxalic acid (C2H2O4) is introduced in this study as an organic alternative that has the potential to selectively decalcify cementitious phases while preserving aggregate integrity.

The special focus of this article is to address the inherent limitations of RA, its inferior physical and chemical properties, by demonstrating oxalic acid as a sustainable, technically viable treatment pathway.

2. EXPERIMENTAL SETUP

RA was obtained from C&D waste and subjected to baseline physical and chemical testing. Three acid treatments were employed, i.e., hydrochloric acid, sulphuric acid, and oxalic acid (an innovative organic treatment). The schematic chemical bond is shown in Figure 2. Each batch was fully immersed in the respective acid solution and left undisturbed. The effectiveness of acid treatment is primarily influenced by solution concentration and immersion duration [9]. H_2SO_4 and HCl were applied at 0.1 M concentration for 24 hours, while $C_2H_2O_4$ (0.1 M) was tested for both 24 and 72 hours (illustrated in Figure 3).

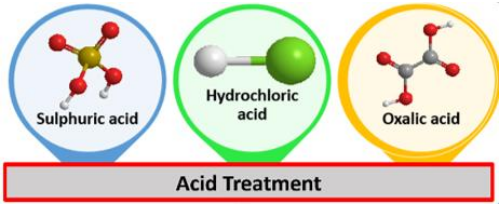

Figure 2. Chemical bond of acids

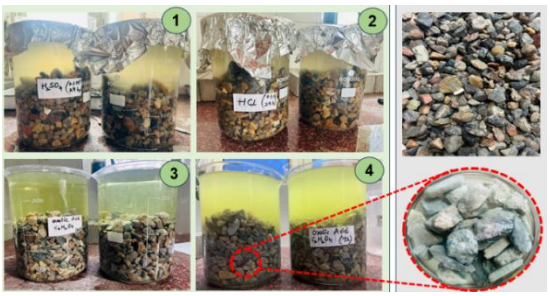

Figure 3. Acid treatment of RA

Mortar removal (%) was assessed through water absorption testing in accordance with IS 383:2025 [10]. Treated RA samples were cured for 24 hours, oven-dried for 4 hours at 105 ± 5 °C, cooled to room temperature, and weighed to determine mortar loss. Acid treatment successfully reduced the quantity of adhered mortar on the RA surface, evidencing chemical dissolution and refinement of microstructural features.

3. RESULTS AND DISCUSSION

The findings demonstrate that targeted acid treatment strategies can fundamentally alter the intrinsic limitations of RAs by reducing adhered mortar and refining their microstructure. HCl-treated aggregates achieved the highest mortar removal (106 g), followed by H_2SO_4 (93 g) and oxalic acid (65 g). Despite lower mortar removal, oxalic acid resulted in a notable reduction in water absorption (1.30%), comparable to HCl (2.12%). Untreated RA showed poor properties compared to NA, with higher AIV (43.2%), lower bulk density (997.9 kg/m³), specific gravity (2.38), and higher water absorption (3.68%). Acid treatments improved performance, with oxalic acid yielding the best results, i.e., the lowest water absorption (2.89%), the highest bulk density (1440 kg/m³), and an AIV close to NA, outperforming H_2SO_4 and HCl. Adoption of such techniques could enable broader utilisation of RA in construction, fostering circular economy practices, lowering dependency on virgin aggregates, and mitigating environmental degradation.

4. CONCLUSIONS

This study demonstrates that acid-treated RAs, particularly those processed with hydrochloric and oxalic acids, possess the requisite physical and mechanical properties to replace NA in concrete applications. The developed methodology provides a scalable and effective solution to the challenge of C&D waste in India and globally, supporting ambitions for greener, more sustainable construction practices. Future work should focus on optimising treatment protocols and exploring long-term durability in field conditions.

ACKNOWLEDGEMENT

The authors are grateful to the CSIR-CBRI for granting permission to publish this work.

REFERENCES

[1] M.H. Javed, A. Ahmad, M. Rehan, M. Farooq, M. Farhan, M.A. Raza, A.S. Nizami (2025). Advancing Circular Economy Through Optimised Construction and Demolition Waste Management Under Life Cycle Approach. *Sustainability*, *17*(11), 4882.

[2] Y.R. Patil, V.A. Dakwale, R.V. Ralegaonkar (2024). Recycling Construction and Demolition Waste in the Sector of Construction. *Advances in Civil Engineering*, *2024*(1), 6234010.

[3] cseindia.org/page/aboutus, Centre for Science and Environment, 2024

[4] Y. Gong, C. Yu, Z. Zhang, Z. Jia, E. Dong, Q. Lin, X. Niu, Y. Zhang, W. Wang, (2025). Enhancement of recycled coarse aggregate concrete properties using a combined adjustable cement slurry coating and mixing

approach. *Construction and Building Materials*, 491, p.142634.

[5] C. Lu, Q. Yu, J. Wei, Y. Niu, Y. Zhang, C. Lin, P. Chen, C. Shi, P. Yang, (2024). Influence of interface transition zones (ITZ) and pore structure on the compressive strength of recycled aggregate concrete. *Construction and Building Materials*, 456, p.139299.

[6] J.V.M. Raman, V. Ramasamy, (2021). Various treatment techniques involved to enhance the recycled coarse aggregate in concrete: A review. *Materials Today: Proceedings,* 45, pp.6356-6363.

[7] R.P. Neupane, N.R. Devi, T. Imjai, A. Rajput, T. Noguchi, (2025). Cutting-edge techniques and environmental insights in recycled concrete aggregate production: A comprehensive review. *Resources, Conservation & Recycling Advances*, 25, p.200241.

[8] H.S. Kim, B. Kim, K.S. Kim, J.M. Kim, (2017), Quality improvement of recycled aggregates using the acid treatment method and the strength characteristics of the resulting mortar. *Journal of material cycles and waste management*, 19(2), pp.968-976.

[9] W. Thaue, M. Iwanami, K. Nakayama, W. Yodsudjai, (2024). Influence of acetic acid treatment on microstructure of interfacial transition zone and performance of recycled aggregate concrete. *Construction and Building Materials,* 417, p.135355.

[10] Bureau of Indian Standards, 2025. Draft Indian Standard: Aggregates, Specification Part 1, Coarse and Fine Aggregates for Concrete (Fourth Revision of IS 383). Document No. CED 02(27866) WC. Approved 27 January 2025.

4th International Symposium on One Health, One World
November 20 – 22, 2025
ABS ID: 72
Code No: IMSBE-OP-18

Characterisation Of Printing and Mechanical Properties Of Agro-Waste Based Binary Cementitious Composite

B. Pal[1], A. Chourasia[2]
[1] Scientist, CSIR-Central Building Research Institute, Roorkee 247 667, India,
[2] Chief Scientist, CSIR-Central Building Research Institute, Roorkee 247 667, India,
Correspond to Dr. B. PAL (biswajitjgec.1992@gmail.com)

Keywords: *Buildability, Open Time, Compressive Strength, Anisotropy, Binary.*

INTRODUCTIONS

In recent years, the construction industry has witnessed rapid advancements through the advent of 3D concrete printing, along with a growing emphasis on sustainability achieved by incorporating agro-industrial waste into 3D printable concrete (3DPC). However, the limited understanding of the printing performance and mechanical behaviour of agro-waste-based 3DPC remains a major challenge, hindering its widespread adoption. Since these properties are crucial for material design and for evaluating the structural performance of printed elements, addressing this knowledge gap is essential.

Hence, to develop a 3D-printable concrete mix, researchers have focused on characterizing early-age printing parameters [1], hardened mechanical properties [2], durability aspects [3], as well as performance under dynamic loading [4] and fire exposure [5], among others. Over the years, numerous studies have explored the use of various industrial wastes, such as fly ash (FA) [6], ground granulated blast furnace slag (GGBFS) [7], ladle furnace slag (LF) [8], and lead–zinc tailings [9], in developing waste-based cementitious binders. Alongside, researchers have also investigated agricultural by-products, including bagasse ash (BA) [10], rice husk ash (RHA) [11], and hazelnut shell ash [12], for the same purpose. In these studies, ordinary Portland cement (OPC) was partially substituted with different agro-industrial wastes to produce binary waste-based cementitious binders.

In general, from the perspective of designing a 3D-printable cementitious mix, only a limited number of studies have simultaneously investigated the combined effects of various supplementary cementitious materials and admixtures on both mechanical and printing properties. Moreover, most existing research on 3D printing has primarily focused on individual aspects, such as characterizing early-age properties [13] assessing mechanical performance [14], or evaluating mechanical anisotropy [15,16].

For example, in [17], researchers investigated two mixed types: a control mix made solely with cement, and another incorporating OPC, FA, and silica with SP as an admixture. In the composite binder, the proportions of the constituents were kept constant. The printed specimens were then evaluated for flow characteristics (via flow table results), as well as compressive and flexural strengths under loads applied from different directions at various printing intervals. In contrast, the present study focuses on examining how different admixtures (SP, VMA, retarder), and their varying proportions simultaneously influence both the mechanical and printing properties.

This study examines the printability characteristics (e.g., extrudability, buildability) and hardened mechanical properties (e.g., compressive strength) of 3D printable concrete (3DPC) mixtures incorporating Bagasse Ash (BA) as a partial cement replacement. The mix design process involves a simultaneous evaluation of printing performance and compressive strength across different proportions of primary constituents and admixture dosages. Subsequently, the mechanical properties are assessed under three distinct loading directions. Finally, the compressive strength of printed specimens is compared with that of conventionally cast specimens.

2. MATERIALS AND METHODS

Among the raw binders, Ordinary Portland Cement (OPC, 43 grade; ASTM C150 [18]) and Bagasse Ash (BA; ASTM C618 [19]) were used in this study. Since the procured BA was not fully burned, it was thermally processed at 650 °C for 2 hours [20]. Following thermal and subsequent mechanical processing, the maximum particle size of BA was reduced to

about 100 µm, with d_{90} and d_{10} values of 75 µm and 4 µm, respectively. X-ray fluorescence (XRF) analysis confirmed that BA primarily consists of SiO_2 (≈84%) along with unburned carbon, indicating incomplete combustion in its raw state. The fine aggregate used in the mix had a fineness modulus of 2.4 and a dry specific gravity of 2.62. To enhance printability and strength, polycarboxylate-based superplasticiser, viscosity-modifying admixture (VMA), and a retarder were incorporated, given their established role in cementitious composites. Trial mixes were prepared with a fixed cement-to-BA ratio of 60:40 to examine the influence of varying admixture dosages. Among the printability tests, flowability, extrudability, buildability, and open time were evaluated, the details of the test processes are provided in a recently published article [16]. For hardened properties, compressive strength was measured on cube samples, extracted from printed specimen, in accordance with [21].

3. RESULTS AND DISCUSSION

3.1 Effect of admixtures on the compressive strength and open time of the binder

This section evaluates the effects of superplasticizer (SP), viscosity-modifying admixture (VMA), and retarder dosages on the compressive strength and open time of binary mixes. In the first set of trials, the SP dosage was varied in binary (C:BA = 60:40, w/b = 0.4, s/b = 1.4) mixes without VMA or retarder, and the optimum SP content was identified. In the second set, the influence of VMA dosage on open time and compressive strength was examined using the optimum SP content obtained earlier, leading to the determination of the optimum VMA level. In the third set, the retarder dosage was varied, and its impact on open time and compressive strength was assessed for the mix containing the previously optimized SP and VMA dosages. Finally, based on the targeted hardened property (compressive strength) and key printability parameter (open time), the optimum combination of the three admixtures was established, and the final binary binder design mix was formulated.

Fig.1(a). illustrates the effect of varying SP content on the compressive strength and open time of the mixes. The open time is defined as the duration over which the mix retains the desired flowability, ensuring pumpability, extrudability, and buildability. From a practical perspective, a longer open time indicates extended printability. As shown in Fig. 1(a), SP dosage has a significant influence on open time. With increasing SP content, the open time of the binary mix increases due to enhanced deflocculation and dispersion of cement particles. However, beyond 1% SP, the mix begins to lose its shape stability, resulting in a reduction in open time. At 1% SP dosage, the mix exhibits the highest open time (~25 minutes) along with the maximum compressive strength, which exceeds the targeted 38 MPa. Here, it is required to be mentioned that Therefore, an SP dosage of 1% was selected as the optimum value for subsequent studies involving VMA and retarder.

Fig.2. illustrates the effect of varying VMA dosages on the compressive strength and open time of the mixes at a fixed SP dosage of 1%. As shown in Fig. 9.4, the binary mix achieves the maximum open time at a VMA dosage of 0.5%. However, at this dosage, the compressive strength decreases to approximately 34.84 MPa, which is about 8% lower than the design strength of 38.25 MPa. Therefore, a VMA content of 0.5% is selected as optimal for the ternary mix and is subsequently used in further trials to investigate the effect of retarder dosage. Fig.3. shows the open time and compressive strength of the binary mix containing SP = 1% and VMA = 0.5%. It can be seen that adding 0.4% retarder extends the open time of the binary mix to 60 minutes. At this retarder dosage, the compressive strength reaches approximately 40.7 MPa, exceeding the target design strength. Therefore, 0.4% retarder (by mass of binder) is considered optimal for balancing both printability and hardened properties. Based on these results, the final mix design for the developed M30-grade 3D printable binary binder, incorporating agro-industrial waste, is established. The buildability performance with the developed mix is shown in Fig. 2. It is observed that upto 15 layers can effectively be printed employing the developed mix.

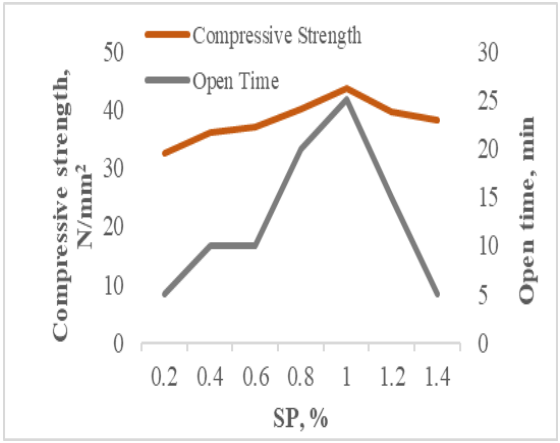

(a)

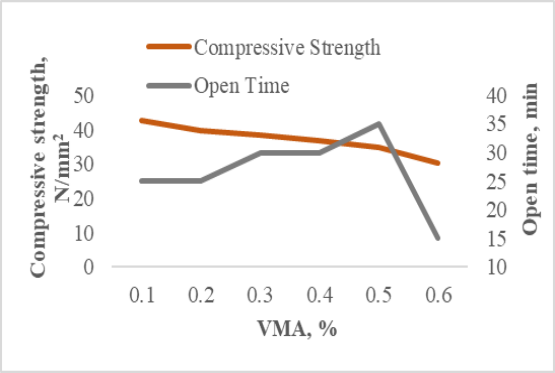

(b)

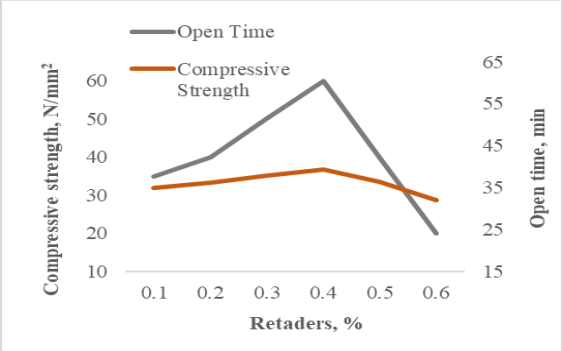

(c)

Fig.1 Effect of varying dosages of (a) Super plasticizer (SP), (b) VMA, and (c) retarders on the compressive strength and open time of BA based binary composite

3.2 Effect of loading direction on the compressive strength

Figure 3 presents a comparison of compressive strength measured along different directions (for details of direction, refer Fig. 2) for the printed mix and the corresponding mould-cast specimen. It is observed that the compressive strength of the printed specimens, regardless of loading direction or mix type, is consistently lower, showing an approximate 20% reduction compared to the mold-cast samples. Similar reductions in strength, ranging from 12% to 26% for printed specimens relative to mold-cast samples, have been reported in [22]. This decrease is attributed to weak interlayer bonding and the presence of pores between adjacent filaments, which reduces the overall strength of printed specimens compared to conventionally cast ones [23].

Moreover, loading in the lateral or Z-direction (for details of direction, refer Fig. 2) results in the lowest compressive strength among the three directions for the binary mix, likely due to interlayer or bond failure along this direction. In contrast, the other two directions exhibit a combination of diagonal shear and interlayer bond failure, leading to comparatively higher strengths. The axial or X-direction demonstrates the highest compressive strength, consistent with previous reports for 3D printed cube specimens under axial loading [24,25]. Such analysis is valuable for practical applications in selecting the printing orientation relative to the anticipated loading direction. However, an opposite trend was observed in [26], which may be attributed to the interaction of multiple nonlinear phenomena affecting the failure of 3D printed specimens. Therefore, further research is needed to fully understand these effects.

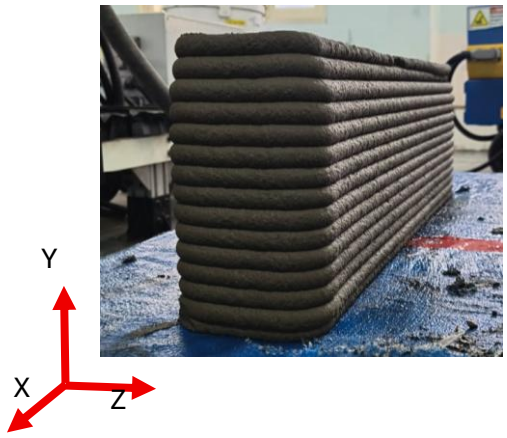

Fig.2 Buildability of the binary mix

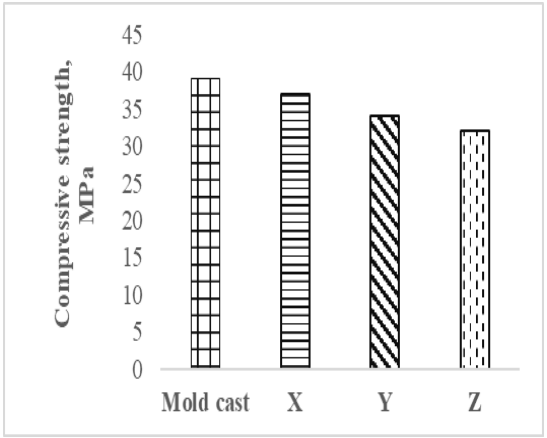

Fig.3 Comparison of compressive strength of printed specimen loaded from three different directions along with the mold cast sample (for details of direction, refer Fig.2)

4. CONCLUSIONS

In this study, bagasse ash (BA) is effectively utilized to develop sustainable, eco-friendly, 3D-printable concrete mixes binary (OPC and BA) mixes, targeting a concrete grade of M30. Accordingly, a series of trial mixes are designed by varying the proportions of different combinations of superplasticizer (SP), viscosity-modifying admixture (VMA), and retarder. These mixes are then evaluated for their printing performance and compressive strength. To assess printing behavior, tests are conducted to determine the printability performance such as buildability, and open time of the designed mixes. Based on the extensive experimental results obtained from the agro-industrial waste-based binary cementitious mixes, the following conclusions are drawn:

- Increasing the VMA dosage has either a negligible or slightly adverse effect on the compressive strength of the mixes. In contrast, increasing SP and retarder dosages enhances compressive strength, but exceeding the optimal levels of these admixtures leads to a reduction in strength for the mix.
- The open time of the 3D-printed cementitious composites improves with the addition of VMA, SP, and retarder. However, beyond the optimum admixture content, the open time begins to decrease.
- Compressive strength of printed specimen is lowest if load is applied lateral to the printed layer direction (Z-direction). Whereas, it is the longitudinal direction that gives the highest compressive strength.

In future, the present work can be extended to investigate the durability and thermal performance of such 3D printed sustainable cementitious composite. Moreover, a physics based numerical model can also be developed that could save significant time and cost associated with experimental work.

REFERENCES:

[1] Q. Wang, J. Xu, D. Feng, W. Li, Y. Zhou, Q. Wang, Properties and printability evaluation of three-dimensional printing magnesium oxychloride cement by fully utilizing aeolian sand, Frontiers of Structural and Civil Engineering (2024) 1–15.

[2] W. Chen, J. Pan, B. Zhu, X. Ma, Y. Zhang, Y. Chen, X. Li, L. Meng, J. Cai, Improving mechanical properties of 3D printable 'one-part'geopolymer concrete with steel fiber reinforcement, Journal of Building Engineering (2023) 107077.

[3] H.G. Şahin, A. Mardani, Mechanical properties, durability performance and interlayer adhesion of 3DPC mixtures: A state-of-the-art review, Structural Concrete (2023).

[4] Y. Yang, C. Wu, Z. Liu, Rate dependent behaviour of 3D printed ultra-high performance fibre-reinforced concrete under dynamic splitting tensile, Compos Struct 309 (2023) 116727. https://doi.org/10.1016/J.COMPSTRUCT.2023.116727.

[5] A.R. Arunothayan, J.G. Sanjayan, Elevated temperature effects on 3D printed ultra-high performance concrete, Constr Build Mater 367 (2023) 130241.

[6] S.F.A. Shah, B. Chen, S.Y. Oderji, M.A. Haque, M.R. Ahmad, Improvement of early strength of fly ash-slag based one-part alkali activated mortar, Constr Build Mater 246 (2020) 118533.

[7] M.S. Reddy, P. Dinakar, B.H. Rao, Mix design development of fly ash and ground granulated blast furnace slag based geopolymer concrete, Journal of Building Engineering 20 (2018) 712–722.

[8] S.K. Singh, P. Vashistha, Development of newer composite cement through mechano-chemical activation of steel slag, Constr Build Mater 268 (2021) 121147.

[9] P. Deng, Z. Zheng, Mechanical properties of one-part geopolymer masonry mortar using alkali-fused lead-zinc tailings, (2023). https://doi.org/10.1016/j.conbuildmat.2023.130522.

[10] V.T. de Sande, M. Sadique, A. Bras, P. Pineda, Activated sugarcane bagasse ash as efficient admixture in cement-based mortars: Mechanical and durability improvements, Journal of Building Engineering 59 (2022) 105082.

[11] V. Jittin, A. Bahurudeen, Evaluation of rheological and durability characteristics of sugarcane bagasse ash and rice husk ash based binary and ternary cementitious system, Constr Build Mater 317 (2022) 125965.

[12] Ü. Yurt, F. Bekar, Comparative study of hazelnut-shell biomass ash and metakaolin to improve the performance of alkali-activated concrete: A sustainable greener alternative, Constr Build Mater 320 (2022) 126230.

[13] P. Zhi, Y.-C. Wu, T. Rabczuk, Effects of time-varying liquid bridge forces on rheological properties, and resulting extrudability and constructability of three-dimensional printing

mortar, Frontiers of Structural and Civil Engineering (2023) 1–15.
[14] L. Kumar, D. Dey, B. Panda, N. Muthu, Experimental and numerical evaluation of multidirectional compressive and flexure behavior of three-dimensional printed concrete, Frontiers of Structural and Civil Engineering (2024) 1–19.
[15] B. Sun, P. Li, D. Wang, J. Ye, G. Liu, W. Zhao, Evaluation of mechanical properties and anisotropy of 3D printed concrete at different temperatures, Structures 51 (2023) 391–401. https://doi.org/10.1016/j.istruc.2023.03.045.
[16] A. Chourasia, B. Pal, A. Kapoor, Influence of printing direction and interlayer printing time on the bond characteristics and hardened mechanical properties of agro-industrial waste-based 3D printed concrete, Journal of Materials in Civil Engineering, ASCE 37 (2025) 04025065. https://doi.org/10.1061/JMCEE7/MTENG-18196.
[17] V.N. Nerella, S. Hempel, V. Mechtcherine, Effects of layer-interface properties on mechanical performance of concrete elements produced by extrusion-based 3D-printing, Constr Build Mater 205 (2019) 586–601.
[18] ASTM Standard C150/C150M-15, Standard Specification for Portland Cement ASTM International, West Conshohocken, PA, 2015, doi: 10.1520/C0150-15, www.astm.org, 2015.
[19] ASTM C618-15, Standard Specification for Coal Fly Ash and Raw or Calcined Natural Pozzolan for Use in Concrete; ASTM International: West Conshohocken, PA, USA, 2015.
[20] J.F.M. Hernández, B. Middendorf, M. Gehrke, H. Budelmann, Use of wastes of the sugar industry as pozzolana in lime-pozzolana binders: study of the reaction, Cem Concr Res 28 (1998) 1525–1536.
[21] IS 516:2014, Method of Tests for Strength of Concrete, IS 516 - 1959 (Reaffirmed 2004), 2004.
[22] A. Singh, Q. Liu, J. Xiao, Q. Lyu, Mechanical and macrostructural properties of 3D printed concrete dosed with steel fibers under different loading direction, Constr Build Mater 323 (2022) 126616.
[23] J. Xiao, H. Liu, T. Ding, Finite element analysis on the anisotropic behavior of 3D printed concrete under compression and flexure, Addit Manuf 39 (2021) 101712.
[24] B. Panda, S.C. Paul, L.J. Hui, Y.W.D. Tay, M.J. Tan, Additive manufacturing of geopolymer for sustainable built environment, J Clean Prod 167 (2017) 281–288.
[25] G. Ma, Z. Li, L. Wang, F. Wang, J. Sanjayan, Mechanical anisotropy of aligned fiber reinforced composite for extrusion-based 3D printing, Constr Build Mater 202 (2019) 770–783.
[26] B. Zareiyan, B. Khoshnevis, Effects of interlocking on interlayer adhesion and strength of structures in 3D printing of concrete, Autom Constr 83 (2017) 212–221.

Mr. Devesh Upadhyay

4th International Symposium on One Health, One World
November 20 – 22, 2025

ABS ID: 32
Code No: IMSBE-OP-20

Development Of a Modular Large-Scale Gantry Based 3-D Concrete Printer

R. Sahai[1], R. S. Bisht[2,1], S. Singh[2,1], Sameer[2], D. Kumar[2], S. K. Panigrahi[2,1]
[1]*Academy Of Scientific & Innovative Research (Acsir), Ghaziabad, Uttar Pradesh, India*
[2]*Construction Automation & Robotics Group, CSIR-Central Building Research Institute, Roorkee, Uttarakhand, India.*
Correspond To Dr. R.S. Bisht (Rsbisht.Cbri@Csir.Res.In)

***Keywords**: Large-scale concrete printer, Design Analysis, Motion Control, Gantry configuration, Modular Design.*

1. ABSTRACT

This study presents the development of a modular large-scale 3-D concrete printer for typical and unique building designs. The printer incorporates a modular framed gantry structure composed of one-meter truss modules connected via bolted joints, allowing adjustable build volumes as per on-site requirements. The system is designed for rapid deployment, with assembly and disassembly time frame of approximately four and two hours respectively, enabling efficient field operations. Design analysis was conducted to validate the structural design parameters, including element cross-sections, fasteners, mountings, motor torque, and motion mechanisms such as ball screws and linear guides. By combining modular structural design with advanced motion control, the printer can be readily scaled up for field applications. A build volume of 3×3×3 m^3 of the printer has been constructed to validate the proposed concept.

2. INTRODUCTION

Three-dimensional concrete printing (3DCP) has emerged as a promising technology for construction, offering rapid and automated construction [1]. While significant progress has been made in small-scale prototyping, the transition toward large-scale, practical systems remains a major challenge [2]. Key barriers include printer scalability, adaptability to varying construction requirements, and maintaining precision over large build volumes [3].

Most studies are focused on custom-built or fixed-geometry printers, which often limit flexibility in on site deployment for large-scale applications. Conversely, the modular design of printers offers a viable solution to these challenges. Modular approach allows the printer to be reconfigured to meet specific site conditions, enabling adjustable print volumes and reducing setup time. Furthermore, modularity enhances transportability, ease of assembly, and system maintenance, making the concept more practical for field implementation [4].

The study focuses on the design and development of a modular framed gantry-based 3DCP, focusing on modularity, scalability and motion accuracy. This work is extension of developed framed gantry concrete printer at laboratory scale (1 × 1 × 1 m^3) [5]. The gantry structure uses one-meter-long truss modules connected by bolted joints, allowing rapid assembly and disassembly. Finite element modelling (FEM) is used to validate structural performance, while kinematic and dynamic models are developed for workspace evaluation and actuator sizing. Motion control is achieved using servo motors, PLC-based instructions, and synchronization algorithms to ensure precise movement in x, y, z axis and material deposition.

3. SYSTEM DESIGN AND ANALYSIS

The large scale 3DCP is designed with a build volume of 3 × 3 × 3 m^3, making it suitable for printing medium-sized rooms as shown in Figure 1. This build capacity provides flexibility to address diverse construction requirements. The printer features a modular framed gantry structure, consisting of one-meter truss modules connected through bolted joints, enabling adjustable build volumes to match on-site demands. The modular configuration allows rapid assembly and disassembly, reducing downtime, improving on-site efficiency, and facilitating relocation and reuse

across multiple projects with significantly less effort than conventional systems.

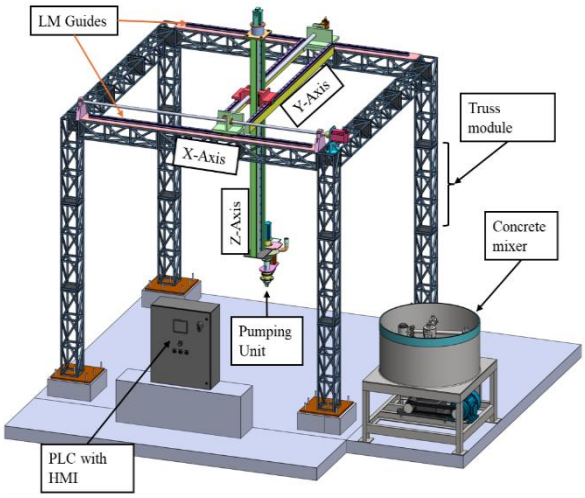

Figure 1. Large-scale 3-D concrete printer

The motion mechanisms comprise of linear motion guides and ball screws for the x, y, and z axes, which provides positioning accuracy within 1 mm. The pumping unit supports both discrete and continuous feeding mechanisms, ensuring consistent material flow. Additionally, the nozzle can rotate about its axis, enabling precise printing of curved surfaces.

Extensive design analysis was conducted to determine motor sizing for the x, y, and z-axes, as well as for concrete pumping and nozzle rotation, leading to the integration of high-torque alternating current (AC) servo motors with feedback control for accurate positioning. Table 1 compares analyzed torque with selected servo motors for each function, higher-rated motors were chosen to ensure reliability and controlled speed ranges for printer operations. Limit switches restrict over travel for safety features. The pumping unit comprises an AC servo motor driven auger with blades for mixing and extrusion, delivering concrete flow at the nozzle tip. A programmable logic controller (PLC) along with human machine interface (HMI) governing motion control as per given instructions in automatic as well as manual modes, enabling precise layer-by-layer printing.

Table 1. Selection of driving motors using dynamic analysis

Purpose	Analysis (Nm)	Selected motors (Nm)	Controlled range (rpm)
x-axis	3.00	3.18	10-40
y-axis	4.75	6.37	10-40
z-axis	7.20	9.55	10-80
Concrete pumping	4.5	5.2	10-40
Nozzle rotation	1.00	1.75	10-20

4. PROTYPE DEVELOPMENT

The developed framed gantry 3DCP at CSIR-CBRI comprises five major components: (i) truss modules, (ii) motion mechanisms (ball screws and LM guides) for x, y, and z-axis movements, (iii) pumping unit with nozzle, (iv) PLC panel, and (v) HMI, as shown in Figure 2.

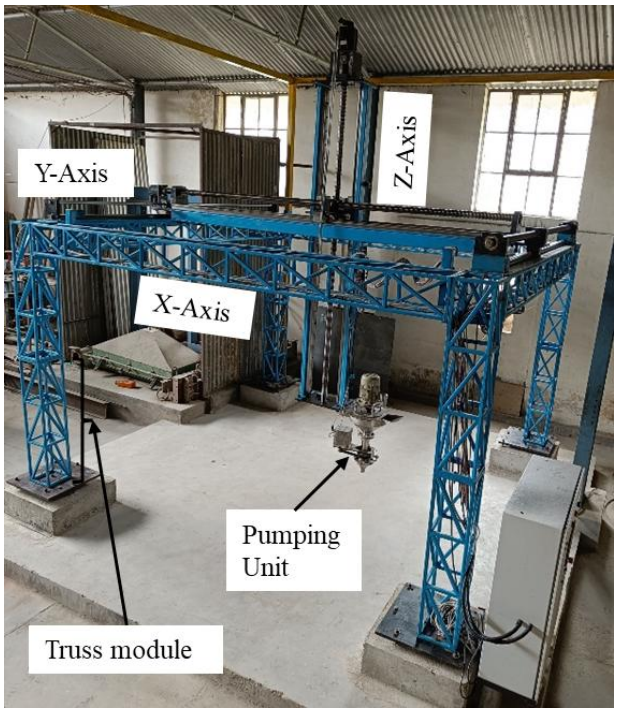

Figure 2. Developed large-scale concrete printer

The truss modules are fabricated from structural steel members of size 0.2 m × 0.2 m × 1 m, designed as per IS:4923 and IS:808. These truss members collectively form the gantry frame, which supports the motion mechanisms for all three axes. Precise linear motion along the x, y, and z-directions is achieved using motorized ball screws along with linear motion guides. Preliminary motion trials for positional tracking are conducted as shown in Figure 3.

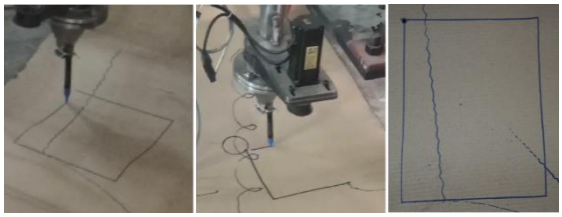

Figure 3. Motion trials using large-scale 3-D concrete printer

5. CONCLUSION

The study presented the design and prototype development of a modular large-scale gantry-based 3D concrete printer, addressing typical and unique building designs. The modular truss-based gantry structure, composed of one-meter steel modules connected by bolted joints, enables rapid assembly and disassembly, of approximately four and two hours, respectively, making the system adaptable to varying onsite conditions. A full-scale printer with build volume of 3×3×3 m^3 has been successfully developed and conducted its motion trials for design validation. Extensive design analysis conducted to optimize the structural size, selection of motors and control system. The mechanisms, incorporating linear guides and ball screws, achieved accuracy within 1 mm.

ACKNOWLEGEMENT

The authors are grateful to the CSIR-CBRI for granting permission to publish this work. The financial support provided by CSIR with project No. MLP042204 is also gratefully acknowledged. We also extend our sincere thanks to Mr. Yash Kumar and Mr. Shivam Kashyap for helping in working trials.

REFRENCES

[1] S. Keating, et al., Rob. Comput. Integr. Manuf. (2019).

[2] A. Puzatova, P. Shakor, V. Laghi, M. Dmitrieva, Buildings 12 (2022) 2023.

[3] S.S. Uppala, M.R. Tadikamalla, i-Manager J. Civ. Eng. 7 (2017) 49.

[4] L.T. Pham, T. Nguyen, T. Trinh, A. Nguyen, Q. Do, B. Bui, J. Xiao, Smart Sustain. Built Environ. 12 (2022) 1056.

[5] R. Sahai, R.S. Bisht, S. Singh, S.K. Panigrahi, Mech. Based Des. Struct. Mach.53 (2024) 1001

4th International Symposium on One Health, One World
November 20 – 22, 2025
ABS ID: 35
Code No: IMSBE-OP-21

Approach To Create Long Term Sustainable Water Source to Solve Water Crisis

Anil Kumar
MC member, Dream Meadows Layout, Kundalahalli, Bangalore-560037, India.
E-mail: anil_karekal@yahoo.com Contact Number: 9886103842

Keywords: *Dream Meadows, STP, KSPCB, Sewage, Statutory, Water Crisis, Sustainability.*

Abstract: The main object of this paper is to highlight the methodology adopted to ensure continuity of STP treated water from waste water, for flushing toilets gardening & rejuvenate the soil in the Dream Meadows layout, Bangalore *and* to be complied with Pollution control board norms with respect to treatment and disposal of waste water. Bangalore being an IT capital of India, experienced a severe water crisis, owing to unethical exploitation of ground water due to increase in population & illegal construction of buildings. With all the news /media raising alerts about fast depletion of ground water, we need to rethink/rework/realign ourselves to arrive at a "Long term permanent sustainable water solution" without which life cease to exist in comfort. While we explored various water resources --Cauvery River water, bore well water, rain water, water tankers and converting atmospheric air into water etc, all of them are temporary in nature and not a successful sustainable models. Our three borewells were dried up as well. Currently, the sewage load on existing Anaerobic plant is to an extent of 125 KLD, which is let out to an external sewer line outside and is a huge loss for the community. This necessitated to upgrade the existing plant to treat the sewage and recycle, to get clear water, thus, be sustainable and raise the bar.

The purpose of this paper is to bring up a *"Transformative Experience"* and we therefore decided to upgrade the existing Anaerobic sewage unit to Aerobic sewage treatment plant of design capacity of 250 KLD considering future growth of population in DM. With little structural modifications, we adopted " *Extended Aeration Activated Sludge Process"* with two levels of disinfection i;e Chlorination and UV treatment to get clear water for flushing to avoid any Urinary tract Infections and thus be healthy.

The test report on various parameters of finally treated water – BOD, COD, PH, TSS and ammoniacal nitrate were conforming to the norms of KSPCB and thus secured clear and stench free usable water. The continuity of supply of treated water on 24/7 basis to all dwellings under pressurization using energy efficient Hydropneumatics pumps was ensured. Our goal – "Net zero discharge" and " Circular economy" was achieved. Now this system is free from Legal hassles and residents have peaceful & purposeful life.

This STP upgrade project was initiated for a *"PURPOSE"* of solving the water crisis and be complied with norms of KSPCB . Finally, delivered well equipped and fully operational state of the art "Sewage Treatement Plant" and quality, time and cost were the essence of this project.

INTRODUCTION:

Dream Meadows is a residential community in the East Bengaluru, developed in the year 2005 and formed a Residential Welfare Association during 2008 and registered under the karnataka Societies Act. The layout is spread across 26 acres of land and has 250+ dwellings as of now and few vacant plots too. Water scaricity encompasses various parts of Bengaluru due to urbanization, increased population & concrete surfacing. A recent study by IISc showed that Bengaluru ground

water is depleting fast, which puts the city at a risk of running out of water. The illegal constructions and increase in population has put a mega demand on water. Research also showed that the underground water is over-exploited and levels are going down and reached a critical stage as per Central Groundwater Board (CGWB), thus started looking for a permanent long term sustainability, which has become a top priority for surviving. Solving water crisis is environmental sustainability and hence need to identify alternative water sources.

There is no Cauvery river water connection to the Dream meadows layout and residents are mainly depending on the Bore well water and water tankers. Our three bore wells in the layout were dried up and we explored different sources of water, but all of them are temporary in nature. We are thriving in a world of change,"reminds us how DM team adapt, innovate and lead in times of uncertainty, ensuring for a *permanent long term Sustainable solution*. The Sustainability initiatives including ESG considerations were also discussd in our meetings.

Currently, we are pumping out about 1.25 lac litres of sewage daily outside the property through external BWSSB sewer line and is a huge loss of water to DM community. DM initiated this STP upgrade for a *PURPOSE* of solving water crisis. Hence, upgraded domestic Anerobic plant from its current capacity to 250 KLD capacity Aerobic STP by adopting " Extended Aeration Activated sludge process", thus delivering sustainability benefits and created tangible impact to all our residents.

Our Goal :

- To arrive at a permanent solution for the water crisis and to ensure Continuity of treated water supply on 24/7, from waste water.
- The treated water shall be in compliance with statutory requirements of KSPCB with respect to treatment and disposal of waste.
- To achieve " net zero discharge " and be self sufficient. The upgraded unit shall be Futuristic, state of the art waste water treatment plant.

Salient Features :

- Name of the Project : Long term sustainable water source to solve water crisis. **(** STP upgrade project of 250 KLD capacity)
- Consultants : M/s Ecotech Engineering Consultants Services Pvt Ltd, Bangalore
- Duration of the project : 75 days,
- Project cost : Rs. 61.5 Lacs + GST .
- Process adopted : "Extended Aeration Activated sludge Process"
- Current status of the Project : STP upgrade project is fully operational, conforming to the norms of KSPCB and ensured continuity of treated water supply to all dwellings.
- Location: Dream Meadows, Kundalahalli , Bangalore. Number of Team members: 04
- Business model : Cost effective high performance futuristic Sewage treatment plant.

Project Planning Phase: All the requirements of STP upgrade were collected ahead of kick off meeting. As per Corrigendum notification, Govt of Karnataka, Dated 12-03-2024, STP was made mandatory for an land area more than 10 acres for townships and Dream Meadows qualifies for it and hence initiated. Filed application with KSPCB for obtaining "Consent For establishment" and be complied with statutory requirements before commencement of works. Calculated electrical load details and secured additional BESCOM power. Chose all raw sewage pumps to be submersible and low RPM Air blowers, thus the noise pollution was totally controlled and

neighbors were not disturbed. Identified the risks, probability of occurance and came up with mitigation plan, held weekly meetings to assure deliverables on time. Appointed Consultant and Vendors with a record history of delivering material/equipment on time. This helped in taking the project out of critical path and led to accelerated mode.

We appointed M/s Ecotech Engineering Consultancy Services Pvt Ltd. as our consultants and also evaluated SBR, MBR,MBBR processes etc. nothing is bad about them. But, we finally chose "Extended Aeration Activated sludge process"as it is cost effective and retrofitting was easy with minimal structural changes for the existing plant.

Funds Mobilization : Created awareness to all residents by organizing presentations about the importance of STP upgrade and consequences from KSPCB, if not taken up, in our AGM/ EGM and Pooled in money from crowd funding. Thus residents dedicated to investing in climate solutions, advocating for a more sustainable future.

CONSTRUCTION METHODOLOGY: We visited several STP units , collected Data, analyzed and adopted DMAIC principles in our project management activities. Basically, we have 3 stages of treatment -- *Primary treatment* where in soild particles ,plastic, diapers ,Napkins etc will be eliminated at Bar screens. *Secondary treatment* -- where in Biological oxidation will take place in presence of oxygen. Sewage flows into equilization tank, Annox tank, Aeration tank , Clarifier, Filter feed & sludge holding tank etc. *Tertiary treatment*-- consists of Pressure sand filter & Activated Carbon Filter and disinfection treatment through Chlorine dosage & U V treatment . The Final treated water after conforming to the norms of all parameters of KSPCB, is pumped to entire layout through CPVC lines using Hydropneumatic pumps , so that water is pressurized and made available to all dwellings on 24/7 X 365 days for flushing toilet, gardening , carwash, construction etc. Reduced load on existing borewells and power consumption charges. This was crucial in an area where water table was significantly declined.

Installation and Commissioning of System: The work was executed as per Design & GFC drawings and Trial run of the plant was undertaken till the system stabilizes**.** Installation & Commissioning of entire system was complete and *PURPOSE* of this project, for which it was intended was achieved.

Key Initiatives that made us proud and unique:

Adopted Agile methodologies by tailoring the execution plan thus mitigated the loss of time and avoided cost over run of the project.

- Held project review meetings every week and milestone dates were tracked to ensure long lead items like -- Air Compressors with Low RPM , Sewage Pumps, ACF & PCF , electrical Panels etc were delivered on time.

- Dependencies were well managed efficiently ahead of Kickoff such that project was executed with out getting into critical path.

- All the parameters of treated water like - PH, BOD, COD,TSS, NH4, were conforming to the norms of KSPCB. Free from stench and improved life style.

- Delivered well equipped and fully operational state of the art STP unit on time , in spite of several site constraints. Certainly, this was a Technology driven project and a game changer going forward.

Operational Excellence : Value creation with our business model adopted :

- Energy efficient Hydropneumatic pumps were installed which ensures treated water supply for flushing toilets /gardening etc, on 24/7 basis, uninterrupted.

- All raw sewage pumps were submersible in nature to contain the noise level

- The existing sewage collection plant with the inflow of continuous sewage on 24/7 basis and diverting the same ensuring that the

work front remains unobstructed, was the biggest challenge.

- The Extended Aeration Activated sludge process adopted was cost effective with minimal structural changes and retrofitting was very easy and hence completed in 75 days period.

Bnefits for Residents :

- " No Legal hassels & penalties" and Peace of mind to all residents , as our STP upgrade project satisfies treatment and disposal of sewage as per norms of KSPCB

- The objective *" Net Zero discharge " and "Circular economy"* is achieved and continuity of treated water was ensured. Thus gave all residents " a meaningful life to enjoy for the rest of their life".

- The water scaricity problem was solved and achieved long term sustainability goal. Thus Environment is well protected and Living conditions of residents are improved. Finally, It reflects community unity ,connectivity and Engg brilliance.

- There was no Cost over run of the project, as we made STP unit operational on time. The dependencies on costly tanker water was avoided.

CONCLUSION :

1. All statutory requirements of KSPCB were met and long term sustainability solution was provided at DM. Thus, contributed to protect environment and human living conditions.

2. The system adopted was hassel free, peaceful & purposefull life for all residents.

3. We have future plan of converting treated water to potable quality water through an Advanced Treatment plant including a Reverse Osmosis Treatment stage as is was done in Singapore for decades.

5. Although , there were huge challenges /surprises at the time of execution , still we managed well and the project was completed in 2.5 months .

6. We have plans of selling treated water to run AC chillers of near by IT Co's and earn money to recover our investment.

7. Although the journey through this project was roller coaster ride, Quality, Time and Cost were the essence of this project. This STP unit is not just a piece of Infrastructure, but it is a symbol of oneness amongst diversified community. Finally, we delivered what we committed in our AGM/EGM and solved water crisis in layout.

The proposal (Detailed)

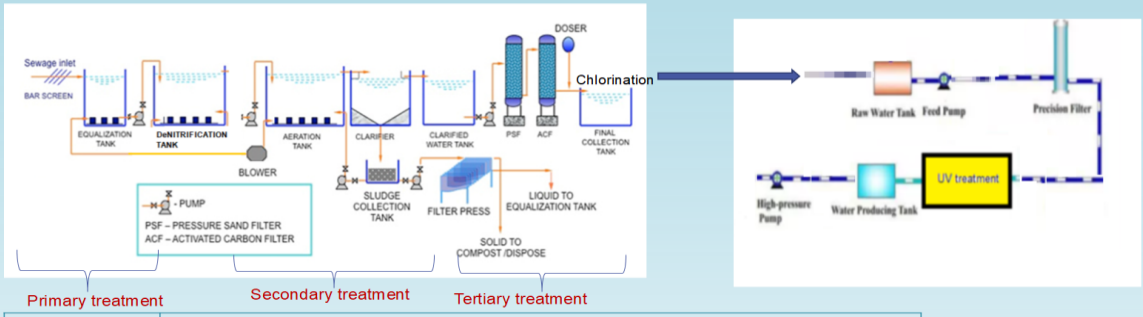

Filter type	Function
Equalization tank	**Detergent, Phenyl and other bathroom cleaning chemicals** are consumed and broken by bacteria here.
DeNitrification tank	**Converts ammoniacal nitrate to nitrogen gas**, thus removing bioavailable nitrogen and returning it to the atmosphere.
Aeration tank	Air is added into the water to **encourage microbial growth** which feed on the organic material.
Clarifier tank	**Solid contaminants will settle down** to the bottom of the tank
PSF	Pressurized sand filter **to remove suspended solids** from water.
ACF	To **remove organic compounds**
Precision filter	To **remove large particle impurities**
UV	Ultraviolet ray **to remove destroy harmful microorganisms**

11

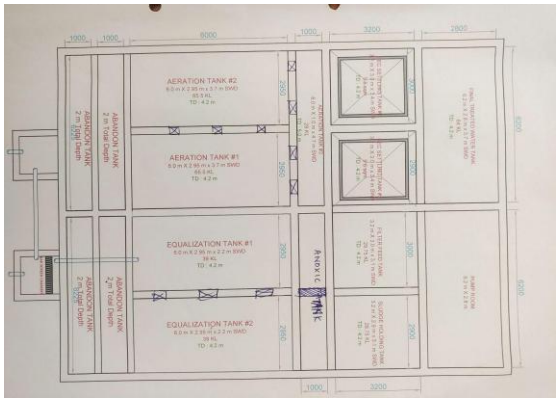

2. STP Execution Plan

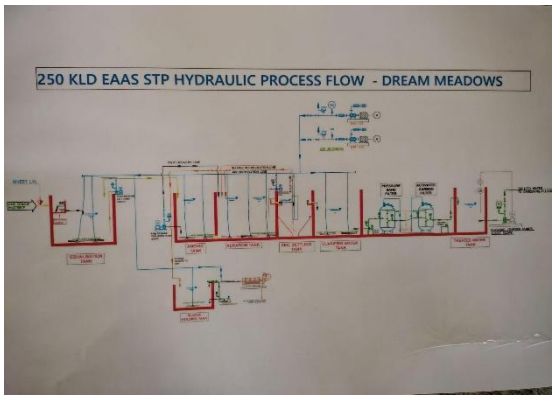

3.Flow Diagram

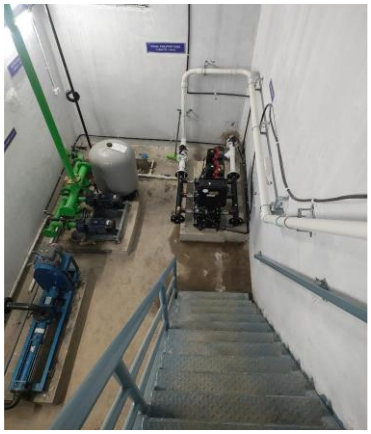

4. Pump Room

5. STP Overview- PCF & ACF, Pipe network

6. Air Blower and Main Electrical P

TREATED WATER TEST RESULTS :

Sl No	Parameters as per KSPCB	Unit	Sewage Quality before upgradation	Final water Quality after upgradation
1	pH		6.5-7.5	7.14
2	BOD	mg/L	18	2.0
3	COD	mg/L	97	4
4	TSS	mg/L	44	1.5
5	Ammonical Nitrogen	mg/L	46.9	1.0
6	Total Nitrogen	mg/L	107.9	4.0

Treated Water for Gardening

Treated water for Construction

Inaguration of Upgraded STP

Reference: 1. The STP Guide by Dr. Ananth kodavasal-- Design, Operation and maintenance, Published by Karnataka state Pollution Control Board. Also, Service Agreement with Consultants.

2. Karnataka Govt Gazette Notification-- Forest, Ecology and Environment Department, dated 12th March 2024.

A**cknowledgement :** The author expresses sincere heartfelt gratitude to Dr. Ananth Kodavasal for his valuable suggestions and guidance at all stages of this project.

ABS ID: 200
Code No: IMSBE-OP-22

Dr. Samreen Bano

4th International Symposium on One Health, One World
November 20 – 22, 2025

ABS ID: 158
Code No: IMSBE-OP-23

Circular Economy Implementation in the Construction Sector Through Use of Alternate Aggregate

P N Ojha[1], Brijesh Singh[2], Amit Trivedi[3], Puneet Kaura[4], Rohit Kumar[5], L P Singh[6]
[1]*Joint Director, National Council for Cement and Building Materials, Ballabgarh, India*
[2] *General Manager, National Council for Cement and Building Materials, Ballabgarh, India*
[3]*Joint Director, National Council for Cement and Building Materials, Ballabgarh, India*
[4]*Group Manager, National Council for Cement and Building Materials, Ballabgarh, India*
[5]*Deputy Manager, National Council for Cement and Building Materials, Ballabgarh, India*
[6]*Director General, National Council for Cement and Building Materials, Ballabgarh, India*
Correspond to Brijesh Singh (brijeshsehwagiitr96@gmail.com)

Abstract

The construction industry is a major consumer of natural aggregates, leading to significant environmental degradation and resource depletion. To address these challenges, this study explores the implementation of a circular economy by utilising industrial by-products such as slags and ash as alternative aggregates in concrete. The research focuses on the feasibility of substituting natural fine and coarse aggregates with copper slag, blast furnace slag (granulated and air-cooled), ferrochrome slag, sintered flyash lightweight aggregate, and bottom ash, while evaluating their impact on the mechanical and durability properties of concrete. Experimental investigations revealed that natural fine aggregate could be replaced up to 50% with copper slag, 100% with air-cooled blast furnace slag (ACBFS), and 60% with granulated blast furnace slag (GBFS) without compromising concrete performance. Ferrochrome slag, evaluated for both fine and coarse aggregate replacement, demonstrated suitability up to 60% substitution, with leaching studies confirming compliance with environmental safety standards. Sintered flyash lightweight aggregate, though unsuitable for wearing surfaces due to lower abrasion resistance, showed promise for structural applications, necessitating revised design codes to account for its unique properties. Bottom ash, when used as a fine aggregate replacement (up to 50%), exhibited comparable strength and durability to conventional concrete, provided the fineness modulus of the composite aggregate was at least 1.35. The study underscores the environmental and economic benefits of adopting these alternative aggregates, including reduced reliance on natural resources, minimized waste accumulation, and lower ecological impact. Standardization efforts, such as revisions to Indian Standards (IS 383:2016, IS 9142) and alignment with international guidelines (ASTM, EN), were highlighted as critical for widespread adoption. The research demonstrates that industrial by-products can effectively replace natural aggregates in concrete, offering a sustainable pathway for eco-friendly construction while aligning with circular economy principles. The findings provide a foundation for future work on optimising mix designs, establishing structural codes, and expanding the utilisation of waste-derived aggregates in diverse construction applications.

significantly depleting day by day and impacting the environment. The linear economy is based on the philosophy of take-make-dispose. The extracted raw materials from the earth are discarded as waste after the end of the useful life of the material. This approach boosted the industrial growth at the cost of resource depletion and environmental degradation, as waste accumulates in landfills and natural reserves. In the circular economy, waste is eliminated by keeping materials in use for as long as possible. Instead of discarding raw materials, it is reused, recycled and regenerated into raw materials. This closed or circular economy minimises the impact on the environment,

***Keywords**: Circular economy, alternative aggregates, slag, flyash, bottom ash, sustainable concrete, mechanical properties, durability.*

1.INTRODUCTION

The major portion of concrete is aggregate, which provides strength and volume to the concrete. A huge quantity of aggregates is required in the construction sector, which is obtained from the river bed or by crushing of rock, which is significantly depleting day by day and impacting the environment. The linear economy is based on the philosophy of take-make-dispose. The extracted raw materials from the earth are discarded as waste after the end of the useful life of the material. This approach boosted the industrial growth at the cost of resource depletion and environmental degradation, as waste accumulates in landfills and natural reserves. In the circular economy, waste is eliminated by keeping materials in use for as long as possible. Instead of discarding raw materials, it is reused, recycled and regenerated into raw materials. This closed or circular economy minimises the impact on the environment, leading to sustainable development. The construction industry is a major consumer of natural resources in the form of cementitious materials and aggregates. This leads to a steeper decline in reserves of materials like sand, gravel, and cementitious components. There is a wide scope for the utilisation of by-products from thermal power plants and steel plants in the construction industry. This utilisation not only conserves natural resources but also reduces the environmental footprint of construction activities. Slags are by-products generated during the smelting of ores and the processing of used metals. They can be broadly classified into three types based on their origin, i.e. Ferrous Slags (Produced during iron and steel manufacturing, such as blast furnace slag and steel slag), Ferroalloy Slags (Generated from the production of ferrochrome slag), Non-Ferrous Slags (Resulting from the recovery of base metals such as copper, nickel, zinc, and phosphorus) [1-3]. The physical, chemical and mineralogical properties of slags, such as their hardness, durability and binding capabilities, make them suitable for use as aggregate. The major portion of slag in India is unutilised. The by-product from a thermal power plant, i.e. bottom ash as a fine aggregate and flyash utilisation for the production of sintered flyash lightweight as coarse aggregate [4]. The historical accumulation of unutilized ash poses a challenge and an opportunity for the construction industry to tap into this resource. To facilitate the utilisation of ash and slags in the construction sector, the National Council for Cement and Building Materials, India, has conducted extensive studies and submitted recommendations for the revision of Indian Standards. The study was focused on enhancing the IS 383:2016 to maximise the utilisation of these products by-products as a replacement for natural sand with copper slag, blast furnace slag, and bottom ash as fine aggregates. Investigations were done to explore the possibility of using ferrochrome slag as a replacement for conventional fine and coarse aggregates in concrete. The formulation of Bureau of Indian Standards IS: 9142 (Part-2)-2018 standard specifying the use of sintered flyash lightweight coarse aggregates in structural concrete applications. The quantity of slag generated during the manufacturing of iron and steel depends upon input raw material quality and process requirements.

India's steel mills produced about 27 Mt of blast furnace slag, 8 Mt of BOF slag, 2.5 Mt of EAF slag, and 1–1.5 Mt of ladle/induction slag in 2017–18. In power plants, the combustion of 759 Mt of coal generated 270 Mt of ash in 2021–22, with fly ash reuse increasing from 56% (2014–15) to 95% (2021–22), although legacy stockpiles remain [5]. Standards (IS, JIS, ASTM, EN) now recognise granulated and crystalline slags as valuable inputs in the production of cement, aggregates, road bases, glass, and soil conditioners. Improper slag and ash disposal can raise water pH, leach heavy metals, and accelerate calcite precipitation, harming aquatic life. To eliminate stockpiles and harness these materials sustainably, India needs stronger policies, research-backed technologies, and broader stakeholder training. With the right legislation and know-how, slag and ash can

become eco-friendly substitutes for natural aggregates. Global initiatives and the National Council for Cement and Building Materials (NCCBM) research are crucial for increasing slag and ash utilisation in construction, necessitating policy implementation and TRL-oriented research. Collaborations between NCCBM, government, and industry stakeholders are vital to these efforts.

The study underscores the environmental and economic benefits of adopting these alternative aggregates, including reduced reliance on natural resources, minimised waste accumulation, and lower ecological impact. Standardisation efforts, such as revisions to Indian Standards (IS 383:2016, IS 9142) and alignment with international guidelines (ASTM, EN), were highlighted as critical for widespread adoption. The research demonstrates that industrial by-products can effectively replace natural aggregates in concrete, offering a sustainable pathway for eco-friendly construction while aligning with circular economy principles. The findings provide a foundation for future work on optimising mix designs, establishing structural codes, and expanding the utilisation of waste-derived aggregates in diverse construction applications.

2. MATERIALS AND METHOD

2.1 Material

The study evaluated five industrial by-products as substitutes for natural aggregates. The slag-based fine aggregates included copper slag (angular particles, specific gravity = 3.4), granulated blast furnace slag (GBFS; specific gravity = 2.9), air-cooled blast furnace slag (ACBFS; specific gravity = 2.7), water-cooled ferrochrome slag (specific gravity = 2.87), and bottom ash from thermal power plants (fineness modulus = 1.33–2.76). For coarse aggregate replacement, air-cooled ferrochrome slag (specific gravity = 2.98) and sintered fly ash lightweight aggregate (LWA; bulk density = 1,250 kg/m^3) were utilised.

2.2 Experimental Design

In this study, investigations were carried out to check the feasibility of increasing copper slag and blast furnace slag as a substitution of natural sand in concrete. Conventional (Natural) sand was replaced (by volume) with copper slag (0%, 25%, 50% & 75%), Granulated Blast Furnace Slag (GBFS) (0%, 30%, 60% & 100%) and Air-Cooled Blast Furnace Slag (ACBFS) (0%, 30%, 60% & 100%). Concrete mixes were examined by substituting conventional sand with copper and blast furnace slag in different proportions and were evaluated for different mechanical properties and durability-related parameters. Leaching studies were also carried out on selected concrete samples. The bottom ash from different sources with fineness modulus varying from 1.33 to 3.01 was used as a percentage replacement of fine aggregate in the concrete. The bottom ash is used to replace natural and crushed fine aggregate of zone II and zone III with varying proportions of 20-50% to study its impact on concrete and to find out the optimum replacement dosage.

3. RESULT AND DISCUSSION

3.1 Study on the substitution of natural fine aggregate in concrete with copper slag and blast furnace slag

In order to explore the possibility of utilising, by-products obtained from different industries as a replacement for natural sand, a study was conducted on the substitution of natural sand in concrete with copper slag and blast furnace slag. Based on experimental analysis, it was observed that copper slag, air-cooled blast furnace slag (ACBFS), and granulated blast furnace slag (GBFS) aggregates show slightly higher water absorption than conventional fine aggregates. Concrete mixes show segregation beyond 50% copper slag and 60% GBFS replacement due to their coarser size, whereas 100% replacement with ACBFS produced cohesive mixes. Mechanical strength is comparable across all replacement levels. Table 1 shows compressive and flexural strength results

for mixes containing different proportions of slags as fine aggregate. These results shows that, despite slight variations, the strength properties of the experimental mixes are within acceptable limits when compared to the control mix. Durability parameters such as Rapid Chloride Penetration Test, carbonation depth, water permeability, and abrasion resistance remained unaffected up to 75% copper slag, 60% GBFS, and 100% ACBFS replacement. The replacement of fine aggregates with copper slag led to a decrease in RCPT values, which still remained within the 'moderate' class but continued to reduce as the replacement percentage increased. In the case of ACBFS and GBFS, the RCPT values were similar to those of natural fine aggregate and showed a decreasing trend up to 60% replacement. The Carbonation depth after 70 days of exposure and water permeability values were observed to be lower than those of concrete with natural fine aggregate, with an increase in the percentage of ACBFS and copper slag. For GBFS, this improvement was observed up to a 60% replacement level. All three mixes also showed reduced abrasion resistance up to 60% replacement, except copper slag, which even showed a reduction at a 75% replacement level. These figures highlight that, despite slight variations, the mechanical and durable properties of the experimental mixes are comparable to the control mix, confirming the feasibility of substituting natural fine aggregate with industrial by-products for sustainable concrete production. Based on the results, natural sand can be safely replaced by up to 50% copper slag, 60% GBFS, and 100% ACBFS without compromising performance [2].

Table 2. Mechanical properties of experimental mixes at 28 days containing different proportions of slags as an aggregate as a replacement of natural fine aggregate

Materials	Air Cooled Blast Furnace Slag		Copper Slag		Granulated Blast Furnace Slag	
Fine Aggregate Replacement (%)	Compressive Strength, MPa	Flexure Strength, MPa	Compressive Strength, MPa	Flexure Strength, MPa	Compressive Strength, MPa	Flexure Strength, MPa
0	25.93	2.72	25.93	2.72	25.93	2.72
25	-	-	28.35	3.13	-	-
30	28.65	2.89	-	-	27.54	2.71
50	-	-	31.43	3.36	-	-
60	30.87	2.95	-	-	28.76	2.83
75	-	-	33.43	3.68	-	-
100	28.50	2.80	-	-	28.16	2.61

3.2 Study on the use of ferrochrome slag as an alternative to natural aggregates in concrete structures

The Ferrochrome slag is generated during the manufacturing of ferrochrome. Based on the cooling process, two types of ferrochrome slag are obtained, i.e. water-cooled and air-cooled ferrochrome slag. Figure 1 and Figure 2 micrographs of air-cooled and water-cooled Ferrochrome slag showing the distribution of mineral grains, respectively. The study examined both water-cooled and air-cooled ferrochrome slag, evaluating their physical and chemical properties concerning the presence of chromium as Cr+3 and Cr+6 in concrete. Concrete mixes were created by replacing natural fine and coarse aggregates with ferrochrome slag at 30%, 60%, and 100% replacement levels, at two different water-cement ratios. Both slags confirm the requirements of IS: 383-2016. Slag samples showed higher specific gravity than that of natural aggregates. Slag shows comparable water absorption with natural aggregates. The air cooled ferrochrome slag showed low values of abrasion, crushing and impact.

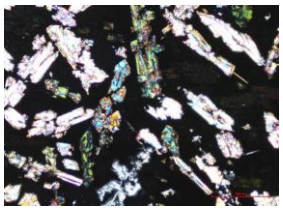

Figure 1. Micrograph of air-cooled Ferrochrome slag showing distribution of mineral grains

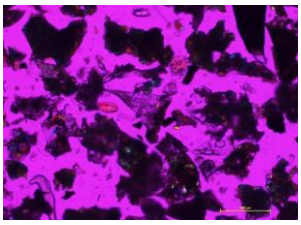

Figure 2. Micrograph of water-cooled ferrochrome slag showing distribution of mineral grains

Concrete mixes at two w/c ratios were prepared in which natural fine aggregates are replaced by water cooled ferrochrome slag and natural coarse aggregates with air-cooled ferrochrome slag. Both ferrochrome slag increased slump loss and mixes showed segregation and bleeding beyond 60% replacement due to its higher specific gravity, the hardened properties (strength, durability) of concrete containing ferrochrome slag were comparable to or better than control mixes. Leaching studies confirmed that heavy metal concentrations (Cr, Fe, Zn, Cu, Mn, Ni, Pb and Ti) in both types of ferrochrome slag and concrete samples were below prescribed environmental limits. Water-cooled Ferrochrome slag can be used to replace natural fine aggregate by up to 60% by weight, while using 100% natural coarse aggregate in concrete. Similarly, air-cooled Ferrochrome slag can be used to replace natural coarse aggregate by up to 60% by weight, while using 100% natural fine aggregate in concrete without compromising performance or environmental safety [3].

3.3 Study of coal based bottom ash as a replacement to fine aggregate in concrete:

The physical and chemical properties of bottom ash samples were evaluated to explore its suitability as a partial replacement for conventional fine aggregate in concrete. Composite fine aggregates were developed by replacing 10% to 50% of natural fine aggregate with bottom ash. A total of 70 concrete mix trials were conducted using these composite fine aggregates, and the mixes were evaluated for fresh, hardened, and durability properties. The results indicated that replacing conventional fine aggregate with bottom ash should not exceed 50% by weight for OPC concrete. The fineness modulus of the resulting composite fine aggregate should be at least 1.35. The compressive strength of concrete at 28 days for all trials using composite fine aggregates was comparable with the compressive strength of control concrete made with 100% conventional fine aggregates. The carbonation depth for the control sample was 6.5-10 while for composite cement it was 5.5-11mm. The RCPT of control and composite mix of concrete were comparable. The control concrete mixes show electrical resistivity values of 6 to 7 k-ohm-cm, while concrete with composite fine aggregate showed 6.5 to 8.5 k-ohm-cm. Based on these findings, the study proposed specifications for the use of coal-based bottom ash as an alternative fine aggregate in concrete, along with mix design guidelines [6].

3.4 Sintered flyash lightweight aggregate for structural concrete

A study on sintered fly ash coarse aggregates (SFA) produced using Class F fly ash in the two size fractions (8–16 mm, 4–8 mm), as shown in Figure 3. The aggregates were evaluated for their microstructural characteristics (Figure 4), as well as their physical and chemical properties, to assess their suitability for use in masonry units, lightweight concrete blocks, and structural lightweight concrete (SLC) for non-wearing surfaces.

Figure 3. SFA

Figure 4. Microstructure of sintered flyash aggregate (10 µm & 1.5x)

Concrete mixes were prepared at water-cement ratios of 0.55 and 0.45, and tested for mechanical (compressive, flexural, tensile strength, drying shrinkage, modulus of elasticity, Poisson's ratio) and durability properties (RCPT, electrical resistivity, chloride migration, water permeability, sorptivity). Results showed that Lightweight Aggregate Concrete (LC) performed comparably to Normal Weight Aggregate Concrete (NC), though modulus of elasticity and flexural strength were lower for LC at similar compressive strengths. The aggregates met IS: 9142, ASTM C331, and IS: 2185 (Part II) standards for use in concrete masonry and lightweight blocks. Due to lower abrasion resistance, these aggregates are not recommended for wearing surfaces. The study [7-12] shows that it can be used as a replacement for the coarse aggregate by 100% in the strength range of 20-55MPa. The findings contributed to the development of IS: 9142 (Part-2): 2018 for the structural use of sintered fly ash aggregates. Codal provisions for lightweight concrete should be stricter than those for normal-weight concrete to ensure durability under similar exposure conditions.

4. CONCLUSIONS

On the basis of a study for the production of coarse aggregate and fine aggregate from different types of ash and slag, the following conclusions are made:

- The natural fine aggregates can be replaced by copper slag up to 50%, 60 % using granulated blast furnace slag aggregates, and 100% by the use of air-cooled blast furnace slag. The percentage replacement is finalised by testing the mechanical and durable properties of concrete.
- Water-cooled ferrochrome slag can replace up to 60% of natural fine aggregate, along with 100% natural coarse aggregate, and air-cooled slag can replace up to 60% of natural coarse aggregate, along with 100% natural fine aggregate in concrete.
- Bottom ash having at least 1.35 fineness modulus can replace up to 50% of natural fine aggregate in OPC-based concrete.
- Sintered fly ash lightweight aggregates conform to the IS: 9142, ASTM C-331, and IS: 2185 (Part-II) standards and are suitable for non-wearing applications like masonry blocks. Its structural use is possible, though flexural strength and modulus of elasticity are lower than conventional concrete.
- Use of industrial by-products like slags and ashes in concrete supports sustainable construction by reducing depletion of natural resources and promoting the circular economy.

REFERENCES:

[1] P.N. Ojha, A. Singh, B. Singh, Experimental investigations on substitution of natural sand in concrete with copper slag and blast furnace slag, J. Asian Concr. Fed. 7 (2021) 1–11.

[2] P.N. Ojha, A. Singh, B. Singh, V. Patel, Experimental investigation on use of ferrochrome slag as an alternative to natural aggregates in concrete structures, Res. Eng. Struct. Mater. 7 (2021) 225–244.

[3] P.N. Ojha, B. Singh, P. Kaura, A. Singh, Lightweight geopolymer fly ash sand: an alternative to fine aggregate for concrete production, Res. Eng. Struct. Mater. 7 (2021) 375–392.

[4] B. N. Mohapatra, P. Kaura, P. N. Ojha, B. Singh, S. Kumar, V. Liju, Fresh, hardened, and durability properties of concrete made with flyash and limestone-based Portland composite cement. Journal of Asian Concrete Federation, (2023) 9(1), 1-16.

[5] Central Electricity Authority, Annual Report 2018–19, Ministry of Power, Government of India, New Delhi, 2019.

[6] P.N. Ojha, A. Singh, A. Trivedi, B. Singh, N. Chowdhury, Evaluation of coal-based bottom ash as an alternative to fine aggregate in concrete: recommendations for specifications of bottom ash and its concrete mix design, Res. Eng. Struct. Mater. 3 (2023) 45-58.

[7] B. Singh, S.B. Singh, S.V. Barai, Performance of concrete made using sintered fly ash lightweight aggregate-A review, Indian Concr. J. 97 (2023) 41–59.

[8] B. Singh, S.B. Singh, S.V. Barai, P.N. Ojha, R. Kumar, Empirical Model for Static and Dynamic Modulus of Elasticity for Sintered Flyash Lightweight Aggregate-Based Concrete, Iran. J. Sci. Technol. Trans. Civ. Eng. 10 (2025) 1–6.

[9] B. Singh, S.B. Singh, S.V. Barai, P.N. Ojha, R. Kumar, Fracture behavior of concrete made with sintered fly ash lightweight coarse aggregate in comparison to normal weight concrete, Res. Eng. Struct. Mater. 11(2) (2025) 761–781.

[10] B. Singh, S.B. Singh, S.V. Barai, P.N. Ojha, R. Kumar, Experimental investigation for the determination of stress-strain relationship for sintered flyash lightweight aggregate concrete, Constr. Build. Mater. 489 (2025) 142339.

[11] B. Singh, S.B. Singh, S.V. Barai, P.N. Ojha, R. Kumar, Empirical model for determining compressive strength using post-installed pull-out test for structural lightweight concrete made with sintered flyash lightweight aggregate. Structural Concrete. (2025).

[12] B. Singh, S.B. Singh, S.V. Barai, P.N. Ojha, R. Kumar, Mechanical properties and fracture behavior of concrete made with sintered fly ash lightweight coarse aggregate and electric arc furnace slag as fine aggregate, Res. Eng. Struct. Mater. (2025) 1–22.

[13] P. N. Ojha, B Singh, P. Singh, A. Singh, M. K. Mandre, Study on effect of fly ash and limestone powder on compressive strength of roller compacted concrete for dam construction. J. Asian Concr. Fed., (2022), 8(1), 37-50.

[14] P. N. Ojha, B. Singh, S. Prakash, P. Singh, M. K. Madre, S. Kumar, Effect of high-ratio fly ash on roller-compacted concrete for dam construction. Res. Eng. Struct. Mater., (2022) 8(2), 233-251.

4th International Symposium on One Health, One World
November 20 – 22, 2025

ABS ID: 93
Code No: IMSBE-OP-24

Evaluating The Thermal Performance of Photovoltaic Cells Using Phase Change Materials and Geometric Enhancements: A Numerical Approach

Tabish Alam[1], Nagesh B. Balam[2], Md Muslim Ansari[3], Kishor S Kulkarni[4], Chandan S Meena[4], Naushad Ali[5], Injamamul Haque[5]

[1]*Senior Scientist, APEE, CSIR-Central Building Research Institute, Roorkee, India,*
[2]*Senior Principal Scientist, APEE, CSIR-Central Building Research Institute, Roorkee, India,*
[3]*Senior Scientist, SE, CSIR-Central Building Research Institute, Roorkee, India,*
[4]*Principal Scientist, APEE, CSIR-Central Building Research Institute, Roorkee, India,*
[5]*Project Associate, APEE, CSIR-Central Building Research Institute, Roorkee, India,*
Correspond to Dr. Tabish Alam (tabish.cbri@csir.res.in)

***Keywords**: Photovoltaic (PV) cell, Phase change material (PCM), Computational fluid dynamics (CFD), Heat transfer enhancement.*

Abstract

Photovoltaic (PV) panels often experience a decline in performance due to the buildup of excessive heat, with over 80% of incoming solar radiation being released as waste heat. The use of passive thermal management through phase change materials (PCMs) has been recognized as an effective approach, thanks to their capability to absorb surplus heat via latent heat storage. In this research, a numerical analysis was conducted on a PV-PCM system that incorporated RT42 PCM and was enhanced with T-shaped fins positioned at a 32° angle to improve heat transfer. Two different fin configurations were examined using a transient CFD model created in ANSYS FLUENT. The findings reveal that the triple-fin setup (Case-2) substantially enhanced thermal performance in comparison to the double-fins configuration (Case-1).

1. INTRODUCTION

The global energy landscape is undergoing a rapid transformation as the demand for sustainable and environmentally friendly power generation continues to rise. Among the available renewable technologies, solar photovoltaic (PV) systems have emerged as one of the most reliable and scalable solutions, suitable for both urban and remote applications. However, the performance of PV modules is highly sensitive to operating temperature. Beyond the reference point of 25 °C, the conversion efficiency declines by approximately 0.4–0.65% for every 1 °C rise in cell temperature, leading to substantial losses during prolonged exposure to high solar irradiance. Excessive heating not only reduces electrical output but also accelerates material degradation, thus shortening the service life of PV systems [1].

To counter this challenge, both active and passive cooling strategies have been explored. Active methods such as forced air or liquid cooling improve heat dissipation but introduce additional complexity, external power requirements, and higher maintenance costs. Passive approaches, by contrast, are simpler and energy-free, making them attractive for large-scale deployment. Conventional passive strategies like natural convection or radiative cooling, however, are often insufficient under peak solar conditions, particularly in hot climates. This limitation has shifted focus toward phase change materials (PCMs), which can absorb and store excess heat through latent heat, thereby stabilizing PV module temperatures.

Despite their potential, PCMs suffer from low thermal conductivity, which limits heat transfer rates and leads to localized hot spots. To overcome this, researchers have incorporated heat transfer enhancers such as fins, foams, and nanoparticles. Among these, fins provide a cost-effective and structurally simple solution by increasing the effective surface area and promoting uniform melting. In this study, a two-dimensional transient CFD model of a PV-PCM system with T-shaped fins inclined at 32° (optimal tilt for Roorkee, India) is developed.

2. MODEL DESCRIPTION AND PROCESS

In this research, a two-dimensional PV–PCM numerical model integrated with T-shaped fins was developed to investigate passive cooling of photovoltaic modules. The PCM container measured 120 mm in height and 50 mm in width, with a 5 mm aluminum plate attached on top to represent the PV absorber. A uniform heat flux of 1000 W/m² was applied to the absorber surface to simulate solar irradiation (figure 1), while the backside wall was subjected to convective cooling with a heat transfer coefficient of 10 W/(m²·K). T-shaped fins of 3 mm thickness and 33 mm length were embedded within the PCM domain to enhance conductivity and promote uniform melting. The PCM selected was RT42 [2].

The enthalpy–porosity method was implemented in ANSYS Fluent to model melting, accounting for conduction in the solid phase and combined conduction-convection in the liquid phase. The governing continuity, momentum, and energy equations were solved using a pressure-based solver with the SIMPLEC algorithm, second-order upwind discretization, and PRESTO pressure interpolation. Mesh independence was ensured using a fine tetrahedral grid, and transient simulations were conducted with a 0.5 s time step. Model validation was achieved by comparing liquid fraction contours with experimental results from Kamkari et al. [3], showing strong agreement and confirming the reliability of the approach.

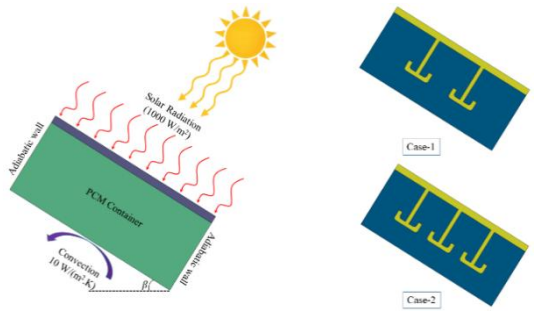

Figure 1. 2D PV-PCM model with T-shaped fins displaying boundary conditions and geometry.

3. RESULT AND DISCUSSION

Figure 2 shows the liquid fraction contours for Case-1 and Case-2 at different time intervals. In both cases, melting begins near the heated top surface and progresses downward, aided by buoyancy-driven convection. The addition of T-shaped fins improves heat transfer by creating multiple melting fronts, but Case-2, with closer fin spacing, develops a denser conductive network and stronger convective circulation. This leads to faster, more uniform melting compared to Case-1, which displays localized heat buildup and slower melt progression in the central and lower regions.

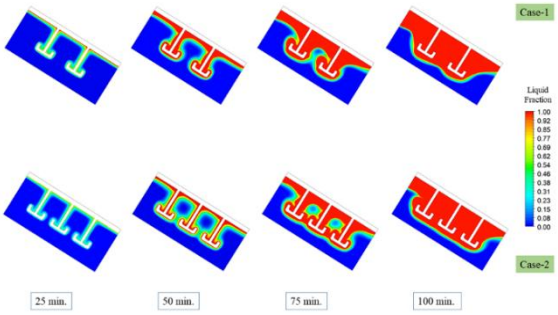

Figure 2. Time-varying liquid fraction contours for Cases 1 and 2.

Figure 3 illustrates the temporal variation of PCM temperature for Case-1 and Case-2. During the early stage (25–50 min), both cases show comparable heating trends, with PCM temperatures around 307–311 K, indicating the onset of melting near the absorber surface. As time progresses, differences emerge due to varying fin arrangements. At 75 min, Case-1 records 313.9 K, whereas Case-2 is slightly lower at 313.2 K, highlighting the effect of improved thermal spreading with closer fin spacing. By 100 min, Case-1 reaches 319.4 K compared to 318.0 K in Case-2, a difference that, while small, signifies more effective heat dispersion in Case-2. This consistent temperature moderation demonstrates that reduced fin spacing enhances conduction pathways and strengthens convective mixing within the PCM, thereby preventing localized overheating. Consequently, Case-2 not only accelerates the melting process but also sustains lower PCM temperatures, ensuring better thermal regulation of the PV module.

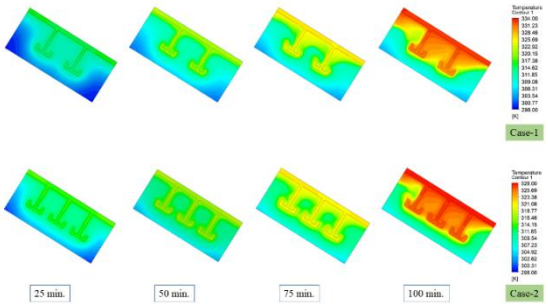

Figure3.Time-varying PV-PCM system temperature contours for Cases 1 and 2.

3. CONCLUSIONS

This study conducted a numerical analysis of the melting performance of a PV-PCM system equipped with T-shaped fins set at an angle of 32° for the passive cooling of photovoltaic modules. The findings indicate that the incorporation of fins improved conductive heat transfer and buoyancy-driven convection, resulting in quicker melting and enhanced heat absorption. Case-2, featuring three fins, achieved complete melting in 265 minutes, in contrast to 291 minutes for Case-1, with a greater liquid fraction at 100 minutes (0.6366 for case-2, 0.6009 for case-1). Furthermore, Case-2 limited the peak PCM temperature to 373.8 K compared to 381.8 K in Case-1. These results validate that optimized fin design significantly enhances PCM-based cooling, effectively reducing overheating and improving PV performance through a straightforward, passive design.

Acknowledgement

The CSIR-CBRI Director's approval of the publishing of this research is much appreciated by the authors. Additionally, we are very grateful for the financing help provided by the CSIR under project number FBR-040304.

REFERENCES

[1]Qu H, Gao B, Kong Q, Xu Z. Experimental study of the effect of ambient temperature on the output characteristics of PV-PCM systems. JEnergy Storage 2024;88:111535. https://doi.org/10.1016/j.est.2024.111535.

[2]Bhakre SS, Sawarkar PD, Kalamkar VR. Numerical study on photovoltaic thermal phase change material system in hot climatic conditions. Appl Therm Eng 2023;227:120423. https://doi.org/10.1016/j.applthermaleng.2023.120423.

[3]Kamkari B, Shokouhmand H, Bruno F. Experimental investigation of the effect of inclination angle on convection-driven melting of phase change material in a rectangular enclosure. Int J Heat Mass Transf 2014;72:186–200. https://doi.org/10.1016/j.ijheatmasstransfer.2014.01.014.

4th International Symposium on One Health, One World
November 20 – 22, 2025

ABS ID: 46
Code No: IMSBE-OP-25

Urban Form And Shadow Impact on Pedestrian Environment

H. Watanabe[1], and Y. Honma[2]
[1]*Proj. Res. Assoc., Institute of Industrial Science, The University of Tokyo, Tokyo, Japan,*
[2]*Assoc. Prof., Institute of Industrial Science, The University of Tokyo, Tokyo, Japan,*
Correspond to Proj. Res. Assoc. H. Watanabe (hiroko@iis.u-tokyo.ac,jp)

***Keywords**: Shadow simulation, Urban form, Pedestrian Environment, comfort, Shading strategies.*

1. GENERAL INSTRCUTIONS

In recent years, the verticalization of urban areas has accelerated, raising challenges for ensuring comfortable pedestrian spaces. In Japan in particular, the intensification of summer heat due to global climate change has increasingly compromised the comfort of outdoor walking. Conversely, during winter, adequate solar access is desired by pedestrians, meaning that the value of shade in urban spaces varies seasonally. In this context, incorporating building-generated shadows into planning can contribute to reducing energy consumption, mitigating the urban heat island effect, maintaining public health, and enhancing urban sustainability.

However, a review of previous studies on the thermal environment of pedestrian spaces shows that discussions have mainly focused on shading provided by street trees [1], while relatively little attention has been given to shadows cast by buildings. Therefore, it is essential to capture the dynamics of building-generated shadows in urban spaces in detail and to obtain knowledge that enables their utilization as a design resource.

The purpose of this study is to clarify the relationship between urban form and shadow conditions, and to conduct large-scale shadow simulations that capture the dynamics of building-generated shade throughout the year. Specifically, we visualize and quantify seasonal and diurnal changes in shadows, and analyze their impacts on urban spaces. By doing so, we evaluate how building configuration and height influence solar access in pedestrian environments and derive knowledge to support the creation of comfortable and walkable urban spaces. This paper presents a case study of Kachidoki 5-chome in Chūō Ward, Tokyo, Japan, where annual variations in shadows are simulated and quantified by season and time of day. Using indicators such as cumulative shadow duration, maximum continuous shadow duration, and time-specific shadow distribution, we sought to extract “comfortable shade zones” for pedestrians.

The findings provide essential knowledge for planning and design, demonstrating the potential of shadow as a planning asset. They also contribute to the realization of walkable urban environments. Furthermore, presenting solar and shadow conditions in both visual and quantitative terms facilitates shared understanding among governments, citizens, and designers, enabling productive discussions for creating sustainable cities. Importantly, these insights highlight how shadow simulation can be systematically incorporated into shading strategies, bridging the gap between urban form, pedestrian comfort, and sustainable design practices.

2. METHODOLOGY

The simulation employed the PLATEAU [2] dataset (2023 edition) provided by the Ministry of Land, Infrastructure, Transport and Tourism, from which building and road data are obtained. Buildings are modeled as simplified box-shaped volumes, and a 2 m × 2 m grid mesh is used for analysis. The target periods are the summer and winter solstices, and simulations are conducted from 8:00 to 16:00 at 15-minute intervals. At each time step, solar positions are calculated, and shadows are projected onto the grid, generating shadow maps for the entire district.

3. ANALYTICAL FRAMEWORK

To capture seasonal extremes, the analysis focuses on the summer solstice, when shadows are shortest, and the winter solstice, when shadows are longest. Three key indicators are employed:

A. Cumulative Shadow Duration

For each grid cell, total shadow hours during the study period are aggregated and mapped by season. Differences between the summer and winter solstices are also calculated to identify locations with high annual variability.

B. Continuous Shadow Duration

The maximum uninterrupted duration of shadow is computed for each cell. This highlighted areas of prolonged shading, which can provide pedestrian comfort in summer but indicate solar deprivation in winter.

C. Time-Specific Shadow Distribution

Shadow duration is separately calculated for the morning (08:00–12:00) and afternoon (12:00–16:00). This allow us to capture the daily movement of comfortable shade zones and to evaluate how pedestrian routes and gathering spaces change throughout the day.

4. CASE STUDY

The study area, Kachidoki 5-chome, has a block area of 108,385 m², of which 28,298 m² is roads. The district contains 61 buildings, with a building coverage ratio of 57%, an average height of 22 m, and a maximum height of 176 m. This high-density urban setting provides a representative context for assessing the influence of tall buildings on pedestrian solar environments.

The simulation results (Figure 1- Figure 4) indicate that during the winter solstice, major

roads are heavily shaded in the afternoon. In contrast, during the summer solstice, streets rarely experienced more than four consecutive hours of shadow. Afternoon conditions in summer showed extended shaded areas along eastern sidewalks of tall buildings, suggesting potential pedestrian comfort. However, these same spaces were found to be severely

deprived of sunlight during winter, highlighting a significant seasonal trade-off.

5. DISCUSSION

The results demonstrate that building configuration and height exert a strong influence on pedestrian solar environments, and that seasonal variability in comfort is

considerable. Shadows serve as a dual resource: in summer they provide valuable relief from heat, while in winter they can inhibit pedestrian activity due to insufficient sunlight. pedestrian

environments. Moreover, analyzing time-specific shadow distributions yields practical insights for designing walking routes and public spaces that adapt to diurnal and seasonal conditions.

REFERENCES

[1] S. Yoshida, Effects of Tree Planting on Ventilation and Thermal Environment in Urban Area, Wind Engineers, JAWE. Vol.2008, Issue 117 (2008) 321-326.

[2] The Ministry of Land, Infrastructure, Transport and Tourism. PLATEA : https://www.mlit.go.jp/plateau/

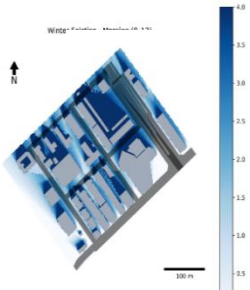

Figure 1.

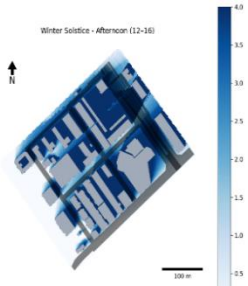

Figure 2.

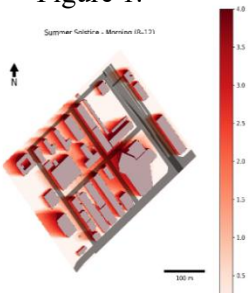

Figure 3.

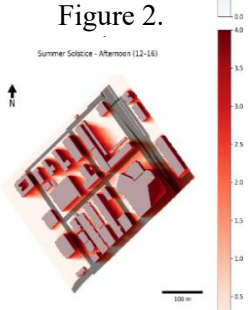

Figure 4.

ACKNOWLEDEMENTS his work was supported by JSPS KAKENHI Grant Number JP24K0783 and the Kajima Foundation for the Promotion of Science.

ABS ID: 122
Code No: IMSBE-OP-26

Dr. P. Pravin Kumar Venkat Rao

4th International Symposium on One Health, One World
November 20 – 22, 2025

ABS ID: 185
Code No: IMSBE-OP-27

Post-Seismic Structural Integrity Assessment of Dams in Northern Myanmar After the 2025 Mw 7.7 Sagaing Earthquake using Multi-Technique InSAR Time-Series

Arliandy Pratama[1], Wataru Takeuchi[2], and Khin Myat kyaw[3]
[1]Ph.D. Student at Dept. of Civil Engineering, The University of Tokyo, Tokyo, Japan, [2]Professor at Institute of Industrial Science, The University of Tokyo, Tokyo, Japan, 3 Research Associate at Institute of Industrial Science, The University of Tokyo, Tokyo, Japan, Correspond to arliandyarbad@g.ecc.u-tokyo.ac.jp

***Keywords**: Dam, Post-Seismic Deformation, InSAR, SHM, Earthquake.*

1.INTRODUCTION

The Mw 7.7 Sagaing earthquake of March 28, 2025, caused catastrophic damage to infrastructure in northern Myanmar, including hundreds of dams across the Sagaing, Mandalay, and Bago regions [1]. Ensuring dam integrity is critical, as failures can trigger cascading hazards, as seen in the Brumadinho and Derna dam disasters [2, 3]. Assessing dam stability after earthquakes is particularly challenging due to dense vegetation and restricted site access. SBAS technique suffers from coherence loss in vegetated terrain [4], and conventional PS-InSAR is limited by scatterer selection [5]. Recent advances, notably Tracy–Widom PS-InSAR (TW-PSI), improve scatterer detection in low-coherence conditions [6]. This study further proposes a new approach for deriving three dimensional (3D) InSAR displacement fields by integrating TW-PSI from dual-orbit Sentinel-1 data with GNSS priors. The aim is to capture both vertical and horizontal deformation patterns, thereby strengthening structural health monitoring (SHM) of dams in seismically active regions [7].

2. DATA AND METHOD

We utilized 171 Sentinel-1 ascending (ASC) and 154 descending (DSC) SAR images provided by ESA, covering the Yeywa and Myogyi Dam region from January 2019 to July 2025. The SAR data were processed using an enhanced Persistent Scatterer Interferometry (PS-InSAR) technique, namely Tracy–Widom PS-InSAR (TW-PSI), based on random matrix theory and introduced by [6], with a particular focus on detecting stable scatterers in highly vegetated areas. The 3D InSAR displacement fields were derived by decomposing dual orbit line-of-sight measurements into vertical (U), east west (E), and north–south (N) components, with the N component constrained using GNSS post-processing data obtained from [8]. Figure 1.

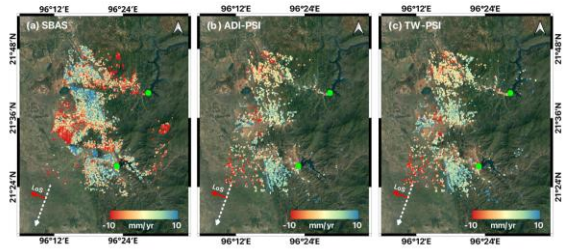

Comparison of point selection among (a) SBAS, (b) ADI-PSI, and (c) TW-PSI from descending-orbit LoS time-series. The locations of Yeywa Dam (21.67°N, 96.45°E) and Myogyi Dam (21.46°N, 96.38°E) are indicated by green dots. 3. RESULTS AND DISCUSSION Figure 1 shows a comparison of InSAR processing results using SBAS, ADI-PSI, and TW-PSI, where SBAS retrieved more points overall but almost none on the dam body, conventional (amplitude dispersion index) ADI based PSI produced more

spatially distributed scatterers including some on both dam structures though still limited, while TW-PSI further increased the number of persistent scatterers particularly on critical sections of the dam, which were then used as the basis for 3D structural deformation analysis.

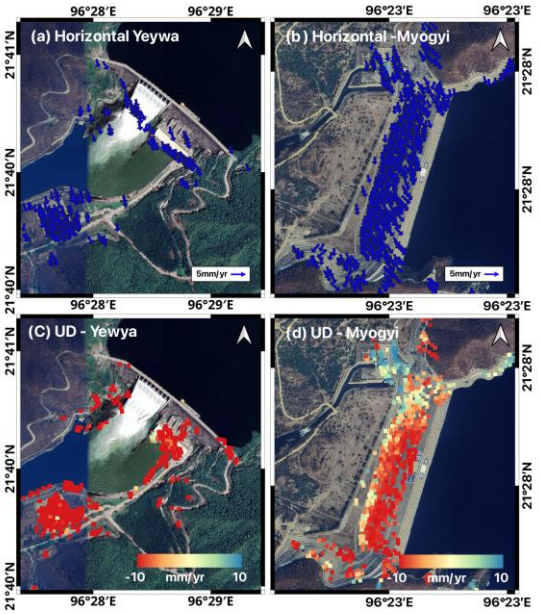

Figure 2. Horizontal (a, b) and vertical (c, d) velocities for Yeywa and Myogyi dams, respectively. At Yeywa Dam, the dominant southward horizontal displacement aligns with the main spillway outflow direction, while at Myogyi Dam the displacement trends more toward the southeast, partly opposing the reservoir pressure. Both dams also exhibit clear vertical subsidence, indicating settlement as a primary deformation mode, with estimated horizontal velocities of about 3.36 mm/yr for Yeywa and 3.20 mm/yr for Myogyi (Figure 2). (a) (b)

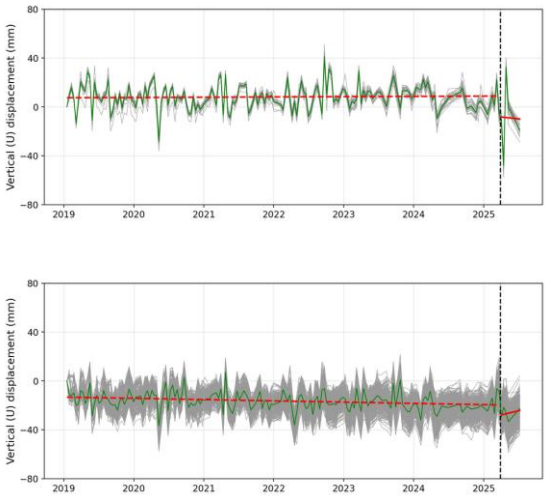

Figure 3. Vertical (U) time-series displacement with pre- and post-seismic trends for (a) Yeywa and (b) Myogyi Dam. Time-series analysis of the vertical component provides direct insights into dam stability under seismic stress. At Yeywa Dam, the detrended time series reveals a minor coseismic step of approximately −4 mm with negligible post-event slope change, indicating stable behavior during the short post-seismic window (Figure 3a).

	Yeywa	Myogyi
Pre-seismic Velocity	0.35 mm/yr	-0.96 mm/yr
Co-seismic displacement	-4.285 mm	-23.1 mm
Post-seismic (Δ Slope)	-7.0 mm/yr	18.8 mm/yr

Table 1. Summary of pre-seismic velocity, co-seismic displacement, and post-seismic (Δslope). Yeywa Myogyi Pre-seismic Velocity Co-seismic displacement 0.35 mm/yr -4.285 mm Post-seismic (Δ Slope) -7.0 mm/yr In contrast, Myogyi Dam shows a clear coseismic settlement of about −23 mm, accompanied by a positive post-seismic slope, suggesting localized deformation and short-term adjustment (Figure 3b). While these displacements do not directly imply structural failure, they highlight zones of potential vulnerability that warrant closer inspection. Such deformation monitoring is central to structural health monitoring (SHM) of dams, as it enables the detection of subtle movements that could compromise long-term performance. Integrating InSAR derived metrics into SHM frameworks supports

proactive safety management and resilience of dam infrastructure in seismically active regions. 4.

CONCLUSIONS

This study demonstrates that advanced PS-InSAR, enhanced with Tracy–Widom scatterer selection and combined with GNSS-constrained 3D decomposition, provides reliable insights into post-seismic dam stability. Yeywa Dam remained stable with minimal coseismic impact, whereas Myogyi Dam experienced significant settlement requiring closer attention. These findings confirm the potential of multi-technique InSAR as a robust framework for remote structural health monitoring (SHM), supporting early warning and risk reduction strategies in earthquake-prone regions. The multi technique InSAR provides cost-effective and scalable for post-seismic risk assessment, supporting resilience planning and disaster-mitigation policies

REFERENCES:

[1] Hussain, S., Pan, B., Hussain, W., Ali, M., Sajjad, M.M., Afzal, Z. and Tariq, A., 2025, October. Analyzing coseismic displacement of the M7. 7 Myanmar earthquake on march 28, 2025, using Sentinel-1 InSAR data. In Structures (Vol. 80, p. 109718). Elsevier.

[2] Grebby, S., Sowter, A., Gluyas, J., Toll, D., Gee, D., Athab, A. and Girindran, R., 2021. Advanced analysis of satellite data reveals ground deformation precursors to the Brumadinho Tailings Dam collapse. Communications Earth Environment, 2(1), p.2. &

[3] Annunziato, A., Santini, M., Proietti, C., de Girolamo, L., Lorini, V., Gerhardinger, A. and Tucci, M., 2024. Modelling and validation of the Derna Dam Break event. GeoHazards, 5(2), pp.504-529.

[4] Fuhrmann, T. and Garthwaite, M.C., 2019. Resolving three-dimensional surface motion with InSAR: Constraints from multi-geometry data fusion. Remote Sensing, 11(3), p.241.

[5] Morishita, Y. and Kobayashi, T., 2022. Three dimensional deformation and its uncertainty derived by -0.96 mm/yr -23.1 mm 18.8 mm/yr integrating multiple SAR data analysis methods. Earth, Planets and Space, 74(1), p.16.

[6] Pratama, A. & Takeuchi, W., 2025. Investigating structural health of rock earth-filled Jatiluhur Dam after a shallow earthquake using multi-technique InSAR time-series. In: Proceedings of the IEEE International Geoscience and Remote Sensing Symposium (IGARSS). Brisbane, Australia, 2025.

[7] Pratama, A. & Takeuchi, W., 2025. Post-seismic structural integrity assessment of Jatiluhur Dam using InSAR-based deformation analysis. In: Proceedings of the International on Remote Sensing (ISRS), Incheon, Korea, 2025.

[8] Lindsey, E., Wang, Y., Aung, L., Chong, J., Qiu, Q., Mallick, R., Feng, L., Aung, P., Tin, T., Min, S. and Bradley, K., 2023. Active subduction and strain partitioning in western Myanmar revealed by a dense survey GNSS network, Earth Planet. Sc. Lett., 622, 118384

4th International Symposium on One Health, One World
November 20 – 22, 2025

ABS ID: 39
Code No: IMSBE-OP-28

Traffic-Compatible Tunnel Health Screening with on-Vehicle Lidar

A. Regmi[1], T. Mizutani[2], And K. Yamamoto[3]
[1] *Doctoral Student, Department of Civil Engineering, The University of Tokyo, Tokyo, Japan,*
[2] *Assoc. Professor, Department of Civil Engineering, The University of Tokyo, Tokyo, Japan,*
[3] *Engineer, Aero Toyota Corporation, Kawagoe, Japan,*
Correspond to Assoc. Prof. T. Mizutani (mizu-t@iis.u-tokyo.ac.jp)

***Keywords**: Tunnel Health, Seepage Mapping, Defect Identification, Lidar, Infrastructure Safety, Asset Management.*

1. INTRODUCTION

Highway tunnels are important parts of the road network, but many are aging and in the process of deterioration. However, condition monitoring of these tunnels is still done mostly by visual inspection [1]. This can be slow, requires lane closures, and sometimes puts inspectors in risky situations. Also, the declining population in many countries has created lack of work force for this kind of monitoring. Thus, for the infrastructure management, we need a sensor-based workflow method that is objective, automatic, quick to repeat, and does not stop traffic[2].

Figure 1: Manual Visual Inspection of Highway Tunnels

This study introduces a traffic compatible workflow using a vehicle mounted LiDAR sensor as shown in the Figure 2 for the monitoring of highway tunnels. In one pass, the system scans the tunnel lining and provides 3D point cloud data consisting of tunnel geometry and reflection intensity from the surface of the tunnel. By using it we have developed a method for complete condition monitoring of the tunnel. We focus on two lining conditions that strongly affect maintenance: (i) water seepage, which can lead to chemical and physical deterioration; and (ii) surface damage such as peeling/spalling and outward bulging

(floating/delamination).Monitoring of Tunnel

Figure 2: On-Vehicle LiDAR system used for tunnel monitoring.

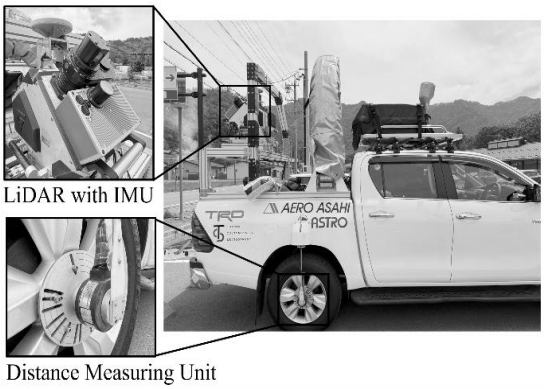

attachments/ fixtures is also necessary for a smooth functioning of the tunnel. Tunnels carry many fixtures—luminaires, signs, cable trays, cables, pipes, etc. Failures in these systems can cause serious incidents even when the concrete lining is sound. The examples of key elements to be monitored in the tunnel lining are shown in Figure 3. A well known example is the 2012 Sasago Tunnel incident on the Chuo Expressway, where the collapse of suspended concrete panels used for ventilation led to tragic outcomes[3]. This case shows why a routine, objective check of attachments (tilt, sag, clearance conflicts, and moisture around fasteners) should be included together with lining checks.

The basic idea in this work is to use the LiDAR's own light to measure both the tunnel's shape and the return intensity, then turn those signals into clear maps for engineers which

includes the detected seepage area, geometric defects as well as the tunnel attachments. The method is designed to be repeatable during traffic, so agencies can compare scans over time.

Figure 3: Key elements to monitor in the lining

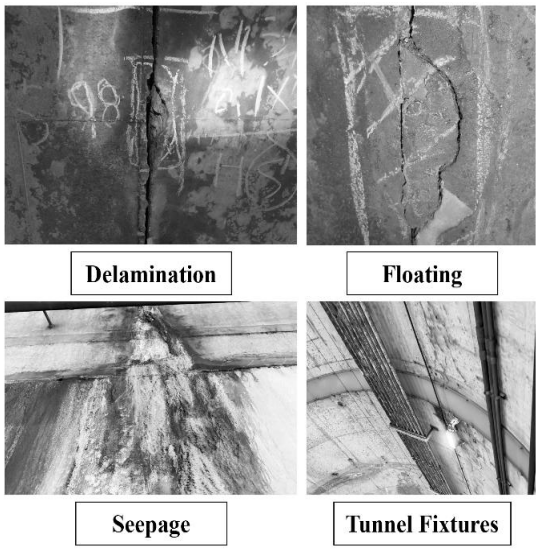

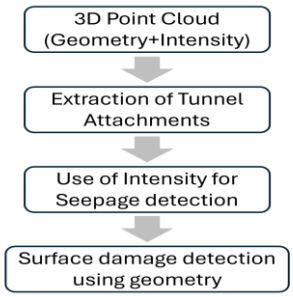

2. METHODS

Figure 4: Overall Methodology

The overall methodological framework is provided in Figure 4. A compact phase-based LiDAR mounted on a survey vehicle scans the tunnel as traffic flows. Each measured point has a 3D position (geometry) and a return intensity value (how "brightly" the surface reflects the laser) as shown in the Figure 5. No special lighting or closures are required unlike the image-based techniques requiring the external light source[4].

First the obtained 3D point cloud data is denoised using the statistical outlier filtering to get clean data. Before further processing for any defect detection in the tunnel lining, the attachments in the lining are removed. This removal of noise and attachments leaves the clean concrete lining. From the 3D coordinates and reflection intensity of the tunnel lining, two major defects are then interpreted:

• Seepage cue (intensity): wet concrete tends to absorb near infrared laser energy, so wet patches look "darker" in the intensity channel.

• Damage cue (geometry): local changes in surface orientation and depth highlight peeling (inward loss of material) and floating/delamination (outward bulging).

Furthermore, we also look at the safety critical tunnel attachments such as luminaires, pipes, cable trays, etc. From the same point cloud, we can check: (i) position and clearance against the tunnel axis, (ii) small tilt or sag that may

Figure 5: 3D point cloud data obtained from LiDAR

indicate looseness, and (iii) darkening near fasteners that can suggest moisture exposure or corrosion risk.

In this way, instead of heavy, site specific deep learning approaches commonly used nowadays [5,6], we use simple, physics guided steps to separate the true signals (patchy wet zones, local geometric departures, attachment misalignment) from other similar features (linear joints, dark sealants, hardware). The end product is a set of easy-to-read overlays: seepage, damage, and attachment status on the tunnel surface.

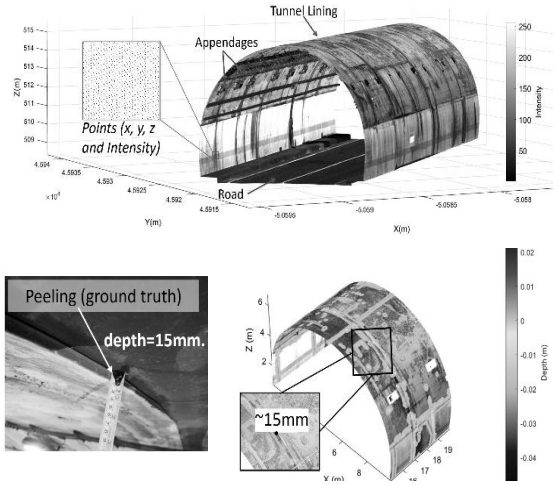

3. FINDINGS

The proposed algorithm was applied on a highway tunnel segment in Japan. Here the ground truth data for the seepage and some

floating and peeling damage were obtained by the visual inspection.

Seepage Condition: By using our technique, we

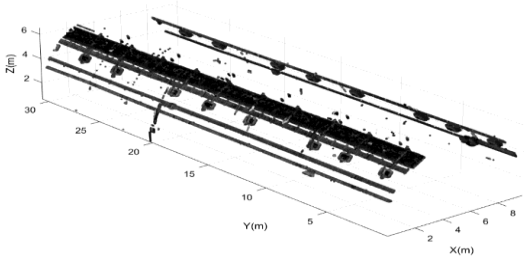

detected the seepage in the tunnel lining. Figure 6 shows the validation of detected seepage area with the photographs collected from the tunnel lining.

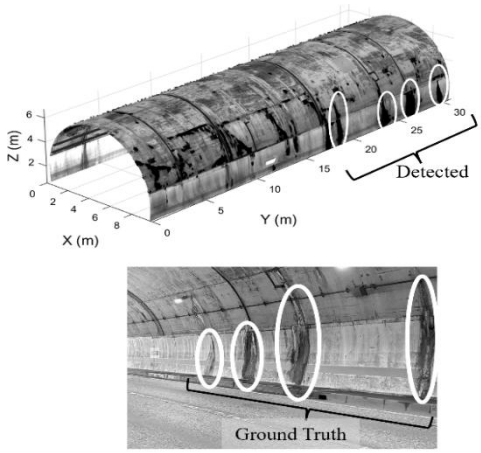

Figure 6: Detected Seepage in the Tunnel lining and validation with ground truth images

Surface condition: The geometric defect detection algorithm flagged two common damage types: an inward peeling and an outward floating. As depicted in Figure 7, the floating area is in good agreement with ground measurements. Additionally, a minor deformation of less than 1 cm was observed, confirming a feature that would not be apparent through normal visual inspection.

While some research focuses only on geometrical defects using 3D geometry [7,8], we have tried to incorporate both seepage and other defects using both geometry and intensity information.

Figure 7: Geometric defect identification and quantification in the tunnel lining (Peeling detected)

Attachments: From the attachment removal step, different tunnel fixtures are obtained as shown in Figure 8. These fixtures are further separated into different segments showing the lights, cables, and pipes present in the tunnel lining, which is highly necessary for tunnel asset management. The proper position and tilt in these attachments can be detected by comparing with the main tunnel axis. Similarly, the records of these fixtures can be kept, and changes can be monitored by scanning the same tunnel in the future.

Thus, a single pass produces quantitative, repeatable outcomes that reduce subjectivity, improve worker safety, and creates a digital record that can be compared over time—for both the lining and the installed attachments.

4.RELEVANCE FOR INFRASTRUCTURE MANAGEMENT

Figure 8: Extraction of Tunnel Fixtures for monitoring

Safety without disruption: Screening from a moving vehicle limits worker exposure and minimizes closures, lowering crash risk and community disruption.

Preventive maintenance: Early recognition of moisture ingress and surface distress helps agencies intervene before deterioration escalates—protecting budgets and extending asset life.

Environmental co-benefits: Better-timed repairs reduce material waste and emissions associated with emergency fixes, aligning infrastructure practice with broader environmental goals.

Clear communication: Map-like outputs is easy to share with operators and contractors.

5. LIMITATIONS

Thin films of moisture can be subtle, and dark textures near joints may occasionally be over-flagged. The tunnel lining behind the fixtures cannot be monitored due to occlusion. The algorithm is tested for only one tunnel and is required to be applied in other different types of tunnels.

6. CONCLUSION AND FUTURE WORK

This work shows that vehicle-based LiDAR is a practical and repeatable way to screen tunnel conditions at network scale without long lane closures. In one pass, the system produces clear maps of the lining and the main attachments and builds a compact “digital twin” that stores the signals needed for maintenance decisions. By combining intensity cues (for seepage and wetting) with geometric cues (for peeling, spalling, and outward bulging), and by checking simple status indicators for fixtures such as luminaires, signs, and cable trays, the workflow supports safer operations and smarter planning in day-to-day infrastructure management. The outputs are objective and easy to compare over time, which also helps teams that are facing fewer inspectors and an aging workforce.

Our next plan is to deploy the workflow across several highway tunnels to confirm repeatability, set practical thresholds, and standardize the data products for agency use. We will also connect the screening results to existing asset systems so that engineers can track locations, attach photos, and schedule targeted follow-up work. Beyond the tunnel lining, a natural extension is the roadway surface: the same pass can be adapted to assess potholes, rutting, and joint steps, creating one integrated highway monitoring stream from a single drive-through. Additional work will study seasonal effects on intensity, define simple quality checks and uncertainty reporting, and link drive-through screening with higher-resolution inspections where needed. The final goal is an integrated, traffic-compatible monitoring system that helps keep tunnels and roads safe, supports timely maintenance, and strengthens long-term infrastructure management.

REFERENCES

[1] Federal Highway Administration, Reliability of Visual Inspection for Highway Bridges, Volume I: Final Report, 2001.

[2] W. Wang, W. Zhao, L. Huang, V. Vimarlund, Z. Wang, Applications of terrestrial laser scanning for tunnels: a review, J. Traffic Transp. Eng. (Engl. Ed.) 1 (2014) 325–337. https://doi.org/10.1016/S2095-7564(15)30279-8.

[3] Ministry of Land IT and T., Sasago Tunnel Ceiling Collapse on the Chuo Expressway (Sequence of Events and Countermeasures), n.d.

[4] Y. Tan, X. Li, J. Lai, J. Ai, Real-time tunnel lining leakage image semantic segmentation via multiple attention mechanisms, Meas. Sci. Technol. 35 (2024). https://doi.org/10.1088/1361-6501/AD1DDB.

[5] Y. Feng, S.J. Feng, X.L. Zhang, D.M. Zhang, Y. Zhao, A two-step deep learning-based framework for metro tunnel lining defect recognition, Tunn. Undergr. Space Technol. 150 (2024) 105832. https://doi.org/10.1016/J.TUST.2024.105832.

[6] S.J. Feng, Y. Feng, X.L. Zhang, Y.H. Chen, Deep learning with visual explanations for leakage defect segmentation of metro shield tunnel, Tunn. Undergr. Space Technol. 136 (2023) 105107. https://doi.org/10.1016/J.TUST.2023.105107.

[7] T. Mizutani, T. Yamaguchi, K. Yamamoto, T. Ishida, Y. Nagata, H. Kawamura, et al., Automatic detection of delamination on tunnel lining surfaces from laser 3D point cloud data by 3D features and a support vector machine, J. Civ. Struct. Health Monit. 14 (2024) 209–221. https://doi.org/10.1007/s13349-023-00731-3.

[8] T. Mizutani, T. Yamaguchi, T. Kudo, K. Yamamoto, T. Ishida, Y. Nagata, et al., Quantitative evaluation of peeling and delamination on infrastructure surfaces by laser signal and image processing of 3D point cloud data, Autom. Constr. 133 (2022) 104023. https://doi.org/10.1016/j.autcon.2021.10403.

ABS ID: 132
Code No: IMSBE-OP-29

Dr. Santha Kumar G.

4th International Symposium on One Health, One World
November 20 – 22, 2025

ABS ID: 15
Code No: IMSBE-OP-30

Mitigating Pedestrian Heat Stress: An Optimization Approach for Shade Placement on Fixed-Routing Networks

N. Adachi[1], H. Hasada[2], H. Watanabe[3], And Y. Honma[4]
[1] *Graduate Student, Dept. Of Architecture, The University Of Tokyo, Tokyo, Japan,*
[2] *Research Associate, Institute Of Industrial Science, The University Of Tokyo, Tokyo, Japan,*
[3] *Project Research Associate, Institute Of Industrial Science, The University Of Tokyo, Tokyo, Japan,*
[4] *Associate Professor, Institute Of Industrial Science, The University Of Tokyo, Tokyo, Japan,*
Correspond To Assoc. Prof. Y. HONMA (Yudai@Iis.U-Tokyo.Ac.Jp)

***Keywords**: Infrastructure, Pedestrian comfort, Street Network, Urban design, Optimal Placement, Heat Stress.*

1. OBJECTIVE

The increasing severity of summer heat due to recent climate change poses a serious social problem. In urban areas, the heat island effect exacerbates this, significantly increasing the risk of heatstroke during outdoor activities. For instance, in Japan, the cumulative number of people transported by ambulance across Japan due to heatstroke from May to September in 2024 reached 97,578, the highest number since the Tokyo Metropolitan Government began its survey in 2008. Pedestrians face prolonged exposure to direct sunlight, making countermeasures against heatstroke an urgent necessity.

Prior research has proposed path-finding algorithms that minimize sun exposure, often estimating insolation from images obtained via Google Street View.[1] However, this approach has limitations, namely: 1) pedestrians are highly likely to choose the shortest path regardless of sun exposure, and 2) heatstroke risk is influenced not only by the total duration of sun exposure but also by the continuity of sun-exposed sections.

To address these issues, this study defines a pedestrian's core body temperature, a key indicator of heatstroke risk, as a non-linear function that changes based on the past thermal state and the current solar exposure. Under the crucial premise that pedestrians will inevitably choose the shortest path, the objective of this research is to solve the optimal shade placement problem: "Where should shade spots be placed to most effectively reduce heatstroke risk along the shortest path?"

2. METHODS

Using open-source building data for the Jinnan area of Shibuya, Tokyo and data on the Sun's altitude for Tokyo, With the Rhinoceros and Grasshopper plugins (on the left in Figure.1), the shaded areas at noon on the Summer Solstice were computed (on the right in Figure.1).

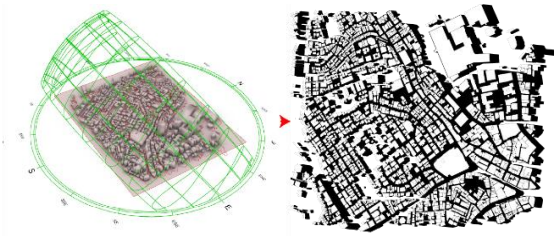

Figure 1. Generating shaded areas from building data

Nodes were placed approximately every 5 meters along the street segments, and a determination was made for each node as to whether it lay inside or outside the closed curves representing the shaded regions generated in the previous step.

The indices, sets, variables, parameters and the optimization problem addressed in this study are presented below.

Indices

i An index for a node ($i \in N$)

p An index for a path ($p \in P$)

Sets

P The set of all origin-destination (OD) pairs (paths) to be evaluated.

N The set of all nodes in the network.

N_p The set of nodes on path p (N_p ⊂ N)

S_0 The set of nodes that are initially shaded ($S_0 \subset N$).

H The set of sunny nodes that are candidates for shade installation (H ⊂ N).

Variables

y_i A binary variable that is 1 if a shade is installed at a candidate node i ∈ H, and 0 otherwise.

t_*ip* A continuous variable representing the deep body temperature of a pedestrian on path p after being affected by the state of node i ∈ p.

zp A binary variable that is 1 if the deep body temperature on path p reaches or exceeds t_k, and 0 otherwise.

si A binary variable that is 1 if node i ∈ N is ultimately shaded, and 0 if it is sunny.

Parameters

qp The pedestrian demand (number of people) for a path p ∈ P.

ci The cost to install a shade at a candidate node

i ∈ H.

b The total budget for facility installation.

t_0 The initial deep body temperature.

t̂ The critical deep body temperature threshold for heatstroke risk.

α A positive coefficient that accelerates the rise in body temperature in the sun.

β A positive constant representing the amount of temperature decrease in the shade.

M A sufficiently large constant used to deactivate constraints.

Formulation

Min. $\Sigma_{(p\in P)} q_p \cdot z_p$ (1)

Subject to.

$s_i = 1 \quad \forall i \in S_0$ (2)

$s_i = y_i \quad \forall i \in H$ (3)

$t_{jp} \geq t_{ip} + \alpha \cdot (t_{ip} - t_0) - M \cdot s_j$ (4)

$t_{jp} \geq t_{ip} - \beta - M \cdot (1 - s_j) \quad \forall p \in P, \forall (i,j) \in N_p$ (5)

$\Sigma_{(i\in H)} c_i \cdot y_i \leq b$ (6)

$M \cdot z_p \geq t_{ip} - \hat{t} \quad \forall p \in P, \forall i \in N_p$ (7)

$y_i \in \{0,1\}$ (8)

$t_{ip} \in \{0,1\}$ (9)

$z_p \in \{0,1\}$ (10)

$s_i \in \{0,1\}$ (11)

Objective Function (1) minimizes the total number of pedestrians who are at risk of heatstroke. Node State Determination Constraints (2) and (3) determine the final state (sunny or shaded) of each node. Deep Body Temperature Update Constraints (4) and (5) calculate the deep body temperature when moving from a node i to the next node j. Equation (4) is activated if the next node j is sunny (s_j=0), increasing the temperature proportionally to its current elevation above the initial temperature. Equation (5) is activated if the next node j is shaded (s_j=1), decreasing the temperature by a constant amount β. Budget Constraint (6) ensures that the total cost of installing shades at the selected candidate nodes does not exceed the total budget b. Heatstroke Risk Determination Constraint (7) forces the risk variable z_p for path p to become 1 if the deep body temperature t_ip at any node i along that path exceeds the threshold t̂.

3. RESULTS

We calculated the optimal placement for 20 shade spots. In the map shown in Figure 2, the intensity of the color on each link indicates its Betweenness Centrality (a value representing how frequently that link is included in the shortest paths). The resulting optimal shade placement was not necessarily selected from areas with high Betweenness Centrality but rather was found to be distributed continuously along two main path segments. Figure 3 shows a comparison of how body

temperature changes on a specific route, with versus without added shades.

Figure 2. optimal placement of 20 shade points

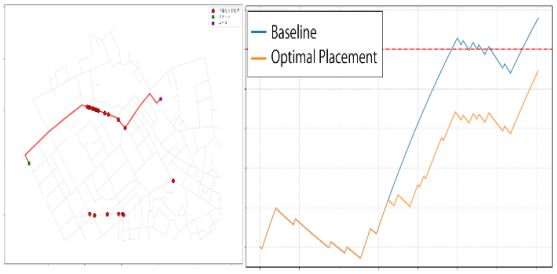

Figure 3. comparison of body temperature transition along a route

3. CONCLUTION

Contrary to the expectation that shade placements would cluster around sun-exposed nodes with high Betweenness Centrality, the results showed the placements were distributed along two distinct linear segments. While placing shade at high-centrality nodes (which often correspond to intersections or key edge junctions) would maximize the number of people who pass through a shaded area, it prevents pedestrians from passing through shade continuously. We hypothesize that although this approach might lower the overall average maximum core body temperature, it would not significantly increase the proportion of pedestrians whose maximum temperature remains below a safe threshold. Instead, the observed configuration—which favors placing continuous shade along relatively long and major path segments—is thought to have emerged because, although it benefits a smaller proportion of all pedestrians, it reliably and substantially reduces the heatstroke risk for those individuals who do use that specific path.

REFERENCES

[1] LI, Xiaojiang, et al. A pedestrian level strategy to minimize outdoor sunlight exposure in hot summer. arXiv preprint arXiv:1910.04312, 2019.

[2] HONMA, Yudai, et al. Locational analysis of In-motion wireless power transfer system for long-distance trips by electric vehicles: Optimal locations and economic rationality in Japanese expressway network. Networks and spatial economics, 2024, 24.1: 261-290.

4th International Symposium on One Health, One World
November 20 – 22, 2025

ABS ID: 84
Code No: IMSBE-OP-31

Numerical Investigation of Interlayer Characteristics on the Mechanical Properties of 3d Printed Concrete

B. Pal[1], A. Chourasia[2]
[1] Scientist, CSIR-Central Building Research Institute, Roorkee 247 667, India,
[2] Chief Scientist, CSIR-Central Building Research Institute, Roorkee 247 667, India,
Correspond To Dr. B. PAL (Biswajitjgec.1992@Gmail.Com)

Keywords: *Numerical Modelling, Mechanical Properties, Finite Element Model, Loading Direction.*

1. INTRODUCTIONS

Modern techniques such as additive manufacturing have created new opportunities in the construction sector, offering significant advantages over conventional concrete practices [1]. However, its widespread adoption still faces several challenges and limitations. One of the major barriers is the lack of comprehensive research that connects printing parameters with the resulting mechanical performance, which hinders the broader application of additive manufacturing in construction [2].

In recent years, a substantial number of research articles have been published in the field of 3D concrete printing, with most adopting experimental approaches to investigate early-stage printing properties such as extrudability and buildability [3]. In addition to these printing characteristics, considerable attention has also been directed toward mechanical properties [4], including compressive and flexural strength, as well as long-term deformations such as shrinkage [5] While experimental studies are essential for understanding the underlying physics of the process and for evaluating the behavior of small-scale samples under mechanical loading, they are often insufficient for assessing the performance of large-scale specimens or exploring the broader applicability of 3D printing in construction. To address this, it is imperative to develop physics-based mathematical models capable of predicting the mechanical response of 3D-printed concrete under loading. The use of such numerical models can significantly reduce the time and cost associated with extensive experimental testing. However, to ensure reliability, these models must realistically represent the governing physics of the problem.

In extrusion-based layering techniques, concrete is deposited sequentially, and both the properties of individual layers and their interactions significantly influence the overall mechanical performance of the additively manufactured composite system. A key distinction between 3D-printed specimens and traditionally cast concrete lies in the weaker interfacial zones formed between successive layers. Consequently, the investigation of interfilament bond characteristics in 3D-printed concrete has become a subject of considerable research interest. However, to date, limited attention has been given in literature to systematically identifying these interfacial bond properties and evaluating their impact on the mechanical behaviour of 3D-printed concrete specimens. These interlayer bond properties are highly dependent on the time interval between successive filament depositions [6]. For example, the experimental results reported in [7] showed that bond strength decreases as the interlayer time gap increases, and for gaps longer than fifteen minutes, failure occurred at the interface region.

The study in [8] reported that, depending on interfacial characteristics, the compressive strength of additively manufactured concrete can decrease by up to 45% compared to conventionally mold-cast samples. Furthermore, experimental investigations have examined the influence of different loading directions on the mechanical behaviour of

printed elements, thereby revealing their inherent anisotropic nature [9].

In contrast to the extensive experimental investigations, only a limited number of studies have employed mathematical frameworks to analyze the mechanical behavior of 3D-printed concrete specimens. Feng et al. [10] utilized a finite element (FE)-based approach with orthotropic material assumptions to numerically examine the influence of printing and loading directions on the load-carrying capacity of 3D-printed arch structures. The orthotropic material properties implicitly account for interlayer bonding characteristics. Similarly, Shakor et al. [11] numerically investigated the mechanical response of printed concrete specimens by incorporating experimentally obtained material properties, with loading applied along different printing directions. However, a key limitation of such models lies in their limited generalizability, as they do not explicitly consider interfilament bond properties. Later, Bos et al. [12] explored the flexural performance of fiber-reinforced 3D-printed concrete using a damage-plasticity-based material model, commonly referred to as concrete damage plasticity (CDP).

However, the work does not account for different bond properties in the numerical model. Following this, a discrete-element method (DEM) was utilised in [13] to study the behaviour of printed concrete specimens subjected to different loading scenarios. However, in DEM, the primary challenge lies in accurately defining the contact properties and it entails significant computational costs. Further, in [14], classical laminate theory was employed to study the mechanical behaviour of printed concrete specimens subjected to tensile load. On the other hand, in [15], CDP model was utilized for the concrete layer and traction-separation type constitutive relation to define the interfilament bond to investigate the influence of interfacial bond on the variability of the mechanical properties of the concrete element in different directions of printing. However, the numerical works [15] lacks with

respect to considering a fix value of interfilament bond properties in the numerical model i.e., the influence of various bond parameters (presence in the constitutive relation of interfilament bond) on the mechanical behavior of the additively constructed concrete specimen have not been investigated. Further, the effect of interlayer pores/gaps (that could arise due to the use of circular nozzle or could be due to the variability in material type or printing process) on the mechanical behavior of concrete samples has not been studied. Very recently, the work of [15] has been extended in [16] and the influence of several printing parameters, that belongs to the interlayer bond, on the load capacity of 3D printed beam under four-point loading has been studied.

A critical review of the existing literature on 3D-printed concrete reveals a lack of mathematical models that account for the governing physical mechanisms of extruded layers and inter-filament bonding under mechanical loading. Moreover, limited efforts have been made to examine how various printing parameters, ranging from bond characteristics to inter-filament pores, influence the directional dependency of compressive strength in printed concrete samples. To address this gap, a continuum-based mathematical modeling framework is required that incorporates the variable strength properties of concrete under compression and tension, along with the shear and tensile bond characteristics, to capture the behavior of printed concrete under compressive loading.

In this study, a finite-element (FE) framework is employed to numerically simulate the compressive behavior of 3D-printed concrete. The developed model represents each extruded filament using a constitutive relation that accounts for both damage and plasticity in concrete, while the inter-filament bond is modeled through a cohesive zone-type constitutive law replicating the zero-thickness interactive zone between adjacent filaments. The required material input properties, such as tensile and compressive strength, are obtained from specific experimental tests [16]. A

comprehensive sensitivity analysis is then performed to evaluate the influence of key printing-related parameters, including bond strength, inter-filament porosity, and the number of extruded layers, on the uniaxial compressive response of 3D-printed specimens tested in different loading directions. Such an extensive parametric investigation provides valuable insights for predicting the compressive strength of 3D-printed concrete under diverse printing conditions and loading orientations, ultimately aiding in the structural design of 3D-printed concrete components.

2. MATERIALS AND METHODS

2.1 Constitutive behaviour of materials

Objects produced using 3D printing typically exhibit highly anisotropic mechanical performance, arising from the adhesive bonding between printed layers. Despite extensive research, a well-established material model for printed concrete has yet to be developed [15]. In this study, the mechanical behavior of the extruded concrete filament is represented using the plasticity and damage-based Concrete Damage Plasticity (CDP) model available in Abaqus® [15,17]. The CDP model accounts for concrete failure under two primary mechanisms: crushing under compression and cracking under tension. Each failure mode incorporates distinct criteria for the initiation and propagation of damage or cracks, which are discussed in detail later in this section. Several studies (e.g.,[17] of concrete under a variety of loading conditions. By employing stress–strain responses from uniaxial compression and tension, the model computes the necessary inelastic or plastic deformations and cracking strains required for numerical analysis. Consequently, the CDP model inherently captures the rapid stress drop observed after peak stress in uniaxial stress–strain curves, a characteristic feature of brittle materials like concrete. For this reason, the CDP model has been extensively used in literature [18] to describe the mechanical behaviour of plain concrete as well as steel-reinforced concrete, and it is adopted in the present work as well.
In the CDP model, a scalar damage variable is employed to represent continuum-based damage in concrete, while a non-associated Drucker–Prager type yield function with predefined cutoffs under tensile loading is used to characterize the plastic behaviour. The Mohr–Coulomb model further defines the flow behaviour in the plastic regime. In addition, the cohesive zone technique is adopted to model the adhesive interaction between successive extruded concrete layers. The response of the system under quasi-static mechanical loading is then governed by the linear momentum balance, expressed [19]:

$$div\,(\boldsymbol{\sigma}) + \rho\bar{b} = 0 \qquad \textbf{(1)}$$

Where, $\boldsymbol{\sigma}$ *is* the stress tensor**, '**div' represents the operator "divergence" that acts on $\boldsymbol{\sigma}$, ρ stands for density and $\underline{b}$ represents the body force. Appropriate boundary conditions must be given in order to solve the governing equation mentioned above. In the CDP model, the description of plasticity and damage through the constitutive relation is represented as

$$\boldsymbol{\sigma} = (1-d)\boldsymbol{D}_0^{el}:\left(\boldsymbol{\varepsilon} - \boldsymbol{\varepsilon}^{\boldsymbol{pl}}\right) = (1-d)\overline{\boldsymbol{\sigma}} \qquad \textbf{(2)}$$

Here, $\boldsymbol{\sigma}$ and $\overline{\boldsymbol{\sigma}}$ present the Cauchy stress and effective stress tensors, d is the scalar damage component, which is isotropic and depends on the $\boldsymbol{\sigma}$, ϵ_{pl}, where ϵ_{pl} represents plastic strain tensor.

2.3 Defining interactions between layers and Building Geometry

The 3D-printed concrete sample is modeled in Abaqus®, using the specified geometry of a cube with sides of 150 mm, constructed from printed layers of 30 mm width and 15 mm thickness extruded through a circular nozzle (see Fig. 1). The 'Solid Extrusion' geometry feature in Abaqus® is employed to develop the detailed structure of the printed cube. During the geometry creation, the curvature across each layer's cross-section is accounted for by defining an average interlayer pore radius. In our previous study [16], using a similar specimen height and layer cross-section, the interlayer pore radius ranged from 0.3 mm at the bottom to 3 mm at the top. Accordingly, this study considers three average interlayer pore radii of 1 mm, 2 mm, and 3 mm. The geometric coordinates of the modeled layers are adjusted to represent these variations. Python scripting is used to define interactions between layers, which can occur horizontally or vertically through one or more faces (see Fig. 3). The constitutive behavior of these

interacting surfaces is defined using Abaqus®'s cohesive zone-based interaction feature. The experimentally measured tensile and compressive strengths of the concrete are 1.78 MPa and 32 MPa, respectively. For simulating compressive behavior, the bottom face of the cube is restrained in all three translational directions, while displacement-controlled loading is applied incrementally in the vertical direction (refer Fig. 1).

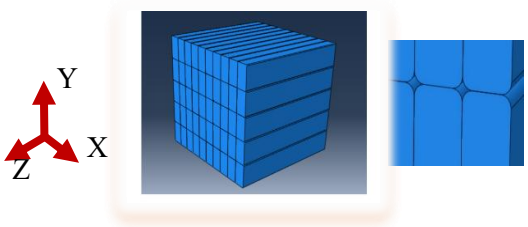

(a) (b)

Fig. 1 (a) Printed cube specimen of side 150 mm with extruded layer of size 30 mm x 15 mm, **(b)** consideration of interlayer pore of radius 'r' in the numerical model

3. RESULTS AND DISCUSSION

3.1 Effect of tensile bond strength and interlayer pore

In this section, influence of tensile bond strength and interlayer pore on the compressive strength of printed specimen is investigated when the load is applied from three different directions with respect to the printed layer orientation. The ratio of shear to tensile bond strength is maintained at 2 throughout. In the present analysis, the bond stiffness is assumed to be 1000 N/mm²/mm, and the failure displacement is set to five times the peak bond displacement.

Figure 2(a–c) illustrates the variation in compressive strength for different tensile bond strengths and interlayer pore sizes under loading from three distinct directions. In all three cases, an increase in interlayer pore size led to a reduction in the compressive strength of the printed specimens. This decreasing trend aligns with physical expectations, as introducing more weak zones reduces the effective load-bearing area. A comparative analysis shows that the Y-direction of loading exhibits the greatest strength reduction, with decreases of 30%, 65%, and 75% corresponding to 1 mm, 2 mm, and 3 mm pores, respectively, compared to mold-cast samples. In contrast, the Z-direction, which is parallel to the printed layers, shows the least sensitivity to interlayer pores, with reductions of 8%, 13%, and 18% for the same pore sizes relative to the mold-cast specimens. Consequently, the relative difference in compressive strength between the Y and Z directions is 12% and 70% for 1 mm and 3 mm pore sizes, respectively. Similar observations of the highest compressive strength—indicating minimal influence of printing parameters—along or parallel to the layer direction (Z direction) have been reported in [16,20], despite variations in material type and printing techniques. Conversely, the lowest compressive strength, reflecting the maximum effect of printing parameters under Y-direction loading, has been documented in [15,16]. These consistent trends in 3D printed concrete specimens underscore the significant influence of printing direction on strength and the resulting anisotropy. Such comparative findings suggest that, regardless of material type or printing method, selecting an optimal printing path can maximize compressive strength.

The higher strength observed in the direction perpendicular to printing may result from the significant compaction caused by the extrusion pressure [20]. A similar explanation for the maximum strength along the perpendicular direction, compared to the other two directions, has also been reported in [20]. The directional dependency of strength in printed specimens is influenced by multiple factors, including printing process parameters, material type, and layer compaction. Therefore, the results reported in the present work may be problem-specific, highlighting the need for further investigation.

Additionally, analysing compressive strength in relation to interfilament pores shows that 3D-printed concrete is significantly affected when loaded transverse to the printing layers (X or Y direction). In contrast, interlayer pores have a relatively minor effect on strength when loaded along the printing direction (Z direction). Such analyses can assist material designers in determining optimal printing paths and orientations to minimize strength reductions for different interlayer pore sizes.

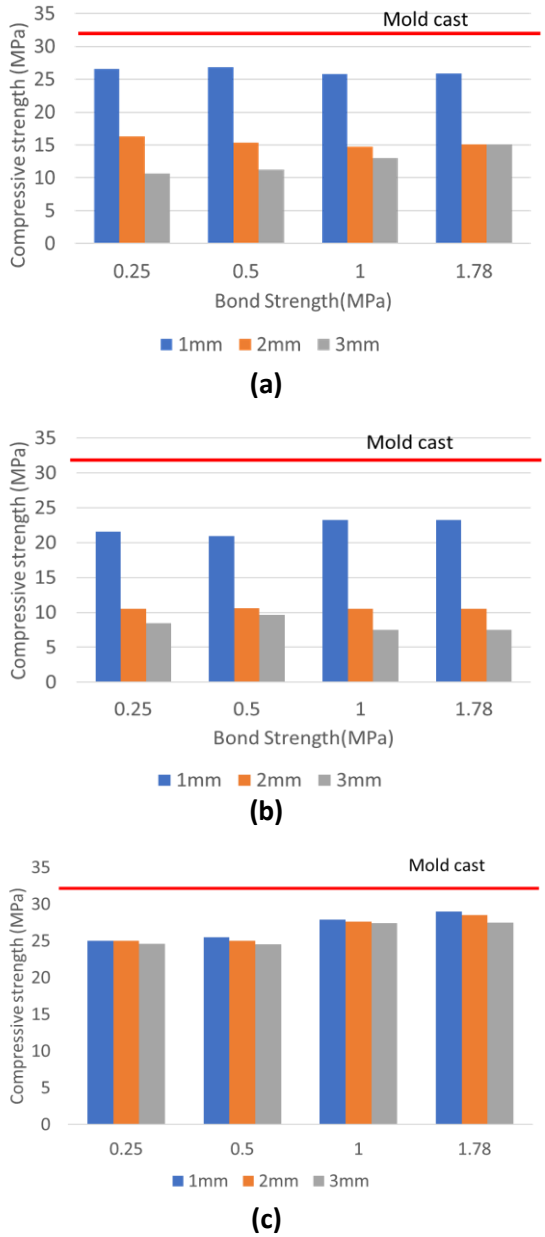

Fig.2 Compressive strength of printed specimen for different bond strength and interlayer pore for load applied in (a) X, (b) Y and (c) Z- direction (refer Fig. 1 for details of direction) along with mold cast specimen (red line)

4. CONCLUSIONS

This study simulates the compressive strength of an additively manufactured concrete cube using a finite element (FE) framework. In the model, each extruded concrete filament is represented by a constitutive relation incorporating both damage and plasticity behaviors. The interfilament bond is modeled using a cohesive zone-type constitutive relation. Comprehensive sensitivity analyses are then conducted to examine the effects of various printing-related parameters on the compressive strength of printed specimen. Based on this study, the following conclusions are drawn**.**

i. Compressive strength of printed specimen i s found to be lower than mold cast sample i rrespective of the loading directions.
ii. The orientation of loading relative to the printed layers (printing direction) significantly influences the compressive strength of 3D-printed concrete. Specimens loaded in the longitudinal direction (Z direction), parallel to the printing direction, exhibit higher strength compared to the other loading directions.
iii. The presence of interfilament pores has a significant impact on the compressive strength of 3D-printed concrete when loaded transverse to the printing layers (X or Y direction). In contrast, interlayer pores have a relatively minor effect on strength when loaded along the printing direction (Z direction).

In future studies, the present work can be extended to investigate the influence of dynamic and cyclic loading on the mechanical behavior of 3D-printed structural members. Such investigations would help identify optimal combinations of printing parameters to enhance both material efficiency and mechanical performance under varied loading conditions.

REFERENCES:

[1] X. Kaikai, G. Yadong, Z. Qiang, Comparison of traditional processing and additive manufacturing technologies in various performance aspects: a review, Archives of Civil and Mechanical Engineering 23 (2023) 1–28.

[2] S. El-Sayegh, L. Romdhane, S. Manjikian, A critical review of 3D printing in construction: Benefits, challenges, and risks, Archives of Civil and Mechanical Engineering 20 (2020) 1–25.

[3] Z. Xu, D. Zhang, H. Li, X. Sun, Effects of the distribution of solid particles on the rheological properties and buildability of 3DPM fresh pastes with different FA/GGBFS content, Archives of Civil and Mechanical Engineering 23 (2023) 82.

[4] B. Sun, P. Li, D. Wang, J. Ye, G. Liu, W. Zhao, Evaluation of mechanical properties and anisotropy of 3D printed concrete at different temperatures, Structures 51 (2023) 391–401. https://doi.org/10.1016/j.istruc.2023.03.045.

[5] L. Zhu, M. Zhang, Y. Zhang, J. Yao, G. Yang, X. Guan, Y. Zhao, Research progress on shrinkage properties of extruded 3D printed cement-based materials, Journal of Building Engineering (2023) 107394.

[6] N. Roussel, F. Cussigh, Distinct-layer casting of SCC: The mechanical consequences of thixotropy, Cem Concr Res 38 (2008) 624–632.

[7] T.T. Le, S.A. Austin, S. Lim, R.A. Buswell, R. Law, A.G.F. Gibb, T. Thorpe, Hardened properties of high-performance printing concrete, Cem Concr Res 42 (2012) 558–566.

[8] J. Kruger, G. van Zijl, A compendious review on lack-of-fusion in digital concrete fabrication, Addit Manuf 37 (2021) 101654.

[9] M. van den Heever, A. du Plessis, J. Kruger, G. van Zijl, Evaluating the effects of porosity on the mechanical properties of extrusion-based 3D printed concrete, Cem Concr Res 153 (2022). https://doi.org/10.1016/j.cemconres.2021.106695.

[10] P. Feng, X. Meng, J.-F. Chen, L. Ye, Mechanical properties of structures 3D printed with cementitious powders, Constr Build Mater 93 (2015) 486–497.

[11] P. Shakor, N. Gowripalan, H. Rasouli, Experimental and numerical analysis of 3D printed cement mortar specimens using inkjet 3DP, Archives of Civil and Mechanical Engineering 21 (2021) 1–16.

[12] F.P. Bos, E. Bosco, T.A.M. Salet, Ductility of 3D printed concrete reinforced with short straight steel fibers, Virtual Phys Prototyp 14 (2019) 160–174.

[13] M. van den Heever, F. Bester, M. Pourbehi, J. Kruger, S. Cho, G. van Zijl, Characterizing the fissility of 3D concrete printed elements via the cohesive zone method, in: Second RILEM International Conference on Concrete and Digital Fabrication: Digital Concrete 2020 2, Springer, 2020: pp. 489–499.

[14] J. Xiao, H. Liu, T. Ding, Finite element analysis on the anisotropic behavior of 3D printed concrete under compression and flexure, Addit Manuf 39 (2021) 101712.

[15] B. Pal, A. Chourasia, A. Kapoor, Intricacies of various printing parameters on mechanical behaviour of additively constructed concrete, Archives of Civil and Mechanical Engineering 24 (2024) 41.

[16] J. Xiao, W. Li, D.J. Corr, S.P. Shah, Effects of interfacial transition zones on the stress-strain behavior of modeled recycled aggregate concrete, Cem Concr Res 52 (2013) 82–99. https://doi.org/10.1016/j.cemconres.2013.05.004.

[17] B. Pal, A. Ramaswamy, Meso-scale study of notched and un-notched plain concrete beam under three-point bending, in: IABSE Congress, Christchurch 2020: Resilient Technologies for Sustainable Infrastructure-Proceedings, International Association for Bridge and Structural Engineering (IABSE), 2020: pp. 890–897.

[18] C.S. Jog, Continuum Mechanics: Volume 1: Foundations and Applications of Mechanics, Cambridge University Press, 2015.

[19] S. Luo, Q. Lin, W. Xu, D. Wang, Effects of interval time and interfacial agents on the mechanical characteristics of ultra-high toughnessnn cementitious composites under 3D-printed technology, Constr Build Mater 374 (2023) 130936.

4th International Symposium on One Health, One World
November 20 – 22, 2025

ABS ID: 73
Code No: IMSBE-OP-32

Numerical Study on Seismic Performance Evaluation of 3d Printed Concrete Buildings

Shubham Singhal[1], Phani Chandra Veligatla, And Dhananjay Tiwari[3]
[1]*Assistant Professor, Earthquake Engineering Research Centre, International Institute Of Information Technology, Hyderabad, India.*
[2]*mtech Student, Earthquake Engineering Research Centre, International Institute Of Information Technology, Hyderabad, India,*
[3]*phd Scholar, Department Of Civil Engineering, Netaji Subhas University Of Technology, New Delhi, India,*
Correspond To Shubham Singhal (Shubham.Singhal@Iiit.Ac.In)

***Keywords**: 3D Printing, Non-linear Analysis, Finite Element Analysis, Seismic Parameters.*

1. INTRODUCTION

3D printed concrete is revolutionizing the construction industry by providing a faster, more sustainable and a very high adaptable alternative to traditional construction methods. One of its main uses is the development of residential buildings, especially for affordable apartments where speed and cost efficiency are very important. This allows for creation of much more complex, curved architectural designs that are difficult and quite expensive with traditional techniques. It is used in commercial and public infrastructures to build office spaces, schools, pavilions, and even pedestrian bridges. 3D printed concrete has been proved valuable for disaster relief measures, allowing emergency shelters to be constructed quickly in areas affected by natural disasters. Urban applications include the production of benches, planters and other street furniture tailored to specific design requirements. The technology also acquires military and remote operations against prosecution, allowing for structure construction in a challenging environment with minimal workers. Additionally, it has shown sustainability through reduced construction waste and the possibility of absorbing recycled materials in concrete mixtures. Despite challenges such as device size limitations, the need for special concrete formulations, and even developed regulations, 3D printed concrete is very promising for future designs of construction.

2. OBJECTIVE

The primary objective of this study is to develop and analyze numerical models of low-rise 3D-printed concrete buildings, including single-storey to represent realistic structural systems. Nonlinear pushover analyses are performed on the model using advanced finite element techniques to evaluate their lateral load–displacement behavior under seismic loading. The obtained pushover curves are compared to assess the relative performance and deformation characteristics of the different structural configurations. Furthermore, the base shear capacities are calculated in accordance with IS 1893 (Part 1): 2016 guidelines to ensure compliance with Indian seismic design provisions. Based on the evaluated lateral load-carrying capacities and overall response, the study identifies the most suitable seismic zones for the safe construction of 3D-printed buildings.,

3. METHODOLOGY

3D finite element models of 3D-printed concrete buildings were developed in ABAQUS using M30 concrete and realistic layer-based geometry. Th model dimensions were 3 mx 3m inline and 3 m storey height. The wall was designed in Zigzag infill pattern to improve lateral resistance, and a 150 mm nozzle size was assumed, producing 50 mm thick layer to simulate the layer-by-layer printing process. As no conventional reinforcement was included, interlayer bonding was represented via tie constraints and surface interactions.

Fixed boundary conditions were assigned at the base, and incremental lateral loads were applied at the top to replicate seismic effects. A nonlinear static pushover analysis was performed using the ABAQUS Explicit solver, which employs a central difference time integration scheme to efficiently handle contact nonlinearities and transient dynamic effects. The solver directly computes

acceleration from equation, ensuring numerical stability and accuracy for high-speed loading scenarios.
Loading-displacement curves were generated for the model for determination of ultimate load capacity, ductility, drift ratio, stiffness, response reduction factor and damage index. The base shear capacity of each structure was further calculated conforming to IS 1893 (Part 1):2016. The results were then compared with codal seismic demand to evaluate structural adequacy

4. MODELLING

The Numerical models of low-rise 3D-printed concrete buildings with single storey configurations was developed in ABAQUS/Explicit to simulate their nonlinear seismic behavior. The structure had a 3 m × 3 m plan with 3 m storey height. The wall system was 150 mm thick, consisting of two 50 mm outer layers and a 50 mm hollow infill with a zigzag grout pattern, replicating the layer geometry of 3D printing as shown in Fig 4.1

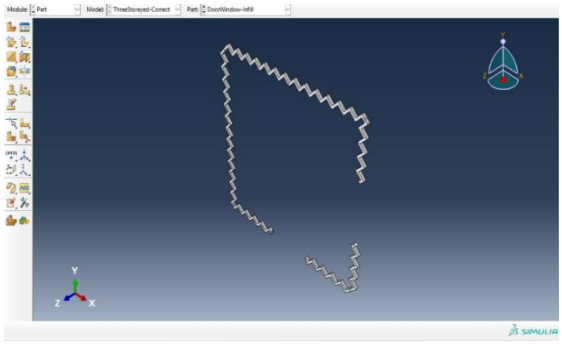

Fig 4.1: ZigZag infill model in part module

The model was meshed with hexahedral elements (150 mm size), with NLGEOM enabled to account for large deformations. Fixed supports were applied at the base to represent a rigid foundation, and a 50 mm roof displacement was imposed to generate pushover curves. Tie constraints ensured perfect bonding between printed layers. The zigzag infill enhanced energy dissipation and lateral stiffness, providing ductile performance without reinforcement. The validated mesh and interaction definitions ensured numerical stability, accurately representing the seismic response of 3D-printed concrete buildings across all configurations.

Tie interactions were assigned between all 3D-printed concrete layers to simulate the strong interlayer bonding observed in experiments. These constraints ensured that adjoining layers moved together without separation, accurately replicating their monolithic behavior under lateral and vertical loads. The infill region was modelled using embedded constraints, assuming full enclosure within the surrounding grout for effective load transfer. Additional ties connected the grout, wall layers, slab, and plinth beam, ensuring unified deformation of the structural system. In all cases, master surfaces were assigned to stiffer parts and slave surfaces to relatively flexible ones for realistic load distribution during seismic analysis.

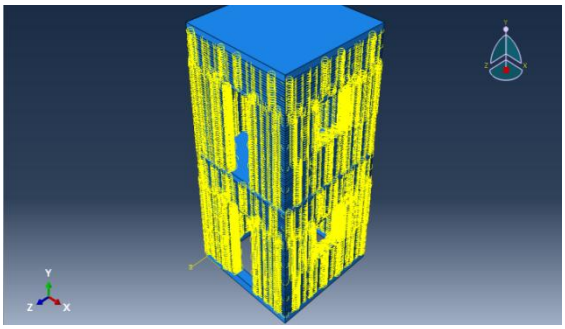

Fig 4.2: Visual of interaction given in between the layers of concrete, embedded infill and grout infill in the model

5. MATERIAL

Material and plasticity properties used in ABAQUS modelling is shown in Table 2.1 and Table 2.2 whereas Table 2.3 and 2.4 shows compressive and tensile behaviour of M30 concrete.

Table 5.1 Properties of considered material

	Grade	Young's modulus	Poisson's ratio
Concrete	30MPa	27386	0.24
Grout	5MPa	11180	0.24

Table 5 2.Plasticity properties considered for non-linearity.

dilation angle (ψ°)	0.30
Eccentricity	0.1
fb_0/fc_0	1.16
K	0.67
Viscosity parameter	0.0003

Table 5.3 Compressive behavior values for concrete grade M30

Yield Stress	Inelastic Strain
2	0
2.711584	0.0001
15.06893	0.0006
25.47806	0.0012
29.76043	0.0019
30	0.002
29.23653	0.0024
26.30684	0.003
20.4045	0.004

Table 5.4 Tensile behaviour values for concrete grade 30

Yield Stress	Inelastic Strain
2	0
2.1	0.00007
3.83406	0.000128
3.03189	0.00035
2.87268	0.25074776
2.7901	0.0007
2.71943	0.00084
2.68752	0.00091
2.64927	0.001
2	0

6. ANALYSIS

In the simulation, a lateral displacement of 50 mm was applied at the top of the building model to examine its resistance to lateral seismic forces as shown in Fig 4.1. The base of the structure was fully fixed, preventing translation or rotation, thereby replicating the real-life condition of a foundation anchored to the ground during an earthquake.

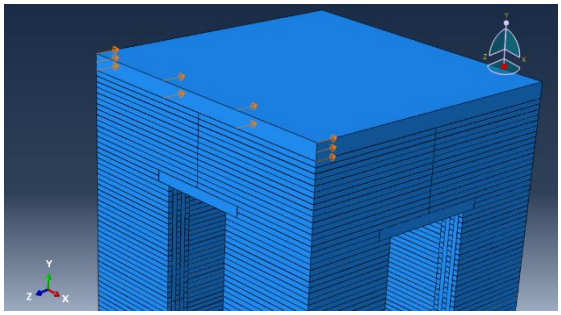

Fig 6.1: Displacement applied at the top of the structure.

This loading configuration enabled the clculation of the lateral stiffness, base shear, and overall deformation response for the structure. The analysis was carried out in the Step module of Abaqus via Dynamic Explicit method instead of a quasi-static approach. This method was chosen due to the complex geometry and numerous contact surfaces in the 3D-printed model, which caused convergence difficulties in quasi-static simulations. The explicit solver allowed for efficient handling of large deformations, contact interactions, and nonlinear material behavior, significantly reducing the overall analysis time. Typically, the number of increment steps ranged from 2000 to 5000, depending on model complexity, with some runs extending up to 10,000 steps to achieve accurate convergence. The NLGEOM (nonlinear geometry) option was enabled to account for geometric nonlinearity during large displacements and rotations. Output data were noted at a single node located at the top, where displacement was applied. Using the History Output Request Manager, displacement and reaction force data were extracted at each time increment to generate load–displacement curves, which form the basis for calculting lateral load-carrying capacity, stiffness, ductility, and overall seismic performance of the 3D-printed concrete structures.

7. RESULT AND DISCUSSION

7.1 Load displacement curves.

From analysis Load versus displacement graph was obtained for the analyzed building as shown below:

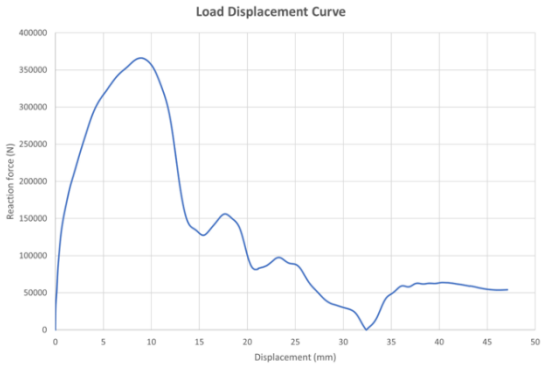

Fig 7.1: Load Displacement curve of Single storey

Structure

From the results obtained Ultimate load carrying capacity, Ductility, Drift capacity, Stiffness and Response reduction factor,overstregth factor and Damage index of the structures can be determined

Δu/ Δy=μ

Where Δu= Ultimate displacement

Δy= Yield displacement

μ = Ductility

Response reduction factor R=(2μ-1)1/2

Drift capacity = Δmax*100/H

Damage Index=1-K/(2K at yeild)

Damage index is calculated at yield point, max point and ultimate

Where H= height of structure

Table 7.1 Parameters obtained from the graphs

Parameter		Value
Load Carrying Capacity (kN)		311.17
Stiffness (kN/mm)	At maximum	32.5
	At ultimate	3.43
Ductility		5.83
Damage index (%)	At yield	0
	At maximum	0.71
	At ultimate	0.82
Response Reduction Factor		3.3
Drift (%)		1.08

From Ultimate Load Carrying capacity and Weight of structure, Seismic coefficient (Ah) can be calculated

Ah= Vb/W

Where Vb= Base shear

W= Weight of structure

From values of Ah zone factor of the structure can be calculated

Ah= (Z/2) *(I/R) *(Sa/g)

Where Z= Zone factor

I = Importance factor =1.5 (assumed)

Sa/g=Design acceleration coefficient = 2.5 (assumed)

Table 7.2. Seismic coefficients and seismic zones determined from the data

A_h	Z
0.5736	1.009

Here we get higher zone factors which means modelis very good at resisting seismic forces,

2. CONCLUSION

The seismic performance evaluation of the single-storey (G) 3D-printed concrete building demonstrated that the structure possesses high initial stiffness and significant load-carrying capacity, making it suitable for resisting lateral forces in low-rise construction. The ultimate load capacity reached approximately 311.18 kN, with a ductility factor of 5.83 and a response reduction factor (R) of 3.3, indicating a moderately ductile behaviour. The structure showed limited lateral displacement, with a drift capacity of 1.08%, which lies well within the permissible limits specified in IS 1893 (Part 1): 2016.

The high stiffness value of 32.5 kN/mm suggests that the single-storey model behaves as a rigid unit under lateral loading, providing excellent resistance against ground-motion effects. However, the limited ductility highlights the need for controlled flexibility or energy-dissipating detailing to prevent brittle failure under severe seismic events.

Based on the evaluated seismic coefficient (Ah = 0.5736) and comparison with codal provisions, the single-storey 3D-printed structure can be categorized under Seismic Zone V, implying that it can perform safely in regions with very high seismic intensity when designed with proper base anchorage and material continuity.

The damage index obtained at Yield point , Maximum point and ultimate point is 0, 0.71 and 0.83 signifies that single storey 3D printed concrete structure shows good seismic resistance with progressive and controlled damage evolution.

REFERENCES:

[1] Narjabadifam, Peyman, Somayeh Mollaei, E. Farsangi, and S. Talebi. "Numerical analysis of seismic behavior of an arched-roof 3D-Printed building." Gradjevinski Mater. i Konstr 67, no. 1 (2024): 1-15.
[2] Liu, Hanqiu, King-James Idala Egbe, Haipeng Wang, Ali Matin Nazar, Pengcheng Jiao, and Ronghua Zhu. "A numerical study on 3D printed cementitious composites mixes subjected to axial compression." Materials 14, no. 22 (2021): 6882.
[3] Wolfs, R. J. M., Freek P. Bos, and T. A. M. Salet. "Early age mechanical behaviour of 3D printed concrete: Numerical modelling and experimental testing." Cement and Concrete Research 106 (2018): 103-116.
[4] Shubham Singhal ,Ajay Chourasia, Yogesh Kajale. “Cyclic behaviour of precast reinforced concrete beam-column connected with headed bars” Journal of Building Engineering 42(2021) 103078.
[5] Xilin Lu, Hao , Ying zhou “Seismic collapse assessment of self-centring hybrid precast walls and conventional reinforced concrete walls”. International Fedration for structural concrete 2017.
[6] Kyung-Ryul Cha,Jihye Seo, Seungjun kim,Young-Jong Kang. “Cyclic response of precast composite hollow reinforced concrete (RC) columns with longitudinal rebars and base-plate connections” International Federation for structural Concrete 2017.

4th International Symposium on One Health, One World
November 20 – 22, 2025

ABS ID: 45
Code No: IMSBE-OP-33

Comparison Of Response Of Single Cell And Double Cell Box Girder Decks

Arunprasath D[1]
Senior Lead Engineering Manager, EDRC, L&T Transportation Infrastructure IC, Chennai, India

Keywords: *Box girder, single-cell, two-cell, bridge analysis, bending moment, shear force, torsional stiffness.*

1.INTRODUCTION

A box girder is a hollow, box-shaped structural element widely used in bridge and building construction, typically made of steel, concrete, or a composite of both. First introduced in the 19th century, notably in the Britannia Bridge (UK, 1850) by Robert Stephenson using wrought iron, box girders gained popularity post-World War II, particularly in Europe and Japan, with the rise of prestressed concrete applications. Modern advancements in construction techniques, computer-aided design, and high-strength materials have further cemented their role in contemporary infrastructure. Structurally, box girders feature a closed rectangular or trapezoidal cross-section that offers high torsional stiffness, making them ideal for curved or asymmetrically loaded bridges. Steel box girders are preferred for long-span and heavily loaded structures, concrete box girders suit short to medium spans such as highway flyovers, and composite versions combine the advantages of both materials to enhance strength and cost-efficiency. Due to their enclosed shape, box girders also provide better resistance to buckling and corrosion in certain environments. Their hollow section allows for easier maintenance access and can house utility lines or cables in bridge applications. Additionally, box girders can be precast or constructed in segments, allowing for faster and more flexible construction, especially in challenging site conditions.

2.OBJECTIVE OF THE STUDY

The primary objective of this study is to investigate the structural behavior and performance of single-cell and two-cell box girders under Indian Standard load conditions, assessing their comparative responses in terms of strength, stability, and efficiency. By analyzing both configurations, the study aims to identify the most suitable cross-sectional design that offers maximum structural capacity while optimizing material usage. Special focus is placed on evaluating how each design performs under ultimate and serviceability limit states, ensuring compliance with national standards. An essential part of the research is to develop a cost-effective solution for box girder bridges that balances structural integrity with economic feasibility. Through this, the study seeks to minimize unnecessary material use, thereby promoting sustainable construction practices. Additionally, the research aims to determine which configuration reduces long-term maintenance needs and enhances durability. Understanding the load distribution and stress patterns in different girder types is crucial to recommending optimal design strategies. The goal is not only to improve performance but also to extend the operational lifespan of bridges. Ultimately, the study will contribute to safer, more economical, and durable infrastructure solutions.

3. ADVANTAGES

Box girders offer several structural and functional advantages that make them a preferred choice in modern construction. One of their key benefits is torsional rigidity, providing excellent resistance to twisting forces, which is especially important for curved bridges or structures exposed to high wind loads. Their clean and simple lines contribute to a sleek, aesthetic appeal, making them suitable for integration into both urban and scenic

environments. The hollow cross-section ensures efficient use of materials, offering a high strength-to-weight ratio that enhances structural performance while minimizing material consumption. Additionally, the interior space of the box girder can be utilized for housing utilities, cables, or providing maintenance access, adding functional value to the structure. These advantages, combined with advancements in design and construction methods, have solidified the box girder's place in contemporary bridge and infrastructure projects around the world.

4.APPLICATIONS

Box girders are widely used across various types of infrastructure due to their structural efficiency and versatility. In bridge construction, they are commonly employed in highway overpasses, railway bridges, viaducts, and even cable-stayed bridges, where their high torsional rigidity and strength-to-weight ratio are critical. In building structures, box girders are occasionally used in high-rise buildings, particularly as transfer girders to support large loads over wide spans without intermediate columns. Additionally, they are found in marine structures such as docks, piers, and offshore platforms, where resistance to torsion and bending is essential due to dynamic loading from waves and wind. Their adaptability to different materials and construction methods makes box girders a reliable choice in both land and marine engineering applications. Furthermore, their enclosed shape helps protect internal components from environmental exposure, extending the lifespan of the structure. In bridge retrofitting or rehabilitation, box girders can also be used to strengthen or replace existing elements without significant structural alteration. The use of precast box girders accelerates construction timelines and minimizes on-site labor. In seismic zones, their stiffness and continuity provide added resistance to earthquake forces. Overall, box girders represent a blend of functionality, durability, and design flexibility across a wide range of engineering scenarios.

5.COMPUTATIONAL MODELLING

5.1 Design Parameters

Box girders are widely used in bridge construction due to their high torsional rigidity, aesthetic appearance, and ability to carry heavy loads over medium to long spans. The use of single-cell or multi-cell box sections depends on various design parameters, including span length, deck width, and the nature of loading.

This study focuses solely on the modeling and structural analysis of the superstructure, without extending into the detailed design or construction aspects. The analysis is carried out using MIDAS civil software, ensuring compliance with IRC standards. The main objective is to compare the structural performance of single-cell and two-cell box girder configurations in terms of key design parameters such as bending moments and shear forces. This comparison will help in understanding the efficiency and suitability of each configuration for the given span and deck width.

This study investigates the structural behavior of single-cell and double-cell box girder configurations for a bridge deck width of 16 meters, based on the provisions outlined in IRC:6- 2017. The focus is on analyzing how each configuration performs under similar loading and span conditions, specifically for a simply supported span of 40 meters. The analysis is conducted using M40 grade concrete, which offers adequate strength and durability for medium-span bridge superstructures. All material properties, load combinations, and structural requirements are considered in accordance with IRC:6-2017 to ensure realistic and code-compliant results.

Table 1. Superstructure Data

Attributes	Data
Span configurations	40m
Type of support	Simply supported
Alignment in plan	Straight
Deck widths	16m
No of cells	Single / Double

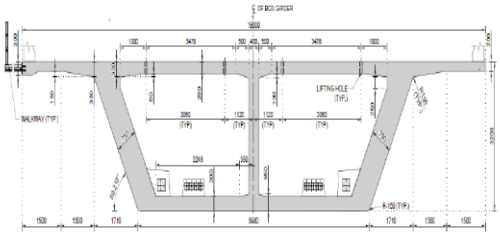

(c)

Figure 1. Typical Two Cell Box for Modelling

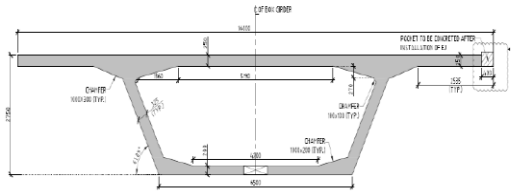

(d)

Figure 2. Typical Single cell Box for Modelling

5.2 Modelling

The modeling of the bridge superstructure was carried out for a simply supported span of 40 meters with a total deck width of 16 meters, considering two different box girder configurations: single-cell and double-cell. The objective was to assess the structural response under standard loading conditions as per IRC:6-2017. For structural analysis, two types of models were developed. Beam model for longitudinal analysis, capturing global behavior such as bending moments and shear forces along the length of the span. Plate model for transverse analysis, enabling a more detailed study of deck behavior, including load distribution and torsional effects.

The models were constructed in structural analysis software with all necessary boundary conditions applied to simulate simply supported behavior. The self-weight of the structure was automatically accounted for using the software's self-weight generation command. Other loads such as the crash barrier and parapet walls were applied as uniform line or surface loads, based on typical IRC-prescribed values. Uniformly Distributed Loads (UDL) and vehicular live loads were applied in accordance with IRC:6-2017, ensuring compliance with specified minimum lateral clearance and positioning of the load as per the standard's guidelines. Appropriate load combinations—including dead load, live load, and impact factors—were used as specified in the IRC code to simulate realistic conditions and evaluate structural responses accurately.

5.3 Loads & Load Combinations

The loads were calculated in accordance with the relevant IRC codes and applied to the model. Load combinations were considered as per Table B.2 of IRC:6-2017 for strength limit state design. Construction stage loads were not included in the analysis.

The following loads were considered:

- Self-weight of the Girders & slabs
- Superimposed dead load – Fixed (crash barrier)
- Superimposed dead load – Variable (wearing coat)
- Live loads

The self-weight of the girders is applied using the self-weight command in MIDAS Civil.

Superimposed dead loads (SIDL) are applied as follows:

- Fixed load: Crash barrier load is taken.
- Variable load: Wearing coat is modeled as a 100 mm thick overlay, applied as a UDL along the span. Live loads are applied as moving loads, considering Class A and Class 70R wheeled vehicles, along with their combinations, as specified in Table 2 of IRC:6-2017. The wearing coat load and the slab load are both applied on the girders as uniformly distributed loads along the span

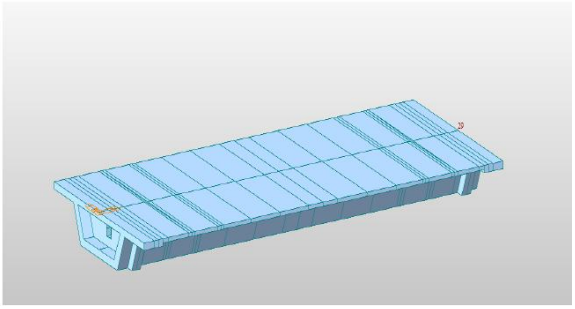

Figure 3. Single Cell Model in Midas Civil

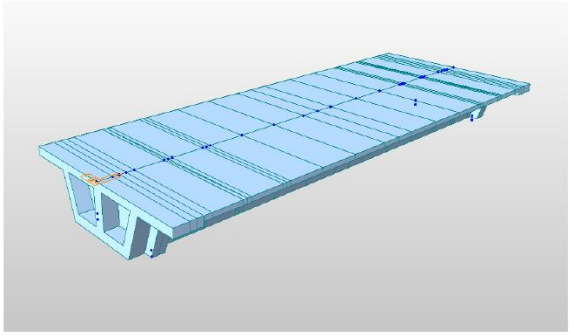

Figure 4. Two Cell Model in Midas Civil

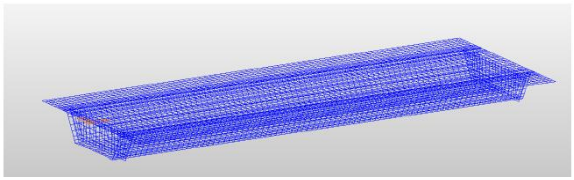

Figure 5. Single Cell Transverse Analysis in Midas Civil

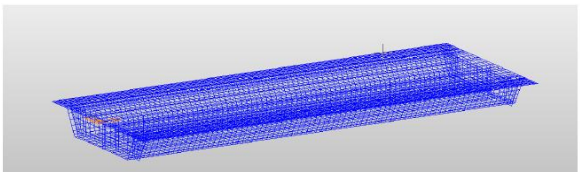

Figure 6. Two Cell Transverse Analysis in Midas Civil

Longitudinal and transverse analyses were carried out on both single-cell and two-cell box girders under ULS and SLS conditions. The structural behavior in terms of bending moment and shear force was compared, and the results are summarized and discussed.

The two-cell box girder demonstrates greater bending moment and shear force capacity under longitudinal loading compared to the single-cell girder. This suggests that two-cell configurations provide better load distribution and enhanced structural performance, especially for longer spans or heavier loads. The increased capacity indicates improved strength and stability, making two-cell girders more suitable for demanding applications. Overall, two-cell girders offer superior longitudinal performance, which can lead to more efficient and durable bridge designs.

In addition to improved strength, the two-cell configuration offers better resistance to deformation and minimizes deflection under service loads. Its symmetrical layout enhances structural redundancy, providing added safety in case of localized damage. The wider cross-section also helps in better distribution of stresses, reducing the concentration of forces at critical points. This results in longer service life and lower maintenance requirements over time. Furthermore, two-cell girders accommodate more efficient placement of tendons in prestressed designs, contributing to enhanced load-carrying behavior and overall performance.

The Results of the analysis are plotted below :

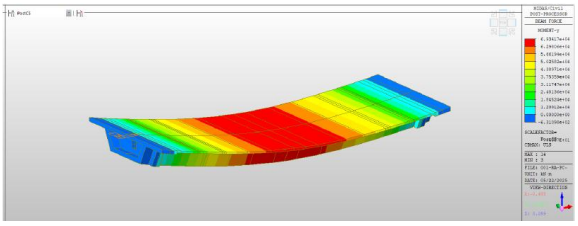

Figure 7. Bending Moment for Single cell

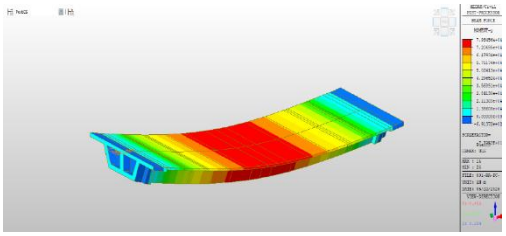

Figure 8. Bending Moment for Two cell

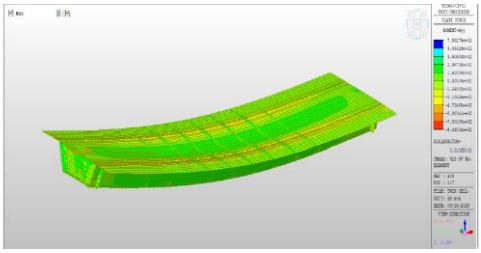

Figure 9. Transverse Analysis – Single Cell

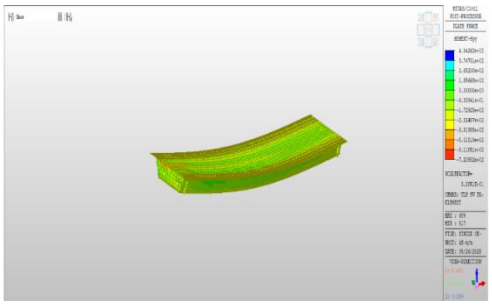

Figure 10. Transverse Analysis – Two Cell

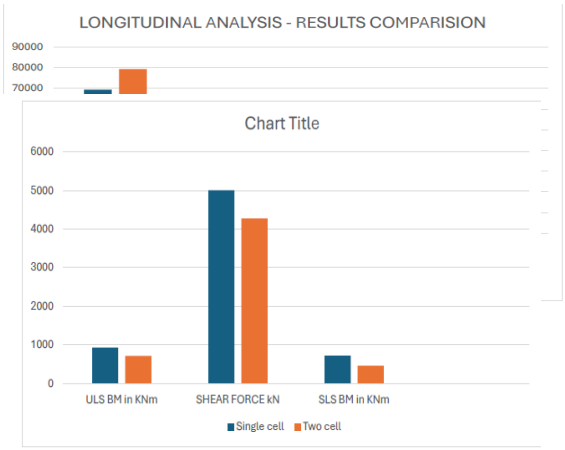

Figure 11. Longitudinal Analysis Results Comparison

Figure 12. Transverse Analysis Results Comparison

6.CONCLUSIONS

Single-cell and two-cell box girders each offer unique performance characteristics, particularly in terms of transverse and longitudinal behavior under load. Single-cell girders tend to exhibit higher transverse bending moments at mid-span under both Ultimate Limit State (ULS) and Serviceability Limit State (SLS) conditions. This makes them slightly more favorable in scenarios where localized transverse loads are dominant, as the increased transverse stiffness can better resist such forces. On the other hand, two-cell girders demonstrate improved longitudinal performance due to better distribution of loads across the cross-section. This makes them ideal for longer spans or structures subjected to higher overall loads, where longitudinal capacity is a primary concern. The presence of an additional cell enhances the girder's ability to handle axial and flexural stresses more efficiently. However, in situations where critical transverse loads or concentrated local forces are expected—such as wheel loads or point loads—single-cell girders might offer more effective resistance. The choice between the two configurations, therefore, depends on specific design requirements, load patterns, and span lengths.

7. REFERENCES:

[1] IRC:6-2017, "Standard Specification and code of practice for Road Bridges Section II: Loads and Load Combinations", Indian Road Congress.

[2] IRC:112-2020, "Code of practice for Concrete Road Bridges", Indian Road Congress.

[3] Analysis and Design of Box Girder and T-Beam BridgevSuperstructure - A Comparative Study - Rao Jang Sher, Muhammad Irfan-ul-Hassan, Muhammad Talha Ghafoor, Atif Qayyum, Vol 39.No.3, 453-465, Mehran University Research Journal of Engineering & technology , July 2020.

[4] Sennah K.M. and Kennedy J.B. "Literature review in analysis of box-girder bridges", Journal of Structural Engineering ASCE, No. 10, 1061(2002) pp.1084-702

[5] W. Y. Li ,L. G. Tham and Y. K. Cheung "Curved Box Girder Bridges" Journal of StructuralEngineering, ASCE, Vol. 114, No.6, June, 1988.

[6] Maisel,W.,& Roll,M.(1971).Methods of analysis and design of concrete box beams with side cantilevers. Cement and concrete Association , London.

[7] N Rajagopalan (2006),Bridge Superstructure, Alpha Science International Ltd., Oxford U

2025 HOW

4th International Symposium on One Health, One World
November 20 – 22, 2025

ABS ID: 174
Code No: IMSBE-OP-34

Non-Contact Bridge Dynamic Displcement Monitoring Using Mimo Radar

Y. Izumi[1], M. Komuro[1], And T. Kawarai[1]
[1] *Graduate School of Engineering, Muroran Institute of Technology, Muroran, Japan,*
Correspond to Y. Izumi (Yizumi@Muroran-It.Ac.Jp)

***Keywords**: MIMO radar, Radar interferometry, Bridge structural health monitoring*

1. Introduction

Multiple-input multiple-output (MIMO) radar interferometry is a powerful, non-contact sensing technique for dynamic displacement measurement of infrastructure, particularly in the field of bridge health monitoring [1]. Despite its advantages in rapid data acquisition and cost-effective operation, the use of MIMO radar in bridge monitoring has not yet been fully explored or widely adopted in practice. This study investigates the applicability of MIMO radar interferometry through operational modal analysis of a steel box girder bridge under normal traffic conditions and discusses its future potential.

2. Dynamic displacement monitoring

MIMO radar is an advanced radar technology that employs multiple transmit and receive antennas, enabling enhanced angular resolution and two-dimensional imaging of targets. In addition to imaging, MIMO radar can monitor displacement and vibration of multiple points within the observation scene by measuring phase changes in radar echoes over time. With rapid data acquisition (~1 millisecond per image), it allows real-time dynamic displacement measurement.

To evaluate the performance of MIMO radar for infrastructure monitoring, we conducted operational modal analysis on a steel box girder bridge located in Hokkaido, Japan, using two MIMO radar systems. Figure 1 shows one of the radars installed beneath the bridge deck. For comparison, a point-wise laser displacement meter was also deployed. Figure 2 presents the vertical displacement time-

Figure 1. Installed MIMO radar unit.

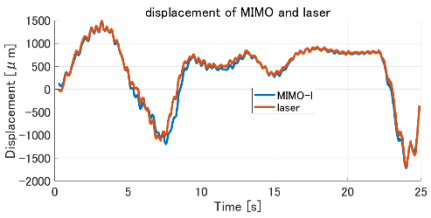

Figure 2. Measured vertical displacement time-series of the bridge.

Figure 3. Developed drone-borne MIMO radar.

hseries measured by both instruments, demonstrating strong agreement. This confirms that modal analysis can be conducted by analyzing the time-series data from multiple observation points.

The MIMO radar system is thus capable of extracting structural dynamic parameters—such as natural frequencies and mode shapes—that are essential for bridge health assessment. Furthermore, the simultaneous use of multiple MIMO radar units expands monitoring coverage and enables retrieval of displacement vectors.

Typically, MIMO radar systems are installed on fixed, stable ground, as shown in Figure 1. To further extend measurement coverage, our research group is currently developing a drone-borne MIMO radar system, illustrated in Figure 3.

3. CONCLUSIONS

MIMO radar has demonstrated high-precision capabilities for non-contact bridge displacement monitoring, achieving sub-millimeter accuracy. Although several successful case studies have been reported, technology still faces technical and practical challenges. Future progress will depend on expanding field applications and addressing existing limitations, paving the way for broader adoption in structural health monitoring.

REFERENCES:

[1] M. Pieraccini and L. Miccinesi, “An interferometric MIMO radar for bridge monitoring,” *IEEE Geoscience and Remote Sensing Letters*, vol. 16, no. 9, pp. 1383–1387, 2019, doi: 10.1109/LGRS.2019.2900405.

ABS ID: 85
Code No: IMSBE-OP-35

Mr. Anshul Agrawal

ABS ID: 153
Code No: IMSBE-OP-36

Dr. Debdutta Ghosh

4th International Symposium on One Health, One World
November 20 – 22, 2025

ABS ID: 56
Code No: IMSBE-OP-37

Brick Kiln Detection Using Geospatial Datasets: A Deep Learning Approach For Environmental Monitoring

A. Mehta[1], P. Chaurasia[2], W. Takeuchi[3], R. Imasu[4], P. Misra[5]
[1]*M. Tech student, Department of Civil Engineering, IIT Roorkee, Roorkee, India,*
[2]*Research Scholar, Department of Civil Engineering, IIT Roorkee, Roorkee, India,*
[3]*Professor, Department of Civil Engineering, The University of Tokyo, Tokyo, Japan,*
[4]*Professor, Atmosphere and Ocean Research Institute, The University of Tokyo, Kashiwa, Japan,*
[5]*Assistant Professor, Department of Civil Engineering, IIT Roorkee, Roorkee, India,*
Correspond to Prof. P. Misra (prakhar.misra@ce.iitr.ac.in)

Keywords: *Air Pollution, Brick Kiln, Classification, YOLO11, IGP.*

1. ABSTRACT

The brick kiln industry in South Asia is a major contributor to construction and economic development. However, it also stands as a significant source of air pollution, emitting large quantities of black carbon and fine particulate matter (PM2.5) that severely impact regional air quality and human health. Despite their contribution to respiratory illnesses and premature deaths, systematic mapping of kiln locations remains limited. This study presents a scalable deep learning-based approach to detect brick kilns across 1.2 million km² in the Indo-Gangetic Plain, including parts of Pakistan, northern India, and Bangladesh. Starting with Sentinel-2 imagery for initial feasibility in Delhi-NCR, the study shifts to higher-resolution Google Maps Static imagery (4.77 m at the equator) and fine-tunes a YOLOv11 object detection model for large-scale application. The pipeline detected over 50,000 kilns with more than 95% validation precision,significantly improving existing datasets. These results support targeted environmental monitoring, compliance enforcement, and pollution source attribution, laying the foundation for emission reduction and public health interventions in one of the world's most polluted regions.

2. INTRODUCTION

Brick kilns are major sources of air pollution and environmental degradation, emitting harmful gases that impact air quality and local ecosystems [1]. These kilns emit large quantities of harmful pollutants, including PM2.5, carbon monoxide (CO), sulfur dioxide (SO2), carbon dioxide (CO2), black carbon, and other substances that degrade air quality [2]. Brick kilns contribute an estimated 8% to 14% of the total air pollution in South Asia [3], with emissions of approximately 0.94 million tons of particulate matter and 127 million tons of carbon dioxide annually. India alone has over 100,000 brick kilns producing around 250 billion bricks annually [4][5]. Brick kilns are known to degrade soil quality, reduce crop and vegetable yields, and pose serious health risks to nearby communities due to their high pollutant emissions. Beyond the environmental impact, the brick kiln industry in South Asia is often associated with exploitative labour practices, where many workers are forced into labour under harsh conditions. A significant proportion of the workforce in this sector is believed to be modern-day enslaved people [6]. Widespread informal employment characterizes the brick industry in South Asia, leaving most workers exposed to vulnerabilities due to inadequate social protection or support. A further concern is the widespread violation of government regulations, with as many as 90% of kilns in the Delhi-NCR region failing to comply with spacing

rules by operating near one another [3]. Thus, detecting brick kilns is essential to mitigate environmental impact, enforce labour regulations, ensure legal compliance, and guide sustainable urban planning in regions with high kiln concentrations.

Monitoring brick kiln emissions has traditionally relied on manual surveys, which are labour-intensive and unsuitable for widespread or remote regions [7][8]. Recent advances in satellite imagery and machine learning have enabled faster and more scalable detection [6]. High-resolution approaches using models such as Faster R-CNN, R-CNN, and Kiln-Net have shown strong precision [6][8], while medium-resolution datasets like Sentinel-2 have also been tested with classification models [7][9]. More recent work has explored transfer learning [7] and self-supervised methods [3]. Building on these developments, this study employs a state-of-the-art YOLOv11 framework with Google Static Maps imagery to detect and map brick kilns across more than 1 million km² in the Indo-Gangetic Plain (IGP), covering Pakistan, India, and Bangladesh.

While previous efforts have demonstrated the potential of both high and medium-resolution imagery for kiln detection, most studies have been limited in geographic scope, dataset size, or model generalizability. Given the scale of the IGP, one of the world's most polluted and densely populated, the absence of a comprehensive, scalable inventory haults emission attribution, compliance monitoring, and policy enforcement. Moreover, the dual challenges of severe environmental degradation and exploitative labour practices linked to the industry underscore the need for systematic, large-scale detection. This study, therefore, addresses a critical gap by developing a robust, deep learning-based framework for kiln mapping, enabling environmental monitoring, regulatory compliance checks, and informed policy interventions.

3. STUDY AREA & DATASETS

The study primarily targets the Indo-Gangetic Plain as the main study area (Figure 1), with an initial analysis focused on the Delhi-NCR region. Delhi-NCR was chosen for this preliminary application due to its persistent air pollution challenges, largely driven by crop residue burning, vehicle emissions, and the high density of surrounding brick kilns. This initial analysis enables testing of the model's performance, identification of any limitations, and iterative improvements to the training dataset before expanding the methodology to the broader Indo-Gangetic Plain.

Figure 1. Study Area-Indo Gangetic Plain

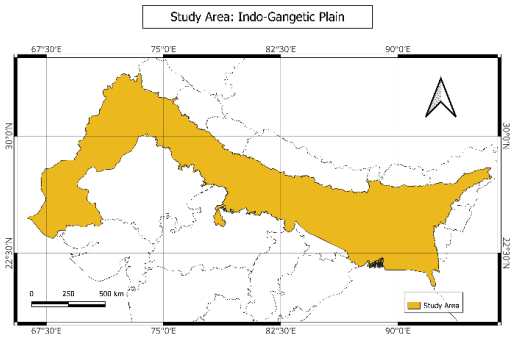

Table 1. Datasets Used

Dataset	IGP Detection	Delhi NCR & UP Brick Kiln classification
Region & Purpose	Indo-Gangetic Plain; Large-scale detection	Uttar Pradesh and Delhi-NCR; Kiln type classification
Zoom level	15	16
Resolution (at scale 2)	2.38 m	1.19 m
Total Images	136,939 (India: 87,381; Pakistan: 33,301; Bangladesh: 16,257)	133,143 (UP: 117,193; Delhi-NCR: 15,950)
Coverage per Image	6-8 km²	1.7-1.9 km²

4. METHODOLOGY

The methodological workflow (Figure 2) followed a structured sequence from data acquisition to analysis. Image patches were downloaded from Google Maps Static API at varying resolutions and curated into two datasets for large-scale detection across the IGP and kiln type classification in Delhi-NCR and Uttar Pradesh, as mentioned in Table 1. Annotation and augmentation were performed using Roboflow, and QGIS and Google Earth Pro supported data validation. The detection dataset contained 2,601 raw kiln instances, expanded to 5,748 after augmentation (Kiln/Non-kiln classes), whereas the classification dataset included 1,603 raw instances, augmented to 3,193 across three classes: Fixed Chimney Bull's Trench Kilns (FCBTK), Zigzag Kilns (ZZK), and Circular FCBTKs. A YOLOv11 model was fine-tuned with these datasets, achieving high detection accuracy. Large-scale inference produced a comprehensive kiln inventory, which GIS analyzed to identify hotspots and evaluate regulatory compliance.

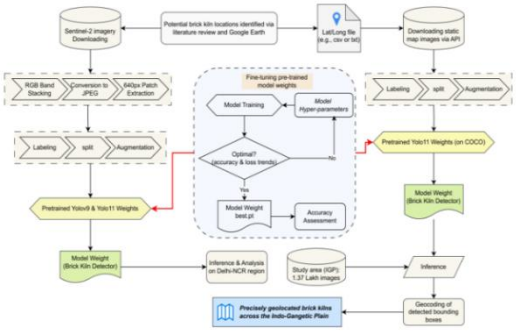

Figure 3. Overall Methodology

5. RESULTS & DISCUSSION

The effectiveness of the proposed model in detecting brick kilns across a broad geographical extent was evaluated using a robust, diverse test dataset, despite environmental variability, seasonal changes, and differences in soil, terrain, and surrounding land use. This dataset includes Maps static images (4.77m pixel size) from various regions of the Indo-Gangetic Plain, selected to represent a wide range of real-world conditions. Representative samples from this unseen dataset are shown in Figure 3.

Figure 4. Representative test data samples demonstrating geographic and seasonal diversity

The fine-tuned YOLO11 model demonstrated strong generalization capabilities, accurately identifying nearly all brick kiln instances in an unseen test region covering approximately 220 km2. The dataset contained 327 kiln instances. As shown in Figure 4(a), the confusion matrix indicates a precision of 97.7% and a recall of approximately 93%. These metrics confirm the model's high detection performance. However, an omission error

of about 7% (i.e., false negatives) was observed. This under-detection is primarily attributable to kilns in Pakistan's Sindh region, where the sandy soil background and visual features differ significantly from those found elsewhere in the Indo-Gangetic Plain. Similarly, for the regional classification model, performance was assessed on a separate unseen dataset comprising 253 kiln instances distributed across three classes: CFCBTK (circular), FCBTK (oval-type), and ZZK (zigzag). Model achieved an overall mAP of 94.8% at an IoU threshold of 0.50 and an F1-score of 91.7%. Class-wise analysis revealed a relatively higher error rate in distinguishing zigzag kilns. Despite being trained predominantly on zigzag and oval FCBTK instances, the model occasionally misclassified between these categories. This challenge arises due to their similar visual appearance in 2.38-meter resolution imagery—the primary distinction lies in the shape of the shorter edge (linear for ZZK and curved for oval FCBTK), which can be subtle at this resolution. As illustrated in the confusion matrix in Figure 4(b), the classification model

produced overall reliable results. To further mitigate omission errors in detection, the outputs of the classification model were cross-referenced with results from our previously developed detection model (which

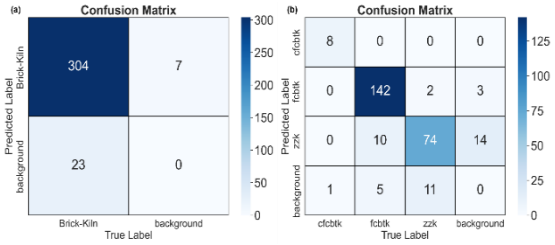

Figure 5. (a) Confusion matrix for brick kiln detection model validation (n=327 instances), (b) Confusion matrix for kiln-type classification model validation, across classes

identified kilns without classifying them), thereby improving the robustness and completeness of the final output.The comprehensive mapping of brick kilns across the Indo-Gangetic Plain (IGP) has yielded significant insights into their spatial distribution and prevalence. Our fine-tuned YOLO11 model identified over 50,000 brick kilns with precise localization across the IGP, as shown in Figure 5.

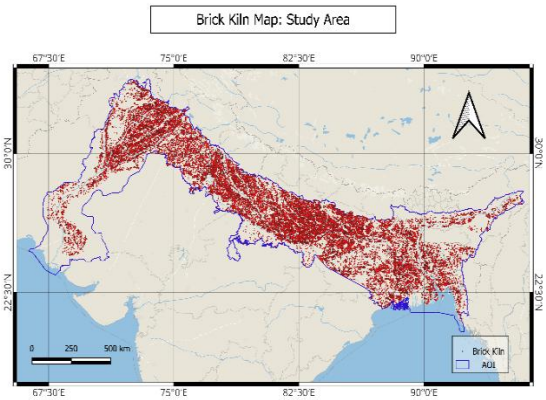

Figure 6 Model-derived brick kiln locations mapped across the IGP

The brick kiln classification results reveal that over 10,290 kilns (more than 60%) in Uttar Pradesh are of oval-shaped FCBTKs. Circular FCBTKs remain in some parts of UP due to historical use, lower upfront costs, and slow industry adaptation. While western Uttar Pradesh, part of the NCR, shows a higher prevalence of zigzag kilns, the broader state-level results highlight the need for more extensive policy interventions to promote cleaner kiln technologies. It is important to note the total number of type-classified kilns detected in Uttar Pradesh.

(approximately 16,200) is lower than the total number of kilns previously detected in this study and the ~19,500 kilns reported by the Uttar Pradesh Pollution Control Board (UPPCB). This underprediction likely stems from the additional complexity of classifying kiln types, small train instances and diversity, which may lead to missed detections. Despite this limitation, the model provides valuable type-specific information. It proves useful when applied at regional scales with appropriate post-processing checks and filters. However, further enhancements are recommended to improve its performance for large-scale applications, such as training on a larger dataset, employing more robust data augmentation techniques, and optimizing hyperparameters.

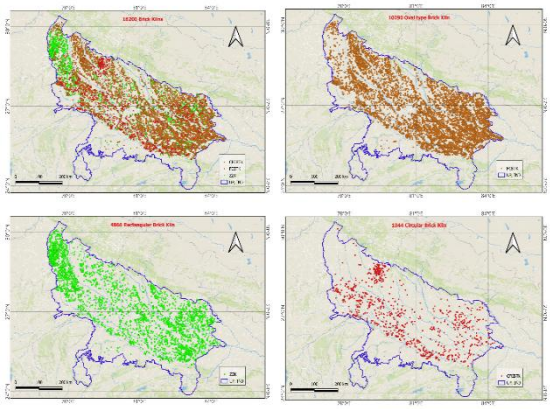

Figure 6. YOLO11-detected brick kiln types in Uttar Pradesh state: (a)

Composite map of three technologies (CFCBTK, FCBTK, ZZK); (b) Oval-type

(FCBTK) distribution; (c) Zigzag (ZZK) and (d) Circular (CFCBTK) kiln distribution.

6. CONCLUSIONS

This study presents a scalable approach to detect and classify brick kilns across the Indo-Gangetic Plain using high-resolution Google Maps imagery and a fine-tuned YOLOv11 model. Over 50,000 kilns were identified with precision and recall exceeding 95%, and kiln types were classified with an F1 score above 90%, enabling detailed regional analysis of

technology transitions. The resulting geolocated dataset supports regulatory monitoring, compliance enforcement, and targeted interventions to reduce environmental and social impacts.

Future integration of thermal and emission data (e.g., NOx, CO) will enhance activity assessment and emission inventories, enabling real-time monitoring of environmental impacts. Overall, this framework offers a robust tool for scalable brick kiln surveillance, supporting sustainable policy implementation, improved air quality modelling, and environmentally responsible practices in the sector.

REFERENCES

[1]A. Sabir, A. Kumar, P. Chauhan, Application of Deep Learning Model in Brick Kiln Information Extraction, pp. 1–15, 2023.
[2]M. S. Bhat, Q. S. Afeefa, K. P. Ashok, A. G. Bashir, Brick kiln emissions and its environmental impact: A Review, Journal of Ecology and The Natural Environment 6(1) (2014) 1–11. doi:10.5897/jene2013.0423.
[3]R. Mondal, Z. B. Patel, V. Jani, N. Batra, Scalable Methods for Brick Kiln Detection and Compliance Monitoring from Satellite Imagery: A Deployment Case Study in India, Feb. 2024.
[4]U. Rajarathnam, V. Athalye, S. Ragavan, S. Maithel, D. Lalchandani, S. Kumar, E. Baum, C. Weyant, T. Bond, Assessment of air pollutant emissions from brick kilns, Atmospheric Environment 98 (2014) 549–553. doi: 10.1016/j.atmosenv.2014.08.075.
[5]K. Tibrewal, C. Venkataraman, H. Phuleria, V. Joshi, S. Maithel, A. Damle, A. Gupta, P. Lokhande, S. Rabha, B. K. Saikia, S. Roy, G. Habib, S. Rathi, A. Goel, S. Ahlawat, T. K. Mandal, M. A. Hashmi, A. Qureshi, A. Dhandapani, J. Iqbal, S. Devaliya, R. S. Raman, Y. Lian, G. Pandithurai, S. K. Kuppili, M. S. Nagendra, S. Mukherjee, A. Chatterjee, T. A. Najar, A. Jehangir, J. Singh, B. Sinha, Reconciliation of energy use disparities in brick production in India, Nature Sustainability 6(10) (2023) 1248–1257. doi:10.1038/s41893-023-01165-x.
[6]G. M. Foody, F. Ling, D. S. Boyd, X. Li, J. Wardlaw, Earth Observation and Machine Learning to Meet Sustainable Development Goal 8.7: Mapping Sites Associated with Slavery from Space, Remote Sensing 11(3) (2019) 266. doi:10.3390/rs11030266.
[7]P. Misra, R. Imasu, S. Hayashida, A. A. Arbain, R. Avtar, W. Takeuchi, Mapping brick kilns to support environmental impact studies around Delhi using Sentinel-2, ISPRS International Journal of Geo-Information 9(9) (2020). doi:10.3390/ijgi9090544.
[8]U. Nazir, U. K. Mian, M. U. Sohail, M. Taj, M. Uppal, Kiln-Net: A Gated Neural Network for Detection of Brick Kilns in South Asia, IEEE Journal of Selected Topics in Applied Earth Observations and Remote Sensing 13 (2020) 3251–3262.
doi:10.1109/JSTARS.2020.3001980.
[9]S. Imaduddin, Y. A. Khan, K. Mirza, B. K. Bhadra, Detection of Brick Kilns Using Multi-Spectral Bands of Sentinel-2 Imagery, in: 2023 International Conference on Artificial Intelligence and Smart Communication (AISC 2023), IEEE, 2023, pp. 496–503. doi:10.1109/AISC56616.2023.10085085. ISBN: 9798350322309.
[10]J. Lee, N. R. Brooks, F. Tajwar, M. Burke, S. Ermon, D. B. Lobell, D. Biswas, S. P. Luby, Scalable deep learning to identify brick kilns and aid regulatory capacity, Proc. Natl. Acad. Sci. U.S.A., 118(17), 2021. doi:10.1073/pnas.2018863118.
[11]W. Liu, D. Anguelov, D. Erhan, C. Szegedy, S. Reed, C.-Y. Fu, A. C. Berg, SSD: Single Shot MultiBox Detector, pp. 21–37, Springer Int. Publ., 2016. doi:10.1007/978-3-319-46448-0_2. ISBN: 9783319464480.
[12]A. Paul, S. Bandyopadhyay, U. Raj, Brick kiln detection in remote sensing imagery using deep neural network and change analysis, Spatial Inf. Res., 30(5), pp. 607–616, Oct. 2022. doi:10.1007/s41324-022-00458-1.
[13]C. K. Saha, J. Hosain, Impact of brick kilning industry in periurban Bangladesh, Int. J. Environ. Stud., 73(4), pp. 491–501, Jun. 2016. doi:10.1080/00207233.2016.1179014.
[14]N. Sadoff, M. C. Sarofim, M. Kolian, B. Seay, A. Adetona, Impact of South Asian brick kiln emission mitigation strategies on select pollutants and near-term Arctic temperature responses, 2021. doi:10.1088/2515-7620/ac0a66.
[15]J. Deng, W. Dong, R. Socher, L.-J. Li, K. Li, L. Fei-Fei, ImageNet: A large-scale hierarchical image database, in: Proc. IEEE Conf. Comput. Vis. Pattern Recognit., 2009, pp. 248–255. doi:10.1109/CVPR.2009.5206848.

ABS ID: 66
Code No: IMSBE-OP-38

Mr. Suraj Jaiswal

4th International Symposium on One Health, One World
November 20 – 22, 2025

ABS ID: 64
Code No: IMSBE-OP-39

Behaviour of Pultruded Gfrp Sections and Local Buckling Under Axial Compression

M.M. Ansari[1], T. Alam[1] and A. Chourasia[1]
[1] *CSIR-Central Building Research Institute Roorkee, 247667, India*

***Keywords**: Pultruded GFRP section, Axial Compression, light-weight frame, FE modelling.*

1. GENERAL INSTRUCTIONS

Pultruded Glass Fibre Reinforced Polymer (Pgfrp) Sections Have Attracted Growing Interest In Civil Engineering Due To Their Outstanding Balance Of Mechanical Performance And Durability Advantages, Particularly For Sustainable And Lightweight Construction Solutions. The Global Imperative For Eco-Friendly And Low-Maintenance Infrastructure Has Motivated The Adoption Of Advanced Composite Materials Such As Pgfrp, Which Offer Distinct Benefits Over Conventional Steel Including Corrosion Resistance, High Strength-To-Weight Ratio, Electrical Insulation, And Simplified Fabrication And Installation Processes. Due To Their Non-Corrosive Nature, Pgfrp Structures Are Ideally Suited For Harsh Environments And Applications Where Long-Term Durability And Minimal Maintenance Are Paramount.[1][2][3]

A Particular Advantage Of Pultruded Gfrp Sections Lies In Their Adaptability For Modular Design, Ease Of Molding Into Complex Shapes, And Reduced Transport Challenges, Thus Supporting Innovative Solutions Such As Photovoltaic Thermal (Pvt) Panel Supports, Solar Lighting Frames, And Rapidly Deployable Modular Infrastructure. These Attributes Have Driven A Paradigm Shift In Engineered Frameworks, Especially Where Sustainability, Energy Efficiency, And Resilience Are Crucial Design Drivers.[4]

Despite These Advantages, The Layered And Relatively Slender Construction Of Pgfrp Sections Necessitates A Rigorous Evaluation Of Their Structural Response—Especially Under Axial Compression, Where Local Buckling May Govern Design Considerations. Unlike Isotropic Steel, The Anisotropic And Orthotropic Properties Of Pgfrp Can Lead To Unique Failure Modes, Including Premature Local Or Global Buckling, Contingent Upon Geometric Slenderness And Boundary Restraints. Buckling Is The Dominant Mode Of Failure In Pgfrp Members Due To The Reduced Modulus Of Elasticity Compared To Steel, With Observed Failure Modes Including Flexural Buckling, Flexural-Torsional Buckling, Or Local Buckling Depending On The Shape, Geometry, And Length Of The Section.

This Study Aims To Systematically Examine The Axial Compression Behaviour And Local Buckling Resistance Of Pgfrp Members Using Finite Element (Fe) Modeling. The Experimental Testing Of Axial Compression Is Also Planned And Will Be Covered In The Next Manuscript. The Outcomes Are Expected To Substantiate Pgfrp's Suitability As A Credible Alternative To Steel For Sustainable Constructions, Supporting Safe, Efficient, And Innovative Infrastructure Development.

2. Results And Discussions

A Lightweight Framed Structure Made Up Of Pgfrp Sections Is Aimed At Constructing A Holding Frame For The Pvt Collector In The Present Project, As Shown In Figure 1. All The Load-Bearing Vertical Members Have A Square Cross-Section.

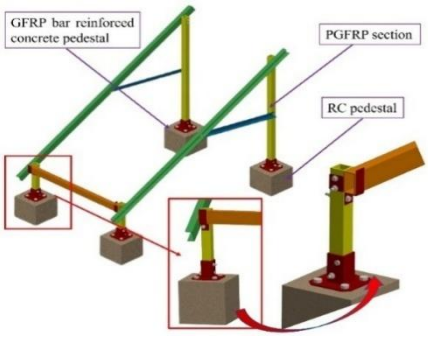

Figure 1. Pgfrp-Based Framed Structure For Holding The Pvt Collector In The Present Project

The Axial Compressive Behavior Of A Pgfrp Section (100 Mm X 100 Mm X 5.2 Mm) Of 500 Mm Length Has Been Analyzed Numerically. The Layup [0/+50/-50/0/-50/+50/0], Material Properties Of Layups And Boundary Conditions Are Taken From The Literature [5]. Continuum Solid Elements Are Considered For Pgfrp Section. The Axial Capacity Of This Stub Pgfrp Section Is Predicted To Be 510 Kn Against The Experimental Test Result [5] Of 505 Kn, As Shown In Figure 2. The Numerically Predicted Behavior Of Pgfrp Under Axial Compression Has Good Agreement With The Test Result.

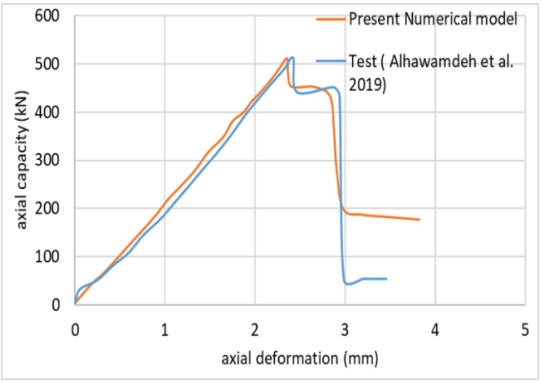

Figure 2. Axial Capacity Of Pgfrp Section, Numerical And Test Result [5]

The Failure In The Hollow Box Sections Is Triggered By Local Buckling As Shown In Figure 3.

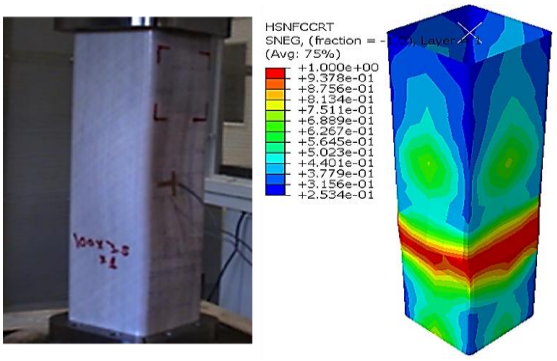

Figure 3. Predicted Failure Pattern In The Pgfrp Section Under Axial Compression Compared To The Test [5

3. Conclusions

Finite Element Modeling Accurately Predicts The Axial Compression Behavior And Local Buckling Response Of Pultruded Gfrp Square Sections, With Validated Numerical Predictions Closely Matching Experimental Results. Local Buckling Is Confirmed As The Dominant Failure Mode In Hollow Pgfrp Sections, Validating The Critical Importance Of Capturing This Failure Mechanism In Design Considerations. The Validated Fe Approach Provides A Reliable Tool

For Assessing The Structural Performance And Load-Carrying Capacity Of Pgfrp Members Without Extensive Experimental Testing. Pgfrp Sections Demonstrate Promising Structural Efficiency And Sustainability Advantages, Particularly For Lightweight Load-Bearing Applications Such As Photovoltaic Thermal Collector Supports Where Corrosion Resistance Is Paramount. The Demonstrated Computational Reliability Establishes Confidence In Numerical Design Methodologies For Optimizing Pgfrp Section Geometries And Layup Configurations In Future Engineering Applications. These Findings Support The Adoption Of Pultruded Composite Sections As Viable Sustainable Alternatives To Conventional Steel For Innovative Lightweight Infrastructure Development.

References:

[1]. Sirajudeen, R.S., Et Al. "Buckling Analysis Of Pultruded Glass Fiber Reinforced Polymer Angle Sections." Materials, Vol. 13, No. 21, 2020, P. 4766.[1]

[2]. Mahmood, E.M., Et Al. "Flexural Performance Of Encased Pultruded Gfrp I-Beam With Shear Connectors And Web Stiffeners." Materials, Vol. 15, No. 13, 2022, P. 4674.[2]

[3]. Harries, K.A., Et Al. "Creep And Creep Buckling Of Pultruded Glass-Reinforced Polymer Columns." Journal Of Composites For Construction, Vol. 21, No. 6, 2017, P. 04017031.[3]

[4]. Allawi, A.A., Et Al. "Encased Pultruded Gfrp Beams With Shear Connectors: A Review." Engineering, Technology & Applied Science Research, Vol. 15, No. 5, 2025, Pp. 27551–27556.

[5]. M. Alhawamdeh, O. Alajarmeh, T. Aravinthan Et Al. Modelling Hollow Pultruded Frp Profiles Under Axial Compression: Local Buckling And Progressive Failure, Composite Structures, 262, 2021, 113650, Https://Doi.Org/10.1016/J.Compstruct.2021.113650

4th International Symposium on One Health, One World
November 20 – 22, 2025

ABS ID: 52
Code No: IMSBE-OP-40

Automated Assessment of Overhead Wires Geometry in Railway Tunnels

F.M. Khan[1], T. Mizutani[2], and A. Regmi[3],
Student, Institute of Industrial Science, The University of Tokyo, Japan,
[2]Assoc. Professor, Institute of Industrial Science, The University of Tokyo, Japan,
[3] Student, Institute of Industrial Science, The University of Tokyo, Japan,
Correspond to Assoc. Prof. Dr. T. Mizutani (mizu-t@iis.u-tokyo.ac.jp)

***Keywords**: Overhead Equipment (OHE), Railways, LiDAR, Tunnel, DBSCAN Clustering.*

1.INTRODUCTION

Our research explores the feasibility of implementing a LiDAR–based system for the assessment of the geometrical configuration of Overhead Equipment (OHE) in Indian Railway tunnels. The OHE system comprises critical components such as the catenary wire, contact wire, cantilever fittings, masts, and dropper wires, all of which are essential for the uninterrupted power supply to electric trains and the overall efficiency of electrified railway operations. In India, the electrified route has increased from around 20,000 Km in 2014 to more than 65,000 Km in 2024, and total electrified track kilometer is near about 100,000 Km [1,2].

With rapid electrification of rail network in India, there is large scale creation of railway assets like masts, cantilevers, catenary and contact wires, dropper wires etc. Height of contact wire is the vertical distance between contact wire and rails, it is the distance measured between contact wire and rails in vertical plane.

In Indian Railways, in general, the height of contact wire is kept about 5.8 meter from rail level and the height of catenary wire is kept as 7.2 meter from rail level [3]. In locations, where there are restrictions or constraints due to overline structures like bridges, tunnels, power line crossings etc , the heights are adjusted according to the site conditions.

The contact wires are provided in a lateral staggered orientation along the track. By providing staggering to the contact wire along the railway route, it serves the important purpose of avoiding excessive friction and rubbing between a single point of contact between pantograph and contact wire.

In Indian Railways, contact wire is provided stagger value of ± 200 mm on alternate masts on tangent tracks, and the stagger is kept within 300 mm on curved tracks [3].

Height and stagger of contact wire are critical parameter of OHE and their correct setting is required for long term reliability and safety of train operations in electrified railways. Also, the correct configuration of OHE parameters is significant for successful commissioning of newly electrified sections in railway electrification projects.

India has diverse set of geographical terrain and vast area including mountains and many railway tunnels. Accurate setting of the height and stagger of the contact wire inside tunnels is complex and very crucial for ensuring safe and reliable operation of electric trains. Since tunnels restrict clearance and have limited space for overhead equipment, any deviation in wire height can lead to insufficient electrical clearance, risking flashovers or damage to pantographs. Inaccurate settings can cause arcing, frequent maintenance issues, and service disruptions. Therefore, maintaining precise wire geometry in tunnels is essential for safety, efficiency, and the longevity of both OHE and rolling stock.

Some previous research in the field of OHE measurements include UAV-LiDAR framework have been proposed for contact wire height and stagger estimation in [4]. Use of Airborne LiDAR data for mast detection was proposed in [5]. While these UAV based methods offer flexibility, they are often constrained in enclosed structures such as truss bridges, dense forests, and tunnels, and involve higher operational costs and airspace restrictions. In [6], Lin et al proposed a novel method based on deep learning to recognize point clouds of

overhead catenary systems (OCS) components. Techniques such as LiDAR–odometer-based trolley systems [7] require manual operation and movement of inspection trolleys on tracks for conducting measurements. Such measurements may have shortcomings in covering large area for measurements and require manpower and time costs for taking measurements.

In our research work, we propose a low cost and time efficient rail car mounted LiDAR based system for identification and extraction of overhead wires in Railway tunnels.

2.METHODOLOGY

Rail car mounted LiDAR-based assessment methodology was employed to evaluate the geometry of OHE within railway tunnels. The sensor suite, comprising a 2D LiDAR, IMU, GPS sensors, was floor-mounted on the guard van of a commercial cargo train to facilitate in-motion field experimentation as seen in Figure 1.

(a) (b) (c)

Fig1(a): Guard van of commercial cargo train

Fig1(b) LiDAR mounted on floor of cargo train

Fig1(c): 2D LiDAR Sensor

Unlike open-route railway environments, GPS-based localization systems like the one proposed in [8] often perform unreliably inside tunnels due to signal attenuation and loss of satellite connectivity. Consequently, the typical method of assigning spatial (longitudinal) `Z` coordinates using GPS data becomes infeasible. To address this limitation, an alternate approach termed the “Frame Accumulation Method” was adopted.

In this approach, the 2D LiDAR captures the environment in discrete frames, with each frame representing a unique 2D scan of the surrounding scene in XY plane. These frames are sequentially numbered (`f`), and the frame number increases linearly with time as the train progresses through the tunnel. Since each frame can be uniquely associated with a scan position, it serves as a proxy for the longitudinal position (Z) of the train. The 3D point cloud of tunnel generated by frame accumulation is shown in Figure 2.

Figure 2: 3D Point Cloud of Tunnel (Frame

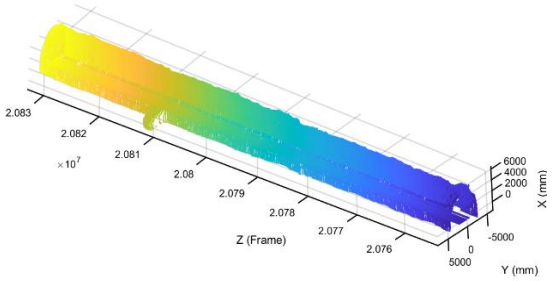

Accumulation Method)

To estimate the spatial `Z` coordinates along the tunnel length, a linear interpolation was performed between the starting and ending frame numbers based on the known tunnel length `l`.

1.The starting frame number of the tunnel was assigned a longitudinal coordinate `Z = 0` meters.

2.The ending frame number was mapped to the tunnel length `Z = l` meters

3.Intermediate frame numbers were linearly interpolated to derive corresponding `Z` values.

This interpolation effectively reconstructs the longitudinal spatial dimension, enabling transformation of the 2D LiDAR data into a 3D point cloud (`x, y, z`).

Once the 3D representation is obtained, point cloud processing technique can be applied for further analysis. The point cloud processing approach for successful extraction of OHE inside tunnels is shown in Figure 3.

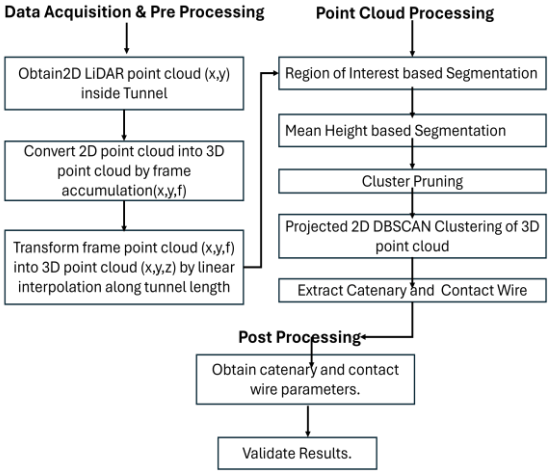

Figure 3: Point Cloud Processing Methodology

After generating the 3D point cloud, the approach applies a series of processing steps to extract OHE wires. These include region-of-interest–based segmentation, mean-height segmentation using wire height as the primary criterion, cluster pruning to remove noise, and projected 2D DBSCAN clustering. Together, these steps enable accurate and efficient isolation of the OHE components from the tunnel environment.

The methodology adopted here assumes linear interpolation based on near constant velocity of the train inside tunnel which is a safe assumptions for distance of few hundred meters for movement of train inside tunnels. The cross-section view of generated point cloud of tunnel and OHE arrangement inside tunnel is shown in Figure 4.

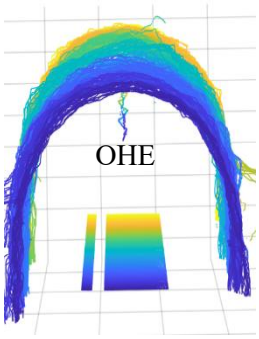

(a) (b)

Fig 4(a) Cross Section of Tunnel Point Cloud

Fig 4(b) Inside view of Jahgirdarwadi Rail Tunnel

3. RESULTS

This section presents the result of OHE geometry assessment in Jahgirdarwadi tunnel under Solapur division of Indian Railways.

The tunnel is 1664 meter long and is critical for train movement in mountainous terrain of the route. The entrance of the tunnel is shown in Figure 5.

Figure 5: Entrance Jahgirdarwadi Tunnel (1.66 Km)

Through Lidar-IMU-GPS system mounted on the floor of commercial cargo train, we obtained the point cloud data for OHE in the tunnel. After application of proposed point cloud processing methodology, we obtained the contact wire height profile for Jahgirdarwadi tunnel. The height plot is shown in Figure 6.

Figure 6: Contact Wire Height profile inside Tunnel

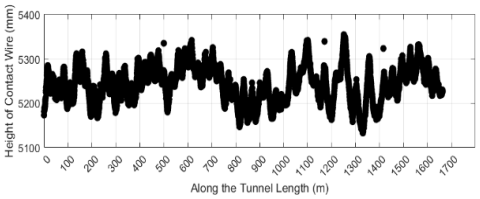

The standard height of contact wire in open route of Indian Railways is 5.8 meter. However, tunnel is a constraint location for maintaining normal profile of contact wire. Also, the minimum permissible height of contact wire is 5.15 metre for safe passage of container cargo trains.

We can see that in Jahgirdarwadi tunnel the height of contact wire is kept just above minimum design value. The height is maintained in range of 5.15 meter to 5.35 meter. This is necessitated to maintain relevant clearance from tunnel walls.

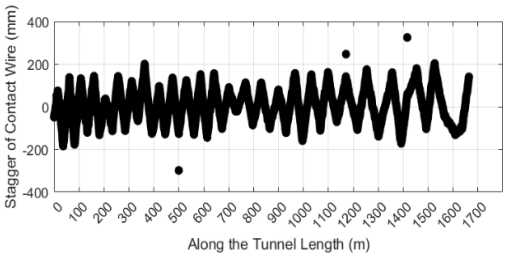

Figure 7: Contact Wire Stagger profile inside Tunnel

The contact wire stagger profile for Jahgirdarwadi tunnel is shown in Figure 7 . From the figure, we see that the contact wire follows 200 mm and -200mm range of stagger values on alternate locations inside tunnel. This is as per the design standards in Indian Railways for stagger of contact wire on tangent tracks.

4. CONCLUSIONS

Our work focused on automated assessment of OHE geometry in difficult terrain like railway tunnels. For locations like tunnels where GPS signal may not be available, we explored alternative approach incorporating 2D LiDAR frame accumulation method which consolidates different 2D frames to generate 3D point cloud. The point cloud processing involved region of interest-based segmentation, projected 2D DBSCAN clustering, mean height-based segmentation for successfully processing the data. The approach worked well for OHE extraction and was implemented on field data of 1.66 Km long tunnel in Indian Railways. The results were successfully validated with design values of OHE. Thus, the proposed method is a viable approach for automated measurements of overhead wires geometry inside railway tunnels.

REFERENCES:

[1] Indian Railways, Ministry of Railways, Indian Railways OfficialWebsite.

https://www.indianrail.gov.in/ (Accessed: May 21, 2025)

[2] Press Information Bureau, Government of India, Indian Railways records Best Ever Monthly Freight Loading of 139 MT in June2024.

https://www.pib.gov.in/(Accessed: June 20, 2025)

Reference to a book:

[3] Indian Railways, 25 kV AC Traction Manual (ACTM), Vol. I and II.

https://indianrailways.gov.in/ (Accessed: September 12th, 2025).

[4] Y. Geng et al., UAV-LiDAR-Based Measuring Framework for Height and Stagger of High-Speed Railway Contact Wire, IEEE Transactions on Intelligent Transportation Systems, vol. 23, no. 7, pp. 7587–7600,

2022.
https://doi.org/10.1109/TITS.2021.3071445.

[5] Ariyachandra, Mahendrini & Brilakis, Ioannis. (2020). Detection of Railway Masts in Airborne LiDAR Data. Journal of Construction Engineering and Management. 146. 10.1061/(ASCE)CO.1943-7862.0001894.

[6] Lin, S.; Xu, C.; Chen, L.; Li, S.; Tu, X. LiDAR Point Cloud Recognition of Overhead Catenary System with Deep Learning. Sensors 2020, 20, 2212. https://doi.org/10.3390/s20082212.

[7] Gutiérrez-Fernández, A.; Fernández-Llamas, C.; Matellán-Olivera, V.; Suárez-González, A. Automatic Extraction of Power Cables Location in Railways Using Surface LiDAR Systems. Sensors 2020, 20, 6222. https://doi.org/10.3390/s20216222

[8] F. M. Khan, T. Mizutani and A. Regmi, "Lidar-IMU-GPS Based System for Over Head Contact Line Geometry Assessment in Railways," 2025 IEEE International Workshop on Metrology for Industry 4.0 & IoT (MetroInd4.0 & IoT), Castelldefels, Spain, 2025, pp. 282-287, doi: 10.1109/MetroInd4.0IoT66048.2025.11121944.

4th International Symposium on One Health, One World
November 20 – 22, 2025

ABS ID: 165

Code No: IMSBE-OP-41

Indigenous antimicrobial polymeric nanofiber membrane as an air filter

R.V.N. Gundloori[1]*, S. Jha[2], S. Ghodke[3], P. Bijjargi[4], K. Sundaraganesan[5], T.R. Gautum[6] and S. Ghosh[7]

[1] *Sr. Principal Scientist, Polymer Science and Engineering, CSIR-National Chemical Laboratory, Pune, India.*
[2, 3, 4,5] *Project Associate, Polymer Science and Engineering, CSIR-National Chemical Laboratory, Pune, India.*
[6]*Senior Research Fellow, Polymer Science and Engineering, CSIR-National Chemical Laboratory, Pune, India.*
[7]*Chief Scientist, PFM Division, CSIR-Indian Institute of Chemical Technology, Hyderabad, 500007, India*
Correspond to Dr. G.V.N.Rathna (rv.gundloori.ncl@csir.res.in

***Keywords**: Air filter, Nanofiber membrane, antimicrobial, polyesteramide, biodegradable, recycled plastic, cellulose.*

ABSTRACT

The demand for air purifiers began to rise to keep away the COVID-19 virus, bacteria, and airborne particles for healthy living. So, the first aid would be using an efficient air filter that can also filter microbes. Particles (< 1 µm) and volatile harmful gases, and the available air filters are antibacterial, but cannot eliminate microbes. Recently, non-woven nanofiber membranes have been investigated as air filters, as they are more efficient than the conventional bulk filters. The nanofiber membranes showed 2.5 times higher efficiency than the bulk materials. Nevertheless, there are no proven studies on polymeric antiviral air filters. This study reports the development of an indigenous low-cost nanomaterial using recycled plastic and natural polymers with antimicrobial properties. Recycled synthetic plastic and the plant-derived cellulose were blended with an indigenous natural polyesteramide that has antibacterial and antiviral properties. And immobilized, a bioactive agent and an inorganic nanocomposite in that blend, before fabricating it in the form of a nanofiber membrane. The morphology of the nanofiber membrane, thermal, mechanical, and antimicrobial properties were evaluated. The results indicated that the developed nanofiber membrane was biodegradable, porous, non-toxic, and possessed good thermal, mechanical, and antimicrobial properties. Hence, this can be demonstrated for the filtering of microbes, in addition to the micro particles and harmful gases

1. INTRODUCTION

The available air purifiers that are in use are non-biodegradable and have a pre-filter made of polypropylene, PP mesh to remove large particles, and a HEPA (high efficiency particulate air) filter to remove fine particles < 1 µm and volatile components and followed by a carbon filter impregnated with spherical carbon material to remove CO, NOx, Ozone, SO2, SiO2, SO4 and NO3. Air cleaners or air filters are used to improve indoor air quality, thus decreasing the impact of air pollutants [1]. There are no proven studies on the anti-viral properties of air filters, although antibacterial properties are occasionally reported [1]. These cleaners or filters, if modified with antibacterial and antiviral agents, the possibility to combat infectious diseases and non-infectious diseases including the pandemic COVID-19-like viruses, will be very high. On the other hand, nanofiber membranes of nanometer range with nanocomposite might replace the now existing filters, because of the enhanced properties fetched by the virtue of their size. Further, using cost-effective, biodegradable, non-toxic polymers of natural and waste resources with nanocomposites for improved polymers shall lead to an advanced filtration of matter (particulate and microbes) more efficiently for clean air, which is the need of the hour. Accordingly, for the universal utility, we aimed to design an advanced biodegradable antimicrobial nanomembrane using recycled PET, (polyethylene terephthalate), cellulose and neem oil based polyesteramide. In this study, we prepared a suitable composition of

nanofiber membrane immobilized with bioactive agents like curcumin (CRMN), an electroactive graphene oxide (GO) and N-doped graphene-oxide (NGO) to enhance physical and antimicrobial properties and demonstrated the cell visibility, biodegradation, antimicrobial properties in addition to thermal and mechanical properties.

2. MATERIALS AND METHODS

PET, micro crystalline cellulose, neem oil, curcumin, graphene oxide, analytical solvents and salts

2.1. Synthesis of neem-oil based polyesteramide

HENA (N, N-bis (2-hydroxy ethanol) castor oil fatty amide)

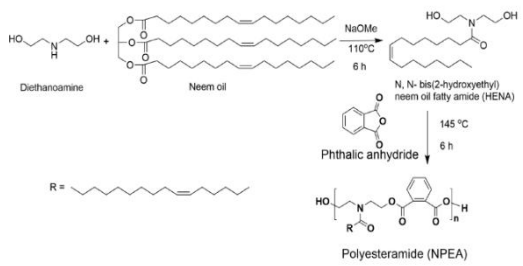

Figure 1. Reaction scheme of synthesis of neem oil polyestramide (NEPA

Neem oil-based polyesteramide was synthesized following the reported procedure [2,3]. Briefly, calculated amounts of di-ethanolamine and sodium methoxide were taken in a 2-necked round-bottomed flask (RB), and stirred for 1 h at 115℃. To this, neem oil was added dropwise and stirred for 6 h under inert atmosphere. Later, the reaction mixture was cooled to room temperature, and extracted it with diethyl ether using a separating funnel to obtain HENA (N, N-bis (2-hydroxy ethanol) neem oil fatty amide). The excess diethyl ether was evaporated to obtain the pure product, HENA. Calculated amount of HENA was taken in a round-bottom flask, to it added phthalic anhydride and dissolved in toluene at room temperature. After 30 min of stirring, the solution mixture was refluxed at 130℃ for 6 h. The byproduct, water (H2O) was collected using Dean-Stark apparatus. The resultant product, neem oil based polyesteramide (NPEA) was extracted with diethyl ether and washed with brine solution to obtain pure product after evaporation of diethyl ether. Figure 1 shows the reaction scheme-1

2.2. Preparation of blends and fabrication of nanofibers

Various compositions (samples) of the blend solutions of PET, cellulose, (MC) and, NPEA were prepared using trifluoroacetic acid and chloroform at 1.0: 1.0 ratio. The blend compositions were with and without CRMN, GO and N-GO. Table 1 shows the various compositions. The blend compositions were fabricated in the form of nanofiber membrane (NM) using electrospinning unit maintained at fixed parameters. The development of nanoformulation is based on our IP[4]

Table 1. Composition of the nanofiber mats

S.No	Code	rPET	MC	NPEA	GO	CRMN	N-GO
1.	rPET (A)	18	0	0	0	0	0
2.	rPET/MC (B)	18	2	0	0	0	0
3.	rPET/MC/NPEA (C)	18	2	1	0	0	0
4	rPET/MC/NPEA/2GO (D)	18	2	1	2	0	0
5	rPET/MC/NPEA/2GO/CRMN (E)	18	2	1	2	15	0
6	rPET/MC/NPEA/2N-GO/CRMN (F)	18	2	1	0	15	2

Characterizations of the synthesized neem oil polyesteramide were studied using FTIR and NMR. The nanofiber membranes (NMs) were characterized using various analytical techniques. The thermal and mechanical studies were done using thermogravimetric analysis and Universal testing machine (Instron). The air permeation studies were done by recording the change in the flux, where the volume of air flow per unit time at a fixed pressure was fixed. The nanofiber membrane of composition E, HEPA and nanofiber membrane immobilized on HEPA filters were studied. The morphology of nanofiber membranes of various compositions was recorded using FESEM. The biodegradation studies were done in the soil to understand the degradation of the NFs after application. The antibacterial studies were done at Acme ProGen Biotech (India) Private Limited, an ISO 9001 certified laboratory using gram-positive (S. aureus) and gram-negative bacteria (E. coli) by dissolving in DMSO/water

and following the well diffusion method. The antiviral studies were done using chikungunya virus at NIV, Pune. The estimation of the virus survived on the filter paper were examined following the method as reported [5, 6].

3. RESULTS AND DISCUSSION

Figure 2 shows the morphology of various compositions. HEPA filters used for air purification were in micron size which ranged from 0.3 nm to 5.0 µm in size. Whereas the nanofibers developed in our lab were below 1µm in size. The nanosize favors more surface area and more bioavailability to inhibit microbial proliferation. The immobilization of GO and curcumin can be observed on the surface of the nanofibers, where the GO and CRMN are impregnated on the surface of the nanofibers.

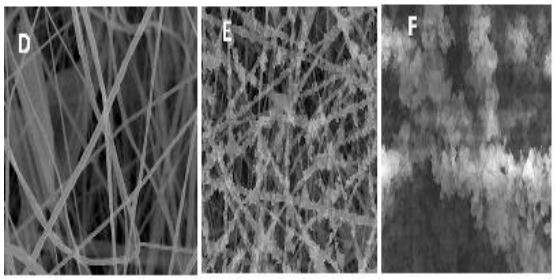

Figure 2. Morphology of the compositions (D) rPET/MC/NPEA/2GO,(E)rPET/MC/NPEA/2GO/ CRMN, and (F)rPET/MC/NPEA/2N-GO/CRMN

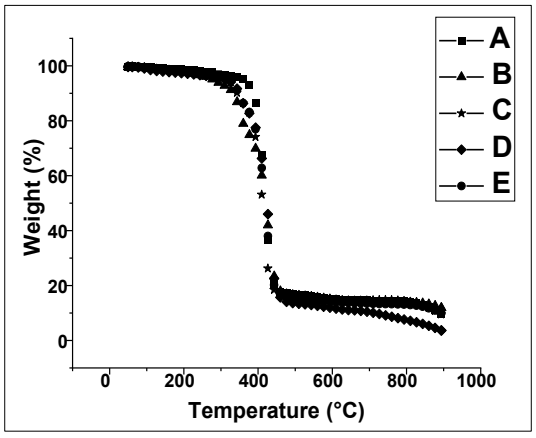

Figure 3. Thermogravimetric analysis of the compositions A,B,C,D,E

The thermogravimetric analysis and the DSC studies proved that the nanofiber membranes were stable. The decomposition temperature for the composition (A), rPET was 376°C and for the blend composition (E), was 326°C, which indicated that the developed nanofiber membrane is well comparable to pure rPET (A). The melting temperature of rPET and the blend composition (E) were 256 and 242 and considered to stable. Figure 3 shows the thermograms of the decomposition temperature of various compositions.

The air permeation studies were done by measuring the difference in the flux (it is measure of air flow perunit time and square centimeter) as a function of pore diameter. The more the porosity the highe-r is the flux. In our studies the nanofiber membrane reco rded higher portosity when compared to the commercial HEPA filter of the same thickness.The fl-ux decreased after the NF immobilized on the HEP-. A filterTable 2 shows the variation in flux as a function of the thickness of NF.

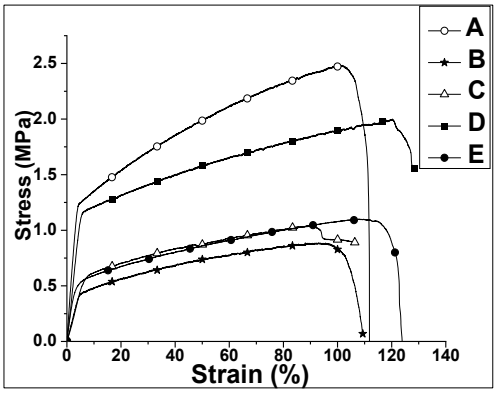

Figure 4. Tensile strength of the composition A, B, C, D, and E

Table 2. Flux of NFs of HEPA, and composition E.

Sample	Thickness (mm)	Flux (ml/sec/cm^2)
HEPA	0.427	0.39
E	0.221	0.62
E	0.539	0.25
E	0.875	0.12
HEPA+E	0.855	0.23

The developed NFs consists of biodegradable compo-nents and therefore considered to be environmentally safe as they get degraded after end applicatio as air filters. To prove this, we havedone soil degradation studies, where the microbes are more responsible to degrade the NFs. Figure 5 shows the biode-gradation of the various compositions (samples) of NFs. The sample E recorded 19% of degradation after 120 days.

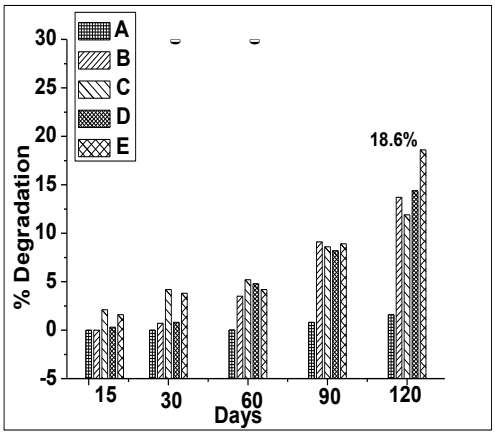

Figure 5. Biodegradation studies in soil for various tions

Antibacterial studies were done using Staphylococcus aureus and Escherichia coli to understand the potential of the antibacterial properties.

Figure 6 shows the antibacterial properties of NFs. The antibacterial activity of the nanofiber mats was assessed against Staphylococcus aureus and Escherichia coli using the well diffusion method was performed on Mueller-Hinton Agar (MHA). Growth inhibition was quantified by measuring the diameter of the

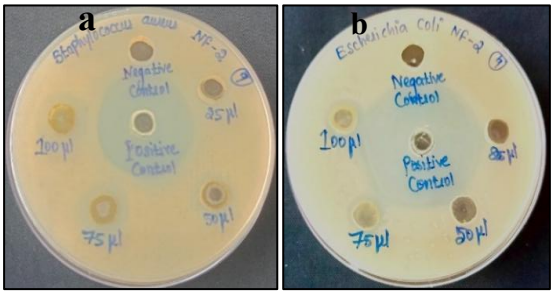

resulting clear zones in millimeters (mm). The sample E recorded antibacterial property with both S. Aureus and E.Coli.

The antiviral efficiency of nanofiber mats was evaluated using a method in which a viral suspension was taken, passed through the mats, and the solution that passed through was called the filtrate.

Table 3. Antiviral studies of nanofiber menmbranes.

Sample	Mean Log10 (Filtrate)	Mean Log10 (on FP)	Log10 Difference
A	6.692	6.529	0.162
B	6.635	6.794	0.07
C	6.757	5.842	1.012
D	6.836	6.647	0.067
E	6.832	0	6.855
F	6.839	5.532	1.303
VC	6.855	6.493	0.361

Figure 7. Antiviral efficiency of nanofiber mats.

The lower value indicated higher filtration efficiency.The virus was retained on the filter paper (FP), called vir-al load on filter paper. A

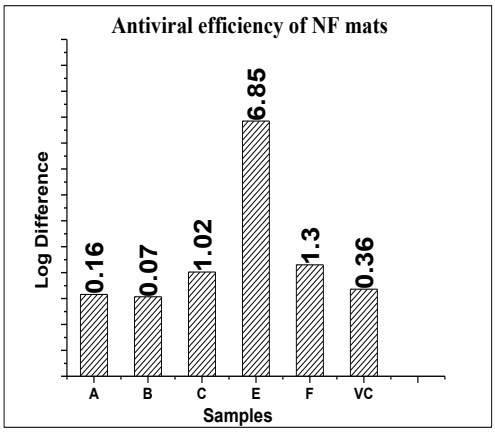

higher value indicated better antiviral properties.

The infectious viral load in all samples, including viral controls (VC), was quantified using a Foc-us Forming Unit (FFU) assay on a susceptible cell monolayer. Following incubation, the visible viral foci werecounted to determine the titer and corresponding Log10 vi-ral copy number for each condition in triplicate. Finally the antiviral efficacy was assessed by calculating the Log-10 Difference between the Filtrate and FP Load samples to quantify the reduction in infectious virus. The antiviral data reveal (Table3) a clear progression in material efficacy across the nanofiber mats. Initial formulations, Sample A (containing rPET), exhibited only minimal antiviral efficiency of 0.16. However, incorporating NEPA led to a marked improvement, achieving significant antiviral properties. The highest level of performance was attained by the final composite systems: Sample E (Graphene Oxide with Curcumin) and Sample F (Nitrogen-doped Graphene Oxide with Curcumin), 6.8 and 1.2, respectively (Figure7).

4. CONCLUSIONS

Designed and synthesized the antimicrobial polymers. Developed blends using recycled plastic, cellulose and NPEA. The air permeation studies for the selected composition E (with Curcumin and GO) recorded porosity higher than commercial filters, where it can be manipulated as desirable. The blend composition (E) containing curcumin and GO showed antibacterial and antiviral properties. The studies are in progress to refine the blend compositions for better efficacy.

REFERENCES

[1] Guoliang Liu, Manxuan Xiao,1, Xingxing Zhang,*, Csilla Gal, Xiangjie Chen, Lin Liu,Song Pan, Jinshun Wu, Llewellyn Tang,*, Derek Clements-Croome, Sustainable Cities and Societies, 32 (2017) 375-396

[2] Killi, N., Dhakare, R. A., Singam, A., Lokanadham, M., Chitikeshi, H., & Gundloori, R. V. N. MedChemComm, 7 (2016) 2299–2308.

[3] Killi, N., Pawar, A. T., & Gundloori, R. V. N.. Applied Bio Materials ,2 (2019) 3341–3351.

[4] Rathna VN Gundlooori, “Bioactive oil-based polyesteramide as nanofibers for wound healing applications”, IP 503536, 1 US 10195158 B2 and 1 EP 3131536 B1, 2013

[5] Habibi, S., & Ghajarieh, A. (2022). Russian Journallf Applied Chemistry, 95 (2022) 486-498.

[6] Lee, J., Bae, J., Youn, D. Y., Ahn, J., Hwang, W. T., Bae, H. & Kim, I. D. Chemical Engineering Journal, 444, (2022) 136460.

ABS ID: 69
Code No: IMSBE-OP-42

Mr. Mickey Mecon Dalbehera

ABS ID: 68
Code No: IMSBE-OP-43

Mr. Mickey Mecon Dalbehera

4th International Symposium on One Health, One World
November 20 – 22, 2025

ABS ID: 17
Code No: IMSBE-OP-01

Commercial Agglomeration Induced By Local Currency Introduction Analyzed Through The Balancing-Mechanism

H. Kato [1], H. Hasada[2], H. Watanabe[3], And Y. Honma[4]
[1]*Graduate Student, Dept. of Architecture, the University of Tokyo, Tokyo, Japan,*
[2]*Research Associate, Institute of Industrial Science, the University of Tokyo, Tokyo, Japan,*
[3]*Project Research Associate, Institute of Industrial Science, the University of Tokyo, Tokyo, Japan,*
[4]*Associate Professor, Institute of Industrial Science, the University of Tokyo, Tokyo, Japan,*
Correspond to Assoc. prof. Y. HONMA (yudai@iis.u-tokyo.ac.jp)
Correspond to Assoc. prof. Y. HONMA (yudai@iis.u-tokyo.ac.jp)

Keywords: *Balancing Mechanism, Commercial Area Agglomeration, Consumer Behavior, Local currency, Huff model.*

1. INTRODUCTION

In recent years, with the rapid spread of cashless payments in Japan, a growing number of municipalities have introduced digital local currencies for use in specific areas. Many of these aim to stimulate the local economy and retain customers by offering point rewards based on local spending.

The success of these currencies has varied among municipalities; some have generated economic impacts exceeding four times the cost of the point rewards, while others have been discontinued due to operational costs. The effectiveness of such policies likely differs depending on the locational characteristics of the region, such as whether it is an urban, suburban, or peripheral area. While various quantitative evaluations and empirical analyses of local currencies exist in previous research [1][2], few studies have focused on these locational factors.

Therefore, this study aims to analyze the effects of a local currency, driven by changes in consumer behavior, while considering locational characteristics such as population, economic scale, and transportation accessibility.

To do this, we build an urban model based on a balancing mechanism. In the process, we identify the parameters needed to properly incorporate locational characteristics. We then use this model to show the features of regions where the local currency is most effective.

2. METHODS

2.1 The Balancing-Mechanism and the Model

The balancing-mechanism used in this study captures the interrelationship where the "attractiveness" of a commercial district determines its "sales," and these sales, in turn, update the district's "attractiveness" for the next period [3].

In our model, the probability of a consumer choosing a commercial district is expressed by a Huff model, which uses the district's attractiveness (retail floor area), travel time from the consumer's residence, and the local currency's reward rate as explanatory variables. Based on these calculated selection probabilities, the sales for each district are estimated. We then attempt to reproduce the distribution of commercial districts by incorporating a feedback loop where these sales determine the attractiveness (retail floor area) for the next period through the balancing- mechanism.

2.2 Case Study

The following simulations are conducted for Nagoya City, using railway network data, OpenStreetMap, and 1km mesh population data from the National Census.

2.2.1 Reproducing the Commercial District Distribution

To reproduce the actual distribution of commercial districts, we identified the model parameters. These parameters are the weights for a district's attractiveness (retail floor area) and travel time from a residence in the Huff

model's consumer choice function. The calibration aimed to minimize the MSLE with the distribution of retail retail floor area from the Commercial Statistics Mesh Data. (The term related to the local currency's reward rate is not considered in this step.)

2.2.2 Analysis of Local Currency Effects

To analyze the effects of the local currency, we simulated its introduction in each of the city's 16 administrative wards individually. Two different reward rate scenarios were established for each ward: (1) a uniform 10% for both local and non-local residents, and (2) a differentiated rate of 20% for local residents and 10% for non-local residents. An evaluation was conducted for a total of 32 cases (16 wards × 2 scenarios). The primary evaluation metric is cost-effectiveness, which is defined as the ratio of the increase in sales to the cost incurred by the point reward program within the ward.

3. RESULTS

3.1 Reproducing the Commercial District Distribution

Fig.1 compares the actual distribution of retail retail floor area (left) with the model-estimated distribution that minimized MSLE (right). While the model generally reproduces the distribution of major commercial districts, it tends to underestimate their overall scale compared to the actual data.

3.2 Analysis of Local Currency Effects

Figure 2 maps the results for all 16 wards. The left panel shows scenario (1): a 10% reward for both local and non-local residents. The right panel shows scenario (2): a 20% reward for local and 10% for non-local residents.

In the left panel (Scenario 1), cost-effectiveness is highest in suburban areas adjacent or well-connected to the urban center containing the major stations (Nagoya and Sakae). This is likely due to a retention effect on local residents who would otherwise shop near these stations. Conversely, in suburban areas with low cost-effectiveness, access to the urban center is poor, and they already have sizable local commercial districts. The cost-effectiveness is lower because rewards are also given to consumers who were already shopping locally.

In the right panel (Scenario 2), the overall cost-effectiveness is reduced compared to Scenario 1, likely because higher rewards are given to already-retained residents. However, the ward shown in red in the center of the map maintains its high effectiveness. This is because it has a station with good access to the major stations but few local commercial districts, making it prone to consumer outflow.

4. CONCLUSION

This model suggests that the effectiveness of a local currency varies with locational characteristics, showing high effectiveness in suburban areas near the urban center. Future work will aim to use game theory to analyze inter-regional competition on reward rates and propose implementation strategies tailored to regional characteristics.

REFERENCES:

[1] Yoshioka, T., Chikaraishi, M., & Fujiwara, A. (2022). An empirical analysis of interaction in two-sided market of local currency. Journal of Japan Society of Civil Engineers, Ser. D3 (Infrastructure Planning and Management), 77(5), I_83–I_93

[2] Hoda, T., & Sakihama, E. (2022). Empirical analysis of effect of digital local currency to regional development: Implications for the introduction of local currency from analysis of users' awareness and purchasing behavior. The Japanese Journal of Regional Policy Studies, 29, 28–37.

[3] Honma, Y., & Kurita, O. (2005). Dynamics of urban commercial developments with respect to customer’s spatial choice behavior: Effects of city shapes and road network patterns on the balancing-mechanism. Journal of the City Planning Institute of Japan, 40(3), 97–102.)

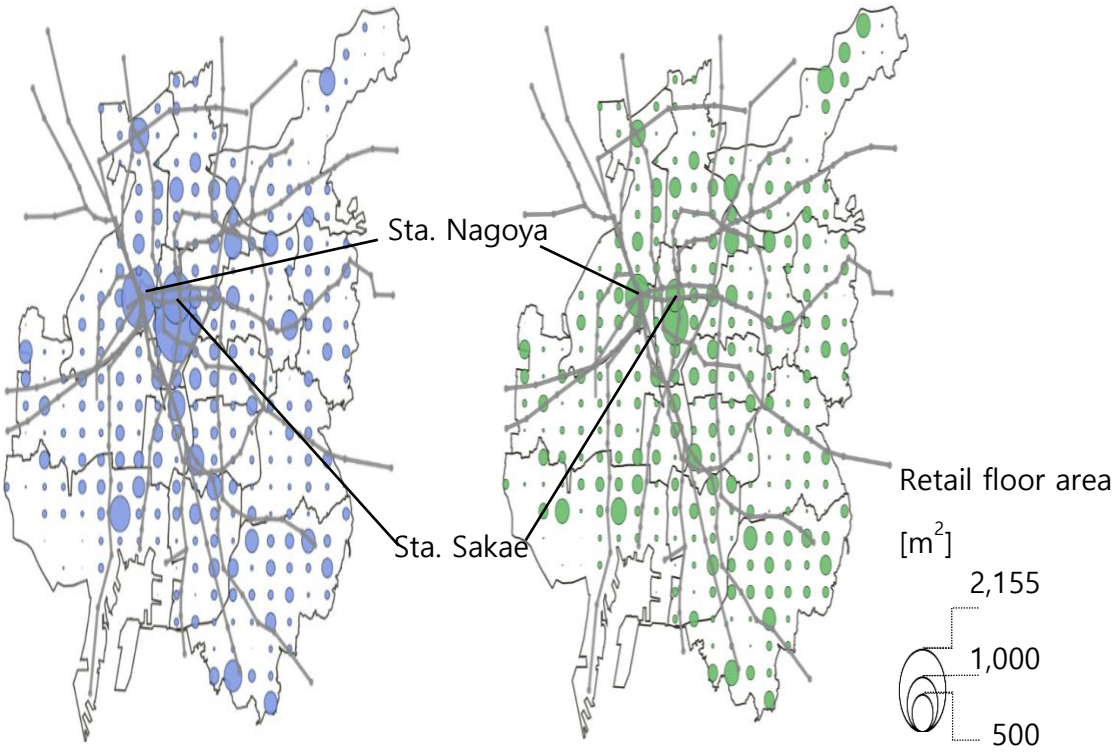

Figure 1. Distribution of Retail floor area: Actual (left) and Model-Predicted (right)

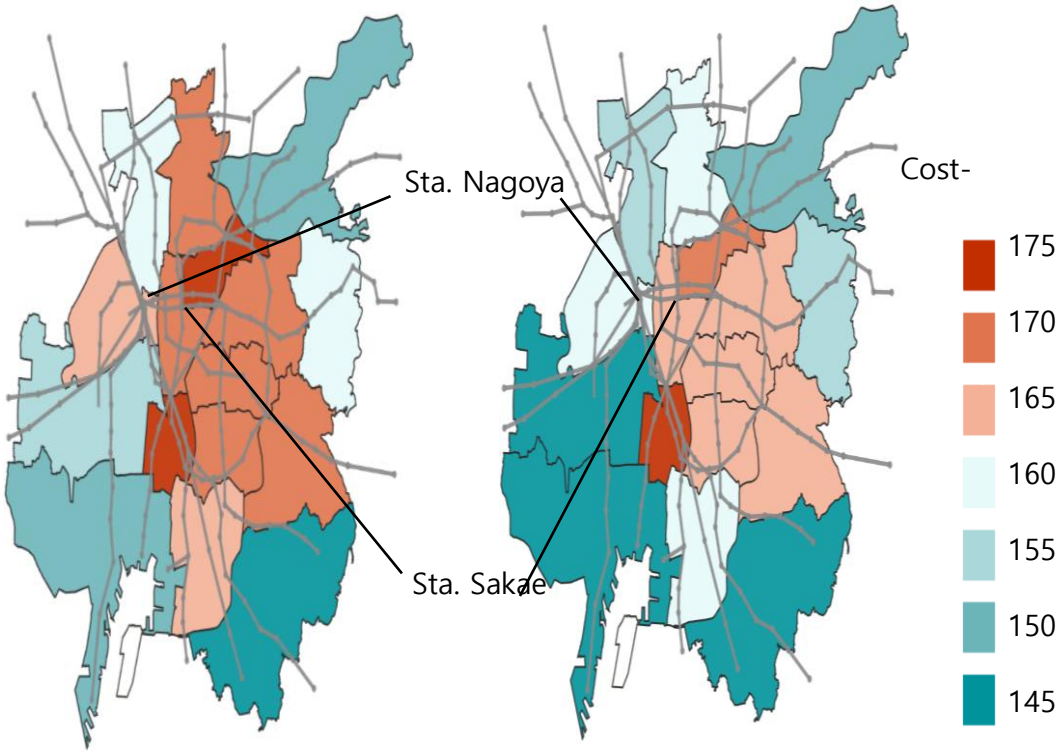

(1) local residents: 10%, non-local residents: 10%

(2) local residents: 20%, non-local residents: 10%

Figure 2. Cost-effectiveness of the Local Currency

4th International Symposium on One Health, One World
November 20 – 22, 2025

ABS ID: 141
Code No: IMSBE-OP-45

Pre-Engineered Buildings –Innovative Structural Systems For Sustainable Built Environment

Dr. Padmaja Gokaraju
Vice President - Engineering, R&D,
M/s Kirby Global, Alghanim Group, Kuwait, Hyderabad, India

Keywords: *Steel, Pre-Engineered Buildings, Innovative Structural Systems, Sustainability, Smart Materials, Built Environment.*

ABSTRACT

Steel Pre-engineered buildings (PEBs) are revolutionizing the construction industry with their efficiency, sustainability, and cost-effectiveness. PEB utilizes a systems approach by combining elements such as roof panels, wall panels, purlins, girts, main frames, and wind bracings, which act integrally. It also relies on standard designs with standard configurations, with each component uniquely profiled to suit the design requirements. They adopt innovative structural systems to enhance sustainability, utilizing smart materials such as high-performance insulation and eco-friendly coatings. This approach reduces energy consumption by maximizing natural light and ventilation, and incorporates renewable energy integration through the use of solar panels and rainwater harvesting systems. These structures adhere to circular economy practices by utilizing steel with bolted connections, facilitating disassembly and reuse, thereby minimizing waste and promoting the recycling of materials. This paper presents a detailed report on the advanced and innovative techniques employed in modern PEB for a sustainable built environment, covering the process from initiation to execution.

1. INTRODUCTION

Pre-engineered Buildings are initiated for low-rise metal buildings following a system's approach, taking advantage of the integrity between the components, namely, primary members made of high-strength (Yst 345Mpa) three-plated I sections, Secondary members made of high-strength (Ys345Mpa) Cold Rolled Steel Sections, and profiled roof and wall panels using high-strength (Yst 345Mpa) Cold Formed Steel, along with longitudinal bracings, which are designed based on prescriptive codes and standards. The components are shown in Figure 1.

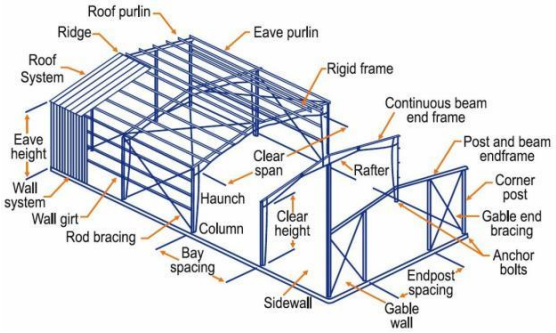

Figure 1. Components of a typical PEB building [1]

The PEBs are specifically designed to meet the unique requirements of each client, utilizing advanced manufacturing facilities and engineering software. PEBs are always produced in factories and delivered to construction sites for assembly, guaranteeing a 100% quality structure from a single supplier with timely delivery. Utilizing environmentally friendly materials and providing cost-effective solutions that meet client needs has made the PEB concept well-liked and profitable. Nonetheless, performance-based design methodologies have been made possible by developments in technology and analysis methods. The goal of performance-based design is to achieve specific performance objectives, such as occupant comfort, energy efficiency, and structural robustness. With this method, more creative and practical designs

can be created that are tailored to specific project needs.

2. INNOVATIVE STRUCTURAL SYSTEMS

There are several innovative structural steel systems and products that go beyond conventional steel framing and that have, in many cases, changed the way designers approach projects.

2.1 Innovative Materials

Modern PEBs aim to utilise innovative materials, including high-strength grade steels for plates in built-up /hot rolled sections and Cold-Formed Steel for use in profiled roof/wall panels, as well as secondary sections (purlins/girts), including corrosion- and fire-resistant grades. Designing structures with steel-concrete composite construction for columns, beams, and slabs, in accordance with the latest codes, enables the extension of PEB concepts to high-rise structures.

2.2 Modular Design and Techniques

Modular and pre-engineered construction techniques are gaining popularity in steel structure design. This approach significantly reduces construction time, enhances quality control, and minimizes waste. They enable the mass production of standardized steel components, ensuring consistency and streamlining construction processes. Some of the recently designed and developed engineering products/systems and techniques enhance the PEB structures to improve sustainability and resilience for high-rise structure construction in severe seismic-prone areas. The following are a few to mention. [2]

2.3 Buckling-Resistant Bracing Systems

BRB frames are a codified building lateral force-resisting system that offers improved seismic behavior, resulting in lower project costs. The ductile BRB response provides reduced frame member sizes, less structural steel weight, and smaller foundations. BRBs significantly exceed the performance requirements of the Seismic Provisions for Structural Steel Buildings (AISC 341).

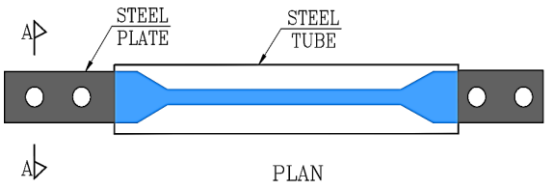

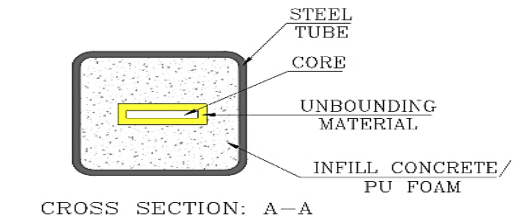

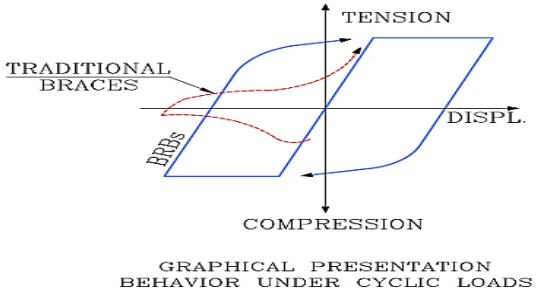

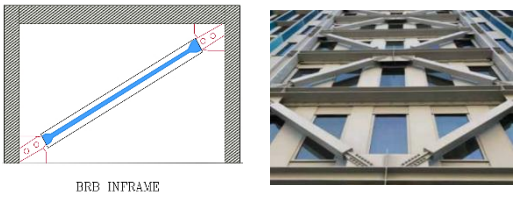

Figure 2. Buckling Resistant Bracing System (BRBs)

2.4 The Re-Fuse Braced Frame (RFBF)

A highly resilient structure is produced by this high-performance lateral load-resisting technology, which features improved reparability characteristics. To accommodate large inelastic deformations under extreme seismic or other hazardous conditions, the system's typical, rolled/built-up section brace members are joined to gusset plates using specifically manufactured, patented steel fuse components with a unique shape. The remaining structure, however, is virtually unaffected because it is still elastic. If the fuse elements are damaged in a hazardous incident, they can be replaced. The device is ideal for renovation, retrofit, and new construction applications due to the small size of the fuse elements, which enables them to be carried through almost any lift, stairs, or elevator.

2.5 Viscous Damping Devices (VDDs)

This bracing system in Steel Special Moment Frames (SMFs) improves seismic resilience and reduces construction costs. The VDD dampens

the motion of the SMF during an earthquake or under cyclic loading. The reduction in the response of the SMF yields a significant decrease in both the steel tonnage of the SMF and the foundation forces and materials. Installation is simple, and fluid viscous dampers do not require replacement after a significant seismic event. VDDs are uniquely capable of protecting a building structure during an earthquake without being damaged.

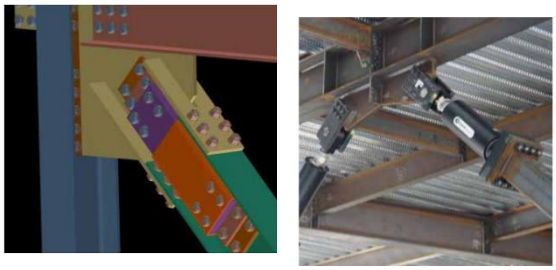

(a) (b)

Figure 3. Bracing Systems with (a) Typical Re-Fuse (b) Viscous Damping Device (VDD)

2.6 Steel Casted Connections

Casted connections simplify the design and enhance the performance of structures by enabling architects and engineers to integrate steel castings into their designs, resulting in more beautiful built environments.

(a) (b)

Figure 4. Casted Connections (a) Column (b) Bracing

2.7 Boltless Steel Clamping System

This is a high-strength bolt-less clamping permanent connection system, an alternative to welding or drilling, designed to resist axial tension and slip due to load combinations that include wind loads or seismic loads. It is suitable for quick installation on-site, is cost-effective, and is ideal for steel structures. It is achieved by clamping two steel sections together with the added convenience of adjustability for easier alignment in the field. Standardized products for columns, girders, trusses, to hang pipe and cable trays, etc, to create safer, innovative, and sustainable connections.

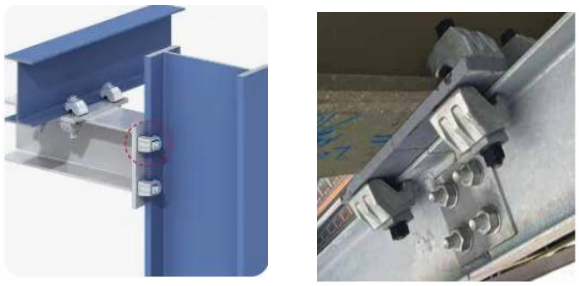

(a) (b)

Figure 5. Clamp Connection for (a) Column (b) Girder

Figure 6. Castellated and Cellular built-up beams

2.8 Castellated/ Cellular Beams

Castellated and Cellular built-up beams offer versatility, reliability, and economy for all types of floor and roof structures while being aesthetically pleasing, lightweight, and structurally sound. They are well-suited for long-span beams, providing faster erection and the ability to pass ductwork and utilities through web openings, which helps achieve lower floor-to-floor heights. Composite design

increases stiffness and improves vibration characteristics.

Steel structures are often subject to environmental factors that can lead to corrosion and degradation over time. Innovations in sustainable coatings and surface treatments have improved the durability and longevity of steel structures [3]. Eco-friendly coatings, such as organic or ceramic-based coatings, provide adequate corrosion protection while minimizing environmental impact. Additionally, self-healing coatings and innovative surface treatments are being developed to detect and repair minor defects or damages, prolonging the service life of steel structures and reducing maintenance needs.

3.Integration Of Smart Technologies (IOT, BIM, AUTOMATION).

The adoption of 3D modelling and visualization tools has significantly improved the design and construction process for steel structures. Building Information Modelling (BIM) platforms enable the creation of detailed 3D models that provide a comprehensive representation of the structure. These models facilitate better coordination among project stakeholders, detect clashes, and provide visualization of the final product, leading to improved communication and reduced errors during construction. The innovative design concept in PEB focuses on integrating sustainability principles, including strategies to reduce energy consumption, optimize material usage, and enhance the environmental performance of steel structures.

3.1 Integration in softwares

The integration of engineering software across the PEB process, from design to detailing, material procurement, production, and execution, enables faster project completion while achieving cost savings by effectively utilising resources and materials, maintaining high quality, and minimising human errors.

Figures 8 (a) and (b) show the 3D model connection of a PEB project in iDea statica, which enhances the construction at the site as shown in (c) and (d). Linking the design software output to detailing software reduces drafting time and errors while generating shop drawings and helps to capture the precise BOQ.

Figure 7. Typical Flow chart for engineering

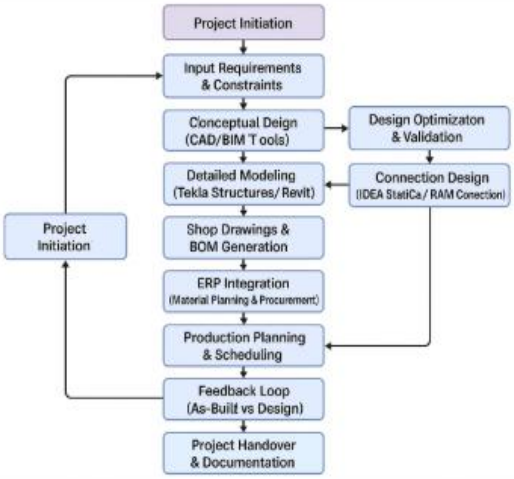

software integration in the PEB industry

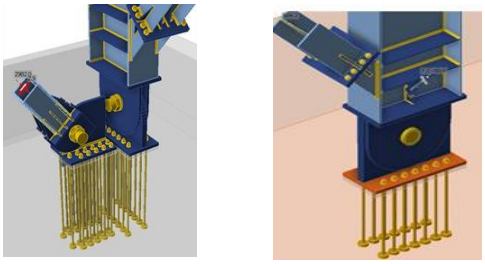

(a) (b)

(c) (d)

Figure 8. (a) & (b) Connection modelled in Software Vs (c) & (d) As executed at Site [3]

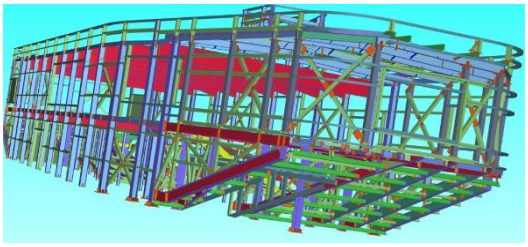

(a)

(b)

Figure 9. (a) 3D Tekla model (b) Executed at Site.

Figure 9 shows a PEB project example.[4]

3.2 Integration in production

Techniques such as life cycle assessment, green materials selection, and energy-efficient design practices are being employed to minimize the environmental impact of steel construction while improving overall project efficiency.

Digital fabrication technologies, such as Computer Numerical Control (CNC) machines and robotics, have revolutionized the manufacturing and assembly of steel structures. Automation also plays a crucial role in material handling, leading to faster construction and improved quality control. These technologies enable the precise fabrication and assembly of steel components, thereby reducing errors and enhancing construction efficiency. [4]

Figure 10. SAW for Built-up sections for PEB [4]

Figure 11. Pod lifting-Advanced Erection Technique [4]

3.3 Integration in execution

In the pod lifting technique of PEB erection, two successive frames, along with a set of purlins, are assembled on the ground and lifted together with tower cranes for execution. This method improves the safety and speed.

Structural health monitoring systems utilize sensors and data analysis techniques to monitor the behaviour and condition of steel structures in real-time. These systems provide valuable information on structural integrity, load distribution, and potential maintenance needs. By continuously monitoring the performance of steel structures, engineers can optimize maintenance schedules, ensure safety, and prolong the service life of the structures. As technology continues to evolve, we can expect further advancements that will push the boundaries of steel structure design, opening up new possibilities for construction efficiency.

Continual research and development efforts have led to the introduction of high-strength, lightweight Cold Rolled Sections into CFS buildings with PEB concepts for various industrial and residential applications, thereby increasing steel consumption.

With the increasing frequency of natural disasters, there is a growing emphasis on designing steel structures that are resilient and disaster-resistant. Engineers are incorporating features such as enhanced seismic design, hurricane-resistant connections, and blast-resistant elements into the design of steel structures. These measures ensure that the structures can withstand extreme forces and mitigate potential damage, contributing to the overall safety and longevity of the built environment.

4. CONCLUSION

The innovations in steel structure design discussed in this article are transforming the construction industry by advancing construction efficiency. The integration of

parametric design, performance-based design with PEB concepts, 3D modelling design and detailing, digital fabrication, sustainable practices, advanced analysis, lightweight materials, and automation technologies is reshaping the way steel structures are conceived, fabricated, and constructed. These advancements not only improve construction efficiency but also enhance safety, durability, and sustainability, ultimately leading to better project outcomes and increased resistance to seismic and wind hazards.

REFERENCES:

[1] Kirby Technical Handbook

[2] AISC Innovative Structural Steel Systems.aisc.org/. 866.ASK.AISC.

[3] Marco, Marcia. “Innovations in Steel Structure Design: Advancing Construction Efficiency.” J Steel Struct Constr 9 (2023): 178.

[4] https://www.kirbyinternational.com

ABS ID: 81
Code No: IMSBE-OP-46

Dr. Govind Gaurav

4th International Symposium on One Health, One World
November 20 – 22, 2025

ABS ID: 48
Code No: IMSBE-OP-47

Affordable Semi-Automatic Casting Machine for Lightweight Panels in Climate-Resilient Construction

Kanti Lal Solanki[1], Dr. SK Panigrahi[1], Chandrabhan Patel[1], Anuj Kumar[1], Dr. Ajay Chourasia[1]
[1]*CSIR-Central Building Research Institute Roorkee, India*

Keywords: Semi-automatic, Climate-Resilient Construction, Panel, MSMEs.

1.ABSTRACT

Climate change has intensified the need for climate-resilient infrastructure, demanding innovative and sustainable construction solutions. This work presents a cost-effective semi-automatic panel casting machine for producing lightweight, durable panels suitable for resource-limited regions. The modular mechanized system integrates semi-automated processes to reduce labor, enhance precision, and ensure consistency in production. Designed for scalability, it supports both small- and large-scale manufacturing. The MS-frame-based setup with a motorized hopper and pneumatic control ensures uniform filling and smooth finishing. By combining automation, modularity, and affordability, this system provides an accessible, efficient, and sustainable solution for MSMEs and local fabricators in climate-resilient construction.

2. INTRODUCTION

Climate change has intensified the demand for resilient, sustainable, and cost-efficient building materials. Mechanized systems enhance production by optimizing manufacturing, reducing labor, and ensuring quality consistency. Bisht et al. (2021) designed and analyzed a machine converting industrial waste into bricks, validating its feasibility through simulations and experiments. Premkumar et al. (2020) integrated IoT into brick-making, enabling real-time monitoring and control but noted economic and user experience challenges. These studies establish a foundation for developing the proposed mechanized system for climate-resistant panels, confirming that integrating sustainable materials with optimized mould design ensures efficiency, durability, scalability, and affordability in modern construction.

3. METHODOLOGY

The development of the mechanized system for manufacturing climate-resistant panels follows a structured methodology encompassing conceptualization, design, analysis, and prototyping of the system. The process begins with extensive research into existing manufacturing techniques, materials, and automation technologies to identify the most efficient and cost-effective approach.

3.1. DESIGN AND ANALYSIS OF MOULD

The mould adopts a vertical casting design, eliminating external vibration by utilizing concrete's self-weight for uniform filling. Panels resemble beam-columns, improving load distribution and stability. Standard dimensions are 3000 mm × 150 mm × 610 mm, with isolated sheets enabling easy de-moulding. Integrated interlocking features ensure precise alignment and structural integrity during assembly.

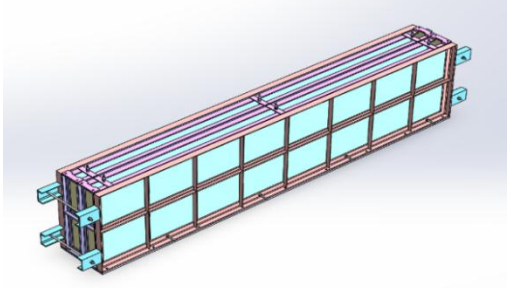

Figure 1. CAD model of mould

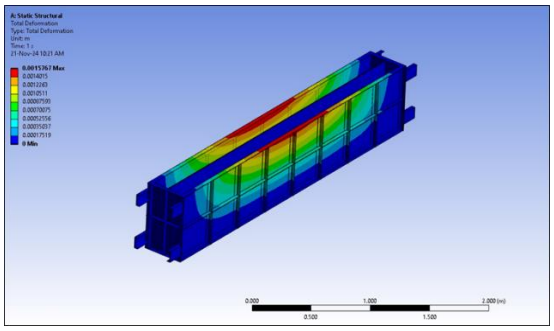

Figure 2. Total deformation of mould

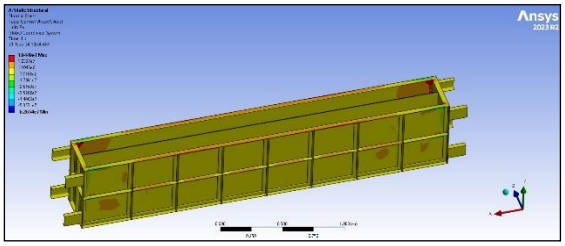

Figure 3. Normal stress variation on mould

3.2 DESIGN AND ANALYSIS OF HOPPER SUPPORTED FRAME

The frame track sustains the total load of the hopper and concrete material. The frame track made up of a rectangular piece of 70 mm in height, 38 mm in width, and 5 mm in thickness (shown in figure 6). The analysis involved applying external loads to the side frame while keeping its bottom edge fully constrained.

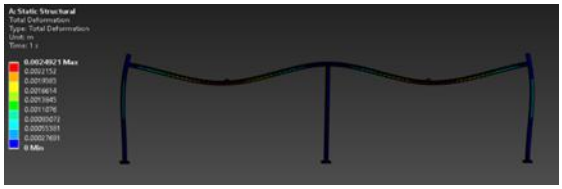

Figure 4. Deformation of supporting frame

4.RESULT

The mechanized system integrates mechanical, electrical, and hydraulic subsystems for efficient automated operation. A mild steel hopper with a hydraulic gate enables precise concrete flow, driven by a 1 HP motor and 1:100 gearbox. Mounted on a rigid MS frame, the system ensures stability, remote operation, minimal labor, and enhanced workplace safety.

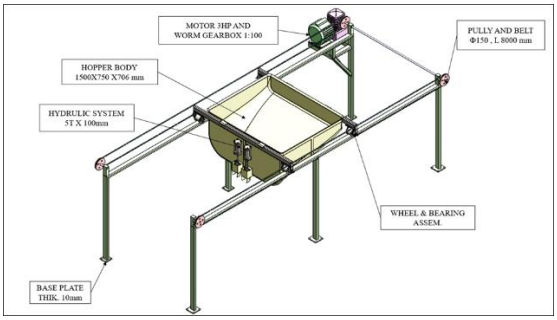

Figure 5. CAD Assembly of semi-automatic panel casting machine

A centralized control panel synchronizes motor, hydraulic, and sensor operations, enhancing automation and safety.

Figure 6. Prototype of semi-automatic panel casting machine

Under the FE analysis, the deformation behaviour shows the deformation is primarily influenced by the structural flexibility in that region and the applied loading conditions. The results indicate that the highest strain occurs at the bottom corner, suggesting significant elongation in this region due to tensile loading. The deformation analysis shows maximum displacement at the top of the side frame, decreasing toward the fixed base, consistent with expected load behaviour.

The deformation analysis of supporting frame revealed that the maximum displacement occurs at the top end of the side frame and it gradually decreases toward the fixed bottom, confirming that the structural response aligns with expected load distribution patterns. The

results indicate that the frame remains stable under the applied loading conditions. The normal elastic strain distribution analysis showed that the maximum strain occurs in the top region of the side frame indicating significant elongation due to tensile loading. Conversely, the minimum normal elastic strain is observed at suggesting minimal deformation or possible compressive behaviour in specific regions.

5.CONCLUSION

Mild Steel (MS) is used for its strength, durability, weldability, and cost-effectiveness. It allows precise fabrication and design flexibility for scalable applications. The vertical mould design ensures uniform casting without vibration, and FEA confirms stability. The modular MS-based system ensures efficient material handling, durability, and sustainability for climate-resilient panel production.

REFERENCES:

1.Bisht, R. S., Panigrahi, S. K., Singh, S., Kumar, D., & Yadav, S.: Design analysis of a machine for manufacturing of bricks from industrial waste: simulations and experiments. International Journal on Interactive Design and Manufacturing, 15, 587-596 (2021).

2.Premkumar, M., Devi, G., Sowmya R.: Design and implementation of brick making machine integrated with smart IoT application. Int. J. Comput. Digit. Syst. 9(3), (2020).

3.Kamaruddin, S.S., Mohammad, M.F., Mahbub, R., Ahmad, K.: Mechanization and automation of the IBS construction approach: a Malaysian experience. Proc. Soc. Behav. Sci. 105, 106–114 (2013).

4.Ponkia, S., Mehta, S., Prajapati, H., Trivedi, R.: Design of a cost effective fly ash brick manufacturing machine. In: Technology Drivers: Engine for Growth, pp. 203–208. CRC Press, Boca Raton (2018).

5.Chen, Y., Sun, Y., Chen, C.: Dynamic analysis of a planar slidercrank mechanism with clearance for a high speed and heavy load press system. Mech. Mach. Theory 98, 81–100 (2016).

4th International Symposium on One Health, One World
November 20 – 22, 2025

ABS ID: OP-01
Code No: IMSBE-OP-48

The Evolution of Evacuation Shelter Management in Japan

O. Murao[1] and K. Matsuzaki[2]
[1]*Professor, International Research Institute of Disaster Science, Tohoku University, Sendai, Japan,*
[2]*Master Course, Department of Architecture and Building Science, Tohoku University, Sendai, Japan,*
Correspond to Prof. O. MURAO (osamu.murao.a6@tohoku.ac.jp)

***Keywords**: 2024 Noto Peninsula Earthquake, Wide-area Evacuation, Paired municipality support, Wajima City, Evacuation shelter management guidelines, Historical transition.*

1. RESEARCH OBJECTIVES AND STRUCTURE

This study first aims to understand how Japan's legal frameworks and guidelines regarding evacuation shelters have evolved based on past disaster experiences. To achieve this, we begin by organizing the historical transitions through a literature review.

Next, the research focuses on spatial elements such as layout and living conditions in shelters, clarifying how their roles and challenges have shifted over time. The usage of shelters during major past disasters has changed in response to evolving needs during evacuation life and broader social transformations. As these realities have been addressed from various perspectives in prior studies, we will clearly present these developments through an extensive review of the literature.

Finally, based on these historical transitions, we analyze the actual management of the wide-area evacuation shelter established after the 2024 Noto Peninsula Earthquake (Gakudani Fureai Gymnasium), aiming to draw insights for future shelter planning and wide-area evacuation responses.

2. EVACUATION FROM WAJIMA TO KANAZAWA

In the 2024 Noto Peninsula Earthquake, the Oku-Noto region—including cities such as Wajima and Suzu—suffered severe damage, and delays in the restoration of lifeline infrastructure were anticipated. As a result, many residents evacuated to less-affected areas such as Kanazawa City and Komatsu City, as well as neighboring prefectures. This phenomenon is referred to as "wide-area evacuation."

Wide-area evacuees were received at secondary evacuation shelters, such as welfare facilities and hotels. In addition, "1.5-stage evacuation shelters" were established as temporary accommodations until evacuees could be relocated to secondary shelters or temporary housing. However, due to difficulty in securing long-term accommodation, these 1.5-stage shelters ended up hosting evacuees for an extended period.

This study focuses on the Gakudani Fureai Gymnasium, a 1.5-stage evacuation shelter located in Kanazawa City that hosted evacuees from the Minamishimi district of Wajima City. Figure 1 illustrates the transition in the number of evacuees at primary shelters in Wajima City, wide-area shelters in Kanazawa City, and the Gakudani Fureai Gymnasium.

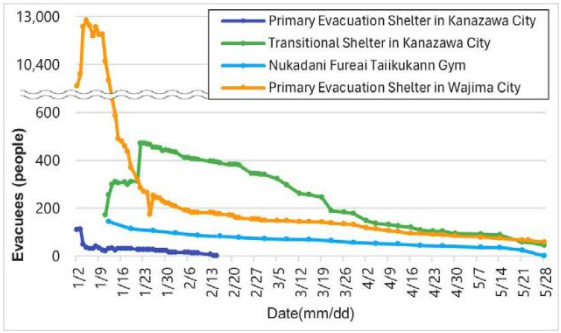

Figure 1. Trends in the Number of Evacuees: Primary Shelters in Wajima, Wide-Area Shelters in Kanazawa, and the Gakudani Fureai Gymnasium (1.5-Stage Shelter)

3. LIVING CONDITIONS IN THE SHELTER

Based on field visits and interviews with shelter staff, the shelter layout and daily life conditions were documented (Figure 2). During the first two weeks, considerable time was required to

establish the reception and management systems. At the reception area, residents from the Minamishimi district of Wajima City were accepted as a group and underwent health screening before being allocated either to the Kakutani Fureai Gymnasium or to other facilities in Kanazawa City.

The alternative facilities included elderly welfare centers and lodging-type learning centers, which offered private rooms with tatami mats or beds and were equipped with heating. Therefore, households with elderly members requiring care or those with children were relocated to these facilities.

4. CONCLUSION

This section briefly introduced the conditions of evacuation shelters in Kanazawa City following the 2024 Noto Peninsula Earthquake.

The presentation will further cover the historical evolution of evacuation shelter operations in Japan.

REFERENCES:

[1] Ishikawa Prefecture: Damage Report, https://www.pref.ishikawa.lg.jp/saigai/202401jishin-taisakuhonbu.html#higai (Date of Access: April 18, 2025)

[2] Ishikawa Prefecture: The Status of Human and Structural Damage Caused by the 2024 Noto Peninsula Earthquake,2024, https://www.pref.ishikawa.lg.jp/saigai/documents/higaihou_201_1400.pdf (Date of Access: May 14, 2024)

[3] Shigeru Ban Architects: Disaster support projects, https://shigerubanarchitects.com/ja/works/?_work=disaster-relief-ja (Date of Access: April 18, 2025)

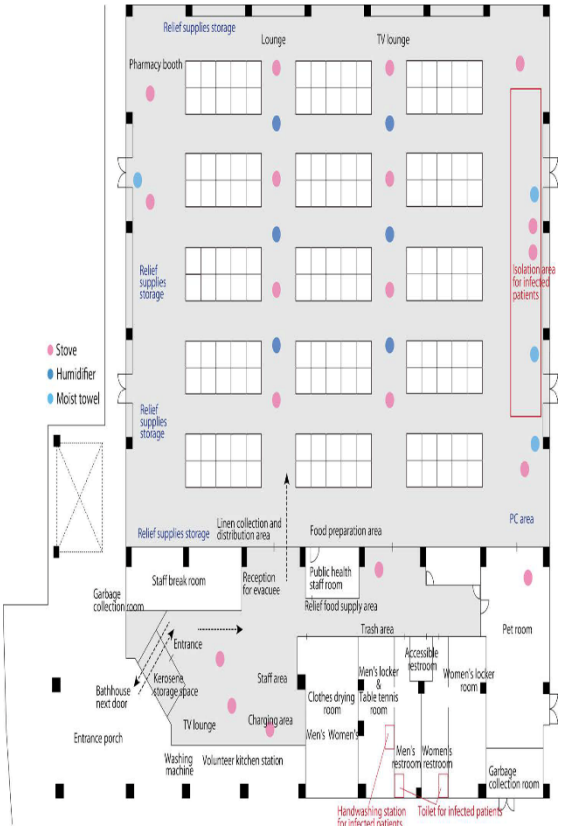

Figure 1. Shelter Layout of Nukadani Fureai Gymnasium: The feature of the layout is that the living area was located within the arena, separated from the operational area. This arrangement ensured the privacy of the evacuees while also allowing the shelter to be open to the media, making it possible to communicate the current situation of the shelter. As a result, many offers of relief supplies and food assistance were received.

In February, as infectious disease cases began to occur daily, a designated area for isolating infected individuals was established. Since this had not been anticipated at the time of the shelter' s opening, several issues arose—such as the area being located near the wall, making it cold, and the traffic flow overlapping with routes to the toilets.

4th International Symposium on One Health, One World
November 20 – 22, 2025

ABS ID: OP-03
Code No: IMSBE-OP-49

Smartphone-Based Ground Penetrating Radar for Millimeter-Scale Damage Assessment in Concrete Structures

T. Mizutani[1], And S. Iwai[3]
[1]*Associate Professor, Institute of Industrial Science, The University of Tokyo, Tokyo, Japan,*
[2]*Graduate Student, Institute of Industrial Science, The University of Tokyo, Tokyo, Japan,*
Correspond to Dr. T. MIZUTANI (mizu-t@iis.u-tokyo.ac.jp)

***Keywords**: Ground Penetrating Radar, Concrete Damage, Frequency Analysis, Spectral Matching, Non-Destructive Testing, Smartphone Sensing.*

1. INTRODUCTION

The degradation of infrastructure systems has become a critical global concern, as bridges, tunnels, and pavements constructed several decades ago are now reaching or exceeding their design life [1]. In Japan and other developed nations, the transition from reactive to preventive maintenance is urgently required to reduce inspection costs and prevent catastrophic failures [2]. Ground Penetrating Radar (GPR) is a promising non-destructive technology in this context, capable of visualizing subsurface conditions based on electromagnetic reflections between materials of different permittivities [3,4].

Traditional handheld GPR systems are widely used for locating rebars or buried utilities but have difficulty identifying subtle defects such as delamination, cracks, or voids due to weak reflections and overlapping signals [5]. Moreover, inspection results often depend on the subjective interpretation of experienced operators. To overcome these limitations, this study develops a smartphone-based handheld GPR system and a frequency-domain algorithm that can automatically and quantitatively estimate internal damage thickness in concrete with millimeter-scale precision and real-time processing capability.

2. SYSTEM AND METHODOLOGY

2.1 GPR System Configuration

The prototype radar system operates within a frequency range of 700–3500 MHz, using an impulse transmission system. The main sensor unit (approximately 1 kg, 149×207 mm) connects wirelessly to a smartphone, which functions as both processor and display. LED guide lines assist the operator in maintaining a constant scanning path, while real-time spectral analysis is executed through a dedicated mobile application. The antenna's broadband frequency ensures high depth resolution and adequate penetration in concrete up to approximately 300 mm.

2.2 Example of GPR Signals and Experimental Setup

Concrete specimens of 300 × 300 × 60 mm were prepared with air gaps between 2 mm and 180 mm to simulate different damage thicknesses. Acrylic spacers with 0.1 mm precision were inserted to form the voids, and the top of each defect was fixed at a depth of 60 mm. Measurements were repeated five times at three positions for each thickness, yielding 1,350 A-scan waveforms. Data from intact specimens were subtracted from

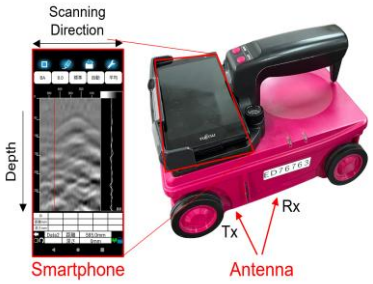

Figure 1. Overview of the Smartphone-Mounted Handheld GPR System

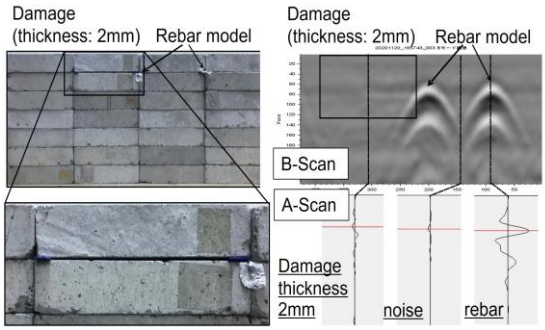

Figure 2. Example of A-Scan and B-Scan Signals from Concrete Specimens (example waveforms showing rebar reflection and 2 mm defect response after background subtraction)

damaged ones to eliminate surface reflections and isolate internal signals [6].

2.3 Frequency-Domain Approach and Spectral Modeling

Estimating the thickness of internal damage from time-domain peaks alone is often unreliable, because multiple reflections and overlapping signals obscure the boundaries of defects. To address this issue, the present study employs a frequency-domain approach that analyzes the overall spectral characteristics of the received radar signal rather than individual peaks.

In this method, the reflected wave from the damaged region is considered as a combination of multiple reflections from the upper and lower boundaries of the void. The interference between these reflections produces distinctive oscillations in the amplitude spectrum. The pattern and periodicity of these spectral oscillations change systematically with the thickness of the defect.

By comparing the measured frequency spectrum with a set of theoretical spectra corresponding to different thicknesses, it becomes possible to estimate the damage quantitatively. Theoretical spectra were generated based on known reflection properties and propagation velocities in concrete, and their relationship to defect thickness was experimentally validated.

Figure 3 illustrates examples of these theoretical spectra for typical damage thicknesses ranging from 2 mm to 180 mm. As the thickness increases, the frequency intervals between adjacent peaks in the spectrum become narrower, providing a clear physical basis for spectral pattern matching.

3. RESULTS AND DISCUSSION

The developed system accurately estimated defect thicknesses between 2 mm and 180 mm. The correlation between measured and estimated values reached $R^2 \approx 0.99$, confirming high precision (Fig. 4). The mean estimation error was below ±3 mm for most specimens, with larger deviations only in thin defects (<10 mm) due to reduced signal-to-noise ratios.

The computation time per waveform was approximately 0.001 s, enabling genuine real-time evaluation. This marks a substantial improvement over conventional time-of-flight or impact-echo methods, which often require extensive post-processing [7]. The frequency-domain approach captured subtle interference effects caused by multiple reflections, which are not easily discernible in time-domain analysis.

In comparison with previous qualitative GPR studies [8,9], the present method provides a truly quantitative evaluation of internal concrete damage, achieving both accuracy and field applicability. Its portability and low cost also make it suitable for bridge decks, tunnel linings, and pavement inspections where rapid measurements are required. The results confirm that handheld GPR integrated with smartphone processing can serve as a practical solution for preventive maintenance and digital inspection programs [2].

4. CONCLUSIONS

This study introduced a compact, smartphone-integrated Ground Penetrating Radar capable of estimating internal concrete damage thickness quantitatively in real time.

By combining amplitude and spectral centroid indicators with optimized spectral pattern matching, the algorithm successfully achieved millimeter-level precision from 2 mm to 180 mm.

The computation time of 0.001 s per waveform demonstrates the feasibility of deploying this technique in real-world field inspections. The developed method

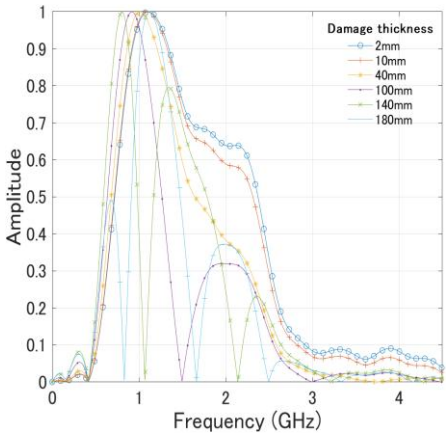

Figure 3.

Theoretical Spectra for Various Damage Thicknesses (frequency-domain spectra for representative damage thicknesses of 2, 10, 40, 100, 140, and 180 mm)

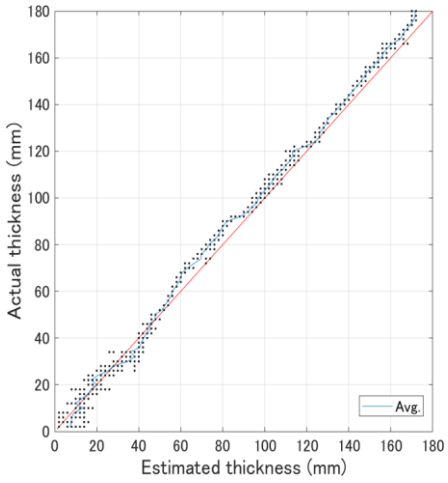

Figure 4. Correlation between Estimated and Actual Damage Thickness

transforms handheld GPR from a qualitative detection tool into a quantitative diagnostic instrument.

Future work will focus on extending this approach to multilayered concrete and reinforcement corrosion evaluation.

REFERENCES:

[1] W. Choate and S. Pat, America in Ruins: The Decaying Infrastructure, Duke Press, 1983.

[2]MLIT, Infrastructure Maintenance Information, Ministry of Land, Infrastructure, Transport and Tourism, Japan, 2022.

[3] J. Hugenschmidt, Construction and Building Materials, 16(3):147–154, 2002.

[4] T. Saarenketo and T. Scullion, Journal of Applied Geophysics, 43(2–4):119–138, 2000.

[5] K. Dinh et al., Automation in Construction, 125:103652, 2021.

[6] R. Kiyoshi, Development of a Method for Detecting Internal Defects in Concrete Using Electromagnetic Radar Method, PhD Thesis, The University of Tokyo, 2021.

[7] C. Cheng and M. Sansalone, Materials and Structures, 26(5):274–285, 1993.

[8] S. Tanaka and M. Yamada, Transactions of the Society of Instrument and Control Engineers, 39(5):432–440, 2003.

[9] T. Uomoto and S.K. Park, Journal of the Japan Society of Civil Engineers, (592):13–24, 1998.

Electronic Poster Presentations

4th International Symposium on One Health, One World
November 20 – 22, 2025

ABS ID: 82
Code No: IMSBE-EP-01

Performance Assessment of Recycled Aggregate Concrete Sourced from Construction and Demolition Waste

Govind Gaurav[1], Vishal Kumar[2]
[1]*Scientist, Advanced Concrete, Steel & Composites, CSIR-CBRI, Roorkee, India,*
[2]*Project Associate, Advanced Concrete, Steel & Composites, CSIR-CBRI, Roorkee, India,*
Correspond to Dr. Govind Gaurav (govindgaurav@cbri.res.in; ggaurav.rkmv@gmail.com)

Keywords*: Natural Aggregates (NA), Recycled Concrete Aggregate (RCA); Recycled Aggregate Concrete (RAC); Valorization; Carbon sequestration; Statistical Analysis; Cumulative density function.*

Abstract: Utilizing recycled concrete aggregates (RCA) in concrete production plays a vital role in enhancing waste management practices and contributes significantly to the sustainable advancement of the concrete industry. In light of this, the present study conducts an experimental investigation to evaluate the mechanical performance through compressive strength at 28 and 56 days on selective substitution (0%, 50% and 100%) of natural aggregates (NA) with RCA sourced from construction and demolition waste (Burari Plant, New Delhi, India) with a nominal aggregate size of 10 mm. One of the key findings observed during the study is a reduction in slump values, indicating a decrease in workability as the proportion of RCA increases in the mix. Compressive strengths of 31 MPa and 35 MPa were obtained for control concrete at 28- and 56–days, respectively, whereas a nominal increase in compressive strength was observed on valorization (using carbonation). At 100% replacement of NA with RCA, a decrease of 24% and 22% in compressive strength was observed at 28- and 56-days, respectively. When RCAs are valorized (using carbonation) and are completely substituted with NA, an increase of 17% and 13% in compressive strength was observed at 28- and 56-days, respectively. Cumulative distribution functions—such as normal, lognormal, weibull, and gamma distributions—are utilized in statistical analysis to identify the most appropriate governing model. It is observed that for NAC and on selective substitution (50% and 100%) of NA with RCA, the Lognormal distribution for the compressive strength best represents the test results at 28 days. In contrast, at 56 days, the lognormal distribution best represents the compressive strength of control concrete and at 100% replacement of NA with RCA. For 50% substitution Weibull distribution best represents the test results for compressive strength. When the valorization of the RCA through carbonation of the RCA is carried out, and is selectively substituted, the lognormal distribution best represents the test results at 28- and 56 days, except for 100% replacement of NA with RCA, where the gamma distribution best represents the compressive strength of concrete.

1.Introduction

The construction industry is primarily reliant on conventional raw materials like cement, sand, and aggregates. However, rising demand and limited natural resources have created questions regarding sustainability, environmental effects, and long-term availability. As a result, there is a greater emphasis on researching alternative materials, such as industrial byproducts, recycled trash, and eco-friendly composites, to prevent the loss of resources and encourage sustainable construction methods. Over the last decade, the rising demand has driven greater reliance on natural aggregate sources, with production climbing from 21 billion tonnes in 2007 to 50 billion tonnes in 2017. This upward trend is projected to continue, reaching an estimated 60 billion tonnes by 2030 [1]. This indicates rapid urban growth, marked by extensive new construction activities and a rise in the demolition of old structures. Construction and demolition (C&D) waste can either be sent to landfills or repurposed for low-value applications such as aggregates in granular base or sub-base layers, non-structural concrete, embankment building, and various

earthworks with limited attention towards its structural applications [2,3].

The mechanical properties of a cementitious system are influenced by several factors, including cement content, aggregate characteristics, water–cement ratio, supplementary materials, fiber content, workability, and the mixing procedure. In concrete containing RCA, the mechanical performance is further affected by the residual mortar adhering to the original aggregate. Enhancing the cement content and using high-quality aggregates can significantly improve the mechanical properties of RAC. Additionally, RCA can be modified through techniques that either remove the porous attached mortar or reinforce it, thereby increasing the overall density and strength of the concrete [4].

Recycled Concrete Aggregate (RCA) is different from natural aggregate (NA) because it includes two additional parts: leftover mortar and a transition area (ITZ) where the NA meets the original cement mortar, resulting in higher porosity and water absorption but lower strength. The adhered mortar on RCA can be removed using various physical and chemical treatments to enhance aggregate quality. Mechanical treatment involves abrasion or crushing to physically detach the mortar, while thermal treatment uses high temperatures to weaken the bond between mortar and aggregate [5–9]. Thermo-mechanical methods combine heat and grinding for more effective removal [10–12]. Electrical treatment applies high-voltage pulses to separate the materials without excessive crushing [13]. Water treatment employs high-pressure jets to erode the mortar, and chemico-mechanical treatment uses chemical agents to soften the mortar before mechanical removal [14,15]. These methods help improve the density, strength, and durability of RCA for use in new concrete. Alternatively, increasing the density of the permeable mortar increases the strength of concrete [16–18].

Duan *et al.* [19] found that using RCAs in self-compacting concrete slightly reduced strength and durability, and that recycled powder further lowered performance due to fine particle agglomeration. Tang *et al.* [20] found that recycled powder had a greater negative impact than coarse RCAs. Adding recycled powder reduces the normalized stress-strain curve of concrete. Wang et al. explored how carbonation affects the performance of concrete with RCAs with various parameters under consideration and concluded that carbonation enhances the interfacial characteristics with the greatest effect for a higher water-cement ratio [21]. The grade of RCAs significantly affects the distribution pattern of concrete containing RCAs. RCAs differ significantly from concrete with natural aggregates due to their non-uniform distribution [22].

2.Research Significance

In recent years, RCA has arisen as a sustainable alternative to NCA, since demand for natural resources has increased. Despite extensive studies comparing NCA and RCA concrete, there is a lack of a variability-based model to estimate the compressive strength of RAC. This investigation is targeted towards the development of a variability-based model for concrete to estimate the compressive strength of concrete made with RCAs and carbonated RCAs at 28- and 56-day, which can aid in probabilistic design of structures and in risk evaluation.

Experimental Program

3.1 Materials

The Portland cement employed in the study is of 43 Grade with the specific gravity of 3.15 and conforms to IS 8112-2013 [23]. Locally available river sand of Zone II and a nominal maximum size of 10 mm (natural coarse aggregates) was used in the investigation (IS 383:2016) [24]. The Recycled Concrete Aggregates of nominal size 10 mm was sourced from the construction and demolition plant at Burari, New Delhi. The granular size distribution of NCA and RCA is comparable. However, RCA (Specific Gravity-2.48) has a lower density than NCA (Specific Gravity-2.70). Additionally, RCA has a larger water absorption rate (5.7%) than NCA (1%). Aggregate crushing and impact values were assessed using IS: 2386 – 2021 [25]. RCA has a higher impact (23.1 for RCA and 18.8 for NCA) and abrasion values (22.2 for RCA and 19 for NCA) compared to NCA. The carbonation of the RCA was carried out using a Carbonation Chamber (Greenovate Instruments Make, India).

3.2 Concrete Mix Proportions

The control mix (AR1) was designed as per IS 10262:2016 [26] with the various ingredients

as displayed in Table 1. The NA and RCA are used in a saturated-surface-dry condition. Coarse aggregates were immersed in water for 24 hours to achieve a saturated surface dry (SSD) condition. Thereafter, selective substitution (50 % and 100%) of NA with RCA is carried out using the equivalent volume method. The control mix (AR1) consisted solely of natural aggregates, whereas AR2 contained an equal proportion of natural aggregates and recycled concrete aggregates (RCAs) by volume. In AR3, natural aggregates were completely replaced with 100% RCAs. Thereafter, valorization of the RCA is carried out through carbonation. During valorization, the RCA is kept in a pressure vessel, and slowly, the CO_2 is injected at a constant pressure of 3 bar. Thereby, carbonated RCAs are used to develop various mixes such as AR2* (50% NA and 50% carbonated RCA) and AR3* (0% NA and 100% carbonated RCA).

Table 1: Proportions of the concrete mixture.

Mix ID	RCA replacement level (%)	Content (kg/m^3)				
		Cement	Fine aggregate	NCA	RCA	Mixing water
AR1	0	360	830	1055	0	194
AR2	50	360	830	528	484	194
AR3	100	360	830	0	970	194
AR1*	0	360	830	1055	0	194
AR2*	50	360	830	528	484	194
AR3*	100	360	830	0	970	194

Mix ID: The alphabet in the first place-holder represents the grade of concrete (A: Normal-strength); the alpha-numeric character at second and third place represents the RCA replacement levels (R1: 0%, R2: 50%, R3:100%, R1*: cubes are valorized (carbonated), R2*: carbonated 50% RCA, R3*: carbonated 100% RCA)

3.3 Methods

Six cubes of size 150 mm × 150 mm × 150 mm are cast in each lot, and compressive strength is calculated at 28- and 56-day ages at a loading rate of 140 kg/cm^2/min, in compliance with IS 516:2021 [27]. Four statistically determined distributions (normal, lognormal, weibull and gamma) were employed for analyzing the compressive strength data for AR1, AR2, AR3, AR1*, AR2* and AR3* samples. To select the best-fitted model for compressive strength data, various strategies were utilized, such as modified Kolmogorov-Smirnov (KS), loglikelihood (LK), and minimal chi-square criterion.

1. Results and Discussion

4.1 Fresh Properties

The slump of the material provides a measurement of the concrete's shear stress at the moment of concreting. In accordance with IS 1199:2023, the workability of the concrete produced using NCA and RCA (AR1, AR2, AR3, AR2* and AR3*) was assessed using the slump test. A slump of 80 mm was obtained for control concrete (AR1). However, slump values increased to 90 mm (AR2, AR2*) and 95 mm (AR3, AR3*), respectively, when the volumetric substitution of RCA with NCA was 50% and 100%. When treated RCA completely replaced NCA, Tam *et al.* [28] reported the greatest reduction. This was attributed to the lower water absorption of RCA, leaving more free water in the mix to increase its slump. Conversely, Nagaraj *et al.* [29] observed that as the RCA replacement level increased from 0% to 100%, the slump also increased, owing to the water demand of RCA.

4.2 Compressive Strength

The compressive strength of the concrete cube of size 150 mm× 150 mm× 150 mm was cast and tested without and with valorized (using carbonation) RCAs, and the results are compiled in **Tables 2** and **3**, respectively, at various levels of substitution (0%, 50% and 100%) of NA with RCA. It is observed that at 28 days for unvalorized RCAs there is 11% and 24% decrease in compressive strength at 50% and 100% replacement, respectively, with reference to control concrete whereas at 56 days there is 17% and 22% decrease in

compressive strength at 50% and 100% replacement, respectively, with reference to the control concrete. Also, it is observed that with valorization (using carbonation) and at 100% replacement of NA with valorized RCAs, there is an increase of 17% in compressive strength at 28 days, and at 56 days, there is an increase of 13% in compressive strength. The increase in the strength is due to the reaction mechanism in which $Ca(OH)_2$, present in attached adhered mortar, reacts with CO_2 during valorization to form the precipitates of $CaCO_3$ in the pores, resulting in densification due to mineral carbonation.

Table 2: Compressive Strength of Control Concrete and Recycled Aggregate Concrete.

Parameter	Compressive Strength (28 days), MPa			Parameter	Compressive Strength (56 days), MPa		
AR1 (Control) Mean: 31.28	33.82	33.90	31.15	AR1 (Control) Mean: 35.44	35.55	37.50	34.29
	32.64	30.65	31.22		36.01	38.83	33.84
	30.21	31.10	32.21		30.94	33.48	34.46
	29.21	32.11	30.16		38.36	36.77	35.93
	32.15	31.15	30.68		37.37	36.64	36.82
	30.62	31.90	29.10		33.52	33.36	39.74
	32.22	30.21	29.64		31.94	34.41	35.61
	31.22	33.21	30.25		35.24	34.29	35.55
AR2 (50% RCA) Mean:	28.94	25.82	28.85	AR2 (50% RCA) Mean:	25.17	32.81	24.16
	30.70	30.43	31.78		31.20	28.25	28.79
27.85	31.96	26.75	32.36	29.40	25.74	28.40	32.73
	24.53	28.87	25.95		31.89	22.84	34.97
	26.22	25.38	28.38		28.56	23.13	32.11
	25.65	26.92	29.30		25.98	27.84	31.48
	30.20	28.80	26.50		33.67	32.12	33.61
	24.20	25.68	24.20		31.27	30.50	28.42
AR3 (100% RCA) Mean: 23.24	21.87	23.44	21.48	AR3 (100% RCA) Mean: 27.42	23.03	21.75	22.08
	22.10	26.30	22.50		36.65	30.59	23.85
	23.45	21.65	25.50		30.20	34.40	28.74
	26.00	24.30	25.60		25.88	25.21	31.17
	21.62	20.62	21.65		23.53	26.77	28.44
	22.62	22.80	21.60		26.91	24.04	30.39
	23.60	23.92	23.51		25.65	27.73	27.58
	22.52	26.51	22.56		27.27	24.68	31.49

Table 3: Compressive Strength of Control Concrete and Recycled Aggregate Concrete with Valorization (*using* Carbonation).

Parameter	Compressive Strength (28 days), MPa			Parameter	Compressive Strength (56 days), MPa		
AR1 (Control)	33.98	32.58	32.55	AR1 (Control)	35.40	34.50	33.90
	34.23	30.65	31.22		36.50	38.40	39.50

Mean: 32.05	30.21	31.10	32.21	**Mean: 36.68**	37.40	35.90	36.00
	33.50	32.11	35.40		37.40	36.50	37.00
	32.15	31.15	30.68		36.00	34.50	36.00
	36.50	31.90	29.10		36.80	38.20	40.10
	32.22	33.30	26.50		37.50	33.50	39.50
	32.44	33.21	30.25		35.40	36.20	38.20
AR2* (50% RCA) Mean: 23.99	22.62	24.19	22.23	**AR2* (50% RCA) Mean: 29.87**	26.52	33.56	24.91
	22.85	27.05	23.25		29.30	29.00	29.54
	24.20	22.40	26.25		26.49	29.15	33.48
	26.75	25.05	26.35		32.64	23.59	34.20
	22.37	21.37	22.40		29.31	23.88	32.86
	23.37	23.55	22.35		26.73	28.59	32.23
	24.35	24.67	24.26		31.20	32.87	34.36
	23.27	27.26	23.31		32.02	31.25	29.17
AR3* (100% RCA) Mean: 27.39	27.98	30.60	27.50	**AR3* (100% RCA) Mean: 30.94**	34.40	30.34	34.09
	26.50	27.50	28.05		28.82	29.62	31.82
	26.50	25.50	27.50		31.50	32.05	29.60
	25.50	27.25	28.60		27.50	29.50	31.05
	28.50	26.50	25.50		31.05	32.20	29.50
	25.50	26.30	25.50		28.50	31.50	32.05
	27.50	28.50	27.50		31.85	32.50	29.50
	28.50	28.05	30.60		31.50	30.50	31.50

Poon et al. [8] observed that on complete replacement of NA with RCA in high-performance concrete, there is a decrease of 7.2% in compressive strength, whereas a marginal decrease in compressive strength was observed on 50% replacement of NA with RCA. Similarly, a decrease [30–32] in compressive strength was observed at various levels of substitutions. On the contrary, Pedro et al. [7] observed an increase in compressive strength with age.

4.3 Statistical analysis for mechanical properties of normal and recycled aggregate concrete

Probability density functions like normal, lognormal, Weibull and gamma distributions can be used to quantify the quality assurance of the concrete made with NCA, RCA and carbonated RCA at selective levels of substitution (0%, 50% and 100%). The various cumulative density functions for the concretes are shown in **Figures 1** and **2**.

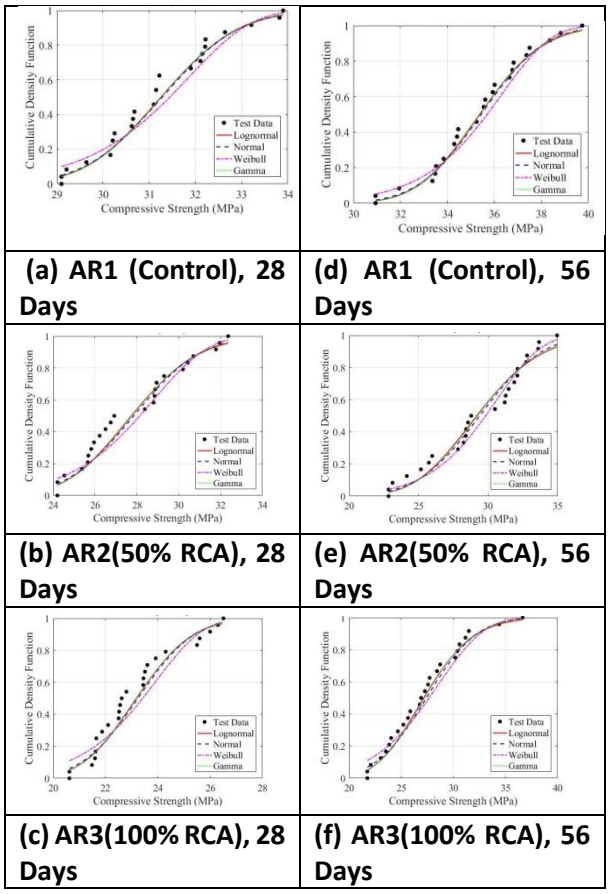

(a) AR1 (Control), 28 Days | (d) AR1 (Control), 56 Days

(b) AR2(50% RCA), 28 Days | (e) AR2(50% RCA), 56 Days

(c) AR3(100% RCA), 28 Days | (f) AR3(100% RCA), 56 Days

Figure 1: Cumulative density function of compressive strength of natural aggregate concrete (NAC) and recycled aggregate concrete (RAC) at 28 and 56 days

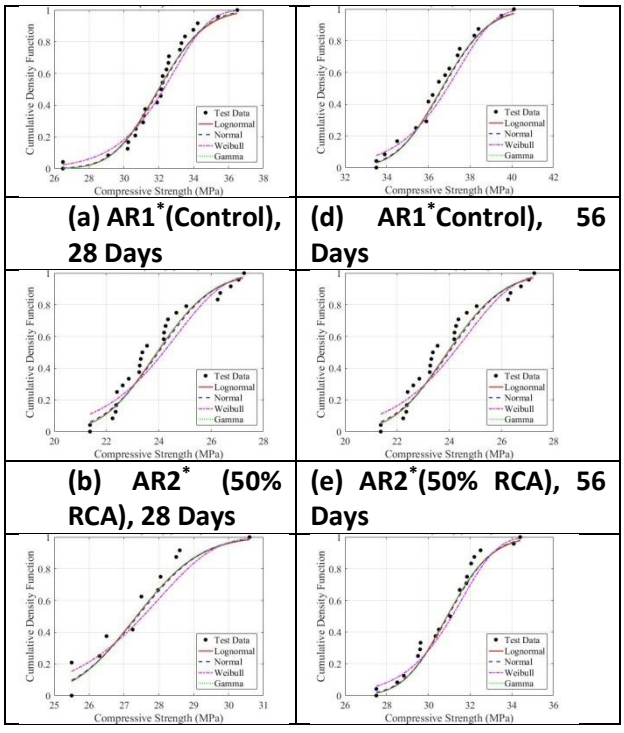

(a) AR1*(Control), 28 Days | (d) AR1*Control), 56 Days

(b) AR2* (50% RCA), 28 Days | (e) AR2*(50% RCA), 56 Days

(c)A R3* (100% RCA), 28 Days	(f) AR3*(100% RCA), 56 Days

Figure 2: Cumulative density function of compressive strength of natural aggregate concrete (NAC) and recycled aggregate concrete (RAC) at 28 and 56 days with valorization (using Carbonation).

Goodness-of-fit tests are used to measure the distribution's suitability for representing mechanical properties. At a significance level of 5%, the KS, LK, and CS goodness-of-fit tests are employed in this investigation. The model with the lowest KS distance and CS value is the one that generates the most suitable probability distribution. Additionally, the probability distribution with the largest LK value is thought to be more appropriate. It's also critical to keep in mind that, in the event that there was any ambiguity between the findings of the three tests, the KS and LK test results were prioritized while doing goodness-of-fit testing. When there are numerous random variables to look at, the CS test is recommended. The goodness-of-fit test parameters (KS distance and CS and LK values) of concrete made without and with carbonation for various statistical distributions are compiled in **Tables 4** and **5**, respectively.

Table 4: Goodness of fit parameters for the statistical distribution of mechanical properties of concrete without carbonation at 28 and 56 days.

Mix ID	Distribution	28 days			56 days		
		KS	CS	LK	KS	CS	LK
AR1	Lognormal	0.125	0.015	-40.064	0.112	0.119	-51.490
	Normal	0.125	0.339	-40.215	0.112	0.054	-51.641
	Weibull	0.170	1.147	-42.256	0.145	0.033	-52.707
	Gamma	0.125	0.266	-40.098	0.112	0.094	-51.650
AR2	Lognormal	0.167	0.188	-55.600	0.140	0.099	-64.286
	Normal	0.167	0.356	-55.822	0.138	0.309	-63.653
	Weibull	0.167	0.044	-56.881	0.138	0.122	-62.887
	Gamma	0.167	0.249	-55.644	0.140	0.162	-64.027
AR3	Lognormal	0.167	0.803	-45.698	0.080	0.066	-64.856
	Normal	0.167	1.040	-46.175	0.105	0.268	-65.586
	Weibull	0.208	1.805	-48.398	0.120	0.624	-67.341
	Gamma	0.167	0.901	-45.834	0.080	0.112	-65.032

Note: Kolmogorov–Smirnov (KS), the loglikelihood (LK), and the minimal chi-square criterion (CS)

Table 5: Goodness of fit parameters for the statistical distribution of mechanical properties of concrete with carbonation at 28 and 56 days.

Mix ID	Distribution	KS	CS	LK	KS	CS	LK
AR 1	Lognormal	0.1167	0.1090	-51.2792	0.1127	0.2102	-46.2360
	Normal	0.1167	0.1436	-50.9059	0.1127	0.2988	-46.8967
	Weibull	0.1483	0.6612	-51.6690	0.1544	1.0314	-48.3570
	Gamma	0.1167	0.1159	-51.1219	0.1127	0.2311	-46.8386
AR 2	Lognormal	0.1667	0.8099	-45.7117	0.1667	0.8099	-45.7117
	Normal	0.1667	1.0397	-46.1751	0.1667	1.0397	-46.1751
	Weibull	0.2083	1.8149	-48.4222	0.2083	1.8149	-48.4222
	Gamma	0.1667	0.9064	-45.8436	0.1667	0.9064	-45.8436
AR 3	Lognormal	0.1894	0.5358	-42.1668	0.1944	0.9079	-45.8163
	Normal	0.1894	0.6925	-42.5056	0.1944	0.7254	-45.8078
	Weibull	0.2955	1.5144	-45.1711	0.2222	0.1936	-47.1844
	Gamma	0.1894	0.5710	-42.2998	0.1944	0.8489	-45.7926

Note: Kolmogorov–Smirnov (KS), the loglikelihood (LK), and the minimal chi-square criterion (CS)

It is observed that for NAC and on selective substitution (50% and 100%) of NA with RCA, the Lognormal distribution for the compressive

strength best represents the test results at 28 days, whereas at 56 days, the lognormal distribution best represents the compressive strength of control concrete and at 100% replacement of NA with RCA. For 50% substitution Weibull distribution best represents the test results for compressive strength. When the valorization of the RCA through carbonation of the RCA is carried out, and is selectively substituted, the lognormal distribution best represents the test results at 28- and 56 days, except for 100% replacement of NA with RCA, where the gamma distribution best represents the compressive strength of concrete.

The distribution pattern changes based on the crack propagation from the old ITZ (interfacial transition zone) and the new ITZ [33]. Also, this is due to the fact that RCAs and natural aggregates have different material properties in terms of crushing, impact, and abrasion values, which influence the shift in the distribution pattern.

5. Conclusion

This investigation is targeted towards the development of variability-based models that best suit the experimental results for compressive strength. Therefore, the following conclusions are drawn from the study:

1. At 28 days, unvalorized RCAs showed compressive strength reductions of 11% and 24% for 50% and 100% replacement levels, respectively, compared to control concrete. By 56 days, these reductions were 17% and 22%, respectively. However, with valorization through carbonation, 100% replacement of NA with valorized RCAs resulted in a 17% strength increase at 28 days and a 13% increase at 56 days.
2. For NAC, when natural aggregates (NA) were partially replaced with RCA at 50% and 100%, the compressive strength at 28 days was best described by a lognormal distribution. At 56 days, the lognormal distribution also best fit the results for control concrete and 100% RCA replacement, while the Weibull distribution was more suitable for 50% replacement. With RCA valorized through carbonation, the lognormal distribution best represented compressive strength results at both 28 and 56 days, except in the case of 100% replacement, where the gamma distribution provided the best fit.

Acknowledgement

The work reported is a part of the work carried out by the funding received in the Project No: OLP 2226 from CSIR-CBRI, Roorkee, India. The assistance & support of the staff and students at Advanced Concrete, Steel & Composites Group are gratefully acknowledged.

References:

[1] G. Gaurav, N. Kotoky, V. Jittin, A. Bahurudeen, Performance assessment of recycled aggregate concrete and its variability, Struct. Concr. (2023) 1–12. https://doi.org/10.1002/suco.202200794.

[2] N. Tošić, S. Marinković, T. Dašić, M. Stanić, Multicriteria optimization of natural and recycled aggregate concrete for structural use, J. Clean. Prod. 87 (2015) 766–776. https://doi.org/10.1016/j.jclepro.2014.10.070.

[3] E. Rigo, G.P. Gava, E.F. Felix, P.M. Borges, E. Possan, Concrete with recycled aggregates from construction: Properties, emissions and carbon capture assessment, Case Stud. Constr. Mater. 23 (2025) e04983. https://doi.org/10.1016/j.cscm.2025.e04983.

[4] M. Ibrahim, W. Alimi, R. Assaggaf, B. Abiodun, An overview of factors influencing the properties of concrete incorporating construction and demolition wastes Heating Air classification System Ordinary Portland cement, Constr. Build. Mater. 367 (2023) 130307. https://doi.org/10.1016/j.conbuildmat.2023.130307.

[5] M.S. de Juan, P.A. Gutiérrez, Study on the influence of attached mortar content on the properties of recycled concrete aggregate, Constr. Build. Mater. 23 (2009) 872–877. https://doi.org/10.1016/j.conbuildmat.2008.04.012.

[6] S. Nagataki, A. Gokce, T. Saeki, M. Hisada, Assessment of recycling process induced damage sensitivity of recycled concrete aggregates, Cem. Concr. Res. 34 (2004) 965–971.

https://doi.org/10.1016/j.cemconres.2003.11.008.

[7] D. Pedro, J. de Brito, L. Evangelista, Structural concrete with simultaneous incorporation of fine and coarse recycled concrete aggregates: Mechanical, durability and long-term properties, Constr. Build. Mater. 154 (2017) 294–309. https://doi.org/10.1016/j.conbuildmat.2017.07.215.

[8] C.S. Poon, Z.H. Shui, L. Lam, Effect of microstructure of ITZ on compressive strength of concrete prepared with recycled aggregates, Constr. Build. Mater. 18 (2004) 461–468. https://doi.org/10.1016/j.conbuildmat.2004.03.005.

[9] S. Yehia, K. Helal, A. Abusharkh, A. Zaher, H. Istaitiyeh, Strength and Durability Evaluation of Recycled Aggregate Concrete, Int. J. Concr. Struct. Mater. 9 (2015) 219–239. https://doi.org/10.1007/s40069-015-0100-0.

[10] K. Bru, S. Touzé, F. Bourgeois, N. Lippiatt, Y. Ménard, Assessment of a microwave-assisted recycling process for the recovery of high-quality aggregates from concrete waste, Int. J. Miner. Process. 126 (2014) 90–98. https://doi.org/10.1016/j.minpro.2013.11.009.

[11] H. Choi, M. Lim, H. Choi, R. Kitagaki, T. Noguchi, Using Microwave Heating to Completely Recycle Concrete, J. Environ. Prot. (Irvine,. Calif). 05 (2014) 583–596. https://doi.org/10.4236/jep.2014.57060.

[12] N. Lippiatt, F. Bourgeois, Investigation of microwave-assisted concrete recycling using single-particle testing, Miner. Eng. 31 (2012) 71–81. https://doi.org/10.1016/j.mineng.2011.09.017.

[13] I. V. Lisitsyn, H. Inoue, S. Katsuki, H. Akiyama, Use of inductive energy storage for electric pulse destruction of solid materials, IEEE Trans. Dielectr. Electr. Insul. 6 (1999) 105–108. https://doi.org/10.1109/94.752017.

[14] F. Kazemian, H. Rooholamini, A. Hassani, Mechanical and fracture properties of concrete containing treated and untreated recycled concrete aggregates, Constr. Build. Mater. 209 (2019) 690–700. https://doi.org/10.1016/j.conbuildmat.2019.03.179.

[15] Y. Kim, A. Hanif, S.M.S. Kazmi, M.J. Munir, C. Park, Properties enhancement of recycled aggregate concrete through pretreatment of coarse aggregates – Comparative assessment of assorted techniques, J. Clean. Prod. 191 (2018) 339–349. https://doi.org/10.1016/j.jclepro.2018.04.192.

[16] X. Fang, B. Zhan, C.S. Poon, Enhancing the accelerated carbonation of recycled concrete aggregates by using reclaimed wastewater from concrete batching plants, Constr. Build. Mater. 239 (2020) 117810. https://doi.org/10.1016/j.conbuildmat.2019.117810.

[17] A.M. Grabiec, J. Klama, D. Zawal, D. Krupa, Modification of recycled concrete aggregate by calcium carbonate biodeposition, Constr. Build. Mater. 34 (2012) 145–150. https://doi.org/10.1016/j.conbuildmat.2012.02.027.

[18] D. Xuan, B. Zhan, C.S. Poon, Durability of recycled aggregate concrete prepared with carbonated recycled concrete aggregates, Cem. Concr. Compos. 84 (2017) 214–221. https://doi.org/10.1016/j.cemconcomp.2017.09.015.

[19] Z. Duan, A. Singh, J. Xiao, S. Hou, Combined use of recycled powder and recycled coarse aggregate derived from construction and demolition waste in self-compacting concrete, Constr. Build. Mater. 254 (2020) 119323. https://doi.org/10.1016/j.conbuildmat.2020.119323.

[20] Y. Tang, J. Xiao, H. Zhang, Z. Duan, B. Xia, Mechanical properties and uniaxial compressive stress-strain behavior of fully recycled aggregate concrete, Constr. Build. Mater. 323 (2022) 126546. https://doi.org/10.1016/j.conbuildmat.2022.126546.

[21] C. Wang, J. Xiao, G. Zhang, L. Li, Interfacial properties of modeled recycled aggregate concrete modified by carbonation, Constr. Build. Mater. 105 (2016) 307–320. https://doi.org/10.1016/j.conbuildmat.2015.12.077.

[22] X. Jianzhuang, L.I. Wengui, P. Chisun, Recent studies on mechanical properties of recycled aggregate concrete in China — A review, 55 (2012) 1463–1480. https://doi.org/10.1007/s11431-012-4786-9.

[23] IS 269:2015 (Reaffirmed 2020), Ordinary Portland Cement-Specifications, BIS. 2015 (2020) 1–13.

[24] IS 383:2016, Coarse and Fine Aggregate for Concrete-Specification, BIS. (2016) 1–21.

[25] IS 2386 (Part-1)-1963 (Reaffirmed 2021), Method of test for aggregates for concrete, BIS. 32 (2021) 1–23. https://doi.org/10.4324/9780203967874-16.

[26] IS 10262:2019, Concrete Mix Proportioning-Guidelines, BIS. 02 (2019) 1–44.

[27] IS 516 : 2020, Hardened concrete - Methods of test, BIS. 54 (2020) 1–20. www.standardsbis.in.

[28] V.W.Y. Tam, X.F. Gao, C.M. Tam, C.H. Chan, New approach in measuring water absorption of recycled aggregates, Constr. Build. Mater. 22 (2008) 364–369. https://doi.org/10.1016/j.conbuildmat.2006.08.009.

[29] V.K. Nagaraj, D.L. Venkatesh Babu, Formulation and performance evaluation of alkali-activated self-compacting concrete, Asian J. Civ. Eng. 19 (2018) 1021–1036. https://doi.org/10.1007/s42107-018-0081-9.

[30] M. Etxeberria, E. Vázquez, A. Marí, M. Barra, Influence of amount of recycled coarse aggregates and production process on properties of recycled aggregate concrete, Cem. Concr. Res. 37 (2007) 735–742. https://doi.org/10.1016/j.cemconres.2007.02.002.

[31] M.C. Limbachiya, T. Leelawat, R.K. Dhir, Use of recycled concrete aggregate in high-strength concrete, Mater. Struct. Constr. 33 (2000) 574–580. https://doi.org/10.1007/bf02480538.

[32] M. Shahria Alam, E. Slater, A.H.M. Muntasir Billah, Green Concrete Made with RCA and FRP Scrap Aggregate: Fresh and Hardened Properties, J. Mater. Civ. Eng. 25 (2013) 1783–1794. https://doi.org/10.1061/(asce)mt.1943-5533.0000742.

[33] J. Xiao, H. Li, Z. Yang, Fatigue behavior of recycled aggregate concrete under compression and bending cyclic loadings, Constr. Build. Mater. 38 (2013) 681–688. https://doi.org/10.1016/j.conbuildmat.2012.09.024.

4th International Symposium on One Health, One World
November 20 – 22, 2025

ABS ID:150
Code No: IMSBE-EP-02

Performance Of Perforated Concrete Filled Steel Tube (Cfst) Under Flexural Loading Condition

Preeti[1,2] And P. Kar[3,4]
[1] *Senior Research Fellow, CSIR-Central Building Research Institute, Roorkee, Uttarakhand, India,*
[2] *PhD Scholar, Academy of Scientific and Innovative Research (AcSIR), Ghaziabad, Uttar Pradesh, India,*
[3] *Scientist, CSIR-Central Building Research Institute, Roorkee, Uttarakhand, India*
[4] *Assistant Professor, Academy of Scientific and Innovative Research (AcSIR), Ghaziabad, Uttar Pradesh, India,*

Keywords: *CFST, Beam, Perforation, Flexure.*

1. INTRODUCTION

A Concrete Filled Steel Tube (CFST) comprises concrete encased in a steel tube, offering delayed local buckling and enhanced load carrying capacity due to the confining effect [1]. Researchers have worked on the CFST beams in the past [2-5], which demonstrate greater stiffness, ductility, and high energy absorption capacity[6]. Perforations serve inspection, maintenance, wiring, as well as optimization [7-8]. This study aims to examine the behaviour of the CFST beams with perforation.

2. EXPERIMENTAL PROGRAM

2.1. Material Properties of Concrete and Steel

Concrete cubes of (150×150×150) mm were cast with each specimen set and were tested under the Universal Testing Machine (UTM), achieving an average compressive strength of ~40 MPa. Table 1 shows the concrete mix details. Tensile coupon specimens were made to determine steel material properties from a 2.8 mm-thick steel tube. The dimensions of coupon and loading protocol was in accordance with ASTM standard [9]. The mean values of Ea, fy, and fu were 199.37, 273, and 353.5 MPa, respectively.

Table 1. Concrete mix design details

Ingredients	Cement	Sand	C.A.	F.A.
Mix (kg/m^3)	400.0	668.7	1177.3	180.0

2.2 Specimens details

Three specimens were tested by varying the number of perforations, maintaining dimensions: CFST-P0 (defines a CFST beam with 0 perforations), similarly, CFST-P1, and CFST-P3. The perforations were made at the compression flange with a welded side at the beam depth. CFST-P1 had a central mid-span perforation, while CFST-P3 had two additional equidistant perforations from the centre. These perforations enabled concrete filling and vibration.

2.3. Test setup

A loading frame with a hydraulic jack of 50T was used to test the specimens with a four-point bending mechanism. A rigid beam distributed two point loads was distributed on the CFST beam. The clear span was 1000 mm, and the shear span of 100 mm between the beam ends and supports. Two LVDTs measured the applied load and the mid-span deflection. The strain was measured at the tensile zone at each loading interval.

3.RESULTS AND DISCUSSIONS

The behaviour of the CFST beams and failure pattern were analysed. The results obtained by the beam specimen are shown in Table 2.

Table 2: CFST Specimen Result

Specimen ID	**Pu (kN)**	**Percentage**
CFST-P0	292.3	-
CFST-P1	266.6	8.79%
CFST-P3	235.7	19.33%

3.1. Load Vs mid-span deflection

Figure 1 shows the load vs. mid-span deflection. It was observed that specimens CFST-P1 and CFST-P3 show a decrease of 8.79 % and 19.33% compared to CFST-P0.

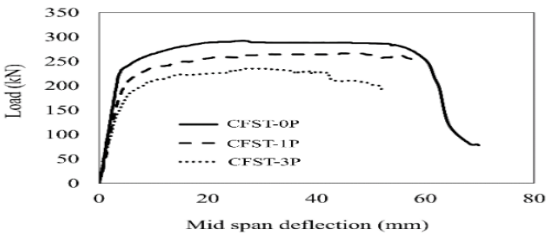

Figure 1: Load vs. mid-span deflection

3.2 Length vs. Deflection

The deflection of the mid span was measured by the LVDTs placed at the bottom. Results are shown in Figure 2. The curves resemble a symmetric half sine wave. Maximum deflection occurred in CFST-0P at the failure, and the CFST-3P showed the least mid-span deflection.

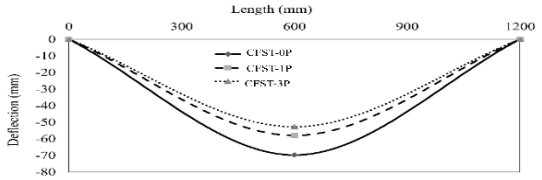

Figure 2: Length Vs Deflection

3.3. Load vs strain curve

The load vs. strain graph is plotted in Figure 3, where a strain gauge was placed at the bottom central mid span of the specimen in the tensile zone. The strain obtained from the tensile zone is positive.

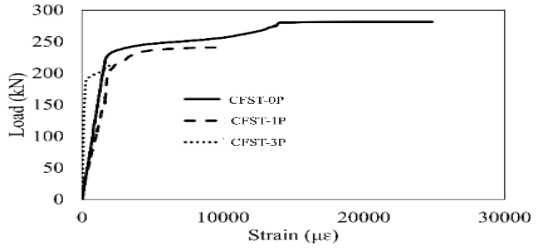

Figure 3: Load Vs Strain

3.4. Failure modes

Figure 4 shows the failure modes of specimens. CFST-0P shows outward buckling and tearing of the steel tube in the tensile zone of the beam (Figure 4(a)). After removing the outer steel skin, cracks were distributed throughout the beam in the local buckling zone, with major cracks at the tearing location. Figure 5 (b) shows CFST-1P specimen failure, where local buckling occurred only at the perforated region. The crack in the steel tube was observed under the perforation location, with inner cracks concentrated near the tearing zone of the steel tube. The CFST-3P specimen showed similar failure patterns, with the failure observed only at the middle perforation site. No effect was seen in the other two perforation sites. Crushing of the concrete occurred at the middle perforation site, along with the crushing of concrete similar to CFST-1P.

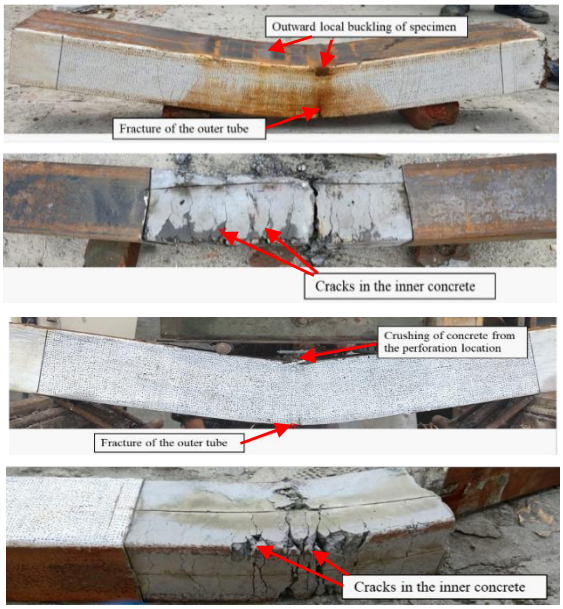

(a)

(b)

Figure 4: Failure modes obtained in specimens (a) CFST-P0 and (b) CFST-P1

4.CONCLUSIONS

From the experimental study conducted, the following conclusions can be drawn-

1) CFST beams primarily showed local buckling in the compression zone and tearing of the steel tube in the tensile region in the controlled specimen. With the introduction of the perforation, the failure location became predefined, and the local buckling occurred only in the central perforated region.

2) It was observed that with the introduction of perforation, the strength of beam drops

significantly and the increase in the number of perforations further reduces the strength.

REFERENCES:

[1] X. L. Zhou, L. H. Han, and H. Lu, Concrete Filled Tubular Members and Connections. 2005.

[2] L. Han, H. Lu, G. Yao, and F. Liao, "Further study on the flexural behaviour of concrete-filled steel tubes," J. of Constructional Steel Res.,vol.62,pp.554565,2006,doi:10.1016/j.jcsr.2005.09.002.

[3] F. H. Abed, Y. I. Abdelmageed, and A. K. Ilgun, "Flexural response of concrete-filled seamless steel tubes," J. Constr. Steel Res., vol. 149,pp.5363,2018,doi:10.1016/j.jcsr.2018.06.030.

[4] F.Abed, Y. Abdelmageed, and Y. Alhoubi, "Effect of different cross-sections and concrete types on the flexural behavior of CFSTs," Compos. Struct., vol.. 276, no. March, p. 114570,2021,doi:10.1016/j.compstruct.2021.114570.

[5] G. Li, D. Liu, Z. Yang, and C. Zhang, "Flexural behavior of high-strength concrete-filled high-strength square steel tube," JCSR, vol. 128, pp. 732–744,2017,doi: 10.1016/j.jcsr.2016.10.007.

[6]L.H. Han, W. Li, and R. Bjorhovde, "Developments and advanced applications of concrete-filled steel tubular (CFST) structures: Members," J. Constr. Steel Res., vol. 100, pp. 211–228,2014,doi: 10.1016/j.jcsr.2014.04.016.

[7] Z.Yao and K. J. R. Rasmussen, "Thin-Walled Structures Inelastic local buckling behaviour of perforated plates and sections under compression," Thin Walled Struct., vol. 61, pp. 49–70, 2012, doi: 10.1016/j.tws.2012.07.002.

[8] T.G. Ghazijahani, H. Jiao, and D. Holloway, "In fl uence of a cutout on circular steel hollow sections under cyclic loading," JCSR, vol. 100, pp.1220,2014,doi:10.1016/j.jcsr.2014.04.015.

[9] A.E8, "ASTM, E8/E8M-15a, Standard Test Methods for Tension Testing of Metallic Materials,in:ASTMInternational,WestConshohocken, PA, 2015", doi: 10.1520/E0008.

2025 HOW

4th International Symposium on One Health, One World
November 20 – 22, 2025

ABS ID:195
Code No: IMSBE-EP-02

Studies On Development of Portland Dolomite Cement (Pdc) Using High Mgo Limestone and Dolomitic Limestone

Varsha Liju, Pinky Pandey, Diksha Rana, Mamta Pawar, S K Chaturvedi, L P Singh
*National Council for Cement and Building Materials**

ABSTRACT

The main aim of this study is to focus on the possibilities of utilizing hitherto unutilized high MgO / dolomitic limestone in cement manufacturing. Cement is manufactured by calcining naturally available argillaceous and calcareous materials at a high temperature releasing large amount of CO2 into the atmosphere. The reduction in the consumption of clinker/ cement will not only reduce the cost of cement production but also the emission of CO2. Lot of limestone quarries have dolomitic limestone inclusions or overburden that cannot be used for cement production. On the other hand, issues like CO2 reduction and natural resource conservation can be mitigated by manufacturing blended cements that have so far stood the test of time and limestone based blended cements are also a viable option. Existing limestone-based cement standards recommend use of high-grade limestone and not low grade or dolomitic limestone. Comparison of mineral characteristics of limestone and dolomite minerals shows that both are similar in nature with minor dissimilarities.

This paper examines the possibility of using dolomitic limestone as partial replacement material to cement. The replacement percentages tried were 5%, 10%, 15%, 20% and 25% as mineral additive. The performance evaluation of the prepared cement blends were carried out as per relevant BIS standard methods. The performance characteristics of cements with dolomitic limestone was compared with cement prepared with cement grade limestone. The results showed the conformity of all the prepared PDC (Portland dolomite cement) & PLC (Portland Limestone Cement) cement blends as per the BIS standard specification for blended cements. On comparison of PDC and PLC cement blends both results revealed marginally enhanced compressive strength in PDC cement blends at latter ages (28 day).

Key Words: Portland Limestone Cement, Dolomite, Dolomitic Limestone, High MgO Limestone

1.0 Introduction

Over the last more than two decades, the effects of using limestone in Portland cement have been well studied. The benefits of limestone as a partial replacement for PC are well established. Its economic and environmental advantages of reducing CO2 emissions are also well known.

One of the major achievements of the cement and concrete industries during the past years is the increasing use of mineral additions. Firstly, since the production of Portland cement clinker is an energy-intensive process, a partial substitution of clinker by mineral additions obviously represents considerable energy savings. Secondly, it makes economic sense to reduce the energy used in the production of cement and concrete and at the same time

make a safe use of what sometimes can be classified as an industrial waste. Lastly, the substitution of mineral additions for clinker lowers the CO2 emission of the cement and concrete industries. Common mineral additions are granulated blast furnace slag,

silica fume, fly ash and limestone filler. Blended cements using uncalcined limestone powder are manufactured and used in many countries as limestone is naturally available, cheap and is a basic raw material in clinker production. Many papers based on investigations of influence of limestone powder on hydration of Portland cement have been reported. Research data revealed that limestone powder not only plays the role of an inert mineral filler (inert additive) but also accelerates the hydration rate of Portland cement at early stage. Portland limestone cement is one of the most widely used cement types in the Europe and is becoming increasingly accepted worldwide. Contrarily, the use of dolomite/ dolomitic limestone/ high MgO limestone as a cement component is rare. The European Standard EN 197-1 defines the minimum requirements for the use of limestone as a cementitious material [1-5]. According to this standard, the calcium carbonate content (CaCO3) of the limestone should be greater than or equal to 75%.

The following tables 1.1 and 1.2 show the % of limestone used in cement in various countries [6-7].

Table 1.1: **Percentages of Limestone Allowed in PLC in Various Countries**

Country/Relevant standard	Year	Per cent of Limestone allowed in PLC
Germany	1965	Allowed 20 per cent limestone to cement
France	1979	Allowed up to 35 per cent addition of slag, fly ash, and limestone in new cement type.
Europe, EN 197-1	1987	Portland Kalkstein cement which consists of 85+/- per cent of clinker and 15+/- of limestone
Canada CSA A 3001	1998	Allowed addition of 5-15 per cent of limestone in cement
United Kingdom BS 7583	1992	Permitted use of 20per cent of limestone in cement in
Europe, EN 197-1	2000	Allowed addition of limestone from 6 to 35 per cent, CEM II/A-L (6-20per cent) and CEM II/B-L (21-35per cent), $CaCO_3 \geq$ 75per cent
U.S., ASTM C-595 and AASHTO M 240	2012	Allowed up to 5-15 per cent limestone in all types of cement, $CaCO_3$ min. 70per cent
Mexico/ NMX C-414	--	Permits up to 35 per cent of Limestone
Brazil/ NBR 11578	1991	Maximum of 10 per cent of limestone is permitted
New Zealand/ NZS 3125	1991	PLC is being produced up to 15 per cent of limestone

Table 1.1: Percentages of Limestone Allowed in

Main type	Notation of the PLC products		Composition (percentage by mass)			
			Main constituents			
			Clinker	Limestone		Minor additional constituents (MAC)
			K	L	LL	
CEM II	Portland limestone cement-PLC	CEM II/A-L	80-94	6-20	-	0-5
		CEM II/B-L	65-79	21-35	-	0-5
		CEM II/A-LL	80-94	-	6-20	0-5
		CEM II/B-LL	65-79	-	21-35	0-5
➢ $CaCO_3$ content ≥ 75 per cent and clay content ≤ 1.20 gram /100 gram. ➢ Type LL limits total organic carbon (TOC) content < 0.20 per cent by weight ➢ whereas Type L restricts TOC < 0.50 per cent by weight.						

Table 1.2: Portland Limestone Cement Types: As per European Standard (EN 197-1)

whereas Type L restricts TOC < 0.50 per cent by weight.

However, with the estimated increase in the requirement of cement in the near future, the limestone with CaCO3 content ≥ 75 per cent is required to be preserved for clinker manufacture. Thus in the present work using dolomitic limestone as partial replacement material to cement is being considered essential. [8-10]. Hence in this work, the replacement of cement was tried with 5%, 10%, 15%, 20% and 25% of dolomitic limestone as mineral additive. The compressive strength of cements with dolomite powder was compared with those prepared with cement grade limestone.

2.0

Experimental work

2.1 Material Used

For the purpose of this study, raw materials are clinker, limestone, dolomitic/high MgO limestone and gypsum were collected from cement plant situated in different zones of the country. The collected samples were crushed using a laboratory jaw crusher and were homogenised by quartering and conning to prepare representative samples. The samples were then ground in a laboratory ball mill to pass 150 micron IS sieve.

The detail of the raw materials collected from different zones is given in the Table 2.1 below:

Table 2.1 List of raw materials collected from cement plants

Sl. No	Clinker obtained from following zones	Notation
1.	Clinker from Central Zone	C-Ct
2.	Clinker from West Zone	C-Wt
3.	Cement Grade Limestone from Central Zone	LST-Ct
4.	Cement Grade Limestone from West Zone	LST-Wt
5.	Dolomitic Limestone obtained from Central Zone	DLS-Ct
6.	Dolomitic Limestone obtained from West Zone	DLS-Wt

2.2 Instrumentation:

All the raw materials used in the study were analyzed to estimate their chemical composition as per the relevant Indian standard codes. The results of chemical analysis is depicted in Table 1. The mineralogical analysis of the samples were done by X-ray diffractometer using the instrument of Rigaku, Japan (Rigaku International, Japan, D-Max 2200V/PC using CuKα radiation). The quantitative analysis of mineral phases were carried out using Rietveld method. The granulometry, microstructure and mineralogy were also studied by using optical microscope, by NIKON 100 POL. The performance evaluation of the prepared blends was carried out by relevant Indian standard codes.

2.3 Experimental method:

2.3.1

Preparation of Portland Limestone and Portland Dolomite Limestone Based Cement Blends

The characterized raw materials from central and western region comprising of clinkers (C-Ct and C-wt) , dolomitic limestone (DST-Ct and DST-Wt), cement grade limestone (LST-Ct and LST-Wt) and Gypsum were used for the preparation cement blends (PDC). For the purpose of comparison Portland limestone cement (PLC) were also prepared.

A total of 20 blends were prepared, 10 cement blends (5 PDC + 5 PLC) each from central and western region. The sulphate content in the prepared blends were maintained at 3.0±0.2%. The percentages of the various raw material constituents of clinker, dolomitic limestone and limestone used for the

preparation of the 20 cement blends are being depicted in Table 2.2. The Blaine fineness was maintained at 350 ± 20 m2/kg.

Results and Discussion

3.1 Chemical analysis of Portland Clinker Samples

The chemical analysis of Portland clinker samples C-Ct and C-Wt collected showed presence of usual oxide constituents with free lime content in the range of 0.83-0.93 indicating well burnt clinker samples (Table 3.1). The chemical analysis of clinker samples showed their conformity to Indian standard specification IS: 16353-2015 Portland clinker. The chemical analysis of dolomitic limestone sample DLS-Ct and DLS-Wt and cement grade limestone samples LST Wt and LST-Ct showed that the CaO content was in the range of 47-48% in cement grade limestone and 30– 41% dolomitic limestone. The silica content was in the range of 6-8% in cement grade limestone and 1-8%% in dolomitic limestone.

The MgO content was in the range of 1.4-2.1% in cement grade limestone and 6.75 -17.8% in dolomitic limestone. The calcite content (CaCO3) calculated from the percentage of lime in the sample was in the range of 77-82% in cement grade limestone, 67-70% in low grade and dolomitic limestone. Similarly, the magnesite content (MgCO3) calculated from the percentage of MgO in the sample was in the range of 1 – 4.5% in cement grade limestone and 32.2% dolomitic limestone. The total carbonates

in the limestone samples was in the range of 77-94% in the limestone samples.

Table 2.2. Designed composition of PDC & PLC cement blends

Oxide Constituents (%)	C-Ct	C-Wt	IS 16353: 2015	DST-Ct	DST-Wt	LST-Ct	LST-Wt	Gypsum
LOI	0.93	0.83	≤1.5	41.76	43.71	40.63	38.34	19.85[a]
CaO	64.19	62.72	-	30.02	40.24	48.28	47.09	32.90
SiO_2	20.10	19.70	-	6.28	2.86	5.96	8.05	1.27[b]
Al_2O_3	6.03	5.44	-	1.68	0.31	1.40	2.14	0.45
Fe2O3	3.54	4.18	-	1.46	0.27	0.44	1.24	0.31
MgO	5.84	2.40	≤6	17.74	11.62	2.65	1.49	1.47
SO3	0.45	1.62	≤2.7	0.01	0.05	0.01	0.01	46.38
Na2O	0.13	0.53	-	0.05	0.38	0.07	0.2	0.02
K2O	0.63	0.76	-	0.48	0.82	0.22	0.33	0.06
IR	0.007	0.022	≤1.0					0.013
Chloride	1.2	1.6	≤0.1					-
Free lime	0.93	0.83	≤3.0					-
Combined Water	-	-	-					15.95

S.No	Cement Samples	Clinker + Gypsum	Dolomitic limestone	Limestone
1	**PDC – 1**	99	1	-
2	**PDC – 2**	98	2	-
3	**PDC – 3**	97	3	-
4	**PDC – 4**	96	4	-
5	**PDC – 5**	95	5	-
6	**PDC – 10**	90	10	-
7	**PDC – 15**	85	15	-
8	**PDC – 20**	80	20	-
9	**PDC – 25**	75	25	-
10	**PLC – 1**	99	-	1
11	**PLC – 2**	98	-	2
12	**PLC – 3**	97	-	3
13	**PLC – 4**	96	-	4
14	**PLC – 5**	95	-	5
15	**PLC – 10**	90	-	10
16	**PLC – 15**	85	-	15
17	**PLC – 20**	80	-	20
18	**PLC – 25**	75	-	25

The chemical analysis of gypsum sample is also given in the Table 3.1. Gypsum sample was analyzed for its oxide constituents and showed 46.38% SO3, 32.9% CaO and 19.85% combined water (Table 3.1). The purity of gypsum based on SO3 content was found to be 95.43% based on the assumption that gypsum present in the form of CaSO4.2H2O.

The moduli value of clinker samples such as Lime Saturation Factor (LSF), Silica Modulus (SM), Alumina Modulus (AM) and potential phases C3S, C2S, C3A and C4AF as determined on the basis of Bogue' calculations are also given in Table 3.2.

Table 3.1: Chemical analysis of raw materials

Table 3.2: Potential Phases and Moduli Values of clinker

	C-Ct	**C-Wt**	**IS 16353: 2015**
Tricalcium silicate (C_3S), %	56.78	51.92	35
Dicalcium silicate (C_2S), %	14.82	17.33	
Tricalcium aluminate (C_3A), %	10.00	7.39	3-12
Alumino-ferrite (C_4AF), %	10.77	12.72	
Moduli Values-			
Lime Saturation Factor (LSF)	0.89	0.80	0.66-1.02
Silica Modulus (SM)	2.11	2.57	-
Alumina Modulus (AM)	1.53	1.73	≥0.66

3.2 Mineral composition Portland Clinker Samples by XRD

XRD analysis of Portland clinker samples showed presence of usual clinker mineral phases; alite, belite, aluminate and ferrite along with periclase [MgO] in small amount as shown in Figures 3.1 and 2.2. Semi-quantitative estimation of clinker mineral phases, in clinker samples C-Ct and C-Wt was carried out Alite and belite contents of clinker samples C-Ct and C-Wt were found to be in between 53.1 & 56.7% and 22.7 & 22.1% respectively as given in Table 3.3 indicating their good quality. The XRD pattern of clinker C-Ct and C-Wt are given in Fig 3.1 and 3.2.

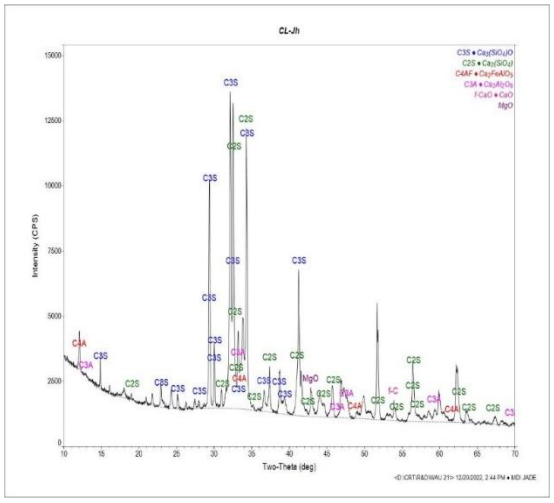

Fig 3.1: X-ray diffraction pattern of clinker C-Ct

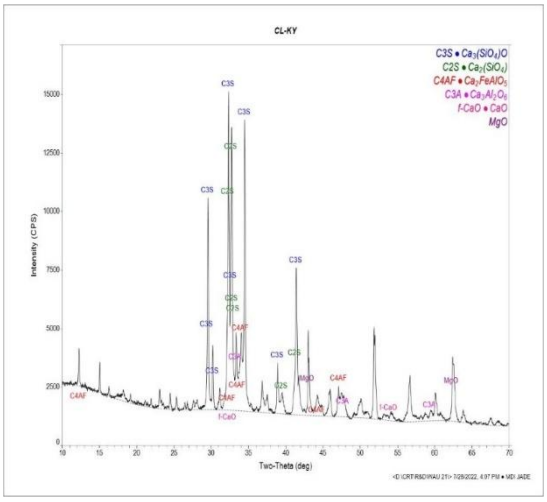

Fig 3.2: X-ray diffraction pattern of clinker C-Wt

Table 3.3: Semi-quantitative estimation of clinker mineral phases by XRD

Phases detected	Clinker Notation	
	C-Ct	C-Wt
Alite [$Ca_{54}MgAl_2Si_{60}O_{90}$]	53.1	56.7
Belite[Ca_2SiO_4]	22.7	22.1
Calcium aluminate [$Ca_3Al_2O_6$]	5.2	5.7
Calcium alumina ferrite [[$Ca_2(Al,Fe)_2{}^2O_5$]	12.8	14.6
Minor phases including periclase	6.2	1.5

3.3 Microstructure of Clinker C-Ct and C-Wt

The clinker phases are moderately developed and inhomogeneously distributed. Majority of alite grains are pseudo hexagonal to lath shaped with both broken and sharp grain margins. Numerous inclusions are present in alite grains. Bleb shaped belite grains are present as inclusions in alite grains. Pitted structure is also observed in alite grains. Grain size variation in alite is too large. Transformation of belite into alite did not reach equilibrium conditions. Majority of alite grains are in the size range of 25 µm to 31 µm. Most of belite grains are sub rounded to rounded in shape with ragged margins. Both one and two set twinning are developed in belite grains. Majority of belite grains are in the size range of 12 µm to 20 µm. Various belite clusters with different shapes and sizes are uniformly developed in the sample. Both alite and belite are developed in various polymorphic forms. Fused alite and belite grains are also developed in the sample. Enlargement of aluminate (C3A) grains are also noticed, which

may be due to slow cooling. Both orthorhombic and cubic forms of aluminate grains are developed. Pores of various shapes and sizes (40 to 450 µm) are uniformly distributed in the nodules. Porosity of the clinker is high. The percentage of alite and belite were 48 and 32% respectively with 21% interstitial matter. The optical micrograph of C-Ct and C-Wt are given in Fig 3.3 and 3.4.

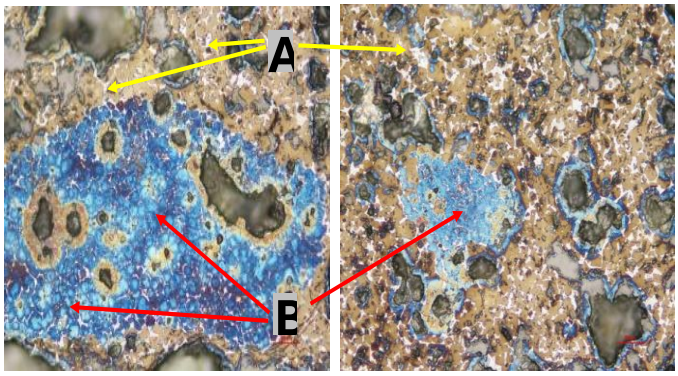

Distribution of alite and belite (20x)

Belite cluster surrounded by grains (20x)

Fig 2.3: Optical micrograph of clinker C-Ct (A-alite, B-belite)

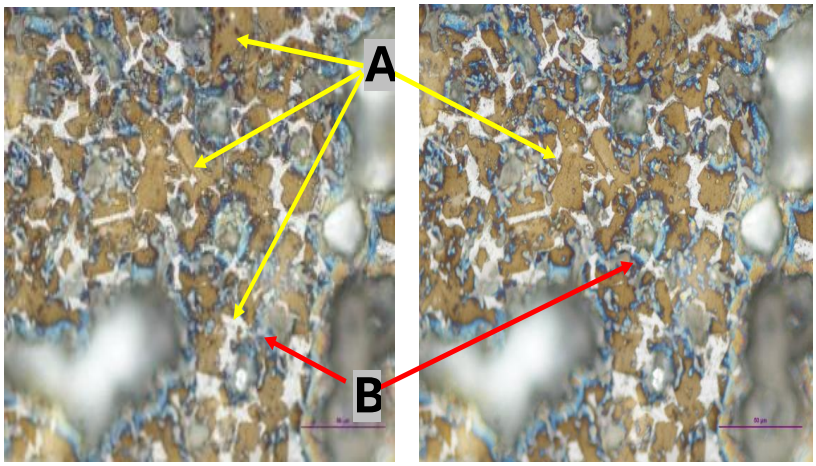

Development of alitegrainswith fractured margins(50x)

Distribution of alite & belite grains(100x)

Fig 2.4: Optical micrograph of clinker C-Wt (A-alite, B-belite)

3.4 Bond Grindability Index of Portland Clinker Samples

The Bond Grindability Indices of clinker samples C-Ct and C-Wt were determined according to test procedure described in Indian standard IS: 10218-2006 and the values are given in Table 2.7.

Table 2.6: Bond grindability index of clinker samples

Clinker code	Bond grindability index (kwh/short- ton)
C-Ct	15.1
C-Wt	16.1

3.5 Performance evaluation of PDC & PLC cement blends

The performance evaluation of the both cement blends were carried out as per relevant BIS standard methods and the results showed the conformity of all the prepared PDC & PLC cement blends as per the BIS standard specification for blended cements. The mechanical properties of the prepared cement blends are given in Table 3.4 and 3.5.

Table 3.4. Performance evaluation of the PDC and PLC of central region

Name	Compressive Strength, MPa (in %)						Setting Time, min	
	1D	3D	7D	28D	90 D	NC	IST	FST
PDC – 5	24.0	33.0	41.0	51.5	59.5	26.0	135	180
PDC – 10	22.0	29.5	40.0)	51.0	56.0	26.0	150	200
PDC – 15	21.0	27.0	35.5	48.5	55.0	25.0	150	210
PDC – 20	16.0	26.0	31.5	40.0	52.5	25.0	170	220
PDC – 25	14.0	22.0	26.5	37.0	45.5	25.3	190	240
PLC – 5	23.0	31.5	38.0	52.0	52.0	24.8	115	175
PLC – 10	20.5	33.0	38.5	47.0	47.0	25.0	140	200
PLC – 15	18.0	27.5	34.5	42.0	42.0	24.8	140	210
PLC – 20	13.5	22.0	30.0	36.0	36.0	25.0	130	205
PLC - 25	10.0	18.5	24.5	32.0	32.0	24.5	140	210

The performance evaluation of PDC and PLC blends of central region depicted that the normal consistency of PDC slightly decreased from 26.0 to 25.0 as dolomitic limestone content is increased to 25%. Also in PLC blends the normal consistency varies. The setting time increases as the dolomitic limestone content in PDC increases and also with addition of limestone. The compressive strength of all the prepared PDC and PLC cement blends comply with the limits given in the specification of blended cement. On comparison of PDC and PLC cement blends with equal clinker replacement it is observed that strength of PDC blends is better than PLC blends.

Table 3.4. Performance evaluation of the PDC and PLC of western region

Name	Compressive Strength, MPa (in %)						Setting Time, min	
East	1D	3D	7D	28D	90 D	NC	IST	FST
PDC – 5	28.5	35.0	41.5	47.0	56.5	22.8	105	140
PDC – 10	23.0	30.5	38.5	41.5	54.5	23.0	115	150
PDC – 15	20.0	27.0	35.0	43.0	49.0	24.3	110	160
PDC – 20	16.5	26.5	32.0	44.5	44.5	24.5	130	170
PDC – 25	19.0	29.5	33.0	40.0	44.0	24.5	110	150
PLC – 5	25.0	31.5	38.0	47.5	54.5	24.5	105	155
PLC – 10	23.5	30.5	37.0	42.5	53	24.3	115	150
PLC – 15	20.5	29.5	36.0	41.0	50.5	24.5	125	170
PLC – 20	19.5	27.0	32.5	36.0	49.5	24.0	115	150
PLC - 25	17.0	26.5	31.0	36.0	49	24.3	100	135

The performance evaluation of PDC and PLC blends of western region The normal consistency of PDC slightly increased from 22.8 to 24.5% as dolomitic limestone content is increased to 25%. In PLC blends the normal consistency is stable. The setting time increases as the dolomitic limestone content in PDC increases and also with addition of limestone but the value decreases after 20% addition. The compressive strength of all the prepared PDC and PLC cement blends comply with the limits given in the specification of blended cement. On comparison of PDC and PLC cement blends with equal clinker replacement it is observed that strength of PDC blends is better than PLC blends. The graph representing the use of dolomitic limestone as mineral additive is shown in Fig 3.2.

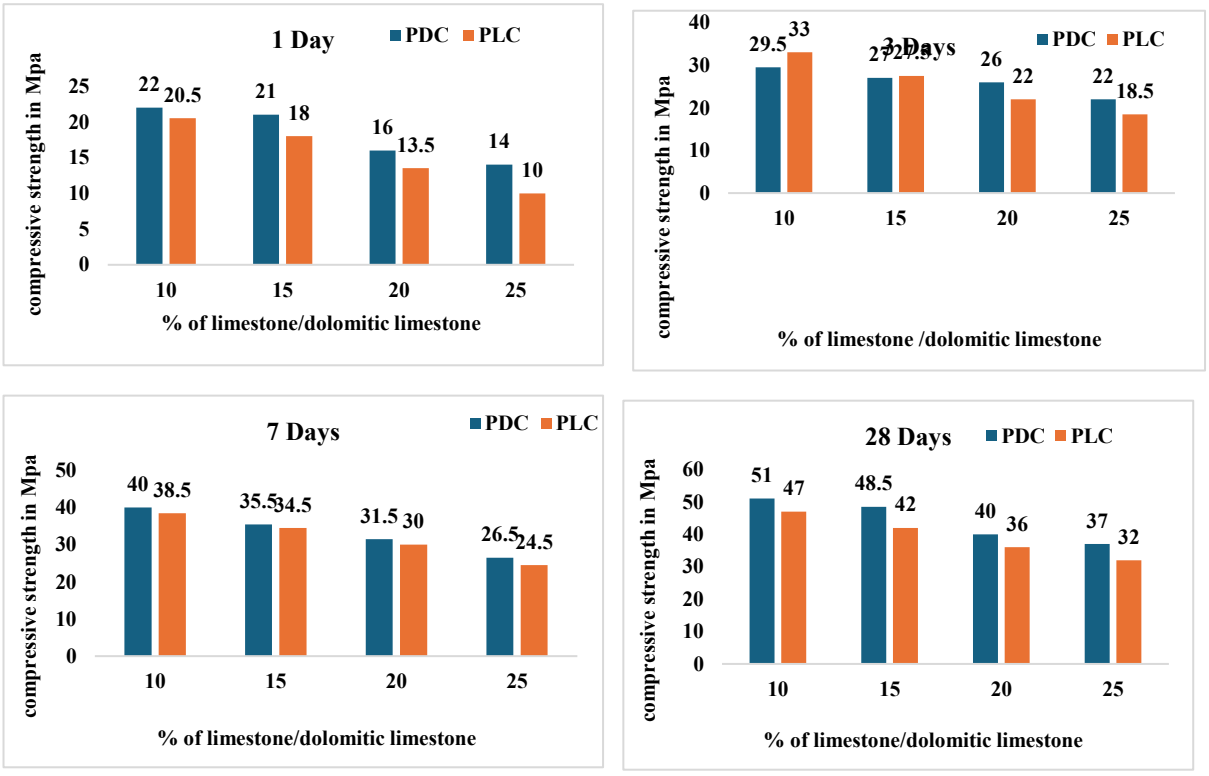

Fig 3.2: Graph representing the use of dolomitic limestone as mineral additive

4.0 Conclusion

•Cement blends were prepared using dolomitic limestone with 11% and 17% of MgO, cement grade limestone, gypsum and clinker samples from two different regions of the country.

•5%, 10%, 15%, 20% and 25% replacement of clinker with dolomitic limestone were designed and Portland limestone cement with similar composition was also prepared for comparison.

•The performance evaluation of PDC and PLC blends of the two region were studied

•The normal consistency of PDC slightly increased from 22.8 to 24.5% as dolomitic limestone content was increased to 25% in cement blends of western region. In PLC blends the normal consistency was stable.

•The setting time increases as the dolomitic limestone content in PDC increases and also with addition of limestone but the value decreases after 20% addition.

•The compressive strength of all the prepared PDC and PLC cement blends comply with the limits given in the specification of blended cement.

•On comparison of PDC and PLC cement blends with equal clinker replacement it is observed that strength of PDC blends is better than PLC blends.

References:

[1] European Standard EN 197-1. EN 197-1: Composition, specifications and conformity for common cements. 2000;1–29.

[2] ASTM C 150. Standard Specification for Portland Cement.

[3] AASHTO M85. Standard Specification For Portland Cement. 2009.

[4] Barbhuiya S. Effects of fly ash and dolomite powder on the properties of self-compacting concrete. Construction and Building Materials. 2011;25:3301–3305.

[5]Tong L, Tang M. Correlation between reaction and expansion of alkali-carbonate reaction. Cement and concrete research. 1995;25:470–476.

[6]Allahverdi A, Salem S. Simultaneous influences of microsilica and limestone powder on properties of portland cement paste. Ceramics-Silikaty. 2010;54:65–71.

[7]Kopanitsa NO, Anikanova LA, Makarevich MS. Fine additives filled with binders based on cement. Journal of Building Materials. 2002;9:2–4.

[8] Mikhailova O, Yakovlev G, Maeva I, et al. Effect of Dolomite Limestone Powder on the Compressive Strength of Concrete. Procedia Engineering. 2013;57:775–780.

[9]Zajac M, Haha M Ben. Hydration of limestone and dolomite cement. Proceedings of the 14th International Congress on the Chemistry of Cement. 2015.

[10] Zajac M, Bremseth SK, Whitehead M, et al. Effect of CaMg (CO3) 2 on hydrate assemblages and mechanical properties of hydrated cement pastes at 40□C and 60□C. Cement and concrete research. 2014;65:21–29.

[11] Xu J, Lu D, Zhang S, et al. Pore structures of mortars with dolomite and limestone powders

ABS ID: -112
Code No: IMSBE-EP-04

Ms. Shrushti Patel

4th International Symposium on One Health, One World
November 20 – 22, 2025

ABS ID: -30
Code No: IMSBE-EP-05

Portable Mud Block Machine for High Altitude Regions

R.S. Bisht[1], D. Kumar[1], S. Singh[1], S. Yadav[1], and S.K. Panigrahi[1]
[1]*Construction Automation & Robotics group, CSIR-Central Building Research Institute Roorkee, Uttarakhand, India,*
Correspond to Dr. R.S. BISHT (rsbisht.cbri@csir.res.in)

***Keywords**: Mechanized process, Traditional and sustainable construction, Modular machine, Machine elements, Design analysis.*

1. ABSTRACT

High altitude regions of India face construction challenges of extreme weather conditions, difficult terrain, and rarefied atmosphere which results in high manpower wages and scarcity of construction materials. Traditional construction practices of manual casting of mud blocks offer several disadvantages like, irregular sizes, low strength and production rates. This work presents a modular mud block machine for high altitude regions. The machine employs a mechanized production system which produces up to 800-1000 blocks per eight-hour shift. The block machine is solely mechanized, modular and operates without electricity requirement. With a weight of approximately 80-100 kg, the machine can be dismantled into sub-assemblies for easy transport and reassembled on-site within 15-20 minutes.

2. INTRODUCTION

Abundance of mud and scarcity of rain fall at high altitude regions viz., Leh and Ladakh in northern part of India presents a potential scope and opportunity of mud, mud-cement based blocks for local construction practices. These two regions are situated at rough geographical terrains and exposed to extreme cold weather conditions due to which the construction practices experience shortage of manpower and construction materials (viz., cement, rebars, etc.) resulting in steep rise in material cost and manpower wages.

Previous developments in field implemented construction machineries viz., egg-laying and stationary concrete block making machines and brick making machine (C-Brick) have marked a significant impact in the building and construction industry, especially within the Indian context [1, 2]. The use of machines enhances strength, consistency in size, and production efficiency of compressed mud/concrete blocks as compared to manual production methods [3].

While manual and semi-automatic machines are commonly employed for small-scale production, most existing designs have not been adapted for use on sloped or rugged terrains, or in high-altitude environments characterized by low temperatures and reduced oxygen levels [3, 4]. Furthermore, only automated machines combine compaction and ejection techniques within a single operational cycle. Instead, many manually operated machines require multiple steps for material feeding, compaction and ejection process. These operations require considerable physical effort, which can lead to worker fatigue in high-altitude conditions [5].

2. DESIGN OF MACHINE

Designing a lightweight block-making machine for high-altitude regions necessitates a robust and portable type solution. The proposed design consists of castor wheel movable base frame with locking and unlocking arrangements, metallic frames to support moulds and plunger units, hopper for material feeding, a single lever arm mechanisms for pressing and ejection for ease of block production as described in Figure 1. The manual arm lever acts as the actuator, providing necessary force to drive the pressing plunger vertically for the ejection mechanism through dual arm and locking linkages.

Mix design with soil and stabilizers is compressed within the fixed mould units, while the base and metallic frames provide structural stability. The design configuration ensures block formation, optimizing local soil utilization for sustainable building applications in demanding environments. The machine is modular and designed in such a way that the whole onsite assembly of the machine can be done within 15-20 minutes to facilitate the effective manufacturing of environmentally friendly mud blocks in difficult, high-elevation areas.

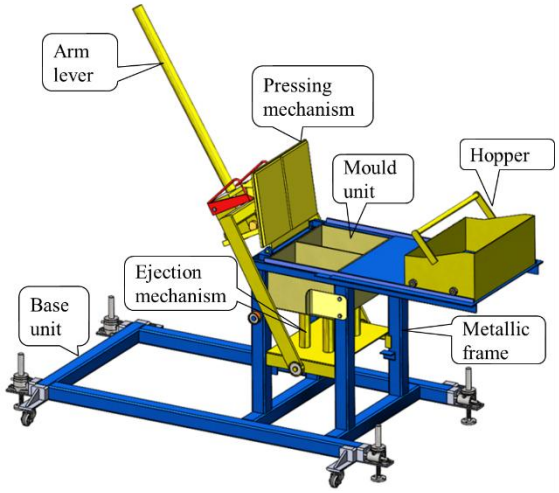

Figure 1. Design elements of the mud block machine

3. PROTOTYPE AND TRIALS

A prototype of the mud block machine has been done after performing extensive design analysis, fabrication and prototype assembly fitting as per Figure 2(a). mechanical fixtures are used for quick onsite assembly of the machine parts. A single lever-operated mechanized system of the machine capable of multiple block production in one operation. It is operated manually, requiring no external power or electricity, thus making it suitable for rural and high-altitude regions. The machine is compact and lightweight, enabling easy transport and deployment at construction sites due to its modular design concept. The machine produces uniform mud blocks with proper edges and shapes compared to manual casting approach, reducing wastage during construction as demonstrated in Figure 2 (b).

Figure 2. (a) Developed block machine, (b) mechanized production of mud blocks

Table 1. Comparative study of mud block production by manual and machine types

Key features	Block production	
	Manual	Machine
Density (kg/m3)	1600-1800	1600-2000
Compressive strength (MPa)	0.5	0.8-1.5
Production (per 8 hours shift)	450-500	800-1000
Cost (₹ per block)	18-20	10-12

Extensive mud block production trials by the developed machine were conducted at CBRI Roorkee and in field conditions at Leh. Results described in Table 1 indicate the blocks achieved a density range of 1600–2000 kg/m³, slightly higher than manually cast blocks (1600–1800 kg/m³). The machine produced blocks exhibit compressive strength improved to 0.8–1.5 MPa compared to only ~0.5 MPa in

manual casting, indicating better load-bearing capacity. With addition of cement, the compressive strength enhances up to 2-3 MPa. The estimated production efficiency of the machine nearly doubled, with 800–1000 blocks (with prepared mix design) produced per shift as compared to 450–500 blocks casted manually, while the cost per block was reduced to ₹10–12 compared to ₹18–20.

The Ladakh region is classified as a cold desert region which experiences much less average annual rainfall of 50-80 mm as compared to average rainfall in Uttarakhand of 1400-1500 mm which makes the mud blocks ideal for building construction in Leh and Ladakh region. Therefore, the developed machinery has a wide potential in high altitude regions due to its ergonomic design and low cost without any skill requirement.

4. CONCLUSIONS

The developed machine can be used for mud and concrete block production with modular design and portable features viz., assembly and easy shifting at work specific site as per requirement. The machine can produce 800-1000 blocks per shift and minimum human effort and produces uniform and compressed blocks with better mechanical features. This machine can be beneficial in high altitude regions where manpower wages and material costs are very high. Blocks with dimension 300 mm × 200 mm × 150 mm for laboratory and field trials were produced by manual casting and machine production for mechanical characterization and trials evaluation. The developed machine demonstrated superior performance over manual casting, producing blocks with higher density, strength, and load-bearing capacity. Laboratory and field trials confirmed nearly double production efficiency and significant cost reduction. The machine highlights the potential for economical, high-quality block production in challenging environments like Leh.

ACKNOWLEDGEMENT

The authors are grateful to the CSIR-CBRI for granting permission to publish this work. The financial support provided by CSIR with project no. IHP250003 are also gratefully acknowledged under high altitude regions of India (HARI) initiative. We extend our sincere thanks to Director CSIR-CBRI, Dr. A. P. Chourasia and Ar. S. K. Negi for mentorship and support. Supplementary information can also be found from the given link:

https://www.youtube.com/watch?v=iyc8XPH6dr0

REFERENCES:

[1] IS 13291 (1992).

[2] R.L. Gupta, D.K. Gautam, S.K. Jain, New Building Materials & Construction World 9 (2004) 32.

[3] J. Bredenoord, Y. Kulshreshtha, Sustainability 15 (2023) 5295.

[4] B.V. Reddy, Current Science, 109(2015) 1651-1659.

[5] R.S. Bisht, S.K. Panigrahi, S. Singh, D. Kumar, S. Yadav, Int. J. Interact. Des. Manuf. 15 (2021) 587-596

4th International Symposium on One Health, One World
November 20 – 22, 2025

ABS ID: OP-55
Code No: IMSBE-EP-06

Gis And Lidar Based Viewshed Analysis of Uncontrolled Intersections

M. Bisht[1], K. Thakur[1], and P. Misra[1]
[1]*M. Tech student, Department of Civil Engineering, IIT Roorkee, Roorkee, India,*
[1]*PhD Student, Department of Civil Engineering, IIT Roorkee, Roorkee, India,*
[1]*Assistant Professor, Department of Civil Engineering, IIT Roorkee, Roorkee, India,*
Correspond to Prof. P. Misra (prakhar.misra@ce.iitr.ac.in)

***Keywords**: Viewshed analysis, LiDAR, GIS, Intersection visibility, Blindspot.*

1. ABSTRACT

Uncontrolled intersections in India pose significant safety challenges, accounting for over 64% of intersection-related accidents in Million-Plus Cities (MoRTH, 2022). Limited visibility due to roadside buildings, vegetation, and parked vehicles reduces drivers' ability to safely assess gaps, increasing collision risk. We propose a GIS- and LiDAR-based framework to evaluate visibility and identify obstructions at such intersections, with complementary benefits. The GIS-based component quickly generates sight triangles aligned with IRC:66-1976 standards and detects building-induced obstructions, enabling scalable blind spot identification across multiple intersections in a large urban area. In contrast, the LiDAR-based analysis provides detailed 3D virtual viewshed modelling for individual intersections, simulating driver line-of-sight under different parameters and allowing assessment of multimodal traffic interactions. Temporary obstructions, such as parked vehicles, can be further incorporated to evaluate their impact on visibility. Application of these methods demonstrates that GIS offers rapid, large-scale visibility screening, while LiDAR enables high-resolution, intersection-specific analysis. Together, the framework provides urban planners and traffic engineers with actionable insights for data-driven interventions to reduce accident risk, supporting both large-area planning and detailed intersection-level safety analysis.

2. INTRODUCTION

Road traffic crashes remain a major safety concern worldwide, causing over one million deaths each year. In India, the situation is particularly critical, with the country ranking first in road traffic fatalities and fourth in injuries globally [1]. Intersections account for 22% of all crashes, and among Million-Plus Cities, uncontrolled crossings without traffic signals or stop signs contribute to over 64% of intersection-related accidents, deaths, and injuries [2]. Limited visibility due to roadside buildings, vegetation, and parked vehicles forces drivers to rely on compromised judgment, elevating collision risks. Despite the significance of the issue, systematic visibility assessment at uncontrolled intersections remains underexplored in road safety planning.

Sight distance (SD) evaluation has been an established key factor in intersection visibility and roadway safety. Early geospatial approaches relied on digital elevation models (DEMs) to simulate road alignments and estimate available sight distance [3–6]. While practical for design stages, DEM-based methods oversimplified road geometry and failed to capture obstructive objects. The incorporation of GIS-based tools, such as viewshed and line-of-sight (LOS) analyses, improved accuracy by accounting for terrain variations [7–10]. Further studies integrated crash data with visibility assessments. However, 2D and 2.5D models, even when using DSMs or TINs, remained limited in representing vertical structures like bridges, overhangs, or tree canopies [11].

The advent of LiDAR introduced more detailed modelling of intersection visibility. Terrestrial and mobile LiDAR-based studies applied voxelization and ray tracing to capture complex urban geometries, including pole- and tree-induced obstructions [12–14]. These approaches enabled high-resolution viewshed simulations, though most focused-on vehicles and static environments. Fewer studies addressed multimodal users or dynamic

obstructions such as parked vehicles, despite their significant role in blind spot formation.

This paper contributes a complementary GIS- and LiDAR-based framework that bridges these gaps. The GIS-based method enables rapid, large-scale identification of sightline obstructions due to buildings, making it suitable for citywide screening. In contrast, the LiDAR-based method provides detailed 3D virtual viewsheds for individual intersections, incorporating multimodal perspectives and temporary parking scenarios. By combining scalability with depth, the framework supports data-driven intersection visibility analysis at both regional and site-specific levels, thereby contributing to sustainable intersection design and broader road safety planning.

3. STUDY AREA & DATASETS

The study was carried out at the Indian Institute of Technology Roorkee campus in Uttarakhand, India. The campus contains academic blocks, residential areas, and landscaped spaces, with several uncontrolled intersections in its internal road network. Data were drawn from multiple sources. Road and building shapefiles were obtained from the ESRI web portal to provide the spatial framework for sight triangle analysis (Figure 1). Stopping sight distances were also measured in the field using a measuring wheel and compared with Indian Roads Congress (IRC) standards. At a particular intersection, high-resolution point clouds were collected with a FARO terrestrial laser scanner from nine positions and processed in CloudCompare (Figure 2). Synthetic car models were inserted to simulate parked vehicles (Figure 3). In addition, UAV imagery was processed in RealityCapture to generate an orthomosaic, which was used as a base for visualising LiDAR-based visibility outputs in QGIS.

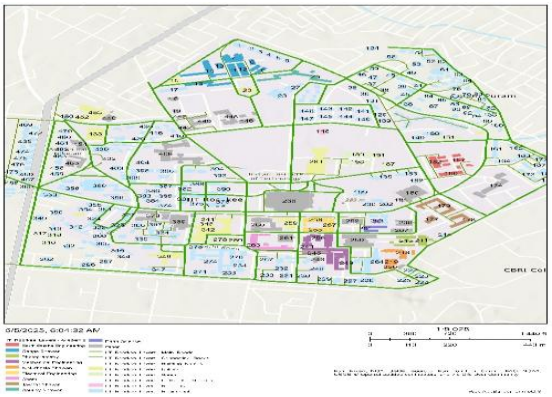

Figure 1. Map of IIT Roorkee obtained from ESRI web portal

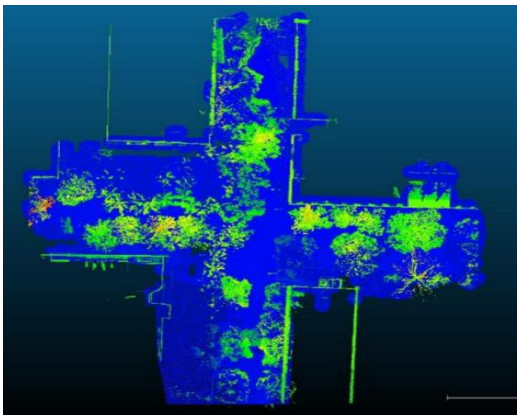

Figure 2. Top view of the intersection point cloud

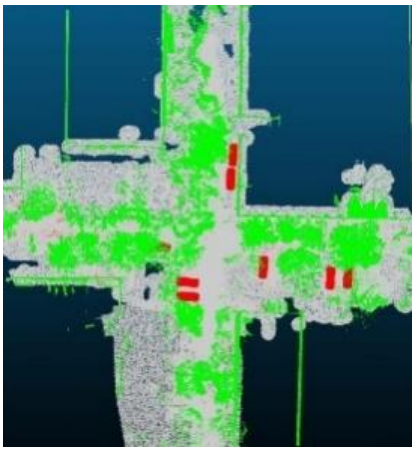

4.METHODOLOGY

The study employed a multi-scale, data-driven approach to evaluate visibility at uncontrolled intersections by combining GIS analysis, LiDAR modelling, and temporary obstruction simulation. Intersections were first identified using road centerlines. Sight triangles were generated based on stopping sight distances, depending on the design speed of the road to detect potential visibility obstructions caused by buildings.

For a detailed, site-specific assessment, LiDAR point clouds of a selected intersection were processed to extract ground surfaces and generate a 2D occupancy grid. Line-of-sight rays were traced from the driver's perspective to identify obstructions, producing a three-dimensional virtual viewshed that captured complex vertical features.

Temporary obstructions, such as parked vehicles, were simulated by inserting synthetic car models into the point cloud, and modified viewsheds were generated to quantify reductions in visibility. This integrated

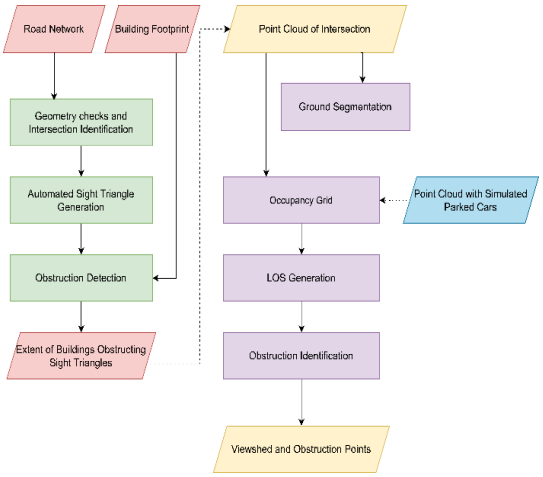

Figure 4. Overall Methodology

methodological workflow (Figure 4) allows scalable screening of multiple intersections while providing high-resolution, intersection-level insights, supporting targeted interventions for road safety planning.

5. RESULTS & DISCUSSION

The total obstructed area at each intersection was calculated by aggregating the obstructions detected in the sight triangles. Intersections were classified based on the proportion of obstruction, highlighting locations with critical visibility deficits (Figure 5). This approach provided a rapid, scalable assessment of multiple intersections within the campus.

For Lidar-based results, obstruction points were extracted, and the 3D viewshed was projected onto a 2D plane for visualization (Figure 6). Combining the obstruction points with the projected viewshed allowed a detailed understanding of visibility limitations at the intersection, capturing vertical features that are not accounted for in traditional methods of measuring sight distances.

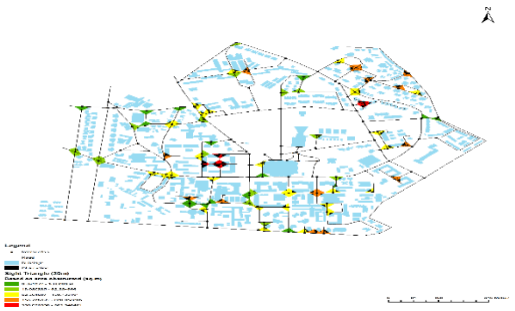

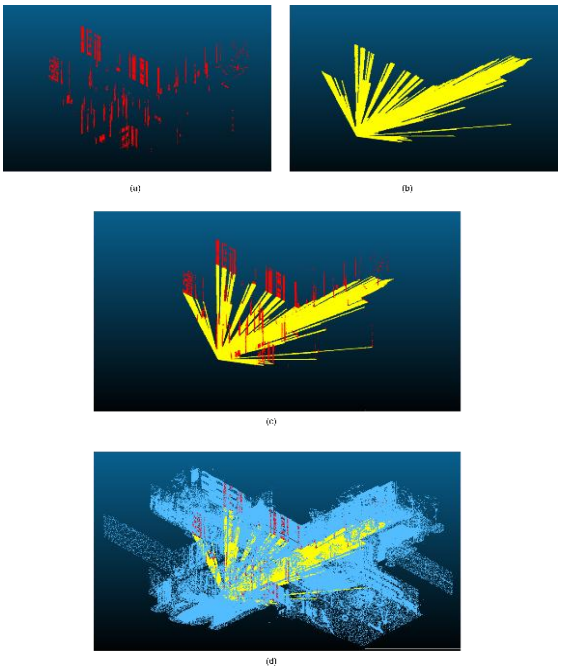

Figure 5. Classification of intersections based on total obstructed area

Figure 6. LiDAR-based viewshed for the eastbound approach—(a) obstruction points, (b) 2D projection, (c) combined view, and (d) overlay on intersection point cloud (visualized in CloudCompare).

Using the LiDAR dataset, 2D projections of 3D viewsheds were generated for different road users: passenger cars, pedestrians, bicyclists, and heavy vehicles (Figure 7). This analysis highlighted differences in visibility for multiple modes.

Figure 7. Viewsheds generated for different

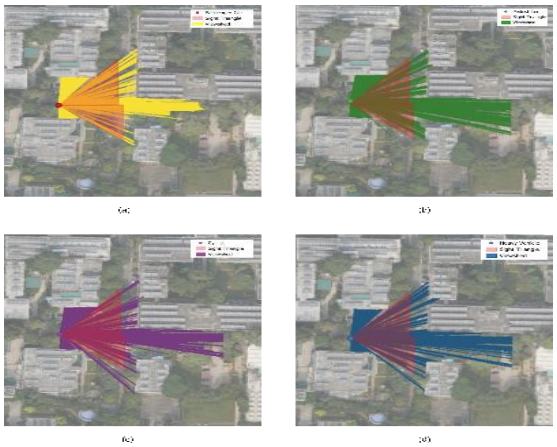

transportation modes—(a) Passenger Car (1.2m), (b) Pedestrian (1.65m), (c) Bicyclist (1.4m), and (d) Heavy Vehicle (3.8m).

The effect of parked vehicles on intersection visibility was evaluated by inserting synthetic cars into the point cloud. Comparative viewshed analysis quantified reductions in visible area (Figure 8). The results indicated that significant blind spots can arise due to temporary obstructions, emphasizing the need for parking management near intersections.

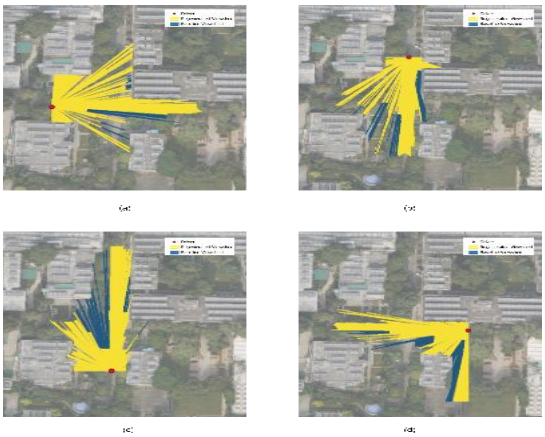

Figure 8. Viewshed reduction for each intersection approach due to simulated parked vehicles— (a) Eastbound, (b) Southbound, (c) Northbound, and (d) Westbound

6. CONCLUSIONS

This study combined GIS-based sight triangle analysis and LiDAR-derived 3D viewsheds to assess visibility at uncontrolled intersections.GIS-based analysis enabled rapid, scalable identification of intersections with building-induced obstructions using sight triangles based on design speed of the road. LiDAR-based viewsheds captured complex vertical obstructions and supported multi-modal perspectives, highlighting variations in visibility for different road users.Simulated parked vehicles revealed measurable reductions in visible area, emphasizing the importance of managing roadside parking.Overall, the integrated GIS–LiDAR approach provides a practical, multi-scale framework for intersection visibility assessment, supporting data-driven planning and targeted safety interventions.

REFERENCES:

[1] International Road Federation, World Road Statistics 2022, Geneva, Switzerland, 2022.

[2] Ministry of Road Transport and Highways (MoRTH), Road Accidents in India 2022, Government of India, New Delhi, 2022.

[3] Y. Hassan, S.M. Easa, A.O. Abd El Halim, Analytical Model for Sight Distance Analysis in 3D Highway Alignments, Transp. Res. Board, Washington, DC, 1996. https://doi.org/10.1177/036119819615230010 1

[4] K. Ismail, T. Sayed, New algorithm for calculating 3D available sight distance, J. Transp. Eng. 133 (2007) 572581 https://doi.org/10.1061/(ASCE)0733-947X(2007)133:10(572)

[5] Jha, M. K., Karri, G. A. K., & Kuhn, W. (2011). New Three-Dimensional Highway Design Methodology for Sight Distance Measurement. *Transportation Research Record*, *2262*(1), 74-82. https://doi.org/10.3141/2262-08 (Original work published 2011)

[6] M.K. Jha, G.A. Karri, Road surface development and sight distance calculation with new visualization methods, Proc. 2nd WSEAS Int. Conf. Sensors & Signals, Visualization, Imaging & Simulation, 2009, pp. 220–225.

[7] A.J. Khattak, H. Shamayleh, Highway safety assessment through geographic information system-based data visualization, J. Comput. Civil Eng. 19 (2005) 407–411. doi.org/10.1061/(ASCE)0887-3801(2005)19:4(407)

[8] Tsai, Y., Yang, Q., & Wu, Y. (2011). Use of Light Detection and Ranging Data to Identify and Quantify Intersection Obstruction and Its Severity. *Transportation Research Record*, *2241*(1), 99-108. https://doi.org/10.3141/2241-11 (Original work published 2011)

[9] M. Castro, L. Iglesias, J.A. Sánchez, L. Ambrosio, Sight distance analysis of highways using GIS tools, Transp. Res. Part C: Emerg. Technol. 19 (2011) 997–1005. https://doi.org/10.1016/j.trc.2011.05.012

[10] M. Castro, J.A. Anta, L. Iglesias, J.A. Sánchez, GIS-based system for sight distance analysis of highways, J. Comput. Civil Eng. 28 (2014) 04014005. https://doi.org/10.1061/(ASCE)CP.1943-5487.0000317

[11] C. De Santos-Berbel, M. Castro, S.L.-C. Medina, M. Paréns-González, Sight distance studies on roads: influence of digital elevation elevation models and roadside elements, Procedia Soc. Behav. Sci. 160 (2014) 449–458. https://doi.org/10.1016/j.sbspro.2014.12.157

[12] M.J. Olsen, D.S. Hurwitz, A.G. Kashani, K. Buker, 3D Virtual Sight Distance Analysis using Lidar Data, Pacific Northwest Transp. Consortium, 2015, p. 74. https://doi.org/10.1016/j.trc.2017.12.004

[13] J. Jung, S. Hong, S. Yoon, J. Kim, J. Heo, Automated 3D wireframe modeling of indoor structures from point clouds using constrained least-squares adjustment for as-built BIM, J. Comput. Civil Eng. 30 (2016) 04015074. https://doi.org/10.1061/(ASCE)CP.1943-5487.00005

[14] E. Che, M.J. Olsen, Fast ground filtering for TLS data via Scanline Density Analysis, ISPRS J. Photogramm. Remote Sens. 129 (2017) 226–240. https://doi.org/10.1016/j.isprsjprs.2017.05.00

ABS ID: 149
Code No: IMSBE-EP-07

Dr. Prasanta Kar

ABS ID: 83
Code No: IMSBE-EP-08

Mr. Mugesh Arumugam

4th International Symposium on One Health, One World
November 20 – 22, 2025

ABS ID: 42
Code No: IMSBE-EP-09

Study of Analysis of Precast / Partially Precast Pier Cap for 4 Lane Elevated Corridor with Cantilever Pier

Thirunavukkarasu M[1]
Lead Engineering Manager, EDRC, L&T Transportation Infrastructure IC, Chennai, India

Keywords: *Pier cap Shell, partially precast Pier cap, fully precast Pier cap, RCC, PSC Macalloy prestressing.*

INTRODUCTION

Bridges play a vital role in road transportation by facilitating trade, connecting rural and urban areas & promoting tourism. It supports industrial growth and provides employment opportunities through infrastructure development. India boasts the World's 2nd largest road network after the USA with 63.72 Lakhs km Approx which is contributing 4.7% of the country's GDP. In contrast to this, the Conventional approach of cast in-situ (CIS) construction methodology, quality related problems leading to a faster deterioration of structures makes the intended service life questionable. Also, these conventional methodologies are time consuming, which cause a lot of disturbance to the public during construction & lead to further increase the traffic congestion. Therefore, an accelerated method of construction incorporating modern technologies, new practices & systems are the need of the hour.

OBJECTIVE OF THE STUDY

The PBES systems adopted for Pier caps in developed countries viz partially Precast Pier caps (Shells) & fully precast Pier caps with RCC / PSC / Macalloy Prestressing system, its analysis for various loading conditions (Permanent loads & variable loads), pros & cons of each system under different atmospheric conditions (Exposure conditions) will be covered.

In the present study, a 4-lane elevated corridor with Precast segmental Box girder with cantilever pier & pier cap system is adopted for the study (span 50m & deck width 14.5m). The Pier cap study will be carried out for all permanent loading conditions in addition to launching girder loads for the erection of segmental box girders, and erection conditions for Pier cap along with IRC loading conditions.

CONFIGURATION FOR THE STUDY

For this study a 5x50m continuous span bridge with a precast prestressed concrete (PSC) box girder superstructure is considered. The bridge has a deck width of 14.5m and a carriageway width of 13.5m. The structure is constructed using segmental construction techniques. Thew super structure rests on elastomeric bearings on hammer head pier cap. The bridge pier is designed as rectangular sections of size 2.3m x 2.3m, ensuring stability and adequate load distribution. The substructure is supported by four piles per pier, each with a diameter of 1.2m, which provides sufficient foundation strength to withstand vertical and lateral forces.

PBES SYSTEM FOR THE PIER CAP UNDER STUDY

The length of Pier cap in transverse direction as per functional requirements is 6.6m for both EJ Piers & intermediate Piers. However, based on the type of PBES system the length varies & is described in detail. The width of pier cap is 3.1m in longitudinal direction in all cases.

1.RCC Pier cap

The depth of Pier cap in case of RCC Pier cap is 1.5m as shown below. The Pier cap Design for Service case & Launching Girder case is manually carried out & the summary is presented below.

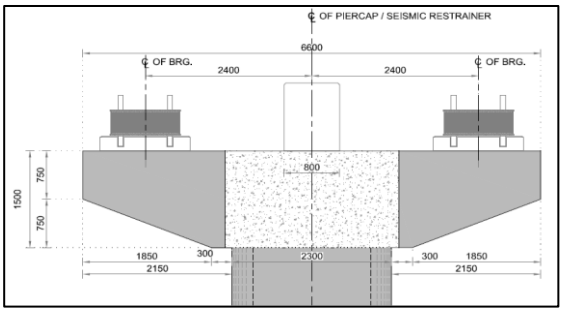

Figure 1.RCC Pier - Fully precast

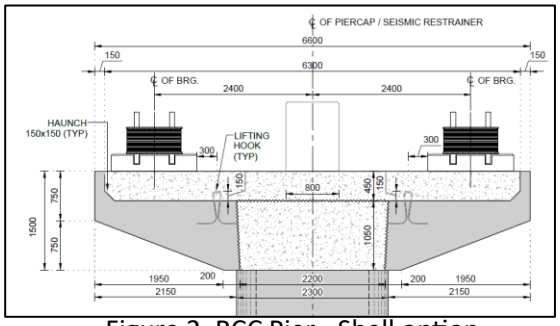

Figure 2. RCC Pier - Shell option

The structural member exhibits deep beam or corbel-type behavior, characterized by a shear span-to-depth ratio of 0.908 under service conditions and 0.073 during the construction stage. Due to this low a/d ratio, the member's load transfer mechanism is dominated by strut-and-tie action rather than conventional flexural behavior. The design has been carried out primarily using the Strut-and-Tie Method (STM), with additional checks for flexure, shear, secondary tensile reinforcement, and torsion–shear interaction to comprehensive structural safety.

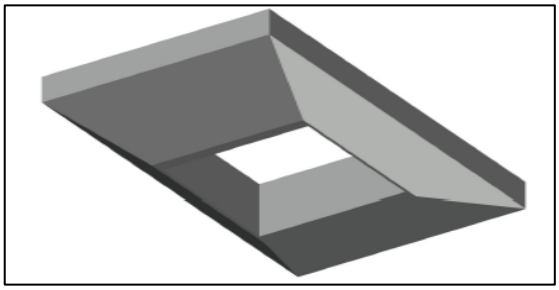

Figure 3. Fully precast - Weight = 70T

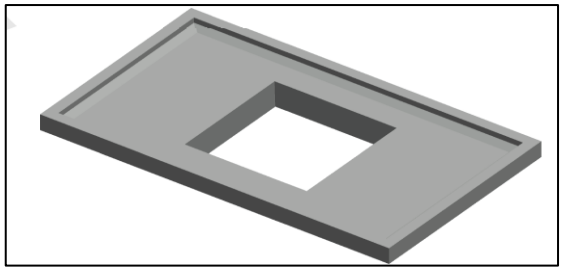

Figure 4. Shell option Weight = 40T

For longitudinal reinforcement, the calculated steel requirement was 45,038 mm², which has been satisfied by providing 56 bars of 32 mm diameter arranged in two layers, achieving an equivalent area of approximately 45,038 mm². This provision not only meets the structural demand but also ensures adequate ductility and load-carrying capacity in the member, confirming that the reinforcement design is fully compliant with code requirements.

1.PSC Pier cap

In this option though the functional requirement of pier cap width is 6.6m, in order to have anchorage blocks not fouling with Pedestal reinforcement, the width requirement is 6.9m with a depth of 1.35m. Like the RCC option the Pier cap is designed & the summary is shown below

The prestressing system consists of 114 high-strength strands, each with a diameter of 15.2 mm and a nominal cross-sectional area of 139 mm², arranged into six cables with approximately 19 strands per cable. Each strand has an ultimate tensile strength of 1860 MPa. The cables are provided in a straight profile to minimize frictional losses and simplify construction.

Serviceability performance has been evaluated using the strain compatibility method, appropriate for bonded tendons. The analysis confirms that no tensile stresses develop under service load conditions, ensuring that the prestressing system remains fully compliant with the service stress limits specified in IRC:112. This design approach provides both structural efficiency and practical constructability, making it suitable for members exhibiting deep beam or corbel-type behavior.

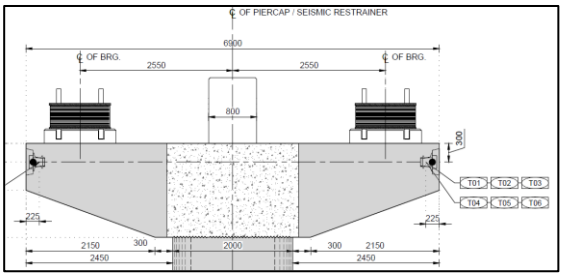

Figure 5. PSC Pier - Fully precast

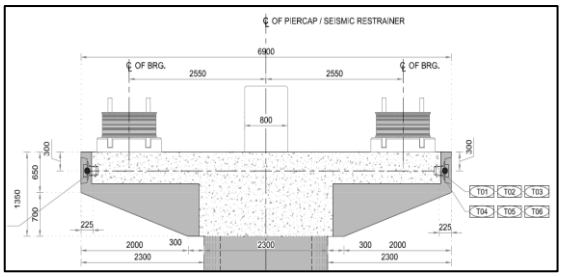

Figure 6. PSC Pier – Shell option

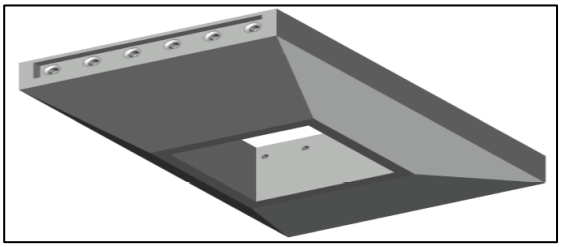

Figure 7. Fully precast - Weight = 75T

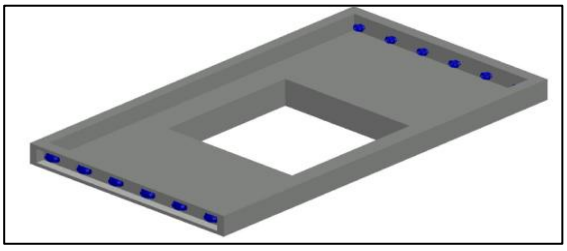

Figure 8. Shell option - Weight = 45T

1.Macalloy Prestressing

The Pier cap of 6.9 m length and a depth of 1.35 m has been prestressed using high-strength bar tendons. Each bar has a diameter of 75 mm, providing a nominal cross-sectional area of 4185 mm² with an ultimate tensile strength of 1030 MPa. A total of nine such bars are employed to satisfy the design requirements. The use of bar tendons, in place of conventional multi-strand cables, facilitates simpler handling and offers practical advantages during construction. In particular, post-erection stressing is feasible, which improves site execution and reduces the complexity associated with tendon profiling and frictional losses.

As the tendons are unbonded, the serviceability performance has been assessed through deformation compatibility analysis. The results confirm that the induced stresses are within the permissible limits prescribed in IRC:112, ensuring that the members remain compliant under service load conditions. Thus, the adoption of 75 mm high-strength prestressing bars provides a technically efficient and construction-friendly alternative to conventional strand-based tendon systems.

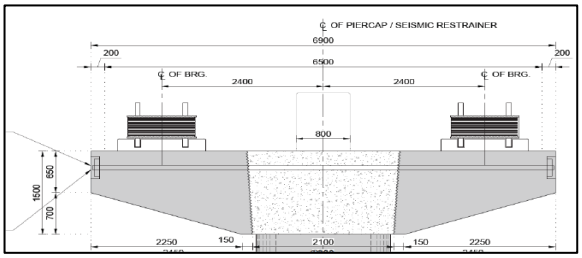

Figure 9. Macalloy prestressing - Fully precast

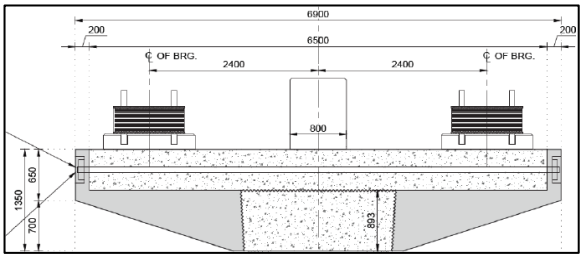

Figure 10. Macalloy prestressing – Partially precast

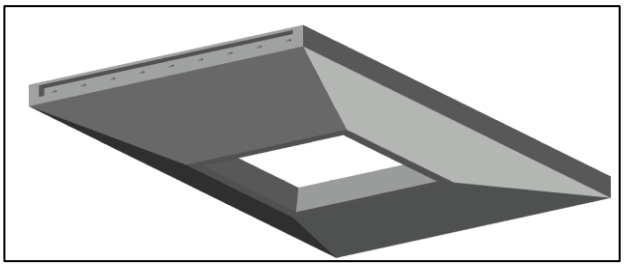

Figure 11. Fully precast - Weight = 75T

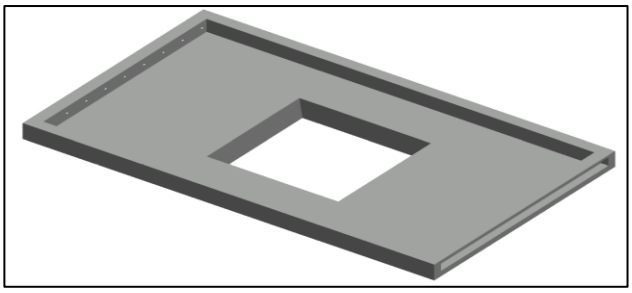

Figure 12. Fully precast - Weight = 45T

Pier cap erection analysis

Fully Precast Pier Cap - Erection Analysis

In case of fully precast analysis the pier cap shall be erected using cranes of suitability capacity. The analysis for this stage involves the following steps depending on the type of lifting system adopted. The lifting arrangement for the precast pier cap has been carefully designed to ensure safe handling during erection. Four lifting points were selected, compatible with various threaded lifting systems, and the anchorage lengths for the lifting inserts were designed based on manufacturer specifications. As an alternative, lifting hooks utilizing prestressing strands or bars can be employed, offering flexibility in the erection procedure.

The structural behavior of the precast pier cap under lifting conditions has been analyzed to verify its stability and to ensure that stresses at the lifting points and surrounding concrete remain within acceptable limits. This evaluation helps prevent local failures, cracking, or excessive deformations during the handling and positioning of the pier cap, ensuring safe and efficient construction practices.

Partially Precast Pier Cap (Shell) – Erection Analysis

In line with the erection analysis of fully precast system, the lifting arrangement shall also be chosen & accordingly the following arrangements shall be carried out.

The erection analysis of a partially precast pier cap (shell) requires careful evaluation to ensure structural stability during construction stages. Similar to a fully precast system, the lifting arrangement must be selected appropriately, and corresponding checks carried out prior to execution.

During the lifting stage, the shell's behavior under crane loads is analyzed to verify that the structural capacity and deformations remain within acceptable limits. Additionally, punching shear at critical sections is assessed under lifting conditions to prevent local failures.

Following placement, the stability of the shell is examined during the pouring of green concrete. The analysis includes both the overall stability of the partially precast assembly and the lateral pressure exerted on the side walls due to fresh concrete. These checks ensure that the pier cap remains safe and stable throughout erection and concreting operations, minimizing the risk of construction-stage failures.

CONCLUSIONS

The study evaluates different construction approaches for RCC (fully and partially precast), PSC (fully and partially precast), and Macalloy post-tensioning systems highlighting their advantages, challenges, and areas of suitability (Refer Figure-13).

RCC – Fully precast	RCC – Partially Precast (Shell)	PSC - Fully precast Partially	PSC –Partially Precast (Shell)	Macalloy Post Tensioning – Fully precast	Macalloy Post Tensioning - Partially Precast (Shell)
Pros: • Rebar preparation at site is Minimum. • Differential shrinkage and creep between precast and in-situ is comparatively less. • Being fully precast, simple collar arrangement from pier may be suitable. • No additional in-place Prestressing activity Cons: • Erection and logistics may be challenging. Suitability: • Suitable for corbels in any environment with proper concreting	Pros: • Ease of erection and logistics. • No additional in-place Prestressing activity Cons: • Support arrangements to be planned. • Heavy rebar preparation to be planned in-place. • Differential shrinkage and creep between precast and in-situ is comparatively high. • Additional reinforcements need to be provided in case of thick shells, whereas Service stage reinforcement can be utilized in case of thin shells. Suitability: • Suitable for corbels in any environment with proper concreting	Pros: • Rebar preparation at site is less. • Differential shrinkage and creep between precast and in-situ is comparatively less. • Being fully precast, simple collar arrangement from pier may be suitable. • Introduction of PT reduces the weight in case of flexural Pier caps. Cons: • Erection and logistics may be challenging. • Additional in-place Prestressing activity Suitability: • Suitable for flexural Pier caps in any environment with proper concreting	Pros: • Ease of erection and logistics. Cons: • Stressing shall be in place. • Support arrangements to be planned. • Heavy rebar preparation to be planned in-place. • Differential shrinkage and creep between precast and in-situ is comparatively high. Suitability: • Suitable for flexural Pier caps in any environment with proper concreting	Pros: • Stressing operation is handy and easy compared to conventional Post tensioning. • Rebar preparation at site is less. • Differential shrinkage and creep between precast and in-situ is comparatively less. • Being fully precast, simple collar arrangement from pier may be suitable. • Introduction of PT reduces the weight in case of flexural Pier caps. Cons: • Macalloy post tensioning is much Costly compared to conventional methods. • Erection and logistics may be challenging. • Additional in-place Prestressing activity. Suitability: • Not Suitable for aggressive environments (Marine, arid and Semi-Arid locations) as it is unbonded tendon.	Pros: • Stressing operation is handy and easy compared to conventional Post tensioning. • Ease of erection and logistics. Cons: • Macalloy post tensioning is much Costly compared to conventional methods. • Stressing shall be in place. • Support arrangements to be planned. • Heavy rebar preparation to be planned in-place. • Differential shrinkage and creep between precast and in-situ is comparatively high. Suitability: • Not Suitable for aggressive environments (Marine, arid and Semi-Arid locations) as it is unbonded tendon.

figure 13. Various lifting arrangements

REFERENCES:

1. T.H. Kim, Y.J. Kim and H.M. Shin (2013) "*Performance assessment of precast concrete pier cap system"* Samsung Construction & Trading Corporation, Daewoo Institute of Construction Technology, School of Civil and Architectural Engineering, South Korea published in Techno-Press, Ltd.

2. Joshua T. Hewes, Ph.D., P.E. (2013) *"Analysis of the State of the Art of Precast Concrete Bridge Substructure Systems"* Arizona Department of Transportation Research Center, Northern Arizona University.

3. ERIC YERMACK, P.E., ARORA and ASSOCIATES, P.C., Lawrenceville *"Accelerated Bridge Construction Using Precast Piers"* New Jersey Transportation Research Board International Bridge Engineering Conference.

4. Eric E. Matsumoto, PE, PhD & Jim Ma, PE (2015), "*Precast Concrete Bridge Substructure Systems And Details for Seismic Regions",* Associate Professor, Department of Civil Engineering, California State University.

ABS ID: 18
Code No: IMSBE-EP-10

Mr. Chakradhar V

2025 HOW

4th International Symposium on One Health, One World
November 20 – 22, 2025

ABS ID: OP-87
Code No: IMSBE-EP-11

Towards Sustainable Architecture: Data-Driven Geometry Optimization of a Funicular Arch

Singh A[1], Deshmukh M.S[2], and George J[3]

[1]*Undergraduate Student, Computer Science and Engineering, IIIT Hyderabad, Hyderabad, India,*
[2]*Undergraduate Student, Electronics and Communication Engineering, IIIT Hyderabad, Hyderabad, India*
[3]*Assistant Professor, Earthquake Engineering Research Centre, IIIT Hyderabad, Hyderabad, India*

Keywords: *-Arches, Optimization, Machine Learning, Limit analysis, Rigid body mechanics.*

ABSTRACT

Funicular structures like arches, vaults, and domes have always captured the attention of architects due to their impressive strength and efficient use of materials. Nowadays, with sustainability being the center of attraction and construction contributing significantly to carbon emissions, these designs are more relevant than ever. This work introduces a computational method aimed at discovering the optimal shapes for funicular arches that can withstand heavy loads. By employing a kinematic approach rooted in limit analysis, we gather data on the failure points of arches, which we then use to train machine learning (ML) models. These models can do a quick prediction of the collapse capacity, allowing us to optimize thickness while ensuring both vertical and horizontal safety standards are met. This study primarily focuses on uniform arches, with plans to move to non-uniform ones in the future.

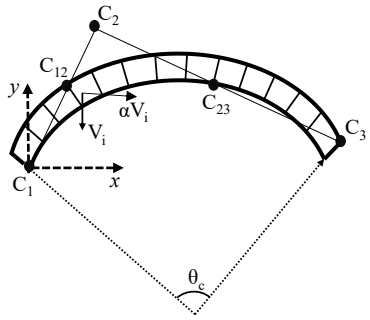

Figure.1 Discretized arch geometry

2.INTRODUCTION

The construction industry is responsible for around 54% the world's CO_2 emissions, a great way to reduce material usage can be finding ways to optimize these structural shapes(Block et al., 2020). In this context, it is imperative for the structural designers to reduce the usage of construction materials without compromising on the structural integrity and aesthetics. Funicular geometries which are primarily compression governing structural systems, gain prominence in this regard. With the advent and wide acceptance of 3-D printing technology, it is possible to create geometries even with varying section properties and perform as good as a traditional section typology(Nodargi & Bisegna, 2020).

In this context, a methodology is introduced for the form optimization of funicular geometries utilizing Machine Learning (ML) techniques for computational efficiency. The study employs a hybrid approach where the structural failure is quantified using traditional limit analysis procedure while the geometry optimization is enabled using an ML enabled optimization scheme.

3.METHODOLOGY

3.1 Limit analysis

The analysis procedure is developed considering an unreinforced masonry arch as the typology(George & Menon, 2021). The failure of the arch is governed by the virtual work equilibrium equation as:

$$\sum_{i=1}^{n} V_i \delta y_i + \alpha \sum_{i=1}^{n} V_i \delta x_i = L_{fi} \quad (1)$$

Where δyi and δxi are the vertical and horizontal virtual displacement components of the ith arch element (Vi) respectively, α is the collapse load factor, and Li is the internal virtual work. Since the formulation is based on rigid block assumptions, Li can be assumed to be zero. By the iterative application of virtual work

equation, the hinge locations (C12, C23) and the governing collapse factor can be identified.

3.2 Collapse scenarios

The primary objective of this research is to attain an optimized arch geometry ensuring safety against possible external loading and self-weight. Once geometry optimization is carried out separately for each case, the scenario where both loads are applied simultaneously is considered for the analysis. Further, for each load case, an arch geometry optimized with uniform (Figure 2(b)) and nonuniform thickness (Figure 2(c)) are considered. To achieve these the critical loading scenarios to which an arch can be subjected to are considered as separate load cases.

Case A: Collapse due to gravity loading: Superimposed loads are applied on the arch barrel at the critical loading position to obtain the collapse factor and corresponding hinge locations.

Case B: Collapse due to lateral loading: Horizontal seismic forces are applied on the arch to simulate a collapse mechanism. The critical acceleration causing failure and corresponding hinge locations are identified.

Case C: Collapse due to combined gravity and lateral loading: To simulate the realistic possible loading scenario, a combination of horizontal and vertical in plane forces are applied on the arch simultaneously to obtain the governing collapse configuration.

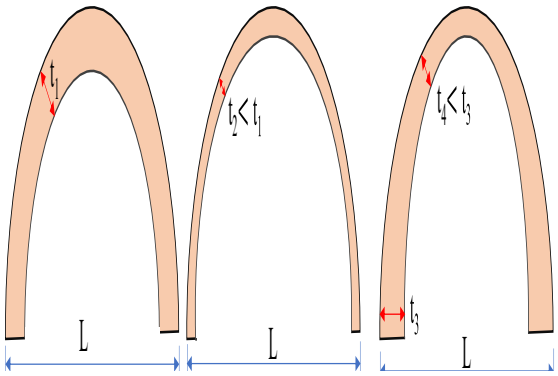

(a)Original geometry (b) Uniform optimized geometry (c)non-uniform optimized geometry

Figure 2 Demonstration of geometry optimization

For the considered loading scenarios, a dataset is created simulating 10,000 arch geometries by varying thickness (t), Span (L), and rise (r), keeping density constant. Each analysis is carried out and the collapse factor and corresponding hinge locations are identified.

3.3 Surrogate Modeling approach

The kinematic limit analysis, while accurate, is computationally intensive. To overcome this limitation, a data-driven surrogate model was developed to serve as a computationally efficient substitute. A comprehensive dataset was first generated by performing the full limit analysis on the 10,000 simulated arch geometries. For each simulation, the key failure characteristics: the governing collapse load factor (α) and the corresponding hinge locations were calculated and stored.

An ML model was then trained on this dataset. To ensure the model accuracy and prevent overfitting, standard cross-validation and regularization techniques were implemented during the training process. Once trained, this surrogate model can predict collapse capacity and failure mode of any new arch geometry

3.3 Geometry Optimization Framework

With a predictive model in place, an optimization framework was established to find the most efficient geometric design of the arch. The primary objective of the framework is to minimize the arch thickness (t), subject to predefined structural safety constraints.

The framework operates through an iterative process:

1. An optimization algorithm systematically proposes a candidate arch geometry.

2. This candidate design is fed into the trained surrogate model, which provides an instantaneous prediction of its vertical and horizontal collapse factors.

3.The predicted factors are checked against the required safety constraints.

The constraints is defined based on the value of collapse factor as:

$$\alpha j \geq \alpha i \quad (2)$$

Where αi is the collapse factor before optimization and αj is the factor of optimized arch. Candidate geometries that violate these constraints are discarded. The optimization algorithm uses the results from the valid

designs to intelligently guide its search, progressively converging towards a solution that minimizes material usage while satisfying all performance requirements. This process allows for the exploration of a vast design space to find an arch that is both lightweight and strong.

4. Concluding remarks

This work integrates classical rigid body mechanics with data-driven modeling to create a fast and accurate framework for structural optimization. The proposed method empowers designers to explore a vast range of geometries, leading to funicular arch designs that minimize material usage and reduce the associated carbon footprint. While this study focused on uniform arches, the methodology is readily extendable to non-uniform and free-form shapes, highlighting its potential for broader applications in sustainable architectural design.

ACKNOWLEDGEMENTS

The authors acknowledge the Earthquake Engineering Research Centre at IIIT Hyderabad for their guidance and resources.

REFERENCES:

1.Jorquera-Lucerga, J. (2018). Form-Finding of Funicular Geometries in Spatial Arch Bridges through Simplified Force Density Method. Applied Sciences.

2. Zhang, J. M., Wang, C. M., Pan, W.H. (2024). Methodology for Determining Optimal Design of Funicular Arches Under Point Loads and Self-Weight Against In-Plane Buckling. Engineering Structures.

3.Block, P., Van Mele, T., Rippmann, M., Ranaudo, F., Calvo Barentin, C., & Paulson, N. (2020). Redefining structural art: Strategies, necessities and opportunities. Structural Engineer.

4.George, J., & Menon, A. (2021). Simplified Performance Assessment for Single-Span Masonry Arch Bridges under Live Load. Journal of Bridge Engineering,.https://doi.org/10.1061/(ASCE)BE.1943-5592.0001723.

5.Nodargi, N. A., & Bisegna, P. (2020). Thrust line analysis revisited and applied to optimization of masonry arches. International Journal of Mechanical Sciences https://doi.org/10.1016/j.ijmecsci.2020.105690.

ABS ID: 103

Mr. Shuta Notsu

ABS ID: 26
Code No: IMSBE-EP-12

Mr. Nikhil Sanjay Nighot

ABS ID: 22
Code No: IMSBE-EP-13

Mr. Vijay Verma

4th International Symposium on One Health, One World
November 20 – 22, 2025

ABS ID: 74
Code No: IMSBE-EP-14

Performance Evaluation of High-Volume Fly Ash Concrete for Sustainable Construction

J.A. Raut[1 2], H.C. Arora[1 2], and B.K. Rao[3 4]
[1]*Academy of Science and Innovative Research (AcSIR), Ghaziabad 201002, India*
[2]*CSIR-Central Building Research Institute, Roorkee 247667, India*
[3]*Academy of Science and Innovative Research (AcSIR), Ghaziabad 201002, India (Superannuated)*
[4]*CSIR-Central Building Research Institute, Roorkee 247667, India (Superannuated)*
Correspond to J.A. RAUT (rautjidnyasaanil@gmail.com)

***Keywords**: High-volume fly ash concrete, Sustainable construction, Fly ash replacement.*

1.GENERAL INSTRCUTIONS

The Indian Construction Industry Is A Major Consumer Of Concrete, And Environmental Concerns Along With Sustainability Goals Motivate Using Industrial By-Products Like Fly Ash As Partial Cement Replacements. Fly Ash Exhibits Pozzolanic Behavior And Improves Long-Term Performance And Durability Of Concrete, But Concerns About Early-Age Strength Remain. This Study Investigates Mechanical And Durability Properties Of Concrete Mixes Containing 50%, 60%, And 70% Fly Ash Replacement At The 28-Day Curing Period, Aiming To Demonstrate Their Applicability For Structural Use.

2.Material And Mixed Design

Ordinary Portland Cement (Opc) 53-Grade Was Used Along With Aggregates And A Superplasticizer For Workability. Fly Ash Sourced From Surathgarh Thermal Power Station Was Incorporated At 50%, 60%, And 70% Replacement Levels By Weight Of Cementitious Material. Mix Designs Targeted M30 And M40 Grades With Optimized Water To Binder Ratios And Admixtures To Maintain Required Workability And Strength.

3.Experimental Methodology

Here Is A Brief Explanation Of The Tests Performed At 28 Days On The Concrete Specimens:

1.Compressive Strength On Cubes (10 Cm):

Concrete Cubes Of 10 Cm Size Were Cast And Cured Submerged For 28 Days. The Cubes Were Tested In A Compression Testing Machine, Where A Gradually Increasing Load Was Applied Until The Cube Failed. Compressive Strength Is Calculated By Dividing The Maximum Load At Failure By The Cross-Sectional Area. This Test Indicates The Ability Of Concrete To Withstand Axial Loads, Which Is Crucial For Structural Performance.

2.Flexural Strength On beam specimens:

Beam-Shaped Concrete Specimens Were Tested For Their Resistance To Bending Under Load. The Flexural Strength (Modulus Of Rupture) Reflects The Tensile Strength Capacity Of Concrete, Important For Evaluating Crack Resistance And Durability Under Bending Stresses.

3.Rapid Chloride Permeability Test (Rcpt):

This Test Measures The Concrete's Resistance To Chloride Ion Penetration By Passing An Electrical Current Through A Concrete Specimen Submerged In Chloride Solution. Lower Charge Passed Corresponds To Lower Permeability, Indicating Better Durability Against Chloride-Induced Corrosion.

4.Corrosion Rate Measurement Via Electrochemical Techniques:

Reinforcing Steel Embedded In Concrete Specimens Was Monitored For Corrosion Activity Using Electrochemical Sensors. This Method Provides Quantitative Data On Corrosion Rates, Indicating The Protective Quality Of The Concrete Cover And Its Resistance To Chloride Attack.

5.Carbonation Depth Measurement Using Phenolphthalein Indicator:

Concrete Specimens Exposed To Co2 Undergo Carbonation, Which Lowers The Ph And Can Reduce Steel Passivation. The Depth Of Carbonation Is Visually Assessed By Applying Phenolphthalein Solution, Which Changes Color In Alkaline Conditions. Measuring Carbonation Depth Helps Evaluate Long-Term Durability.

6.Sulphate Resistance Evaluation By Compressive Strength After Exposure:

Specimens Were Exposed to Sulphate-Rich Environments, And Their Compressive Strength Was Tested Afterward. Retention Of Strength Indicates Resistance to Sulphate Attack, Which Causes Expansion and Cracking.

7.Drying Shrinkage on Prism Specimens:

Concrete Prisms Were Monitored for Length Changes Due To Moisture Loss Over Time. Drying Shrinkage Can Cause Cracking and Durability Issues, So Measuring This Helps in Assessing Dimensional Stability.

4. Result And Discussion

1. Compressive Strength

Concretes With 50% And 60% Fly Ash Replacement Achieved 28-Day Compressive Strengths Close To the Control (Opc Only), Suitable for Structural Applications:

Fly Ash Replacement (%)	Compressive Strength (Mpa) M30	Compressive Strength (Mpa) M40
50	29.8	41.7
60	26.5	37.2
70	18.5	35

These Values Confirm the Potential Use of High-Volume Fly Ash (Hvfa) Concretes for Durable Structures.

2.Flexural Strength

Fly Ash Replacement (%)	Flexural Strength (Mpa) M30	Flxural Strength (Mpa) M40 Days
50	31.33	36
60	31.33	36
70	22.67	22.67

Flexural Strength For Hvfa Concretes Was Comparable Or Slightly Lower Than Control Mixes At 28 Days, With 50% Fly Ash Replacement Showing Good Performance Indicating Adequate Tensile Resistance.

3.Chloride Ion Permeability

Fly Ash Concretes Exhibited Lower Chloride Ion Permeability Compared to Control, Indicating Improved Resistance to Chloride Ingress and Enhanced Protection Against Reinforcement Corrosion.

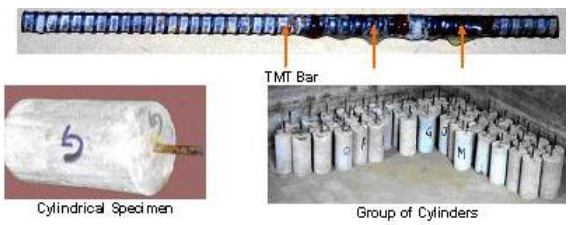

4.Corrosion Resistance

Reinforcing Steel Embedded in Hvfa Concretes Showed Lower Corrosion Rates At 28 Days and Beyond, Attributed to Improved Microstructure and Reduced Permeability of Fly Ash Concretes.

5.Carbonation And Sulphate Resistance

Hvfa Concretes Maintained Comparable Resistance to Carbonation and Sulphate Attack as Control Mixes At 28 Days, Indicating Durability Under Aggressive Environmental Exposures.

6.Drying Shrinkage

Drying Shrinkage Values for Hvfa Concretes Were Lower Than for Control Concrete, Reducing the Risk of Cracking and Enhancing Long-Term Durability.

5.Conclusion

Fly Ash Replacement Up To 70% Produces Concrete with Satisfactory 28-Day Compressive and Flexural Strengths Suitable for Structural Use. The Improved Chloride Ion Resistance and Reduced Corrosion Rates Benefit Durability. Carbonation And Sulphate Resistance Remain Adequate, While Shrinkage Reduction Reduces Cracking Risk. These Findings Support the Adoption of Hvfa Concretes for Sustainable And Durable Construction

6.References:

1.Atiş, C.D. (2002). "High Volume Fly Ash Abrasion Resistant Concrete," American Society of Civil Engineers. This Study Investigated Abrasion Resistance and Durability of Mixes With 50-70% Fly Ash Replacement.

2.Sivasundaram Et Al. (1990). Strength Development of High Volume Fly Ash Concrete Monitored Over 3 Years, Showing High Long-Term Strength Gains And Durability.

3.Mehta, P.K. (2004). "High-Performance, High-Volume Fly Ash Concrete for Sustainable Development," International Workshop on Sustainable Development and Concrete Technology, Highlighting Strength And Durability Benefits.

4.Gebler, S.H. And Klieger, P. (1986). "Effect of Fly Ash on the Durability of Air-Entrained Concrete," Proceedings of the 2nd International Conference on Fly Ash And Pozzolans In Concrete.

5.Siddique, R. (2004). "Performance Characteristics of High Volume Class F Fly Ash Concrete," Cement and Concrete Research, Vol. 34, Pp. 487-493, Discussing Strength and Durability Improvements.

6.Rao, B.K., And Kumar, V. (1996). "Fly Ash in High Strength Concrete," National Seminar on Advances in Civil Engineering, Focusing on Structural Grade Concretes With Fly Ash.

7.Haque, M., Langan, B., And Ward, M. (1984). "High Fly Ash Concretes," Aci Materials Journal, Jan-Feb 1984, DETAILING STRENGTH AND DURABILITY CHARACTERISTICS.

4th International Symposium on One Health, One World
November 20 – 22, 2025

ABS ID: PO-01
Code No: IMSBE-EP-15

Axial Strength and Buckling Behavior of Cold-Formed Steel C-Sections and Built-Up Members: Experimental Investigation and Semi-Analytical Approach

S. Uniyal[1] C. Sonkar[2] and S. Narayan[3]
[1]*Research Scholar, Civil Engineering, NIT Uttarakhand, Srinagar Garhwal, India,*
[2] *Principal Scientist, Structures, CSIR-CBRI, Roorkee,*
[3]*Assistant Professor, Civil Engineering, NIT Uttarakhand, Srinagar Garhwal, India,*
Correspond to S. Uniyal(dt23cej005@nituk.ac.in)

Keywords*: distortional, lateral torsional, nested.*

1. GENERAL INTRODUCTION

Cold-formed steel sections are increasingly used in construction due to their high strength-to-weight ratio and flexibility in design. However, the axial behavior and failure mechanisms of configurations such as C-section, Built-up-I (I/IL-), and Nested (BO-) members under compression remain inadequately Cold-formed steel sections are increasingly used in construction due to their high strength-to-weight ratio and flexibility in design. explored, especially in light of design code limitations. This study aims to evaluate and compare the ultimate axial strength and buckling performance of these sections, considering the effects of geometrical variables and connection details.

2. EXPERIMENTAL INVESTIGATION

Five full-scale monotonic concentric axial compression tests were conducted in this study on cold-formed steel specimens: one C-sections, three built-up I-sections (back-to-back channel sections), and one built-up box section (face-to-face channel section), all tested under simply supported boundary conditions.

Figure 2.1 presents the cross-sections of all cold-formed steel (CFS) specimens.

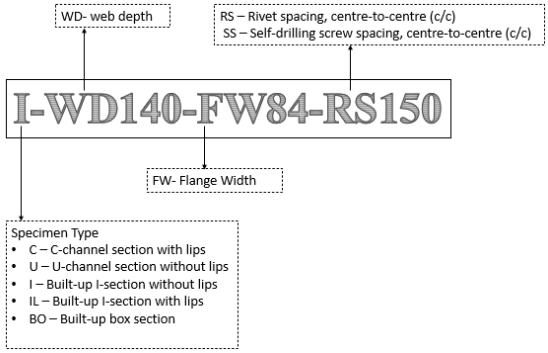

Figure 2.1 Nomenclature adopted for the specimens

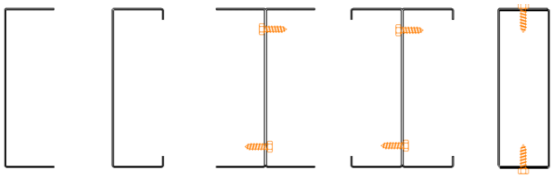

Figure 2.2 Cross sections of the CFS specimen

3. OBSERVATIONS AND CONCLUSIONS

The axial load–displacement curves revealed a distinct elastic stage followed by nonlinear deformation and progressive local buckling. The control specimen (C-WD90-FW42-L10) exhibited the lowest peak load (27.9 kN) with early buckling, while the built-up I specimens with riveted connections (RS series) achieved superior load capacity and ductility. The IL-WD120-FW84-RS150 specimens recorded the highest peak loads (83.32 kN), outperforming their screw-connected counterparts (IL-WD120-FW84-SS150) by approximately 19%. Also, built-up I section with 100 mm screw spacing provided up to 68% greater axial strength than C-sections due to enhanced torsional rigidity.

Axial compressive strength results confirmed that increasing web depth and adopting riveted joints significantly improved stiffness and strength. Riveted built-up I section (RS) exhibited enhanced load transfer between components, delaying local and distortional buckling. In contrast, screw-connected built-ups (SS) displayed earlier stiffness degradation and lower post-peak resistance.

Failure modes were dominated by local buckling of flange elements, distortional buckling in the web, and eventual fastener slip or pull-out. Riveted specimens maintained structural integrity longer, indicating improved connection rigidity and energy dissipation capacity.

Overall, the IL-WDW120-FW84-RS150 configuration demonstrated the most favorable combination of strength, stiffness, and ductility. The results highlight that riveted built-up I configurations can enhance axial performance by up to threefold compared to conventional screw-connected CFS members.

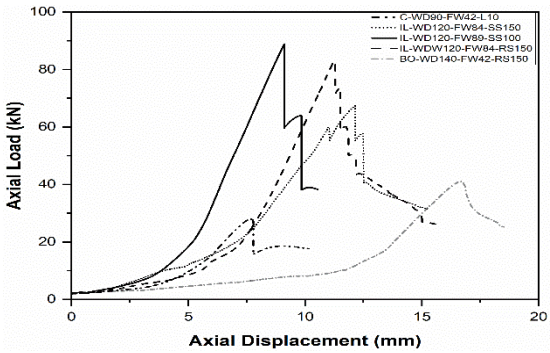

Figure 3.1 Axial load vs displacement curve of all the specimen tested

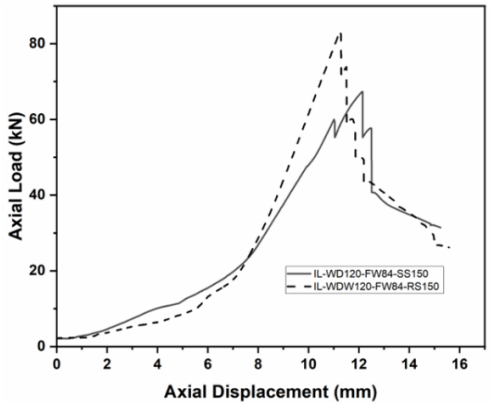

Figure 3.2 Comparison of Built-up I specimen with riveted and screw connection.

Table 1 Axial compressive strength of all the specimens

S. No	Specimen Id	Axial Compressive strength (kN)
1.	C-WD90-FW42-L10	27.9
2	IL-WD120-FW84-SS150	67.36
3.	IL-WD120-FW90-SS100	88.9
4.	IL-WD120-FW84-RS150	83.32
5.	BO-WD140-FW42-RS150	41.03

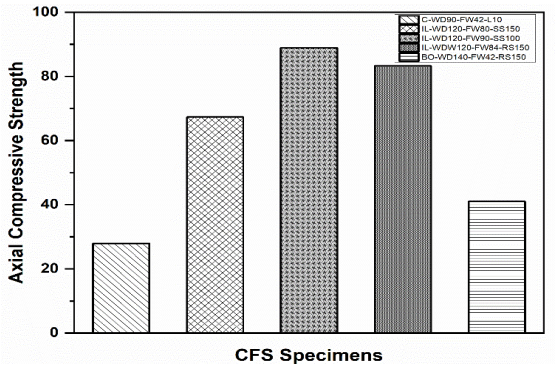

Figure 3.3 Comparison of axial compressive strength of all the CFS specimen

REFERENCES:

[1] Glauz, R. S. (2023). Enhancements to the Direct Strength Method of cold-formed steel member design. Thin-Walled Structures, 183, 110421. https://doi.org/10.1016/j.tws.2022.110421

[2] Schafer, B. W. (2008). Review: The Direct Strength Method of cold-formed steel member design. Journal of Constructional Steel Research, 64(7–8), 766–778. https://doi.org/10.1016/j.jcsr.2008.01.022

[3] Mahar, A. M. (2022). Buckling and post-buckling behaviour of cold-formed steel built-up columns [Queensland University of Technology]. https://doi.org/10.5204/thesis.eprints.232829

[4] Piyawat, K., Ramseyer, C., & Kang, T. H.-K. (2013). Development of an Axial Load Capacity Equation for Doubly Symmetric Built-Up Cold-Formed Sections. Journal of Structural Engineering, 139(12). https://doi.org/10.1061/(asce)st.1943-541x.0000780

4th International Symposium on One Health, One World
November 20 – 22, 2025

ABS ID: PO-02
Code No: IMSBE-EP-16

Bond Shear Tests of Polyester Geo-Grids Strengthened on Masonry Substrates

Deekshitha M K[1], Siva Chidambaram R[2]
[1]*PhD Scholar, Academy of Scientific and Innovative Research (AcSIR), Ghaziabad, India*
Advanced Concrete, Steel and Composites (ACSC) Group, CSIR-CBRI, Roorkee, India
deeksh2901@gmail.com
[2]*Principal Scientist, Advanced concrete, Steel and Composites (ACSC) Group, CSIR-CBRI, Roorkee, India*
Correspond to Siva Chidambaram R (dr.krsiitr@gmail.com)

Keywords: *Bond Shear Test, Masonry, Textile-reinforced Mortar (TRM).*

1. INTRODUCTION

The textile meshes are embedded in the inorganic cementitious, lime or cement-lime matrices to obtain textile-reinforced mortar or textile-reinforced concrete. Usually, the textiles like aramid, basalt, carbon and glass with a higher modulus of elasticity, a considerable amount of strain before rupture, are preferred to provide strength, stiffness and ductility for strengthening. Bond shear tests of textile-strengthened mortar or textile-reinforced concrete are carried out to study the interfacial bond characteristics between the matrix and the substrate, and the textile and the matrix itself. However, there are disadvantages in each existing textile; there is a need for affordable high-strain textiles rather than the existing ones to provide enough ductility to the substrate. This study analyses the bond shear behaviour of polyester geo-grids embedded in the polymer-modified cementitious mortar for a bond length of 300mm.

2. SPECIMEN CONFIGURATIONS

The bond shear test specimens were cast according to the specifications mentioned in RILEM 250 CSM. The bond length and the unbonded lengths of the specimens were fixed as 300mm and 400mm, respectively, as shown in Fig.1. The masonry prisms of height 500mm were cast and cured for 14 days. The surface of the strengthening was grooved at equal intervals for better adhesion between the cementitious matrix and the masonry substrate. The grooved surface was wetted with a thin cementitious slurry, followed by the application of a 5mm-thick polymer-modified cementitious matrix. Then, a single ply of uniaxial polyester geogrids with a tensile strength of 100 kN/m was embedded in the matrix and covered with another 5mm-thick matrix. The specimens were cured for 28 days before testing. The specimens are named after the geo-grid used, where “G” represents “Geo-grid”, “U” is Uniaxial, 100 is the tensile strength of the geo-grid, followed by the bond length of the specimen, which is 300mm on the substrate. The single lap shear tests were carried out by pulling the unbonded end of the textiles after clamping in the clevis grips.

Fig. 1. Bond shear test specimens

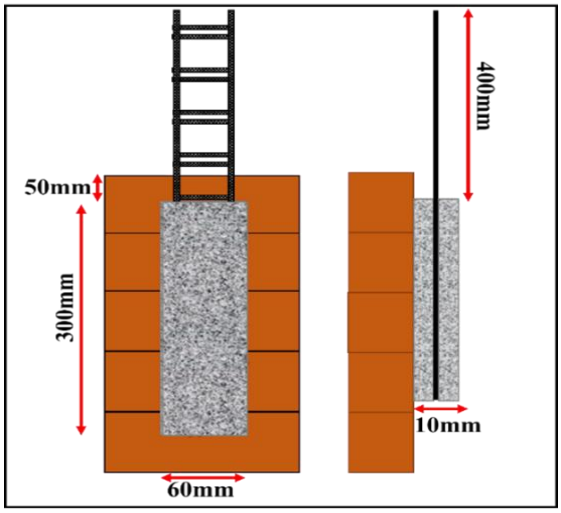

3. RESULTS AND DISCUSSION

The specimens were analysed for the failure patterns and the axial load-global slip behaviour through the tests.

Failure patterns

The failure patterns of the specimen are discussed in Fig.2. In the initial stage of the axial pull, the unbonded textiles experienced yielding at the junctions. When the tensile stress was further increased, the matrix in the bond length cracked, indicating a stress transfer from the textiles to the mortar. The cracks in the mortar are attributed to the lesser tensile strength than that of the geo-grids embedded. The specimens failed with the mortar spalling and the rupture of textiles in the matrix being embedded in the intact lower matrix, indicating better bonding between the masonry substrate and the matrix.

Fig.2. Rupture of textiles in the bonded regions

Axial load – Global slip behaviour

The axial load–global slip response of the GU100_300(1L) series (Fig.3.) specimens exhibits a typical behaviour associated with the bond–slip mechanism between the textile reinforcement and the matrix substrate. All three specimens exhibit a linear ascending branch followed by a nonlinear phase, indicating gradual debonding of the textile–matrix interface rather than sudden brittle failure. The stiffness in the initial stages is defined by the shear rigidity and adhesion developed between the matrix-substrate and within the textile-matrix interfaces. The stepped pattern in the graph suggests the engagement of geo-grid yarns subsequently in the stress transfer, further pointing at a ductile pull-out mechanism, beneficial for energy dissipation and indicating the ability of the geo-grid to sustain loads even after peak stress. The sudden drop in the axial load represents the rupture of the textiles at the bonded region. The variation in the ultimate slip values is due to the heterogeneity of the matrix impregnation and yarn alignment in the matrix during the specimen preparation.

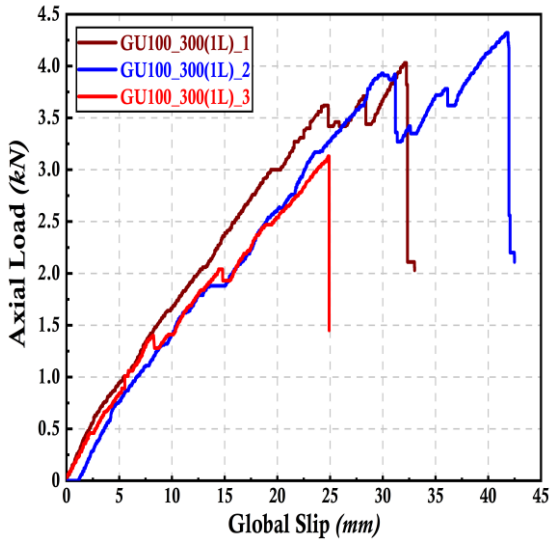

Fig.3. Axial load – Global slip behaviour

CONCLUSIONS

Three masonry prisms strengthened with 100 kN/m uniaxial geogrids embedded in polymer-modified cementitious mortar have been studied for the bond shear behaviour.

1.The cracks on the mortar matrix and ruptured geo-grid yarns indicated better bonding between the system.

2.The absence of a pronounced softening branch or plateau region after the peak suggests that interfacial debonding occurred almost simultaneously along the bonded length, instead of a progressive pull-out mechanism.

3.The observed brittle response due to the poor matrix impregnation can be solved with the improved surface treatment of the textile and anchorages at definite spacings.

REFERENCES:

[1] M. Rafieizonooz, J.-H.J. Kim, H. Varaee, Y. Nam, E. Khankhaje, Testing methods and design specifications for FRP-prestressed concrete members: a review of

current practices and case studies, J. Build. Eng. 73 (2023), 106723, https://doi.org/10.1016/J.JOBE.2023.106723.

[2] X. He, C. Zhou, M. Lv, Y. Wang, Y. Liu, Interfacial stresses of beams hybrid strengthened by steel plate with outside taper and FRP pocket, J. Build. Eng. 75 (2023),107034, https://doi.org/10.1016/J.JOBE.2023.107034.

[3] G. Ferrara, C. Caggegi, A. Gabor, E. Martinelli, Experimental study on the adhesion of basalt textile reinforced mortars (TRM) to clay brick masonry: the

influence of textile density, Fibers 7 (2019) 103, https://doi.org/10.3390/fib7120103.

[4] K.B. Goliath, D.C.T. Cardoso, F. de A. Silva, Influence of mechanical characterization technique on Carbon-TRC constitutive relations, J. Build. Eng. 67 (2023),

106058, https://doi.org/10.1016/J.JOBE.2023.106058.

[5] G. de Felice, M.A. Aiello, C. Caggegi, F. Ceroni, S. De Santis, E. Garbin, N. Gattesco,Ł. Hojdys, P. Krajewski, A. Kwiecie´n, M. Leone, G.P. Lignola, C. Mazzotti, D. Oliveira, C. Papanicolaou, C. Poggi, T. Triantafillou, M.R. Valluzzi, A. Viskovic, Recommendation of RILEM Technical Committee 250-CSM: Test method for Textile Reinforced Mortar to substrate bond characterization, Mater. Struct. 51 (4) (2018), https://doi.org/10.1617/s11527-018-1216-x

Theme

Urban Safety & Disaster Mitigation (USDM)

Distinguished Speakers

ABS ID: KN-197

Towards Ideal Disaster Countermeasures in Japan

K. Meguro[1]
[1]*Dean, Professor, Interfaculty Initiative in Information Studies/ Graduate School of Interdisciplinary Information Studies, The University of Tokyo*
Correspond to Prof. K. MEGURO (meguro@iis.u-tokyo.ac.jp)

Keywords: *National Critical Disaster, 1923 Great Kanto Earthquake Disaster, Aging and Depopulation Society, From Cost to Value, Phase-Free Disaster Countermeasures.*

1. INTRODUCTION

In 2023, 100 years passed since the Great Kanto Earthquake of 1923, which had caused damage of over 40% of the national budget at the time. Furthermore, the risk of disasters called national critical disasters, such as a Tokyo Metropolitan inland earthquake and a great earthquake(s) along the Nankai Trough, is now being pointed out. The disaster countermeasures that Japan should promotes most now are efforts to correct the so called "Japan's unfair disaster discounts" due to under evaluated Japanese disaster management capacity.

2.DIRECTION OF DISASTER COUNTERMEASURES OF JAPAN

In Japan, where the population is declining and the financial constraints are severe, it is impossible to maintain the traditional disaster countermeasures led by public support. The only way to make up for the lack of public support is through self-help and mutual assistance, but the traditional method of appealing to people's and companies' conscience and morality is limited. The keywords for future disaster countermeasures are "from cost to value" and "phase-free." Disaster countermeasures that have traditionally been considered costs have little continuity, and it is difficult to invest in measures that only work during disasters that rarely happen. Disaster countermeasures from now should be phase-free measures that do not distinguish between peacetime and emergency situations, with the main purpose of increasing value (quality of life and business performance, etc.) in peacetime, and can be used in emergency situations as well. This will create an environment that continuously brings value to those who implement measures, regardless of whether a disaster occurs or not.

3. WHAT DISASTER DISCOUNT IS

As shown in the upper part of Figure 1, Japanese cities such as Tokyo, Yokohama and Osaka are rated as having very high disaster risks by overseas companies. Disaster risk is generally evaluated as "hazard x exposed value x vulnerability." Hazards are earthquakes and typhoons (natural threats), and specifically, the magnitude and extent of external forces multiplied by the probability of occurrence. Exposed value x vulnerability is the weak human lives, property, and functions located in the area affected by the hazard. Japan is disadvantaged due to that it is located in an area where a wide variety of hazards occur, and the great amount of exposed value by the concentration of value in the metropolitan area. However, both the governments (nation, prefectures, and municipalities) and companies have been taking measures at a much higher level than other countries, but these measures are not being properly evaluated. As a result, Japanese companies are valued significantly lower than Western companies with similar corporate

performance. This phenomenon is called disaster discount.

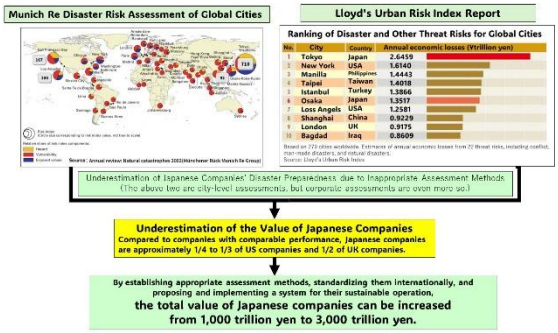

4. WHAT JAPAN SHOULD TACKLE FOR IMPLEMENTATION OF DISASTER RESILIENT SOCIETY

The reasons behind disaster discount are that Japanese society (governments and private companies) is reluctant to disclose information related to disaster risks (without information, assessment results become conservative) and that the current assessment methods used internationally are inappropriate. Japan had better need to propose correct assessment methods, make them the international standard, and create a system in which various efforts made in advance are properly rewarded. For companies, an increase in the assessed value of their own company will be a major incentive, and the concentration of functions in the capital region will also be alleviated. An increase in the value of Japanese companies as a whole will not only make Japan and Japanese people themselves more prosperous but will also create an environment in which future damage can be significantly reduced. This kind of total system, which is not normally considered disaster countermeasures, should be promoted.

ABS ID: KN-01

Disaster Multi-Risk Reduction and Urban Resilience: A Selection of Concepts, Methods and Applications

P.b. Lourenço
Professor, ISISE, ARISE, Department of Civil Engineering, University of Minho, Guimarães, Portugal
Correspond to pbl@civil.uminho.pt

Keywords: *Masonry; Cultural Heritage Buildings; Multi-hazard; Risk; Earthquakes.*

1. INTRODUCTION

Numerous large-scale disasters are causing severe economic losses and affecting millions of people. These, associated with a rapidly increasing rate of urbanisation, demonstrate the need for specific approaches to assess and manage natural and man-made disaster risks over these areas. Earthquakes, fires or floods are inevitable hazards with the potential to generate large-scale social, cultural and economic impacts and long-last disruption of the urban systems. However, these impacts can be significantly reduced through the implementation of a systematic risk assessment process. One of the most important research challenges in the field of systemic risk analysis is how to define new advanced analysis methods able to consider the interdependencies between these different components. The evaluation of the risk is considered essential to define strategic urban and emergency planning management actions and should be based on the analysis of the buildings, the exposed population and their emergency interaction. Such an approach is urgently needed for complex scenarios, particularly in the case of multiple hazards involving e.g. earthquakes, liquefaction, floods and fire.

Natural disasters continue to produce large human and economic losses. Between 1998 and 2017, disasters caused about 1.3 million deaths and affected 4.4 billion people, with economic losses on the order of trillions of dollars. Although most recorded disaster events were climate related, a large share of disaster fatalities arose from geophysical events, particularly earthquakes [1].

Unreinforced masonry (URM) buildings constitute a substantial portion of the global building stock, especially in historic centres and archaeological sites. Their prevalence is well documented in exposure databases and building taxonomies intended for seismic risk assessment. The Global Earthquake Model has developed a worldwide exposure model that organizes information on building types and occupancies, confirming that masonry accounts for a significant fraction of construction [2]. This global evidence reinforces the need to address URM behaviour in risk management strategies for historic environments.

The 2017 Lesvos earthquake in Greece is a recent example that underscores these concerns. Damage patterns recorded in traditional masonry, including out-of-plane failures of façades and gables, highlight the influence of construction typology, existing defects, and past interventions on seismic performance [3]. Such field observations help engineers calibrate and validate assessment approaches and provide a quality check for laboratory testing and numerical models.

2. BUILT SCALES AND EXAMPLES

Conservation engineering offers a bridge between empirical knowledge and modern structural analysis. The discipline integrates historical research, detailed on-site surveys,

experimental characterization, monitoring, and calibrated modelling to support decisions that satisfy safety, authenticity, and compatibility. It requires a strong foundation in both science and ethics, since interventions must be minimal, compatible, durable, and reversible where feasible, and should be justified by transparent analysis of uncertainties and alternatives. This perspective has been distilled in the ICOMOS principles and the Iscarsah Guidelines [4], which provide a holistic framework for the analysis, conservation, and structural restoration of architectural heritage (Figure 1). The most recent edition of the Iscarsah Guidelines reiterates core requirements such as the use of knowledge-based models, sensitivity analyses, and quality control of interventions within a documented process from diagnosis to maintenance.

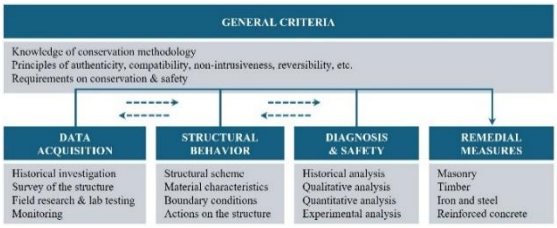

Figure 1. ICOMOS/Iscarsah methodology [4].

Risk and resilience provide a useful framework for analysing seismic safety in cultural heritage. Risk is typically defined as a function of hazard, exposure, and vulnerability, while resilience relates to the capacity of assets, systems, and communities to resist, adapt, and recover. In historic urban areas, these concepts are especially relevant because the consequences of earthquakes are magnified by factors such as aging building stocks, deferred maintenance, and competing institutional responsibilities [5]. Therefore, addressing these challenges requires approaches that operate across multiple scales. At the building scale, the Iscarsah methodology supports rigorous, case-specific analysis and design. At urban and territorial scales, index-based and parametric methods, complemented by open-source geospatial workflows and, where appropriate, machine learning algorithms, enable comparable assessments across large inventories and facilitate prioritization in planning and emergency management. The combination of these scales translates assessment outputs into actionable decisions for preparedness, mitigation, and phased retrofit.

The National Museum of Archaeology in Lisbon (Portugal) illustrates the challenges posed by a large, monumental masonry structure (Figure 2). In this case, inspections, ambient vibration testing, nonlinear pushover analyses, and displacement-based verifications in line with Eurocode provisions were combined in a comprehensive assessment [6]. The results indicated adequate performance under design-level earthquakes but vulnerabilities in severe scenarios, particularly in the vaulted galleries. Retrofitting options, such as roof reinforcement and stainless-steel tie rods, were analysed, highlighting the trade-offs between safety improvements and cost or visual impact.

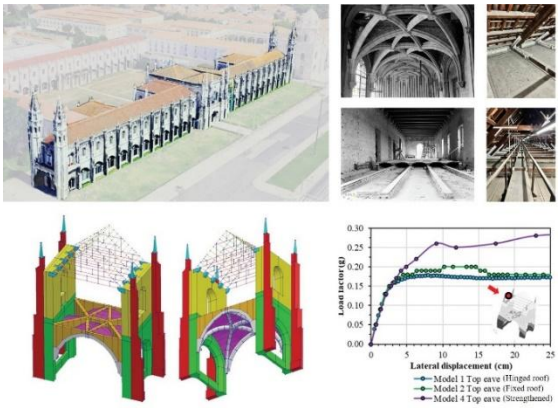

Figure 2. Seismic vulnerability assessment of the National Museum of Archaeology in Lisbon [6].

Complementing these methodological advances, an open-source information system was implemented to manage seismic vulnerability data across large sets of historical buildings (Figure 3) [7]. This system integrates survey data into a GIS environment, enriched with Python-based tools for calculating indices, managing uncertainty, and publishing results

through web services. The workflow was designed to function even with limited infrastructure, allowing both proactive (pre-disaster) and reactive (post-disaster) surveys. By lowering technical and financial barriers, this approach proves how digital tools can democratize vulnerability assessment, making it feasible for small institutions and local authorities to adopt systematic strategies for seismic risk management.

3. CONCLUSIONS

URM structures, which form the backbone of historic towns and archaeological sites, remain particularly vulnerable due to their inherent material limitations, complex morphologies, and the cumulative effects of age and environmental exposure. The scale of potential human and cultural losses underscores the urgency of developing and applying robust methodologies for their assessment and protection.

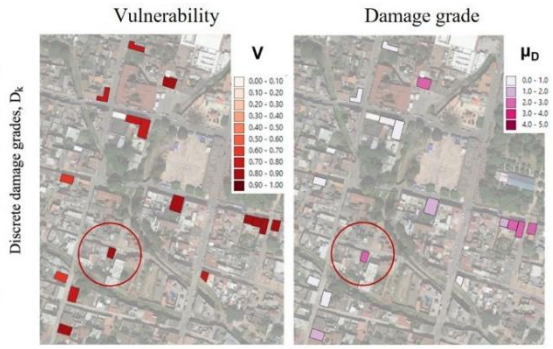

Figure 3. Open-source GIS framework for seismic vulnerability assessment [7].

The concepts of risk and resilience provide a coherent lens for approaching this challenge. Risk highlights the combined influence of hazard, exposure, and vulnerability, while resilience emphasizes the capacity to absorb, adapt, and recover. Applied to heritage contexts, these ideas call for action at the scale of individual monuments and across urban and territorial levels. Large-scale screening tools can help authorities prioritize resources, while detailed building-scale studies reveal the mechanisms of failure and the safety margins of specific structures. Both scales are necessary to move from diagnosis to effective preparedness and intervention strategies. Methodological advances have progressively strengthened this field. At the same time, conservation engineering remains not only a technical endeavour but also an ethical one, demanding interventions that respect authenticity, minimize intrusion, and ensure compatibility and reversibility. Safety is therefore pursued not as an abstract engineering goal but as part of a broader responsibility to protect cultural values.

REFERENCES:

[1] UNDRR & CRED, Economic Losses, Poverty & Disasters: 1998-2017, 2018.
[2] Silva, V. et al., Development of a global seismic risk model. Earthquake Spectra, 36(1), 372–394, 2020.
[3] Vlachakis, G., Vlachaki, E., Lourenço, P.B., Learning from failure: Damage and failure of masonry structures, after the 2017 Lesvos earthquake (Greece). Engineering Failure Analysis, 117, 104803, 2020.
[4] ICOMOS/Iscarsah, Guidelines for the Analysis, Conservation and Structural Restoration of Architectural Heritage, 2024.
[5] Mascheri, G. et al., A framework for multi-risk assessment in a historical area of Lisbon. International Journal of Disaster Risk Reduction, 108, 104508, 2024.
[6] Karanikoloudis, G. et al. (2025). Seismic Assessment of the National Museum of Archaeology in Lisbon, Portugal. Int. J. of Architectural Heritage, 1–29, 2025.
[7] Ramírez Eudave, R. et al., Implementing Open-Source Information Systems for Assessing and Managing the Seismic Vulnerability of Historical Constructions. Buildings, 13(2), 540, 2023.

ABS ID: KN-03

Ncree-niar's contributions to earthquake disaster mitigation and Community resilience in taiwan

J.-f. Chai[1]
[1]*Deputy Director General, National Center for Research on Earthquake Engineering (NCREE), National Institutes of Applied Research (NIAR), Taipei, Taiwan*
Correspond to Dr. J.-F. Chai (chai@niar.org.tw)

Keywords: *Structural Retrofit Program, Earthquake Early Warning System, AI Application in Earthquake Engineering, Non-structural Components and Systems*

1. INTRODUCTION

This article presents the earthquake mitigation strategies and advanced technologies developed at the National Center for Research on Earthquake Engineering, National Institutes of Applied Research (NCREE-NIAR) after the 1999 Chi-Chi earthquake, aimed at enhancing the community sustainability and resilience in Taiwan. It encompasses the structural retrofit program for public and private buildings in Taiwan, the seismic performance enhancement of non-structural components and systems, the development of earthquake early warning system and smart city management platform, and the application of AI in earthquake engineering.

2. STRUCTURAL RETROFIT PROGRAM

Since 2000, after the Chi-Chi earthquake, NCREE- NIAR helps Taiwanese government to launch a program to assess and strengthen the seismic performance of school buildings, hospitals, government offices and other public buildings. Taking school buildings as an example, approximately US$ 4 billion has been invested in the seismic evaluation and strengthening of 9,550 schools, with 626 schools having completed retrofitting to enhance earthquake resilience. The typical retrofit methods for school buildings include the jacked column, shear wall and wing wall. Figure 1 demonstrates the effectiveness of retrofit by comparing the seismic performance of two adjacent buildings after an earthquake.

Figure 1. Two adjacent buildings: left one without retrofit was severely damaged, and the right one with retrofit by shear wall performs well after the 2024 Hualien Earthquake (ML6.2)

For private building, it was observed that the mixed residential and commercial buildings were collapsed during earthquakes because of the soft and weak floors. Hence, NCREE-NIAR proposed the structural retrofit strategy to reduce the collapsed risk due to soft and weak

story. It means that the retrofit in current stage is only for the soft and weak story, and the retrofit for whole building is essential in the future. Buckling Restrained Braces (BRBs) offer stability, energy dissipation, and ease of construction, thereby enhancing the seismic resistance of buildings and protecting life and property. They have also been applied in the retrofit of existing structures (as shown in Figure 2).

Figure 2. After 2016 Hualien EQ, one building (6-story) was classified as moderately damaged and was retrofitted with BRB. In the 2024 Hualien EQ, only minor cracks appeared on the walls and ceiling.

3. NON-STRUCTURAL COMPONENTS AND SYSTEMS

In order to enhance the seismic performance of the non- structural components and systems to keep the function of buildings during and after earthquakes, the seismic- resistant strategy on critical equipment design was developed at NCREE-NIAR, and it focused especially for the suspended systems as well as the mechanical and electrical components and equipment in hospitals, Hi-tech fabs, nuclear power plants and renewable power systems. Based on the shaking table test and numerical analysis, the dynamic behavior and effectiveness of strengthening strategies for suspended systems (fire-protection piping systems, ceiling, busway and spring isolated suspended unit) and displacement-sensitive components (ALC wall) were investigated and qualified (Fig. 3). It should be noted that the study of busway and ceiling systems installed at a full scale 10-story steel building was executed at E- Defense (Fig.4) under the collaboration project between NIED and NCREE-NIAR.

The seismic behavior of the equipment inside a wind turbine nacelle was studied at NCREE-NIAR. Based on the numerical analysis, the seismic response at the top of supporting tower of a wind turbine corresponding to the design earthquake was determined first, and it was used as the input motions of a full-scale wind turbine nacelle shaking table test (Fig. 5). In addition, the FEM model of the nacelle and inside equipment was developed and

verified by the aforementioned experiment results. Furthermore, the critical component was selected and put onto the shaking table for detailing test (Fig. 5), while the input motion being the responses at anchorage point obtained from previous nacelle tests. The purpose is to develop seismic qualification methods for the critical components in large wind farm assets

Figure 3. Shaking table test for non-structural components and systems at NCREE-NIAR

platform which can deliver earthquake information by administrative district to designated re-broadcasters (specific users) for rapid application. As shown in Fig, 6, the hybrid platform integrates NCREE-NIAR's existing on-site system data with regional information provided by Central Weather Administration. When a predicted seismic intensity above the warning threshold level is expected to affect specific administrative districts (townships, towns, or city districts), the information is sent to re-broadcasters. These re-broadcasters then provide services to enterprises or the public through functions such as disaster mitigation control and warning. In addition, applications include dynamic evacuation, elevator control to the nearest floor, automatic gas shut- off, school broadcast alerts, electronic bulletin

board warnings in public buildings, construction site safety alerts, radio announcements, and energy management services for charging stations.

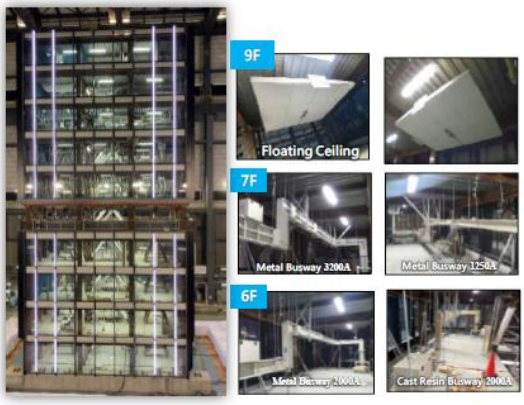

Figure 4. Shaking table test for non-structural components and systems (busway and ceiling) installed at a full scale 10-story steel building at E-Defense

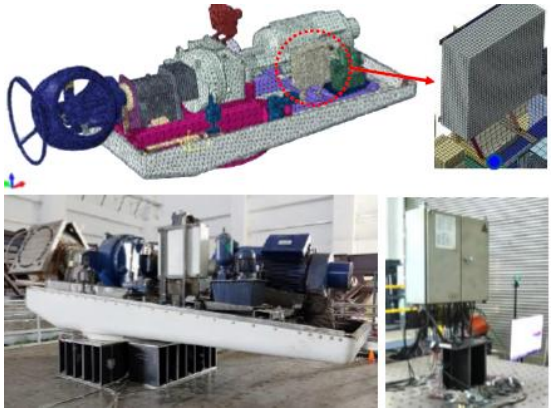

Figure 5. FEM model and shaking table test for full-scale wind turbine nacelle and critical component at NCREE- NIAR

4. EARTHQUAKE EARLY WARNING SYSTEM

NCREE-NIAR has integrated both regional and on-site systems to develop a hybrid earthquake early warning

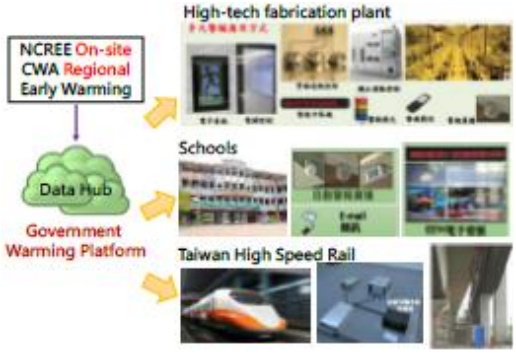

Figure 6. Hybrid earthquake early warning platform integrating both on-site and regional information

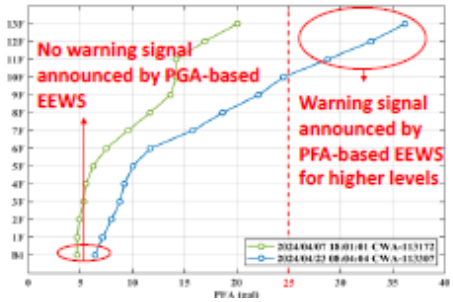

Figure 7. PFA-based EEWS for high-rise building considering the resonance effect

Currently, the earthquake early warning messages are mainly based on whether the PGA reaches the warning threshold. However, even earthquakes that do not reach this threshold at the ground surface may still cause severe swaying in high-rise buildings due to the interaction between seismic waves and the natural characteristics of tall structures, leading to the resonance effect (Fig. 7). To address this, the NCREE-NIAR has developed the High- Rise Building Strong Motion Early Warning System. This system utilizes structural monitoring data to identify in advance the natural vibration period of buildings and the seismic response characteristics of upper floors. During an earthquake, it uses the initial P-waves to assess whether the subsequent S-waves are likely to induce strong shaking in high-rises. Based on this assessment, the system determines whether to issue a warning message, enabling residents on upper floors to take protective measures beforehand and reduce potential damage.

5. AI APPLICATION IN EARTHQUAKE ENGINEERING

For disaster relief, NCREE-NIAR developed the AI- enhanced digital twin to quickly identify large-scale building damage and road pass-ability using satellite or aerial images with machine learning. It takes 7-10 minutes for City-level recognition with 75% accuracy (Fig. 8). In addition, it can automatically generate 3D digital models for buildings and key features, such as entry points and tilt angles, using optical radar and drone photography in 1 hour (Fig. 8). It can help decision-making for rescue plans in impacted zones. Furthermore, NCREE-NIAR developed the AI technology to quickly evaluate the remaining seismic-resistant capacity of buildings from architectural drawings, structural diagrams, and on-site damage photos, which speeds up the classification of disaster damage for reconstruction.

Figure 8. AI-enhanced digital twin for large-scale damage recognition and key feature analysis of impacted zones after earthquakes

NCREE-NIAR developed a digital twin for quality control of on-site rebar assembly, including the rebar dimensions, spacing, and seismic hook angles for walls, columns, and slabs. This system has been used in the actual project of the MRT Line. In addition, a localization and measurement technology was developed for drones, overcoming the challenges of navigation in GNSS-lack zones (Fig. 9). This technology enables detailed surface inspections of structural elements, including detection of cracks, efflorescence, and concrete spalling in critical bridge components. In collaboration with four leading steel structure manufacturers, NCREE-NIAR developed an AI-based expert system for internal diaphragm plates in steel columns and established an integrated automated welding platform (Fig.10).

Figure 9. AI-assisted surface inspection for structures at GNSS-lack zones

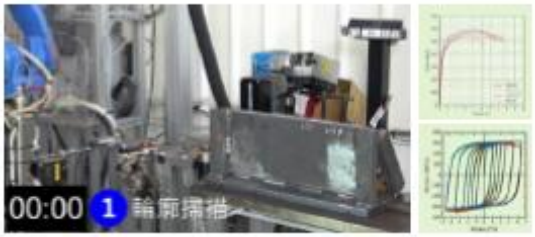

Figure 10. AI-Assisted automated welding technology for steel structures

6. CONCLUSION

The research achievements of NCREE-NIAR in earthquake mitigation fully reflect its missions and visions:

(1) pre-quake preparation, emergency response, and post- quake recovery; (2) integration of research capacities across earthquake engineering institutes in Taiwan to enhance the nation's overall research capability; and (3) promotion of international cooperation in earthquake hazard mitigation, establishing NCREE-NIAR as a key contributor to the global earthquake engineering research community."

ACKNOWLEDGMENTS

This article summarizes the research and development results on earthquake disaster mitigation conducted at the National Center for Research on Earthquake Engineering, National Institutes of Applied Research, and incorporates the contributions of all research colleagues. I would like to express my gratitude to them for their dedication.

ABS ID: KN-07

Prof. C V R Murty

ABS ID: KN-13

Dr. Shantanu Sarkar

ABS ID: KN-14

Prof. Daniel Vitorino de Castro Oliveira

ABS ID: KN-15

Shri. Krishna S vatsa

Keynote Speakers

ABS ID: KN-210

Mr. Jitendra Bothara

ABS ID: KN-04

The Impact of the 2025 Myanmar Earthquake on Tall Buildings in Bangkok

P. Warnitchai
Professor, School of Engineering and Technology, Asian Institute of Technology, Pathumthani, Thailand Correspond to Prof. P. Warnitchai (pennung@ait.ac.th)

Keywords: *Bangkok, Tall Buildings, Long-period Ground Motions, Soil Amplification, Resonance, Damping, Mandalay Earthquake.*

1. OVERVIEW

Bangkok, the capital of Thailand, was significantly affected by the 2025 M7.7 Mandalay earthquake, even though it is located about 1000 km from the earthquake epicenter. The city lies on a large, 800 m deep soil basin, which can strongly amplify long-period ground motions. A large number of high-rise buildings with long natural periods were strongly shaken by the resonance effect of these amplified ground motions, causing great panic among building occupants. Several hundred of these buildings suffered minor to severe damage to non-structural components (e.g. partition walls, ceilings, elevators), about ten of them suffered significant damage in structural walls (concrete crushing and buckling of reinforcing bars), and one 30-storey building collapsed completely. This event is the most severe earthquake Bangkok has ever experienced in modern times. Bangkok is indeed prepared for the effects of such distant large earthquakes, as high-rise buildings have been designed and built since 2007 to withstand the expected long-period ground motions. The design spectrum was determined based on a comprehensive study of basin amplification and a probabilistic seismic hazard assessment. During this earthquake, ground motions were recorded at five seismic stations in Bangkok. Although the spectral accelerations of these recorded motions are lower than those of the design-basis earthquake, their impact on high-rise buildings appears to be disproportionately high. Subsequently, an investigation was conducted using the acceleration records at rooftop of two high-rise buildings and the time histories of lateral roof displacements of several high-rise buildings obtained from video clips using a pixel tracking technique. The result shows that the critical damping ratio of the fundamental vibration modes of these buildings is much lower than expected; it is about 1% instead of 2.5%--the value recommended by the Tall Buildings Initiative and adopted by the Thai national standard for earthquake-resistant design. This finding could explain the higher-than-expected impact on high-rise buildings in Bangkok from the distant large earthquake. It could also mean that the seismic design criteria for Bangkok will need to be significantly adjusted in the near future. It also suggests an effective method to suppress the seismic response: increasing the damping level by installing energy-absorbing devices in high-rise buildings.

2. SOIL AMPLIFICATION OF GROUND MOTIONS

The earthquake occurred along the Sagaing Fault in Myanmar, with its epicentre nearly 1,000 km from Bangkok. At such a large distance, the seismic waves travelling through the regional tectonic plate should have weakened to a level that would cause no significant harm to buildings and structures. However, due to the presence of a large, deep soil basin beneath Bangkok and the surrounding provinces, the seismic waves, particularly long-period ones (about 2 to 8

seconds), were greatly amplified, making them strong again.

The sedimentary soil basin is more than 100 km wide, measured from north to south and east to west, and is about 800 m deep beneath Bangkok. The uppermost layer is soft clay, underlain by alternating layers of stiffer clay and sand. Our research team has spent many years determining its key dynamic properties using a technique based on array microtremor measurements. We created a dynamic model of the soil basin, and our model predicted that the basin can amplify long-period seismic waves several times, making the surface ground motions strong and of long-period type.

This type of long-period ground motions can produce strong shaking effects on structures with long natural periods through resonant amplification, and Bangkok has a large number of such long-period structures—tall buildings. Many of these were shaken strongly and suffered some degree of damage. However, the effects on low- to mid-rise buildings with short natural periods were much less significant, as there is no resonant amplification in such cases.

3. THE MAIN SEISMIC THREATS TO BANGKOK

Based on our seismic hazard assessment, the following are three possible earthquake scenarios with the greatest potential impact on Bangkok:

• An earthquake of magnitude 7.0–7.5 occurring along an active fault in Kanchanaburi province, about 200 km from Bangkok.

• An earthquake of magnitude 8.0 occurring along the Sagaing Fault, the longest and most active fault running through several cities in Myanmar into the Andaman Sea.

• An earthquake of magnitude 8.5–9.0 occurring in the Arakan Subduction Zone.

Although all these earthquake scenarios are possible, the likelihood of any occurring in our lifetime is quite low (less than 10%). However, the March 2025 earthquake, which was very similar to the second scenario, has already occurred and demonstrated that Bangkok is vulnerable to such distant earthquakes. We need to prepare ourselves for the other possible scenarios.

4. DAMAGE TO TALL BUILDINGS

The Thailand Structural Engineers Association (TSEA) surveyed the damage and found that several hundred tall buildings in Bangkok and surrounding provinces suffered damage to their non-structural components (cracked partition walls, fallen ceilings, damaged facades, elevator problems, and drainage issues), while around ten buildings showed structural damage. In one 25-storey hospital, for example, reinforced-concrete shear walls experienced concrete crushing and buckling of vertical reinforcement near the base of the walls, which might have been due to improperly overlapped vertical bars, creating weak zones that behaved in a brittle manner. One 33-storey office building under construction completely collapsed during the event.

5. GROUND MOTION RECORDS

Five seismic stations in Bangkok recorded ground accelerations. These records indicate that the ground shaking was of long duration (more than 2 minutes), long period (about 2 to 8 seconds), and low intensity (peak ground acceleration about 0.02g). Compared to the code spectra (DBE and MCE spectra), the spectral accelerations for natural periods of 3 seconds or less were well below code provisions. However, for natural periods of 5 seconds or more, the spectral accelerations were comparable to those of the code spectra, with some even slightly higher.

6. RESONANCE IN TALL BUILDINGS

Resonance occurs when the period of ground shaking matches a building's natural period. The response spectra of ground motion records from stations in Bangkok show several spectral peaks within a period range of 2 to 8 seconds, indicating that the ground shaking contains motions of many different periods. Therefore, resonance can occur in buildings ranging from 'not-so-tall' to 'super-tall', as long as their natural period matches one of these spectral peaks.

The Bangkok skyline has only around ten super-tall buildings (about 60 storeys or higher) with natural periods of around 6 to 8 seconds. However, the city has more than a thousand tall buildings ranging from 10 to over 50 storeys, with natural periods between 1 and 5 seconds. Within this period range, the most dominant spectral peak occurs at a period of about 3 seconds. This indicates that tall buildings of about 25 to 30 storeys were likely to be most affected by the earthquake. The initial damage data appears to support this point well.

7. DAMPING RATIO OF TALL BUILDINGS

The damping ratio, which quantifies how well a building dissipates energy, has a major influence on the response of the building, particularly when the resonance occurs. The lower the damping ratio, the higher the structural response. It is generally assumed that the damping ratio of tall buildings is about 2.5%, which is lower than that of low- and mid-rise buildings (5%). However, based on vibration records from a few instrumented tall buildings and tall building movement data obtained by a research team from the Institute of Science Tokyo using a pixel tracking method to analyse available video records, we found that the damping ratio of several tall buildings could be as low as 1%. This lower-than-expected damping ratio could be a key factor for the higher-than-expected damage observed in many tall buildings in Bangkok.

7. STRATEGIES TO IMPROVE SEISMIC PERFORMANCE OF HIGH-RISE BUILDINGS

Ground motions typically consist of a wide range of frequencies. In Bangkok, the presence of deep soft soil basins tends to amplify specific frequency components, particularly those associated with long-period ground shaking. This amplification results in the acceleration response spectra with several spectral peaks and valleys within the long period range.

Increasing structural stiffness or strength (by adding or enlarging structural components) may inadvertently shift the building's natural period towards one of these spectral peaks, thereby increasing seismic demands. Consequently, this approach could be counterproductive in soft soil conditions.

As previously discussed, structural damping plays a crucial role in mitigating seismic responses under long-period ground motions. The most effective strategy in this context is the incorporation of supplementary damping systems, which can reduce seismic demands regardless of the structure's natural period. Devices such as viscous dampers, viscoelastic dampers, friction dampers, and metallic dampers are particularly beneficial.

In conjunction with supplementary damping systems, structural walls should be carefully designed to be more ductile by mitigating brittle failure modes. These brittle failure modes include diagonal tension and compression failures due to shear forces, sliding shear at construction joints, instability in slender wall sections, compression reinforcement buckling, and failures related to lap splices and anchorage. Addressing these vulnerabilities can substantially reduce damage and significantly lower the risk of collapse during seismic events.

Bright Spark Lecture

ABS ID: KN-05

Mandalay Supershear Earthquake: Lessons Learned and Mitigation

S.h. Zaw[1]
[1]*Vice President, Myanmar Earthquake Committee,*
Federation of Myanmar Engineering Societies, Myanmar

Keywords: *Mandalay Earthquake, Mitigation.*

1. GENERAL

The Mandalay Earthquake on March 27, 2025, was a rare Supershear event (M 7.7) that ruptured the middle Sagaing Fault. It caused over 5,000 deaths and major infrastructure collapses, including the Mandalay and Myitnge bridges. Striking during peak conflict, it severely affected cities like Mandalay and Naypyidaw, impacting about 33% of the population. The extent of the damage was comparable to the historical 1839 Innwa earthquake (M 7.8)

2. RESPONSE AND ASSESSMENT

Response efforts were led by the Myanmar Earthquake Committee and the Myanmar Earthquake Clinics, an impartial, independent volunteer team. Major actions included rapid building assessments. The Post Disaster Rapid Assessment (PDRA) used the ATC-20 standard, training 400 engineers and incorporating mobile and GIS tools. This was followed by the Post-Disaster Structural Review (PDSR), which covered all building types, unlike standards focused solely on concrete structures.

2.1 Timeline and Lessons Learned

The response phase lasted five months and was notably efficient. The first two weeks focused on emergency rescue and restoring lifelines, followed by two months of damage assessment, emergency stabilization, SOP development, and trust building. Key lessons included the value of local decision-making, which enabled rapid, practical solutions, and the ongoing need to adapt and foster trust.

3. MITIGATION AND FAULT ZONE RESTRICTIONS

Future earthquake mitigation in Myanmar centers on enforcing strict Fault Zone restrictions for land use, guided by maps that classify areas into risk zones. The highest-risk Red Zone, extending 50 feet each side of the fault, forbids permanent structures and underground utilities to prevent surface rupture and protect lives. The moderate-risk Yellow Zone allows only lightweight, low-rise buildings with enhanced seismic design and geotechnical review, while the low-risk Blue Zone applies standard seismic codes but restricts major developments and prohibits public or essential facilities. These measures aim to reduce seismic hazards and guide safer development in areas near active faults.

4. CONCLUSIONS

The 2025 Mandalay Supershear Earthquake exposed severe vulnerabilities in densely populated, unstable areas. The efficiency of the recovery effort relied heavily on ad hoc, localized, professional response teams and the successful cooperation among stakeholders. Key lessons included the value of local decision-making for fast, practical solutions. To mitigate future risks, enforcing Fault Zone restrictions—especially the 50 ft Red Zone ban on permanent structures—and adopting better seismic design and community preparedness are essential for cities like Yangon and Bago.

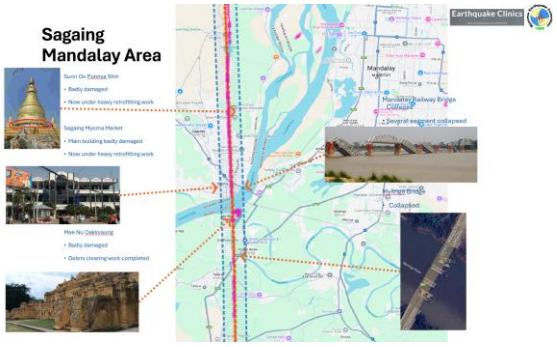

Figure 1. Fault Zone around Sagaing and Mandalay Areas

Figure 2. Mandalay University celebrating 100 years anniversaries after repairing severe damaged in Mandalay earthquake.

REFERENCES:

[1] Henry Yule, A Narrative of the Mission to the Court of Ava in 1885 (London: [Publisher, Year]), 349–351.
[2] https://sites.google.com/view/earthquakeclinics

Oral Presentations

4th International Symposium on One Health, One World
November 20 – 22, 2025

ABS ID: 95

USDM-OP-01

Investigation on Shear Strength and Behaviour of Reinforced Concrete Short-Span T-Beams Strengthened by Concrete Jacket

Vishnu t. Unni[1] and amlan k. Sengupta[2]

[1]*Ph.D Student, Department of Civil Engineering, Indian Institute of Technology Madras, Chennai, India,*

[2]*Professor, Department of Civil Engineering, Indian Institute of Technology Madras, Chennai, India,*
Correspond to VISHNU T. UNNI (ce20d025@smail.iitm.ac.in)

Keywords*: short beam, concrete jacketing, micro-concrete, seismic strengthening, shear reinforcement, inclined stirrups.*

1. ABSTRACT

The present study investigated the improvement in shear strength and behaviour of short span beams due to concrete jacketing. Specimens with portions of slabs as flanges (subsequently referred to as T-beams) were tested. The objective of testing T-beams was to study the fabrication and effect of the three-sided retrofit scheme. In the study, two reference T-beam specimens (without retrofitting jacket) and two retrofitted T-beam specimens were tested under monotonic transverse loading and cyclic loading to study the behaviour under shear failure. All the specimens were designed to fail in shear, with their shear-span to effective depth ratios about 1.5. The tests examined the application of micro-concrete as a jacketing material with inclined stirrups. The details of the specimens, test set-up and results are briefly described in this paper. A method to estimate the shear strength of a jacketed beam based on the strut-and-tie method and sandwich model is presented.

2. INTRODUCTION

Reinforced concrete multi-storey buildings with deficiencies to resist the effect of earthquakes can be retrofitted with global strategies or using member level techniques such as concrete jacketing, bonding of steel plates, fiber-reinforced polymer (FRP) sheet wrapping, and use of composites made with cement based matrix. The present study addressed the strengthening of shear deficient short-span T-beams by employing concrete jacketing as a retrofitting technique.

In the experimental study, two original specimens (without jacketing) and two retrofitted specimens were casted (Table 1). One specimen from each set was tested under monotonic transverse loading and the other under repeated cyclic loading as described later. High-strength micro-concrete was used as the jacketing material, along with additional longitudinal reinforcement and inclined stirrups. The stirrups were inclined at 135° to the longitudinal axis of a beam in the left shear-span and symmetrically placed in the right shear-span. Since reversed cyclic loading was not applied, stirrups inclined at 45° were not provided. All the specimens were designed to fail in shear, with their shear-span to effective depth ratios nearly about 1.5.

3. DETAILS OF SPECIMENS

This section covers the geometry, reinforcement details, materials used and the preparation of the specimens.

Specimen Dimensions

The details of the specimens are shown in Figure 1. BSO1 and BSO2 represent the reference beams. The inner portions of the jacketed beams were same. There were minimum stirrups in the shear span regions. Two stirrups were provided at each of the loading and support locations to avoid local crushing of concrete. BSJ1 and BSJ2 denote the jacketed beams. Jacketing was provided only on three sides of the beams. The thickness of a jacket was 70 mm on the sides and 50 mm at the soffit. Minimum thickness of the jacket was adopted so as to provide adequate cover to the additional bars. To reduce the drilling of

slab for anchoring the additional stirrups, a scheme with holder bars supported by widely spaced J-hooks was attempted. All the beams were designed to fail in shear by providing adequate amount of longitudinal tension reinforcement.

Concrete

Two types of concrete were used: (a) conventional low grade concrete for the reference beams and inner portions of the jacketed beams, (b) micro-concrete for the jacket portions (Table 1). The surface of the inner portion was adequately roughened for adhesion of the micro-concrete.

Table 1. Concrete mixes and compressive strengths

Specimen	**Type of concrete**	**Mix proportion**	**f_{cm}^* (N/mm²)**
BSO1, BSO2	Normal	Cement : FA : CA: Water = 1:2.7:4.1: 0.66 *	25
Inner portions of BSJ1, BSJ2			34
Jackets of BSJ1, BSJ2	Micro-Concrete	Water : Premix powder =1:0.16	56
*f_{cm}: Mean cube strength *CA: Coarse Aggregate, FA: Fine Aggregate			

4. DETAILS OF EXPERIMENTS

All the beams were tested using a 600-tonne load-controlled compression testing machine (Fig. 2). Each specimen was simply supported, with a hinged support at one end and a roller support at the other. A single vertical load was applied at mid-span over a small loading patch. The load was measured using a load cell. The deflection at mid-span and strains in the shear spans were measured using linear variable differential transducers (LVDTs).

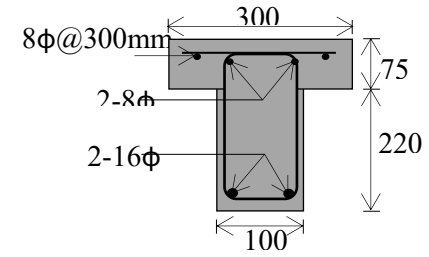

(i) Cross-section A-A

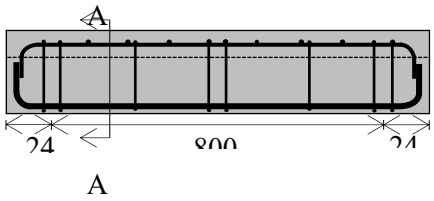

(ii) Longitudinal section

(a) Reference beam

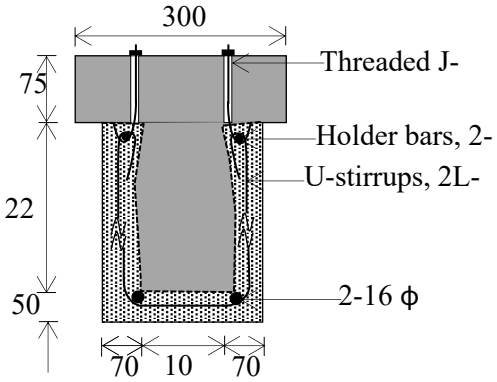

(i) Cross-section B-B

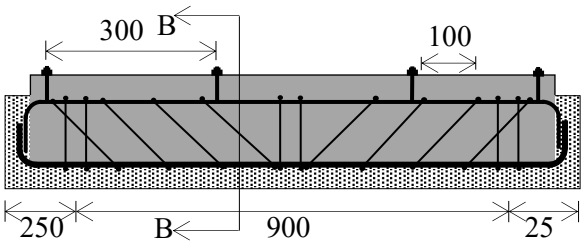

(ii) Longitudinal section

(b) Jacketed beam

Figure 1. Details of specimens (all dimensions are in mm)

Figure 3 shows the load versus mid-span deflection curves for the beams tested under monotonic loading. Figure 4 shows the same for the beams tested under repeated cyclic loading.

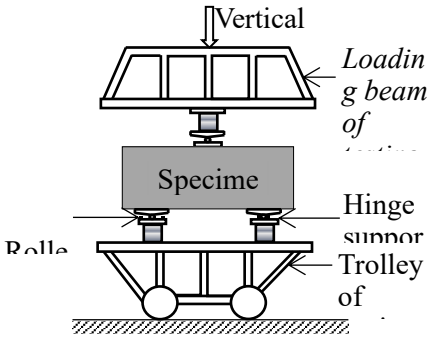

Figure 2. Schematic representation of test setup

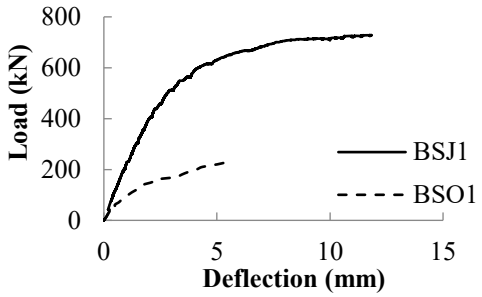

Figure 3. Load versus deflection under montonic loading

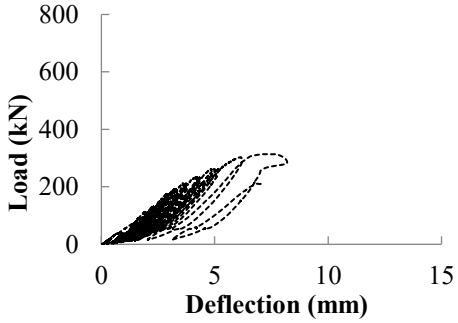

(a) BSO2

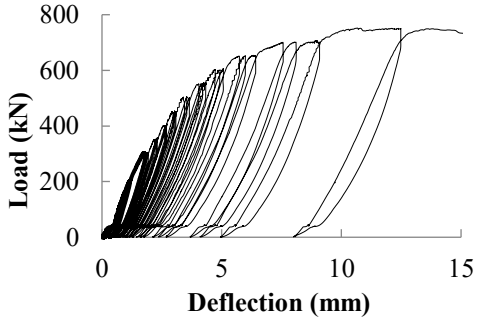

(b) BSJ2

Figure 4. Load versus deflection under cyclic loading

5. PREDICTION OF SHEAR STRENGTHS

For the deep beams, the strut-and-tie model (STM) was adopted for predicting the shear strengths [1]. Direct struts between the load and the supports were chosen based on the observed cracking and failure patterns (Fig. 5). Since the contribution of flange in resisting shear is small, a T-beam section was considered equivalent to a rectangular section. The transverse widths (dimensions in-plane of the shear panel) at the ends of a strut were obtained based on the in-plane dimensions of the loading and support plates. The failure of a strut was computed based on the lower width. Since, the out-of-plane dimensions of the plates covered the breadth of a specimen, the later was considered as the thickness of a strut. In the STM for the design of a conventional beam, the shear strength is considered as the lower of the following: a) crushing strength of a strut, b) yield strength of the stirrups. For a tested specimen, since the failure load corresponded to the crushing of a strut, the shear strength of a beam was determined based on the crushing strength of strut.

Reference Beams

The shear capacity (V_{uR}) corresponding to the crushing of a strut is calculated from Equations 1 and 2. Equation 1 relates the failure load (P_u) with the compressive force in the strut (C_d) based on the equilibrium of the nodal zone adjacent to the loading. The crushing strength of strut is estimated from the softened compressive strength of concrete (f_{cd}) and the section normal to the axis of the strut. The softening coefficient for cracked concrete (ζ) was determined using Equation 3 [2], which is a function of the diagonal tensile strain (ε_r) in the web. This was experimentally obtained from an inclined LVDT (L1 in Fig. 6). This was applied to the cylinder compressive strength of concrete (f_c'), which was taken as 0.8 times the cube compressive strength (f_{ck}).

$$V_{uR} = \frac{P_u}{2} = C_d \sin\theta \quad \textbf{(1)}$$

$$C_d = f_{cd} b_w w_d \quad \textbf{(2)}$$

$$\zeta = \frac{0.9}{\sqrt{1+400\varepsilon_r}} \quad \textbf{(3)}$$

The variables in the equations are as follows.

b_w = thickness of a strut = breadth of the beam web
w_d = least width of a strut
θ = angle of inclination of a strut

Jacketed Beams

The STM was extended to the vertically layered section of a jacketed beam web by using a sandwich model (Fig. 7). Here, the properties of concrete and reinforcement in the inner portion and the jackets outside are combined for the composite action. The distance between the centroids of the longitudinal reinforcement in the tension and compression zones is considered as the depth of an idealised shear panel. A key assumption in this model is that there is no slip at the prepared interface between the inner concrete and the jacket micro-concrete. The assumption of strain compatibility is based on the observation that no spalling of the jacket concrete was detected. The resultant crushing strength of the strut is based on the compressive strengths of the inner concrete and the jacket concrete (Equation 4). For design, the shear strength of a jacketed specimen is considered to be lower of the resistance offered by the struts or stirrups (Equations 5 and 6). The values of the variables for calculating the shear strengths of the specimens are provided in Tables 2 and 3.

$$C_d = (f_{cdi} b_i + 2 f_{cdj} t_j) w_d \quad \textbf{(4)}$$

$$V_{uR} = C_d \sin\theta \quad \textbf{(5)}$$

$$V_{uR} = \frac{A_{sv}}{s} z f_y (\cot\theta + \cot\alpha) \sin\theta \quad \textbf{(6)}$$

The variables in the equations are as follows.

$A_{st,i}$, $A_{st,j}$ = areas of longitudinal tension reinforcement of the inner and jacket portions
$A_{sc,i}$, $A_{sc,j}$ = areas of longitudinal compression reinforcement of the inner and jacket portions
A_{sv} = $A_{sv,j}$ = total area of the additional stirrups at a section
b_i = breadth of the inner portion
b_j = total breadth of the jacketed portion
f_{cdi} = softened compressive strength of inner concrete = $\zeta\, 0.8\, f_{ck,i}$
f_{cdj} = softened compressive strength of inner concrete = $\zeta\, 0.8\, f_{ck,i}$
f_y = yield strength of stirrups
s = horizontal spacing of the stirrups
t_j = thickness of jacket
z = distance between the centroids of tension and compression longitudinal reinforcement
α = angle of inclination of the additional stirrups

Figure 8 shows the predicted and experimental values of shear strengths. It is observed that the strut-and-tie method combined with the sandwich model predicted the shear strength reasonably well (Fig. 9).

Table 2. Variables for calculation of shear strengths

Specimen	w_d (mm)	θ (°)	ζ
BSO1	113.0	30.4	0.60
BSO2			
BSJ1	118.4	31.1	0.64
BSJ2			

Table 3. Softened compressive strength of concrete

Specimen	f_{cdi} (N/mm²)	f_{cdj}(N/mm²)
BSO1	12.0	-
BSO2		
BSJ1	16.3	27.4
BSJ2		

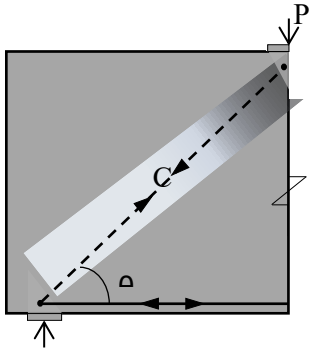

Figure 5. Formation of strut in a shear panel of a reference beam

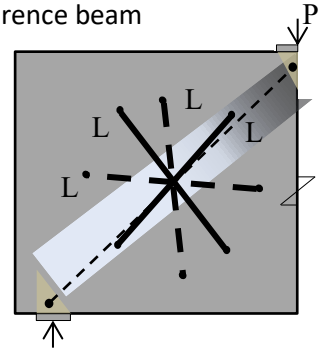

Figure 6. LVDT rosette (left shear-span) (F-front side, R-rear side)

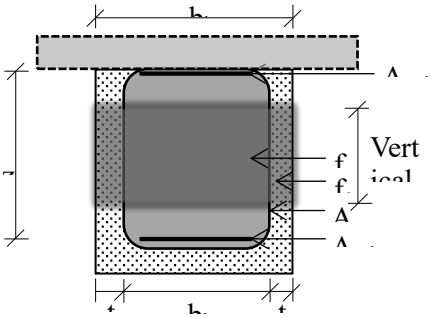

Figure 7. Sandwich model for a jacketed section

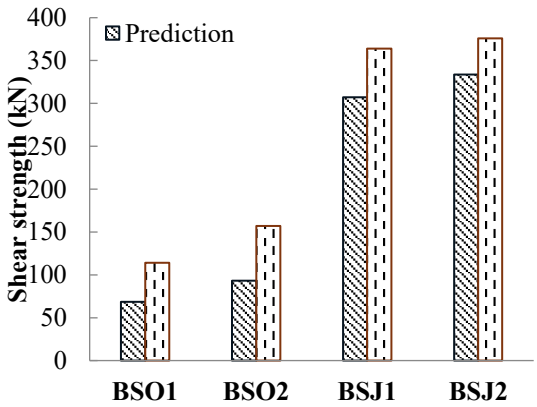

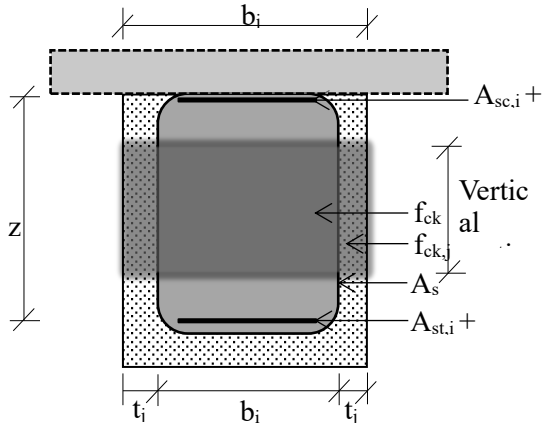

6. BEHAVIOUR OF SPECIMENS

A reference specimen failed in shear at the peak load, with the formation of diagonal cracks throughout the depth. However for a jacketed specimen, since the shear cracks were bridged by the inclined stirrups, flexural cracks occurred simultaneously. Failure patterns of jacketed specimens are shown in Figure 10. When a specimen was loaded, first thin flexural cracks formed around the middle of the tension face. Upon increased loading, one or more diagonal shear cracks appeared, propagating between the outside edges of the loading plate and the inside edges of the

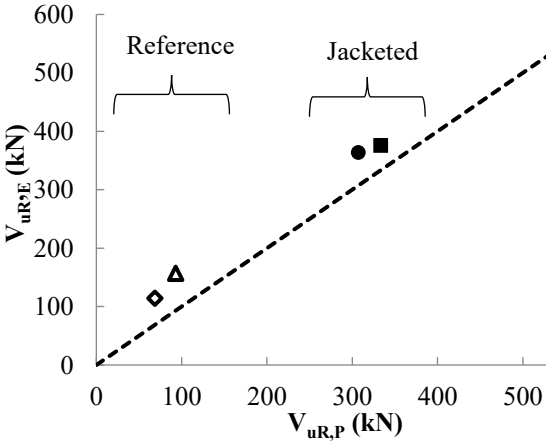

Figure 9. Correlation of predicted ($V_{uR,P}$) and experimental ($V_{uR,E}$) values

support plates. The development of diagonal cracks caused the mid-span deflection to increase rapidly. This showed the significance of shear deformation. With increasing strut action, each shear panel behaved like a truss panel. An average shear strain in a panel was computed from the strains measured by the diagonal LVDTs. An average shear stress was computed by dividing the shear force across a vertical section of a beam by the sectional area of a shear panel. Figure 10 shows the non-linear variations of average shear stress across the depth with average shear strain for beams tested under monotonic loading.

The following are salient observations from the tests.

(a) The nonlinear load versus deflection behaviour curves of the short-span beams were governed by shear deformation, especially after the formation of diagonal cracks. The failure loads corresponded to the crushing of the diagonal concrete struts in shear spans.

(b) A shear crack occurred across the entire width of a specimen, and not restricted in the jacket portions. For a jacketed specimen, there was no delamination of the jacket until the peak load under both monotonic and cyclic loadings. This showed that the roughened interface performed adequately.

(c) The shear strength of the jacketed beam (BSJ1) increased by 207% as that of the reference beam (BSO1) under monotonic loading. Similarly under cyclic loading, the shear strength of the jacketed beam (BSJ2) increased by 123% as that of the reference beam (BSO2).

(d) It was observed that the shear strain in the jacketed beam (BSJ1) at a certain shear stress was lower than that in the reference beam (BSO1) (Fig. 11). This was because the shear cracks in the jacketed beam were smaller compared to those in the reference beam. It was concluded that the inclined stirrups were effective in bridging the cracks.

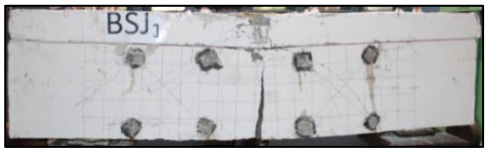

(i) Under monotonic loading

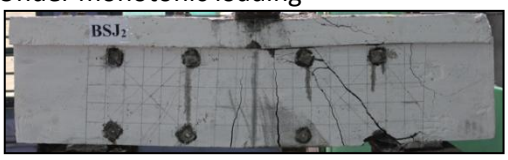

(i) Under cyclic loading

Figure 10. Failure patterns of jacketed beams

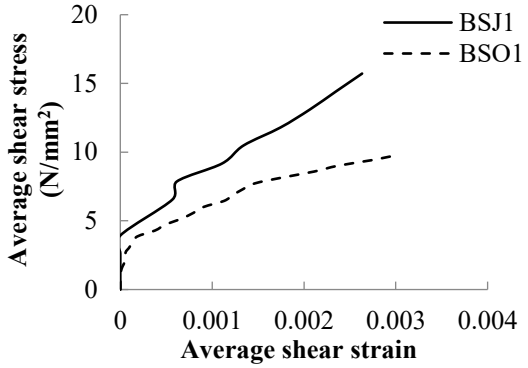

Figure 11. Variations of average shear stress versus average shear strain in shear panels

7. CONCLUSIONS

Following are the conclusions from the present study.

- The adopted concrete jacketing scheme substantially increased the shear strength of the beams. No delamination occurred at least up to the peak load, under either monotonic or cyclic loading.
- Since the load versus deflection behaviour of a specimen was governed by nonlinear shear deformation, a generalised truss approach can be adopted to predict the shear behavior [3].
- The envelope of the load–deflection behavior under cyclic loading was consistent with that observed under monotonic loading.
- The prediction of a shear strength using the strut-and-tie method combined with the sandwich model, was reasonably good.

The above conclusions can be furth”r investigated by testing specimens under reversed cyclic loading.

REFERENCES:

1. U. S. Pillai and D. Menon, Reinforced Concrete Design, Tata McGraw-Hill Education Private Limited, New Delhi, 2022.

2. T.T.C. Hsu Unified Theory of Reinforced Concrete, Taylor and Francis Group, USA, 1993.

3. K. Murugan and A. K. Sengupta, Formulation of a generalized truss analogy for the analysis of shear behavior of short jacketed columns, Structures, 55(2023), 1572-1583.

ABS ID: 58
USDM-OP-02

Mr. Ganesh Ashok Suryawanshi

ABS ID: 51
USDM-OP-03

Rehabilitation of severely deteriorated rcc elements in operational healthcare facility: a case study on material techniques and execution monitoring

Aishwarya gupta[1], niharika nanduru [2], pradeep kumar ramancharla[3]
[1] *sr. Project engineer, technical dept., nvln constructions pvt ltd, hyderabad, india,*
[2] *director, nvln constructions pvt ltd, hyderabad, india,*
[3] *professor, csir and director of csir-central building research institute, roorkee, india*

Keywords: *concrete rehabilitation, healthcare structures, corrosion mitigation, repair materials.*

1. ABSTRACT

The restoration of healthcare infrastructure—including hospitals, pharmaceutical manufacturing units, and bulk drug storage facilities—is vital to ensuring safety, operational efficiency, and uninterrupted medical services. Neglecting the upkeep of healthcare infrastructure can compromise safety and functionality. Regular maintenance is essential and must be carried out by experienced structural engineers who can accurately assess and identify deterioration in critical structural components. The common issues affecting these buildings typically start from damp conditions, water seepage, chlorides or aggressive agent's ingress, substandard construction practices, and insufficient concrete cover of structural elements.

The paper emphasizes material selection, execution techniques, and quality control strategies employed to meet structural and functional demands. This case illustrates how systematic, material-driven rehabilitation—executed without disrupting facility operations—can restore performance, extend service life, and improve resilience in aging concrete structures.

2. METHODOLOGY ADOPTED

The adopted methodology emphasized a lifecycle-oriented and sustainable approach to structural rehabilitation. Repair interventions were designed not only to restore immediate safety and serviceability but also to ensure durability under future environmental and operational demands. Selection of repair systems prioritized:

Lifecycle Extension: Materials and techniques were chosen to slow down deterioration processes, reduce frequency of future interventions, and extend the functional life of the facility.

Sustainability Considerations: Rehabilitation was preferred over demolition and reconstruction, thereby conserving resources, minimizing construction waste, and reducing embodied carbon.

Healthcare-Specific Constraints: All methods complied with hospital hygiene protocols, low-VOC material requirements, and non-intrusive application procedures to ensure uninterrupted operation of medical services.

By integrating modern repair technologies with sustainability principles, the methodology provided a balanced framework that addressed structural needs while aligning with environmental and institutional priorities.

Approach	Rehabilitation	Replacement
Service Life Extension	15–25 years (with periodic maintenance)	40–50 years (new structure)
Resource Use	Moderate (repair materials only)	Very High (cement, steel, demolition)
Environmental Impact	Low – reduced demolition waste, lower	High – large material footprint,

	embodied carbon	disposal issues
Suitability for Healthcare Facilities	High – non-intrusive, maintains hospital operations	Low – disruptive to ongoing services, requires relocation

3. CONCLUSIONS

The rehabilitation approach demonstrated that sustainable repair practices can achieve technical, environmental, and operational objectives simultaneously. Through the use of advanced protective coatings, compatible repair mortars, and durable waterproofing systems, the structure's service life was significantly extended without resorting to energy- and resource-intensive reconstruction.

From a sustainability perspective, the intervention reduced environmental footprint by lowering material consumption, limiting demolition waste, and supporting long-term durability. From a healthcare perspective, compliance with hygiene and operational standards ensured that the rehabilitation process aligned with the sensitive requirements of medical facilities.

Overall, the study highlights that adopting a lifecycle-based and sustainability-driven perspective in structural rehabilitation enables resilient, resource-efficient, and future-ready infrastructure for critical healthcare services.

REFERENCES:

[1] IS 15988:2013. Seismic Evaluation and Strengthening of Existing Reinforced Concrete Buildings — Guidelines. Bureau of Indian Standards.

[2] EN 1504-9:2008 – Products and Systems for the Protection and Repair of Concrete Structures

2025 HOW

4th International Symposium on One Health, One World
November 20 – 22, 2025

ABS ID: 09
USDM-OP-04

Field data-based landslide hazard assessment in parts of munsyari, pithoragarh, uttarakhand, india

Kaushal Singh Barfal[1], Siddhant Vaish[1,2] And Ajay Kumar Arya[3]
[1]*Research Scholar, Department of Geology, University of Lucknow, Lucknow, India,*
[2]*Research Scholar, Birbal Sahni Institute of Paleosciences, Lucknow, India*
[3]*Professor, Department of Geology, University of Lucknow, Lucknow, India*
Correspond to Prof. A.K. ARYA (aryageology2014@gmail.com)

Keywords: *Landslide, Geospatial, Disaster Management Plan, Main Central Thrust, Landslide Hazard Zone*

ABSTRACT

Landslides are one of nature's most devastating natural hazards. They come in various form and shape and are caused due to a number of factors. It is thus not easy to simply apply learning from one place to another without understanding the causative and triggering factors that may be unique to a specific area. Geologically, Munsyari and the villages within the Tehsil are strewn on either side of the Munsiari Thrust (MT) plane or, the approximately 10 km zone of the LHS between the MT and the Main Central Thrust (MCT) north of it. Literature is abundant with geology, tectonics, seismicity, mass wasting studies in the River Goriganga valley. Field evidence in the region has shown sufficient indicators of neo-tectonic activities, with innumerable joints, fractures, schistosity, gneissosity, ground water seepage, broken breast and retaining walls, buckled, broken, subsided roads any many more. Incessant rainfall, unplanned civic development, increasing tourism and population, decreasing forest cover and road construction using heavy dynamite blasting are adding further stress to the already fragile ecological environment.

Given that temporal prediction of a landslide event is a challenge, best alternative is to place barriers between the hazard, event and impact. Identification of Hazardous zones is the first step and currently literature is abundant with various methodology, however most methods generate results within an acceptable geological uncertainty range. We therefore use a simple multi-criteria Wight of Evidence (WoE) method to identify the hazard zones, which is also very similar to the BIS 1998 proposed method.

Hazard zones are classified based on severity and consequence of the potential mean mass wasting event, deciphered from historical data in the region. Zones that fall in the high impact zones are re-analyzed with field technical and non-technical data, to assess possible barriers.

These assessed barriers can be classed as Pre-event barriers (B-pre) implies making use of all the relevant information to stay away from line of sight of the potential event, as much as possible for all socio-economic activities. Similarly, post-event barriers (B-pos) that reduce reaction time for rescue and rehabilitation after any event. Identification of both these barriers require almost the same type of information, however the urgency in decision making is crucial for B-pos. Detailed geospatial information combining geologic, technical, environmental, administrative and social data if readily available with multiple event scenarios and their respective mitigation measures would immensely accelerate disaster management or prevent major loss in the case of an event.

This Disaster Management Plan (DMP) containing decision maps requires a seamless involuntary integration of multiple activities at the site, village and/or tehsil level between government, non-government agencies and local population. Having such a plan may not always prevent the event from occurring but severity of the consequences to life, livelihood and environment could be dramatically reduced by speeding decision making and focusing on recovery measures, or where

possible, ensuring urban designs, both policy and enforcement, takes this plan into account. “Life of many, or the Ecosystem as a whole cannot be put at ransom for the greed of few.”

This work aims to combine Geospatial information to highlight Landslide Susceptible Zones in the River Goriganga watershed and use it to propose probable meso-scale DMP for high-impact zones as a template that can be employed in similar seismic and eco-sensitive areas.

ABS ID: 53
USDM-OP-05

Real-Time Landslide Hazard Assessment at Narendra Nagar Using Acoustic Emission Sensor Technology

Ashish pippal, kanti l solanki, chandrabhan patel, s. K. Negi
[1]*CSIR-Central Building Research Institute, Roorkee, India*
Correspond to Mr. Ashish Pippal (ashish@cbri.res.in)

***Keywords**: Landslide, Acoustic Emission, high-frequency stress waves*

1. INTRODUCTION

The Indian Himalayan region has complex geology, rugged terrain, steep slopes, intensified seismic-tectonic processes, and excessive rainfall which make it vulnerable to landslides and cause frequently fatalities and substantial economic damage. Landslide risk and hazard assessment has recently gained a lot of pay attention. Urbanization increases the likelihood of slope instability in sloping metropolitan regions Shazan et al. (2023) [1].

We are all aware that the Himalayan region's slant disappointment can be attributed to a number of normal factors, such as temperamental steep inclines, helpless stone construction, and heavy precipitation Ahlawat et al. (2021) [2].

Making almost 17% of all recorded natural hazards, landslides rank as the seventh deadliest natural hazard worldwide. Landslides are predicted to become more common in the future as a result of growing urbanization, deforestation, and climate change. Shrestha et al. (2025) [3] have made putting in place Landslide Early Warning Systems (LEWS) essential for lowering the risk of disasters and fostering community resilience. LEWS offer vital time for precautionary actions and evacuation, which could save lives. By issuing warnings from minutes to several hours before to a landslide event, LEWS can dramatically lower the number of fatalities, according to research by Intrieri et al. (2013) [4]. With the use of early warnings, authorities can be prevent the damage of infrastructure, roads, bridges and economic loss.

The acoustic emission (AE) sensor technology is a promising non-invasive technique for real-time monitoring of slope instability in landslide hazard assessment. AE systems function on the principle that they detect elastic waves produced by micro fractures, particle dislocation, or soil shearing and hence enable early identification of deformation patterns in slopes.

Song et al. (2025) [7] offer an in-depth overview of AE technology in landslide monitoring, highlighting its singular ability to identify precursory signals preceding slope failure. AE sensors can identify high-frequency elastic waves produced by internal material deformation, enabling slope stability conditions to be categorized on the basis of AE event rates. Their review cites that AE systems, particularly when coupled with waveguides, are able to sense deep-rooted slope movements with sensitivity and dependability. The integration of AE with satellite-based SAR and pore pressure sensors also augments diagnostic capability, making AE a useful tool in field and laboratory applications. In spite of such challenges as signal degradation in complicated geological media, the continuing development of sensors, processing of signals, and machine learning is increasingly enhancing the applicability of AE systems.

Dixon et al. (2022) [8] investigate the practical use of AE systems using the Community Slope SAFE (CSS) project based in Myanmar. With this

method, AE sensors are incorporated in steel waveguides that are pushed into potentially unstable slopes. The sensors measure slope displacement rates, and when deformation exceeds a set level, they will set off visual and audio alerts. This study in Myanmar found that AE systems can be installed, operated, and maintained by trained community voluntary workers in circumstances where resources were limited. Their results confirmed there are strong correlations between AE rates and rates of slope deformation, and suggested that the CSS system could be used as real-time, low-cost early warning in high-risk places.

Dixon et al. (2022) created and implemented the Community Slope SAFE landslide early warning system using both wired and wireless AE sensors installed in steel waveguides in Myanmar. The Community Slope SAFE landslide early warning system observed slope deformation using RDCs and was automated to send SMS alerts when criteria were exceeded. The study reported its emphasis on community engagement and training so locals received the capability to deploy, maintain, and adjust the disposal for their local contexts. The AE activities correlated with rainfall and slope activity, indicating that AE could be used for an alerting system with good reliability. The system was powered by solar panels, was affordable, and designed to be low maintenance purposes setting, in communities that were remote and hazard prone. The project demonstrated that AE technology could successfully be implemented to develop a community disaster preparedness framework. The study would provide significant insight into future developments of community disaster alerting systems in the Indian Himalayan region such as Narendra Nagar where community-led real-time monitoring systems are needed for improving resilience towards landslides.

Ahlawat (2021) [2] describes the root causes of slope failure in the Himalayas, citing factors such as excessive rainfall, seismicity, poor rock formations, and surging human activities like deforestation and road construction. It cites that anthropogenic factors—particularly road development and deforestation—amplify natural susceptibilities, resulting in recurrent landslides. Further, landslides in the country are not only environmentally destructive but also interrupt social and economic life as they destroy infrastructure, degrade arable land, and result in loss of human life.

Codeglia et al. (2017) investigated the use of Acoustic Emission (AE) technology for monitoring slow-moving rock slopes at the Passo della Morte site in the Italian Alps. For their analysis, the researchers installed steel waveguides, imbedded into boreholes, to transfer the AE signals generated by internal rock deformation to piezoelectric surface sensors. AE activity was measured as Ring Down Counts (RDC), recorded every 15 minutes, which identified micro-crack behaviour. The authors employed a 20–30 kHz band-pass filters for their monitoring system, utilizing a 0.25 V threshold to avoid excess background noise. The researchers achieved long-term monitoring with minimal power supply demands, suggesting AE technology for passive measurements was suitable for remote areas. The authors also correlated AE readings with rainfall, snow depth and groundwater changes. In doing so, they were able to demonstrate that AE signals reliably represent the stages of deformation. This work demonstrates the legitimacy of using AE sensors to monitor under unstable slope conditions and provides a method for an autonomous system for long-term AE monitoring - one which would be perfect for landslide impacted areas of the Himalayan region like Narendra Nagar.

Dixon et al. (2015) [6] consider a technological solution to such risks, focusing on the use of Acoustic Emission (AE) monitoring systems for slope stability in real time. Their work describes a field trial of AE sensors embedded within steel waveguides at a railway slope in Southampton, UK. The AE sensors were able to detect geophysical conditions of micro-seismic

activity associated with ground movement and provided alerts to operators when rates of slope displacement exceeded preset threshold values. The findings indicate that AE systems are sensitive and viable, at a modest level of cost due to the capability of gathering high-temporal resolution, which makes for an impactful early warning system, particularly when included in a communication system.

This study uses Acoustic Emission (AE) sensor technologies to monitor and evaluate landslide dangers in real-time in the geologically vulnerable area of Narendra Nagar, Uttarakhand. The site Narendra Nagar, Uttarakhand is identified and characterized as the landslide-prone zones based on our preliminary geotechnical and geomorphological analysis. The purpose of the study is to assess response from AE sensors to identify micro-seismic or micro-crack activity linked to slope deformation. System deployment, sensor calibration, real-time data collection, AE activity correlation with slope movement, and early warning alert generation are all included in the scope. The study highlights the potential for community-level integration of AE-based landslide early warning systems in susceptible Himalayan terrains, as well as their cost-effectiveness and field usability.

- To install and implement AE sensor-ba sed monitoring systems capable of cap turing real-time micro-crack activity in unstable slopes
- To correlate AE event rates with slope displacement and deformation trends for early detection of potential landslid e events.

2. METHODOLOGY:

2.1 Study Area

The study was carried out at Narendra Nagar, a town near to Rishikesh in the Indian state of Uttarakhand. It is located between 30°09’00 N and 30°11’00 N latitude and between 78°16’00 E and 78°19’00 E longitude. The steep terrain, delicate geology, and exposure to intense monsoonal rains make this area of the Lesser Himalayas extremely susceptible to landslides. Real-time landslide hazard monitoring and early warning systems are necessary due to its close proximity to important road infrastructure and growing residential areas.

Figure 1: Landslide area at Narendra Nagar

2.2 Material Specification

To monitor slope stability using Acoustic Emission (AE) sensor technology, four (4 Nos.) boreholes one (1 Nos.) at the crown zone, two (2 Nos.) transition zone and one (1 Nos.) at the toe zone were drilled at marked (shown in Fig.) high risk zones identified through preliminary geotechnical and geomorphological mapping.

Each borehole had a diameter of 200 mm and was drilled to an average depth of 17 meters. The loose aggregates of size 5–10 mm gravel were used to backfill the annular space surrounding the waveguides in the boreholes. This created an active waveguide that improves the generation and transmission of AE signals.

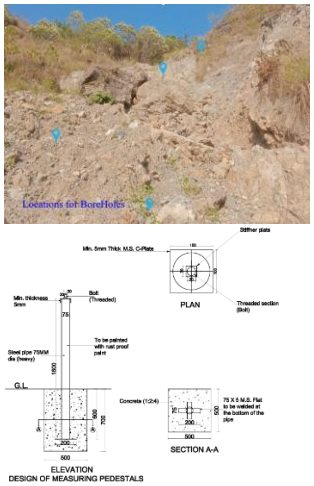

Figure 2: Borehole location and details

Four (4 Nos.) AE sensors were installed in each borehole. All four (4 nos.) wired AE sensors were installed Borehole 1, Borehole 2 and Borehole 3 in a pattern where three were placed near the top of the borehole at different depths for surface-near monitoring, and one at the bottom for sub-surface monitoring. Whereas three (3 Nos.) wired AE sensors and one wireless (1 Nos.) AE sensor are similarly placed in Boreholes 4. Both shallow and deep-seated slope deformation zones are vertically covered by this configuration, and wireless sensors increase the system's adaptability for remote signal transmission in situations where cabling is limited.

2.3 Data Collection

In this study, acoustic emission (AE) data gathering and collecting were planned to provide for long-term, continuous monitoring of unstable slopes in high-risk, remote locations. In order to identify micro-seismic activity caused by stress-induced fracture in soil or rock masses, the system used AE sensors that were mounted via steel waveguides placed into boreholes. In order to record AE activity in the form of Ring Down Counts (RDCs), which measure the frequency with which the signal amplitude crosses a predetermined threshold within a 15-minute period, these sensors were connected to a data acquisition system (DAS) made up of microcontroller-based components. After removing background noise from the analog signals using a band-pass filter (usually operating between 20 and 30 kHz), a voltage threshold was used to guarantee that only pertinent AE events were recorded. The system was perfect for distant and independent operation because it just kept RDC values, which drastically reduced power and memory usage. Both wired and wireless AE sensors were used; when important thresholds were surpassed, real-time alerts, including SMS notifications, were made possible by wireless nodes sending data via GSM modules and solar-powered controllers. To increase the accuracy of interpretation, AE data was also gathered concurrently with environmental and geotechnical factors such slope displacement, groundwater levels, and rainfall. In susceptible areas like the Himalayan terrain of Narendra Nagar, this integrated approach offers a dependable, field-ready solution for landslide hazard monitoring and helps the early detection of slope movement.

4. RESULT AND DISCUSSION

5. CONCLUSIONS

REFERENCES:

[1] Shazan, M., Pandit, K., Sarkar, S., & Uniyal, P. (2023). A brief review on landslides in Indian Himalayas. Proceeding on Innovative and Sustainable Materials & Technologies. CSIR-Central Building Research Institute, Roorkee.
[2] Ahlawat, S. (2021). Landslides in Himalayan Region: Occurrence, Cause and Effect, Volume 8, Issue 2, pp 731-739.

[3] Shrestha, M., Sharma, S., & Pradhan Shrestha, R. (2025). Landslides in the Himalayas: A Comprehensive Review of Hazards, Impacts, and Adaptive Strategies. Rural and Regional Development, 3(1), 10002.

[4] E. Intrieri, G. Gigli, N. Casagli, and F. Nadim (2013), Landslide Early Warning System: toolbox and general concepts, Nat. Hazards Earth Syst. Sci., 13, 85–90, 2013

www.nat-hazards-earth-syst-sci.net/13/85/2013/ doi:10.5194/nhess-13-85-2013.

[5] Deng, L., Yuan, H., Chen, J., Sun, Z., Fu, M., Wang, F., ... & Chen, T. (2021). Correlation between acoustic emission behaviour and dynamics model during three-stage deformation process of soil landslide. Sensors, 21(7), 2373.

[6] Codeglia, D., Dixon, N., Fowmes, G. J., & Marcato, G. (2017). Analysis of acoustic emission patterns for monitoring of rock slope deformation mechanisms. Engineering Geology, 219, 21-31, http://dx.doi.org/10.1016/j.enggeo.2016.11.021

[7] Song, J., Leng, J., Li, J., Wei, H., Li, S., & Wang, F. (2025). Application of Acoustic Emission Technique in Landslide Monitoring and Early Warning: A Review. Applied Sciences, 15(3), 1663. https://doi.org/10.3390/app15031663.

[8] Dixon, N., Smith, A. & Pietz, M. A community-operated landslide early warning approach: Myanmar case study. Geoenviron Disasters 9, 18 (2022). https://doi.org/10.1186/s40677-022-00220-7

[9] Dixon, N., Smith, A., Spriggs, M., Ridley, A., Meldrum, P., & Haslam, E. (2015). Stability monitoring of a rail slope using acoustic emission. Proceedings of the Institution of Civil Engineers-Geotechnical Engineering, 168(5),373-384, http://dx.doi.org/10.1680/geng.14.00152

[10] Shiotani, T. (2006). Evaluation of long-term stability for rock slope by means of acoustic emission technique. Ndt & E International, 39(3), 217-228, doi:10.1016/j.ndteint.2005.07.005.

[11] Dixon, N., Smith, A., Flint, J. A., Khanna, R., Clark, B., & Andjelkovic, M. (2018). An acoustic emission landslide early warning system for communities in low-income and middle-income countries. Landslides, 15, 1631-1644, DOI 10.1007/s10346-018-0977-1.

ABS ID: 166
USDM-OP-06

Ms. Siya Srivastava

ABS ID: 154
USDM-OP-07

Mrs. Hina Gupta

ABS ID: 148
USDM-OP-08

Dr. Suman Kumar

ABS ID: 147
USDM-OP-09

Dr. Suman Kumar

ABS ID: 102
USDM-OP-10

Need for Structural Health Monitoring (Shm) Code in India

P. D. Velani[1], A. Bhalkikar[2], H. C. Dasari[3], and R. Pradeep kumar[4]
[1]*Specification Engineer, Development Team, MIDAS Research and Development Centre India Pvt. Ltd, Navi Mumbai, India*
[2]*Assistant Professor, Civil Engineering Department, CHRIST University, Bangaluru, India*
3Assistant Professor, Civil Engineering Department,
Aditya Institute of Technology and Management, Srikakulam, India
[4]*Director, CSIR-Central Building Research Institute (CBRI), Roorkee, India,*
Correspond to Dr P D Velani (pulkit@midasit.com or velani.civil@gmail.com)

Keywords: *Structural failures, Sensors, Structural Health Monitoring, Infrastructure safety, National Standard, Mitigation, Resilience*

1. INTRODUCTION

India is witnessing rapid urbanization and infrastructure development, but this growth has also exposed critical vulnerabilities in the structural integrity of buildings, bridges, and public infrastructure. A large portion of the country's infrastructure, particularly in urban and semi-urban areas, is either aging, poorly maintained, or constructed without adequate quality control. Many structures lack periodic inspection or systematic assessment frameworks, resulting in undetected deterioration over time. Recent incidents such as the Morbi bridge collapse in Gujarat (2022), Siliguri flyover collapse (2023), and several high-rise building collapses in cities like Mumbai and Indore have underscored the urgent need for proactive measures.

Further, the current practices involve visual inspection and NDT tests which are done by engineers with years of experience in dealing with maintenance and monitoring. As there are no specific guidelines for assessment or health monitoring of structures, the procedure for the assessment of the strength of the structure is done by independent procedure. This may lead to underestimation or overestimation of deterioration in structures.

2. SHM IN INDIA AND AROUND THE WORLD

The application of SHM in India is used for buildings to get structural response (dynamic parameters such as natural period and damping) using ambient vibration (Arlekar & Murty, 2000; Velani et al., 2024; Velani & Ramancharla, 2023) as well as for long term continuous monitoring (Dasari & Kumar, 2024; Velani et al., 2022). There is also evidence of use of SHM for dams(Technical Manual on Instrumentation of Dams, 2022), bridges, heritage structures (Pradeep Kumar et al., 2020) and recently published guideline on SHM(ISHMS, 2024) by Indian Structural Health Monitoring Society.

Globally, SHM has been in use for the past two to three decades. Countries such as Australia, China, Canada, members of the European Union, the United Kingdom, and the United States are among those where SHM applications are more common, supported by established guidelines or codes. However, despite numerous guidelines and extensive research, the overall penetration of SHM applications remains limited (Limongelli, 2019; Moreu et al., 2018). This is mainly due to ambiguity or the lack of clear guidelines regarding sensor types and their lifespan. In cases of permanent vibration monitoring, data

handling can become cumbersome. Additionally, SHM results are often highly technical and may not be easily interpretable by decision-makers, and the cost–benefit ratio of such systems remains uncertain or inadequately documented.

Among several new Chinese codes for bridges, many important aspects are addressed, such as the type of sensors to be used in different situations, expected sensor lifespan, and SHM recommendations based on the bridge type and span. Such detailed provisions can help owners, engineers, and sensor manufacturers gain better clarity and scope in their work, thereby making the application of SHM more meaningful.

3. OPPORTUNITIES AND CHALLANGES/ NECESSITIES

India currently holds the position of the fourth-largest economy globally and is rapidly aspiring to reach the third position in the near future. This growth is supported by one of the largest road and rail networks in the world. However, this vast infrastructure presents a duality: some assets are decades old, with parts of the network dating back over 50 years, while new high-speed highways and railway lines are being rapidly added. To sustain the pace of development, safety must be paramount and never compromised in the new build environment. Simultaneously, sufficient resources must be allocated not only for rigorously maintaining the existing infrastructure but also for upgrading it to meet the ever-increasing demand from vehicular traffic and railway rolling stock. These critical needs are further compounded by the constant threat of degradation due to natural disasters like earthquakes and floods. Structural Health Monitoring (SHM) offers a technology-driven solution that can effectively address many of these challenges by providing real-time condition assessment and predictive maintenance insights. Given this context, the time is right to introduce a comprehensive, national SHM code in India to ensure the long-term safety and resilience of its vital infrastructure.

4. PROPOSAL & CONCLUSIONS

Taking inspiration of research carried out around the world and in India, India should come with code on SHM where Part I of a code act as a mother code on SHM giving overview of SHM and basic framework of SHM. Followed by parts of the same code addressing the specific needs of SHM for different civil structures such as bridges, buildings, dams, nuclear installment, offshore installment etc.. Implementation of SHM guidelines will lead to better infrastructure management and achieve the sustainable goals. And for this Academia, Government and industry needs to come forward to contribute towards development of this code.

REFERENCES:

Arlekar, J. N., & Murty, C. V. R. (2000). Ambient vibration survey of RC-frame buildings having brick masonry infill walls. Indian Concrete Journal, 74(10), 581–586.

Dasari, H. C., & Kumar, R. P. (2024). A case study on model updating of long uniform buildings. Journal of Civil Structural Health Monitoring, 14(2), 465–484. https://doi.org/10.1007/s13349-023-00717-1

ISHMS. (2024). GUIDELINES FOR STRUCTURAL HEALTH MONITORING.

Limongelli, M. P. (2019). Toward the development of standardized procedures for structural health monitoring.

Moreu, F., Li, X., Li, S., & Zhang, D. (2018). Technical Specifications of Structural Health Monitoring for Highway Bridges: New Chinese Structural Health Monitoring Code. Frontiers in Built Environment, 4. https://doi.org/10.3389/fbuil.2018.00010

Pradeep Kumar, R., Srinagesh, D., Seshunarayana, T., Chadha, R. K., Bodige, N., Suresh, G., Hima Chandan, D., & Murty, C. V. R. (2020). Vulnerability Assessment of a Heritage Structure Subjected to Blast-Induced Ground

Motions. Current Science, 119(7), 1131–1141. https://doi.org/10.18520/cs/v119/i7/1131-1141

Technical Manual on Instrumentation of Dams. (2022).

Velani, P. D., Dasari, H. C., Bhalkikar, A., & Ramancharla, P. K. (2024, June). DAMPING OF RC TALL BUILDINGS IN INDIA BY AMBIENT VIBRATION TEST. 18th World Conference on Earthquake Engineering.

Velani, P. D., Patnala, N., Prakke, B., Shastry, S. L. N., & Kumar, R. P. (2022). Tremors and built environment of Hyderabad, Telangana, India: safety of buildings using recorded ground motions. Current Science, 122(10), 1174–1184. https://doi.org/10.18520/CS/V122/I10/1174-1184

Velani, P. D., & Ramancharla, P. K. (2023). Approximate natural period expression for reinforced concrete tall buildings in India. Current Science, 124(12), 1412–1421.

4th International Symposium on One Health, One World
November 20 – 22, 2025

ABS ID: 99
USDM-OP-11

Structural performance assessment of buildings A key to earthquake disaster preparedness

P.A. Bansode[1], R. Goswami[2]
[1]*Assistant Professor, Department of Civil Engineering, Pandit Deendayal Energy University, Gandhinagar, India*
[2]*Professor, Department of Civil Engineering, Indian Institute of Technology Madras, Chennai, India*
Correspond to Dr. P.A. BANSODE (bansodeprashant.a@gmail.com)

Keywords: *Moment-Resisting Frame, Nonlinear Analysis, Ground Motions, Hazard, Fragility, Risk.*

1. INTRODUCTION

Earthquake safety of buildings is of paramount importance and design standards are enforced to ensure that buildings withstand anticipated design earthquake demand with the intent of minimizing risk to lives and properties. The design standards provide earthquake hazard estimates based on available ground motion data, which are revised over time due to improved understanding of tectonic features and availability of updated datasets of ground motions. With the revision of hazard, the performance of existing buildings that were designed according to the previous standards may not any more meet the demand of updated hazard levels, thereby posing higher risk. Given this challenge, a comprehensive risk evaluation of existing buildings is essential. Thus, the intent of this study is to emphasize the importance of structural performance assessment as a key component of earthquake risk evaluation, necessary for improved disaster preparedness.

In India, about 80% of the total population lives on approximately 60% of the landmass which have moderate to severe seismicity [1]. Many inter and intraplate earthquake events in past have resulted in loss of several lives and damage to thousands of buildings over the past few decades. Therefore, this study attempts to investigates the earthquake risk associated with mid-rise regular reinforced concrete (RC) moment-resisting frame (MRF) buildings of different categories (viz., normal, important, critical building) located in different earthquake zone (Zone II to V) (Figure 1a), designed according to IS 1893(1): 2016 [2], under the impact of revised earthquake hazard of India as prescribed in Draft IS 1893(1): 2025 [3]. A summary of key changes related to revised earthquake hazard for buildings and seismic zoning (Figure 1b) are discussed elsewhere [4]. The occurrence of an earthquake corresponding to the updated seismic hazard estimate would significantly affect the overall performance of RC buildings, especially in the regions of high seismicity. This study helps identify the vulnerability and demonstrates the inadequacy of MRF buildings in the regions of high seismicity, highlighting the need for retrofitting.

2. BUILDING DESCRIPTION

The numerical study considers 3D 9-storey RC MRF buildings. In total, 12 MRF buildings, of three different categories, namely, normal, important, and critical building, located in four different zones (i.e., Zone II to V) of India, are designed and detailed as per the provisions of IS 456: 2000, IS 1893 (1): 2016 and IS 13920: 2016 [2, 5-6]. The buildings have rectangular plan configuration as shown in Figure 2. The typical floor height is 3.7m, with a floor diaphragm of 180 mm in thickness. Apart from self-weight, super-imposed load, floor finish, and roof finish considered are 2.5 kPa, 0.5 kPa, and 1.0 kPa, respectively. The buildings are considered to be founded on hard soil with fixed base condition. Further, the design stress resultants are obtained using Response Spectrum Method along with appropriate gravity loads. The member dimensions of the building components are based on minimum stiffness requirements by limiting inter-story drift ratio to 0.4%, and axial compressive stress in columns to 0.4fc. Since, the building comprises special moment-resisting frames

oriented along two mutually orthogonal horizontal directions, they are designed for full design earthquake force in one direction at a time, and the corresponding load combinations are used.

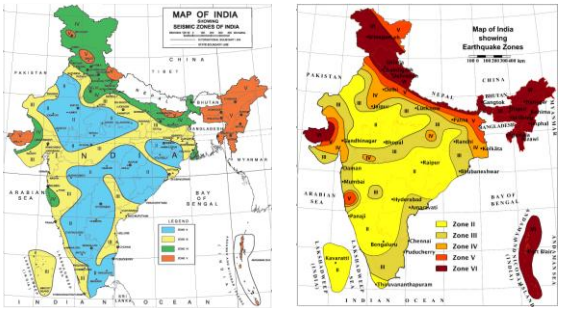

(a) (b)

Figure 1. Seismic Zone Map of India (a) current (2016 version) and (b) revised (2025 version

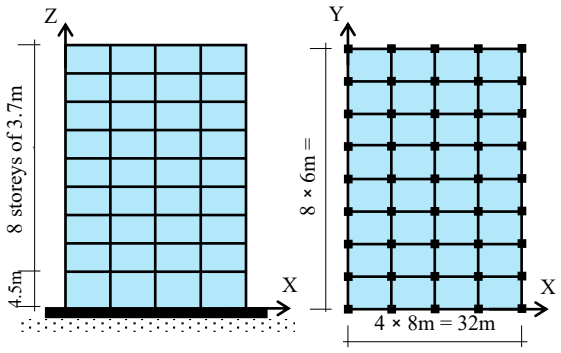

(a) (b)

Figure 2. (a) Elevation and (b) plan of study buildings

3. NONLINEAR MODELS AND METHODS

The nonlinear numerical models of study buildings consider the inelastic force-deformation behaviour of material, section, and member. It captures the attainment of different damage states in the building components (viz., yielding of reinforcing steel, spalling of cover concrete, and crushing of core concrete), and considers the effect of strength deterioration and stiffness degradation, and redistribution of forces during inelastic excursions [4].

The seismic risk evaluation of buildings involves integration of earthquake hazard and fragility curves. The latest draft of Indian earthquake design standard provides probabilistic seismic hazard analyses-based estimates of design peak horizontal ground acceleration [3]. For the purpose, earthquake events of 2,475-year return period (TR) are considered as benchmark and the hazard curves are derived in terms of exceedance probabilities [7], as represented by Eq.(1) (Figure 3). Multiple stripe analysis (MSA) is performed and standard lognormal cumulative distribution function is used to represent fragility curves for different damage states using Eq.(2) (Figure 4) [8]; and the seismic risk of buildings is quantified as the probability of attaining a specified damage state (DS) that are conditional on the occurrence of a single intensity measure (IM) level. The IM considered is spectral acceleration at fundamental natural period of a building (T1). For the purpose, nonlinear dynamic analyses are carried out to estimate a range of possible displacement demands that are likely to appear on a building under different earthquakes. This requires appropriate selection and scaling of ground motions. Therefore, a suite of 20 far-fault ground motions (Table 1) is selected based on reasonable randomness in terms of PGA, earthquake magnitude (Mw) and source-to-site distance (RRup) [9-11].

Table1. Far-fault earthquake ground motion suite [9-11]

Year	Earthquake	Station	PGA, g	Mw	RRup, km
1952	Kern County	TLS	0.18	7.36	38.89
1971	San Fernando	LH#9	0.17	6.61	22.57
1979	Imperial Vall.	CC#4	0.13	6.53	50.10
1979	Imperial Vall.	Delta	0.35	6.53	22.03
1979	Imperial Vall.	NFS	0.11	6.53	36.92
1987	Super. Hills	WLA	0.21	6.54	23.85
1989	Loma Prieta	A2RC	0.27	6.93	43.23
1989	Loma Prieta	HSP	0.37	6.93	27.93

1992	Cape Mendo. 41.97	EMW	0.18	7.01	
1992	Landers	DHS	0.15	7.28	21.78
1992	Landers	PSA	0.09	7.28	36.15
1994	Northridge-1 41.17	LA	0.21	6.69	
1994	Northridge-1 35.81	LH#1	0.09	6.69	
1995	Kobe	Kako.	0.32	6.90	22.50
1995	Kobe	Mori.	0.21	6.90	24.78
1999	Chi-Chi	T.047	0.30	7.62	35.00
2001	Bhuj Ahme. 306.00		0.11	7.60	
2011	Sikkim Sili. 179.00		0.16	6.90	
2015	Nepal	Kant.	0.16	7.80	59.90
2023	Turkey-Syria 142.15		3125	1.09	7.80

The 5% damped pseudo-spectral acceleration response spectra of these ground motions, are scaled to target spectra based on spectral acceleration values at the fundamental natural period (T1) of the study buildings [12], as represented in Figure 5. Further, the product of hazard curve and fragility curve corresponding to collapse state (CS) obtained from above set of equations Eq.(1) and (2), respectively, are integrated to estimate the absolute risk of collapse P[CS] over the design life (TD) of a building (Eq.(3)) [13].

$$\lambda\left[IM > x_j\right] = 1 - \left(1 - \frac{1}{Z_{T_R}}\right)^{T_D} \quad (1)$$

$$P\left(DS \mid IM = x_j\right) = \Phi\left[\frac{1}{Z_{2\beta}} \ln\left(\frac{x}{\theta}\right)^{1/k}\right] \quad (2)$$

$$P[CS] = \int_0^{\infty} P\left(CS \mid IM = x_j\right) \cdot \left| d\lambda\left(IM > x_j\right) \right| \quad (3)$$

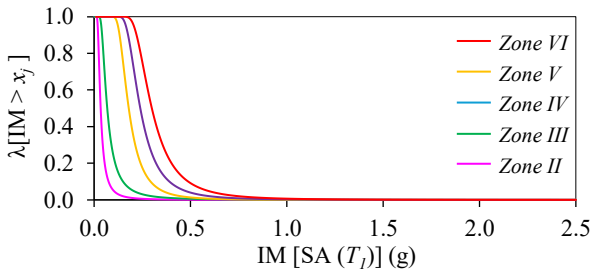

Figure 3. Hazard curves of the five earthquake zones in terms of exceedance probabilities

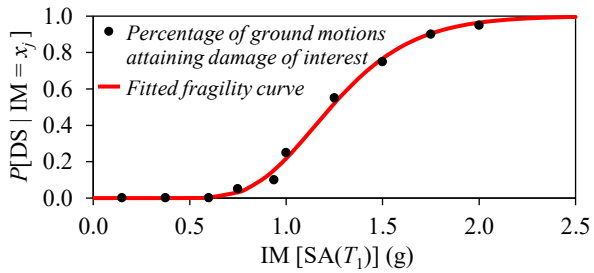

Figure 4. Fractions of damage state attained as a function of IM and corresponding fragility

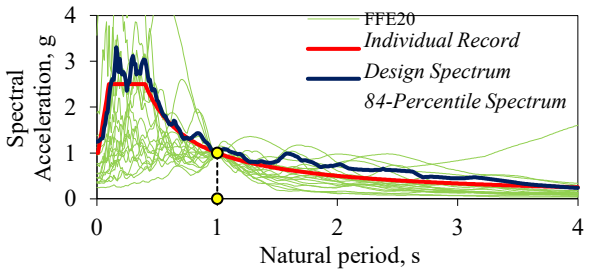

Figure 5. 5%-damped elastic pseudo-spectral acceleration spectra of the 20 far-fault earthquake records, scaled to 1g at 1 second natural period

The 12 study buildings discussed in Section 2, are evaluated through a series of nonlinear dynamic analysis using the suite of 20 far-fault ground motions (Table 1). The ground motions are scaled at different intensities of shaking (x_j) ranging from 0.1g to 1.5g, and the resulting fragility curves for the three damage states (*viz.*, yielding of reinforcing steel, spalling of cover concrete and crushing of core concrete) are presented in Figure 6. The fragility parameter θ and β for each damage state are graphically represented in Figure 7. It can be observed that the median capacity (θ) of buildings at yielding, spalling and crushing damage states range from 0.29g to 0.37g, 0.42g to 0.69g and 0.49g to 0.84g, respectively. The dispersion (β) values obtained for different damage states are in the range of 0.25 to 0.40, indicating relatively lower variability and a consistent correlation between the structural response and the intensity measure. It also implies that the uncertainty associated with modeling parameters and ground motion variability has been reasonably captured within the analysis framework.

In earthquake zone II and III, the ratio of median collapse capacity (θ) to earthquake hazard of the region ($2475T_R$) is observed to be greater than 2 (~2.3 to 4.3), indicating that the designed buildings exhibit a higher capacity relative to expected earthquake demand (Figure 8a). Conversely, in zone IV and V, this ratio is found to be less than 2 (~1.2 to 1.9), implying that the MRF buildings in the regions of high seismicity are more vulnerable, with their median collapse capacity being close to the $2475T_R$

4. FRAGILITY ANALYSIS

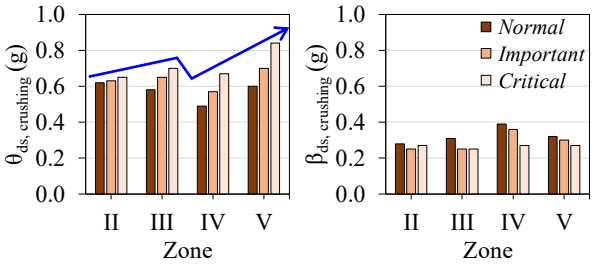

(a) (b)

Figure 7. Variation in fragility parameters (a) θ and (b) β

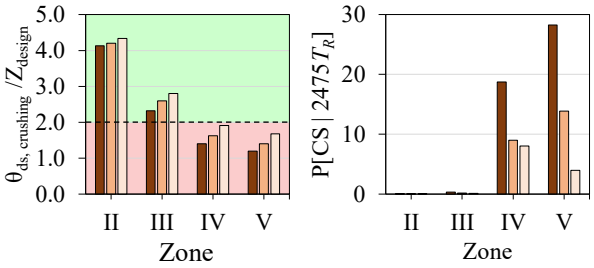

(a) (b)

Figure 8. (a) Ratio of median collapse capacity to earthquake hazard of the region and (b) Probability of collapse conditional at $2475T_R$

hazard of the region. Further, the probability of collapse state (CS), *i.e.*, crushing of core concrete, conditional at $2475T_R$, P[CS | $2475T_R$], are reported in Table 2. Buildings

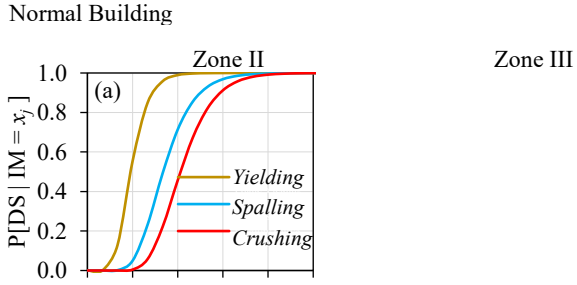

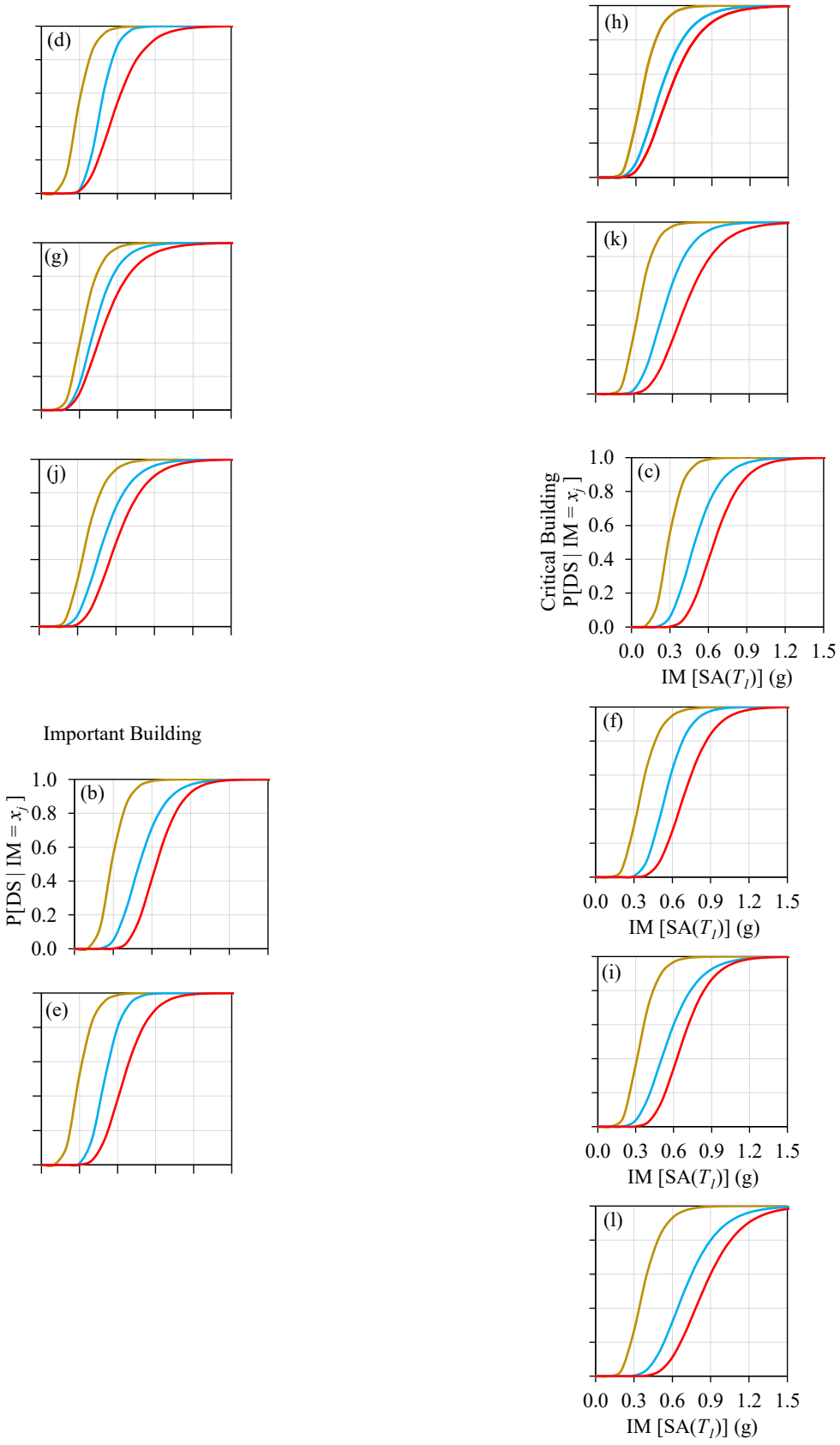

Figure 6. Fragility curves for study buildings of different categories in different earthquake zone

in zone II and III, have very low probability of attaining collapse state; the values observed are well below the acceptable limits set by international guidelines (Figure 8b). This is essentially due to the overall design wherein the design of vertical members is governed by gravity load in these lower zones, and thus, they tend to have high reserve strength against lateral forces. But, all buildings in zone IV and V fail by a wide margin; hence, the probabilistic performance expectations are not fulfilled.

5. ABSOLUTE RISK

The evaluation of absolute risk metric accounts for the cumulative probability of collapse, P[CS], over the entire design life of buildings. The absolute risk for all buildings in zone II and III falls well below the acceptable limit (Table 3), except critical buildings in zone III that fails by a narrow margin (0.31% against a desirable value of 0.25% or less). Such lower values of absolute risk in lower earthquake zone suggests that these buildings are unlikely to experience significant damage leading to collapse. In contrast, all buildings in zone IV and V surpasses the acceptable risk limits, highlighting the potential inadequacies of MRF structural system in regions of high seismicity. Therefore, it is evident that the existing stock of buildings in zone IV and V are at risk and require immediate attention towards retrofitting. In this context, there is urge to carry out extensive structural performance assessment of existing buildings in higher earthquake zones of India.

Table 2. Conditional Probability of attaining collapse state in MRF buildings P[CS | 2475T_R]

Zone	Normal	Important	Critical
II	0.00	0.00	0.00
III	0.31	0.00	0.00
IV	**18.75**	**8.98**	**8.02**
V	**28.26**	**13.85**	**3.98**
Acceptable Limit (%)	10.00	5.00	2.50

Table 3. Absolute probability of collapse in MRF buildings

Zone	Normal	Important	Critical
II	0.08	0.07	0.07
III	0.53	0.37	**0.31**
IV	**3.74**	**2.02**	**0.75**
V	**3.90**	**2.16**	**0.94**
Acceptable Limit (%)	1.00	0.50	0.25

6. CONCLUSION

Following are the key conclusions drawn from this study:

1. Earthquake risk associated with MRF buildings in zone II and III are within acceptable limit, but those in zone IV and V exceeds the limit.
2. Damage expected under the revised hazard is considerably large. This is of concern and highlights urgent need of assessment and retrofit of buildings in India.

REFERENCES:

[1] Annual Report, *National Disaster Management Authority*, Government of India. New Delhi, India

[2] IS 1893 Part 1 (2016). Criteria for Earthquake Resistant Design of Structures—Part 1: General Provisions and Buildings. *Bureau of Indian Standards*, New Delhi, India

[3] Draft IS 1893 Part 1 (2025). Design Earthquake Hazard and Criteria for Earthquake Resistant Design of Structures - Part 1: General Provisions and Buildings. *Bureau of Indian Standards*, New Delhi, India

[4] P. Bansode, R. Goswami (2024). Seismic Performance of Existing RC Moment Frame Buildings under Revised Seismic Hazard of India. Proceeding of 18th *World Conference on Earthquake Engineering*, Milan, Italy

[5] IS 456 (2000). Plain and Reinforced Concrete—Code of Practice. *Bureau of Indian Standards*, New Delhi, India

[6] IS 13920 (2016). Ductile Design and Detailing of Reinforced Concrete Structures Subjected to Seismic Forces – Code of Practice. *Bureau of Indian Standards*, New Delhi, India

[7] Raghukanth, S. T. G., Podili, B., Sreejaya, K. P., Gupta, I. D., Roshan, A. D., Sinha, R., Chopra, S., Srinagesh, D., Sheth, A., Goswami, R., Mandal, H. S., Singh, R. J., Chaudhary, J. K., Kumar, S. A., and Murty, C. V. R. Draft earthquake zone map of India. *Journal of Earth System Science*, 133 (2024)

[8] Baker, J. W., Bradley, B. A., and Stafford, P. J. *Seismic Hazard and Risk Analysis*. Cambridge University Press, United Kingdom, 2021. ISBN: 9781108348157

[9] PEER NGA-West2 (2024). Ground motion database. Viewed on 28.01.2024.

[10] CESMD (2024). CESMD archive. Viewed on 28.01.2024.

[11] PESMOS (2024). PESMOS archive. Viewed on 19.01.2024.

[12] NIST GCR 11-917-15 (2011). Selecting and Scaling Earthquake Ground Motions for Performing Response-History Analyses. *National Institute of Standards and Technology*, USA

[13] Baker, J. W. Efficient analytical fragility function fitting using dynamic structural analysis. *Earthquake Spectra*, 31 (2015) 579-599

4th International Symposium on One Health, One World
November 20 – 22, 2025

ABS ID: 38

USDM-OP-12

Analysis Of The Congestion Conditions of Highway Parking Area In Japan Using Probe Data And Drone Movie Data

S.Y. Mon[1], and D. Watanabe[2]

[1]Graduate Student, Graduate School of Marine Science and Technology,

Tokyo University of Marine Science and Technology, Tokyo, Japan,

[2] Professor, Department of Logistics and Information Engineering,

Tokyo University of Marine Science and Technology, Tokyo, Japan,

Correspond to Prof. D. WATANABE (daisuke@kaiyodai.ac.jp)

***Keywords**: Freight Transportation, Parking Congestion, Probe Data Analysis, Drone Footage.*

1. INTRODUCTION

Japan's extensive and well-developed highway network is critical to its transportation infrastructure. It includes national expressways, urban expressways, and national highways designed for efficient travel across regions. The Tomei Expressway, spanning approximately 410 kilometers from Tokyo to Nagoya, serves as a crucial artery for passenger and freight transport, featuring modern amenities and advanced traffic management systems. Strategic Service Areas (SAs) and Parking Areas (PAs) along its route provide essential rest stops and amenities for drivers and travelers[1]. Especially, the Ashigara SA on the inbound side of the Tomei Expressway in Kanagawa Prefecture faces significant parking and safety challenges due to high demand, especially from Heavy vehicles[2].

This study investigates congestion patterns in Ashigara SA through a detailed analysis of probe data combined with drone footage. The research will identify barriers to parking,

correlate probe data with drone videos, and explore daily congestion changes, peak hours, and short-term versus long-term parking behaviors. By comparing probe data with real-time conditions, the study seeks to accurately reflect on-ground realities and propose solutions to enhance parking efficiency and manage the growing demand for freight transport.

2. DATA OVERVIEW

2.1 PROBE DATA

The probe data used for this study includes comprehensive statistics such as serial number, record time, travel start time, speed, engine RPM, travel distance, GPS latitude, longitude, direction, and car model.

Table 1. Period of surveys in Ashigara SA

Date	**Time**	
	Category	**Duration**
Dec. 4(Sun) to Dec. 5(Mon)	Evening to Midnight	PM6 to AM2
Dec. 5(Mon)	Noon	AM11 to PM1
Dec.6(Tue)	Afternoon to Evening	PM2 to PM7
Dec.7(Wed)	Early morning	AM4 to AM8
Dec.7(Wed) to Dec. 8(Thu)	Evening to Midnight	PM4 to AM3

Covering the period from December 4, 2022, to December 8, 2022 as shown in Table 1, the dataset encompasses over 2.4 million data points (2,442,833 points). This extensive dataset provides valuable insights into vehicle movement and performance, capturing detailed information on each vehicle's journey and operating conditions.

2.2 DRONE RECORDED DATA

The drone videos are recorded as shown in Figure 1 from an altitude of at least 100 meters or more and from 50 meters away from the service area premises in the period as shown in Table 1. The drone did not enter the SA compound; it took off and landed outside the area on the public road and conducted fixed-point observations. The main purpose of these recorded videos is to digitize the behavior of each vehicle in seconds within the SA. These videos can capture the number of vehicles inside the SA at the recorded time, and the total number of parked vehicles can be calculated. This data can provide information on the number of parked cars and the flow rate of entry and exit. In this study, the drone video, and the results of the analysis of the probe data can reveal the movement behavior within the Ashigara SA.

Figure 1. Sample of drone video in Ashigara SA

3. COMPARISON BETWEEN PROBE DATA AND DRONE RECORDED DATA

Since probe data are not installed in all vehicles, the number of observations is smaller than that of drone data, accounting for approximately 30–40%. Figure 2 summarizes the parking space selection behavior upon

entering SA. From evening to midnight, many vehicles are observed parking outside parking spaces or leaving without parking. In contrast, in the early morning and daytime, almost all vehicles are able to park within parking spaces.

(i)Probe data

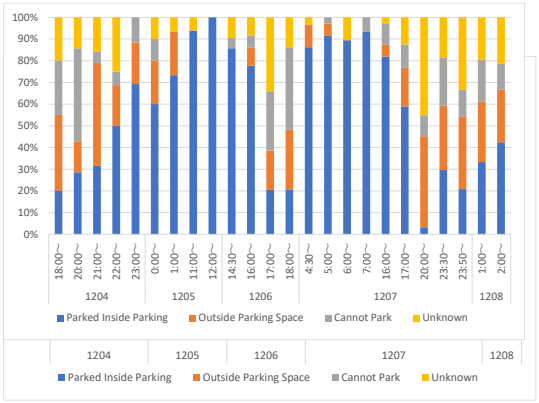

(ii)Drone recorded data

Figure 2. Parking decision-making in Ashigara SA

4. OBSERVED PARKING BEHAVIOR BY PROBE DATA

4.1 DURATION FOR PARKING CHOICE

The time taken to find a parking space after entering the SA based on probe data is shown in Figure 3. In the evening and at night, it takes about 5–8 minutes, while at midnight it takes more than 8 minutes. In the morning, a parking space is generally found within 5 minutes. As seen in Figure 3, it is difficult to find a parking space from evening to midnight, which explains the longer search time.

4.2 PARKING DURATION

The parking duration based on probe data is shown in Figure 4. Long-term parking of more than two hours accounts for about 20–30% across all time periods. One possible reason for this is that SA is being used not merely for short breaks, but for long rest periods or time adjustments

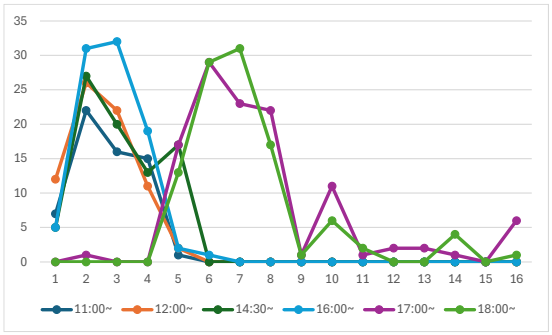

5. CONCLUSIONS

This research identified barriers to parking, correlate probe data with drone videos, and explore daily congestion changes, peak hours, and short-term versus long-term parking behaviors. By comparing probe data with real-time conditions, the study seeked to accurately reflect on-ground realities and propose solutions to enhance parking efficiency and manage the growing demand for freight transport.

(i)1204

(ii)1206

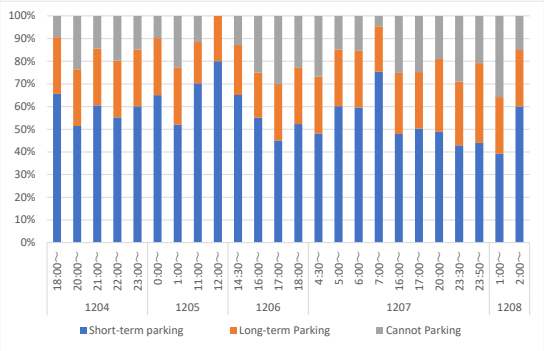

Figure 3. Duration for parking choice in Ashigara SA

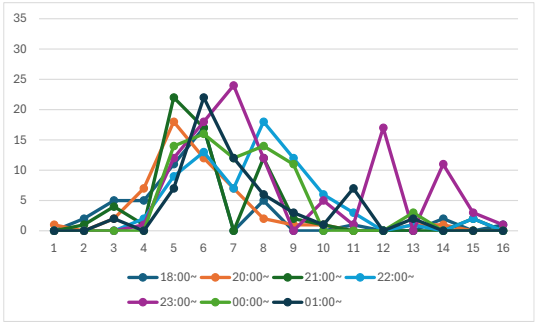

Figure 4. Parking duration in Ashigara SA

REFERENCES

[1] Y. Misui, T. Nemoto, T. Goto, T. Kagabu: Demand analysis of large-truck parking at expressway rest areas in Japan, ITS World Congress 2022 Conference Proceedings, 2022.

[2] D. Watanabe, Y. Misui, T. Nemoto, T. Hyodo, T. Kagabu, H. Tanabe, Analysis of the parking behavior of heavy-duty vehicles at expressway SA/PAs and suggestions for solutions to parking problems by using drone imagery, Journal of Japan Logistics Society, 32 (2024) 87-94[in Japanese].

ABS ID: 90

USDM-OP-13

Mr. Ajay Dwivedi

ABS ID: 92

USDM-OP-14

Dr. Ajay Chourasia

ABS ID: 179

USDM-OP-15

Dr. Rajesh Kumar Dash

ABS ID: 168

USDM-OP-16

Prof. Saurabh Panditsh

ABS ID: 03
USDM-OP-17

Smartphone-Based Ground Penetrating Radar for Millimeter-Scale Damage Assessment in Concrete Structures

T. Mizutani[1], and S. Iwai[3]
[1]*Associate Professor, Institute of Industrial Science, The University of Tokyo, Tokyo, Japan,*
[2] *Graduate Student, Institute of Industrial Science, The University of Tokyo, Tokyo, Japan,*
Correspond to Dr. T. MIZUTANI (mizu-t@iis.u-tokyo.ac.jp)

Keywords*: Ground Penetrating Radar, Concrete Damage, Frequency Analysis, Spectral Matching, Non-Destructive Testing, Smartphone Sensing.*

1. INTRODUCTION

The degradation of infrastructure systems has become a critical global concern, as bridges, tunnels, and pavements constructed several decades ago are now reaching or exceeding their design life [1]. In Japan and other developed nations, the transition from reactive to preventive maintenance is urgently required to reduce inspection costs and prevent catastrophic failures [2]. Ground Penetrating Radar (GPR) is a promising non-destructive technology in this context, capable of visualizing subsurface conditions based on electromagnetic reflections between materials of different permittivities [3,4].

Traditional handheld GPR systems are widely used for locating rebars or buried utilities but have difficulty identifying subtle defects such as delamination, cracks, or voids due to weak reflections and overlapping signals [5]. Moreover, inspection results often depend on the subjective interpretation of experienced operators. To overcome these limitations, this study develops a smartphone-based handheld GPR system and a frequency-domain algorithm that can automatically and quantitatively estimate internal damage thickness in concrete with millimeter-scale precision and real-time processing capability.

2. SYSTEM AND METHODOLOGY

2.1 GPR System Configuration

The prototype radar system operates within a frequency range of 700–3500 MHz, using an impulse transmission system. The main sensor unit (approximately 1 kg, 149×207 mm) connects wirelessly to a smartphone, which functions as both processor and display. LED guide lines assist the operator in maintaining a constant scanning path, while real-time spectral analysis is executed through a dedicated mobile application. The antenna's broadband frequency ensures high depth resolution and adequate penetration in concrete up to approximately 300 mm.

2.2 Example of GPR Signals and Experimental Setup

Concrete specimens of 300 × 300 × 60 mm were prepared with air gaps between 2 mm and 180 mm to simulate different damage thicknesses. Acrylic spacers with 0.1 mm precision were inserted to form the voids, and the top of each defect was fixed at a depth of 60 mm. Measurements were repeated five times at three positions for each thickness, yielding 1,350 A-scan waveforms. Data from intact specimens were subtracted from

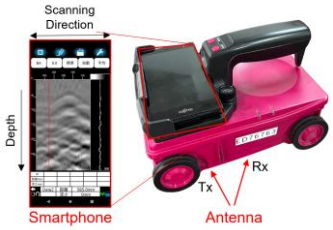

Figure 1. Overview of the Smartphone-Mounted Handheld GPR System

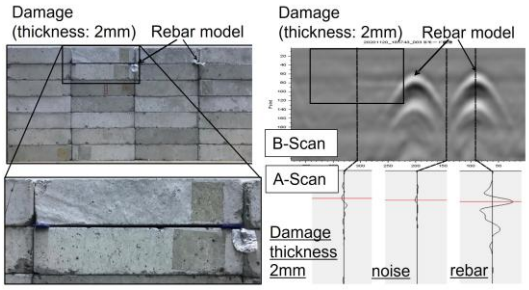

Figure 2. Example of A-Scan and B-Scan Signals from Concrete Specimens (example waveforms showing rebar reflection and 2 mm defect response after background subtraction)
damaged ones to eliminate surface reflections and isolate internal signals [6].

2.3 Frequency-Domain Approach and Spectral Modeling

Estimating the thickness of internal damage from time-domain peaks alone is often unreliable, because multiple reflections and overlapping signals obscure the boundaries of defects. To address this issue, the present study employs a frequency-domain approach that analyzes the overall spectral characteristics of the received radar signal rather than individual peaks.

In this method, the reflected wave from the damaged region is considered as a combination of multiple reflections from the upper and lower boundaries of the void. The interference between these reflections produces distinctive oscillations in the amplitude spectrum. The pattern and periodicity of these spectral oscillations change systematically with the thickness of the defect.

By comparing the measured frequency spectrum with a set of theoretical spectra corresponding to different thicknesses, it becomes possible to estimate the damage quantitatively. Theoretical spectra were generated based on known reflection properties and propagation velocities in concrete, and their relationship to defect thickness was experimentally validated.

Figure 3 illustrates examples of these theoretical spectra for typical damage thicknesses ranging from 2 mm to 180 mm. As the thickness increases, the frequency intervals between adjacent peaks in the spectrum become narrower, providing a clear physical basis for spectral pattern matching.

3. RESULTS AND DISCUSSION

The developed system accurately estimated defect thicknesses between 2 mm and 180 mm. The correlation between measured and estimated values reached $R^2 \approx 0.99$, confirming high precision (Fig. 4). The mean estimation error was below ±3 mm for most specimens, with larger deviations only in thin defects (<10 mm) due to reduced signal-to-noise ratios.

The computation time per waveform was approximately 0.001 s, enabling genuine real-time evaluation. This marks a substantial improvement over conventional time-of-flight or impact-echo methods, which often require extensive post-processing [7]. The frequency-domain approach captured subtle interference effects caused by multiple reflections, which are not easily discernible in time-domain analysis.

In comparison with previous qualitative GPR studies [8,9], the present method provides a truly quantitative evaluation of internal concrete damage, achieving both accuracy and field applicability. Its portability and low cost also make it suitable for bridge decks, tunnel linings, and pavement inspections where rapid measurements are required. The results confirm that handheld GPR integrated with smartphone processing can serve as a practical solution for preventive maintenance and digital inspection programs [2].

4. CONCLUSIONS

This study introduced a compact, smartphone-integrated Ground Penetrating Radar capable of estimating internal concrete damage thickness quantitatively in real time.

By combining amplitude and spectral centroid indicators with optimized spectral pattern matching, the algorithm successfully achieved millimeter-level precision from 2 mm to 180 mm.

The computation time of 0.001 s per waveform demonstrates the feasibility of deploying this technique in real-world field inspections. The developed method

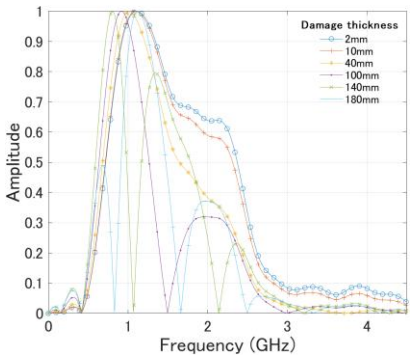

Figure 3. Theoretical Spectra for Various Damage Thicknesses (frequency-domain spectra for representative damage thicknesses of 2, 10, 40, 100, 140, and 180 mm)

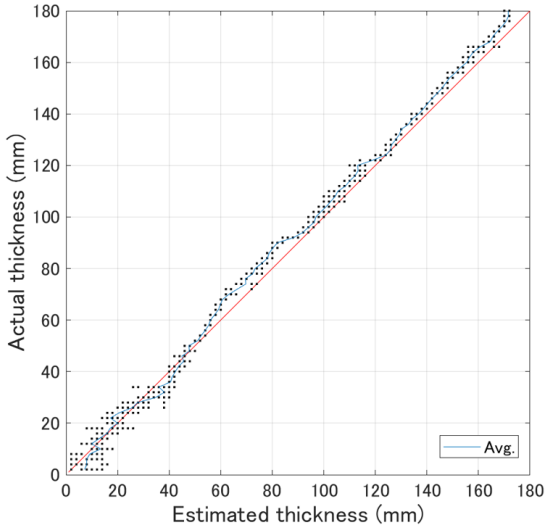

Figure 4. Correlation between Estimated and Actual Damage Thickness

transforms handheld GPR from a qualitative detection tool into a quantitative diagnostic instrument.

Future work will focus on extending this approach to multilayered concrete and reinforcement corrosion evaluation.

REFERENCES:

[1] W. Choate and S. Pat, America in Ruins: The Decaying Infrastructure, Duke Press, 1983.

[2] MLIT, Infrastructure Maintenance Information, Ministry of Land, Infrastructure, Transport and Tourism, Japan, 2022.

[3] J. Hugenschmidt, Construction and Building Materials, 16(3):147–154, 2002.

[4] T. Saarenketo and T. Scullion, Journal of Applied Geophysics, 43(2–4):119–138, 2000.

[5] K. Dinh et al., Automation in Construction, 125:103652, 2021.

[6] R. Kiyoshi, Development of a Method for Detecting Internal Defects in Concrete Using Electromagnetic Radar Method, PhD Thesis, The University of Tokyo, 2021.

[7] C. Cheng and M. Sansalone, Materials and Structures, 26(5):274–285, 1993.

[8] S. Tanaka and M. Yamada, Transactions of the Society of Instrument and Control Engineers, 39(5):432–440, 2003.

[9] T. Uomoto and S.K. Park, Journal of the Japan Society of Civil Engineers, (592):13–24, 1998.

2025 HOW

4th International Symposium on One Health, One World
November 20 – 22, 2025

ABS ID: 115
USDM-OP-18

2d digital image correlation-based impact analysis of rockfall protection tunnels incorporating energy dissipation systems

Sarath Rajeev[1], Ganesh Kumar S[2]
[1]*Project Associate, GE&GH Division, CSIR- Central Building Research Institute, Roorkee, India.*
[2]*Principal Scientist, GE&GH Division, CSIR- Central Building Research Institute, Roorkee, India*

***Keywords**: Rockfall, Impact forces, Slope stability, Energy dissipator, DIC, VIC 2D.*

1. INTRODUCTION

In steep mountainous regions like the Himalayas, the detachment of rock masses from slopes poses a threat to people and nearby infrastructure [1]. The energy induced by the falling rock mass is typically several hundred kilojoules, depending on its size, mass, height of fall, and slope conditions. Among protective systems, rockfall shelters play a critical role in steep terrain. However, variation in impact energy affects structural performance and may compromise integrity. By introducing hybrid measures, the impact capacity of the structure can be enhanced to withstand energy up to 6 MJ [2]. In most protection systems, soil is used as an energy dissipator. The soil layer acts as a cushion by distributing stress, dissipating energy, and providing damping characteristics [3]. However, increasing cushion thickness raises the dead weight of the structure, limiting its performance. In this study, geotextile-filled bags containing various buffering materials as cushion layers were attempted to minimize rockfall-induced impact energy. The scaled model system response was monitored by a two-dimensional Digital Image Correlation (2D-DIC). The impact force, velocity, and displacement were measured and compared to study the energy dissipation mechanism of each configuration.

2. MATERIALS AND EQUIPMENT

Locally available Solani sand (Roorkee, India) and rubber was used as an infill material for the development of geotextile bag cushioning system. The grain size distribution characteristics are shown in Fig.1. A 1.5mm thick non-woven polypropylene geotextile was used for the cushioning material. The tensile strength of the geotextile as per ASTM-D4595,1986 was 13N/mm at 45% strain level. The geotextile used in the study is shown on Fig.2. For monitoring, 2D DIC technique was deployed. The 2D DIC system in the study consists of 1 CMOS-based DIC camera with 1920 x 1200 pixels at 155 frames per second (fps). Since the impact study is a quick test, the use of a high-speed camera has been used for capturing high-quality images.

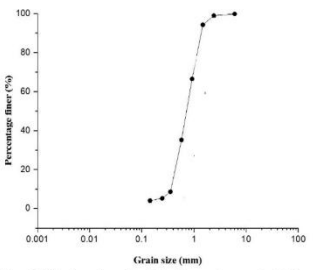

Fig. 1 Grain size distribution characteristics

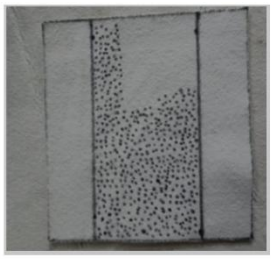

Fig. 2. Geotextile used in the study

3. METHODOLOGY

Developing a scale-down model involves complexities in simulating model structures equivalent to prototype structure and its material properties. By adopting proper similitude relationship, the experimental investigations were performed in this study. A box-type reinforced concrete tunnel was taken as a rockfall protection structure for impact load testing. To derive uniformity in the similarity ratio, a geometric similarity ratio of 22 (CL=22) was chosen for the tunnel model. The model tunnel was 740 mm in length, measuring 280 mm x 280 mm in size, with a thickness of 25 mm. The tunnel was coated with white paint for speckling for the DIC analysis. To replicate the rockfall mass, a circular concrete ball of 160 mm diameter, having a density of 2100 kg/m^3, was used. The weight of the concrete ball was 4.5 kg. To mitigate the impact created by falling rock mass, geotextile-infilled bags of dimensions 150 mm x 150 mm were placed on the top of the structure. In the first series of the study, the geotextile-infilled sandbags were placed in a 3-layer stacking arrangement on the structure. The concrete block weighing 4.5 kg was dropped from a height of 2 m, and in the second series, geotextile-infilled sandbags were replaced with geotextile-infilled sand and rubber combination. The impact force generated from a drop height of 2 m with and without cushioning system were estimated and compared for evaluating the efficiency of the system. The experimental test setup is shown in Figure 3.

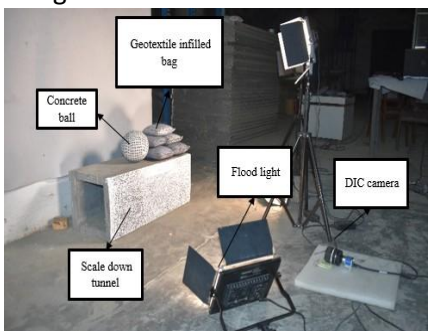

Figure 3. Experimental test set-up

4. RESULT AND DISCUSSION

The observations made during the experimental study are discussed in this section. After the impact, recorded images were analysed using the 2D DIC technique. For the image analysis, VIC 2D software was used, and velocity before and after impact were analysed and compared for structure with and without cushioning system. Using first-order differentiation with respect to time, acceleration time history was estimated and impact force was then calculated by multiplying the mass of the concrete ball with acceleration-time history. It was observed that the tunnel model without a geotextile infilled bag experiences a peak force of 485N, and it can be clearly observed that the introduction of a geotextile infilled sandbag and a geotextile having sand and rubber material reduces the peak force to 45N and 33N, showing the efficient absorption of impact force. Compared with a tunnel without a geotextile infilled bag system and a geotextile infilled (sand and rubber) system, approximately 13.8 times and 10.77 times reductions in reaction force were observed. The impact force-time response for all three cases, i.e. tunnel without a geotextile infilled bag, with geotextile infilled sand bags, and a geotextile infilled (sand + rubber) bag shown in the figure.5 The influence of a 3-layer stacking arrangement of geotextile infilled bags was further validated by comparing the deformation response of the tunnel and the geotextile infilled bag, are shown in Table 1. In the case of geotextile infilled bags, only the average deformation representing the deformation of the stacking arrangement was considered. Since the tunnel without geotextile infilled bags shows failure for a 2m drop weight. The failed tunnel model is shown in the figure.6 In both testing conditions geotextile bag experiences maximum deformation compared to the tunnel model, and exhibits the energy dissipation characteristics. To illustrate the energy dissipation of the developed geotextile infilled

bag cushioning system against impact loading, the overall behaviour of the geotextile infilled bag was studied. The overall behaviour of geotextile-infilled bags for the energy efficiency assessment is shown in Table 2. It was evident the structure with cushion showed improved energy reduction characteristics compared to the structure without a cushioning system

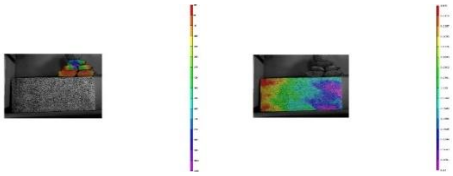

Fig. 4. Image processing in VIC 2D software

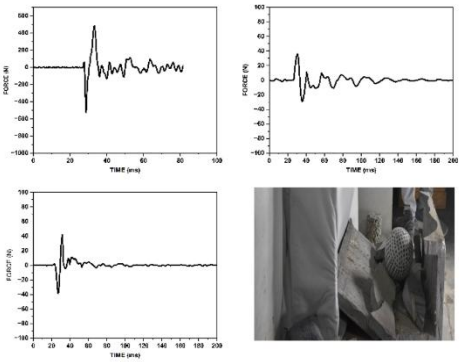

Fig.5. Impact force response of different systems and failed tunnel model

Table 1: Deformation response of tunnel and geotextile infilled bags

Test condition	Tunnel	Geotextile bag
	Deformation (mm)	Deformation (mm)
Geotextile infilled sandbag on top of tunnel	0.166	7.08
Geotextile bag with sand and rubber material	0.15	4.591

Table 2. Overall behaviour of geotextile infilled bag against impact loading

Stacking material	Sand	Sand & Rubber
Height of fall (m)	2	2
stacking	3 layers	3 layers
Initial velocity(v_i)	6.26	6.26
Final velocity(V_f)	0.60	0.49
Initial energy(E_i)	82.06	82.06
Final energy(E_f)	0.7524	0.501
Energy dissipated (%)	99.08	99.3

4. CONCLUSION

1. The developed geotextile-infilled bag-based cushioning system showed improved performance in energy dissipation against rockfall-induced impact force. An overall reduction of approximately 99% in energy dissipation was observed when using the geotextile-infilled sandbag system and the geotextile-infilled (sand and rubber) bag system, resulting in minimized structural deformation.
2. Provision of geotextile infilled bag cushioning systems reduce the dead weight of the structure as compared to conventional sand cushioning systems.
3. 2D DIC technique predicts deformation and strain measurements accurately in impact studies. The observations made during the study evidenced that, 2D DIC system can be an effective and quantitative tool for determining the deformation mechanism of different materials under any type of loading

REFERENCES:

[1] S.K. Bartarya, K.S. Valdiya, Landslides and erosion in the catchment of the Gaula River, Kumaun Lesser Himalaya, India, Mountain Res. Dev. 9 (1989) 405–419.

[2] S. Ghadimi Khasraghy, Numerical simulation of rockfall protection galleries, IBK Bericht 334 (2012).

[3] K. Schellenberg, On the design of rockfall protection galleries, Doctoral dissertation, ETH Zurich, 2008.49 (1) (2021) 45–56.

ABS ID: 05
USDM-OP-19

Mr. Deepak Gupta

4th International Symposium on One Health, One World
November 20 – 22, 2025

ABS ID: 27
USDM-OP-20

Artificial Intelligence-Based Modelling of Urban Pm 2.5 Concentration Considering Key Performance Indicators

J. Pandya[1], D. Kaul[2], and D. Sarkar[2]
[1]*PhD Scholar, Civil Engineering Department, Pandit Deendayal Energy University, Gandhinagar, India,*
[2]*Associate Professor, Civil Engineering Department, Pandit Deendayal Energy University, Gandhinagar, India,*
[3]*Professor, Civil Engineering Department, Pandit Deendayal Energy University, Gandhinagar, India,*
Correspond to Ms J. PANDYA (pandyajanki867@gmail.com)

***Keywords**: PM2.5, Urban Area, Key Performance Indicators, Artificial Intelligence, Modelling.*

1. INTRODUCTION

Urban areas are concentration points of pollutants in all components of the environment. This issue is particularly pronounced in South Asia, including countries like China and India, due to their high population density. These pollutants have a number of health challenges for living beings [1]. Particulate matter 2.5 (PM2.5) poses a significant health threat across the world, as it deeply penetrates the human respiratory system and causes chronic diseases, including lung cancer [2]. To overcome this issue, it is necessary to have an understanding of the pollutant concentration in urban areas and then adopt a strategic approach to reduce its concentration. In any urban area, there are many factors which affect pollutant levels, including anthropogenic and natural [3]. In 2025, [4] identified many factors which are responsible for the Air Quality Index (AQI) after performing a Multi-Criteria-Decision-Making (MCDM) tool, and they have taken out the major affecting factors, which include geodetic information, population density, meteorological factors and other categorical data, which are daytime, traffic density (based on daytime and peak hours), month and area type (residential, commercial and industrial). These parameters are considered as an input for machine learning (ML) models for this study. ML is a subpart of artificial intelligence (AI), which can effectively handle complex data, as this study includes. This research is centric to one urban area; for this, the wind direction is also included as an input, shown in Table 1.

Table 1. List of Factors affecting urban PM2.5 levels

Sr No	Factors
1	Relative Humidity
2	Wind Speed
3	Wind direction
4	Atmospheric Temperature
5	Daytime
6	Solar Radiation
7	Longitude
8	Latitude
9	Altitude
10	Population Density
11	Traffic Density
12	Month
13	Area Type

2. STUDY AREA

For this study, India's capital, Delhi, has been chosen as the study area, as it is densely populated with more than 33 million people [5], and its AQI mostly exceeds safer limits, especially in winter. Data has been collected from Central Pollution Control Board (CPCB) monitoring stations, which are shown in Figure 2.

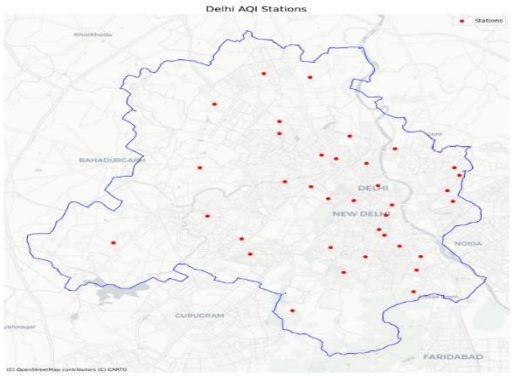

Figure 1. The Delhi map shows the location of monitoring stations with red dots from where the data has been collected.

3. METHODOLOGY

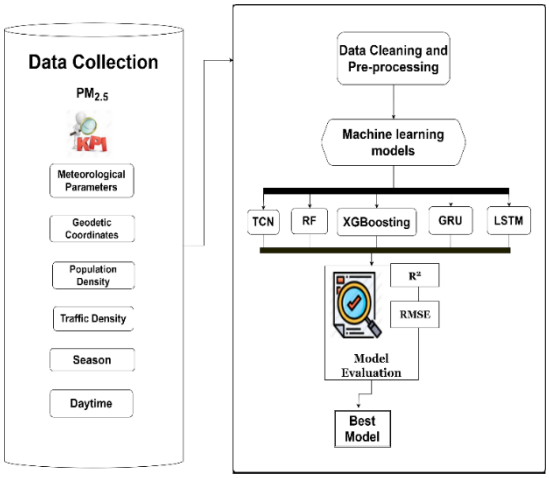

Figure 2. Flow diagram of the proposed framework for PM2.5 prediction in Delhi, India

The methodology adopted for this study is mentioned in Figure 2. Firstly, data from 1st January 2020 to 20th October 2024 has been collected from the CPCB official website, and then the dataset was pre-processed by removing outliers and handling missing values. After this, five ML models, Random Forest (RF), Extreme Gradient Boosting (XGBoost), Temporal Convolutional Networks (TCNs), Gated Recurrent Unit (GRU) and LSTM (Long-Short Term Memory), are employed to predict PM2.5 concentration, and for better accuracy, hyperparameter tuning has also been performed. Then, these models are evaluated using two metrics, R2 (Coefficient of Determination) and RMSE (Root Mean Square Error), and the best model has been identified based on these criteria.

4. RESULT AND DISCUSSION

All five ML models are being evaluated by applying two evaluation metrics, R2 and RMSE. Their evaluation scores are mentioned in Table 2.

Table 2. Show R2 and RMSE values of two datasets: Training and Testing of all models

Model's Name	R-Square Score		RMSE Score	
	Training	Testing	Training	Testing
RF	0.7647	0.6924	29.519	33.787
XGBoost	0.7846	0.7281	28.2413	31.77
TCNs	0.6885	0.6688	33.9668	35.029
GRU	0.7418	0.7073	30.928	32.927
LSTM	0.9145	0.8965	17.8664	19.550

As Table 2 shows, LSTM has the highest accuracy with the highest R2 value of 0.8965 and the lowest RMSE value of 19.55. In contrast, TCNs have the lowest accuracy with the highest RMSE value, 35.029 and the lowest R2 value, 0.6688, of the testing datasets.

5. CONCLUSION

Key performance indicators (KPIs) are quantifiable factors that contribute to PM2.5 concentrations in any area. For this study, these factors are used as an input to build the best model, which efficiently predicts its concentration for a particular area. Since the KPIs encompass both natural and anthropogenic factors, the resulting models can effectively capture and simulate human-induced pollution. ML models can effectively work with complex data and can forecast PM2.5 concentration without requiring fancy tools, which makes the study easier.

The approach of considering KPIs as an input in ML models to predict PM2.5, which gave an around ninety per cent accurate model (LSTM), demonstrates the capability of models in capturing both natural and human-induced pollutants. This approach can give the root cause of exceeding pollutant concentration and help in making a strategy to reduce the PM2.5 level in the air.

REFERENCES:

[1] A. J. Cohen, M. Brauer, R. Burnett, H. R. Anderson, J. Frostad, K. Estep, K. Balakrishnan, B. Brunekreef, L. Dandona, R. Dandona, V. Feigin, G. Freedman, B. Hubbell, A. Jobling, H. Kan, L. Knibbs, Y. Liu, R. Martin, L. Morawska, C. A. Pope, H. Shin, K. Straif, G. Shaddick, M.

Thomas, R. van Dingenen, A. van Donkelaar, T. Vos, C. J. L. Murray, and M. H. Forouzanfar, The Lancet 389, 1907 (2017).

[2] X. Liu, H. Zhou, X. Yi, X. Zhang, Y. Lu, W. Zhou, Y. Ren, and C. Yu, Asia-Pac. J. Oncol. Nurs. 12, (2025).

[3] J. Pandya, D. Sarkar, and D. S. Kaul, J. Inst. Eng. India Ser. A (2024).

[4] J. Pandya, D. Sarkar, and D. Kaul, in Comput. Model. Sustain. Energy, edited by B. K. Jha, N. Jha, J. Brahma, and M. Yavuz (Springer Nature Singapore, Singapore, 2025), pp. 687–698.

[5] A. S. Mohan and L. Abraham, Earth Sci. Inform. 17, 1923 (2024).

4th International Symposium on One Health, One World
November 20 – 22, 2025

ABS ID: 20

USDM-OP-21

Optimal subsidy to reduce Co2 emissions by promoting energy-efficient Housing with a balanced approach to demolition and renovation

K. isawa[1], and Y. honma[2]
[1]*Proj. Res. Assoc., Research Centre for Advanced Science and Technology, The University of Tokyo, Tokyo, Japan,*
[2]*Assoc. Prof., Institute of Industrial Science, The University of Tokyo, Tokyo, Japan,*
Correspond to Assoc. Prof. Y. Honma (yudai@iis.u-tokyo.ac.jp)

***Keywords**: Urban Metabolism, Incentive Design, Housing Policy, Household Income, Mathematical Optimization.*

1. INTRODUCTION

Reducing CO_2 emissions is a key global issue. The International Energy Agency reported that Asia produced about two-thirds of global CO_2 emissions in 2019, with China at 29%, India at 7%, and Japan at 3%. Then, reducing CO2 emissions in Asia is urgent under the Paris Agreement. Japan faces significant CO_2 emissions from the residential sector, promoting energy-efficient houses, i.e. Zero Energy Houses (ZEHs) with subsidies [1]. ZEHs are more costly than conventional homes; thus, some households might prefer standard houses despite subsidies. Renovating existing homes may be more cost-effective and eco-friendlier than demolition and rebuilding. Future policies should balance renovation and new construction.

This study aims to develop an effective subsidy allocation pattern based on household income to promote energy-efficient housing and cut CO_2 emissions. It offers insights into designing incentives that strike a balance between economic constraints and environmental goals. While prior studies often use discrete optimization for resource allocation or bin-packing problems, this research applies an analytical approach to find solutions. We believe our study will help achieve a balanced urban metabolism by integrating demolition and renovation strategies sustainably and affordably.

2. OVERVIEW OF MATHEMATICAL MODEL

This study examines certain households to understand trends and develop a framework for household and government decisions, especially regarding rental houses influencing homeownership. The government aims to reducing CO2 emissions with minimal subsidy, so total subsidy is outlined, ignoring budget constraints.

$$\min_{I_{\mathrm{rep.}}(p),I_{\mathrm{new}}(p)} F\left(I_{\mathrm{rep.}}(p), I_{\mathrm{new}}(p)\right) \quad (1)$$

$$F\left(I_{\mathrm{rep.}}(p), I_{\mathrm{new}}(p)\right) = I_{\mathrm{rep.}}(p)\mathrm{N}_{\mathrm{rep.}}(p) + I_{\mathrm{new}}(p)N_{\mathrm{new}}(p) \quad (2)$$

$$s.t. \quad Z_{\mathrm{rep.}}(p)\mathrm{N}_{\mathrm{rep.}}(p) + Z_{\mathrm{new}}(p)N_{\mathrm{new}}(p) = ZP \quad (3)$$

$$I_{\mathrm{rep.}}(p), I_{\mathrm{new}}(p) \geq 0 \quad (4)$$

Each parameter is detailed in Table 1. Households usually select options based on utility, but some regard "building a new house (or renovating a second-hand one)" as the best, regardless of cost. The probability of irregular behavior is modelled via the logit model:

$$P_{\mathrm{rep.}}(p) = \frac{e^{\gamma V_{\mathrm{rep.}}(p)}}{e^{\gamma V_{\mathrm{rep.}}(p)} + e^{\gamma V_{\mathrm{new}}(p)}} \quad (7)$$

$$N_{\mathrm{rep.}}(p) = N(p) \times P_{\mathrm{rep.}}(p) \quad (5)$$

$$N_{\mathrm{new}}(p) = N(p) - P_{\mathrm{rep.}}(p) \quad (6)$$

Here, rearranging Eq. (3) and Eq. (6),Eq. (8) is obtained:

$$\mathrm{N}_{\mathrm{rep.}}(p) = \frac{\left(I_{\mathrm{rep.}}(p) - N(p)Z_{\mathrm{new}}(p)\right)}{Z_{\mathrm{rep.}}(p) - Z_{\mathrm{new}}(p)} \quad (8)$$

And Substituting Eq. (8) into Eq. (2), the objective function becomes as follows:

$$F\left(I_{\text{rep.}}(p), I_{\text{new}}(p)\right) = \frac{ZP - N(p)Z_{\text{new}}(p)}{Z_{\text{rep.}}(p) - Z_{\text{new}}(p)} I_{\text{rep.}}(p) + \left(N(p) - \frac{ZP - N(p)Z_{\text{new}}(p)}{Z_{\text{rep.}}(p) - Z_{\text{new}}(p)}\right) I_{\text{new}}(p) \quad (9)$$

Given the current strong preference for new houses, households' utility is expected to vary depending on whether they choose to renovate an existing house to improve energy efficiency or to build a new energy-efficient house. If they select renovation, they may not see the purchase as being worth the full-face value of the expenditure, and there is a risk that they will experience a sense of loss. The aversion to second-hand properties leads households to perceive the amount spent on renovation costs as less than their full-face value; the perceived loss is denoted by $H(p)$. On the other hand, when a subsidy is received, households feel as though they have gained by that amount, and thus their utility increases by $I(p)$.

Table 1. List of parameters.

rep.	Options : Repairing a second-hand house
new	Options : Building a new house
p	Household income
$I_x(p)$	Subsidy per household belonging to income zone p that chooses option x
$N_x(p)$	Households belonging to income zone p that choose option x
$Z_x(p)$	CO2 reduction per household belonging to income zone p that chooses option x
$N(p)$	Distribution of households relative to household income p
$P_x(p)$	Probability of households belonging to the income zone p that choose option x
γ	Coefficient of the effect of utility difference on choice probability
ZP	Total household CO2 reduction in income zone p

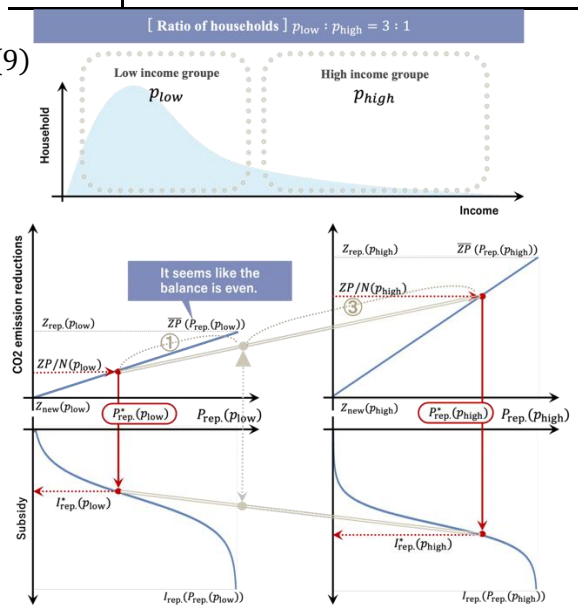

Figure 1. Diagram of the correlation equation via $P_{\text{rep.}}(p)$

At this point, if both the reduction in CO_2 emissions and the perceived out-of-pocket cost of renovation exceed those of new construction, government subsidies for households choosing renovation become necessary. Conversely, if renovation's perceived out-of-pocket cost is lower than new construction, the probability of renovation being chosen—due to greater CO_2 reduction, making subsidies unnecessary. The relationship between renovation probability and subsidies is given by Eq. (7).

・When $Z_{\text{rep.}}(p) > Z_{\text{new}}(p)$ and $T_{\text{rep.}}(p) \geq T_{\text{new}}(p)$,

$$I_{\text{rep.}}(p) = \frac{1}{\gamma}\log\frac{P_{\text{rep.}}(p)}{1 - P_{\text{rep.}}(p)} + T_{\text{rep.}}(p) - T_{\text{new}}(p) \quad (16),$$

$$I_{\text{new}}(p) = 0 \quad (17).$$

・When $Z_{\text{rep.}}(p) > Z_{\text{new}}(p)$ and $T_{\text{rep.}}(p) \leq T_{\text{new}}(p)$,

$$I_{\text{rep.}}(p) = 0 \quad (18),$$

$$I_{\text{new}}(p) = \frac{1}{\gamma}\log\frac{1 - P_{\text{rep.}}(p)}{P_{\text{rep.}}(p)} - T_{\text{rep.}}(p) + T_{\text{new}}(p) \quad (19).$$

- In all other cases,

$$I_{\text{rep.}}(p) = I_{\text{new}}(p) = 0 \quad (20).$$

Here, ZP is the total reducing CO_2 emissions for households in income zone p. In other words, the average reductions per household are determined, $ZP/N(p)$. Thus, converting $ZP/N(p)$ into an equation for $P_{\text{rep.}}(p)$, we can find the probability of households belonging to income zone p choosing renovation, $P^*_{\text{rep.}}(p)$:

$$\overline{ZP}\left(P_{\text{rep.}}(p)\right) = \left(Z_{\text{rep.}}(p) - Z_{\text{new}}(p)\right)P_{\text{rep.}}(p) + Z_{\text{new}}(p) \quad (21)$$

$$P^*_{\text{rep.}}(p) = \left(ZP/N(p) - Z_{\text{new}}(p)\right)/\left(Z_{\text{rep.}}(p) - Z_{\text{new}}(p)\right) \quad (22)$$

As illustrated by the dotted line in Fig. 1, we can obtain $I^*_{\text{rep.}}(p)$ by substituting $P^*_{\text{rep.}}(p)$ into Eq. (7). In the absence of subsidies ($P_{\text{rep.}}(p) = 0$), households choose new house, which entails a lower perceived out-of-pocket cost. Consequently, the total CO_2 emissions of households with income level p amount to $Z_{\text{rep.}}(p) \times N(p)$, which is below ZP. However, with the introduction of subsidies, as the perceived out-of-pocket cost of renovation increases, the probability of households choosing renovation $P_{\text{rep.}}(p)$ also rises, leading the CO_2 emission reductions to approach $Z_{\text{rep.}}(p)$. Accordingly, it was found that the required $P^*_{\text{rep.}}(p)$ to achieve the average household CO_2 reduction $ZP/N(p)$ is uniquely determined, and thus the optimal subsidy $I^*_{\text{rep.}}(p)$ can be specified.

3. HOW TO CONSIDER DIVERSE HOUSEHOLD

In Chapter 2, we formulate the objective function of households with a given income level p. However, when households are distributed across different income levels, how should this relationship be considered? We try to consider the situation where there are multiple household income levels. For s

implicity, we limit the discussion to two income levels, namely high-income p_{high} and low-income p_{low}. Fig. 1 illustrates the relationship

between the subsidy and the household's probability. Due to variations in budget constraints across income classes, higher-income households can purchase higher-quality housing. Consequently, disparities in housing quality emerge among different income groups, which in turn lead to differences in the amount of CO_2 reduction achieved per unit of expenditure.

Therefore, when we determine the optimal solution, it is necessary to consider two conditions: the presence of heterogeneous households, where differences in achievable quality and efficiency lead to disparities in the reduction effect per unit of investment across income groups; and, consequently, the need to establish differentiated optimal subsidy levels according to income groups, which means that household utility must be treated as a constraint within the optimization framework.

4. CONCLUSIONS

In this paper, we explain how the optimal subsidy amount for households with a given income level p is determined using a mathematical model. Building on this result, our future work will extend the analysis to develop an optimal subsidy allocation pattern that considers the entire household income distribution by approximating the distribution with a lognormal distribution [2][3].

ACKNOWLEDEMENTS

This work was supported by JSPS KAKENHI (Grant Numbers JP 24K22990).

REFERENCES:

[1] Ministry of Land, Infrastructure, Transport and Tourism (MLIT). Housing: Page on the Act on the Improvement of Energy Consumption Performance of Buildings, https://www.mlit.go.jp/jutakukentiku/house/shoenehou.html (Accessed: July 13, 2024).

[2] Masahiko Aoki, The Theory of Distribution, Chikuma Shobo, Tokyo, 1979.

[3] Osamu Kurita, Mathematical Models of Cities and Regions, Kyoritsu Shuppan, Tokyo, 2013.

ABS ID: 77

USDM-OP-22

Dr. Chanchal Sonkar

ABS ID: 180

USDM-OP-23

Dr. Debi Prasanna Kanungo

ABS ID: 205

USDM-OP-24

Dr. Philips Omowumi Falae

4th International Symposium on One Health, One World
November 20 – 22, 2025

ABS ID: 142

USDM-OP-25

Negative stiffness damper for damage mitigation of rc buildings

Ramyashree[1], p. Kamatchi[2], g. Raghava[3]

[1]M. Tech Project Student, CSIR- Structural Engineering Research Centre, Chennai, India
[2]Chief Scientist & Head, ASTaR, CSIR- Structural Engineering Research Centre, Chennai, India
[3]Professor, NITTE Meenakshi Institute of Technology, Bengaluru, Karnataka, India
Correspond to Dr. P. Kamatchi(kamatchi.serc@csir.res.in)

***Keywords**: Negative Stiffness damper, Seismic response, Viscous Damper, Damage Mitigation, RC building.*

1. INTRODUCTION

Dampers and isolators are passive energy dissipation devices which are used for seismic protection of buildings. As reported in literature [1], the concept of negative stiffness is being widely adopted in the automobile sector for vibration isolation. Limited applications of negative stiffness damping (NSD) have been reported in literature[2-4] for seismic damage mitigation. In this paper, in order to investigate the applications of NSD in buildings an effort has been made to numerically simulate the response of G+5 RC framed building for three earthquakes with and without NSD and also with viscoelastic damper (VD).

2.NEGATIVE STIFFNESS DAMPER

Negative stiffness Damper (NSD), is a mechanical device used for seismic damage mitigation of structures (Fig.1a-1d). The NSD is a device that initiates the motion in same direction as the displacement due to applied force. Molyneux was the first to suggest the negative stiffness motion, which is foundation of Negative Stiffness Vibration Isolation Devices (NSVID), 1959. A “negative stiffness” from the Negative Stiffness Device (NSD), which is a self-contained device generating force acting in the same direction as the imposed displacement. The NSD consists of double chevron bracing and a vertical pre-compressed spring with stiffness (Fig. 1). Additionally, the bottom of frame has an elastic-bilinear spring that connects the top of the brace to bottom of the frame. The pivot plate transfers the vertical forces operating on the spring to the frame braces instead of structure. A system of self-contained double chevron to fends against preload. Gap Spring Assembly (GAP) is a system type that offers positive stiffness till certain displacement. The structural application of NSD was first given by Nagarajaiah et al, [5].

3. BUILDING MODEL

A six storey Reinforced Concrete(RC) framed building is considered in the present study and modelled in SAP2000 software[6]. The building has four bays in longitudinal direction and thee bays in transverse direction with equal bay width of 4 m each. The NSD and VD are added in the 1st, 2nd, and 3rd bays at ground floor(Case 1) and at first floor (Case 2) of one of the frames of the six storey building as shown in Fig. 3. Addition of NSD causes reduction in time period, but addition of VD do not alter the time period of the building as given in Table 1. Time history analyses of the building with and without damper are carried out with three ground motions viz., Loma Prieta, North Ridge, Zone 5[7] with accelerations multiplied with a factor of 3. Results of the time history analyses in terms of base shears, Peak roof displacement are compared in Tables 2 and 3. Variations in storey drift of building for different earthquakes for different cases are given in Fig. 4.

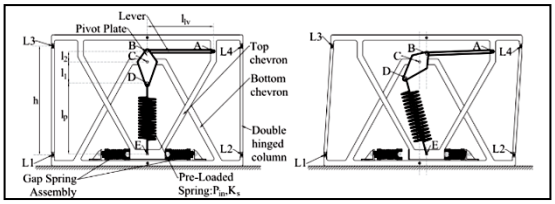

Fig. 1 Schematic representation of Negative Stiffness Damper: Undeformed NSD and Deformed NSD [5]

Fig. 2 Experimental model of NSD Undeformed NSD and Deformed NSD [5]

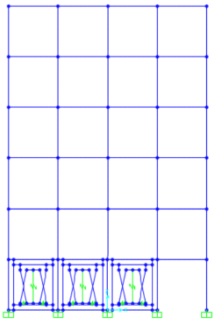

a) With NSD- Case 1

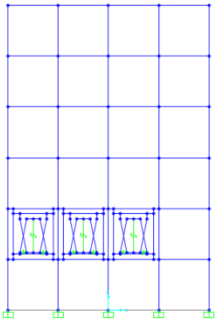

(b) With NSD- Case 2

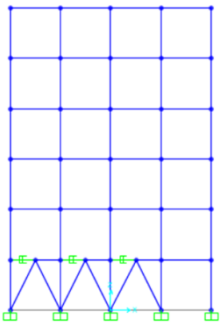

(c) With VD- Case 1

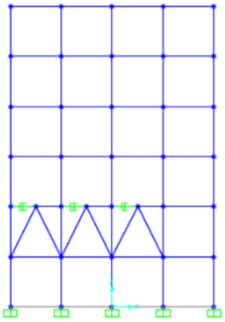

(d) With VD- Case 2

Fig. 3 Front frame of six storey building fixed with NSD and VD in the ground floor and First floor

Table 1 Time period of the building (in seconds)

Undamped	Damped Case 1		Damped Case 2	
	NSD	VD	NSD	VD
0.891	0.750	0.891	0.680	0.891
0.891	0.750	0.891	0.680	0.891
0.891	0.750	0.891	0.680	0.891

Table 2 Base shear of the building (in kNs)

Ground motion	Undamped	Damped, Case 1		Damped, Case 2	
		NSD	VD	NSD	VD
Loma Prieta	1744.1	1514.2	1778.7	1135.3	1616.8
North Ridge	1209.0	860.3	1161.0	780.2	1076.0
Zone 5	496.4	499.6	450.7	460.6	500.0

Table 3 Peak roof displacement of the building

(in mms)

Ground motion	Undamped	Damped, Case 1		Damped, Case 2	
		NSD	VD	NSD	VD
Loma Prieta	56.44	37.23	58.43	22.51	52.51
North Ridge	34.08	20.94	29.33	16.50	26.08
Zone 5	15.51	13.24	12.55	7.86	13.40

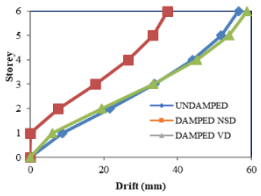

(a) Loma Prieta Case 1

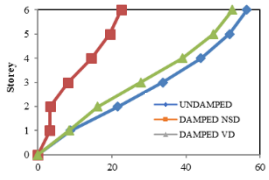

(b) Loma Prieta Case 2

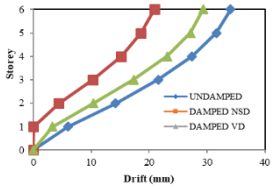

(c) North Ridge Case 1

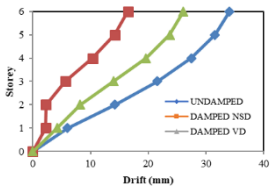

(d) North Ridge Case 2

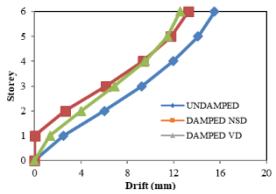

(e) Zone 5 spectrum compatible ground motion Case 1

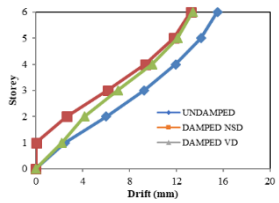

(f) Zone 5 spectrum compatible ground motion Case 2

Fig. 4 Storey drift of building for different earthquakes

4. CONCLUSIONS

From the results obtained, it is clear that adding the NSD to structure brings down the seismic responses viz., Base shear, Maximum roof displacement and storey drifts. From the results it is seen that installation of NSD in first floor *ie* Case 2 seems tohave maximum response reduction compared to Case1. The reduction of response of building with NSD is significant compared to the building with VD.The reduction in responses in NSD are due to negative stiffness property of device, friction in device, and also due to stiffness of pre-compressed spring in device.

ACKNOWLEDGEMENT

This paper has been assigned a registration number of CSIR-SERC- 1365/2025. This research is carried out as a part of OLP22441 project on Mitigating Effects of Wind and Seismic Hazards on Tall Buildings. The first author carried out the work as a part of her M. Tech thesis. The third author is the internalguide of the M. Tech project student. This paper is being published with the kind permission of the Director, CSIR-Structural Engineering Research Centre.

REFERENCES

[1] Huan Li1, Yancheng Li1, and Jianchun Li,. "Negative Stiffness Devices for Vibration Isolation Applications", Review Article, Advances in Structural Engineering, Sage Journals, 2000.

[2] Satish Nagarajaiah, Lin Chen, Meng Wang, "Adaptive Stiffness Structure with Damper: Seismic and Wind Response Reduction using Passive Negative Stiffness and Inerter Systems", Technical Paper, Journal of Structural. Engineering, (2022). Vol-148, Issue-11.

[3] Priyanka A. Jadhav, Suhail Ahmed Shaikh, "Optimization of Seismic Response of Steel Structure using Negative Stiffness Damper", International Journal of Advances in Mechanical and Civil Engineering, 2018. Vol-5, Issue-4.

[4] A. Sarlis, D. T. R Pasala., et al, "Negative Stiffness Device for Seismic Protection of Structure: Shake Table testing of a Seismically Isolated Structure", Journal of Earthquake Engineering, 2016, Vol-19, Issue-2.

[5] Nagarajaiah, Satish & Pasala, Dharma Theja & Reinhorn, Andrei & Constantinou, Michael & Sarlis, Apostolos & Taylor, D... Adaptive Negative Stiffness: A New Structural Modification Approach for Seismic Protection. Advanced Materials Research. (2013), 639-640. 54-66. 10.4028/www.scientific.net/AMR.639-640.54.

[6] Computers and Structures, Inc., SAP2000 – Integrated Software for Structural Analysis and Design, Version 25: Analysis Reference Manual, Berkeley, California, USA, 2025.

[7]IS 1893:2016 (Part 1):(2016) "Criteria for earthquake resistant design of structures-Part1: General provisions and buildings." Bureau of Indian Standards, New Delhi.

ABS ID: 108
USDM-OP-26

Ms. Yerramsetty Lakshmi Supriya

2025 HOW

4th International Symposium on One Health, One World
November 20 – 22, 2025

ABS ID: 24
USDM-OP-27

Enhancing Urban Flood Resilience: A Flood Parameter Predictive Modelling With Uav-Dem and 1d Hydrodynamic Simulation For Non-Perennial River

M. H. Rana[1], d. P. Patel[2] and v. Vakharia[3]
[1]*Ph.D. Research Scholar, Department of Civil Engineering, Pandit Deendayal Energy University, Gandhinagar, India,*
[2]*Professor, Department of Civil Engineering, Pandit Deendayal Energy University, Gandhinagar, India,*
[3]*Associate Professor, Department of Mechanical Engineering, Pandit Deendayal Energy University, Gandhinagar, India*
Correspond to Ms. Mrunalini H. Rana (mrunalini.rphd20@sot.pdpu.ac.in)

***Keywords**: 1D hydrodynamic model, Non-perennial River UAV-DEM, Urban flood mamagement.*

1. INTRODUCTION

The flooding continues to be among the most catastrophic natural disasters, necessitating sophisticated, data-informed strategies for precise forecasting and prompt intervention (1). Flood has become intense and frequent due to altered precipitation patterns and rising extreme weather events with gradual increase in sea level. The dense urban set-up faces challenge during flooding leading to property destruction and human fatalities. Throughout the history, understanding, evaluating and predicting flood events for better flood management have remained the critical pursuit. To achieve these goals flood inundation models have evolved as an essential tools for simulating flood dynamics including extent, depth, velocity and timing and assessing the extent of inundation under various hydrological conditions (2). For any flood study accurate terrain depiction and appropriate data resolution are most crucial, especially when it is Non-perennial River where there is irregular flow patterns with highly variable channel condition. Satellite image are the sources but now a days Unmanned Aerial Vehicle (UAV's) provide high-resolution aerial data, enabling accurate bathymetry for non-perennial rivers. Such data improves hydrodynamic modeling and enhances flood prediction by capturing the impact of input resolution on simulations (3). This study outlines a clear framework for predicting flood parameters along a specific 5 km segment of the Sabarmati River, a non-perennial river, utilising high-resolution Digital Elevation Models (DEM's) created with Unmanned Aerial Vehicles (UAV's). The collected topographic data was incorporated into a 1D hydrodynamic model to replicate water levels and flow patterns across various cross-sections using CivilGeo HEC-RAS (4). Key characteristics from the simulated outputs and input datasets were identified through established feature selection methods to improve model efficacy. In this paper XGboost was performed and evaluated on RMSE and MAE. This integrated approach showcases the efficacy of merging UAV-derived topographic data, one-dimensional hydrodynamic modeling, and machine learning methods to enhance flood forecasting in non-perennial river sections where traditional data is scarce. The findings of this study play a significant role in improving urban safety and disaster mitigation, offering valuable insights for local municipal bodies in the effective planning and management of flood-prone areas.

2. STUDY AREA

A 5 km stretch of the Sabarmati River in Gujarat in Gandinagar was surveyed using Phantom 4RTK to produce 3.69 cm high resolution DEM. The origin of the rives is from Rajasthan state but majorly flowing in Gujarat state. The survey area coverage is about 8 sq.km. encompasses strategic urban hub such as GIFT city and Knowledge Corridor hoisting Institutes and Universities. The UAV-based survey provides detailed bathymetry, offering a pilot

framework for flood modeling and urban river management in similar set up.

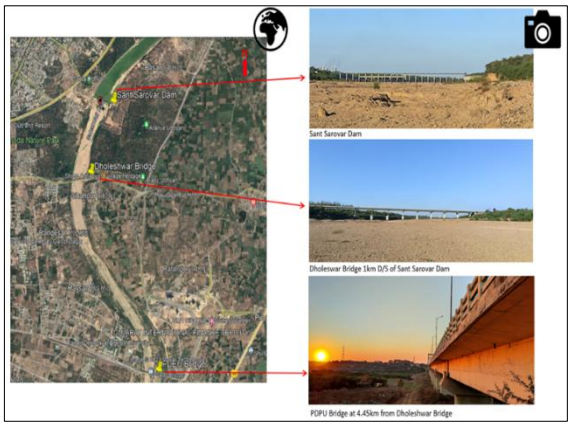

Figure 1. Study area surveyed by Phantom 4RTK

3. METHODOLOGY

The workflow for the study is basically handled in three stages: UAV Survey and DEM generation, followed by Hydrodynamic modelling and application of machine learning model. The high resolution DEM were generated from UAV survey. These DEM were one of the input parameter in 1D hydrodynamic modelling along with the flood record of August 2006 acquired from the State Water Data Centre, Gandhinagar. The 1D hydrodynamic simulation gives out put like discharge, velocity, energy gradient elevation etc. using the Saint-Venant equation which comprise of continuity and momentum equation.

$$\frac{\partial A}{\partial t} + \frac{\partial Q}{\partial x} = 0$$

$$\frac{\partial Q}{\partial t} + \frac{\partial \left(\frac{Q^2}{A}\right)}{\partial x} + gA\frac{\partial H}{\partial x} + gA\left(S_o - S_f\right) = 0$$

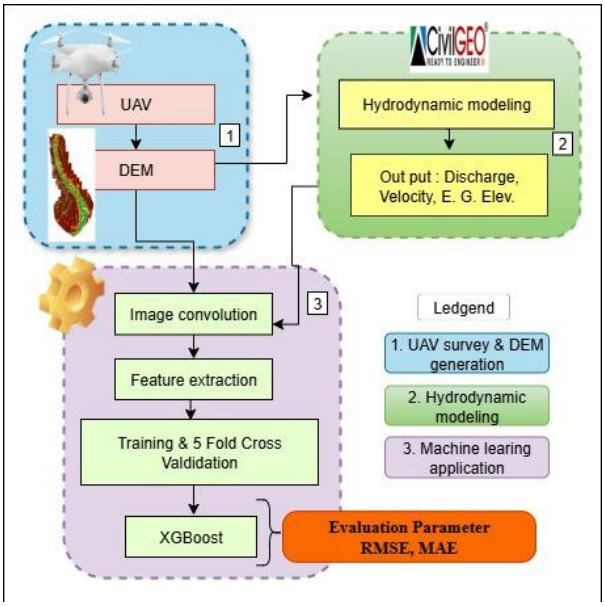

Figure 2. Work flow for the case study

For flood parameter prediction the images were convoluted using GAN advanced deep learning model named ConSinGAN (4). The improved DEMs generated by ConSinGAN enhance spatial resolution and topographic details, allowing more accurate flood simulations by better capturing micro topographic features. Supervised learning uses labeled data to train models, enabling them to accurately predict the outcomes from new unseen data based on learned pattern. In this study we have used XGBoost model. This is an optimised gradient boosting algorithm that built decision tree sequentially to improve prediction accuracy and prevent over fitting. Widely used for speed, scalability and strong performance (5).

4. RESULT AND DISCUSSION

The XGBoost model is evaluated by applying two evaluation metrics, RMSE and MAE with training and testing of datasets.

Table1: Results of XGBoost model on flood parameters

XGBoost	RMSE		MAE	
	Training	Testing	Training	Testing
Discharge	0.5657	1.5186	0.4013	0.9349
Velocity	0.0004	0.0008	0.0002	0.0005
E.G.Elev.	0.0084	0.0211	0.0061	0.0135

The XGBoost model demonstrate strong predictive performance across all parameters. Here discharge has low training and high testing indicates slight variable due to complex flow behavior. Velocity show low errors indicates high accurate model fit. E.G. Elev. Both training and testing errors are minimal shows models robustness and reliability in predicting flood parameters with negligible over fitting.

5. CONCLUSIONS

The study highlights that accurate flood modeling using advanced DEM enhancement and machine learning techniques like XGBoost significantly improves urban safety and disaster mitigation efforts. It supports policy innovation and informed political decision-making for effective resource allocation and risk management. By improving forecasting accuracy, it strengthens preparedness in multi-disaster environments, enabling faster response and minimizing damage to life and infrastructure.

REFERENCES:

[1] Kuhaneswaran B, Sorwar G, Alaei AR, Tong F. Evolution of Data-Driven Flood Forecasting: Trends, Technologies, and Gaps—A Systematic Mapping Study. Vol. 17, Water. 2025.

[2] Kheswa N, Bloodless Dzwairo R, Kanyerere T, Singh SK. International Journal of Water Resources and Environmental Engineering Current methodologies and algorithms used to identify and quantify pollutants in sub-basins: A review. 13(2):154–64. Available from: http://www.academicjournals.org/IJWREE

[3] Rana MH, Patel DP, Vakharia V, Jodhani KH, Gupta N, Singh SK, et al. UAV-Derived DEM Bathymetry for Enhancing 1D Hydrodynamic Modeling for Non-perennial River. J Indian Soc Remote Sens [Internet]. 2025;(0123456789). Available from: https://doi.org/10.1007/s12524-025-02254-4

[4] HEC-RAS User's Manual. HEC-RAS River Analysis System HEC-RAS User's Manual. 2023.

[5] Chen T, Guestrin C. XGBoost: A Scalable Tree Boosting System. In: Proceedings of the 22nd ACM SIGKDD International Conference on Knowledge Discovery and Data Mining [Internet]. New York, NY, USA: Association for Computing Machinery; 2016. p. 785–794. (KDD '16). Available from: https://doi.org/10.1145/2939672.2939785

ABS ID: 186
USDM-OP-28

Eye-Tracking Based Analysis of Driver Distraction Patterns in Urban Environments: A Delhi Study

Romy Mathew[1], Merin Sara Mathew[1], Meenakshi Prasad[1], Kamini Guptha[2], Vinod Karar[3] and s. Velmurugan[3]
[1]*Student, Department of Civil Engineering, Saintgits College of Engineering (Autonomous), Kottayam, Kerala, India,*
[2]*Senior Technical Officer, Traffic Engineering and Safety, CSIR-Central Road Research Institute (CRRI), Delhi, India,*
[3] *Chief Scientist, Traffic Engineering and Safety, CSIR-Central Road Research Institute (CRRI), Delhi, India,*
Correspond to Dr. Vinod Karar (vinodkarar.crri@nic.in)

***Keywords**: Urban traffic safety, Eye-tracking, Driver behavior, Gaze distribution, Cognitive load.*

Abstract: In a crowded city like Delhi, urban traffic is getting more complicated. Driver behaviour plays an important role in these situations and this is crucial for enhancing road safety. Understanding driver behaviour is vital in the development of better driver assistance systems. The eye-tracking technology helps to examine physical behaviour of driver which helps in study of their patterns during city driving situations. Here, the eye movement information is taken from the professional drivers of different age without considering the gender. The eye movement information captured include assess fixation duration, saccades, and gaze distribution. The reaction to different situation like traffic situations, such as pedestrians, traffic lights, and nearby vehicles are taken from the drivers on how they react to visual elements. Here, we study how the driver's eye-gaze whereabouts and duration are impacted by heavy traffic, whether the road layouts puzzle them and in-car distractions like touchscreen use. It is observed that they get stressed when they are in busy locations. Usually these drivers only focus on a particular areas and looks around very less. This makes them to slow down in unexpected situation like pedestrian crossing, or sudden brake of the vehicle in front. It is noticed that the professional and skilled drivers move their eyes very quickly and widely on each and every elements very carefully. The purpose of the study is to shed light on mental workload and how it affects safety and how they get distracted while driving in urban areas. By following these conditions properly, we will be able to create better driver education and more intelligent automotive systems that helps to assist drivers more effectively.
Keywords: Urban traffic safety, Eye-tracking, Driver behavior, Gaze distribution, Cognitive load

INTRODUCTION

Road safety especially in a traffic -congested and densely populated cities like Delhi has become a major issue in today's urbanized world. The studies say driver distraction is one of the primary problems in road traffic accident, and it is increased in urban environments where drivers should find complex situations which involves vehicle movement, pedestrian crossings, and traffic signals. It was observed that the distractions can be visual, cognitive, or manual in nature, and these can be either from internal sources like mobile phone use, conversations or external sources like roadside advertisements, activities. In contrast to highways or rural areas, urban cognitive load driving in urban areas requires continuous visual scanning and

rapid decision-making, which makes drivers more prone to distraction.

The detailed analysis of driver attention and cognitive load in real world scenarios were taken using an eye-tracker. The eye tracker helped to measure where, how long and how regular the driver looks on various objects in their environment. From analysing, it helps to understand the distraction patterns which the traditional methods failed to notice. The observation thus helps in understanding the driver's behavior and for developing the measures to improve the road safety in congested traffic systems.

The study mainly focuses on identifying and analysing the driver distraction patterns in real scenarios in urban environment using modern technology particularly Tobii eye tracker. This study was done in a high densely populated routes of Delhi. It helps to observe various underlying conditions in traffic. The main objective of this study was to determine and analyse the driver's distraction for various objects or elements in the road environment and to categorize their behaviour which helps in developing the road safety. The data were collected from the drivers of different ages without considering their gender. They have a high experienced level in driving. The data of eye movement like the fixation duration, glance frequency were recorded during live drives. Also, parameters like the vehicle speed, pedestrian density, environmental clutter, and the signal placement were taken into consideration to connect the gaze behavior with the given situation for collecting the data.

1. METHODOLOGY

The study of driver behaviour plays an important role in these situations which is crucial for enhancing the road safety. This study is vital as it helps to develop the better driver assistance systems. The developed eye-tracking technology helps to identify the driver's physical behavior which is used to study the driver distraction patterns during the given situations to drive.

The evaluated patterns of driver distraction and visual behaviour was done in densely populated and unpredictable traffic conditions using the eye tracking technology in the urban environments The core objective was to understand the driver visual focus while driving in the real time conditions and how different elements seen in the environments and cognitive stressors influence the efficiency. The study mainly aims to measure specifically the gaze distribution and fixation patterns among the skilled drivers in order to find the visual behavior under various traffic conditions to explore the impact of distractions inside the vehicle and the layouts outside the vehicle. This helps to improve the road safety, driver training, and intelligent assistant systems.

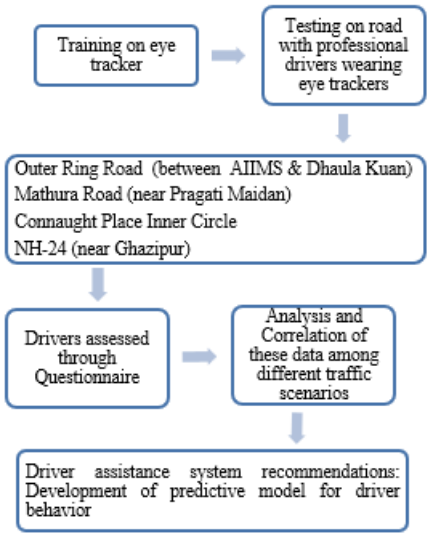

Fig. 1 Adopted Methodology

The participants include the drivers who were professional and skilled of varying age groups irrespective of their genders. All selected drivers have their valid driving license and each have at least three-year experience on driving in a congested roads like Delhi. The study helps to identify the different behavioral patterns of these drivers in a metropolitan driving obstacle.

An eye tracker specifically named, Tobii Pro Glasses 2 were used to record the driver eye movements. This is a wearable eye-tracking

device designed for real-time detection. The device is fitted with a high-definition front camera to capture the road view, infrared sensors for recording saccades, fixations, and gaze plots, and synchronization with analysis software for comprehensive visual behavior analysis. Each driver went through pre-orientation and calibration session for about 15-20 minutes for ensuring the proper fitting, accurate data capture and the alignment, followed by a brief trial drive for their familiarization with the device. The on-road driving session were taken for about 30 minutes which covered almost all the routes with high density vehicle speeds. During the driving period, the data like fixation duration, saccades, and gaze distribution were recorded and research team member became a part in order to ensure the road safety and to analyse the real time behavior.

After completing the drive, a questionnaire session was structured for the evaluation of the difficulty of the drivers while driving, attention-diverting elements such as roadside billboards, pedestrian movement, and in-car distractions, as well as perceived stress and mental workload. Tobii Pro Lab software was used to record the data which focused on Areas of Interest (AOIs) including traffic lights, pedestrians, vehicles, and mirrors. Different patterns of visual behavior and the lapses which generates the fixation heatmaps and gaze plots. Different analysis of varying age groups, road types, and traffic densities, as well as based on the frequency and duration of visual distractions were taken and conducted which further provides a deep information on driver behavior and develop different measures to enhance the road safety, driver training, and intelligent assistance systems in urban areas.

2. RESULTS AND DISCUSSIONS

The study for eye tracking using Tobii Pro Lab in congested cities like Delhi provides a detailed information about driver distraction patterns which focus on Areas of Interest (AOIs). The data collected from the professional drivers describes the diverse traffic scenarios and analysed for fixation duration, saccades, gaze distribution, and AOI-specific metrics:

- Outer Ring Road between AIIMS & Dhaula Kuan
- Mathura Road near Pragati Maidan
- Connaught Place Inner Circle,
- NH-24 (near Ghazipur)

The analysis using the Tobii Pro Lab's highlights that in a high traffic condition the drivers showed an extended fixation duration on specific AOIs, such as the vehicle directly ahead (AOI-1) and traffic signals (AOI-2), with limited attention to peripheral AOIs like pedestrians (AOI-3) or adjacent vehicles (AOI-4). It was observed that the average fixation duration ranges from 0.3 to 0.7 seconds in the congested areas which when compared to 0.2 to 0.4 seconds in less dense traffic regions. Gaze distribution in busy locations while driving showed that it was (e.g., Connaught Place Inner Circle) allocated 65% of their gaze to AOI-1 (road ahead), 20% to AOI-2 (traffic signals), 10% to AOI-3 (pedestrians), and 5% to AOI-4 (adjacent vehicles).

The professional drivers expressed a faster and more frequent gaze changing patterns across AOIs, covering a wider visual field. The data collected indicates that the experienced driver's transition these between AOIs (e.g., from AOI-1 to AOI-3) with an average saccade velocity 20% higher than novices, enabling quicker responses to dynamic elements like pedestrian crossings. In contrast, less experienced drivers showed slower saccades, with transition times averaging 0.15 seconds longer in high-traffic areas like Mathura Road.

The AOI tools of Tobii Pro Lab highlights different attention patterns. For instance, on NH-24, drivers spent 30% less time fixating on AOI-3 (pedestrians) when distracted by in-car touchscreens (AOI-5). In complex layouts like Connaught Place, fixation entropy was higher, indicating irregular shifts between AOIs due to increased cognitive load. The AOI analysis also showed that drivers on Outer Ring Road

maintained a balanced gaze distribution across AOI-1 (road ahead) and AOI-4 (adjacent vehicles), reflecting more predictable traffic flow.

The consolidation of Tobii Pro Lab metrics with questionnaire responses helps to find out further findings of driver distraction patterns. Reported stress levels were steady with longer fixations on AOI-1 and this helps to reduce attention to peripheral AOIs, confirming the influence of cognitive load on visual behavior. AOI-based observations offered a detailed view of attention distribution, making the outcomes applicable to real-world driving contexts. Moreover, the study's predictive model, informed by AOI data, offers potential for developing intelligent vehicular systems which are capable of monitoring gaze allocation in real time—such as triggering alerts when insufficient attention is given to pedestrians (AOI-3). The study also supports broader interventions which results in including driver education on gaze distribution and infrastructure improvements like road layouts and enhanced pedestrian signage in high-density areas such as Connaught Place, Mathura Road, and NH-24. This helps to reduce cognitive overload and improve urban road safety.

CONCLUSION

The modern technology specially the Tobii Pro Lab was used to find the driver distraction patterns in Delhi's complex urban traffic environment. The fixation duration, saccades, gaze distribution, and blink behavior, and mapping these onto defined Areas of Interest (AOIs) which also includes the road ahead, mirrors, pedestrians, adjacent vehicles, and in-vehicle interfaces were recorded and thus helps research by providing an objective assessment of visual behavior. Through the study, results indicated a strong tunneling effect in high-density traffic, where drivers focused mostly on the road ahead, often neglecting other secondary cues such as pedestrians or nearby vehicles. This behavior helps to develop delayed decision-making and slower hazard response in proper manner. In contrast, experienced drivers exhibited broader scanning patterns, faster gaze changing movements, and smoother transitions between AOIs, leading to improved situational awareness and hazard anticipation. In car distractions was a significant driver distraction in urban environments, with gaze durations which frequently exceeds by two seconds, thereby reducing attention to mirrors and pedestrian zones. Validation through heatmaps, gaze plots, and self-reported stress levels confirmed these patterns.

The findings had been done to highlight the practical importance of pointing out the behavioral evidence into transport engineering, road signage placement, and in-vehicle interface design. Developing driver training programs using the eye tracking data also provide valuable inputs that emphasize peripheral scanning. It also helps in informing predictive ADAS models which is capable of issuing real-time alerts. Looking from a wider perspective, the study illustrates the potential of eye-tracking research to make a connection with behavioral science, road safety, and urban planning, contributing to safer and more intelligent transport systems.

REFERENCES:

[1] J.D. Lee, Fifty years of driving safety research, Hum. Factors 50 (2008) 521–528.

[2] T.W. Victor, J.L. Harbluk, J.A. Engström, Sensitivity of eye-movement measures to in-vehicle task difficulty, Transp. Res. Part F: Traffic Psychol. Behav. 8 (2005) 167–190.

[3] M.F. Land, B.W. Tatler, Looking and Acting: Vision and Eye Movements in Natural Behaviour, Oxford University Press, Oxford, 2009.

[4] A. Doshi, M.M. Trivedi, On the roles of eye gaze and head dynamics in predicting driver's intent to change lanes, IEEE Trans. Intell. Transp. Syst. 10 (2009) 453–462.

[5] W.W. Wierwille, Visual and manual demands of in-car controls and displays, in: Proc. Hum. Factors Ergonom. Soc. Annu. Meet., vol. 37, no. 7, 1993, pp. 542–546.

[6] Y. Tochihara, H. Yamato, M. Suzuki, Eye tracking measurements for evaluating cognitive load and visual behavior in urban driving in Tokyo, Int. J. Hum. Comput. Interact. 36 (2020) 950–962.
[7] M.S. Young, J.M. Mahfoud, N.A. Stanton, Visual clutter in the urban driving environment: Effects on driving behaviour and implications for design, Ergonomics 55 (2012) 34–49.
[8] L. Gugerty, Situation awareness during driving: Explicit and implicit knowledge in dynamic spatial memory, J. Exp. Psychol. Appl. 17 (2011) 247–265.
[9] M.A. Recarte, L.M. Nunes, Effects of verbal and spatial-imagery tasks on eye fixations while driving, J. Exp. Psychol. Appl. 6 (2000) 31–43.
[10] K.A. Brookhuis, D. de Waard, Monitoring drivers' mental workload in driving simulators using physiological measures, Accid. Anal. Prev. 42 (2010) 898–903.
[11] D.E. Haigney, R.G. Taylor, S.J. Westerman, Concurrent mobile (cellular) phone use and driving performance: Task demand characteristics and compensatory processes, Transp. Res. Part F: Traffic Psychol. Behav. 3 (2000) 113–121.
[12] S. Velmurugan, S.S. Arkatkar, G. Joshi, Behavioral study of road users under mixed traffic conditions on urban roads in India, Central Road Research Institute (CRRI), Report No. CRRI/2015/UBD/TR, 2015.
[13] R. Pal, A. Ghosh, A. Chattopadhyay, Evaluation of driver's visual scanning behavior under mixed traffic conditions using eye tracking, J. Mod. Transp. 25 (2017) 193–201.
[14] V. Sharma, A. Roy, S. Mishra, Urban intersection violations and driver gaze behaviour in Indian cities: An eye tracking study, Transp. Res. Procedia 48 (2019) 175–182.
[15] CRRI Pilot Study, Preliminary observations on gaze patterns in Delhi urban roads using wearable eye-trackers, Central Road Research Institute, Unpublished Internal Report, 2020.
[16] R.R. Mourant, T.H. Rockwell, Mapping eye-movement patterns to the visual scene in driving: An exploratory study, Hum. Factors 12 (1970) 81–87.

ABS ID: 181
USDM-OP-29

Ms. Kamini Gupta

4th International Symposium on One Health, One World
November 20 – 22, 2025

ABS ID: 173
USDM-OP-30

Enhancing urban traffic safety through optimized heads- up display systems

Bhavika Arora[1], Divya Agrawal[2], Kamini Gupta[3], S. Velmurugan[3], Vinod Karar[3]
[1] *Department of Physical Sciences, Banasthali University, Jaipur, India*
[2] *CSIR - Central Scientific Instruments Organisation, Chandigarh, India*
[3] *Traffic Engineering & Safety Division, CSIR - Central Road Research Institute, New Delhi, India*
vinodkarar.crri@nic.in

Keywords: *Augmented Reality, Heads-Up Display, Dashboard Displays, Opaque Screens, Mil- itary Vehicles, Automotive Safety Introduction.*

Abstract

Dashboards as well as heads-up and augmented reality displays are aiding in the evolution of human interaction with machines in automobiles, military vehicles, and aircrafts. These modern systems facilitate understanding of the information provided, minimizes loss of attention to the task, and increases safety by depicting essential information through the opera- tor's line of sight. This review integrates findings from recent academic studies focusing on the technological stimulation, impacts on safety and cognitive workload, and barriers to implemen- tation across various domains. The literature portrays how AR-HUDs have potential for faster response times and improved situational awareness, though considerable obstacles such as lim- ited visibility, information overload, and lack of standardization still pose challenges. This work consolidates evidence from existing research on augmented reality integration into a conducive high-stakes operations environment. Two display configurations were developed viz. Micro-Ac- tive Matrix Organic Light Emitting Diode Display (AMOLED) system with projection optical system and a DWIN TFT LCD display with STM32 microcontroller, both employing semi-re- flective combiner glass. The literature survey and limited experimentation shows 40% decrease in data access time and 35% improvement in situational awareness while maintaining operational focus when compared to conventional dashboard displays. The understanding of critical human factors considerations including cognitive load reduction, visual accommodation processes, and multi-sensor integration challenges, was made in this study.

1. Introduction

The switch from old analog gauges to modern display technologies in cars is a huge step forward. Wickens and Dixon (2007) explain that automated diagnostic systems can be a big help for drivers, especially when things get stressful, while traditional setups often do not cut it in tough situations [1]. Research on transportation safety hammers home the need for drivers to stay aware of their surroundings, with Endsley (1995) laying out a solid framework for how people keep track of what's happening in fast- moving situations [2].

Head-up displays take things up a notch by putting key info right in the driver's line of sight, unlike standard dashboards. Gabbard et al. (2014) provided analysis regarding advanced driver-assistance systems (ADAS), emphasizing their advantages and chal- lenges concerning driver information overload [3]. Horrey and Wickens (2007) remark that older interfaces presented to the drivers are no solution, as they require continual looking away. This, in their opinion, increases the collision risk due to the momentary, fleeting looks drivers sneak at the road [4].

High-level architecture integrating CAD and data from all graphical interfaces de- sign systems integrates both drivers and passengers. Davis et al. (2007) focus on the vehicle data distribution digital bus or popularly the Controller Area Network (CAN) bus, showing how peripheral devices of the vehicle are optimally utilized for a flawless operation [5].

2. Literature review

2.1 Display Technologies in Automotive and Military Applications

2.1.1 Head-Up Display Fundamentals

Weintraub and Ensing (1992) documented the design theory of HUDs in detail for hu- man factors issues [6] while HUDs were still in prototypes stages, Charissis and Naef (2007) tried to carry out evaluations of HUD interfaces concerning driving performance and system usability alongside usability testing for driving performance [7]. Their out- comes provided fundamental baseline metrics on efficacy of HUDs.

Specific to the demand of attention and driving with heads up displays in automo- biles, Liu (2003) brought the context with supportive evidence [8]. This study, while showing some degree of measurable gains in certain performance metrics, showed a great deal of variability in the magnitude of gains based on implementation and condi- tions.

2.1.2 Sensor Integration

As far as the actual sensing technologies and their integration with display systems are concerned, in a different setting, Hess et al. (2004) explored the autonomous logistics capability enabled by Prognostic and Health Management (PHM) systems. These re- searchers stressed the need for seamless integration of sensors and displays [9]. In an- other aspect, Young et al (2007) studies driver distraction investigating various types of displays and how they influences the driver's focal point of attention [10]. Under- standing the impact of display technologies is important as seen from the results of these studies.

2.1.3 Advanced Display Technologies

Den Boer (2005) provides a thorough exploration of active-matrix liquid crystal dis- plays, breaking down how they function and why they are valuable [11]. These displays shine for their energy efficiency and crisp visuals, making them ideal for use in vehi- cles. MacDonald et al. (2007) discuss advancements in flexible electronics substrates, which could pave the way for exciting new possibilities in car displays [12]. Yamamoto et al. (1989) focused on improving LCD viewing angles, a crucial consideration when multiple people need a clear view of the screen [13].

Azuma (1997) offers a foundational overview of augmented reality technology, lay- ing out its core concepts and challenges [14]. Tang et al. (2003) studied how augmented reality performs in assembly tasks, providing in-sights that apply to real-world opera- tions [15]. Milgram et al. (1995) introduced the reality-virtuality continuum, a frame- work that helps us under-stand the different levels of augmented reality systems [16]. This concept remains key to classifying AR technologies.

2.1.4 Human Factors and Safety Considerations

Wickens (2002) came up with the multiple resource theory, which offers a way to un- derstand how different types of displays impact mental workload [17]. This framework is key to figuring out why some display setups work better than others do. Levy et al. (2006) studied the psychological refractory period, revealing basic limits in how people process information that shape display design [18]. These mental constraints are critical to keep in mind when designing advanced display systems.

Wickens and Long (1995) investigated object versus space-based models of visual attention, with specific implications for head-up display design [19]. Their findings provide important guidance for information placement and presentation in HUD sys- tems.

Yeh and Wickens (2001) studied display signaling in augmented reality, examining how cue reliability and image realism affect attention allocation and trust calibration [20]. This work is particularly relevant for military applications where trust in displayed information is critical. Holmqvist et al. (2011) offer a detailed look at eye-tracking methods, which are crucial for objectively measuring how well different display tech- nologies perform [21]. These techniques provide a solid way to evaluate display sys- tems.

Fadden et al. (2001) took a meta-analytic approach to weigh the pros and cons of head-up displays, pulling together evidence from multiple studies to draw stronger con- clusions about their effectiveness [22].

2.1.5 Application Domains

Lee et al. (2019) studied how drivers' visual behavior differs between traditional dis- plays and head-up displays, offering solid evidence that HUDs change how drivers fo- cus their attention [23]. Their findings show clear shifts in driver behavior when using these systems.

Park et al. (2008) examined automotive head-up displays, focusing on their safety and usability, and offered practical insights tailored to driving scenarios [24]. Kim and Dey (2009) studied augmented reality windshield displays as navigation aids, pointing out benefits for specific user groups [25].

Gish and Staplin (1995) explored the human factors of using head-up displays in vehicles, highlighting important safety considerations [26]. Liu and Wen (2004) com- pared head-up and head-down displays in commercial vehicle operations, providing useful insights for professional drivers [27].

Livingston et al. (2002) developed augmented reality systems for military operations in urban settings, establishing key standards for AR in high-stakes military contexts [28]. Their work underscores the unique requirements and solutions needed in these environments.

Hou et al. (2007) explored adaptive interfaces for controlling multiple unmanned aerial vehicles, demonstrating how advanced display technologies can meet the chal- lenges of complex military operations [29]. Their findings highlight the potential of these systems to support demanding missions.

Prinzel et al. (2003) examined synthetic vision display concepts for both retrofit and forward-fit commercial aircraft applications [30]. Their comprehensive evaluation pro- vided important insights for aviation display system design. Prinzel et al. (2003) also investigated CFIT (Controlled Flight Into Terrain) prevention using synthetic vision, demonstrating life-critical applications of advanced display technology [31]. This work shows the potential safety benefits of properly implemented display systems.

2.1.6 Technical Challenges and Limitations

Drascic and Milgram (1996) highlighted key perceptual challenges in augmented real- ity that still pose problems for system designers [32]. These include ensuring accurate registration, managing depth perception, and minimizing visual interference (2019) specifically studied the effects of luminance and color on driver performance and safety in AR automotive displays [33]. Their work provides important guidelines for display calibration and environmental considerations.

Farsi et al. (1999) provide an overview of Controller Area Network implementation, highlighting both capabilities and limitations [34]. The Controller Area Network (CAN) bus system is reliable but comes with limitations in bandwidth and latency that could influence real-time display applications. Kaptein et al. (1996) explored the valid- ity of driving simulators, which is crucial for testing display

systems [35]. Their work emphasized the need for realistic testing environments for proper evaluation of dis- plays.

Tufte (1983) outlined essential principles for presenting numerical data visually, which remain incredibly relevant for modern display systems [36]. These guidelines ensured that information was displayed clearly and effectively, even when space was tight. Rasmussen (1983) created frameworks to understand how skills, rules, and knowledge influence human performance, providing a strong basis for designing dis- play systems [37]. This work helps explain why certain display configurations are more effective than others do.

3 Discussions

3.1 Sensor Diversity and Augmented Reality Head-Up Displays (AR-HUDs)

The combination of various sensing modalities with AR-HUDs represents a major ad- vance for vehicle safety and efficiency, particularly in military applications. Modern vehicles may carry a host of sensors viz. thermal imaging cameras, LIDAR, radar, acoustic sensors, chemical detectors and obtain a full 360-degree view of an environ- ment [38]. This, effectively, increases the things that drivers or operators can see be- yond the natural limits of human senses.

Thermal imaging is particularly valuable in military operations, where detecting heat signatures from people, vehicle engines, or fires can provide a crucial tactical advantage [39]. Arrue et al. (2000) demonstrated how thermal imaging could identify forest fires, laying the groundwork for its use in vehicle fire detection systems [40]. When com- bined with AR displays, thermal data could be projected right into the user's field. The key challenge is to display this information in a way that boosts, rather than over- whelms, the operator's natural awareness.

3.2 Silent Notification Architectures for Stealth Operations

Military vehicles operating in hostile environments require advanced notification sys- tems that provide essential operational threat information while maintaining secrecy. Haptic feedback systems paired with AR displays, as well as notification systems that keep silent, can ensure operators remain informed without compromising stealth [41]. Cao et al. (2008) studied vibrotactile and visual alert systems, showing how combining different alert methods works well in noisy environments [42]. The development of priority-based notification hierarchies becomes essential in these systems [43]. Life-threatening situations such as incoming projectiles or improvised explosive devices re-quire immediate, unmistakable alerts, while lower-priority information like wildlife de-tection or environmental changes could be presented through subtle visual indicators. Multiplexed responses Mid-layering in this way lets the body cull overly reactive re- sponses while harvesting the appropriate response to fluctuating threat levels.

Color-coding and pictograph embedding of AR overlays can quickly communicate- difficult-to-explain data [44]. For example, red overlays might highlight human threats right away, orange overlay could highlight things that might be a threat, like fire or chemical signatures, and blue overlay could represent friendly forces or safe locations.

The trick is in coming up with standardized iconography that stays the same across all units and vehicle types.

3.3 Wildlife and Environmental Hazard Detection

Military and civilian vehicles operating in varied environments face risks be-yond hu- man threats, including wildlife encounters and environmental hazards. Large animals can cause serious collisions, especially in low-visibility conditions, while smaller crea- tures may signal environmental shifts or chemical

dangers [45]. Huijser et al. (2009) offer a detailed study of animal-vehicle collision patterns and strategies to reduce these risks [46]. The use of infrared and motion detection systems allow for the detection of animal body heat and movement, enabling advanced warning for the possible collisions [47]. As noted by Malo et al. (2004), infrared sensors have shown significant promise in wildlife detection systems and have the potential to greatly reduce animal-vehicle collisions [48]. Such systems, when interfaced with AR displays, may highlight the position of animals with adequate threat assessment evaluation. For example, a deer about to cross a road may pro-duce moderate warning such as 'speed limit advised' while a large feline predator close to a military camp may elicit more serious notifica- tions.

Environmental monitoring does not only focus on biological threats, but also in- cludes potential fires, detection of chemical hazards, and changes in weather [49].

Gardner and Bartlett (1999) provide comprehensive coverage of electronic nose technologies for chemical detection, which could be integrated into vehicle sensor suites [50]. The advance warning of critical situations can be equipped with smoke de- tectors, gas analyzers, and atmospheric pressure sensors. With the integration of AR, this information could be provided contextually, such as the showing of wind direction for smoke dispersal, or indicating safe evacuation routes during chemical incidents.

3.4 Integration Challenges and Technical Considerations Challenges in Sensor Integration

Merging information from different types of sensors poses serious challenges. Real- time processing of different sensor inputs necessitates the use of high-level information handling techniques [51]. In their work, Hall and McMullen (2004) discuss in detail all the different mathematical frameworks for fusing data from multiple sensors and the issues related to integrating different types of sensors [52]. The trade off with trying to minimize false alerts is that real threats might be masked and ignored.

Vehicle communication bandwidth restrictions became critical problems with the integration of several sensors that offer high accuracy imaging [53]. Prioritizing and compressing data must negotiate a tradeoff between precision and speed. Local pro- cessing in the vehicle can manage routine information generated by the sensors, while only sending critical messages or unexpected results to lower command systems for central processing [54].

Another issue of concern are power requirements especially if military operations are for long durations [55]. Sensor systems need to be power-efficient; during inactivity periods of silence, sensor systems may need to be in a low-power stand-by mode but need to respond to stimuli. For use in remote regions, other than normal batteries, en- ergy from the vehicle's motion or solar power can be used [56].

3.5 Human Factors in Multi-Sensor AR Systems

Displaying multi-sensor information through AR interfaces must account for human cognitive limits. Too much information can overwhelm operators, reducing their situa- tional awareness, so careful interface design is essential [57]. Cummings and Mitchell (2008) studied how operators manage multiple autonomous vehicles, offering insights into handling complex displays [58]. Systems that adjust to operator needs and prefer- ences show promise for improving human-machine interaction.

Training for operators using sensor-integrated AR systems goes beyond standard vehicle operation [59]. Personnel need to understand what different sensors can and cannot do, recognize potential system failures, and stay skilled in manual operation if automated systems go down. Simulation-based training

provides a safe way to build these essential skills [60].

Building the right level of trust in automated systems is crucial [61]. Relying too much on sensors can lead to complacency, while distrusting them might cause operators to ignore important alerts. Lee and See (2004) provide a detailed analysis of trust in automation, offering frameworks to achieve balanced trust levels [62]. Regular checks on system accuracy and clear reporting of sensor reliability help operators maintain appropriate confidence.

3.6 Cybersecurity and System Resilience

Augmented reality (AR) systems that integrate multiple sensors are prime targets for adversaries, particularly in military settings [63]. Robust cybersecurity measures are essential to protect against attacks on sensors and attempts to insert false data into the system [64]. Checkoway et al. (2011) revealed vulnerabilities in automotive systems, highlighting the need for strong security in connected vehicle technologies [65]. Tools like encryption, authentication protocols, and systems to detect unauthorized access are critical for secure setups.

Building in redundancy and the ability to keep functioning despite failures ensures systems stay operational even if parts were attacked or break down [66]. Using different sensor types to monitor the same environmental factors allows for cross-checking and continued performance if primary systems are compromised. Manual override capabil- ities must remain accessible to operators in all circumstances [67].

The development of tamper-evident and self-diagnostic capabilities helps identify when systems have been compromised [68]. Regular integrity checks and behavioral analysis can detect anomalous operation patterns that might indicate interference or component failure [69].

3.7 Related Experimental Work

The evolution from conventional analog gauges to advanced AR heads-up displays (HUDs) represents a paradigm shift in human-machine interaction within automotive and military applications. This study presents a comprehensive comparative analysis of transparent see-through display technologies, specifically examining their implementa- tion in high-stakes, attention-sensitive environments where maintaining situational awareness is critical for operational safety.

Two display configurations were developed and evaluated: (1) Micro-AMOLED with projection optics, and semi-reflective combiner glass, and (2) DWIN TFT LCD 5.5-inch display with STM32 microcontroller. Each configuration was tested using simulated CAN bus data transmission, displaying critical parameters including speed, RPM, navigation directions, temperature, and fuel levels.

Performance evaluation and testing demonstrated significant advantages of AR-HUD systems over conventional dashboard displays. Key findings include a 40% re- duction in data access time (1.2 seconds vs. 2.0 seconds), 35% improvement in situa- tional awareness, and reduced cognitive load while maintaining focus on the opera- tional environment. Further details are covered in the following sections.

3.7.1 Display Interface Design

The Display (Micro-AMOLED or AMLCD) presents information in an organized lay- out:

- Speed: Top left (e.g., “68 km/h”)
- RPM: Top right (e.g., “3000 RPM”)
- Fuel: Bottom left (e.g., “Fuel: 66%”)
- Temperature: Bottom center (e.g., "Temp: 90°C")
- Directions/Road Signs: Bottom right (e.g., “L” for left turn)
- System architecture and Test environment are shown in Fig. 1. and Fig. 2, respectively.

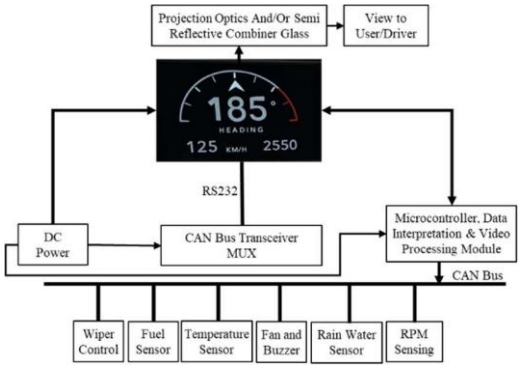

Fig. 1. System Architecture

Fig. 2. Within an in-car environment for Display Validation at the Driver Behaviour Simulation Lab, CSIR-CRRI

3.7.2 Micro-AMOLED based AR Heads-Up Display with Projection & Magnifying Optics, & Semi-reflective Combiner Glass - Configuration-1

The developed system was tested in simulated conditions. The PC was used to transmit data to the microcontroller board without communication errors, the Micro AM-OLED displayed the drive parameters. The Configuration-1 utilized Micro-AMOLED display with control electronics coupled with Projection and magnifying optics and Semi-re- flective transparent combiner glass. The following performance metrics were checked:

- Data transmission reliability - 100% successful data packets
- Image projection quality - Sharp, clearly readable
- System response time - Average 1.2 seconds for data access

The Micro AM-OLED display (size 1" – diagonal) was driven with microcontroller (refer Fig. 3(a)). The vehicle parameters were displayed in certain format making sure that cluttering is not there (refer Fig. 4(a)). The Heads-up display in AR format under- goes left-right mirroring two times – one through folding mirror to reflect the display information (vehicle parameters displayed a symbology) towards the combiner glass and second reflected from the combiner glass, which acts as mirror for the symbology, towards the viewer.

3.7.3 Prototype Testing Results: DWIN TFT LCD 5'5 based AR Heads-Up Display with Semi-reflective Combiner Glass - Configuration-2

In the second configuration (refer Fig. 3(b)), the symbology display is obtained in right- left mirror format (Fig. 4(b)), where one reflection from the semi-reflective (~ 30% reflection) makes it correctly oriented and which is also see-through to enable see the forward view through that glass window. The symbology is made right-left mirror through programming on microcontroller.

The 5.5" Active Matrix Liquid Crystal Display (AMLCD) with a resolution of 720x480 pixel, maximum luminance of 800 Nits is used. The DWIN TFT LCD 5'5

Inch is driven using STM32 Microcontroller. The display (symbology) obtained is hy- brid, that is, mixture of analog and digital for study purpose. The Display is driven using +12V DC Adapter while STM32 Microcontroller board is driven using +5 V supply with +12 V as Input from the Adapter. This configuration is used as AR config- uration with no projection optics but only DWIN TFT LCD 5'5 Inch Display along with the semi-reflective glass to facilitate simultaneous viewing of the forward view through the glass on which the symbology view obtained through the semi-reflective glass surface.

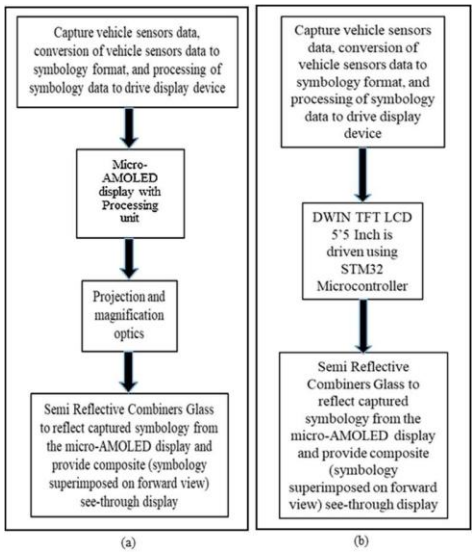

Fig. 3. (a) Display Configuration – 1: Micro-AMOLED display with control electronics coupled with Projection and magnifying optics and Semi-reflective transparent combiner glass, (b) Display Configuration – 2: DWIN TFT LCD 5.5” driven using STM32 Micro-controller coupled with Semi-reflective transparent combiner glass.

Fig. 4. (a) Symbology display obtained on Micro-OLED Display (b) DWIN TFT LCD 5’5 Inch display (Mirror)

3.7.4 Hardware Components and Configuration

- PC for execution of script for simulated CAN bus data transmission to Ar- duino
- Microcontroller to process serial data and controls MicroOLED display/5.5” Active Matrix Liquid Crystal Display (AMLCD)
- Display for Configuration-1: Micro-AMOLED, the compact, high-contrast display with SPI interface
- Display for Configuration-2: 5.5” Active Matrix Liquid Crystal Display (AMLCD), resolution of 720x480 pixel, maximum luminance of 800 Nits
- Lens system comprising convex and concave lenses configured for projection onto glass surface AND/OR Glass surface, the transparent surface (wind- shield or helmet visor) for reflected image display

3.7.5 CAN Bus

Vehicle data simulation occurs on the PC, with data transmission to Arduino for organ- ization into structured bytes using Can Data struct:
Data encoding:

- Speed - speed & 0xFF (e.g., 68 km/h → 0x44)
- RPM - rpm & 0xFFFF (e.g., 3000 RPM → 0x0BB8)
- Fuel - fuel & 0xFF (e.g., 66% → 0x42)
- Temperature - temp & 0xFF (e.g., 90°C → 0x5A)
- Directions/Road Signs - ASCII character encoding (e.g., "L" → 0x4C)

The Microcontroller receives this data through serial communication and refreshes the Micro-AMOLED display every 500ms.

3.7.6 Comparison with Conventional Dashboard Displays

The comparison of performance of conventional dashboard displays, and see-through augmented reality display in the heads-up display format is as under:

- Response time: AR-HUD system almost half that for Conventional dash- board display
- 40% reduction in data access time

– The significant improvement stems from eliminating the need for the drivers (participants) to divert their attention from the primary opera- tional environment to view dashboard information.

- Situational awareness enhancement

– Situational awareness improvement - 35% increase compared to con- ventional systems

– Attention maintenance - Focus on environment while accessing critical information
- Cognitive load reduction - Decreased mental effort required for information gathering
- Errors: Comparable

3.8 Future Technological Developments

Innovative technologies offer substantial opportunities to enhance the functions of sensor integrated AR systems. Algorithms of artificial intelligence and machine learning can enhance the detection of threats while minimizing false "positive" detections [70]. The work by Darms et al. (2009) illustrated the use of machine learning algorithms for the processing of automotive sensor data [71]. AI Edge Processing allows for a greater level of analysis to be done on the vehicle as opposed to relying on external communi- cation networks.

For detection of some chemical and biological hazards, quantum sensing technolo- gies could be beneficial for detection sensitivity and accuracy [72]. Advanced materials science could also be helpful in formulating new durable sensors suited to extreme op- erating conditions with high performance [73].

More developed network systems allow single vehicles to access collective sensing technologies [74]. Military units mesh networks can share threat data across operational areas and civilian use could use infrastructure based sensors to aid threat awareness at the level of the single vehicle [75]. Biswas et al. (2006) on vehicle-to-vehicle commu- nication illustrates the prospects of cooperative sensing systems [76].

The innovation of comprehensive sensor fusion with AR display technology marks a new era in vehicle safety and operational efficiency. The implementation of such sys- tems requires strong attention to human elements, sound technical design, and consid- eration of operational demands across multiple application environments. Billinghurst et al. (2015) provide a comprehensive survey of augmented reality research directions, identifying key areas for future development [77]. Their work suggests that adaptive, context-aware systems represent a promising research direction.

Merenda et al. (2016) investigated augmented reality interface design approaches for different driving tasks, showing the potential for task-specific adaptations [78]. This work suggests that one-size-fits-all approaches may be less effective than adaptive sys- tems. The lack of standardization across AR and HUD systems represents a significant challenge for widespread adoption. Pfannmüller et al. (2009) compared different dis- play concepts for automotive navigation systems, highlighting the need for systematic evaluation criteria [79]. Regan et al. (2008) discuss driver distraction theory, effects, and mitigation strategies, providing a framework for understanding long-term implica- tions of advanced display systems [80].

4 Conclusion

This review of augmented reality displays in automotive and military applications re- veals a field with significant promise but also substantial challenges. The literature demonstrates clear evidence for potential benefits of AR-HUD systems, including im- proved response times and enhanced situational awareness under specific conditions.

The discussion of advanced sensor integration and silent notification systems high- lights the transformative potential of combining multiple sensing modalities with AR display technology. Military applications particularly benefit from silent threat detec- tion capabilities that maintain operational security while providing essential situational awareness. The integration of thermal imaging, motion detection, and environmental monitoring creates comprehensive awareness systems that extend far beyond traditional visual perception.

However, the research also reveals important limitations and challenges that must be

addressed for successful implementation. These include visual performance issues in varying lighting conditions, cognitive workload considerations, security concerns for sensor networks, and the need for standardized evaluation criteria across different sen- sor types and display modalities.

Driving environments create serious challenges for managing driver attention, espe- cially on tough terrains, highways and traffic flyovers. In these situations, the distance of vehicle to vehicle is often less than 5 meters. Drivers frequently need to shift their focus from the road to the dashboard instrument panel. This diversion can delay visual adjustments and lead to information overload, which can compromise road safety and performance during critical events.

The study presented in this works has conducted thorough review and experimenta- tions exploring the importance of heads-up display (HUD) systems to reduce attention shifts by showing only essential and useful information directly through the windshield. The analysis has been made on how visual accommodation processes and cognitive load factors interact, focusing on the effects of display brightness and surrounding light conditions on driver performance across analog, digital, and augmented display formats in busy urban traffic settings.

The key features of the study include: 40% reduction in data access time compared to conventional dashboards, 35% improvement in operator environmental awareness, and Seamless combination of multiple sensor inputs with AR display technology

The study demonstrates that transparent see- through display technologies offer sub- stantial benefits for automotive applications, particularly in high-stakes environments where maintaining situational awareness is critical. The developed system successfully addresses key challenges in information presentation while maintaining operational simplicity and cost-effectiveness.

While primary objectives were achieved, there were some limitations such as the current MicroOLED resolution limits information density and detail. System perfor- mance may vary under different lighting conditions, and the microcontrollers - Arduino UNO and STM32 have computational limitations restricting advanced sensor integra- tion. The testing constraints due to testing conducted in controlled laboratory conditions rather than real-world operational environments, Testing involved few participants, which may not represent broader user populations, and Short-term testing may not re- veal long-term usability or reliability issues. In future, more sophisticated sensor fusion and data processing capabilities, higher resolution displays with improved visibility characteristics, extended evaluation in real-world operational environments, and indus-try-wide standards for transparent display implementation, may be considered.

REFERENCES:

1. Wickens, C. D., & Dixon, S. R. (2007). The benefits of imperfect diagnostic auto-mation: a synthesis of the literature. Theoretical Issues in Ergonomics Science, 8(3), 201-212.

2. Endsley, M. R. (1995). Toward a theory of situation awareness in dynamic sys-tems. Human Factors, 37(1), 32-64.

3. Gabbard, J. L., Fitch, G. M., & Kim, H. (2014). Behind the glass: Driver challenges and opportunities for AR automotive applications. Proceedings of the IEEE, 102(2), 124-136.

4. Horrey, W. J., & Wickens, C. D. (2007). In-vehicle glance duration: distributions, tails, and model of crash risk. Transportation Research Record, 2018(1), 22-28.

5. Davis, R. I., Burns, A., Bril, R. J., & Lukkien, J. J. (2007). Controller Area Network (CAN) schedulability analysis: Refuted, revisited and revised. Real-Time Systems, 35(3), 239-272.

6. Weintraub, D. J., & Ensing, M. (1992). Human factors issues in head-up display design: The book of HUD. Crew System Ergonomics

Information Analysis Center, Wright-Patterson AFB.
7. Charissis, V., & Naef, M. (2007). Evaluation of prototype automotive head-up display in- terface: driving performance and system usability. Proceedings of the 4th International Con- ference on Universal Access in Human-Computer Interaction, 622-631.
8. Liu, Y. C. (2003). Effects of using head-up display in automobile context on attention de- mand and driving performance. Displays, 24(4-5), 157-165.Fleming, W. J. (2001). Over- view of automotive sensors. IEEE Sensors Journal, 1(4), 296-308.
9. Hess, A., Calvello, G., & Dabney, T. (2004). PHM a key enabler for the JSF autonomic logistics concept. Proceedings of IEEE Aerospace Conference, 3543-3550.
10. Young, K., Regan, M., & Hammer, M. (2007). Driver distraction: A review of the literature. Austroads Report, AP-R298/07.
11. Den Boer, W. (2005). Active matrix liquid crystal displays: fundamentals and applications. Newnes.
12. MacDonald, W. A., Looney, M. K., MacKerron, D., Eveson, R., Adam, R., Hash- imoto, K., & Rakos, K. (2007). Latest advances in substrates for flexible electronics. Journal of the Society for Information Display, 15(12), 1075-1083.
13. Yamamoto, T., Nishikawa, S., Honma, M., & Ishii, Y. (1989). Liquid crystal display device having improved viewing angle dependence of color. Journal of Ap-plied Physics, 65(11), 4362-4365.
14. Azuma, R. T. (1997). A survey of augmented reality. Presence: Teleoperators & Virtual Environments, 6(4), 355-385.
15. Tang, A., Owen, C., Biocca, F., & Mou, W. (2003). Comparative effectiveness of augmented reality in object assembly. Proceedings of the SIGCHI Conference on Human Factors in Computing Systems, 73-80.
16. Milgram, P., Takemura, H., Utsumi, A., & Kishino, F. (1995). Augmented reality: A class of displays on the reality-virtuality continuum. Proceedings of SPIE, 2351, 282-292.
17. Wickens, C. D. (2002). Multiple resources and performance prediction. Theoreti-cal Issues in Ergonomics Science, 3(2), 159-177.
18. Levy, J., Pashler, H., & Boer, E. (2006). Central interference in driving: Is there any stopping the psychological refractory period? Psychological Science, 17(3), 228-235.
19. Wickens, C. D., & Long, J. (1995). Object versus space-based models of visual attention: Implications for the design of head-up displays. Journal of Experimental Psychology: Ap- plied, 1(3), 179-193.
20. Yeh, M., & Wickens, C. D. (2001). Display signaling in augmented reality: Ef-fects of cue reliability and image realism on attention allocation and trust calibration. Human Factors, 43(3), 355-365.
21. Holmqvist, K., Nyström, M., Andersson, R., Dewhurst, R., Jarodzka, H., & Van de Weijer,
J. (2011). Eye tracking: A comprehensive guide to methods and measures. OUP Oxford.
22. Fadden, S., Ververs, P. M., & Wickens, C. D. (2001). Costs and benefits of head-up display use: A meta-analytic approach. Proceedings of the Human Factors and Ergonomics Society Annual Meeting, 45(1), 16-20.
23. Lee, S. C., Neale, V. L., Klauer, S. G., & Dingus, T. A. (2019). Comparison of visual be- havior between conventional and head-up display interfaces. Transporta-tion Research Rec- ord, 2673(6), 8-19.
24. Park, K. S., Choi, S. H., Lee, K. W., & Lee, C. W. (2008). Design evaluation of automotive head-up displays in terms of safety and usability. Proceedings of the Human Factors and Ergonomics Society Annual Meeting, 52(23), 1851-1855.
25. Kim, S., & Dey, A. K. (2009). Simulated augmented reality windshield display as a cogni- tive aid for elder driver navigation. Proceedings of the SIGCHI Conference on Human Fac- tors in Computing Systems, 133-142.
26. Gish, K. W., & Staplin, L. (1995). Human factors aspects of using head up dis-plays in automobiles: A review of the literature. Report DOT HS, 808, 320.

27. Liu, Y. C., & Wen, M. H. (2004). Comparison of head-up display (HUD) vs. head-down display (HDD): driving performance of commercial vehicle operators in Taiwan. Interna- tional Journal of Human-Computer Studies, 61(5), 679-697.
28. Livingston, M. A., Rosenblum, L. J., Julier, S. J., Brown, D., Baillot, Y., Swan, J. E., ... & Hix, D. (2002). An augmented reality system for military operations in urban terrain. Pro-ceedings of the Interservice/Industry Training, Simulation & Education Conference.
29. Hou, M., Kobierski, R. D., & Brown, M. (2007). Intelligent adaptive interfaces for the con- trol of multiple UAVs. Journal of Cognitive Engineering and Decision Mak-ing, 1(3), 327-362.
30. Prinzel, L. J., Comstock, J. R., Glaab, L. J., Kramer, L. J., Arthur, J. J., & Barry, J. S. (2003). The efficacy of head-down and head-up synthetic vision display concepts for retro-and for- ward-fit commercial aircraft applications. The International Journal of Aviation Psychology, 13(1), 33-66.
31. Prinzel, L. J., Kramer, L. J., Arthur, J. J., Bailey, R. E., & Parrish, R. V. (2003). CFIT pre- vention using synthetic vision. Proceedings of SPIE, 5018, 170-181.
32. Drascic, D., & Milgram, P. (1996). Perceptual issues in augmented reality. Pro-ceedings of SPIE, 2653, 123-134.
33. Gabbard, J. L., Smith, M., Tanous, K., Kim, H., & Jonas, B. (2019). AR displays in auto-motive environments: Effects of luminance and color on driver performance and safety. IEEE Computer Graphics and Applications, 39(4), 77-88.
34. Farsi, M., Ratcliff, K., & Barbosa, M. (1999). An overview of controller area network. Com-puting & Control Engineering Journal, 10(3), 113-120.
35. Kaptein, N. A., Theeuwes, J., & Van Der Horst, R. (1996). Driving simulator va-lidity: Some considerations. Transportation Research Record, 1550(1), 30-36.
36. Tufte, E. R. (1983). The visual display of quantitative information. Graphics Press.
37. Rasmussen, J. (1983). Skills, rules, and knowledge; signals, signs, and symbols, and other distinctions in human performance models. IEEE Transactions on Systems, Man, and Cy- bernetics, (3), 257-266.
38. Luo, R. C., Yih, C. C., & Su, K. L. (2002). Multisensor fusion and integration: approaches, applications, and future research directions. IEEE Sensors Journal, 2(2), 107-119.
39. Rogalski, A. (2012). Progress in focal plane array technologies. Progress in Quantum Elec-tronics, 36(2), 342-473.
40. Arrue, B. C., Ollero, A., & De Dios, J. M. (2000). An intelligent system for false alarm reduction in infrared forest-fire detection. IEEE Intelligent Systems, 15(3), 64-73.
41. Van Erp, J. B., Saturday, I., & Jansen, C. (2006). Vibrotactile waypoint naviga-tion at sea and in the field: Two navy studies. Proceedings of the IEEE Virtual Reali-ty Conference, 47-54.
42. Cao, A., Chintamani, K. K., Pandya, A. K., & Ellis, R. D. (2009). NASA TLX: Software for assessing subjective mental workload. Behavior Research Methods, 41(1), 113-117.
43. Woods, D. D. (1995). The alarm problem and directed attention in dynamic fault manage- ment. Ergonomics, 38(11), 2371-2393.
44. Treisman, A. M., & Gelade, G. (1980). A feature-integration theory of attention. Cognitive Psychology, 12(1), 97-136.
45. Romin, L. A., & Bissonette, J. A. (1996). Deer–vehicle collisions: status of state monitoring activities and mitigation efforts. Wildlife Society Bulletin, 276-283.
46. Huijser, M. P., Duffield, J. W., Clevenger, A. P., Ament, R. J., & McGowen, P. T. (2009). Cost–benefit analyses of mitigation measures aimed at reducing collisions with large ungu-lates in the United States and Canada: a decision support tool. Ecolo-gy and Society, 14(2).
47. Coulombe, P., Huot, J., & Poupart, J. (2006). Intensive hunting as a major mor-tality factor of an expanding white-tailed deer

population in the boreal forest. Cana-dian Journal of Zo- ology, 84(9), 1342-1353.
48. Malo, J. E., Suárez, F., & Díez, A. (2004). Can we mitigate animal–vehicle acci-dents using predictive models? Journal of Applied Ecology, 41(4), 701-710.
49. Baum, K. A., Haynes, K. J., Dillemuth, F. P., & Cronin, J. T. (2004). The matrix enhances the effectiveness of corridors and stepping stones. Ecology, 85(10), 2671-2676.
50. Gardner, J. W., & Bartlett, P. N. (1999). Electronic noses: principles and appli-cations. Ox- ford University Press.
51. Steinberg, A. N., Bowman, C. L., & White, F. E. (1999). Revisions to the JDL data fusion model. Proceedings of SPIE, 3719, 430-441.
52. Hall, D. L., & McMullen, S. A. (2004). Mathematical techniques in multisensor data fusion. Artech House.
53. Kenney, J. B. (2011). Dedicated short-range communications (DSRC) standards in the United States. Proceedings of the IEEE, 99(7), 1162-1182.
54. Shi, W., Cao, J., Zhang, Q., Li, Y., & Xu, L. (2016). Edge computing: Vision and challenges. IEEE Internet of Things Journal, 3(5), 637-646.
55. Zorzi, M., Gluhak, A., Lange, S., & Bassi, A. (2010). From today's intranet of things to a future internet of things: a wireless-and mobility-related view. IEEE Wire-less Communi- cations, 17(6), 44-51.
56. Priya, S., & Inman, D. J. (Eds.). (2009). Energy harvesting technologies. Spring-er.
57. Sweller, J. (1988). Cognitive load during problem solving: Effects on learning. Cognitive Science, 12(2), 257-285.
58. Cummings, M. L., & Mitchell, P. J. (2008). Predicting controller capacity in su-pervisory control of multiple UAVs. IEEE Transactions on Systems, Man, and Cyber-netics-Part A: Systems and Humans, 38(2), 451-460.
59. Salas, E., Wilson, K. A., Murphy, C. E., King, H., & Salisbury, M. (2008). Com-municating, coordinating, and cooperating when lives depend on it: tips for team-work. Joint Commis- sion Journal on Quality and Patient Safety, 34(6), 333-341.
60. Hays, R. T., Jacobs, J. W., Prince, C., & Salas, E. (1992). Flight simulator training effec-tiveness: A meta-analysis. Military Psychology, 4(2), 63-74.
61. Parasuraman, R., & Riley, V. (1997). Humans and automation: Use, misuse, disuse, abuse. Human Factors, 39(2), 230-253.
62. Lee, J. D., & See, K. A. (2004). Trust in automation: Designing for appropriate reliance. Human Factors, 46(1), 50-80.
63. Petit, J., & Shladover, S. E. (2015). Potential cyberattacks on automated vehi-cles. IEEE Transactions on Intelligent Transportation Systems, 16(2), 546-556.
64. Parkinson, S., Ward, P., Wilson, K., & Miller, J. (2017). Cyber threats facing au-tonomous and connected vehicles: Future challenges. IEEE Transactions on Intelli-gent Transportation Systems, 18(11), 2898-2915.
65. Checkoway, S., McCoy, D., Kantor, B., Anderson, D., Shacham, H., Savage, S., ... & Kohno,
T. (2011). Comprehensive experimental analyses of automotive attack surfaces. Proceedings of the 20th USENIX Security Symposium, 447-462.
66. Avizienis, A., Laprie, J. C., Randell, B., & Landwehr, C. (2004). Basic concepts and taxon-omy of dependable and secure computing. IEEE Transactions on Depend-able and Secure Computing, 1(1), 11-33.
67. Sheridan, T. B., & Parasuraman, R. (2005). Human-automation interaction. Reviews of Hu- man Factors and Ergonomics, 1(1), 89-129.
68. Anderson, R., & Kuhn, M. (1996). Tamper resistance: a cautionary note. Pro-ceedings of the Second USENIX Workshop on Electronic Commerce, 1-11.
69. Chandola, V., Banerjee, A., & Kumar, V. (2009). Anomaly detection: A survey. ACM Com- puting Surveys, 41(3), 1-58.

70. Jordan, M. I., & Mitchell, T. M. (2015). Machine learning: Trends, perspectives, and pro- spects. Science, 349(6245), 255-260.
71. Darms, M., Rybski, P., Baker, C., & Urmson, C. (2009). Obstacle detection and tracking for the urban challenge. IEEE Transactions on Intelligent Transportation Systems, 10(3), 475- 485.
72. Degen, C. L., Reinhard, F., & Cappellaro, P. (2017). Quantum sensing. Reviews of Modern Physics, 89(3), 035002.
73. Chen, P. Y., Soric, J., & Alù, A. (2012). Invisibility and cloaking based on scatter-ing can- cellation. Advanced Materials, 24(44), OP281-OP304.
74. Hartenstein, H., & Laberteaux, K. P. (2008). A tutorial survey on vehicular ad hoc networks. IEEE Communications Magazine, 46(6), 164-171.
75. Li, F., & Wang, Y. (2007). Routing in vehicular ad hoc networks: A survey. IEEE Vehicular Technology Magazine, 2(2), 12-22.
76. Biswas, S., Tatchikou, R., & Dion, F. (2006). Vehicle-to-vehicle wireless commu- nication protocols for enhancing highway traffic safety. IEEE Communications Magazine, 44(1), 74- 82.
77. Billinghurst, M., Clark, A., & Lee, G. (2015). A survey of augmented reality. Foundations and Trends in Human–Computer Interaction, 8(2-3), 73-272.
78. Merenda, C., Kim, H., Gabbard, J., Wooters, N., & Hix, D. (2016). Augmented reality in- terface design approaches for goal-directed and stimulus-driven driving tasks. IEEE Trans- actions on Visualization and Computer Graphics, 22(11), 2107-2118.
79. Pfannmüller, L., Kramer, M., Senner, B., & Bengler, K. (2009). A comparison of display concepts for a navigation system in an automotive contact analog head-up display. Proceed- ings of the 1st International Conference on Automotive User Inter-faces and Interactive Ve- hicular Applications, 143-150.
80. Regan, M. A., Lee, J. D., & Young, K. (2008). Driver distraction: Theory, effects, and mit- igation. CRC Press.

2025 HOW
4th International Symposium on One Health, One World
November 20 – 22, 2025

ABS ID: 134
USDM-OP-31

Route Choice Modeling Based on The Riding Environment of Bicycle Users

Rina Mizunoue[1], Kazuyuki Takada[2]
[1]*Undergraduate student, Tokyo Denki university, Saitama, Japan,*
[2]*Professor, Tokyo Denki university, Saitama, Japan*

***Keywords**: Bicycle, Route choice, ETC2.0, Bike-sharing.*

1. INTRODUCTION

In recent years, bicycles have been increasingly recognized as a sustainable, low-impact mode of daily transportation. However, the quality of cycling environments varies across regions, and safety and comfort issues often arise where cyclists share space with pedestrians and motor vehicles. In this context, developing and allocating bicycle lanes has become a key issue in urban transport policy. Yet, further study is needed to determine where lanes should be built and how they affect travel behavior and safety.

Kanazawa City, a medium-scale compact city, provides a valuable case study. Its bicycle-sharing program “Machinori” is widely used by both residents and tourists. Although bicycle lanes have been developed mainly along major roads, coverage remains limited and uneven. These conditions highlight the need to analyze cyclists’ route choice behavior. However, the effects of dynamic traffic and safety factors on such behavior remain unclear.

Figure 1. Bicycle-Sharing Station in Kanazawa City

(Reference: Official Website of Kanazawa City)

2. Literature Review

2.1 Studies on Bicycle Route Choice

Bicycle route choice has been extensively examined in transportation planning and urban design. Many studies have analyzed how infrastructure, road environment, and perceived safety affect cyclists’ behavior. However, most rely on static or localized data and rarely capture dynamic traffic conditions or potential conflicts with motor vehicles.

Broach, Dill, and Gliebe [1] developed one of the most influential revealed-preference route choice models using GPS trajectories from cyclists in Portland, Oregon. Their model incorporated travel time, distance, slope, and several types of bicycle facilities, such as separated cycle tracks and painted lanes. The results indicated a strong preference for physically separated facilities, even at the cost of longer distance, while painted lanes had a much smaller positive effect. This research established the methodological foundation for GPS-based route choice modeling but did not account for time-varying traffic situations or interactions with vehicles.

Hood, Sall, and Charlton [2] applied a similar GPS-based approach to San Francisco, focusing on how gradient and intersection density affect cyclists’ choices. They found that cyclists often avoid steep slopes and congested intersections, preferring flatter and simpler routes even if travel time increases. Their findings emphasized the importance of urban form and road geometry, but the study was limited to one metropolitan area and short-term observation, constraining generalization.

Lu et al. [3] extended this approach using trip data from a public bike-sharing system, comparing *dominant routes*—those most frequently chosen by users—with their *shortest path counterparts*. Their analysis revealed that cyclists deviate from shortest paths to avoid heavy traffic and signalized intersections and to follow continuous bicycle

lanes. The study introduced the concept of dominant route analysis, offering a practical way to understand real-world behavior at the network level. However, it still lacked integration with dynamic traffic data that could explain why users avoided specific areas or times of day.

In contrast, Aldred et al. [4] used a stated-preference survey in the United Kingdom to examine perceived safety and comfort under various cycling environments. They found significant gender differences in sensitivity to traffic stress and infrastructure type, suggesting that psychological and social factors play a crucial role in cyclists' decision-making. Yet, SP surveys inherently depend on hypothetical scenarios and may not capture actual behavior in complex urban environments.

In Japan, Kawai et al. [5] analyzed cyclists' route choice using SP data from urban areas, focusing on the continuity and comfort of bicycle lanes. Their study confirmed that perceived comfort strongly influences route choice, but the analysis was limited in both spatial and temporal scope. Such limitations are common among domestic studies, which rarely incorporate real-time traffic flow or safety dynamics from surrounding vehicles.

2.2 Studies on Traffic Safety and Near-Miss Analysis

While bicycle route choice has been studied extensively, relatively few works have examined the relationship between cyclists' routes and potential conflict points with motor vehicles.

Recent traffic safety research has increasingly focused on the use of **vehicle probe data**—such as ETC2.0 and floating car data—to detect hazardous driving behavior and to identify near-miss zones.
These studies have demonstrated that **hard-braking events** and **sudden decelerations** are effective indicators of potential risk locations, as they often correspond to unexpected obstacles, intersections with limited visibility, or mixed-traffic zones involving pedestrians and cyclists.

For example, several Japanese studies (Ishibashi et al. [6]; Suga et al. [7]) have applied ETC2.0 data to extract high-risk locations based on the density of sudden braking records, validating that such points frequently overlap with intersections or road segments with complex geometry. These findings highlight the potential of ETC2.0 data as an objective source for identifying "near-miss" or "almost-accident" situations. However, these analyses have primarily targeted motor vehicle behavior and have not yet integrated bicycle trajectory data or cyclist exposure patterns.

2.3 Research Gaps and Objectives of This Study

Collectively, previous studies have clarified how infrastructure, environment, and perceived safety influence cyclists' route choice. However, few have considered how dynamic traffic conditions—such as vehicle speed changes or sudden braking—affect cyclists' behavior. In addition, near-miss analyses using vehicle probe data have rarely examined fine-scale interactions between bicycles and motor vehicles.

Building on these gaps, the present study focuses on Kanazawa City and applies ETC2.0 probe data in combination with bicycle-sharing trajectory and OD data. This approach enables quantitative analysis of the spatial relationship between cyclists' routes and potential near-miss points. The framework aims to provide empirical evidence supporting the development and prioritization of safer, more comfortable bicycle networks.

3. DATA

This This study analyzes the origin-destination (OD) data and trip records from Kanazawa City's bicycle-sharing system "Machinori." As explanatory variables, the development status of bicycle lanes is included as an infrastructure factor, and the locations of signalized intersections are considered as a road environment factor. For safety, open data on high-frequency traffic accident intersections published by the Ishikawa Prefectural Police are utilized, while population distribution and the number of tourist attractions are incorporated as surrounding environmental factors. The analysis period covers one year, from January 1 to December 31, 2024.

Figure 2. Bicycle Network and Related Factors in Kanazawa

4. METHODOLOGY

The analysis focuses on origin-destination (OD) pairs with high travel demand, examining route choice behavior among bicycle users between these locations. A route choice model is constructed using a multinomial logit framework, using road and geographical attributes—such as the presence or absence of bicycle lanes—as explanatory variables.

REFERENCES:

[1] Broach, J., Dill, J., & Gliebe, J. (2012). Where do cyclists ride? A GPS-based route choice model for Portland, Oregon. Transportation Research Part A: Policy and Practice, 46(10), 1730–1740.

[2] Hood, J., Sall, E., & Charlton, B. (2011). A GPS-based bicycle route choice model for San Francisco, California. Transportation Letters, 3(1), 63–75.

[3] Lu, Y., Zhu, L., Yu, C., & Chen, J. (2018). Understanding bike share cyclist route choice using GPS data: Comparing dominant and shortest paths. Journal of Transport Geography, 69, 79–90.

[4] Aldred, R., Elliott, B., Woodcock, J., & Goodman, A. (2016). Cycling provision separated by traffic stress: Perceived safety, gender differences, and route choice. Transportation Research Part F: Traffic Psychology and Behaviour, 41, 68–80.

[5] Kawai, Y., Sato, K., & Takahashi, T. (2021). Analysis of cyclists' route choice considering comfort and continuity of bicycle lanes. Proceedings of the Japan Society of Civil Engineers, D3 (Infrastructure Planning and Management), 77(5), I_121–I_130.

[6] Ishibashi, T., Kawakami, T., & Okada, M. (2020). Identification of high-risk locations using ETC2.0 probe data based on hard-braking events. Journal of the Eastern Asia Society for Transportation Studies, 14, 1250–1260.

[7] Suga, M., Fujita, A., & Ishikawa, H. (2022). Detection of hazardous driving behavior using ETC2.0 probe data and its application to traffic safety analysis. Proceedings of the Japan Society of Civil Engineers, D3 (Infrastructure Planning and Management), 78(5), I_215–I_223.

ABS ID: 133
USDM-OP-32

Dr. Saurabh Shiradhonkar

2025 HOW

4th International Symposium on One Health, One World
November 20 – 22, 2025

ABS ID: 176
USDM-OP-33

A Preliminary Seismic Risk Assessment of Built Environment

D. Yogeswar[1], C. Sashidhar[2]
[1]*Research Scholar, Department of Civil Engineering, JNTUA, Ananthapuramu, India,*
[2]*Professor, Department of Civil Engineering, JNTUA College of Engineering, Ananthapuramu, India,*
Correspond to D. Yogeswar (yogeswar65@gmail.com

Keynotes: *Seismic Risk Assessment, Disaster Preparedness, Risk Mapping, Hazard Zonation, Risk Perception.*

1. ABSTRACT

Rapid urbanization is driving towards uneven settlements in the existing built environments of the urban areas. Focus on the seismic safety of built environments is key towards achieving zero tolerance to avoidable life loss. Particularly, in the low – to – moderate seismic zones, a macro level view of seismic risk aids in understanding the perception of the potential disaster and acts as an initial step to raise awareness towards safety of the built assets. Also, the factors contributing to the overall seismic risk helps to prioritize the mitigation efforts of a region. The southern peninsular region of India, that is characterized by lower frequency of earthquake occurrence is considered for the current study. The preliminary assessments conducted using the prevalent hazard represented as peak ground acceleration values and the exposure of the building assets from 2011 census of India. Based on the studies carried out a seismic risk map at a sub district level of the region is developed.

2. INTRODUCTION

The peninsular Indian region is considered to be a seismically stable compared to the Himalayan region. The most notable past earthquakes like Koyna in 1967 and Latur in 1993 (6.2 Magnitude) showed that even regions which are considered as tectonically safe can also be affected with severe damage with minimum seismic events [1][6]. Due to the rapid urbanization, the density of population and the infrastructure in cities and towns is more, where the rapid infrastructure construction is designed in line with the seismic provisions [3]. Due to the less supervision on enforcement of IS 1893 provisions and poor construction practices the buildings are also affected by the minimum ground shaking which in turn cause significant human and economic losses [1][4]. These factors exhibit the importance in studying about the seismic risk even in the low to medium zones of peninsular India.

The probabilistic seismic risk assessment developed by [6] and [8] nationwide, gives important overview and are not designed to see the fine patterns of exposure and vulnerability which has its impact at district and sub district level. Another challenge lies in the availability of empirical vulnerability functions and limited availability of small parts of exposure data for diverse Indian building types [5]. Addressing these gaps requires complementary approaches that rely on observed data and broad regional perspectives. In this context for creating awareness among all the stakeholders and also for preparedness and risk sensitivity planning a macro level empirical assessment will play a vital role by identifying spatial trends of risk. The present study contributes to this effort by developing a preliminary seismic risk assessment of the built environment in peninsular India, providing thoughts which

support future requirement for refining in models, codes and policies.

3.METHODOLOGY

The seismic risk of a region is computed as a combination of hazard, vulnerability, and exposure. For a preliminary understanding of the distribution of risk among the regions a model based on the two factors, hazard, exposure contributing to the earthquake risk are considered. The relative seismic risk of the region is computed as the interaction between the hazard and the housing stock, as per census, in the region as computed in equation (1).

"Relative Risk= " Hazard x Exposure (1)

The Zero Period Acceleration (ZPA) computed in the National Disaster Management Authority (NDMA) report on Probabilistic Seismic Hazard Analysis (PSHA) of Indian land mass, 2011 is considered. The ZPA values are considered for two cases, for a return period of 475 years (10% probability in next 50 years, ZPA1) and 2475 years (2% probability in next 50 years,ZPA2) are adopted.

The regions considered for the study are subdistricts (tehsils or taluks) defined as per 2011 census of India. Developing seismic risk maps at the subdistrict level of less seismically active regions help to understand and strengthens the ability to prioritize mitigation and preparedness accordingly. The number of buildings as per census of India is used as the parameter of the exposure. Two types of buildings, buildings with concrete wall-concrete roof (CWCR) and burn brick wall with concrete roof (BWCR) are chosen. The risk computed is a relative risk which helps to compare the subdistricts within a district and then eventually within the state.

4. Results and Discussion

The subdistrict wise distribution map of concrete wall concrete roof buildings and burnt brick wall concrete roof provides a spatial representation of how buildings are concentrated across the peninsular India. The subdistricts in the urban region of all the states have higher concentration of CWCR buildings (Figure 1). The distribution of the BWCR buildings is in the states of Maharashtra, Karnataka, Tamil Nadu and Kerla (Figure 2). The map helps for understanding the extent of exposure to seismic hazards. The risk maps for the CWCR indicate that though some regions are having high concentration of the buildings the risk is less due to the less hazard factor (Figure 3). The number of regions having the higher risk increased in case of higher hazards and the important hospital and school buildings should be addressed in these regions for detailed assessments (Figure 4).

Brick masonry building type is a dominant typology in India, especially in the semi-urban regions.The distribution of the risk of the BWCR buildings considering the ZPA1 is presented in the figure 5. It can be observed that there is a more number of the subdistrict are at a higher risk and the risk increases in the case of ZPA2and the pattern can be attributed to the more number of the buildings exposed (Figure 6).

The data used is of the 2011 census of India and there are many subdistricts created after 2011.

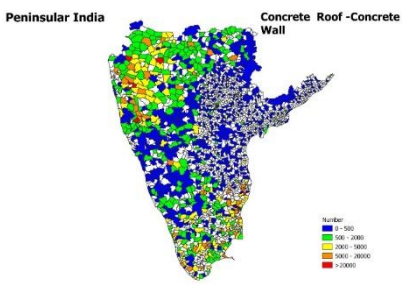

Figure 1: Distribution of Concrete Roof Concrete Wall Structures.

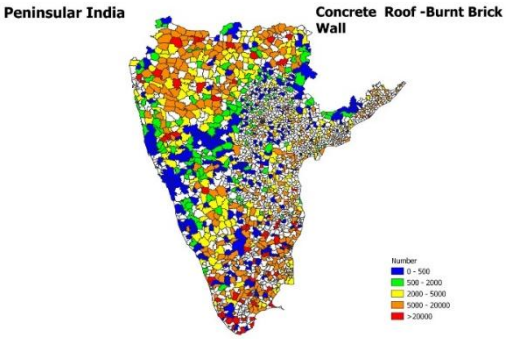

Figure 2: Distribution of Concrete Roof – Burnt Brick Wall Structures

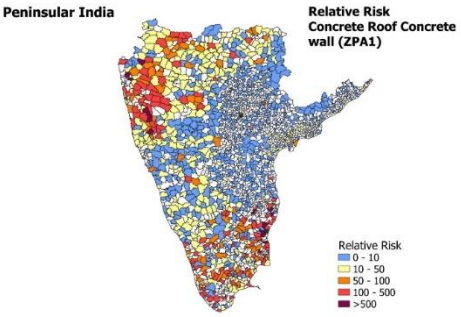

Figure 3: Relative Risk Concrete Roof Concrete Wall (ZPA1)

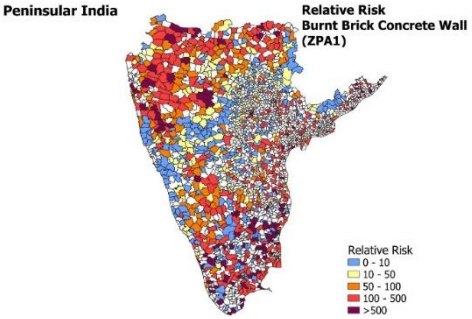

Figure 4: Relative Risk Burnt Brick Concrete Wall (ZPA1)

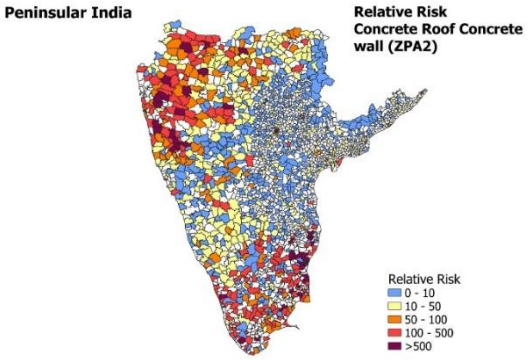

Figure 5: Relative Risk Concrete Roof Concrete Wall (ZPA2)

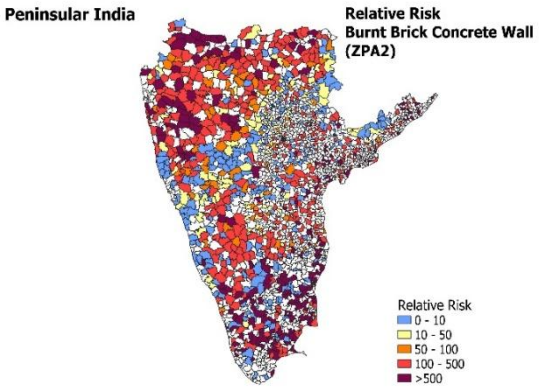

Figure 6: Relative Risk Burnt Brick Concrete Wall (ZPA2)

5. CONCLUSION

A comprehensive overview at subdistricts of peninsular India to evaluate earthquake disaster risk is presented in the paper. Such a method is easy to compute and supports in identifying the regions that require immediate action for mitigation and preparedness, especially in the seismically less active zones. However, a sensitivity analysis is required to

improve and validate the model, which is reserved for further study.

REFERENCES:

[1] Ashish Lindholm CD, Parvez IA and Kuhn D (2016) Probabilistic earthquake hazard assessment for Peninsular India. Journal of Seismology 20(2):629-653.

[2] Iyengar RN, Sharma D and Siddiqui JM (1999) Earthquake history of India in medieval times. Indian Journal of History of Science 34(3): 181-237.

[3] Jain SK (1998) Indian earthquakes: An overview. Indian Concrete Journal 72(11): 555-561.

[4] Jain SK (2016) Earthquake safety in India: Achievements, challenges and opportunities. Bulletin of Earthquake Engineering 14(5): 1337-1436.

[5] Lahiri A, Jena PR, Rao RK and Sen TK (2001) Economic Consequences of the Gujarat earthquake. Economic and Political Weekly 36(16):1319-1332.

[6] National Disaster Management Authority (NDMA) (2010) - Development of Probabilistic Seismic Hazard Map of India.

[7] National Disaster Management Authority (NDMA) (2013) Catalogue of Building Typologies in India. 15 September. New Delhi, India: National Disaster Management Authority.

[8] National Disaster Management Authority (NDMA) (2019) - Earthquake Disaster Risk Index Report.

[9] Nath SK, Thingbaijam KKS (2011) Peak Ground Motion predictions in India: An appraisal for rock sites,. Journal of Seismology 15(2) 295-315.

[10] Pagani M, Monelli D, Weatherill GA, Danciu L, Crowley H, Silva V, Henshaw P, Butler L, Nastasi M, Panzeri L, Simionato M and Vigano D (2014) OpenQUake engine: An open hazard (and risk) software for the global earthquake model. Seismological Research Letters 85(3) :692-702.

[11] Rao A, Dutta D, Kalita P, et al. Probabilistic seismic risk assessment of India. Earthquake Spectra. 2020;36(1_suppl):345-371.

[12] Ramancharla Pradeep & Murty, C.V.R.. (2014). Earthquake Safety of houses in India: Understanding the bottlenecks in implementation. Indian Concrete Journal. 88. 51-63.

[13] Silva V, Crowley H, Pagani M, Monelli D and Pinha R (2013) Development of the OpenQuake engine, the Global Earthquake Model's open-source software for seismic risk assessment. Natural Hazards 72(3):1409-1427.

[14] Singh Y, Lang DH, Prasad JSR and Deoliya R (2013) An analytical study on the seismic vulnerability of masonry buildings in India. Journal of Earthquake Engineering 17(3):399-422.

[15] United Nations Office for Disaster Risk Reduction (UNDRR) (2015) Making Development Sustainable: The future of Disaster Risk Management. Global Assessment Report on Disaster Risk Reduction 2015 (GAR15). Geneva: United Nations Office for Disaster Risk Reduction.

2025 HOW

4th International Symposium on One Health, One World
November 20 – 22, 2025

ABS ID: 19

USDM-OP-34

Earthquake risk assessment of wooden houses for spatial delineation Of critical areas in tokyo prefecture

Arpan Singh[1], Kenjiro Yamamoto[2], And Kimiro Meguro[3]
[1]*PhD Student, Dept. of Civil Engineering, The University of Tokyo, Tokyo, Japan,*
[2]*Research Fellow, Institute of Industrial Science, The University of Tokyo, Tokyo, Japan,*
[3] *Professor, Institute of Industrial Science, The University of Tokyo, Tokyo, Japan,*
Correspond to Arpan Singh (singh-arpan97@g.ecc.u-tokyo.ac.jp)

Keywords*: Wooden Houses, Exposure Index, Physical Risk, Exposure Dataset.*

1. INTRODUCTION

Japan features diverse building typologies. Based on type of construction material the houses are classified as Reinforced Concrete (RC), steel-framed buildings, and wooden houses. Among these, wooden houses constitute the largest proportion, with consistent construction over the decades (Figure 1). Nearly 50% of them are in dilapidated condition [1], emphasizing the need to locate and retrofit them to improve their seismic capacity. The 1995 Kobe, 2016 Kumamoto, and the recent 2024 Noto earthquake highlighted the damage to such structures, resulting in human, property, and functionality losses. Therefore, to minimise such losses and increase awareness of earthquake-resistant design, subsidies are provided to encourage improved earthquake safety.

Japan consists of 47 prefectures and 1,741 municipalities [2]. The subsidy systems in these prefectures vary, as the funding originates from a combination of national, prefectural, and municipal government contributions. Different prefectures and municipalities receive distinct subsidies allocated by their respective prefectural and municipal governments [3]. Furthermore, as per a past study the subsidy amount for the prefectures of Aichi and Kochi differed despite having the same number of old wooden houses [4]. Thus, understanding the seismic risk linked to wooden houses at the municipal, prefectural, or ward level is essential for identifying hotspot areas and assessing how well subsidies match those risks and existing frameworks. Hence, the study focuses on identifying areas with higher adverse impact on wooden houses at the finer ward level to understand the risk associated with wooden houses using the existing defined quarter grid cell (250 m) hazard mesh developed by the Japan Seismic Hazard Information Station.

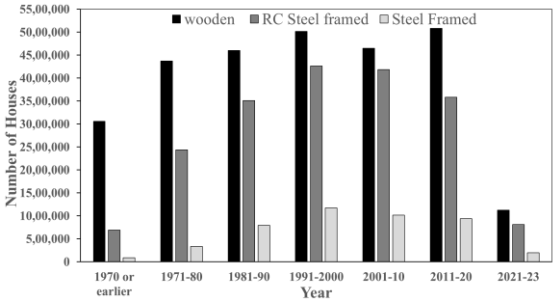

Figure 1. Number of houses built in each decade [5]

2. CASE STUDY

Tokyo prefecture is considered for the study. The prefecture comprises of 23 special wards (tokubetsu-ku), 26 cities (shi), 5 towns (machi), and 8 villages (mura). Among these 3 towns and all 8 villages are excluded due to lack of data. Furthermore, wooden dwellings account for 32% of the total housing stock in the administrative areas considered, while the remaining are non-wooden housing types [5].

3. METHDOLOGY

Two distinct types of earthquake risk are evaluated: one in which the relative risk across the administrative divisions is determined using hazard, and exposure parameters; and the other in which risk is computed as the expected number of houses completely destroyed from the combination of hazard, vulnerability, and exposure parameters. The

former, method 1, follows a qualitative approach and latter, method 2, based on quantitative approach.

Relative Risk = Hazard X Exposure (1)

Risk=Hazard X Vulnerability X Exposure (2)

Seismic hazard of the region is based on the dataset developed by Japan Seismic Hazard Information Station (J-SHIS), estimated at the center of quarter grid cells (250m x 250m). The average case of the earthquake occurrence probability of the probabilistic seismic hazard is considered this study. The probability of exceedance of JMA intensities 5 lower, 5 upper, 6 lower and 6 upper for a period of next 50 years constitutes the hazard for computation of relative risk. The seismic intensity of the region with a 2% & 39% probability of exceedance for the next 50 years is used for the computation of risk.

The exposure dataset of wooden houses is developed from the inventory of houses from the Housing and Land Survey [5]. A systematic 250 mesh wise distribution of the wooden houses is carried out to create a grid wise exposure dataset. The exposure dataset data values obtained using the proposed methodology are validated against census values for wooden houses in administrative regions.

Vulnerability is considered based on the damage index functions of the wooden houses that relate seismic input parameter JMA intensities to expected damage states (Table 1) [6,7]. The damaged index functions express the earthquake damage state of the individual building on a numerical scale of degree of damage, with 0 implying No Damage State and 1.0 Total Collapse. The probability of the buildings completely destroyed, total collapse, is considered in the current study.

The thematic maps for both approaches are created using QGIS, an open-source geographic information system [8]. The vector dataset was created in Microsoft Excel using existing datasets obtained from Housing and Land Survey updated in 2023 [5]. The flowchart in Figure 2 shows the brief steps of the methodology.

Damage Index	For JMA Intensity	Average	Stand. Deviation
Damage Index D5		7.37	0.582
Over Damage Index D4		6.85	0.565
Over Damage Index D3		6.42	0.600
Over Damage Index D2		5.96	0.621
Over Damage Index D1		5.04	0.574

Table 1. Parameters proposed for Damage Functions [6,7]

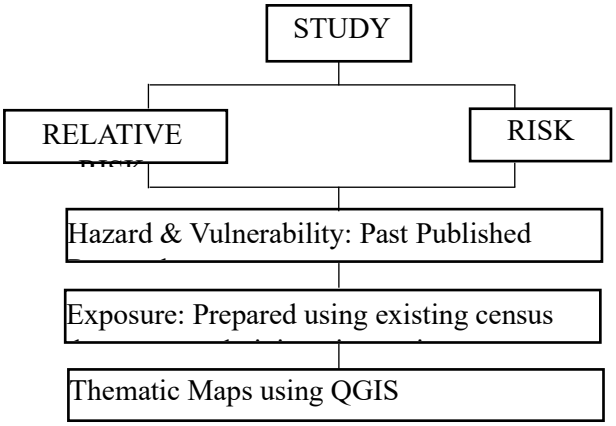

Figure 2. Brief outline of methodology

4. OBSERVATIONS AND RESULTS

Tokyo prefecture is considered for the estimation of risk for both the methods. Quarter grid wise exposure data set of wooden buildings is developed. The number of wooden houses of each ward from census, and data obtained from aggregation of wooden houses from each grid in that ward as from the proposed methodology is compared (Figure 3 (a), (b)). The results show good agreement with existing census data values available ward-wise with a percentage error less than 0.05%.

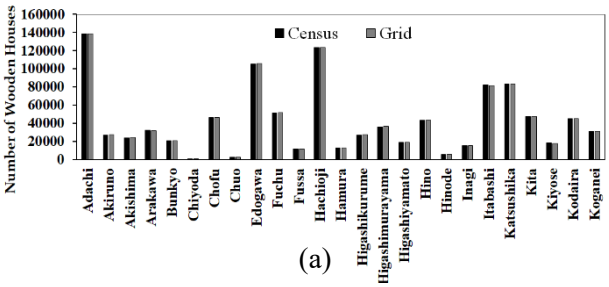

(a)

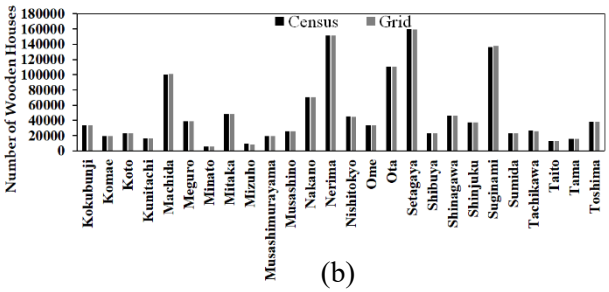

(b)

Figure 3. Comparison of exposure dataset Census data Vs Developed grid data

In method 1, the hotspots for intensities JMA 5 lower and 5 upper are Suginami, parts of Nakano, and the southeastern parts of Nerima. Similarly for intensities 6 lower and 6 upper are Arakawa, Adachi, Ota, Katsushika, and Edogawa, compared to other parts of the prefecture. This can be attributed to higher probability of occurrence of JMA 5 lower and upper intensity in these regions are higher. Furthermore, when examining these regions for increased intensity, such as JMA 6 upper or lower, the relative risk in these areas decreases. This is due to the probability of the occurrence of higher intensity levels in such regions in the next 30 years are less. In addition, in the areas of Adachi, Katsushika and Edogawa, these areas present relative values higher in case of IJMA all intensities. This is because the regions comprise of maximum wooden houses compared to other regions. Alongside, it also depicts that the probability of occurrence of JMA intensities of higher level is more (figure 4).

For physical risk, for exceedance of probability 39% in next 50 years, regions like Adachi, Arakawa, Katsushika and Edogawa depict a significant number of houses to be completely destroyed. The regions have high exposure as mentioned above, coupled with the higher number of the dilapidated wooden houses. So, low intensity events have also an impact in the region. Furthermore, exceedance probability of 2% in next 50 years, the impact is higher and distributed across the prefecture as shown in the Figure 5 (a), (b).

5. CONCLUSION AND WAY FORWARD

Two methods of risk assessments, one based on the qualitative approach and the other quantitative approach, are introduced. The method 1 helps to identify the hotspot regions and allows to have a bird's eye view of the risk prone areas. The data requirements are straightforward for this method and are easy to evaluate. The method 2 gives a full picture of the expected number of wooden houses collapsing and helps for a focused mitigation measures (retrofitting) to reduce the adverse consequences in the future earthquake events.

Further, the study should be conducted to effectively assess the seismic risk of wooden houses throughout Japan. In addition, physical risk for various exceedance probabilities, such as 3%, 5%, and 10%, occurring over the next 30 and 50 years should be conducted to enhance understanding of the potential damage to wooden houses.

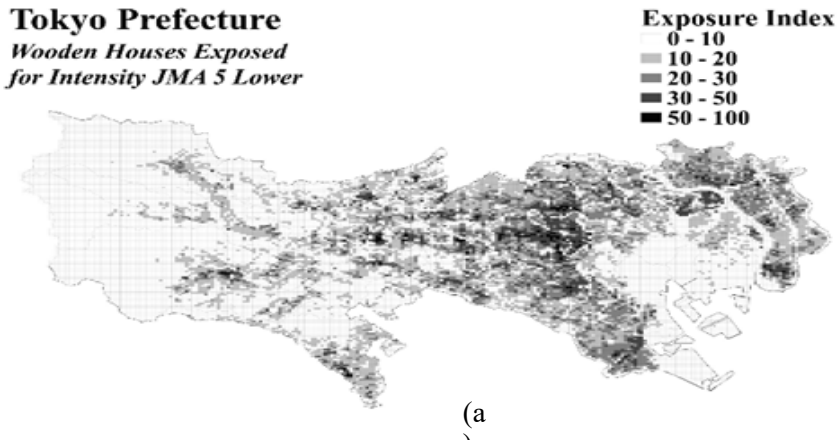

(a

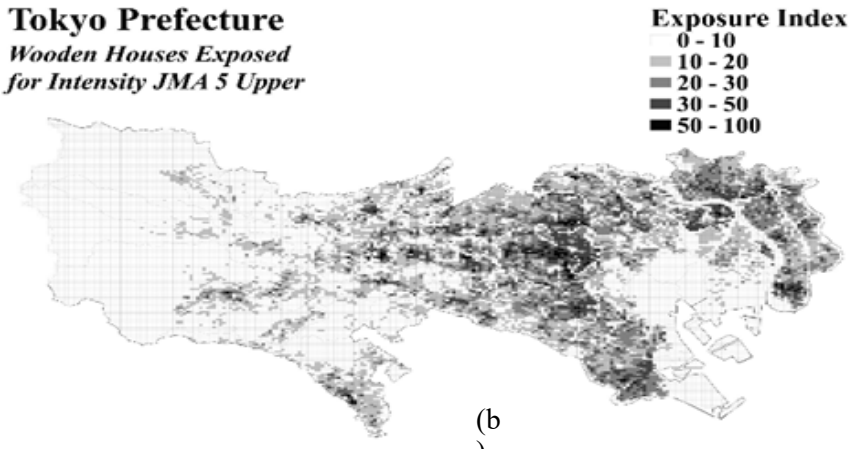

(b

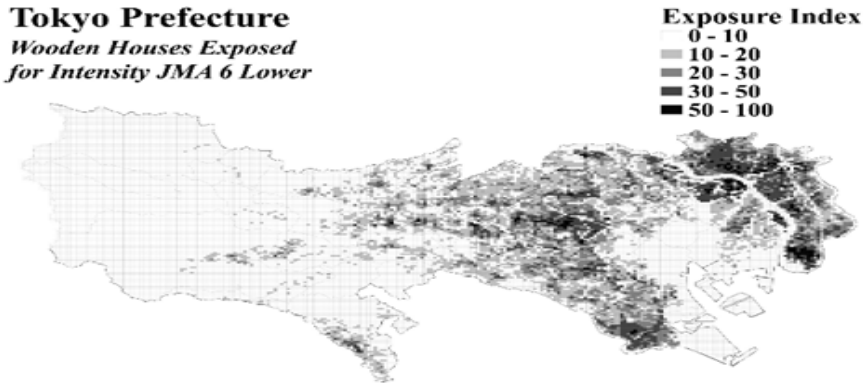

(c

Figure 4 (a,b,c). Thematic Maps: Relative Risk - Methode 1

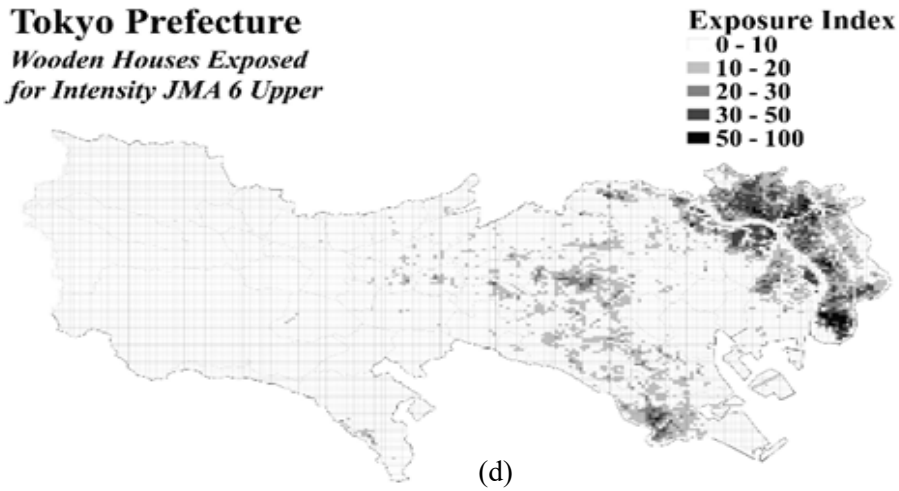

(d)

Figure 4 (d). Thematic Maps: Relative Risk - Method 1

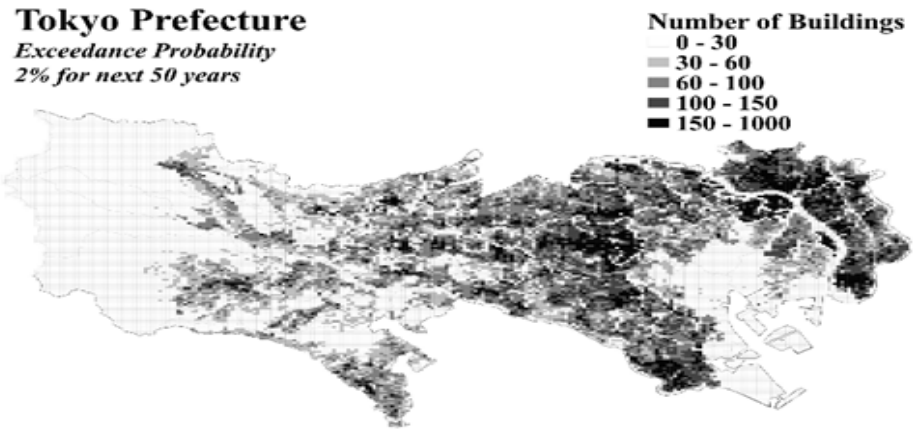

(a)

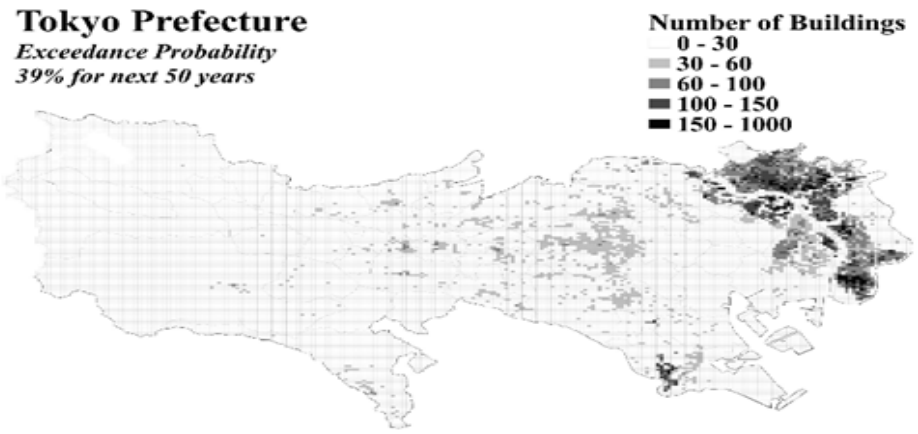

(b)

Figure 5. Thematic Maps: Risk - Method 2

REFERENCES:

[1] I. Kazuhiro, J. Takagi, and S. Minami, *Seismic Reinforcement of Existing Japanese Wooden Houses Using External Galvanized Thin Steel Plates*, Proceedings of the 12th World Conference on Earthquake Engineering, Lisboa, 2012.

[2] Ministry of Internal Affairs and Communications. (2024). *List of local government codes in Japan (as of April 1, 2024).* https://www.soumu.go.jp/denshijiti/code.html

[3] Ministry of Internal Affairs and Communications. (2024). *List of local government codes in Japan (as of April 1, 2024).* *https://www.mlit.go.jp/jutakukentiku/house/content/001878940.pdf*

[4] H. Kawabata, H. Itoda, and T. Hanai, *Investigation on seismic retrofit of old wooden houses in Kochi Prefecture*, AIJ J. Technol. Des. Vol. 25, No.59 (Feb., 2019), 135-140.

[5] Statistics Bureau, Ministry of Internal Affairs and Communications, *e-Stat Portal Site of Official Statistics of Japan*. https://www.e-stat.go.jp/en

[6] S. Okada and N. Takai, *Classifications of structural types and damage patterns of buildings for earthquake field investigation*, Proceedings of the 12th World Conference on Earthquake Engineering, Auckland, New Zeeland. Paper no.705, 2000.

[7] S. Okada and N. Takai, *Damage index functions of wooden buildings and reinforced buildings for seismic risk Management*, Proceedings of the 13th World Conference on Earthquake Engineering, Vancouver, BC, August 1–6, 2004, Paper No. 727.

[8] QGIS Development Team. QGIS Geographic Information System (Version 3.40.3). QGIS Association, 2025. https://www.qgis.org.

ABS ID: 152
USDM-OP-35

Dr. R. Siva Chidambaram

ABS ID: 78
USDM-OP-36

Mr. Ashish Kapoor

4th International Symposium on One Health, One World
November 20 – 22, 2025

ABS ID: 75
USDM-OP-37

Third-Party Quality Assurance: A Strategic Approach to Disaster Management in Construction

J. Raut[1 2], and H.C. Arora[1 2]
[1]*PhD Scholar, AcSIR (Academy of Science and Innovative Research), Ghaziabad 201002, India*
[2]*Senior Principal Scientist, CSIR-Central Building Research Institute, Roorkee 247667, India*
Correspond to J. RAUT (rautjidnyasaanil@gmail.com)

***Keywords**: Third-Party Quality Assurance, Construction Quality Management, Regulatory Compliance, Risk Mitigation, Project Transparency, Mass Timber, Disaster Resilience.*

1. GENERAL INSTRCUTIONS

Construction quality is a critical determinant of disaster resilience, particularly in earthquake-prone, coastal, and densely urbanized regions. Failures in construction not only compromise safety but also result in major economic losses and social disruption. Conventional in-house quality control is often hindered by conflicts of interest, limited expertise, and inadequate monitoring.

Third-Party Quality Assurance (TPQA) provides an independent evaluation of design specifications, materials, workmanship, and codal compliance. It bridges communication between contractors, consultants, and clients, thereby enhancing accountability and transparency. By ensuring compliance with standards such as IS 456:2000, IS 883:2016, MoRTH, IRC, ISO, and ASTM, TPQA strengthens both safety and sustainability. With increasing use of innovative materials such as cross-laminated timber (CLT) and glulam, TPQA has become vital in assessing performance, fire resistance, and long-term durability.

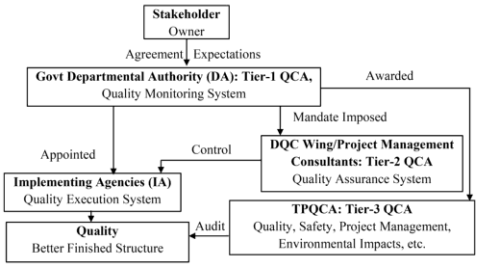

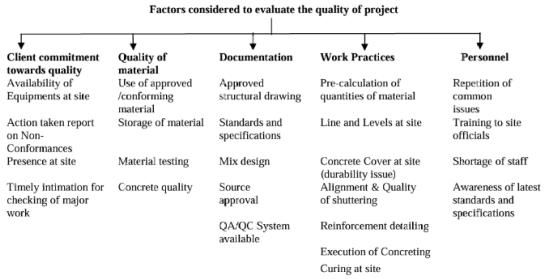

2.METHODOLOY

TPQA methodology covers three stages: pre-construction, construction, and post-construction. In each stage, independent oversight ensures that compliance and quality objectives are achieved.

- Pre-construction phase: review of design documents, verification of material specifications, and audits of procurement processes.
- Construction phase: on-site inspections, material testing, monitoring of workmanship, non-destructive testing (NDT), and verification of safety practices.
- Post-construction phase: final inspections, serviceability checks, load testing, and validation of as-built drawings before handover.

Typical TPQA checkpoints for different structures include:

- Reinforced Concrete (RC) Frames:
- Mix proportion verification, cement grade checks, water-cement ratio control.

• Reinforcement spacing, cover, lap length, and anchorage validation.
• Shuttering alignment, vibration of concrete, curing (7–28 days).
• Non-destructive testing such as Rebound Hammer and Ultrasonic Pulse Velocity.
• Masonry Structures:
• Brick quality, compressive strength, and water absorption checks.
• Mortar ratio (1:4 to 1:6), bond pattern, and joint thickness verification.
• Alignment at plinth and roof levels, curing practices, and fire resistance measures.
• Steel Structures:
• Steel grade verification, mill certificates, and welding inspection.
• Bolted joint torque checks, ultrasonic testing of welds, and corrosion protection.
• Stability inspections during erection and surface preparation for coatings.
• Timber Structures:
• Moisture content, dimensional stability, and certified timber species checks.
• Adhesive bonding integrity, fastener placement, and joint performance.
• Fire resistance, protective coatings, and termite/fungal protection.

3.CASE STUDY

Case Study 1 (2024):

This study emphasized common quality-related deficiencies in concrete and reinforcement. Issues included poor cement storage, improper mortar reuse, inadequate formwork, and reinforcement misplacement. TPQA interventions detected these issues early, minimizing long-term durability concerns and preventing costly rework.

a. Cement storage over wet place **b.** Unevenness of the formwork

c. No provision of bond over old concrete **d.** Extra projected concrete

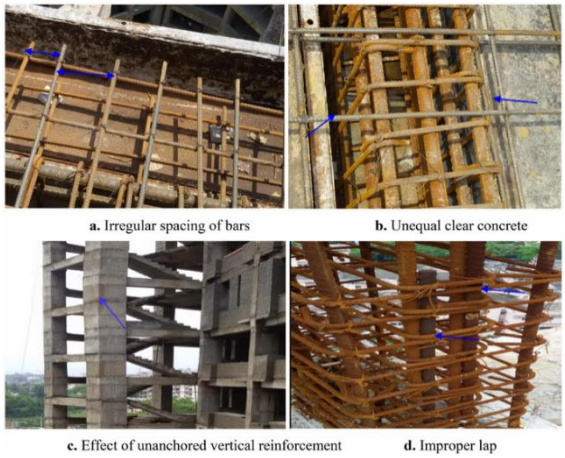

a. Irregular spacing of bars **b.** Unequal clear concrete

c. Effect of unanchored vertical reinforcement **d.** Improper lap

Case Study 2 (CSIR-CBRI, 2024):

A sports complex inspection revealed significant deficiencies such as honeycombing in concrete, misaligned beams, missing members, and inadequate foundations. Non-destructive tests including Rebound Hammer and Ultrasonic Pulse Velocity confirmed medium-quality concrete. Chemical analysis revealed high sulfate content, exceeding permissible limits, raising long-term durability concerns. Structural modeling with ETABS categorized the structure as unsafe under seismic loads. Corrective measures, including redesign checks and reinforcement of deficient members, were recommended.

4. RESULTS AND CONCLUSION

The findings from both case studies demonstrate that TPQA is instrumental in detecting construction defects and enforcing corrective actions. Independent oversight fosters accountability and prevents disputes among contractors, consultants, and clients.

Adoption of TPQA ensures compliance with IS codes, MoRTH, and IRC requirements, as well as international benchmarks such as ISO and ASTM. Moreover, modern digital technologies—including AI-based inspections, IoT-enabled sensors, and digital quality management systems—are revolutionizing TPQA practices by enabling real-time defect detection and predictive maintenance.

The outcomes show that TPQA not only enhances quality control but also strengthens disaster resilience by ensuring structural robustness, reducing risks of collapse, and promoting sustainable infrastructure development.

5. CONCLUSIONS

TPQA transforms construction quality control from a compliance-oriented activity into a proactive disaster risk management strategy. By offering unbiased verification across pre-construction, construction, and post-construction stages, TPQA minimizes risks of failure, reduces costs associated with rework, and enhances stakeholder confidence.

The integration of digital inspection tools, predictive analytics, and codal compliance frameworks further amplifies TPQA's relevance in today's complex infrastructure landscape. Broader adoption of TPQA is strongly recommended to achieve resilient, safe, and sustainable built environments.

REFERENCES:

[1] Karmakar, S. (2024, September 4). Third-party quality control concept, methodology, and implementation in the building and housing construction industry in India. International Journal of Construction Management. https://doi.org/10.1080/15623599.2024.2397227

[2] Patel, V., Ojha, P. N., Singh, B., & Sagar, A. (2021, November). Case study on quality assurance system in construction. SSM Journal. https://doi.org/10.26392/SSM.2021.04.01.012

[3] Burati, J. L. Jr., Matthews, M. F., & Kalidindi, S. N. (1991, June). Quality management in the construction industry. Journal of Construction Engineering and Management, 117(2), 341-359. https://doi.org/10.1061/(ASCE)0733-9364(1991)117:2(341)

4th International Symposium on One Health, One World
November 20 – 22, 2025

ABS ID: 59
USDM-OP-38

Smart Geosynthetics for Monitoring Dynamic Response of Geosynthetic-Reinforced Structures

G. Sakthivel[1], S. Ganesh kumar[2]
[1]*Project Associate, GEGH, CSIR- Central Building Research Institute, Roorkee, India,*
[2]*Principal Scientist, GEGH, CSIR- Central Building Research Institute, Roorkee, India,*
[2]*Assistant professor, Academic of Scientific & Innovative Research, Ghaziabad, India.*

***Keywords**: Geosynthetic- Reinforced wall, Smart geosynthetics, Dynamic loading, slope stability, earthquake hazard.*

1. INTRODUCTION

The use of geotextiles and geogrids has become indivisible aspect in reinforced earth systems due to its better tensile properties which improve stability, and deformation resistance. Despite its established structural effectiveness, reinforced earth structures equally vulnerable on the event of natural disaster. The degradation or excessive loading of reinforcement strata and associate strain variation within the reinforcement member during precipitation, seismic loading and combined hydro seismic actions [1] induces failure in the structure.

This research paper is a systematic investigation of the dynamic behavior of the geogrid-reinforced retaining walls under the influence of different levels of soil saturation in conjunction with seismic excitations to support the need for monitoring strain development within the reinforcement member for the varying in-situ and loading conditions. Two different configurations were examined, namely a traditional concrete-block retaining wall, having dry backfill soil and 75% water-saturated conditions. Further, the dry and saturated backfill reinforced structure was subjected to repeated incremental shaking of 0.2 (g), 0.3 (g), and 0.4 (g) to assess the influence of saturation and repeated shaking on the long-time performance assessment. The observations highlighted the behavior of coupled hydro-seismic nature under seismic conditions and necessitate the need for SHM applications to identify structural distress in a timely manner for disaster mitigation.

2. EXPERIMENTAL TESTING

Soil used for the study

The backfill soil used for the study was collected from nearby site in Roorkee, Uttarakhand. The properties of the soil is given in Table 1.

Table 1. Material Characterization

Material	Properties	Value
Backfill Sand	Specific Gravity (Gs)	2.66
	Mean particle size	0.206 mm
	Void ratio (at 70%)	0.79
	Permeability (cm/s)	13.5×10^{-3}

For reinforcement, biaxial geogrid having aperture size 30 mm × 40 mm has been used in this study. The ultimate tensile strength was 22.42 kN/m where the stiffness at 5% strain was 283 kN/m.

Model Testing

A 1:5 scaled reinforced structure as per similitude laws [2] has been developed in this study for dynamic performance assessment. The dynamic behaviour of geogrid-reinforced retaining walls was assessed under dry and saturated backfill conditions using uniaxial shake-table facility. Using conventional modular elements having size 0.15 m × 0.15 m × 0.15 m, reinforced earth structure having 900 mm height and 1700 mm length was constructed. 5 layers of geosynthetic reinforcement were used as a reinforcing member. Two series of experiments were then conducted viz. dry backfill and 75% saturated backfill. For dynamic assessment repeated

incremental acceleration 0.2g, 0.3g and 0.4g were given as sequential input motions. The experimental setup of the retaining wall model in a uniaxial shake table and schematic diagram of the geogrid-reinforced wall is shown in Fig.1.

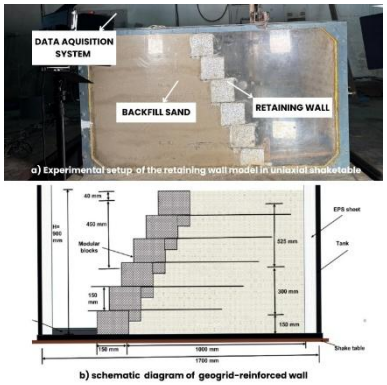

Fig.1 Experimental and Schematic test set-up

For monitoring, three 350ohm strain gauges were installed on the central rib at 15cm, 30cm and 45cm intervals at each geogrid layer to record the tensile-strain distribution of the dynamic loading (Fig.2 (a) and (b)). Using advanced data acquisition system, the strain development during each shaking was monitored and recorded.

3. RESULTS AND DISCUSSIONS

Observations on tensile behavior of geogrid

Tensile strength and axial strain properties of geogrid were investigated at two loading rates i.e. 5mm/min and 30mm/min for determining the effect of strain rate on mechanical behavior. It was evident that the tensile strength-strain curves were almost similar despite of loading rates. The time to failure at higher loading rates indicated the improved mobilization of the tensile capacity which underlines the importance of structural health monitoring (SHM) for regular monitoring in reinforced earth structure in real time for indicating possible overstressing of reinforced soil structures and for developing warning regarding health of the structure.

Influence of backfill soil saturation

The tensile behavior of geogrid-reinforced retaining walls under dynamic loading for the dry and saturated conditions is shown in Fig. 3 (a) and (b). In saturated conditions, tensile stiffness increased by about 31-75% upon exposure to incremental shaking intensities of 0.2-0.4g, relative to the base level. Conversely, the dry state showed a reduced stiffness gain between 12.2% and 44% which showed that part of the saturation and pore-water interaction significantly altered the stress-strain behavior of the reinforcement.

The high stiffness in saturated conditions can also due to increase in pore pressure and the partial loss of effective stress that increases confinement in the upper layers which increases strain localization. Further, the joint action of hydro-seismic effects causes variations of the mobilization of the tensile strain of the geogrid layers, leading to a non-linear distribution of the strain along the height. The variation in strain development within the geogrid members also highlights the need for the early detection after rainfall event which can minimize distress in the structure on the event of earthquake occurrences

Influence of multiple shaking events

The strain development experienced in the geogrid evidenced that the strain development in geogrid is highly sensitive to the underlying soil condition and the magnitude of the input excitation. The strain values recorded under repeated shaking of 0.2 g, 0.3 g, and 0.4 g is shown in Fig. 4.

Figure 2 (a) Location of strain gauges on the geogrid specimen

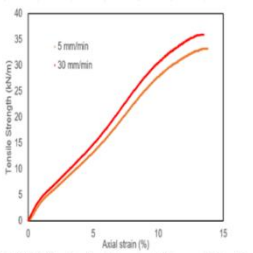

Fig. 2 (b) Strain development in geogrid with varying loading conditions

A systematic increase in strain accumulation was observed during successive shaking on the reinforcement layers confirming cumulative deformation in the reinforcement layers.

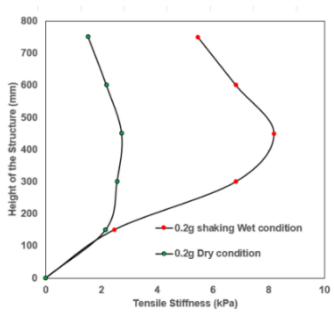

Fig.4 Tensile strain response for different ground conditions subjected to dynamic loading conditions

The layer of geogrid at approximately the mid-height provided the highest response of strain. In dry soil conditions, the strain distribution is comparatively lesser than dry soil conditions due to in-situ densification with minimum load transfer between the soil and geogrid. The overall increase in stiffness was between the conditions was 12.2% to 44%. For the saturated backfill, the stiffness increases ranged between 31% and 75%. The observations highlights the variation in strain localization and stiffness in the geogrid reinforcement for the varying conditions which provides the need for SHM for providing early warning towards the stability of the structure

4. CONCLUSION

The current experiment study has demonstrated that the loading rate as well as the level of soil saturation have a significant effect on tensile and dynamic characteristics of geogrid reinforced walls of retention. The tensile test showed that stiffness and ultimate strength are found similar but with variation in failure time/strain mobilization time. The Uniaxial shake-table experiments showed that saturation significantly increases strain evolution, and tensile stiffness was found to change by 31-75% under 75% saturation compared to the 12.2-44% change under dry conditions. The highest strain response was always observed in the central geogrid layer and created localized progressive strain in a repeated seismic loading. The observations evidenced the need for Structural Health Monitoring (SHM) to enable the real-time measurement of strain change, the early warning of stiffness loss, and the assessment of the integrity of reinforced earth structures.

REFERENCES:

[1] R.J. Bathurst, T.M. Allen, D.L. Walters, Reinforcement loads in geosynthetic walls and the case for a new working stress design method, Geotextiles and Geomembranes 20 (2002) 343–366.

[2] Iai, Susumu. "Similitude for shaking table tests on soil-structure-fluid model in 1g gravitational field." Soils and foundations 29, no. 1 (1989): 105-118.

2025 HOW
4th International Symposium on One Health, One World
November 20 – 22, 2025

ABS ID: 79
USDM-OP-39

Out-of-Plane Behaviour of Aac Wall Panels Reinforced with Prefabricated Wire Reinforcement in Comparison to Rcc Bands

C. Sonkar[1], R. Chowdhury[2], A. Chourasia[3], R. Paswan[4], M. M. Dalbehera[5], S. Kumar6, K. Sharma[7] and m.k. Yadav[8]

[1]*Principal Scientist, Structural Engineering Group, CSIR-Central Building Research Institute (CBRI), Roorkee, Uttarakhand, India,*
[2]*Business Head, VAP & AAC-TPO, Biltech Building Elements Ltd., New Delhi, India*
[3]*Chief Scientist, Structural Engineering Group, CSIR-CBRI, Roorkee, Uttarakhand, India,*
[4]*Senior Scientist, Advance Concrete and Steel Composites, CSIR-CBRI, Roorkee, Uttarakhand, India,*
[5]*Principal Scientist, Structural Engineering Group, CSIR-CBRI, Roorkee, Uttarakhand, India,*
[6]*Technical Officer, Structural Engineering Group, CSIR-CBRI, Roorkee, Uttarakhand, India.*
[7]*Student, Civil Engineering Department, Thapar Institute of Engineering and Technology, Punjab, India*
[8]*Research Scholar, CSIR-CBRI, Roorkee, Uttarakhand, India,*

Keywords*: AAC Masonry, Out-of-Plane Loading, Prefabricated Wire Reinforcement, RCC Bands, Masonry Strengthening, Energy Dissipation.*

1. INTRODUCTION

Reinforced concrete (RC) frame structures with masonry infills are widely adopted in Indian multistory buildings. Although considered non-structural, these infills play a crucial role in the global seismic response of RC frames [1,2]. Post-earthquake investigations have consistently shown that infill walls, rather than RC members, are more vulnerable to damage, particularly under out-of-plane (OOP) loading, which poses serious risks to safety and serviceability [3,4]. Hence, a clear understanding of the OOP behavior of masonry infills is essential for accurate seismic performance assessment and design improvement. This study presents full-scale out-of-plane tests on RC frames infilled with autoclaved aerated concrete (AAC) masonry, focusing on a 100 mm thick, slender wall representative of modern construction practices. The experimental investigation evaluates load capacity, stiffness degradation, energy dissipation, and crack propagation mechanisms under monotonic loading, providing valuable insights into the OOP response characteristics of slender AAC infills in RC frames.

2. EXPERIMENTAL PROGRAM

Four full-scale experimental investigation was conducted on a 100 mm thick AAC wall panel (3.0 m × 3.0 m) at the National Earthquake Engineering Test Facility (NEETF), CSIR–CBRI, Roorkee, to examine its OOP behavior under monotonic loading. The selected wall thickness corresponds to a slenderness ratio of 30, representing a highly flexible configuration. The test setup (Figure 1) comprised a rigid RC reaction frame firmly anchored to the strong floor. OOP loading was applied using two synchronized servo-controlled hydraulic actuators delivering uniform displacement at a rate of 0.5 mm/min. Wall deformations were continuously monitored using Linear Variable Differential Transformers (LVDTs) and Laser Displacement Sensors (LDSs) positioned along the wall surface. The structural response was assessed in terms of ultimate load capacity, mid-span displacement, stiffness degradation, energy dissipation, and cracking behavior. The energy dissipation was computed as the area under the load–displacement curve up to 0.8 Pu, where Pu denotes the ultimate load corresponding to the 100 mm thick, slender wall. The various specimen configurations tested are provided in Table 1.

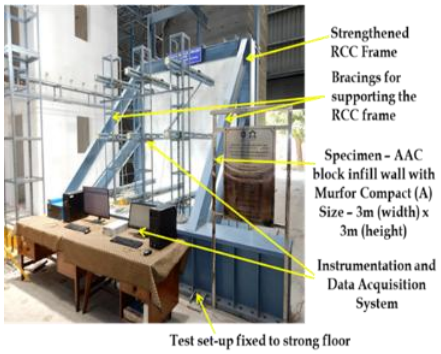

Figure 1. Out-of-plane test set up

Table 1: Details of 100 mm AAC wall specimen tested

Specimen ID	Reinforcement Details
AAC_100_0_1	Control specimen of 100 mm thick wall
AAC_100_5_WOEA_1	With 5 Single layers of prefabricated wire reinforcement A40 without edge-anchoring
AAC_100_5_EA_1	With prefabricated wire reinforcement A40 and edge-anchoring
AAC_100_2_RCCB_1	With two RCC bands at lintel and sill level

3. RESULTS AND DISCUSSION

Figure 2 presents the observed crack patterns in 100 mm thick wall specimens, highlighting distinct failure mechanisms under out-of-plane loading. The unreinforced wall exhibited a brittle flexural–shear failure with major cracks forming at mid-height, while the prefabricated wire reinforced walls showed delayed crack propagation and improved crack distribution. The inclusion of edge anchorage further stabilized crack development, preventing sudden failure. In contrast, the RCC-banded wall demonstrated well-confined cracking with limited propagation, indicating enhanced integrity.

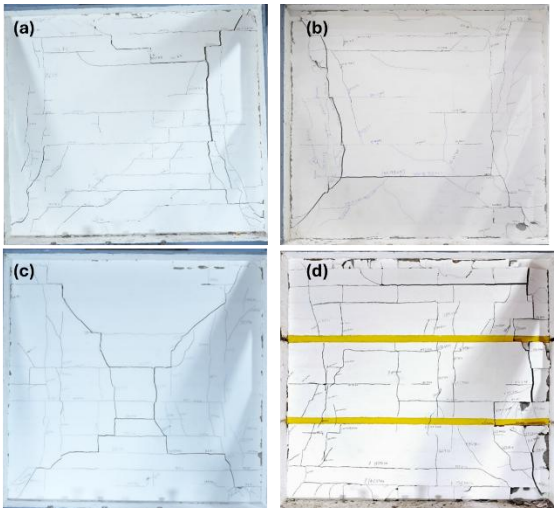

Figure 2. Observed crack patterns in 100 mm thick AAC wall specimens (a) AAC_100_0_1; (b) AAC_100_5_WOEA_1; (c) AAC_100_5_EA_1; (d) AAC_100_2_RCCB_1.

Figure 3 shows the corresponding load–displacement behavior. The unreinforced wall failed abruptly with low displacement capacity, whereas the PWR-reinforced wall without edge anchorage attained higher strength and ductility. The addition of edge anchorage improved post-peak stability and energy absorption. The RCC-banded wall achieved the highest load capacity and exhibited the most gradual strength degradation, signifying strong confinement and superior energy dissipation. Overall, PWR reinforcement enhanced crack control and flexibility, while RCC bands provided the most effective confinement and ductility improvement.

Figure 3 illustrates the corresponding load–displacement response. The unreinforced control wall exhibited initial cracking at mid-height between 30–36 kN and sudden failure beyond the peak load of 150.76 kN at 11.39 mm displacement. The prefabricated wire reinforced wall without edge anchorage showed delayed crack initiation and a more gradual failure, reaching 173.64 kN at 14.76 mm displacement-indicating a 15% strength and 30% ductility improvement over the control. When edge anchorage was provided, peak load reached 158.49 kN with 15.58 mm displacement, reflecting a smoother post-peak response and enhanced stability. The specimen with RCC lintel and sill bands demonstrated the most stable behaviour, attaining 167.53 kN at 16.02 mm displacement, with significantly improved energy dissipation (about 67% higher than the control) due to effective confinement.

Overall, prefabricated wire reinforcement displayed enhanced ductility and energy absorption like RCC reinforced masonry described in previous works [4].

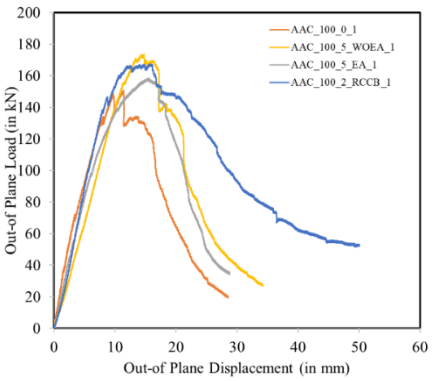

Figure 3. Out-of-plane load vs. displacement curves of 100 mm thick walls

4. CONCLUSIONS

The experimental results on 100 mm AAC walls show that reinforcement governs the OOP behavior. Prefabricated wire reinforcement delayed cracking, improved ductility, and stabilized response, while edge anchorage enhanced stress distribution. RCC bands achieved maximum strength and energy dissipation with enhanced deformability. Overall, prefabricated wire reinforcement provides a lightweight, economical alternative to RCC bands for improved seismic performance.

5. REFERENCES:

[1] Akhoundi F. et al., Experimental Out-of-Plane Behavior of Brick Masonry Infilled Frames, International Journal of Architectural Heritage, 14(2), 221-237, 2020.

[2] Rodrigues H. et al. Experimental Evaluation of Out-of-Plane Capacity of Masonry Infill Walls, Engineering Structures, 111, 48–63, 2016.

[3] Ricci P. et al. Experimental Investigation of the Influence of Slenderness Ratio and In-Plane/Out-of-Plane Interaction on URM Infill Walls, Construction and Building Materials, 191, 507–522, 2018.

[4] Al-Jaberi Z. et al. Experimental and Analytical Approach for Prediction of Out-of-Plane Capacity of Reinforced Masonry Walls, Engineering Structures, 196, 109297, 2019.

ABS ID: 02
USDM-OP-40

Structural Performance of Bamboo – Eps Sandwich Core Panel Under Uniaxial Compression

Ajay Chourasia[1], Mickey Dalbehera[2], and Chanchal Sonkar[3]
Chief Scientist, SE Group, CSIR-Central Building Research Institute, India
Principal Scientist, SE Group, CSIR-Central Building Research Institute, India
Correspond to Ajay Chourasia (ajayc.cbri@csir.res.in)

***Keywords**: Bamboo – EPS Core panel, CCB treated, Bambusa Balcoa, Bamboo dowel Bar, Composite action.*

1. Introduction

Bamboo, renowned for its rapid growth, exceptional strength-to-weight ratio, and renewability, has emerged as a promising sustainable construction material (Morales et al., 2017). Its inherent composite-like structure, characterized by strong longitudinal fibers embedded in a lignin matrix, imparts remarkable mechanical properties, surpassing those of many other natural materials. However, the anisotropic nature of bamboo, exhibiting weakness in the transverse direction, presents challenges in its structural application. To address this limitation and harness the full potential of bamboo, researchers have explored its integration into composite structures, such as sandwich panels (Morales et al., 2017). Sandwich panels, comprising two stiff face sheets bonded to a lightweight core, offer an exceptional combination of high strength, stiffness, and low weight, making them ideal for a wide range of structural applications. The utilization of bamboo as a face sheet material in sandwich panels offers a unique opportunity to leverage its high tensile and compressive strength along the grain, while the core material provides shear resistance and enhances the overall stability of the panel.

Expanded polystyrene, a lightweight, closed-cell foam material, has gained considerable attention as a core material in sandwich panels due to its excellent thermal insulation properties, low cost, and ease of processing. Combining bamboo face sheets with an EPS core creates a sustainable composite material with enhanced structural performance, potentially suitable for applications in building construction etc. The structural performance of such panels under compressive loading is crucial for ensuring their safe and reliable application. Understanding the behavior of bamboo-EPS sandwich panels under uniaxial compression will help in understanding the behavior of material properties of each component, the failure pattern etc.

2. Experimental Program

Nine scaled down (1000 x 100 x 230) experiments have been performed in the present study to investigate the failure behavior, load-deformation curve and ultimate strength of Bamboo – EPS panel. The subsequent section discusses about the taken up experimental investigation in this study.

2.1Specimen details

Table 1 discusses about the test matrix. Nine specimens have been tested to assess their performance under compression. For scaled down specimens, two types of vertical bamboo mesh's were prepared for the study. One was 50 x 50mm and the other was 100x 100mm mesh opening. Bamboo strips of 25 mm width were sliced from bamboo culms and used in bamboo mesh. The outer skin of bamboo strip was removed and cleaned. Then the longitudinal and transverse strips were joined using binding wires. Sikadur 32 gel was used over the bamboo strips on both the side to

develop a better bonding with concrete. Two types of shear connectors (steel rebar of 3 mm and bamboo dowel pin of 15mm have been used to connect the bamboo mesh. Concrete of M20 grade, has been used for concerting of the panels.

Table 1: Experimental matrix

Type of vertical mesh	Vertical Reinforcement spacing (mm)	Steel shear connector with 50mm spacing (B)	Steel shear connector with 100mm spacing (C)	Bamboo shear connector with 50mm spacing (D)	Bamboo shear connector with 100 mm. spacing (E)
Bamboo	50	BB50	BC50	BD50	BE50
	100	BB100	BC100	BD100	BE100
	50	SB50			
CCB treated Bamboo species of Bambusa Balcoa sourced from upper assam has been used in the study.					

CCB treated Bamboo species of Bambusa Balcoa sourced from upper assam has been used in the study.

3. Experimental results and discussion

The H/t slenderness ratio of all the specimens was kept at 9.35 for bamboo reinforced sandwich panels and 11.49 for steel reinforced sandwich panels. Table 2 shows the ultimate load carrying capacity of the panels. The ultimate load carrying capacity of BB50 panel (with 50mm bamboo wire mesh spacing and steel shear connector with 50mm spacing) was found to be 167 kN, From the 50mm spaced bamboo mesh spaced panel an increase in load carrying capacity was observed as the spacing of shear connectors increased. This may be due to an increase in compositeness in-between the bamboo mesh.

Table 2: UTM axial test results

Steel panels	Ultimate load carrying capacity (kN)
SB50	208.3
BB50	167
BC50	196.8
BD50	118.8
BE50	149.03
BB100	222.48
BC100	190.35
BD100	211.98
BE100	158.9

3.1 Load Deflection Profile

The axial deflection of the panel was observed to increase with increase in load in the axial testing machine. As per ACI-318, Panels with H/t ratio<25 is expected to fail by crushing. All the panels in the study has H/t ratio of 9.35 or 11.45 and it all failed due to crushing at the top or bottom as specified by ACI-318. No buckling was observed in the study.

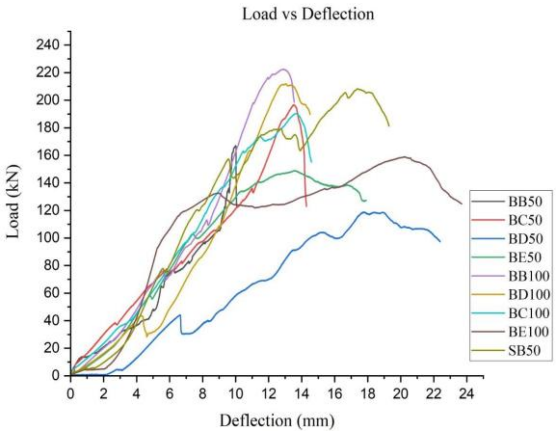

4. Conclusion

1. Bamboo as new material for shear connector has been used and its load carrying capacity compared to that of steel has been studied. The load carrying capacity of bamboo was found to be around 75-95% of that of the steel panel when half-scale panels were tested.
2. Bamboo shows considerably good load carrying capacity when compared to conventional steel EPS panels of the same

dimensions but more deflection (around 18-20%)was observed.

3. Load carrying capacity of panels decreased as the spacing of bamboo shear connectors increased.

4. As the bamboo vertical mesh spacing increased, decrease in load carrying capacity was observed

5. Study of cracking pattern showed that the panels mostly failed by crushing on the top and bottom as expected by them to fail as per ACI-318.

REFERENCES

Zhang, Wei, et al. "Shear resistance behavior of partially composite Steel-Concrete-Steel sandwich beams considering bond-slip effect." Engineering Structures 210 (2020): 110394.

Mohamad, N., Goh, W. I., Abdullah, R., Samad, A. A. A., Mendis, P., & Sofi, M. (2017). Structural performance of FCS wall subjected to axial load. Construction and Building Materials, 134, 185-198.

Amran, Y. M., Rashid, R. S., Hejazi, F., Safiee, N. A., & Ali, A. A. (2016). Response of precast foamed concrete sandwich panels to flexural loading. Journal of Building Engineering, 7, 143- 158.

Benayoune, A., Samad, A. A., Ali, A. A., & Trikha, D. N. (2007). Response of pre-cast reinforced composite sandwich panels to axial loading. Construction and Building materials, 21(3), 677-685.

Gara, F., Ragni, L., Roia, D., & Dezi, L. (2012). Experimental tests and numerical modelling of wall sandwich panels. Engineering Structures, 37, 193-204.

Chen, A., Norris, T. G., Hopkins, P. M., & Yossef, M. (2015). Experimental investigation and finite element analysis of flexural behavior of insulated concrete sandwich panels with FRP plate shear connectors. Engineering Structures, 98, 95-108.

Akinyemi, A. B., Omoniyi, E. T., & Onuzulike, G. (2020). Effect of microwave assisted alkali pretreatment and other pretreatment methods on some properties of bamboo fibre reinforced cement composites. Construction and Building Materials, 245, 118405.

ABS ID: 10
USDM-OP-41

Mr. V Srinivasan

ABS ID: 49
USDM-OP-42

Iot-Based Subsurface Snow Temperature Profiling Unit for Avalanche Forecasting

Chandrabhan Patel[1], Kanti Lal Solanki[1], Prateek Kumar[1], Komal Joshi[1], Dr. DP Kanungo[1]
Dr SK Panigrahi[1]
[1]*CSIR-Central Building Research Institute, Roorkee, India*

Keywords: *Bamboo – Avalanche; Temperature; Layers; Temperature measurement.*

1. INTRODUCTION

The Himalayan regions of India is highly exposed to several weather-related disasters. Avalanche is considered as one of the most destructive hazards since it poses significant threat to lives and infrastructure. Therefore, monitoring the occurrence of avalanche in hilly regions is vital for risk reduction. The snowpack has a temperature difference between its base layer and surface layer. Under low temperature gradient, snow crystals become rounded and bond well, creating a strong layer, whereas under high temperature gradient, growth of faceted crystals or depth hoar is dominant. Faceted grains form weak layers that fail under stress and are a common cause of slab avalanche. This work presents the development of an IoT enabled 8-channel temperature monitoring unit specifically designed for snow profile temperature at multiple depths in avalanche prone areas.

2. METHODOLOGY

The system integrates 8 temperature sensors, and a depth sensor with a microcontroller for data acquisition and real time data logging. Each of the eight channel captures temperature variation across different snow layers, which allows detailed thermal profiling to assess snow metamorphism and weak layer formation. The system is designed for long term field deployment and has solar charging capabilities.

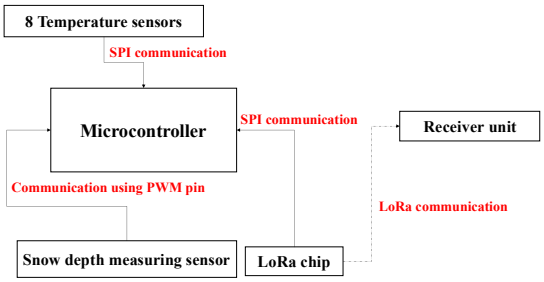

Figure 1: Block diagram of the snow avalanche profile system

3. INSTRUMENTATION

The sensor measures temperature at various depths, AND snow depth. The data from all sensors is logged to an SD card and then transmitted to the receiver unit via LoRa communication. The LoRa transmitted is integrated in the PCB to send data to over long range, this data is then received by our receiver unit which further transmits it to our webserver.

4. EXPERIMENT

An experiment was carried out to evaluate the performance of the IoT-enabled snow temperature profile sensor under controlled ice conditions. For this purpose, a wooden setup was constructed, and eight temperature sensors were installed at equal intervals along its vertical length. These sensors were positioned to capture the temperature variations across different layers of ice.

Figure 2: Experimental setup

5. RESULTS AND DISCUSSION

During the experiment, the system successfully recorded the gradual decrease in temperature across the layers, demonstrating the sensor's capability to monitor thermal changes over time. The graph illustrates temperature variation over time for eight sensors (T1-T8) placed at different depths in the snow profile. Initially, the upper layers (T6-T8) recorded higher temperatures around 25-30°C, while the lower layers (T1-T3) remained cooler at 5-15°C. Around 16:23 to 16:37, a sharp temperature drop occurred across all sensors, nearing 0°C, indicating melting conditions. Later temperatures rose again, with upper layers reaching about 28-30°C and lower layers increasing gradually to 10-20°C. This demonstrates the system's effectiveness in capturing vertical thermal gradients and dynamic temperature changes within the snowpack.

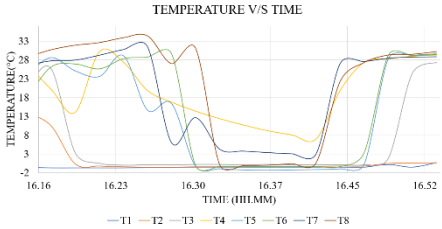

Figure 3: Temperature V/S Time graph

6. CONCLUSION

The developed IoT-enabled 8-channel temperature monitoring system effectively measures and records snow temperature variations across multiple depths, providing valuable insight into snowpack stability and metamorphism. The integration of LoRa communication and solar-powered operation makes it suitable for long-term deployment in remote, avalanche-prone Himalayan regions. Experimental results validate the system's reliability and accuracy in capturing thermal gradients within snow layers, which is crucial for identifying weak layers and predicting potential avalanche occurrences. This technology contributes to improved monitoring, early warning, and mitigation of avalanche risks.

REFERENCES:

[1] S. Ramalingam, H. Priya R, A. D. M, H. Lekha N and G. P. S, "Integrated Avalanche Detection And Rescue System Using IoT and Communication Networks," 2025 International Conference on Computational Innovations and Engineering Sustainability (ICCIES), Coimbatore, Tamilnadu, India, 2025, pp. 1-6, doi: 10.1109/ICCIES63851.2025.11033028.

[2] P. K. Indukala, U. G. Gosh and M. Vinodini Ramesh, "IoT-Driven Microseismic Sensing System and Monitoring Platform for Landslide Detection," in IEEE Access, vol. 12, pp. 97787-97805, 2024, doi: 10.1109/ACCESS.2024.3427386.

ABS ID: 209
USDM-OP-43

Dr. Nawal Kishor Banjara

4th International Symposium on One Health, One World
November 20 – 22, 2025

ABS ID: 201
USDM-OP-44

Numerical Assessment of Topographic-Soil–Structure Interaction Effects on Mid-Rise Buildings Adjacent to Slopes

Adnan Ansari[1] and Manojit Samanta[2]
[1]*Research Scholar, GEGH Division, CSIR-CBRI, Roorkee;*
Academy of Scientific & Innovative Research (AcSIR), Ghaziabad, India
[2]*Principal Scientist, GEGH Division, CSIR-CBRI, Roorkee;*
Associate Professor, Academy of Scientific & Innovative Research (AcSIR), Ghaziabad, India
Correspond to Dr. M. Samanta (manojit@cbri.res.in)

***Keywords**: Topographic-soil-structure interaction (TSSI), Hilly terrains, Slope amplification, Finite element modelling, Urban seismic design, Seismic response.*

1. INTRODUCTION AND BACKGROUND

Construction on sloped ground has significantly increased due to the scarcity of flat land, rapid population growth, and the demand from the tourism industry, particularly in seismically active hilly regions [1] [2]. Structures built on slopes often exhibit irregularities in both plan and elevation, leading to non-uniform distribution of mass and stiffness, which causes inherent torsional behaviour and eccentricity. Consequently, many existing buildings on hill slopes are anticipated to perform unsatisfactorily even during minor earthquake shaking.

The seismic response of structures in these regions is governed by Topography-Soil–Structure Interaction (TSSI), a complex phenomenon where the effects of topography, soil mechanics, and structural response are mutually dependent [3] [8]. The presence of topography irregularities, such as slopes, induces intensified ground motion (amplification) during earthquake shaking. Seismic waves reflected from the slope surface amplify ground surface motions, particularly in the area near the crest. Figure 1 shows the field investigations following disastrous events, such as the 1999 Chamoli earthquake, indicate that the negative impacts of slope topography on the ground surface can exacerbate seismic performance and cause severe damage to structures. Previous seismic assessments often relied on simplistic models, assuming fixed bases (FB), or performing analyses that account only for Soil-Structure Interaction (SSI) on flat terrain. However, modelling conditions must be realistic, encompassing both soil and structural nonlinearity under 3D conditions to accurately capture the seismic demands on these structures. TSSI analyses, therefore, are critical to quantify the increased seismic vulnerability resulting from combined topographical effects and structural irregularities.

Figure 1. Damaged buildings due to Chamoli Earthquake

2. METHODOLOGY

In the present study, advanced three-dimensional nonlinear numerical simulations has been adopted to assess the seismic performance of buildings subjected to topographic soil–structure interaction (TSSI) using the Finite Element (FE) software Abaqus.

The soil domain was modeled using an advanced kinematic hardening constitutive model to represent nonlinear soil behavior under cyclic seismic loading condition. This model helps to accounts for both isotropic and kinematic hardening effects, enabling a more realistic description of stress–strain relationships, hysteretic damping, and accumulation of plastic strains during earthquake shaking [3].

The study included reinforced concrete buildings of 3, 5, and 10 stories, configurations to evaluate height-dependent response characteristics. To evaluate the influence of site conditions, the analyses incorporated varying slope angles of 20°, 30°, and 40°. These slope inclinations were adopted to represent realistic ranges of topographic gradients encountered in hilly terrains. By systematically combining structural height and slope

inclination as parametric variables, the coupled effects of topography and structural configuration on seismic demands has been examined.

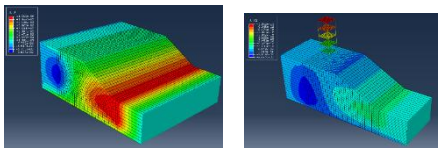

(a) (b)

Figure 2. (a) Free field analysis (b) Fixed base analysis of 5-storey building at 30o slope.

3. CONCLUSION

The assessment of TSSI in this study confirms that slope topography substantially amplifies seismic demands on adjacent buildings, particularly mid-to-high rise reinforced concrete frames. Results show that ignoring slope effects leads to significant underestimation of seismic fragility across all damage states [3] [4]. The most critical responses such as increases in lateral displacements and base shear were observed in buildings of 5 stories and above located near the slope crest, where the combined influence of topographic amplification and inherent irregularities of hillside construction was most evident. In addition, the analyses revealed that buildings close to the slope crest experienced more severe foundation rocking [2] [5] [6] [7].

These findings highlight that slope-foundation-structure interaction is a dominant factor governing seismic performance in hilly terrain, underscoring the need for engineers to explicitly incorporate TSSI effects in design and assessment to ensure safety and reliability.

4. REFERENCES:

[1] Kassem, M. M., Nazri, F. M., & El-Maissi, A. M. (2024). The influence of slope angle variation on structures resting on hilly region considering soil–structure interaction under earthquake loadings using capacity curves and probabilistic approach. Journal of Earthquake Engineering, 28(7), 1818-1836.

[2] Raj, D., Singh, Y., & Kaynia, A. M. (2018). Behavior of slopes under multiple adjacent footings and buildings. International Journal of Geomechanics, 18(7), 04018062.

[3] Shabani, M. J., Shamsi, M., & Ghanbari, A. (2021). Dynamic response of three-dimensional midrise buildings adjacent to slope under seismic excitation in the direction perpendicular to the slope. International Journal of Geomechanics, 21(11), 04021204.

[4] Shabani, M. J., Shamsi, M., & Zakerinejad, M. (2022). Slope topographic impacts on the nonlinear seismic analysis of soil-foundation-structure interaction for similar MRF buildings. Soil dynamics and earthquake engineering, 160, 107365.

[5] Fatahi, B., Huang, B., Yeganeh, N., Terzaghi, S., & Banerjee, S. (2020). Three-dimensional simulation of seismic slope–foundation–structure interaction for buildings near shallow slopes. International Journal of Geomechanics, 20(1), 04019140.

[6] Bahuguna, A., & Firoj, M. (2022, October). Numerical simulation of seismic response of Slope–Foundation–Structure interaction for mid–rise RC buildings at various locations. In Structures (Vol. 44, pp. 343-356). Elsevier.

[7] Qi, S., He, J., & Zhan, Z. (2022). A single surface slope effects on seismic response based on shaking table test and numerical simulation. Engineering Geology, 306, 106762.

[8] Tripe, R., Kontoe, S., & Wong, T. K. C. (2013). Slope topography effects on ground motion in the presence of deep soil layers. Soil Dynamics and Earthquake Engineering, 50, 72-84.

4th International Symposium on One Health, One World
November 20 – 22, 2025

ABS ID: OP-04
USDM-OP-45

Applicability of Hilbert Huang Transform Based Approach In Structural Health Monitoring

G. Devi[1], S.K.Panigrahi[2], A. Kumar[3], N. K. Banjara[4] N. Kumar[5]
[1]*Sr. Tech Officer, CSIR-CBRI, Roorkee, Uttarakhand, India and Ph.D Scholar, ACSIR,*
[2]*Chief Scientist, CSIR-Central Building Research Institute, Roorkee, India*
[3]*Principal Scientist, CSIR-Central Building Research Institute, Roorkee, India*
[5]*Ex- Proj. Assistant, CSIR-Central Building Research Institute, Roorkee, India*
Correspond to Gayatri Devi(gayatrikapil@gmail.com)

***Keywords**: Empirical Mode Decomposition, Hilbert Huang Transform, Joint Time-frequency, Non-stationary signal analysis, damage Indices, Structure Health Monitoring.*

To model nonlinear and non-stationary signal systems Empirical Mode Decomposition(EMD) is a commanding signal analysis technique. By combining the EMD with Hilbert transform a new transform obtained known as Hilbert Huang Transform (HHT). Using this a time-frequency representation may be obtained, which gives a full time-frequency-energy distribution of the signal. Such a representation would be idyllic for the analysis of nonlinear and non-stationary data. Empirical Mode Decomposition can capture the non-stationary features from the seismic vibration data of a damaged structure by extracting Intrinsic mode function (oscillating mode embedded in the data). Hilbert Huang Transform (HHT) based technique may be used to find out damage indices existing in a structure. This paper evaluates the applicability of Hilbert Huang Transform (HHT) by verifying its effectiveness considering one non-stationary and non-linear synthetic signals and then show its utility in Structural Health monitoring purpose by analyzing the vibration signals of a benchmark structure of UBS (University of British Columbia). The results demonstrate the efficacy of HHT for identifying damages in a real structure.

INTRODUCTION

In engineering structure, damage decreased the natural frequency of the structures, which caused a rapid change in structure's stiffness. As the event of damage took place in a structure, the acceleration signals recorded in the surrounding of that particular location will change evidently in comparison with undamaged state. The analysis of these signals based on Fourier transform is very difficult as it have some limitations. FT don't provide simultaneous time-frequency statistics and is not appropriate for non-stationary signals analysis varying with time. For damage identification of structures many signal processing techniques like wavelet transform (WT), Autoregressive models and Hilbert-Huang transform (HHT) have been implemented in SHM in recent years. (H. Li et al.,2009), (H. Li et al., 2014), (Bo Chen et al., 2014).

Hilbert Huang Transform technique developed (Huang et al, 1998) is a quite innovative approach for the processing of non-stationary signals. This approach has two main dealings. First is the empirical mode decomposition (EMD), by which the original signal is decomposed in its Intrinsic Mode Functions(IMFs). Next is implementation of Hilbert transform on these IMFs, the time-frequency representations of these oscillating modes may be obtained. (J. Liu et al, 2006),.The preface of EMD is the most inventive part of this process. (Bo Chen et al, 2014).

In structural engineering the application of Hilbert Huang transform have been proposed for SHM by Vincent et al. (1999). Yang and Lie (1999, 2000) and Yang et al. (2001) carried out Hilbert Huang Transform based study for damage detection in structures. J. Liu et al (2006) also used HHT approach in SHM by applying this method on the test data of actual benchmark structure of University of British Columbia.

In structural Health Monitoring, the HHT centered techniques are regulating creating great attention. Number of studies are performed regularly involving theory, field based measurement and experiments. (Bo Chen et al., 2014). Assessment and localization of active discontinuities using energy distribution between intrinsic modes has been done by Ghazi &Buyukozturk (2014). and Bagchi (Dec 2017) gave an overview for seismic assessment. However it is still unease the application of HHT technique practically in SHM for a variety of civil engineering structures. This technique based assessment, detection is still challenging. Therefore it is essential to explore the applicability and validity of HHT based approaches for SHM. To access the applicability of HHT in SHM, it is introduced to identify the damage in a structure.

HILBERT HUANG TRANSFORM

This method was offered by Huang et. al. (1998) include the decomposition of signal into its Intrinsic mode function by empirical mode decomposition and these IMFs acknowledge a well acted Hilbert transform. By extracting the IMFs, EMD captures the non-stationary feature of the signal. (Huang et al.,1998)(Bekara and Vander Bann, 2009) (Han & Baan, 2013)(Tary et al. 2014). A joint time-frequency representation is achieved by combining EMD with Hilbert transform to calculate instantaneous frequencies (Taner et al.,1979) (Chagnolleau&Baraniuk, 1999) which is known as the Hilbert Huang spectrum (Huang et al. ,1996).

The original signal is finally expressed as the sum of the IMF components plus the final residue:

$$X(t)=\sum_{j=1}^{m} [B_j(t)+ r_m(t)]$$

Where Bj(t) is the jth IMF component; m describes here the total number of IMF components; and rm(t)

Based on time dependent amplitude a(t) and instantaneous phase θ(t) the Instantaneous frequency ω(t) be computed via a Hilbert Transform

$$\omega(t)=(-d\theta(t))/dt= (-d)/dt ([\tan]^{-1} H\{B(t)\}/B(t))$$

Hilbert Spectrum is shown as

$$H(\omega,t)=Re\sum_{j=1}^{n} [a_j(t)e^{i\int \omega(t)dt}]$$

Where Bj(t) is the jth IMF component; m describes here the total number of IMF components; and rm(t) defines final residue.

RESULT AND DISCUSSION

To evaluate the effectiveness of HHT, one non-stationary synthetic signal with familiar solutions are executed. Then the real experimental results are analyzed. The non-stationary synthetic cases mentioned here:

case I

The synthetic signal is a submission of three components which consists of sine waves of different frequencies. The length of signal is 10 Sec. and sampling frequency is 1000 Hz. The details of synthetic signal is given by the following equation and is represented in figure.1 with its three components.

$$X = \begin{cases} 2\sin(2\pi 8t) & 0 \le t \le 3 \\ 1.5\sin(2\pi 15t) & 3 \le t \le 6 \\ 3.5\sin(2\pi 5t) & 6 \le t \le 10 \end{cases}$$

----------eqn.1

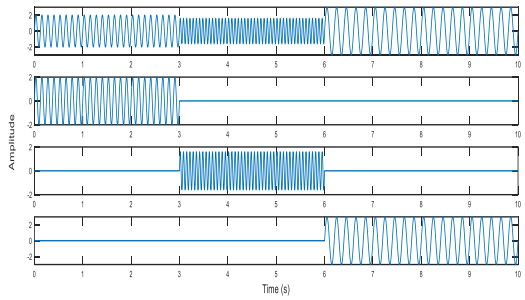

Figure 1. First synthetic signal (time domain)

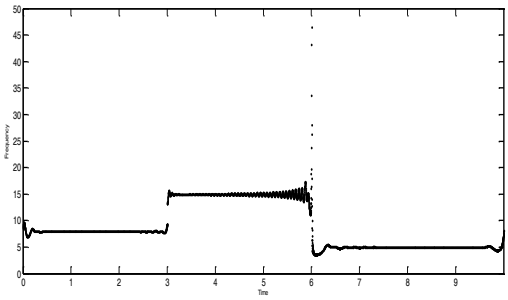

Figure 1.1 Time-frequency representation

of first synthetic signal using HHT

First Signal is a sine function and its frequency is changing from 8 hz to 15 hz at the instant of 3sec. and 15 hz to 5 hz at the instant of 6 sec. displayed in figure 1. Figure1.1 consist the time-frequency features of this signal achieved by HHT. It can be evaluated through figure 1.1 that very correct time-frequency representation is achieved, namely freq.≈8hz(0≤t≤3s); freq.≈15hz(3s≤t≤6s); freq.≈5hz(6s≤t≤10s).

Case 2

The experiment taken here is a numerical benchmark SHM problem established by IASC-ASCE SHM task group. (Johnson et al.2001). Building the models and simulating their response has been done through the DATAGEN Package in matlab environment.

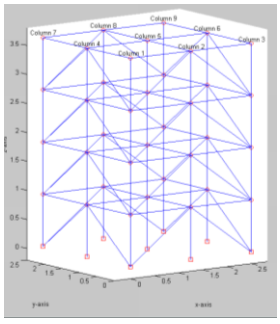

Figure 4: Definition of different column numbers of model

IDENTIFICATION OF DAMAGE LOCATION

To locate the damage at different location, a proper case study has been done, for which data have been generated based on following damage pattern.

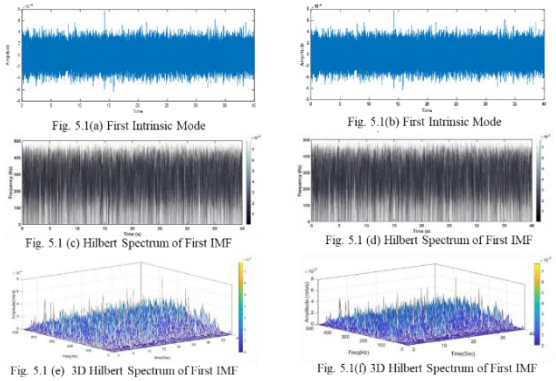

Test U:Undamaged Case

Test P1:damage pattern 1: all braces of first story are broken.

Figure 5: Comparison of results for first IMFs of Sensor data at Column 2 of First floor (left: undamaged structures and right:damaged structures) & Column 6 also.

The damage index computed by taking the difference of median of frequency of both cases (undamaged & damaged) for all the acceleration signals data.

Fig.8 Bar plot of damaged Index

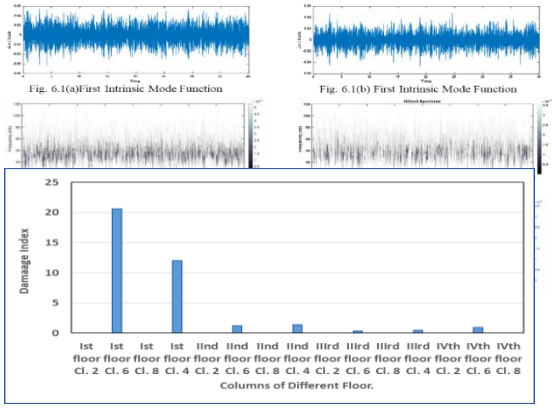

CONCLUSION :

The applicability of Hilbert- Huang Transform (HHT) based approach has been tested for Structural Health Monitoring. One synthetic examples are defined to check the effectiveness of this approach and a famous benchmark problem example demonstrated to

evaluate the performance of this approach in Structure Health Monitoring. The results describe that this method is capable to accomplish the detection of damage and its location. This new JTF method has a good potential to show its applicability for structural health monitoring. Based on the results, it may be concluded that Hilbert Huang Transform based approach is a beneficial tool in Structural Health Monitoring.

REFERENCES:

H. Li, T. Yi, M. Gu, and L. Huo, Evaluation of earthquake induced structural damages by wavelet transform, Progress in Natural Science, 19(2009) 461–470

Bo Chen, Sheng-linZhao, and Peng-YunLi, Application of Hilbert-Huang Transform in Structural Health Monitoring: A State-of-the-Art Review, Mathematical Problems in Engineering, 2014

Hilberh Huang, N.E., Shen, Z., Long, S.R., Wu, M.C., Shih, H.H., Zheng, Q., Yen, N.C., Tung, C.C. and Liu, H.H., The Empirical Mode Decomposition and The Hilbert Spectrum for Nonlinear and Nonstationary Time Series Analysis, Proceedings of the Royal Society, London A, 454 (1996) 903–995

Jianbo Liu, Xinwei Wang, Shenfang Yuan and Gang Li, On Hilbert–Huang Transform Approach for Structural Health Monitoring, Journal of Intelligent Material Systems and Structures, 17(2006).

Ghazi R.M. and Buyukozturk O., Assessment and localization of active discontinuities using energy distribution between intrinsic modes, Proc. 32nd IMAC, Soc. for Expe. (2014)

B. Vincent, J. Hu, and Z. Hou, Damage detection using empirical mode decomposition and a comparison with wavelet analysis, Proceedings of 2nd International Workshop on Structural Health Monitoring, Stanford University, Stanford, Calif, USA, (1999)891–900

J. N. Yang and Y. Lei, Identification of natural frequencies and damping ratios of linear structures via Hilbert transform and empirical mode decomposition, Proceedings of the International Conference on Intelligent Systems and Control, Anaheim, Calif, USA, (1999)310 –315 IASTED/ActaPress ,

J.N. Yang and Y. Lei, System identification of linear structures using Hilbert transform and empirical mode decomposition, Proceedings of 18th International Modal Analysis Conference SanAntonio, Tex, USA, 1(2000) 213–219

J. N. Yang, Y. Lei, and N. E. Huang, Damage identification of civil Engineering structures using Hilbert-Huang transform, In: Proceedings of 3rd International Workshop on Structural Health Monitoring Stanford, Calif, USA (2001), 544–553,

E. A. Johnson, H. F. Lam, L. S. Katafygiotis and J. L. Beck, A benchmark problem for structural health monitoring and damage detection, Structural control for civil and infrastructure engineering, F. Casciati and G. Magonette, eds., World Scientific, Singapore, (2001) 317– 324.

Taner, M. T., F. Koehler, and R. E. Sheriff Complex seismic trace analysis, Geophysics, 44,11(1979)1041–1063.

Magrin-Chagnolleau, and R. Baraniuk , Empirical mode decomposition based time-frequency attributes, Proc. 69th(1999)1949–1952, SEG Meeting,

Bekara, M., and M. Van der Baan, Random and coherent noise attenuation by empirical mode decomposition, Geophysics, 74(5) (2009) 89–98, doi:10.1190/1.3157244.

Han, J., and M. van der Baan, Empirical mode decomposition for seismic time-frequency analysis, Geophysics, 78(2) (2013) 9–19, doi:10.1190/geo1(2012-0199).

J. B. Tary, R. H. Herrera, J. Han, and M. Van Der Baan, Spectral estimation-What is new? What is next?, Rev. Geophys., 52 (2014)723-749.

2025 HOW
4th International Symposium on One Health, One World
November 20 – 22, 2025

Sustainable On-Demand Transit Under Demographic Shift Via A Scenario-Based Behavioral Modeling Framework

H. Hasada[1], A. Mizuno[2], S. Kitamura[3], and R. Kanamori[4]

[1] Research Associate, Institute of Industrial Science, The University of Tokyo, Tokyo, Japan,
Project Research Fellow, The Institute of Behavioral Sciences, Tokyo, Japan,
[2] Researcher, The Institute of Behavioral Sciences, Tokyo, Japan,
[3] Group Manager, The Institute of Behavioral Sciences, Tokyo, Japan,
[4] Project Professor, Institutes of Innovation for Future Society, Nagoya University, Aichi, Japan,
Correspond to Dr. H. HASADA (hasada@iis.u-tokyo.ac.jp)

***Keywords**: Attitudinal preference, Demand responsive transit, Integrated choice and latent variable model, Mobility policy planning framework, Shared socio-economic pathways, Scenario-based demand forecasting*

1. INTRODUCTION

As urban populations around the world experience rapid shifts and structural transformation, ensuring equitable and sustainable mobility systems remains a key challenge for city and regional planners. On-demand transit (ODT) services, also referred to as demand responsive transit, offer a flexible alternative to fixed-route systems, especially where demand is dispersed and private car access is limited. However, their long-term effectiveness depends on aligning service design with local demographic trends and behavioral preferences [1]. This study presents a structured demand analysis framework that integrates socio-demographic projections with behavioral choice modeling.

2. DEMAND ANALYSIS FRAMEWORK

The proposed framework integrates socio-demographic projections with behavioral choice modeling to provide insights into future mobility demand under demographic shifts. This demand analysis framework consists of the following three key steps (Figure 1).

Targeting: This step involves identifying the new service introduced to complement the existing local transportation system. A comprehensive household travel survey is conducted to analyze travel decisions in diverse contexts. It collects revealed preference (RP) and stated preference (SP) data, including travel mode choices, socio-demographic factors, and diverse indicators related to ODT and personal mobility.

Modeling: This step develops an integrated choice and latent variable model [2-3] composed of a mode choice part and an indicator part using the survey results. This model captures the relationship between service attributes, user characteristics (e.g., age, license ownership), and latent psychological factors shaping ODT attitudes, ensuring consistency with real-world travel patterns [4].

Forecasting: This step uses the estimated model to simulate long-term demand patterns under multiple socio-economic scenarios. The forecasting uses the Japanese Shared Socio-economic Pathways (J-SSPs) shown in Figure 2. SSPs are the five scenarios that are internationally recognized and describe possible future socio-environmental conditions, including aging trends. The results help policymakers evaluate the feasibility and impact of ODT over time and support strategic policy planning, such as licensing policies.

3. FUTURE FORECAST RESULTS

This study focuses on Kozoji New Town, a suburban residential area in Japan. Figure 3 presents the changes in the total demand, which is projected to continue declining until around 2035. This trend is primarily driven by a continuing decrease in the overall population of the area, which is expected due to persistently low birth rates. Figure 4 shows the population decline in each scenario predicted by the National Institute for Environmental Studies. However, after 2035, the trend in Figure 3 is projected to change. Especially in J-SSP1, J-SSP2, and J-SSP5, the demand is estimated to slightly increase. This is attributed to the aging of the second baby boomer generation. While this overall pattern of decline followed by stabilization is consistent across all population scenarios, the forecasted values for 2050 vary by up to nearly 10% depending on the scenario. This highlights the importance of accounting for a range of possibilities when forecasting demand under uncertain future conditions.

Table 1 shows the improvement in log-sum accessibility by age group and gender following the introduction of ODT in 2035 under the J-SSP2 scenario, as calculated using the developed model. The results clearly indicate that the greatest improvements are seen among the oldest population segment, particularly individuals aged 85 and over. Among them, females experience the highest improvement in accessibility. This suggests that conventional transportation systems may fall short in serving the mobility needs of older adults,

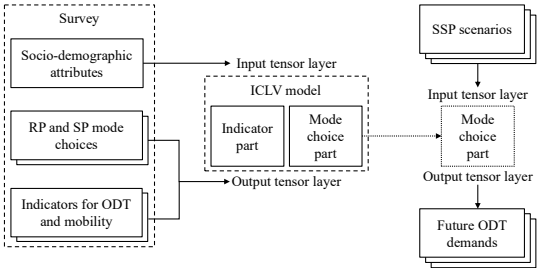

Figure 1. Concept of demand analysis framework for ODT

especially elderly women, and that ODT can effectively bridge this accessibility gap. This analysis underscores the importance of promoting license

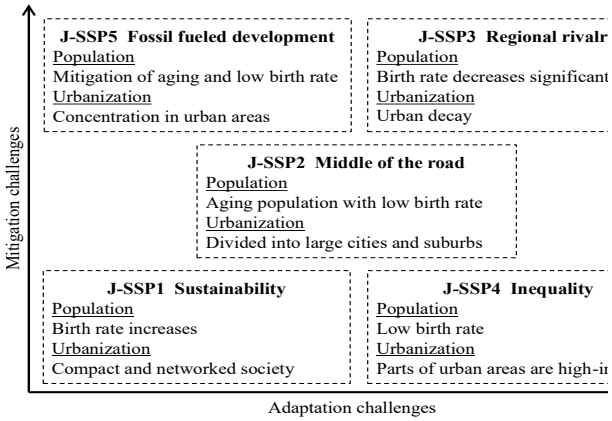

Figure 2. Summary of J-SSP scenarios developed by the National Institute for Environmental Studies

surrender among these groups to support the transition toward ODT.

Policies encouraging voluntary license surrender may change license holding rates over time. Table 2 illustrates how demand for ODT varies by age group if the number of licensed individuals changes by ±100 due to shifts in license holding rates. The results show that a reduction of 100 licensed individuals leads to the greatest increase in demand among those aged 75 to 84, with an estimated rise of 2.4 trips per day. These findings help identify which age groups are most responsive to license surrender policies and suggest that encouraging license surrender among them can be an effective way to increase demand for ODT.

4. CONCLUSIONS

This study applies the framework for ODT demand analysis to a suburban area undergoing rapid population aging and decline. The findings highlight the importance of targeted deployment strategies that prioritize vulnerable demographic segments and ensure financial and operational sustainability. By linking individual-level behavioral heterogeneity with long-term planning scenarios, our framework

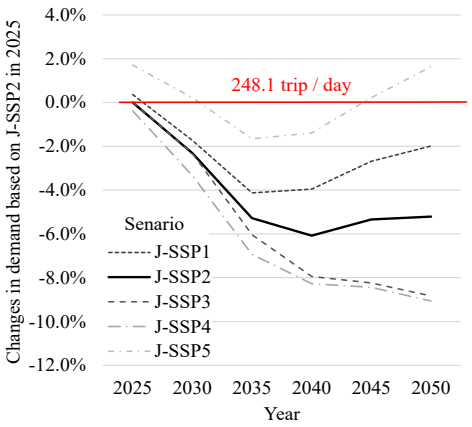

Figure 3. Projected change in total demand for ODT

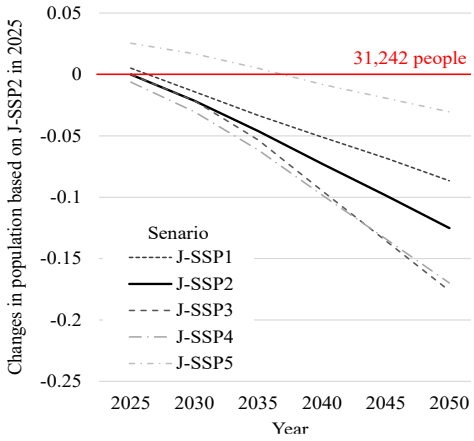

Figure 4. Projected change in population aged 15 and over

offers a practical tool for adaptive and inclusive transit policy in diverse urban settings across Asia.

REFERENCES

[1] Currie, G., Fournier, N., Res. Transp. Econ., 83 (100895).
[2] McFadden, D, Mark. Sci. 5 (4), 275–297.
[3] Train, K. E., McFadden, D. L., Rev. Econ. Stat., 69 (3), 383–391.
[4] Hasada, H., Mizuno, A., Kitamura, S., Kanamori, R., Journal of the City Planning Institute of Japan, 54 (3), 1107–1114.

Table 1. Log-sum accessibility improved by introducing ODT in 2035 under the J-SSP2 scenario

		Gender	
		Female	Male
Age	15-64	0.00006	0.00005
	65-74	0.00019	0.00012
	75-84	0.00092	0.00039
	85-	0.00282	0.00122

Table 2. Demand sensitivity for the number of people with driving licenses in 2035 under the J-SSP2 scenario

		Numbers of driving license holders		
		-100	**±0**	+100
Age	65-74	49.4	**47.3**	45.2
	75-84	61.2	**58.8**	56.3
	85-	36.8	**35.6**	34.5

2025 HOW
4th International Symposium on One Health, One World
November 20 – 22, 2025

ABS ID: OP-159
USDM-OP-47

Police Activities at the Time of the Great Kanto Earthquake and the Future Great Tokyo Earthquake

Tetsuro Ito

Visiting Professor, The University of Tokyo, Tokyo, Japan

***Keywords**: Great Kanto Earthquake, police activities, the rumors and false reports, future great Tokyo earthquake,*

1. Introduction

More than 100 years have passed after the Great Kantō Earthquake that struck in 1923.

The Great Kantō Earthquake occurred on September 1st of that year. An earthquake originating from the seabed of Sagami Bay caused a seismic intensity of 6 (at the time, the maximum intensity scale only went up to 6, an intensity of 7 had not yet been established), resulting in extensive damage throughout the Kantō region, centered on Tokyo Prefecture and Kanagawa Prefecture.

Looking at police activities at the time of the earthquake, police forces, including the Tokyo Metropolitan Police Department(MPD), immediately launched multifaceted operations. They engaged in rescuing and aiding victims, preventing the spread of rumors, cracking down on crime, and preventing and suppressing economic crimes such as hoarding and price gouging.

By reviewing how the police operated at that time, focusing on the activities of the MPD, we will examine the police activities and challenges then. We will also consider the role and challenges facing the police should a massive earthquake directly beneath the capital strike the metropolitan area again.

2, Police Activities During the Great Kanto Earthquake

The Great Kanto Earthquake of 1923 became a major disaster, resulting in over 500,000 homes completely or partially destroyed by fire and over 100,000 dead or missing. Immediately after the earthquake struck, the MPD organized a temporary emergency headquarters, conducted emergency summonses of police officers, and carried out emergency duties. Simultaneously, exercising the authority of the Superintendent General of the MPD, it requested the deployment of the Imperial Guard Division to engage in emergency disaster response measures.

3. Specific Activities

One of the primary emergency measures undertaken by the MPD was the rescue and relief of disaster victims. The number of victims in Tokyo alone exceeded 1.9 million, with over 3.4 million affected throughout the Kanto region.

One relief measure involved attending to the injured and sick. At that time, the Sanitary Department and Fire Department were divisions within the MPD. Therefore, relief teams were formed using Sanitary Department personnel. These teams were dispatched to various disaster-stricken areas to provide emergency treatment to the injured and sick on-site. They also admitted the injured and sick to temporary shelters set up by the MPD, accommodating approximately 5,000 people.

Furthermore, securing food and water for the victims was an urgent priority. Police stations were instructed to collect food supplies, prepare meals, and distribute them. Police officers borrowed materials to prepare and distribute food. Approximately 300,000 disaster victims flooded the Imperial Palace Plaza and Hibiya Park area alone. It is said that distributing water and food helped stabilize public sentiment. Securing water proved particularly difficult; after obtaining water in the Itabashi area where is 20km away from the center of Tokyo, it was transported in sake barrels via cargo trucks for distribution.

4. Characteristic Activities of the Police During the Great Kanto Earthquake

One particular concern for the police at this time was the rumors and false reports fueled by the anxiety of disaster victims. Rumors such as “Socialists and Koreans are setting fires,” “Koreans are taking advantage of the situation to incite riots and are plotting to poison the well water,” and “Koreans are coming to attack us.” caused great anxiety and outrage among the populace. The panic among citizens caused by these rumors and false reports became a major obstacle to maintaining vigilance and security. Many citizens, misled by these baseless rumors, organized vigilante groups. Driven by their fury, they killed and injured citizens and resisted against the police. Consequently, the MPD ordered police stations under its jurisdiction to protect Koreans and crack down on rumors and vigilante groups, while also conducting round-the-clock patrols alongside the military.

By September 5th, the MPD had sheltered over 6,000 Koreans at police stations and other facilities. It also cracked down on radical vigilante groups, arresting 161 individuals for 45 murders and 85 individuals for 16 cases

of assault. Consequently, the vigilante violence subsided. A major factor contributing to the spread of rumors was the suspension of news media functions and the absence of radio broadcasting at the time.

5. Government actions

Meanwhile, as an emergency measure, the government convened an emergency cabinet meeting on the day after the disaster, establishing the "Provisional Earthquake Relief Bureau" to implement rescue and relief measures for victims. It also issued an "Emergency Requisition Order" under Article 8 of the Imperial Constitution, requisitioning food, building materials, sanitary supplies, transport equipment, and other items necessary for victim relief. Furthermore, martial law was imposed on the same day in Tokyo Prefecture and Kanagawa Prefecture, followed by Saitama and Chiba Prefectures. Consequently, the police coordinated and cooperated with the Martial Law Command Headquarters, undertaking security patrols and providing relief to disaster victims.

Fires following the earthquake and the disruption of transportation systems led to an extreme shortage of daily necessities. The shortage of foodstuffs became particularly severe. Meanwhile, hoarding and withholding goods from sale occurred, with some items being sold at prices up to fifty times their normal cost. Consequently, on September 7, the government promulgated and immediately enforced the Emergency Imperial Decree "Concerning the Suppression of Exorbitant Profits on Daily Necessities." Police acted on citizen reports to enforce this decree. Violators who engaged in profiteering faced relatively severe penalties, including up to three years' imprisonment, leading to a gradual cessation of hoarding, withholding, and profiteering.

Police officers were dispatched from across the nation to support these enforcement efforts, arriving from as far north as Karafuto and as west as the Kinki region.

However, these police activities could not have been accomplished without the selfless dedication of police personnel who worked day and night without regard for their own safety. During the disaster relief efforts, the number of police officers who lost their lives in the line of duty reached as high as 94, primarily in the eastern area of Tokyo, including police station chiefs.

6. Modern Police Activities in the Event of a Major Earthquake Directly Beneath the Capital

The police are formulating plans for various disaster scenarios and corresponding police responses in preparation for a major earthquake directly beneath the capital in future.

Regarding responses to a major earthquake directly beneath the capital, various circumstances differ significantly between the time of the Great Kantō Earthquake and the present day. Concerning the fires that caused extensive damage during the Great Kantō Earthquake, numerous wooden structures with low seismic resistance still exist and locations where large quantities of combustible materials, including fuel tanks, are concentrated are scattered across various areas, particularly along the Tokyo Bay coastline.

Furthermore, population growth due to the concentration in the capital region and the development of various infrastructure, which was limited at the time, mean that new types of damage are anticipated. Even if buildings avoid collapse from the earthquake, maintaining daily life will become difficult due to the disruption of lifelines, including electricity, and transport networks. Additionally, the severing of roads will halt the supply of goods, people trapped in lifts within numerous buildings, including high-rises, the emergence of stranded commuters in office districts and commercial areas, and the risk to the lives of hospitalized patients and residents due to reduced functionality and shortages of supplies in medical institutions and care/nursing facilities are anticipated to pose significant challenges for rescue operations.

Furthermore, the rumors and misinformation experienced during the Great Kanto Earthquake remain a challenge even today, despite the development of broadcasting infrastructure and the internet. There is a high likelihood that the spread of false information via social media and the escalation of anxiety could occur again. To eliminate such rumors and misinformation, establishing reliable sources of information is essential.

CONCLUSIONS

The activities of the police and other administrative bodies during a major earthquake directly beneath the capital will be diverse and protracted. However, even with substantial support from across the nation, these activities are expected to be impossible to carry out to a degree that fully meets the demands of those affected. This is because the scope of the activities is simply too vast, and the personnel available to undertake them are limited.

In disasters, in addition to public assistance from the police, fire service, and administrative bodies, mutual aid from neighbors such as residents' associations and self-reliance – helping oneself – are will be crucial.

In the event of a major earthquake directly beneath the capital, even with public assistance maximized, its activities will have limits. Self-reliance to help oneself and one's family, and mutual aid between neighbors, will be paramount. However, self-help and mutual aid are not being practiced sufficiently when compared to the severity of the anticipated situation.

Therefor it is imperative that we reflect on the past, prepare ourselves for the possibility that such a disaster could strike us in the near future, and make the necessary preparations to survive it. As the saying goes, "Better safe than sorry". We must recognize that once a massive earthquake strikes directly beneath the capital, it could lead to unimaginably dire circumstances. It is our earnest

hope that this does not become a case of “No worry, no preparation”.

Mr. Katsumi Tsukagoshi

Mr. Ku Yamamoto

Electronic Poster Presentations

2025 HOW
4th International Symposium on One Health, One World
November 20 – 22, 2025

ABS ID: 193
USDM-EP-02

Developing evidence based guidelines for bollard placement to Project children on school routes

Hiroaki Noguchi[1], Kazuyuki Takada[2]
[1]*Undergraduate student, Tokyo Denki University, Saitama, Japan*
[2]*Professor, Tokyo Denki University, Saitama, Japan*

Keywords: *Vision Zero, Bollard, Risk Factor Analysis.*

1. INTRODYCTION

Reducing the number of traffic accidents to near zero is one of the most critical challenges facing modern society. An advanced concept pursuing this ideal is “Vision Zero,” originating in Sweden. Vision Zero sets the goal of eliminating all traffic fatalities and serious injuries. Rather than attributing responsibility solely to individual driving errors, it focuses on designing safe transportation systems that operate on the premise that humans make mistakes.

In Japan, traffic accidents involving elementary school children commuting to and from school have become a social issue. According to Cabinet Office data, while fatal and serious injury accidents involving elementary school children are decreasing, approximately 700 incidents still occur annually. Notably, accidents while walking account for over 50% of the total. A contributing factor is that many traffic safety measures in Japan remain focused on identifying dangerous locations based on past accident statistics—essentially a reactive approach.

Therefore, this study aims to bridge the gap between this philosophy and practice by creating a flowchart to determine the priority for implementing Vision Zero and verifying the feasibility of installing bollards. Specifically, we will digitize and analyze road environment risk factors such as “presence of sidewalks” and “actual usage as a shortcut” using GIS to identify areas where risks are concentrated. This enables strategic planning for installing measures like bollards—which physically separate pedestrians and vehicles—in the most effective locations.

A bollard is a post designed to physically prevent vehicle entry in order to protect people and buildings.

Fig1. Image of the bollard

2. OVERVIEW OF THE TARGET AREA

The study area for this research is Shibuya Ward, Tokyo. This ward features a complex mix of high-density residential areas, commercial districts, and major thoroughfares with heavy traffic, presenting diverse traffic safety challenges. It serves as a representative field for analyzing risk factors on urban school routes, offering multifaceted insights. The specific analysis scope is limited not to the entire ward but to elementary schools in Shibuya Ward, particularly residential streets closely tied to children's daily living spaces.

3. SUMMARY OF USED DATA

The list of used data in this study is shown in Table 1.

Table1. List of used data

Data Name	Source	Data Created
Location data for elementary schools	Shibuya Ward	List of Schools and School District Maps Published on the Shibuya Ward Board of Education Website.
Shibuya Ward Road Register Plan Data	Shibuya Ward	Information regarding road widths and other details in Shibuya Ward is recorded.

Figure 2 shows all 18 elementary schools in Shibuya Ward and a 500-meter radius zone around each school.

According to traffic accident statistics from the Metropolitan Police Department and other sources, pedestrian accidents involving children tend to occur frequently within a 500-meter radius of schools.

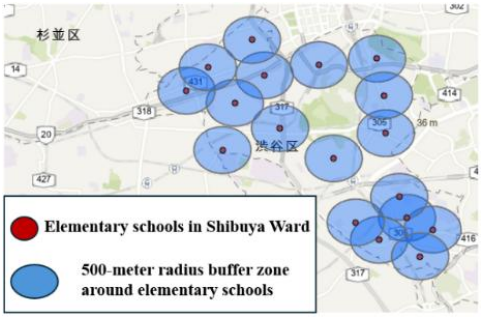

Fig 2. Elementary schools in Shibuya Ward and the surrounding 500-meter area

3. METHODLOGY

The Vision Zero Implementation Priority Decision Flowchart is based on the core Vision Zero principles of preventive safety and protection of vulnerable road users. It proposes specific barrier installation plans for areas identified through this process.

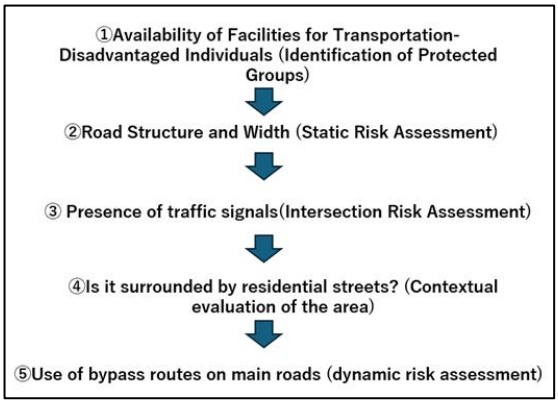

Fig3. Vision Zero Priority Flowchart

4. THE IMAGE OF OUTPUT

The Vision Zero implementation priority decision flowchart developed in this study was applied to 18 elementary schools in Shibuya Ward, Tokyo. As an example, we cited the area around Hatomori Elementary School located in the Sendagaya district.

The reason is that the surrounding roads, particularly the ward roads running along the north and west sides of the site, pose a structural risk due to either lacking sidewalks or being extremely narrow (②). Furthermore, while this area is largely a quiet residential neighborhood and should primarily serve as a local street for residents (③), its location sandwiched between two major arterial roads, Gaien Nishi-dori and Meiji-dori, has led to it being used as a shortcut by vehicles seeking to bypass congestion, traveling at high speeds (④). This is also a contributing factor.

Considering these multiple risks, we propose installing

bollards at the following locations.

Install retractable or removable bollards at the locations indicated by the arrows and blue circles in Figure 4.

Installing these bollards first at Point ①—the entrance from the main road in the southwest of the area enables the physical blocking of the primary inflow route where this area is most frequently used as a shortcut. Furthermore, installing them at intersections within the area

identified as high-risk (blue circles) prevents vehicles that might enter during restricted hours from taking dangerous shortcuts, ensuring these intersections remain safe zones for children. Installing bollards at intersections near the school gate also eliminates the possibility of contact between children and vehicles if they suddenly run out.

5. CONCLUSION

This study developed a hazard assessment flowchart for school routes based on the Vision Zero philosophy. When subsequently applied to Shibuya Ward, Tokyo, the Hatomori Elementary School area was identified. The surrounding area contained multiple intersections used as shortcuts off major roads, with narrow widths and poor visibility, presenting high risks for contact accidents.
Consequently, examples of locations where installing bollards could reduce the risk were identified.
Future research will deepen understanding of Vision Zero and advance studies to further reduce the risk of traffic accidents.

REFERENCES:

[1] National Institute for Land and Infrastructure Management Policy, Pedestrian Traffic Safety Measures at Intersections
[2] Shibuya City Official Website, Viewing of Road Register Plans, District-Owned Path Plans, and Route Maps Figure 4. Bollard Installation Diagram Near Elementary School

[3] Cabinet Office, Traffic Safety White paper

4th International Symposium on One Health, One World
November 20 – 22, 2025

ABS ID: 191
USDM-EP-03

Analysis of Shared Bikes Combined with Actual Usage Records

Takashi Miyazawa[1], Kazuyuki Takada[2]
[1]*Master student, Tokyo Denki university, Saitama, Japan*
[2]*Professor, Tokyo Denki university, Saitama, Japan*

Keywords: *shared bike, demand, tourist.*

1. INTRODUCTION

In recent years, bike-sharing systems have been widely introduced across cities in Japan, serving diverse travel demands ranging from daily commuting and school trips to tourism and leisure activities. A bike-sharing system is a service in which multiple bicycles are made available at designated docking stations (hereafter referred to as “ports”), allowing users to borrow and return bicycles freely. In tourist cities, both visitors and local residents utilize the same system, resulting in mixed travel demand and complicating the identification of distinct usage characteristics.

Such a situation can also be observed in Kanazawa City, Ishikawa Prefecture, where the number of tourists has increased since the opening of the Hokuriku Shinkansen. Given that the travel behavior of tourists and local residents differs substantially, analyzing them together may obscure their specific characteristics. Therefore, this study aims to clarify the differences in usage patterns between tourists and local residents based on one year of bike-sharing usage data from 2024.

Fig.1 Machinori

(Source: Kanazawa Tabimono-gatari website)

2. DATA

This study focuses on Machinori, the bike-sharing system in Kanazawa City, Ishikawa Prefecture. Machinori is a type of community-based service that utilizes the nationwide system operated by Docomo Bike Share Co., Ltd. In recent years, the number of tourists visiting Kanazawa has been steadily increasing, accompanied by a rise in bike-sharing usage. For this study, we analyze trip data collected over one year, from April 1, 2024, to March 31, 2025. After removing missing values, a total of 522,970 trips remain for analysis. An overview of the dataset is presented in Figure2. Among the user attributes, the dataset includes the variable “User registration area,” which indicates the regional operator through which a user registered for the Docomo Bike Share service.

User ID (After anonymization)	Aggregation key	User registration area	Bike ID	Start port	Start time	End port	End time
20	一般ユーザ月額会員	金沢	KNZ0341	89001	2024/4/1 7:46	89014	2024/4/1 7:56
20	一般ユーザ月額会員	金沢	KNZ0232	89001	2024/4/2 7:49	89014	2024/4/2 8:00
20	一般ユーザ月額会員	金沢	KNZ0252	89001	2024/4/3 7:48	89014	2024/4/3 7:58
20	一般ユーザ月額会員	金沢	KNZ0383	89001	2024/4/4 7:52	89014	2024/4/4 8:02
20	一般ユーザ月額会員	金沢	KNZ0037	89001	2024/4/5 7:50	89014	2024/4/5 8:02
20	一般ユーザ月額会員	金沢	KNZ0051	89001	2024/4/8 7:48	89014	2024/4/8 8:00

Fig.2 Overview of trip data

3. METHODOLOGY

In this study, users of Machinori were classified into three groups based on one year of trip records: (1) local residents, (2) tourists using a 1-day pass, and (3) tourists who have experience using bike-sharing systems in other regions. The usage characteristics of each group—such as trip start time, trip duration, travel distance, and spatial distribution—were then compared. The classification criteria for users are as follows.

(1) Local residents : Users who registered in the Kanazawa area or subscribed to a monthly membership plan.

(2) 1-day pass tourists : Mainly foreign visitors and short-term users who purchased a one-day pass.

(3) Users registered in other regions: Domestic tourists who had pre-registered with the Docomo Bike Share system in other cities.

4. RESULTS

4-1. TRIP DURATION AND TRAVEL DISTANCE

Figures 3 and 4 show the distributions of trip duration and travel distance for each user type. The average trip duration for local residents is approximately 21 minutes, and the average travel distance is about 2.2 km, indicating that most trips are short-distance rides for daily activities such as commuting to work or school.

In contrast, 1-day pass tourists tend to have longer trip durations despite their relatively short travel distances. This suggests that these users often keep bicycles for extended periods during sightseeing activities. Furthermore, the proportion of circular trips—defined as trips where the origin and destination ports are the same—was notably higher among 1-day pass tourists (about 32%) than among local residents (about 6%).

Meanwhile, users registered in other regions (domestic tourists) exhibited average trip durations of approximately 39 minutes and average travel distances of around 1.9 km, showing characteristics intermediate between those of local residents and 1-day pass tourists.

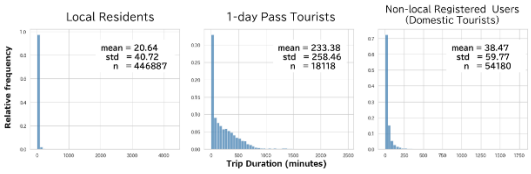

Fig.3 Distribution of trip duration by user type (minutes)

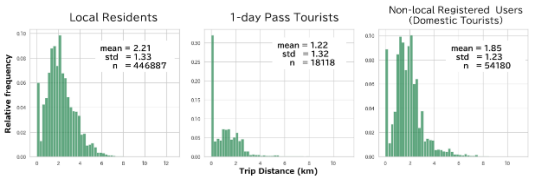

Fig.4 Distribution of travel distance by user type (km)

4-2. HOURLY DISTRIBUTION OF TRIP COUNTS BY USER TYPE (WEEKDAY VS HOLIDAY)

Figure 5 presents the distribution of trip counts by time of day, separated by weekdays and holidays, for the three user types: 1-day pass tourists, users registered in other regions, and local residents. For 1-day pass tourists, trip counts are highly concentrated between 10:00 and 12:00 in the morning, reflecting travel behavior associated with sightseeing activities. Users registered in other regions show a broader distribution of trips extending from morning to afternoon, suggesting that they use bicycles not only for sightseeing but also for a variety of other activities. In contrast, local residents exhibit distinct peaks during 7:00–9:00 in the morning and 17:00–19:00 in the evening on weekdays, clearly reflecting commuting and school-related travel demand.

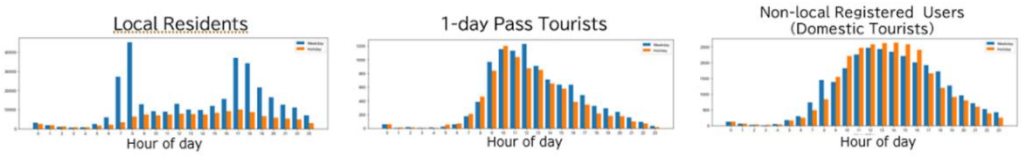

Fig.5 Hourly Distribution of Trip Starts by User Type (Weekday vs Holiday)

Table.1 Top Three Origin–Destination Port Combinations by Usage Frequency

	No.1	No.2	No.3
Local Residents	Kanazawa station ⇒ Kanazawa station 3561 trips	Kanazawa station ⇒ Korimbo Seseragi 2421 trips	Kanazawa station ⇒ Lawson Kanazawa Wakamiya-cho Store 2188 trips
1-day Pass Tourists	Kanazawa station ⇒ Kanazawa station 2275 trips	Kanazawa Station East ⇒ Kanazawa Station East 833 trips	Kanazawa Station East ⇒ Kanazawa station 288 trips
Non-local Registered Users (Domestic Tourists)	Kanazawa station ⇒ Kanazawa station 1423 trips	Higashiyama Shusei-no-Michi Path ⇒ Kanazawa station 572 trips	Kanazawa station ⇒ Higashiyama Shusei-no-Michi Path 542 trips

4-3. SPATIAL DISTRIBUTION

Table 1 presents the top three origin–destination (OD) pairs with the highest trip counts for each user type. For all three user groups, the most frequent OD pair was within the same railway station port. However, differences were observed in the second and third most frequent pairs.

1. CONCLUSION

In this study, the differences in usage characteristics between tourists and local residents were examined based on trip records, focusing on travel distance, trip duration, time-of-day trip counts, and spatial distribution. Significant differences were observed between the two groups. Future research will investigate how tourist usage affects the usage patterns of local residents.

4th International Symposium on One Health, One World
November 20 – 22, 2025

ABS ID: 114
USDM-EP-04

Seismic Response Control of Buildings Using Fe-Based Shape Memory Alloy Base Isolators

M.eswar[1,2] and A. Chourasia[1,2]
[1]*CSIR – Central Building Research Institute, Roorkee – 247667, India*
[2]*Academy of Scientific and Innovative Research (AcSIR), Ghaziabad – 201002, India*
Correspond to Dr. A. CHOURASIA (ajayc@cbri.res.in)

Keywords: *Seismic Response Control; Shape Memory Alloys; SMA Isolator; Fe-based SMA Plate.*

1. INTRODUCTION

A Seismic events pose a significant threat to structural integrity, particularly when a building's fundamental frequency aligns with the dominant frequencies of an earthquake. This alignment amplifies the acceleration response, leading to severe damage. A widely implemented mitigation strategy is base isolation, which decouples the superstructure from its foundation to shift its frequency away from peak seismic energy, thereby minimizing damage. Researchers around the world studied several advanced techniques to mitigate these effects [1–3].

Recent research has focused on enhancing seismic control systems with smart materials [4]. Shape Memory Alloys (SMAs) are particularly promising due to their unique superelastic effect and energy dissipation capabilities, which have led to the development of various SMA-based seismic devices (e.g., braces, dampers, and connectors) [5–7]. This paper builds on that work, presenting a numerical investigation into the performance of a novel base isolator design that incorporates SMA U-Shaped plates.

2. NUMERICAL MODEL

A three-dimensional finite element (FE) model was developed in ABAQUS to investigate the performance of the proposed isolator. The study was conducted in two stages as described below.

2.1 SMA Material Property

First, the superelastic behavior of the Fe-based SMA was validated by simulating a single 150 mm x 60 mm x 10 mm plate. The model utilized the built-in superelastic material capabilities in ABAQUS, with parameters for transformation stresses, elastic moduli, and maximum transformation strain based on existing literature. The plate was modeled with eight-node linear brick elements (C3D8R), fixed at one end and subjected to a 5 mm cyclic displacement at the other. The simulation successfully reproduced the characteristic flag-shaped hysteresis loop, confirming the material's recentering capabilities and validating the modeling approach for the complete isolator.

Table 1. Material Properties of Superelastic SMA Plate

Material Properties	Values
Martensite's Young's Modulus, E_M (GPa)	30
Martensite's Poison's Ratio, ν_M	0.33
Transformation Strain, ε_l	0.03
Start of Transformation (Loading), σ^t_{Ms} (MPa)	340
End of Transformation (Loading), σ^t_{Mf} (MPa)	450
Start of Transformation (Unloading), σ^t_{As} (MPa)	250
End of Transformation (Unloading), σ^t_{Af} (MPa)	100
Start of Transformation in Compression (Loading), σ^c_{Ms} (MPa)	459

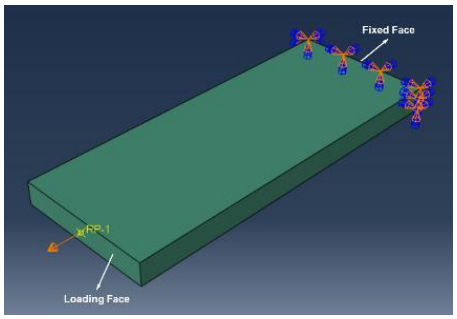

Figure 1. SMA Plate Element showing Fixed and Loading Faces

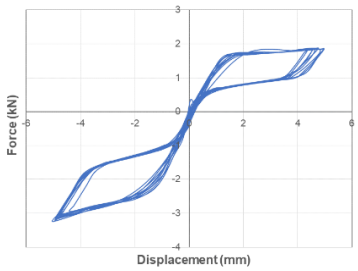

Figure 2. Hysteresis Graph of SMA Plate for a Displacement of 5 mm.

2.2 Proposed SMA Isolator Model

Subsequently, a detailed FE model of the novel base isolator was created. The proposed design features four U-shaped SMA plates (5 mm thick, 16 mm wide) connected to top and bottom steel fixing plates. This assembly works in conjunction with a central bearing composed of alternating layers of rubber and steel with a lead core. The entire system is placed between two large steel loading plates. All components were modeled using 3D solid elements (C3D8R), with hybrid elements (C3D8RH) used for the hyperelastic rubber layers. A finer mesh was employed for the SMA plates to accurately capture stress distribution. The isolator model was subjected to a constant vertical load of 50 kN and a cyclic horizontal displacement protocol to simulate seismic action. For benchmarking, the performance of the SMA isolator was compared against an identical isolator modeled with conventional steel U-shaped plates.

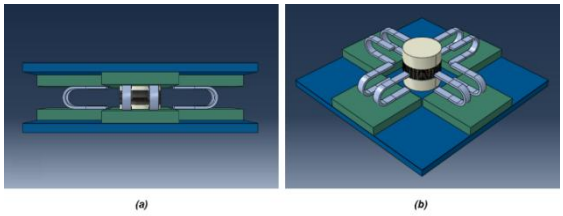

Figure 3. Design of Isolator from (a) Side View (b) Isometric View by removing Top Loading Plate and Fixing Plates

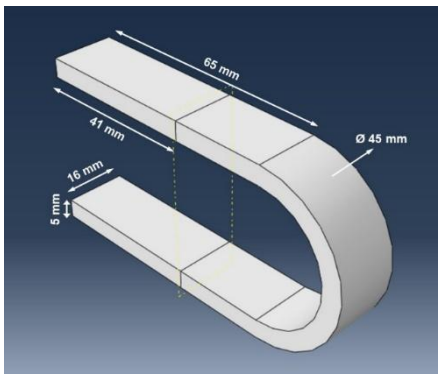

Figure 4. Dimensions of U-shaped Plate

3. RESULTS

The validated finite element model of the single SMA plate, subjected to a 5 mm cyclic displacement, successfully reproduced its characteristic "flag-shaped" hysteresis. This confirmed its excellent re-centering capability with minimal residual displacement, despite an expected asymmetry in force (1.9 kN in tension vs. 3.2 kN in compression).

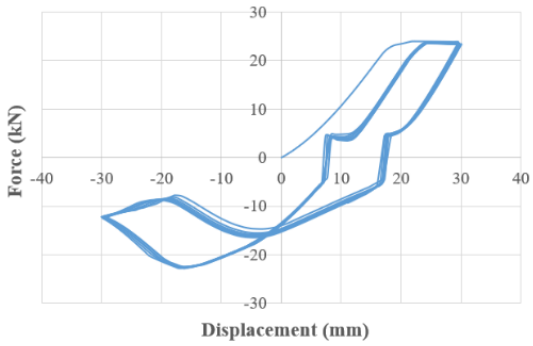

Figure 5. Force-displacement response of SMA and Steel isolators (40 mm displacement)

When the full isolator models were compared under a 50 kN constant vertical load and a 40 mm cyclic horizontal displacement, the proposed SMA isolator demonstrated comparable energy dissipation to an identical isolator using conventional steel plates. However, the SMA isolator showed vastly superior performance in re-centering; it returned to its original position after the protocol, whereas the steel model retained large permanent deformations. Furthermore, the SMA isolator's hysteretic performance remained stable and repeatable over numerous loading cycles.

4. CONCLUSIONS

These findings demonstrate that the proposed Fe-based SMA isolator is a highly effective solution for seismic control. It successfully combines robust energy dissipation with the critical advantage of re-centering, a combination that minimizes permanent structural damage and enhances post-earthquake serviceability. The ability to re-center significantly reduces the need for post-event repair and realignment, unlike conventional systems that sustain permanent yield. Furthermore, the use of Fe-based SMAs presents a potentially more cost-effective alternative to other SMA types, making this a promising practical solution for resilient structures.

REFERENCES:

1. Robinson WH (2011) Lead-rubber hysteretic bearings suitable for protecting structures during earthquakes. Seism Isol Prot Syst 2:5–19. https://doi.org/10.2140/siaps.2011.2.5

2. Guo T, Xu W, Song L, Wei L (2014) Seismic-Isolation Retrofits of School Buildings: Practice in China after Recent Devastating Earthquakes. J Perform Constr Facil 28:96–107. https://doi.org/10.1061/(asce)cf.1943-5509.0000411

3. Gu X, Yu Y, Li Y, et al (2019) Experimental study of semi-active magnetorheological elastomer base isolation system using optimal neuro fuzzy logic control. Mech Syst Signal Process 119:380–398. https://doi.org/10.1016/j.ymssp.2018.10.001

4. Jani MJ, Leary M, Subic A, Gibson MA (2014) A review of shape memory alloy research, applications and opportunities. Mater Des 56:1078–1113. https://doi.org/10.1016/j.matdes.2013.11.084

5. DesRoches R, Smith B (2004) Shape Memory Alloys in Seismic Resistant Design and Retrofit: A Critical Review of their Potential and Limitations. J Earthq Eng 8:415–429. https://doi.org/10.1080/13632460409350495

6. Gur S, Mishra SK, Chakraborty S (2014) Performance assessment of buildings isolated by shape-memory-alloy rubber bearing: Comparison with elastomeric bearing under near-fault earthquakes. Struct Control Heal Monit 21:449–465. https://doi.org/10.1002/stc.1576

7. Dezfuli FH, Alam MS (2014) Performance-based assessment and design of FRP-based high damping rubber bearing incorporated with shape memory alloy wires. Eng Struct 61:166–183. https://doi.org/10.1016/j.engstruct.2014.01.008

4th International Symposium on One Health, One World
November 20 – 22, 2025

ABS ID: 98

USDM-EP-05

Methods for Improving Earthquake Resistance of Non-Structural Elements

S. Saranya[1], and P. Sunitha[2]

[1]*Doctoral student, Earthquake Engineering Research Centre, IIIT Hyderabad, India,*

[2]*Assistant Professor, Earthquake Engineering Research Centre, IIIT Hyderabad, India,*

Correspond to Prof. P. SUNITHA (sunitha.palissery@iiit.ac.in)

***Keywords**: Non-Structural Elements, Damages, Mitigation Methods, Earthquake Resistanc.*

ABSTRACT

Non-Structural Elements (NSEs) such as building contents, appendages to buildings, utilities and services are highly vulnerable during earthquakes and can pose significant risks if not properly secured to th supporting structure. Consequences of unsecured NSEs in the aftermath of earthquakes are significant losses to human life, property, and functionality of buildings. This is because, NSEs are susceptible to sliding, rocking, toppling, overturning, stretching, shortening, and shearing. These movements are compounded by: (a) NSE-structure anchorage conditions, (b) geometry, weight, and friction with the supporting surface and NSE, and (c) NSE types. Recent earthquakes in Turkey and Myanmar also witnessed damage in NSEs, reiterating the criticality. In general, earthquake resistance of NSEs can be improved by 3 broad mitigation approaches recommended in literature. They are: (i) non-engineered (based on judgement) (ii) pre-engineered (based on calculations, experiments, and experience from past earthquakes), and (iii) engineered (based on detailed design recommended in design standards). These approaches typically employ anchor bolts, braces, slack chains, snubbers, flexible connections, and shock absorbers tailored to the specific type and performance requirements of NSE. This paper presents a detailed discussion of commonly adopted methods that help improve earthquake resistance of NSEs and enhance overall safety of buildings in urban areas.

1. INTRODUCTION

Non-Structural Elements (NSEs) are broadly classified based on their (i) function – architectural, Mechanical, Electrical and Plumbing (MEP) and Furniture, Fixtures & Equipment (FF&E), and (ii) seismic response – acceleration-sensitive, displacement-sensitive, and acceleration-and-displacement sensitive [1, 2]. Acceleration-sensitive NSEs, being heavy and stiff, are prone to sliding, rocking, or toppling if unanchored, while displacement-sensitive NSEs, which are light and flexible, are prone to stretching, shortening, or shearing if anchored. Acceleration-and-displacement sensitive NSEs are both massive and flexible, are prone to both acceleration and displacement effects. For example, in doors and windows, the primary effect is caused by displacements, while accelerations have a secondary effect. Conversely, in staircases, the effects appear in reverse order [1].

Improving earthquake resistance of NSEs is crucial because it helps to (i) reduce financial loss, as NSEs typically account for approximately 75–85% of the total project cost in commercial buildings, (ii) ensure continued functionality of NSE after an earthquake, and (iii) prevent serious injuries or fatalities [1, 2]. In general, earthquake resistance of NSEs can be improved by 3 broad mitigation approaches recommended in literature. They are: (i) non-engineered (based on judgement), (ii) pre-engineered (based on calculations, experiments, and experience from past earthquakes), and (iii) engineered (based on detailed design

recommended in design standards) tailored to the specific type and performance requirements of NSE [1, 2]. Further, earthquakes induced damage in architectural NSEs had been widespread and resulted in greater damage compared to other NSE types in past earthquakes. For example, the 1971 San Fernando earthquake resulted in 90% of the damage in architectural NSEs, whereas only 7% was due to MEP components in commercial buildings [3]. This paper presents a concise and focused discussion on the design guidelines or techniques that help improve earthquake resistance of *architectural NSEs*.

2. ARCHITECTURAL NSEs

Architectural NSEs are primarily displacement-sensitive when fixed to supporting structure using adhesives but display acceleration sensitivity when anchored. Typically, wall elements, partitions and ceiling systems constitute the major architectural NSEs. Displacement-sensitive NSEs are subjected to deformation or rotation depending on the differential movement of the supporting structure [1, 2]. Therefore, it is necessary to either limit the seismic displacement of the supporting structure by adopting a stiff structural system or designing the NSEs to accommodate or imposed design seismic demands without sustaining any damage in the NSEs [2].

The selection of an appropriate design or technique depends on the type of NSE, its functional importance, and performance requirements. For example, lineal NSEs such as water mains must accommodate relative displacements between supports, while planar NSEs like glass must accommodate displacements along their edges. Displacement-sensitive NSEs are protected by using sliding connections or expansion joints to accommodate seismic deformations and relative displacements.

3. SEISMIC RELATIVE DISPLACEMENTS

In general, the design seismic relative displacement (D_{pl}) of the NSEs is calculated using the following equation:

$$D_{pl} = D_p I_e \quad [1]$$

where I_e Importance factor of the structure, and D_p is the relative seismic displacement of the NSE. Further, displacements within the structure can be estimated using (Figure 1(a)):

$$D_p = \delta_{xA} - \delta_{yA} < \frac{(h_x - h_y)\Delta_{aA}}{h_{sx}} \quad [2]$$

and displacements between the structure can be estimated using (Figure 1(b)):

$$D_p = |\delta_{xA}| + |\delta_{yB}| < \frac{h_x \Delta_{aA}}{h_{sx}} + \frac{h_y \Delta_{aB}}{h_{sx}} \quad [3]$$

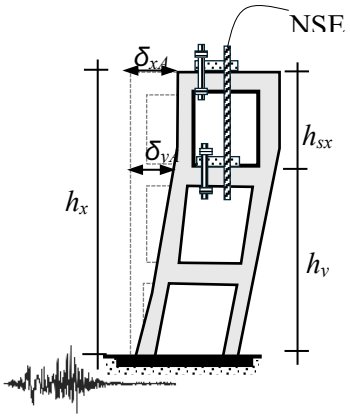

(a)

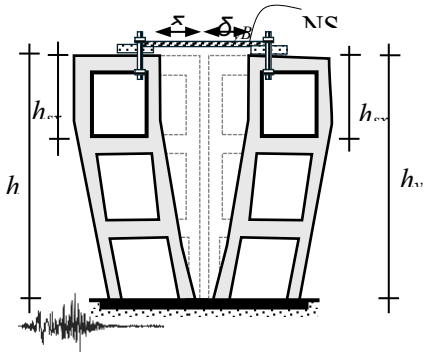

(b)

Figure 1: (a) Displacements within structure, and (b) Displacements between structure. Adapted from [1]

where δ_{xA} & δ_{yA} deflection at building level *x* & *y* of structure A, δ_{yB} deflection at building level *y* of structure B, h_x & h_y height of level *x* & *y* to which upper and lower connection point is attached, Δ_{aA} & Δ_{aB} allowable storey drift for structure A & B, respectively, and h_{sx} storey height [4]. And, for tall buildings Equation (2) is multiplied by 1.2 to obtain D_p [5]. For certain architectural NSEs such as *exterior wall elements*, and *glass glazing systems*, distinct equations are available to estimate their seismic displacement demands [4].

(a) Exterior wall elements

Wall elements and their connections must allow D_{pl}, as determined from equation [1] or a minimum of 13 mm, whichever is greater. For sliding connections using slotted or oversize holes, the threaded rods shall have length-to-diameter ratios ≤ 4. If the connections accommodate storey drift by bending of threaded rods, it shall satisfy:

$$\frac{(L/d)}{D_{pl}} \geq 0.24\left(\frac{1}{mm}\right) \quad [4]$$

where *L* clear length of rod between nuts or threaded plates, and *d* rod diameter [4].

(b) Glass glazing systems

Glass in glazing systems such as curtain walls, storefronts, and partitions shall meet:

$$\Delta_{fallout} \geq 1.25D_{pl} \text{ or } 13\text{mm} \quad [5]$$

where $\Delta_{fallout}$ is the relative seismic displacement at which the glass fallout from the glazing systems. However, this requirement is not applicable if adequate clearance is provided to prevent contact between the glass and the frame at design drift. For rectangular glass panels, this clearance can be estimated by:

$$D_{clear} \geq 2c_1\left(1+\frac{h_p c_2}{b_p c_1}\right) \quad [6]$$

where D_{clear} is relative horizontal displacement, measured over the height of the glass panel which causes initial glass-to-frame contact, h_p & b_p height & width of the rectangular glass panel, c_1 & c_2 average of the clearances on both sides & at top and bottom, respectively [4]. In addition, several guidelines are recommended in design codes and documents to improve earthquake resistance in commonly used architectural NSEs.

4.Available Guidelines in Design Codes and Documents

FEMA E-74 and other international codes recommend design guidelines to improve earthquake resistance of major architectural NSEs such as exterior wall components, interior partitions, and ceiling systems which are summarized in Table 1.

Table 1. Design guidelines to improve earthquake resistance of select Architectural NSEs

Exterior Wall Components	
Adhered Veneer	Design a structural canopy to resist the weight and impact of falling veneer, particularly above exits or walkways. Provide connections to attach the veneer to the structure [2].
Anchored Veneer	Compare tie spacing with code requirements to evaluate anchorage adequacy. Add seismic anchors with an extra horizontal wire in the mortar bed tied to the anchor to reduce falling hazards [2].
Prefabricated Panels	Design for an expected inter-storey drift of the structure or 12.7 mm, whichever is greater, using ductile connection with sufficient rotation capacity to prevent failure. Use push-pull connectors or sliding connections with slotted or oversized holes to handle out-of-plane forces while allowing in-plane movement [2].
Glazing	Adopt stiff structural systems that limit inter-storey drift or provide larger edge clearances at mullions. Avoid storefront windows to eliminate soft-storey and torsional behaviour; if required, use laminated glass to enhance seismic safety [2].
Glass Block	Limit panel size to 13.4 m^2 (exterior) and 23.2 m^2 (interior), with maximum dimensions of 7.6 m wide and 6.1 m high, and provide lateral support at intervals of 406 mm. Isolate panels from structure using rigid mortar at the sill, slip joints with steel angles, channels, or anchors at the top and sides, and horizontal reinforcement in alternate mortar joints [2].
Interior Partitions	
Heavy Partition Walls	Provide out-of-plane restraint for heavy full-height partitions using in-plane slip joints with steel angles fixed to the slab above. Partial-height walls should be self-supporting and isolated from structural frames by a 25 mm clearance to avoid captive column failure (Figure 2(a)) [2]. For non-uniformly distributed masonry partitions with various positions and properties, perform 3D analysis excluding infills with multiple significant openings and incorporating twice the design code stipulated accidental eccentricity [6]. Special care is required for slender partitions (slenderness ratio > 15), which may be strengthened with anchored wire meshes, wall ties, and concrete posts and belts across the wall thickness; edges of large openings should also be reinforced with concrete belts [6].
Light Partition Walls	*High-rise buildings*: Isolate non-load bearing partitions from the structure to minimize damage using out-of-plane restraint with in-plane slip joints for full-height partitions [2]. *Low-rise buildings*: Anchor full-height walls to the diaphragm to add lateral resistance, and brace partial height partitions every 1.8 to 2.4 m [2].
Glazed Partitions	Ensure the glazing is self-supporting and does not load the glazing or mullions. Support wall elements above glazing with lintel. Provide extra bracing to satisfy code recommended drift limits and maintain isolation with adequate glass-to-frame clearance [2, 7, 8].
Ceiling Systems	
Suspended Acoustic Lay-in Tile Ceiling Systems	Ceilings must resist vertical and horizontal seismic forces without collapse and main runners of the ceiling system must be oriented perpendicular to the primary structural elements, such as roof purlins [9, 10]. The terminal ends of runners shall be supported at a maximum distance of 200 mm from the supporting structure,

	and runners along with their connectors, designed ≥ 80 kg test load [11]. The ceiling system should withstand earthquake forces by (i) preventing dislodgement of suspension components, (ii) accommodating inter-storey drift without impacting structural elements, services, or other NSEs, and (iii) ensuring elements ≥ 7.5 kg do not fall more than 3 meters. The limiting vertical deflections for ceiling frame are span/360 to span/500, depending on the finish, while for ceilings, the limit is span/200 [10]. Wall Partitions should be attached to the ceilings only if they permit lateral movement of the ceiling, ensuring a minimum clearance of 10 mm from the wall, and their connections should be made at the primary framing members [11]. S_{DS}<*0.5g* (Design Spectral Acceleration at short period): Design ceilings weighing below 120 N/m^2 as unrestrained with special perimeter detailing to accommodate structural movement. If the weight is above 120 N/m^2 design as restrained, with seismic bracing assemblies (Figure 2(b)) [2]. S_{DS} ≥*0.5g:* Design ceilings as restrained, with perimeter wall connection, rigid or non-rigid bracing, perimeter closure angles with minimum leg length of 50 mm, and edge clearances. Provide *perimeter closure* with fixity on two adjacent sides with 19 mm clearance on the others, for ceilings over 92.9 m^2, and *seismic separation joints* for ceilings over 232 m^2 [2].
Ceiling Systems	
Ceilings applied directly to structure	Ensure appropriate fasteners are used for each successive layer with adequate penetration into the joist. Subdivide large ceilings with flexible diaphragms into areas < 232 m² and provide seismic expansion joints to allow relative movement [2].
Suspended Heavy Ceilings	Provide special seismic detailing similar to acoustic ceiling with more frequent bracing using vertical compression struts and diagonally splayed wire braces or rigid struts. Install 50 mm perimeter closure angles fixed to two adjacent walls, with 19 mm clearance at the opposite walls [2].

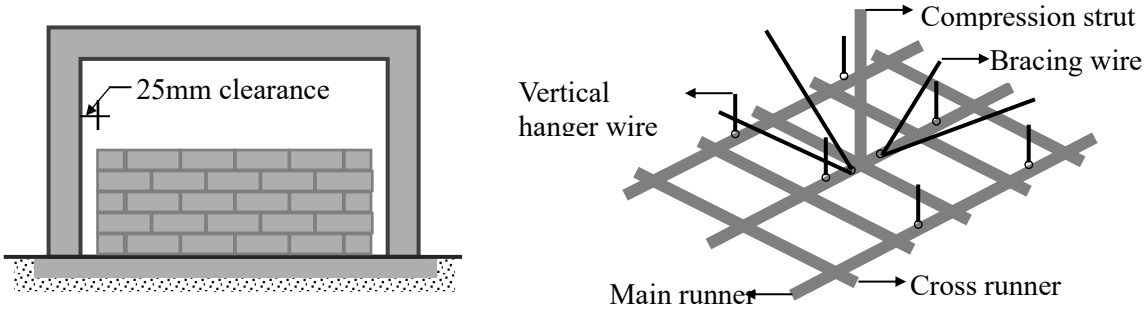

Figure 2: (a) Partial heavy-weight partition, and (b) Seismic bracing assembly in ceilings. Adapted from [2]

5. SUMMARY

The paper provides a comprehensive overview of the guidelines or techniques recommended

by design codes and documents to improve earthquake resistance of NSEs. They emphasize the importance of implementing proactive measures such as anchorages, lateral bracing, push-pull connectors, sliding connections, seismic isolation, seismic restraints and proper seismic detailing to minimize NSE damage during earthquakes.

Further, dynamic analysis using numerical 3D modelling of buildings with NSE, finite element modelling of NSE sub-assemblages, and shake table tests of critical NSEs can provide crucial insights of the behaviour of NSEs under earthquakes. These methods will enable a more accurate assessment of the interaction between structural and nonstructural systems, including their connections, thereby enhancing earthquake resistance of NSEs and urban safety.

REFERENCES

[1] C.V.R. Murty, R. Goswami, A.R. Vijayanarayanan, R. Pradeep Kumar, V.V. Mehta, Introduction to Earthquake Protection of Non- Structural Elements in Buildings, Gujarat State Disaster Management Authority, Gandhinagar, India, 2012.

[2] FEMA E-74, Reducing the Risks of Nonstructural Earthquake Damage – A Practical Guide, ATC, CA, USA, 2011.

[3] K. V. Steinbrugge, E. E. Schader, Earthquake Damage and Related Statistics in San Fernando, California, Earthquake of February 9, 1971, National Oceanic and Atmospheric Administration, Washington D.C, 1973, pp. 709-710 & 713.

[4] ASCE 07, Minimum Design Loads for Buildings and Other Structures, American Society of Civil Engineers, Virginia, USA, 2022.

[5] IS 16700, Criteria for Structural Safety of Tall Concrete Buildings, Bureau of Indian Standards, New Delhi, 2017.

[6]Comité Européen de Normalisation (CEN) Eurocode 8: Design of Structures for Earthquake Resistance. Part 1: General Rules, Seismic Actions and Rules for Buildings, European Standard EN 1998-1, Brussels, Belgium, 2004.

[7]EAK, Greek Code for Seismic Resistant Structures, 2000.

[8] NCh 433.Of1996, Modified in 2012, Seismic Design of Buildings, National Institute of Standardization, Inn-Chile, 2012.

[9] Comité Européen de Normalisation (CEN), BS EN 13964, Suspended ceilings requirements and test methods, European Standard , Brussels, Belgium, 2014.

[10] AS/NZS 2785, Suspended Ceilings — Design and installation, Joint Australian/New Zealand Standard, Joint Technical Committee BD-035, 2020.

[11] ASTM E580 / E580M (USA), Standard Practice for Installation of Ceiling Suspension Systems for Acoustical Tile and Lay-In Panels in Areas Subject to Earthquake Ground Motions, U.S. Department of Defense, 2024.

ABS ID: OP-106

Mr. Keisuke Yasuda

ABS ID: 207
USDM-EP-06

Dr. Dasari Hima Chandan

2025 HOW

4th International Symposium on One Health, One World
November 20 – 22, 2025

ABS ID: 206
USDM-EP-07

Deformation in Geosynthetic Reinforced Soil Wall During Seismic Event for Improved Risk Reduction

G. Das[1,3], and M. Samanta[2,3]
[1]*Phd Research Scholar, GEGH Group, CSIR-Central Building Research Institute, Roorkee-247667, India,*
[2]*Sr. Pr. Scientist, GEGH Group, CSIR-Central Building Research Institute, Roorkee-247667, India*
[3]*Academy of Scientific and Innovative Research (AcSIR), Ghaziabad- 201002, India*
Correspond to M. Samanta (manojit@cbri.res.in)

Keywords*: Geosynthetic, Reinforcement stiffness, Seismic, Dynamic deformation, Acceleration amplification, Stress distribution.*

1. INTRODUCTION

Geosynthetic Reinforced Soil (GRS) walls are widely used as an alternative to conventional retaining walls because they are economical, flexible, and easy to construct. Their ability to deform without losing stability makes them suitable for seismic regions. However, during past earthquakes, several GRS walls have shown large deformations or even collapse. These failures highlight the importance of understanding their behavior under seismic loading and improving design methods to ensure internal stability.

The internal stability of a GRS wall depends on the proper design of reinforcement length, spacing, and strength. It ensures that the reinforcement layers do not rupture or pull out during shaking. Traditional pseudo-static methods ([1], [2], [3]) are commonly used to estimate these parameters. These methods assume a linear failure plane through the wall base, which simplifies calculations but does not accurately represent the actual curved failure surface formed during earthquakes. Even recent design guidelines ([4], [5]) continue to use this linear assumption.

Various experimental and numerical studies ([6], [7]) show that the GRS walls generally fail along nonlinear or log-spiral surfaces ([8], [9]). Researchers such as [2], [3] proposed log-spiral models, while others adopted multilinear failure surfaces. Although these approaches improve accuracy, they are complex and require iterative analysis.

In the present study, the seismic stability of wrap-around geosynthetic reinforced soil (GRS) walls has been investigated using both analytical formulations and numerical modeling. The influence of the horizontal seismic acceleration coefficient on the failure mechanism and reinforcement demand has been examined. Results from the finite element analysis has also been compared with the failure surface obtained from the analytical studies to confirm the reliability of the model.

2. METHODOLOGY

To pursue the present investigation, a wrap-around vertical Geosynthetic Reinforced Soil (GRS) wall of height H has been analyzed to assess its seismic behavior. The wall is horizontally reinforced with geosynthetics (geogrid), and a simplified model has been used to evaluate stability and deformation. The backfill has been assumed homogeneous, isotropic, dry, and cohesionless with constant unit weight (γ) and friction angle ($\phi°$). A uniform surcharge (q_s) has been applied on top, and a rigid rock foundation was

considered. Seismic loading was represented using a pseudo-static approach with a horizontal acceleration coefficient (Kh) constant along the wall. Under static conditions, a linear Rankine failure plane was assumed.

For seismic conditions, a polynomial failure surface (y=ax^n) described by [10] has been adopted. Based on formulation the failure plane has been identified and total tensile force has been calculated by the force equilibrium in both directions for active and passive resistance zone of GRS wall as shown in figure 1.

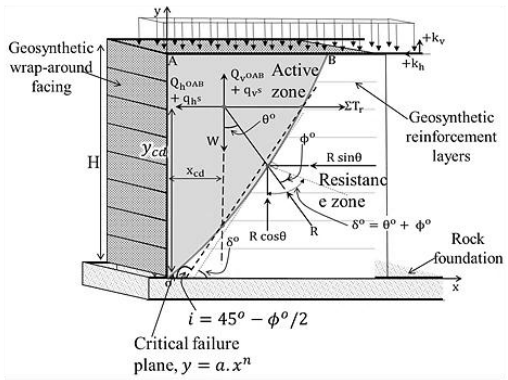

Figure 1. Critical failure surface and force equilibrium of GRS wall

The reinforcement strength T_j has been expressed as $K_r=(\Sigma T_r)/(0.5\gamma H^2)\approx(T_j)/((\gamma z+q_s)\ S_v)$, where S_vis layer spacing. The anchorage length preventing pullout was $L_r^j=T_j/(\mu_p\ (1-K_v).(2\sigma_v^j\ C_r\ \tan\psi))$, where μ_p, C_r, and ψ represent pullout resistance factors. The total reinforcement length has been obtained by adding active and anchorage portions, ensuring safety against rupture and pullout failure.

3. RESULTS & DISCUSSION

A numerical model has been developed to validate the seismic behavior of a wrap-around geosynthetic reinforced soil (GRS) wall resting on a rigid foundation. Seismic loading was applied as base displacement over a 7 m wide domain. The backfill was modeled using four-node bilinear quadrilateral elements following the Mohr–Coulomb criterion, while the 1 mm thick geotextile reinforcement and facing were represented by two-node beam elements resisting only tension. Ten reinforcement layers spaced at 0.5 m were incorporated. An absorbent boundary using a spring–dashpot system (stiffness 1 × 10^6 kN/m) minimized wave reflections. Mesh refinement from 0.01 m near the face to 0.1 m beneath the wall ensured accuracy, resulting in 8,807 elements. The input motion from the Northridge earthquake (PGA = 0.4338 g, kh=0.347) produced a failure surface consistent with the proposed analytical profile.

Figure 2 shows that the plastic strain contours from the numerical investigation confirmed that the formulation effectively captures seismic failure behavior and improves the resilience of GRS wall design.

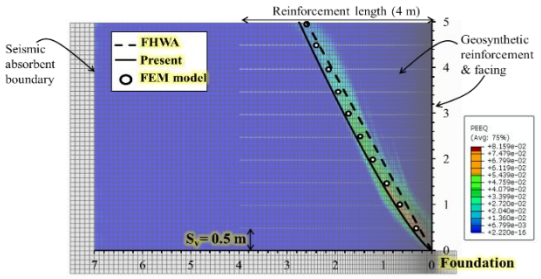

Figure 3. Comparison of failure plane using FEM

4. RESULTS & DISCUSSION

A parametric study was conducted to examine the influence of the seismic acceleration coefficient using the proposed formulations. The study also involves a comparison between the polynomial failure plane and the results obtained from finite element analysis. The parameters for the study has been provided in Table.1.

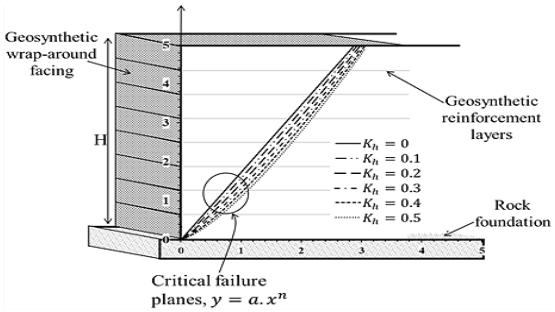

Table 1. Parameter values for present investigation

Parameter	Values
K_h	0, 0.1, 0.2, 0.3, 0.4, 0.5
K_v	0
H ; (m)	9
γ ; (kN/m^3)	18
ϕ ; $(degrees)$	35
ψ ; $(degrees)$	ϕ
q_{ls} ; (kPa)	0
S_v; (m)	0.5
C_r	0.8
μ_r	1
μ_p	1

4.1. Effect of seismic acceleration coefficient (Kh)

Figure 3 illustrates the critical failure planes for different horizontal seismic acceleration coefficients (kh = 0 – 0.5) in a 5 m high wrap-around geosynthetic reinforced soil (GRS) wall founded on rigid rock. As kh increases, the failure surface shifts outward, expanding the active soil zone affected by seismic forces. Under static conditions (kh=0), the failure plane is steep and close to the wall face, while higher kh values produce flatter planes and a larger sliding mass due to increased inertia. This outward shift indicates greater reinforcement length and strength requirements for stability. The results demonstrate that seismic acceleration significantly affects both the failure mechanism and reinforcement demand in GRS walls.

Figure 3. Failure planes at different Kh values

3. CONCLUSIONS

The study concludes that increasing the horizontal seismic acceleration coefficient (k_h) significantly alters the failure mechanism of wrap-around GRS walls. Higher k_h values lead to outward movement of the failure plane, indicating a larger active soil zone and increased reinforcement demand. Numerical analysis validated the analytical model, showing close agreement in predicted failure surfaces and plastic strain patterns. The proposed formulation effectively represents seismic behavior, offering improved accuracy for stability evaluation and design optimization of GRS walls under dynamic loading conditions, enhancing their overall seismic performance and structural reliability.

REFERENCES:

[1] R.J. Bathurst, Z. Cai, Pseudo-static seismic analysis of GRS segmental retaining walls, Geosynth. Int. 2 (1995) 787–830.

[2] H.I. Ling, D. Leshchinsky, Effects of vertical acceleration on seismic design of GRS structures, Geotechnique 48 (1998) 347–373.

[3] B.M. Basha, G.S. Babu, Seismic reliability of reinforced soil walls using pseudo-dynamic method, Geosynth. Int. 18 (2011) 221–241.

[4] AASHTO, LRFD Bridge Design Specifications: Customary U.S. Units, American Association of State Highway and Transportation Officials, Washington, D.C. (2020).

[5] FHWA, Design of Mechanically Stabilized Earth Walls and Reinforced Soil Slopes, Federal Highway Administration, Washington, D.C. (Vol. 1, 2009).

[6] C.C. Huang, Soil retaining structures damaged in the Chi-Chi earthquake, J. Chin. Inst. Eng. 23 (2000) 417–428.

[7] N. Kato, F. Tatsuoka, C. Huang, M. Tateyama, J. Koseki, Seismic stability of retaining walls on sand slopes, Geosynth. Eng. J. 16 (2001) 61–68.

[8] J. Koseki, A. Wakai, K. Mitsuji, Damage report from 2011 Tohoku earthquake in inland Miyagi Prefecture, Geotech. Eng. Mag. 59 (2011) 40–73.

[9] S.B. Mohamed, K.H. Yang, W.Y. Hung, Finite element analysis of two-tier GRS walls compared with centrifuge and limit equilibrium results, Comput. Geotech. 61 (2014) 67–84.

[10] Das, G., & Samanta, M.: Investigation on seismic internal stability of geosynthetic reinforced soil wall. Proceedings of 18th World Conference on Earthquake Engineering, (2024).

ABS ID: 188
USDM-EP-09

Mr. Binay Karna

ABS ID: 120

Mr. Yuki Minematsu

ABS ID: 117

Mr. Koki Nakabayashi

ABS ID: 121

Mr. Taiki Mashio

ABS ID: 123

Mr. Taiyo Matsuzaki

2025 HOW
4th International Symposium on One Health, One World
November 20 – 22, 2025

ABS ID: 137
USDM-EP-10

Assessment of The Impact of Reduced Rps on Doctor Helicopter Operations in the Noto Peninsula

Ryoma arai[1], kazuyuki takada[2], makoto fujiu[3], yuma morisaki[4], and junichi takayama[5]

[1]*Undergraduate Student, Tokyo Denki University, Saitama, Japan,*
[2]*Professor, Tokyo Denki University, Saitama, Japan,*
[3]*Professor, Kanazawa University, Ishikawa, Japan,*
[4]*Assistant Professor, Kanazawa University, Ishikawa, Japan,*
[5]*Professor, Komatsu University, Ishikawa, Japan*

***Keywords**: Noto Peninsula Earthquake, Doctor-Helicopter, Rendezvous Point, temporary housing, Emergency medical care.*

1. INTRODUCTION

The Noto Peninsula Earthquake that occurred at 4:10 PM on January 1, 2024, caused significant damage as of 2:00 PM on May 13, 2025*1, including 592 fatalities (including 364 disaster-related deaths), 2 missing persons, and 1,395 injuries. Additionally, numerous homes collapsed or sustained damage.

Residents whose homes suffered significant damage evacuated immediately after the disaster to local shelters or relatives' homes. While many residents hoped to move into temporary housing, delays in its preparation led some to seek stable living environments elsewhere. These individuals engaged in “secondary evacuation,” staying in hotels or public housing within and outside the prefecture. Regarding temporary housing, a total of 164 complexes has been prepared to date, with 7,168 households having moved in.

Many of the established temporary housing units are located in parks or school grounds, which also served as RPs (RP) for transferring patients between ambulances and doctor helicopters. Consequently, nearly half of these RPs are currently unusable, simultaneously highlighting the conflicting challenges of rebuilding residents' lives and ensuring emergency medical services.

So, this study aims to compare and analyze the medical care provision systems before and after the disaster by clarifying the deployment status of RP facilities, the actual operation and transport performance of doctor helicopters, and the impact of changes in the surrounding environment of RP facilities. It seeks to gain insights that will contribute to strengthening the emergency medical care system in disaster-affected areas.

2. DATA

This study utilizes operational performance data from the Doctor Helicopter service in the Noto Peninsula, Ishikawa Prefecture, covering the two-year period from April 1, 2023, to March 31, 2025.

Table.1 Doctor Helicopter Operational Performance Data

No.	Date		Requesting Fire Department	Destination	Rendezvous Point	Request Time	Departure time	RP arrival time	Treatment Start Time	RP Departure Time	Time of arrival at the hospital
1610	April	1	Nomi	Ishikawa Prefectural Central Hospital	Tetori River Waterside Plaza	12:30	12:37	12:45	12:46	12:57	13:03
1614	April	5	Hakui	Kanazawa University Hospital	Industrial Center Nexus	15:40	15:46	15:56	15:56	16:07	16:17
1615	April	9	Hakusanmono	Ishikawa Prefectural Central Hospital	Hakusan Roku Theme Park Kawai/Shimono Park	10:12	10:18	10:30	10:32	10:47	10:55
1616	April	9	Hakui	Ishikawa Prefectural Central Hospital	Kennin Furai Hockey Hall	15:29	15:35	15:54	15:59	16:36	16:56

Fig.1 The scene of the doctor-helicopter and ambulance parked at the RP.
(Reference: Toyooka City Fire Department Website)

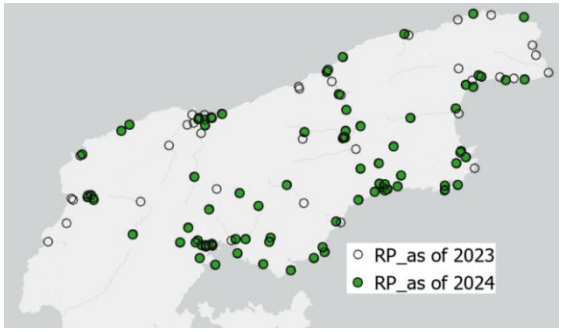

Fig.2 Change in position of RP

3. METHODOLOGY

The specific analytical methods are outlined below. We compared the time from the request for the doctor helicopter to its arrival at the rendezvous point, and the time from the request to the start of treatment, for each fiscal year. Furthermore, Table 4 shows the time from the doctor helicopter's arrival at the rendezvous point to the start of treatment. Furthermore, assuming the time required from helicopter arrival to treatment initiation follows a log-normal distribution, this was graphically illustrated. Since cases with prolonged response times were identified, robust estimation was performed to account for the presence of outliers. Robust estimation is a method that calculates weights for observed values and sets an optimal threshold using a chi-squared test. The robust estimation formula is as follows:

x_i: observed values
$\hat{\mu}$: Position estimated by Huber's M-estimator
scale: Robust Scale based on MAD
k=1.345: Standard values selected with an efficiency of 95% as a guideline for normal distributions

4. RESULTS

Fig.3 Comparison of time (minutes) for each fiscal year

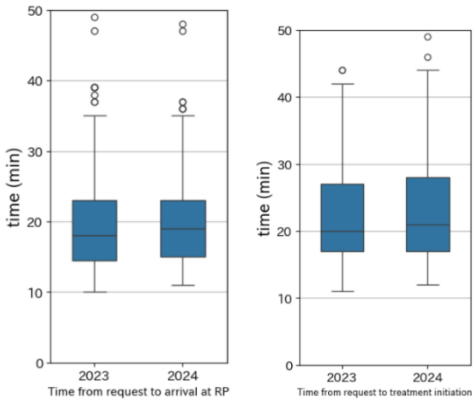

Fig.3 shows that there was no statistically significant difference in the time required from the request for the doctor helicopter to the arrival at the RP, or from the request for the doctor helicopter to the start of treatment.

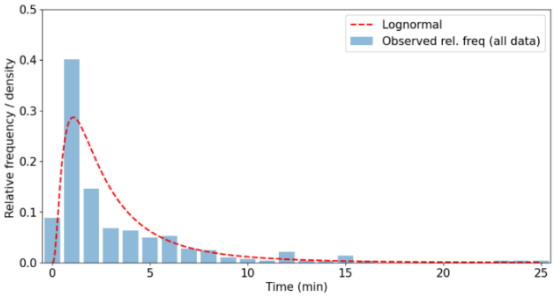

Fig. 4 The time from RP arrival to treatment initiation

Fig. 4 shows that there were several instances where a significant amount of time elapsed between the helicopter's arrival and the start of treatment.

Threshold(Huber)	Chi-squared statistic
0.50	44.32
0.40	59.59
0.30	51.95
0.20	43.95
0.10	69.99

Table2, Threshold determination using the chi-squared statistics

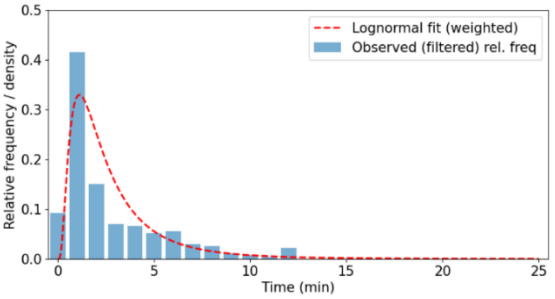

Fig.5 The elapsed time from helicopter arrival to treatment initiation (result of estimated Robust)

Fig. 5 shows the results after excluding outliers by setting the threshold to 0.20 based on Huber weights and the chi-squared statistic.

5.CONCLUSION

This study quantitatively evaluated the impact of the decrease in RPs before and after the Noto Peninsula Earthquake on the operational system of the Doctor Helicopter, based on actual operational data.
In the initial phase of the operational system, no changes are thought to have occurred.

Furthermore, in the vicinity of RPs, delays in ambulance transport may have occurred due to factors such as road closures.

In addition, analysis of outliers revealed that significant time was spent at RPs in northern Noto. This is thought to be influenced by the greater extent of earthquake damage in that area.

Going forward, we aim to further analyze the impact of the disaster through comparative analysis with ambulance transport data.

REFERENCES:

[1] Cabinet Office, Damage Situation Caused by the 2024 Noto Peninsula Earthquake, accessed July 19, 2025 https://www.bousai.go.jp/updates/r60101notojishin/r60101notojishin/pdf/r60101notojishin_57.pdf

[2] Takehiro Furuta, ken-ichi Tanaka, Location models for maximizing the average survival rate in “doctor-helicopter” system, Journal of the City Planning of Japan, Vol.46, No.3, pp. 823-828, 2011,

[3] Motomune Kataoka, Toshio Yoshii, Toru Futagami, Takashi Oguchi, Development of model of the transportation time sent to a hospital by amburance, Seisan kenkyu, Vol.67, No.2, pp. 137-142, 2015

[4] Yuki Bingo, Shuji Ozawa, Makoto Fujiu, Junichi Takayama, Shoichiro Nakayama, Hajime Tatsuno, The study on Doctor-Car and Doctor-Helicopter area setting method at the time of huge scale earthquake -case in Ishikawa prefecture, Japan Society Journal of JSCE, Vol.72, No.2, PP I_107- I_114, 2016

ABS ID: 29
USDM-EP-11

Mr. Satyam Murlidhar Shukla

2025 HOW
4th International Symposium on One Health, One World
November 20 – 22, 2025

ABS ID: 50
USDM-EP-12

Snow avalanche susceptibility zonation mapping along the leh– Manali highway of himachal pradesh and ut of ladakh, india

J.Yadav[1,3], R.K Dash[1], C.B patel[2,3], kanti l. Solanki[2,3], D.P. Kanungo[1,3], and S.K. Panigrahi[2,3]
*Corresponding author: cpatel.cbri@csir.res.in
[1]Geotechnical Engineering and Geohazards (GEGH) Group,
CSIR-Central Building Research Institute, Roorkee, India
[2]Construction, Automation and Robotics (CAR) Group,
CSIR-Central Building Research Institute, Roorkee, India
[3]Academy of Scientific and Innovative Research (AcSIR), Ghaziabad 201 002, India

Keywords: *Snow Avalanche Susceptibility; Leh Manali Highway; Statistical Model.*

1. INTRODUCTION

The Indian Himalaya is highly vulnerable to various natural hazards, including earthquakes, landslides, flash floods, cloudbursts, glacial lake outbursts (GLOFs), and snow avalanches. Among these, snow avalanches are particularly destructive, posing serious threats to human life, infrastructure, and the surrounding environment (Yadav et al., 2025; Dash et al., 2022). Therefore, assessing avalanche susceptibility in such mountainous terrain is crucial for disaster risk reduction and informed regional planning. The study aims to identify snow avalanche susceptible zones along the Leh-Manali Highway by applying and comparing different statistical models, and to determine the most suitable model for snow avalanche prediction in the Himalayan terrain under changing climatic conditions.

2. STUDY AREA

The study area expands approximately 9,934.4 km² across Himachal Pradesh and the Union Territory of Ladakh, extending between 32°3’11.72”N to 32°57’8.94”N latitude and 76°41’11.07”E to 77°43’31.97”E longitude. It encompasses parts of the districts of Leh, Lahaul and Spiti, Chamba, Kangra, and Kullu. The disaster-prone districts of Himachal Pradesh and UT of Ladakh is located in the NW Indian Himalayas (Figure 1). The elevation ranges from 1144 to 6544 m, and the area is known for frequent occurrences of various natural hazards.

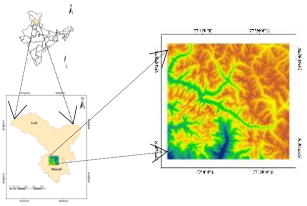

Figure 1. Location map of the study area.

3. METHODOLOGY

A snow avalanche inventory was prepared using remote sensing data, field observations, and a literature survey along the Leh–Manali Highway. The avalanche inventory of 114 events was used to verify and validate the SASM models, with 70% (80 events) for training and 30% (34 events) for validation. Eleven conditioning factors, including slope, aspect, elevation, plan curvature, profile curvature, Topographic Wetness index (TWI), Stream power index (SPI), Topographic position index (TPI), distance to road, distance to drainage and Normalized Difference Vegetation Index (NDVI), were selected based on their relevance to avalanche initiation. These factors were statistically analysed using three bivariate statistical models: Frequency Ratio (FR), Information Value (IV), and Certainty Factor

(CF). Each model produced a susceptibility map classified into five categories ranging from very low to very high susceptibility. Model performance was validated using success and prediction rate curves based on area under the curve (AUC) values.

4. RESULT AND DISCUSSIONS

The susceptibility maps derived from the FR, IV, and CF models successfully identify potential avalanche-prone areas along the Leh–Manali Highway. Regarding slope angle, the maximum FR, IV and CF values come under classes>60°, strongly correlating with snow avalanche susceptibility. The elevation class ranges between 500-1000m, with observed maximum FR, IV, and CF. Validation using ROC curves showed that all three models performed satisfactorily, with AUC values ranging between 0.80 and 0.82. However, the IV model effectively delineated high-risk zones, as demonstrated by their high verification (AUSC of 0.828) and prediction (AUPC of 0.809) accuracies. The final susceptibility map clearly identified critical avalanche-prone stretches of the highway, particularly around high passes and steep valley slopes, offering valuable insights for hazard mitigation and planning.

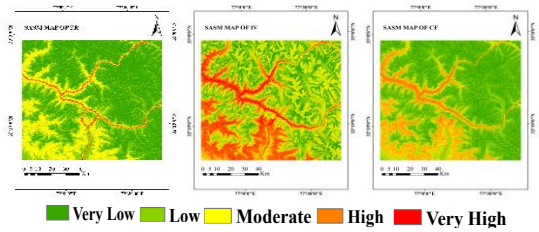

Figure 2. Snow Avalanche susceptibility zonation (SASM) maps using different statistical models: (a) Frequency ratio (b) Information value and (c) Certainty factor.

5. CONCLUSION

Using three statistical models, the study successfully developed and highlighted the effectiveness of snow avalanche susceptibility mapping along the Leh-Manali Highway. Among these, the IV model performed better in verification and validation, effectively identifying very high susceptibility zones with a strong spatial correlation to observed snow avalanche occurrences. The IV model produced the most accurate SASM maps with a success rate of 82.8% and a prediction rate of 80.9%. Avalanche density analysis also confirmed its reliability, showing higher density values in the Very High and High Susceptibility zones (4.97 and 1.73 for success rate, and 3.18 and 2.10 for prediction rate). The FR and CF models showed less reliable results with ambiguous susceptibility classification. The generated maps and methodology provide a valuable tool for disaster risk reduction, spatial planning, and managing snow avalanche hazards in Himalayan regions facing dynamic climatic conditions.

REFERENCES:

[1] Dash, R.K., Falae, P.O., Kanungo, D.P., Debris flow susceptibility zonation using statistical models in parts of Northwest Indian Himalayas—implementation, validation, and comparative evaluation, Nat. Hazards. 111 (2022) 2011–2058.

[2] YADAV, J., DASH, R.K. and KANUNGO, D.P., Spatial prediction of landslides in Pithoragarh district, Kumaon Himalaya, India.

4th International Symposium on One Health, One World
November 20 – 22, 2025

ABS ID: 208
USDM-EP-13

Application of Seismic Method with in-ground Sensors for Detecting Geotechnical Cavities

S. Watanabe[1], H. Yuki[1], Y. Hara[2], and R. Kuwano[3]
[1]*Master's Student, Graduate School of Engineering, The University of Tokyo, Tokyo, Japan,*
[2]*PhD Student, Graduate School of Engineering, The University of Tokyo, Tokyo, Japan,*
[3]*Professor, Institute of Industrial Science, The University of Tokyo, Tokyo, Japan,*
Correspond to Prof. R. KUWANO (kuwano@iis.u-tokyo.ac.jp)

***Keywords**: Cavity Detection, Underground Cavity, Cavity Collapse, Elastic Wave, Granular Material.*

1. INTRODUCTION

The detection of deep subterranean cavities is critical for urban safety, with aging infrastructure causing up to 10,000 road collapses annually in Japan [1]. While Ground Penetrating Radar (GPR) is effective, its penetration is limited to shallow depths of approximately 1.5 meters, failing to detect deeper, hazardous voids [1]. Seismic exploration thus offers a promising alternative for these targets.

Building previous work with surface sensors [2], a new paradigm utilizes buried infrastructure like Distributed Acoustic Sensing (DAS) as in-ground sensors. This approach leverages existing networks but is hindered by a knowledge gap concerning the data differences between in-ground and surface sensors. This study therefore aims to investigate cavity detection using in-ground sensors via elastic wave exploration methods.

2. METHODS

We conducted 1/10th scale model experiments in a soil box containing a homogeneous granular medium to investigate the effects of a buried cavity. Dried No. 6 silica sand was used as the ground material, and the air pluviation method was employed to create a ground model with uniform density. A polycarbonate box with dimensions of 100 mm x 300 mm x 50 mm was used as the cavity. To detect vibrations, piezoelectric elements (RS PRO Piezo Element 30Vp-p, 35mm diameter) were used. The positional relationship of these components is shown in Figure 1.

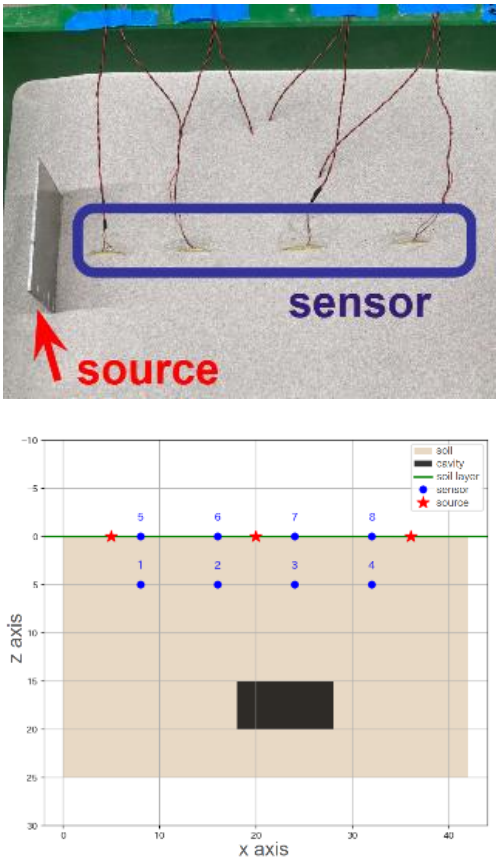

Figure 1. Configuration of the cavity, sensors, and source

A source plate was struck at three locations shown in Figure 1 (x = 5, 20, and 35 cm) in the positive and negative y-directions to generate pulse shear waves, and the vibrations were recorded by the piezoelectric elements. For the recorded vibrations, environmental noise was first removed. The waveforms were then stacked to further reduce noise. Finally, phase migration was performed to clarify the degree of phase coherence in the cross-section of the soil layer [2].

3. RESULTS & DISCUSSION

Figure 2. shows the results of the migration analysis, presenting the averaged and normalized degree of phase coherence for the case with a cavity (Case 1) and without (Case 2). A comparison of the two cases clearly identifies an area with a high degree of phase coherence (exceeding 0.35) only in Case 1, at a depth of 15 cm to 20 cm. This high-coherence area is considered to correspond to the reflective surface of the buried cavity. Although some areas of high phase coherence are also present in Case 2, these are presumed to be reflections from the walls of the soil box. These results suggest that it is possible to detect the reflective surface of the cavity using migration analysis with in-ground sensors, indicating the feasibility of this detection method.

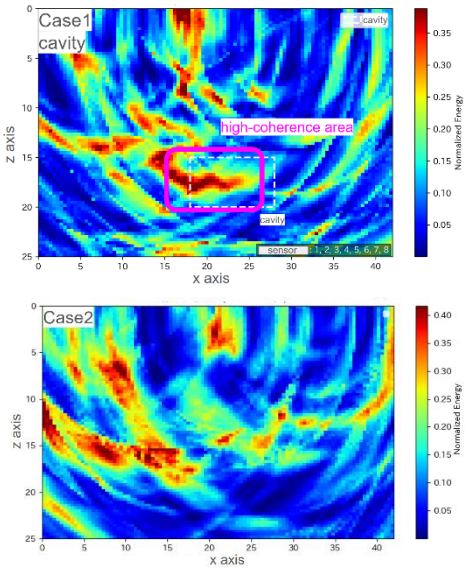

Figure 2. The results of the migration analysis

4. CONCLUSIONS

This study's model experiment suggested the feasibility of detecting a cavity's reflective surface using in-ground sensors and migration analysis, providing a basis for developing detection algorithms for practical systems like Distributed Acoustic Sensing (DAS).

REFERENCES:

[1] R. Kuwano, J. Kuwano, R. Sera, T. Ihara, N. Kozakai, Japanese Geotechnical Journal 18 (2023) 299–315.
[2] Y. Nakata, R. Kuwano, M. Otsubo, Seisan Kenkyu 72 (2020) 397–400.
[3] W. A. Schneider, Geophysics 43 (1978) 49–76.

ABS ID: PO-03
USDM-EP-14

Experimental Evaluation of the Impact Resistance of Gfrp-Reinforced Concrete Slabs

S. Lokesh[1], R. Siva chidambaram[2], T. Sai sheshu[3]
[1]*PhD Scholar, Academy of Scientific and Innovative Research (AcSIR), Ghaziabad 201002, India,*
[2]*Principal Scientist, ACSC Group, CSIR-Central Building Research Institute, Roorkee 247667, India,*
[3]*Project Associate, ACSC Group, CSIR-Central Building Research Institute, Roorkee 247667, India,*
Correspond to schidambaram.cbri@csiri.res.in

***Keywords**: Impact strength, GFRP rebars, Steel Reinforcement, Corrosion, Sustainable.*

1.INTRODUCTION

The corrosion of steel reinforcement remains a major challenge to the durability of concrete structures, necessitating the use of alternative reinforcement materials like Fiber Reinforced Polymer (FRP) bars which are composed of fibers such as glass, carbon, or basalt, provide a durable and efficient solution owing to their lightweight nature, high tensile strength, and complete resistance to corrosion. The use of such bars significantly enhances the service life of structures which are often exposed to severe impact loads [1].

The behaviour of steel-reinforced concrete under dynamic loading has been extensively studied, there is a significant research gap regarding the performance of FRP-reinforced structures under impact [2]. While some studies have begun to investigate the dynamic performance of GFRP- and steel-reinforced concrete slabs, a comprehensive analysis that evaluates the influence of specific failure modes and all key parameters in a single study is still needed. This study aims to fill that gap by providing a comprehensive experimental analysis of steel- and GFRP-reinforced concrete slabs under drop-weight impact loads [3]. Our research evaluates the influence of key parameters and contributes critical data to support the design of safer, more durable, and sustainable infrastructure.

Fig 1. GFRP bars (ribbed surface)

2. METHODOLOGY

To evaluate impact resistance, three full-scale concrete slabs (1000 mm x 1000 mm x 100 mm) were fabricated. Two sets of reinforced concrete slabs were cast and tested under drop-weight impact loading — one reinforced with conventional steel bars and the other with GFRP bars of equivalent reinforcement ratio [4]. The slabs were designed with identical dimensions and material properties to enable direct comparison of impact behavior. A drop-weight impact setup was used, where a 23.5 kg steel mass was released from a height of 2.8 m to generate a controlled impact energy on the slab's center [5]. Load and acceleration responses were measured using a load cell and a triaxial accelerometer connected to a high-speed data acquisition system. Each slab was subjected to a single impact, and parameters such as peak load, acceleration, and failure mode were recorded. After testing, visual examination and crack mapping were carried

out to assess the extent of damage, crack width, and failure mode. Comparative analysis between steel- and GFRP-reinforced slabs was performed based on impact load characteristics, acceleration response, and observed failure patterns.

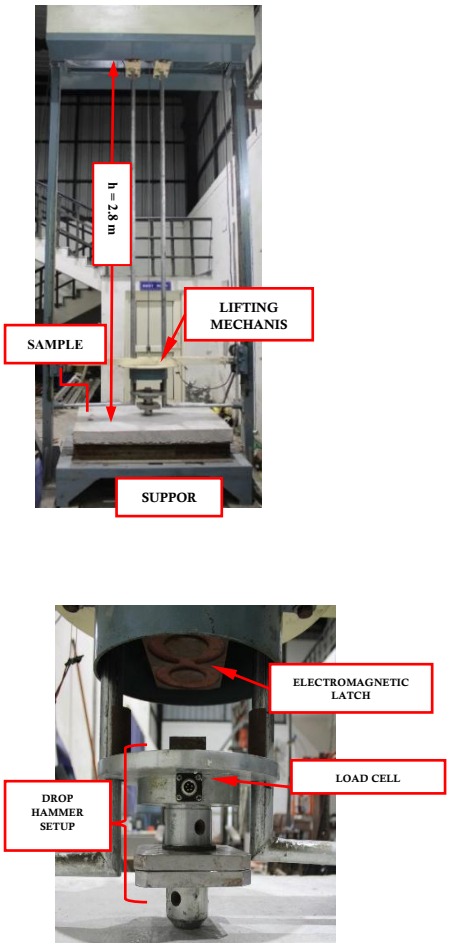

Fig 2. Drop impact experimental setup

3. RESULTS AND DISCUSSION

Failure observations showed concentrated punching cracks around the impact point in the steel slab shown in figure 3 with average diameter of puncture around 77mm, whereas the GFRP slab developed wider but more uniformly distributed cracks with limited spalling with diameter of puncture around 100mm shown in figure 4. Overall, GFRP-reinforced slabs demonstrated enhanced ductility, energy absorption, and post-impact integrity compared to steel-reinforced slabs, highlighting their suitability for structures exposed to dynamic or accidental loads.

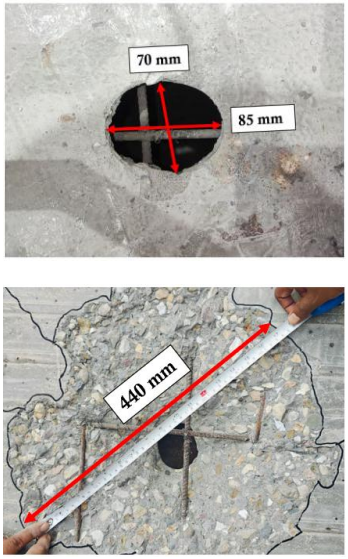

Fig 3: Failure pattern and damage in steel reinforced slab

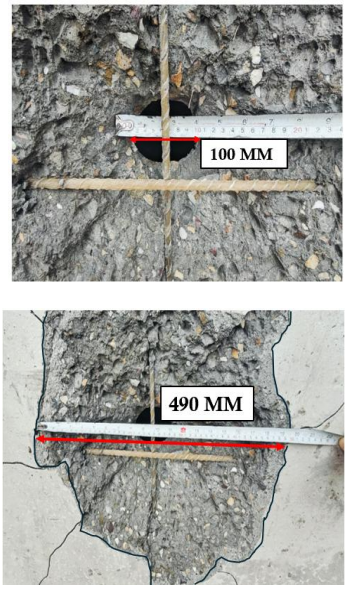

Fig 4: Failure pattern and damage in GFRP reinforced slab

The steel-reinforced slab showed a sharp impact load peak with rapid decay, indicating a stiff and brittle response under impact shown in figure 5. In contrast, the GFRP-reinforced slab exhibited a lower peak load but a broader pulse duration, reflecting better energy absorption and a more gradual stress transfer shown in figure 6.

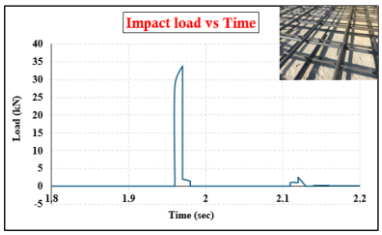

Fig 5: Impact load response of steel slab

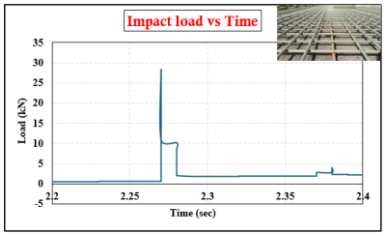

Fig 6: Impact load response of GFRP slab

Acceleration–time data revealed that the steel-reinforced slab experienced sharp and high-magnitude acceleration peaks immediately after impact, indicating a stiffer response and rapid transfer of impact energy with minimal damping. This sudden rise and quick decay in acceleration reflect brittle energy release and limited ability to absorb vibration. In contrast, the GFRP-reinforced slab showed reduced peak acceleration values with a broader and smoother response curve, suggesting better energy dissipation through the concrete–GFRP composite action.

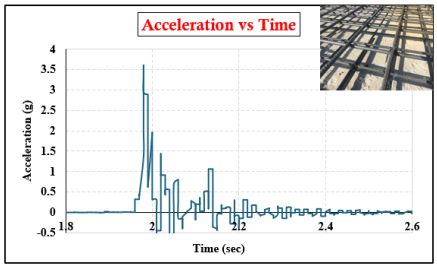

Fig 7: Acceleration vs time of steel slab

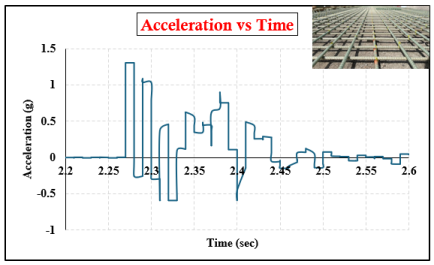

Fig 8: Acceleration vs time of GFRP slab

4. CONCLUSION

GFRP-reinforced concrete slabs exhibited lower peak impact loads but higher energy absorption and better crack distribution than steel-reinforced slabs. The results confirm that GFRP reinforcement enhances ductility, reduces acceleration response, and maintains structural integrity under impact loading. In addition to superior performance, the non-corrosive and lightweight nature of GFRP bars contributes to longer service life and reduced maintenance needs, offering an environmentally sustainable alternative to conventional steel reinforcement.

5.REFERENCE:

[1] ACI committee 440. Report on fiber-reinforced polymer (FRP) reinforcement for concrete structures. ACI 440R-07, American Concrete Institute, Farmington Hills; MI; 2007.

[2] Al-Rousan RZ, Alhassan MA, Al-Salman H. Impact resistance of polypropylene fiber reinforced concrete two-way slabs. Struct Eng Mech 2017;62(3):373–80.

[3] Kishi N, Konno H, Ikeda K, Matsuoka KG. Prototype impact tests on ultimate impact resistance of PC rock sheds. Int J Impact Eng 2002;27(9):969–85.

[4] Xiao Y, Li B, Fujikake K. Behavior of reinforced concrete slabs under low velocity impact. ACI Struct J 2017;114(3):643–50.

[5] Weizhang L, Miao L, Wei Z, Zhimin T. Experimental studies and numerical simulation of behavior of RC beams retrofitted with HSSWM-HPM under impact load. Eng Struct 2017;149:131–46